ADVANCES AND APPLICATIONS OF THE EEG-FMRI TECHNIQUE ON EPILEPSIES

EDITED BY: Brunno Machado De Campos, Fernando Cendes,
Maria Centeno and Ana Carolina Coan
PUBLISHED IN: Frontiers in Neurology

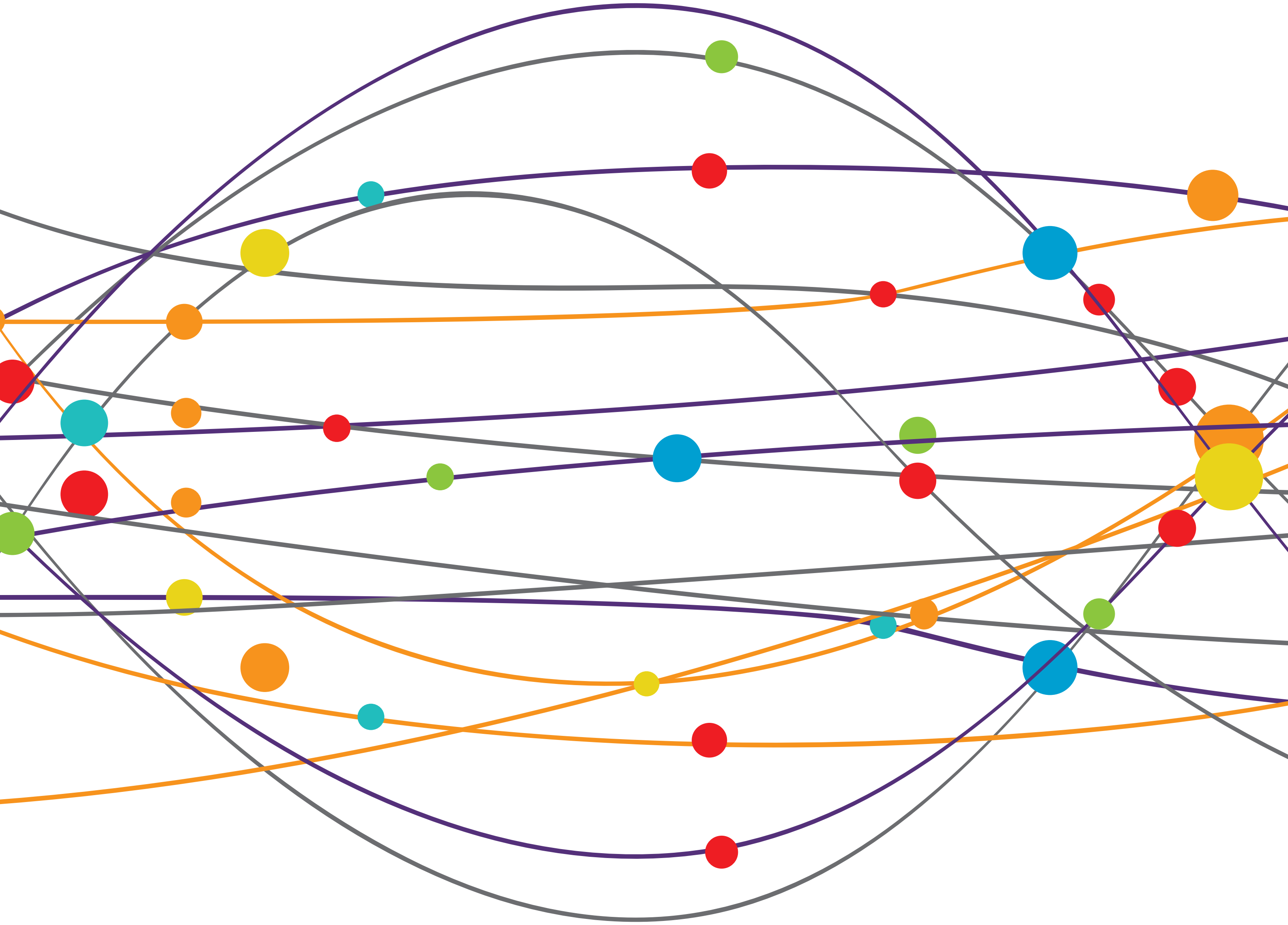

frontiers Research Topics

ISSN 1664-8714
ISBN 978-2-88974-438-1
DOI 10.3389/978-2-88974-438-1

About Frontiers

Frontiers is more than just an open-access publisher of scholarly articles: it is a pioneering approach to the world of academia, radically improving the way scholarly research is managed. The grand vision of Frontiers is a world where all people have an equal opportunity to seek, share and generate knowledge. Frontiers provides immediate and permanent online open access to all its publications, but this alone is not enough to realize our grand goals.

Frontiers Journal Series

The Frontiers Journal Series is a multi-tier and interdisciplinary set of open-access, online journals, promising a paradigm shift from the current review, selection and dissemination processes in academic publishing. All Frontiers journals are driven by researchers for researchers; therefore, they constitute a service to the scholarly community. At the same time, the Frontiers Journal Series operates on a revolutionary invention, the tiered publishing system, initially addressing specific communities of scholars, and gradually climbing up to broader public understanding, thus serving the interests of the lay society, too.

Dedication to Quality

Each Frontiers article is a landmark of the highest quality, thanks to genuinely collaborative interactions between authors and review editors, who include some of the world's best academicians. Research must be certified by peers before entering a stream of knowledge that may eventually reach the public - and shape society; therefore, Frontiers only applies the most rigorous and unbiased reviews.
Frontiers revolutionizes research publishing by freely delivering the most outstanding research, evaluated with no bias from both the academic and social point of view. By applying the most advanced information technologies, Frontiers is catapulting scholarly publishing into a new generation.

What are Frontiers Research Topics?

Frontiers Research Topics are very popular trademarks of the Frontiers Journals Series: they are collections of at least ten articles, all centered on a particular subject. With their unique mix of varied contributions from Original Research to Review Articles, Frontiers Research Topics unify the most influential researchers, the latest key findings and historical advances in a hot research area! Find out more on how to host your own Frontiers Research Topic or contribute to one as an author by contacting the Frontiers Editorial Office: frontiersin.org/about/contact

ADVANCES AND APPLICATIONS OF THE EEG-FMRI TECHNIQUE ON EPILEPSIES

Topic Editors:
Brunno Machado De Campos, State University of Campinas, Brazil
Fernando Cendes, State University of Campinas, Brazil
Maria Centeno, University College London, United Kingdom
Ana Carolina Coan, State University of Campinas, Brazil

Citation: De Campos, B. M., Cendes, F., Centeno, M., Coan, A. C., eds. (2022). Advances and Applications of the EEG-fMRI Technique on Epilepsies. Lausanne: Frontiers Media SA. doi: 10.3389/978-2-88974-438-1

Table of Contents

frontiers in Neurology

EDITORIAL
published: 13 January 2022
doi: 10.3389/fneur.2021.827705

Editorial: Advances and Applications of the EEG-fMRI Technique on Epilepsies

Brunno Machado De Campos[1,2]*, **Maria Centeno**[3], **Ana Carolina Coan**[1,2] and **Fernando Cendes**[1,2]

[1] Neuroimaging Laboratory, Department of Neurology, University of Campinas, Campinas, Brazil, [2] Brazilian Institute of Neuroscience and Neurotechnology (BRAINN), São Paulo, Brazil, [3] Department of Neurology, Hospital Clinic Barcelona, Barcelona, Spain

Keywords: editorial, EEG, fMRI, EEG-fMRI, connectivity, epilepsy

Editorial on the Research Topic

Advances and Applications of the EEG-fMRI Technique on Epilepsies

In this special issue of Frontiers in Neurology, we compiled a collection of articles focused on Applied Neuroimaging in Epilepsy. More specifically, this topic includes advances in the methodological development, application, and interpretation of the EEG-fMRI technique and its sub-fields. The main goal of this Research Topic was to collect data describing the progress of the technique's reliability on the localization of the epileptogenic zone. However, the articles herein also discuss scientific advances on EEG and fMRI data techniques individually, opening new horizons for data exploration and subsequent disease characterization. The use of EEG-fMRI for the localization of the epileptogenic zone relies on the understanding of each modality separately and the consequences of physical interactions intrinsic to this combination.

In this special issue, Bullock et al.'s systematic review summarizes the state of the art of EEG artifact removal proposing a standardized pipeline from hardware positioning to the most effective post-processing procedures for EEG data acquired during fMRI sessions. Complementary, the review article of Sadjadi et al. discusses the clinical applications of EEG-fMRI, elucidating its validity as a localization tool for the epileptogenic zone and the perspectives for the near future based on ongoing methodological advances.

In a study by Pinte et al., EEG electrode positioning relevant for EEG-source localization algorithms is explored. The MRI-compatible EEG-electrodes commonly used in EEG-fMRI sessions present minimal effect on MRIs. They propose an additional acquisition of an ultra-short echo-time image whereby the MR signal of the electrodes is detectable. This acquisition enables the localization of the electrodes through an automated pipeline based on a pre-trained deep-learning network, reaching good sensibility and accuracy. This approach has great potential for multimodal imaging, scalp EEG, and video-EEG analyses, as well as pre- and post-operative correlations with the surgical lacuna and EEG-fMRI data (1–3).

Piper et al. performed functional connectivity (FC) analyses of the anterior thalamic nucleus (ATN) using fMRI derived from EEG-fMRI acquisitions, demonstrating altered connectivity in children with refractory focal epilepsy using the EEG-informed interictal epileptiform discharges (IED) as a temporal regressor on the fMRI processing. The effect of IED events on brain function is a common bias in functional connectivity studies. Although IEDs are not associated with evident clinical manifestations, studies using PET and even EEG-fMRI could demonstrate that they alter basal hemodynamics (or rest condition), with the potential to bias analysis with the random prevalence of epileptiform events. Currently, the effects of IEDs are not considered in most FC

OPEN ACCESS

Edited and reviewed by:
Jan Kassubek,
University of Ulm, Germany

****Correspondence:***
Brunno Machado De Campos
brunno@unicamp.br

Specialty section:
This article was submitted to
Applied Neuroimaging,
a section of the journal
Frontiers in Neurology

Received: *02 December 2021*
Accepted: *14 December 2021*
Published: *13 January 2022*

Citation:
De Campos BM, Centeno M,
Coan AC and Cendes F (2022)
Editorial: Advances and Applications
of the EEG-fMRI Technique on
Epilepsies. Front. Neurol. 12:827705.
doi: 10.3389/fneur.2021.827705

studies (4). Accounting for IED effects improves the accuracy of connectivity studies and may offer some insight into the role of important therapeutic targets such as the ATN (5).

The FC based on fMRI acquired with EEG is also the subject of studies by Kassinopoulos et al., and Fu et al.. The first evaluates the relation between heart rate variability (HRV), a metric recently associated with refractory seizures and the severity of the epilepsies, and large-scale FC metrics. They describe relations between the HR and thalamic signals and connectivities, suggesting that these associations can play a role in the cardiac and blood pressure dysfunctions involved in SUDEP. Fu et al. explored FC in patients with refractory mesial temporal lobe epilepsy (MTLE) and benign epilepsy with centrotemporal spikes (BECT) compared to healthy controls. The findings showed different aberrations in the network-based interactions in MTLE and BECT, accessed throughout distinct global metrics, reinforcing that epileptic sub-syndromes should be considered distinct network diseases (6).

Chaudhary et al., Cohen et al., Ebrahimzadeh et al., Labounek et al., and Suarez et al. focused on the localization of the epileptogenic zone (EZ) and its related networks. Chaudhary et al. performed intracranial EEG during fMRI sessions (icEEG-fMRI) in refractory focal epilepsy patients. The authors investigate the effective reach of the hemodynamic changes related to icEEG IEDs, finding that these events can lead to associated BOLD changes across the whole brain. Furthermore, the authors investigate the correspondence between the BOLD and the topographic distributions of the IEDs, indicating that non-focal epileptiform discharges can generate a more accurate localization of the EZ. Cohen et al. investigate patients with epilepsy secondary to Polymicrogyria (PMG), a malformation of cortical development commonly associated with an intricate and widespread pattern of structural malformation (7). The results show that for this specific syndrome, the BOLD activations overlap the lesions in agreement with the scalp EEG detection in all studied cases. The choice for the hemodynamic response function (HRF) and its time delay relative to the target event is the subject of many EEG-fMRI studies (8, 9). Each epileptic syndrome is characterized by a constellation of factors that lead to specific epileptiform discharge propagation and hemodynamic behavior. The standard general linear model (GLM) with the canonical HRF provides robust results, but the model can benefit from a syndrome- or subject-specific response function modeling to improve the sensibility (10).

Labounek et al. performed a controlled experiment aiming to characterize data-driven EEG-fMRI fusion models in identifying task-related networks. They compared four EEG power models (two spectral and two spatial-spectral) as input on GLMs for individual EEG-fMRI fusion. The results indicate that the variable HRFs methodology significantly improves task-related BOLD responses throughout an entirely data-driven methodology.

The study of Ebrahimzadeh et al. proposes new modeling for the GLM variable of interest on EEG-fMRI analysis, finding promising results in terms of SOZ localization. The methodology consists of a data-driven EEG independent component selection using a previously defined subject-specific spike template. The regressor of interest is the select EEG component convolved with the canonical HRF.

Finally, Suarez et al. investigated the mechanisms that underlie negative BOLD responses (NBR) using the Windkessel (balloon) hemodynamic models. Based on four commonly discussed mechanisms, these findings indicate that an optimized GLM that considers the biophysical nature of the epileptic brain networks would improve the EEG-fMRI technique in precisely defining the SOZ. This study provides further insight into the meaning of NBR that is often seen in the EEG-fMRI maps of patients with epilepsy.

In conclusion, the articles in this Research Topic cover several aspects that are sensitive to the EEG-fMRI field, addressing each technique separately and the peculiar challenges of its combination. Studies have shown successful SOZ localization and indicate promising clinical applications for the method; however, there is still space for improvements regarding new methodological approaches and hardware development. We understand that the field can benefit from a standardization of acquisition and processing protocols among centers, aiming to increase reliability and reproducibility to favor a consolidated clinical application.

AUTHOR CONTRIBUTIONS

All authors listed have made a substantial, direct, and intellectual contribution to the work and approved it for publication.

REFERENCES

1. Casseb RF, de Campos BM, Morita-Sherman M, Morsi A, Kondylis E, Bingaman WE, et al. ResectVol: a tool to automatically segment and characterize lacunas in brain images. *Epilepsia Open.* (2021) 6:720–6. doi: 10.1002/epi4.12546
2. Koupparis A, von Ellenrieder N, Khoo HM, Zazubovits N, Nguyen DK, Hall JA, et al. Association of EEG-fMRI responses and outcome after epilepsy surgery. *Neurology.* (2021) 97:e1523–36. doi: 10.1212/WNL.0000000000012660
3. Coan AC, Chaudhary UJ, Grouiller F, Campos BM, Perani S, De Ciantis A, et al. EEG-fMRI in the presurgical evaluation of temporal lobe epilepsy. *J Neurol Neurosurg Psychiatry.* (2016) 87:642–9. doi: 10.1136/jnnp-2015-310401
4. Omidvarnia A, Pedersen M, Vaughan DN, Walz JM, Abbott DF, Zalesky A, et al. Dynamic coupling between fMRI local connectivity and interictal EEG in focal epilepsy: a wavelet analysis approach. *Hum Brain Mapp.* (2017) 38:5356–74. doi: 10.1002/hbm.23723
5. Bagshaw AP, Hale JR, Campos BM, Rollings DT, Wilson RS, Alvim M, et al. Sleep onset uncovers thalamic abnormalities in patients with idiopathic generalised epilepsy. *Neuroimage Clin.* (2017) 16:52–7. doi: 10.1016/j.nicl.2017.07.008
6. de Campos BM, Coan AC, Lin Yasuda C, Casseb RF, Cendes F. Large-scale brain networks are distinctly affected in right and left mesial temporal lobe epilepsy. *Hum. Brain Mapp.* (2016) 37:3137–52. doi: 10.1002/hbm.23231
7. Kobayashi E, Bagshaw AP, Jansen AZ, Andermann F, Andermann E, Gotman J, et al. Intrinsic epileptogenicity in

polymicrogyric cortex suggested by EEG-fMRI BOLD responses. *Neurology*. (2005) 64:1263–6. doi: 10.1212/01.WNL.0000154640.23656.A3

8. Bagshaw AP, Aghakhani Y, Bénar CG, Kobayashi E, Hawco C, Dubeau F, et al. EEG-fMRI of focal epilepticspikes: analysis with multiple haemodynamic functions and comparison with gadolinium-enhanced MR angiograms. *Hum Brain Mapp*. (2004) 22:179–92. doi: 10.1002/hbm.20024
9. Hawco CS, Bagshaw AP, Lu, Dubeau F Y, Gotman J. BOLD changesoccur prior to epileptic spikes seen on scalp EEG. *NeuroImage*. (2007) 35:1450–8. doi: 10.1016/j.neuroimage.2006.12.042
10. Proulx S, Safi-Harb M, LeVan P, An D, Watanabe S, Gotman J. Increased sensitivity of fast BOLD fMRI with a subject-specific hemodynamic response function and application to epilepsy. *Neuroimage.* (2014) 93:59–73. doi: 10.1016/j.neuroimage.2014.02.018

Conflict of Interest: The authors declare that the research was conducted in the absence of any commercial or financial relationships that could be construed as a potential conflict of interest.

frontiers
in Neurology

SYSTEMATIC REVIEW
published: 11 March 2021
doi: 10.3389/fneur.2021.622719

Artifact Reduction in Simultaneous EEG-fMRI: A Systematic Review of Methods and Contemporary Usage

Madeleine Bullock[1,2], *Graeme D. Jackson*[1,2,3] and *David F. Abbott*[1,2,3]*

[1] Florey Department of Neuroscience and Mental Health, The University of Melbourne, Melbourne, VIC, Australia, [2] Florey Institute of Neuroscience and Mental Health, Melbourne, VIC, Australia, [3] Department of Medicine (Austin Health), The University of Melbourne, Melbourne, VIC, Australia

Simultaneous electroencephalography-functional MRI (EEG-fMRI) is a technique that combines temporal (largely from EEG) and spatial (largely from fMRI) indicators of brain dynamics. It is useful for understanding neuronal activity during many different event types, including spontaneous epileptic discharges, the activity of sleep stages, and activity evoked by external stimuli and decision-making tasks. However, EEG recorded during fMRI is subject to imaging, pulse, environment and motion artifact, causing noise many times greater than the neuronal signals of interest. Therefore, artifact removal methods are essential to ensure that artifacts are accurately removed, and EEG of interest is retained. This paper presents a systematic review of methods for artifact reduction in simultaneous EEG-fMRI from literature published since 1998, and an additional systematic review of EEG-fMRI studies published since 2016. The aim of the first review is to distill the literature into clear guidelines for use of simultaneous EEG-fMRI artifact reduction methods, and the aim of the second review is to determine the prevalence of artifact reduction method use in contemporary studies. We find that there are many published artifact reduction techniques available, including hardware, model based, and data-driven methods, but there are few studies published that adequately compare these methods. In contrast, recent EEG-fMRI studies show overwhelming use of just one or two artifact reduction methods based on literature published 15–20 years ago, with newer methods rarely gaining use outside the group that developed them. Surprisingly, almost 15% of EEG-fMRI studies published since 2016 fail to adequately describe the methods of artifact reduction utilized. We recommend minimum standards for reporting artifact reduction techniques in simultaneous EEG-fMRI studies and suggest that more needs to be done to make new artifact reduction techniques more accessible for the researchers and clinicians using simultaneous EEG-fMRI.

Keywords: simultaneous EEG-fMRI, artifact, motion, ballistocardiogram, electroencephalography, BOLD

Edited by:
Fernando Cendes,
State University of Campinas, Brazil

Reviewed by:
Li Dong,
University of Electronic Science and Technology of China, China
Jean Gotman,
McGill University, Canada

***Correspondence:**
David F. Abbott
david.abbott@florey.edu.au

Specialty section:
This article was submitted to Applied Neuroimaging, a section of the journal Frontiers in Neurology

Received: *29 October 2020*
Accepted: *29 January 2021*
Published: *11 March 2021*

Citation:
Bullock M, Jackson GD and Abbott DF (2021) Artifact Reduction in Simultaneous EEG-fMRI: A Systematic Review of Methods and Contemporary Usage. Front. Neurol. 12:622719. doi: 10.3389/fneur.2021.622719

1. INTRODUCTION

Simultaneous electroencephalography (EEG) and functional MRI (fMRI) is a non-invasive imaging method first described over 25 years ago, and early on was mostly used for characterizing seizure location in epilepsy patients (1, 2). By combining the temporal resolution of scalp EEG with the spatial resolution of fMRI, it is possible to gain more information about brain activity than is possible with either technique alone (3). While simultaneous EEG-fMRI started out as a technique to locate epileptic activity, it is now used much more widely in neuroscience research (4), from studies looking at brain function in disease states such as schizophrenia (5, 6), to those investigating brain dynamics during behaviors such as decision making (7, 8) and sleep onset (9, 10).

A technical challenge with recording simultaneous EEG-fMRI is that EEG recorded inside the MR environment is subject to large sources of noise, which can obscure neuronal activity, or induce artificial artifacts in the EEG recording (11). The four main sources of noise in EEG recorded during fMRI are outlined below, and some examples are shown visually in **Figure 1**.

- Gradient artifact (GA) is the largest source of noise in EEG-fMRI, and is used for fMRI acquisition due to the magnetic field gradients, which induce current in EEG electrodes up to 400 times larger than neural activity, therefore obscuring the EEG information of interest (15).
- Motion artifact occurs when movement of the subject's head within the scanner creates artifacts on the EEG due to induced current at electrodes when moved inside the magnetic field—occurrence explained by Faraday's law (16).
- Ballistocardiogram (BCG) artifact occurs due to the subject's cardio-respiratory patterns, specifically scalp pulse and cardiac-related motion, as well as the changes in magnetic properties of blood flow under the scalp (17).
- Environmental artifact occurring on the EEG recording is mostly due to interference from power line noise, ventilation, and lights in the MR room, as well as the vibration arising from the helium cooling pump used to ensure stability of the scanner's magnet (18).

Given the many artifacts and their impact, methods to reduce all artifacts are crucial to ensuring that the EEG recorded during EEG-fMRI is an accurate representation of brain activity. The earliest algorithm for artifact removal in EEG-fMRI was the average artifact subtraction (AAS) method, which was adapted to remove either BCG (19) or GA (15), and permitted the first fully simultaneous EEG-fMRI. However, due to temporal non-stationarities in template sampling, AAS-filtered EEG still contains residual artifact (15). In the years since the publication of the AAS method, many novel methods have been proposed to improve accuracy of EEG-fMRI, and research in this area is ongoing (20). An aim of this review is to distill the literature from these 21 years and provide updated recommendations about artifact reduction to those interested in practicing EEG-fMRI.

Previous published reviews, such as a recent paper from (20), have given a broad overview of the methods to reduce artifact in EEG-fMRI, but have not systematically reviewed all literature, nor given specific recommendations for researchers not familiar with this field. Perhaps the best example of practical recommendations is a visual article by Mullinger et al. (21), which shows step-by-step optimization for specific EEG-fMRI equipment. While these reviews are useful, there remains a gap: a systematic review of artifact reduction methods in EEG recorded during EEG-fMRI is provided to underpin a set of clear recommendations that make it easier for researchers to make informed decisions about reducing artifact in any EEG-fMRI study.

We aim to:

1. Systematically review EEG-fMRI artifact reduction methods and provide some clarity regarding a potential "gold standard" approach;
2. Systematically review all papers published in the last 4 years that have used EEG-fMRI to determine the artifact reduction techniques used in contemporary practice.

The results of our review lead to guidelines for EEG-fMRI usage, and recommendations to help ensure best practice techniques are widely used.

2. METHODS

2.1. EEG-fMRI Artifact Reduction Techniques

The objective of the first literature search was to identify novel artifact reduction techniques for EEG-fMRI from literature published since the first EEG-fMRI artifact reduction paper appeared in 1998. This review has a specific focus on EEG-informed fMRI, where results of EEG are used to inform the fMRI analysis. Web of Science database was searched for papers related to artifact reduction in EEG-fMRI, in English, from years 1998 to 2019 (January 17, 2020). Document types were categorized into article, proceedings paper, review, data paper, early access, or book chapter (exclusion of editorial material, meeting abstracts, and corrections). The search terms are outlined as follows:

(TS = (((eeg OR electroencephalography) AND ("functional mri" OR fmri OR "functional magnetic resonance imaging")) AND (artifact OR artifact* red* OR filter* OR denois* OR classif*))) AND LANGUAGE: (English)

The title, abstract, and, if required, methods sections of resultant papers were then manually interrogated to include only literature which fitted the following criteria: data from *human* subjects, recorded using *EEG and fMRI*, where EEG and fMRI are recorded *simultaneously*, i.e., EEG recorded inside the MR environment, while fMRI scanning is occurring.

The final step was to determine which of the resultant papers outlined *novel artifact reduction* techniques for the EEG data recorded during EEG-fMRI. Artifact was defined as any source of activity, which appears in the EEG dataset, but is not neuronal in origin. Artifact reduction can include (1) methods to reduce the raw recording of artifact during EEG-fMRI acquisition, and (2) methods to filter out artifact during the post-processing of EEG. A method was considered novel if there were no previous publications outlining its use for reducing *any* artifact on EEG data recorded during EEG-fMRI. By this definition, papers that outline the use of an existing published method, but implemented to reduce another type of artifact, are not considered novel. Although this review focuses on methods that improve EEG clarity, it is accepted that some techniques that improve EEG quality may also impact fMRI quality, positively or negatively. Other literature has covered the impact of the EEG system on artifact in the fMRI recording: for most commercial EEG-fMRI

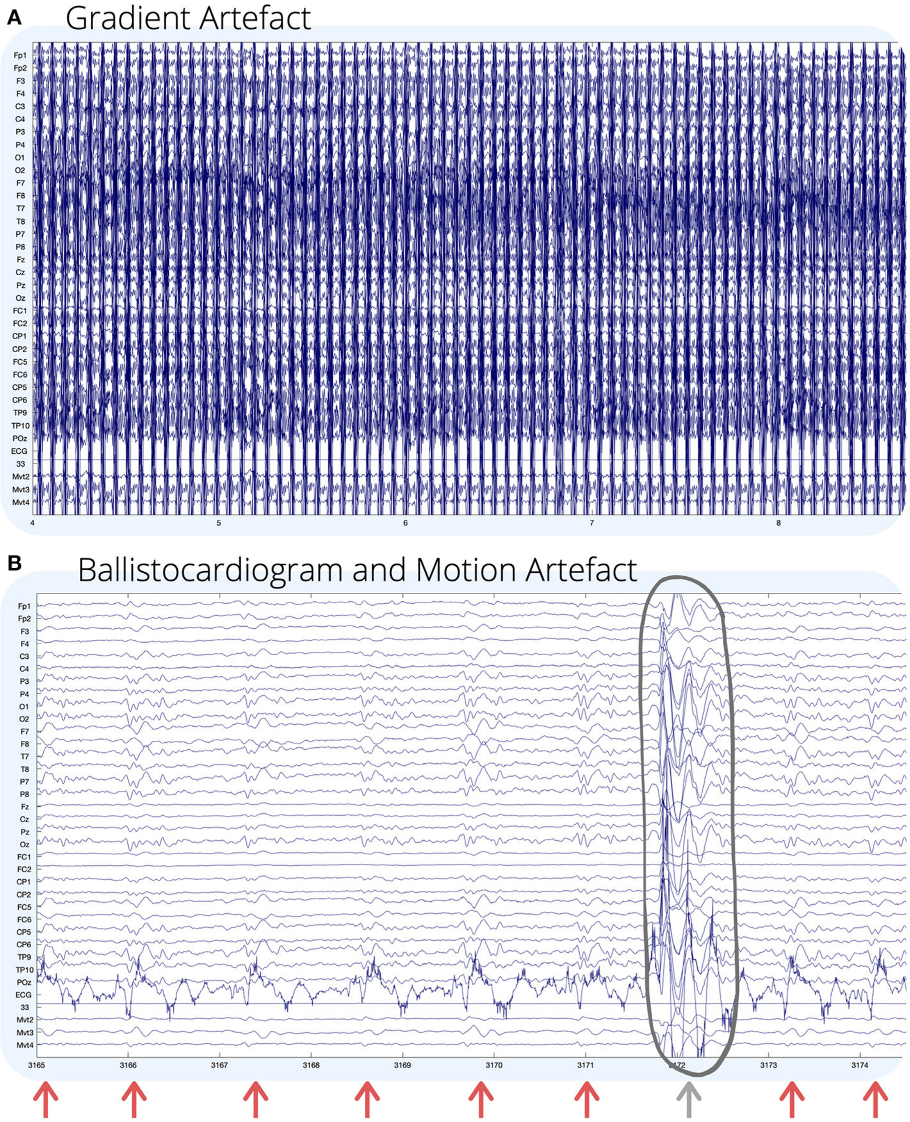

FIGURE 1 | Visual examples of **(A)** gradient; and **(B)** ballistocardiogram (shown by arrows) and motion (circled) artifact on EEG recorded during fMRI. For **(B)**, GA has been removed using an adaptive average artifact subtraction (AAS) method (12). EEG channel numbers are given on the left of each figure. Channels below the ECG (mvmt 2–4) are recordings from carbon wire motion loops for measuring motion. The horizontal axis of each figure shows time in seconds. Environmental artifact is not seen visually in this recording, and for visual examples of environmental artifact, we refer the reader to (13, 14).

systems, artifact from EEG is considered far lower than that generated by fMRI (11, 22–24).

2.2. Contemporary Use of Artifact Reduction Techniques in EEG-fMRI Studies

The primary aim of the second review was to acquire information about the setup and post-processing methods employed by researchers for reducing artifact in contemporary EEG-fMRI studies (2016–2019) (Aim 1). A secondary aim was to understand the level of diversity in recently published studies using EEG-fMRI (Aim 2). Given these aims, there were three primary areas of interest for the included studies: (1) Methods of EEG-fMRI setup (pre-recording) for artifact reduction (Aim 1); (2) post-processing (post-recording) methods for artifact reduction (Aim 1); and (3) measure of interest on EEG used to drive the EEG-fMRI analysis (Aim 2).

The literature search covered the databases—Web of Science, PubMed, and Scopus—and included all articles between January 1, 2016 and December 31, 2019, with the following terms: EEG-fMRI, ERP-fMRI, EEG-BOLD, and their derivatives, including long hand spelling, and words in alternate orders. Key search fields were as follows: Title, Abstract, and Keywords. The inclusion criteria for EEG-fMRI studies is fully simultaneous EEG-fMRI in human population. The definition of simultaneous EEG-fMRI and human population is the same as outlined in part 1, with EEG-fMRI studies using interleaved scanning not considered fully simultaneous. Studies included in this review must have a full methods section, and be either English language publications, or have a translation readily available.

3. SEARCH RESULTS

3.1. EEG-fMRI Artifact Reduction Techniques

The Web of Science search returned 894 articles (891 unique), of which 457 fitted the criteria of simultaneous EEG-fMRI as outlined in the methods, and of those, 136 described novel artifact reduction methods (**Figure 2**). Many of the papers that did not meet the criteria for simultaneous EEG-fMRI described either only EEG *or* only fMRI data. Some papers described data from both modalities, but these data were not simultaneously acquired. Sixteen papers detailed imaging in animal models, without any human imaging. When assessing whether the remaining papers described novel artifact reduction techniques for *EEG* data, 273 were excluded, with the most common reasons being:

1. Applications of EEG-fMRI for answering a clinical, neuroscience, or behavioral question, with no novel artifact reduction technique shown;
2. Characterization of EEG artifact during EEG-fMRI, but no method to remove it;
3. Other reasons, such as:
    a. EEG-fMRI review articles;
    b Methods for EEG-fMRI data fusion;
    c. Methods for artifact reduction in *fMRI* data only;
    d. Proposals of methods for improving EEG-fMRI acquisition, but with no data validation.

The search also identified 48 papers that described comparisons of EEG artifact reduction methods for EEG-fMRI, without proposing any new method. While, these papers do not describe novel methods, they were used to inform the discussion in the following sections in order to provide an objective measure of best practice in EEG-fMRI artifact reduction.

3.2. Contemporary Use of Artifact Reduction Techniques in EEG-fMRI Studies

Figure 3 shows the search strategy used for finding literature relating to artifact use in contemporary EEG-fMRI studies. The original search returned 506 original articles, after excluding duplicates from each of the databases. Screening of papers by title and abstract excluded 132 papers, and full text screening of papers excluded another 130 papers. The most common reasons for exclusions were as follows: animal studies (n = 5), review papers with no original data (n = 81), papers where data are not from simultaneous EEG-fMRI (n = 121), and papers discussing technical aspects of EEG-fMRI without original data in human subjects (n = 49). After exclusion, the review includes 244 EEG-fMRI papers for analysis.

4. ARTIFACT REDUCTION: RECOMMENDATIONS AND CONTEMPORARY USE

This section is divided into subsections based on the four main EEG-fMRI artifact types [GA, BCG artifact, motion artifact, and environmental artifact] and includes results from both reviews in each section. For each artifact type, recommendations are made for the best practice for reduction of that artifact, followed by contemporary usage statistics to contrast best practice vs. current practice. In the interests of space, not all 130 novel artifact reduction techniques revealed in the literature search are covered in detail in the following discussion. A comprehensive list of all techniques is provided in additional tables in the **Supplementary Material.**.

A final subsection details the software toolboxes used to reduce artifact in contemporary studies. Although we do not evaluate software toolboxes in this review, understanding the most commonly used software could help to identify the reasons researchers are using a particular artifact reduction technique in contemporary studies.

4.1. Gradient Artifact Reduction

GA, or imaging artifact, is the largest artifact seen on EEG recorded during fMRI, and occurs due to the strong magnetic field changes during fMRI scanning. GA amplitude can be over 400 times larger than the EEG of interest (15), making its removal crucial for a successful EEG-fMRI study. Early EEG-fMRI studies avoided GA by altering the time of scanning, so that fMRI was acquired either in response to an EEG event such as an epileptic spike (2), or by interleaving EEG and fMRI acquisition (26). However, alternating fMRI and EEG acquisition cannot be considered simultaneous, and useful neuronal information is lost when data are acquired in this way. In order to be simultaneous but still to avoid GA, a method known as Stepping Stone Sampling (27) was developed, which avoids GA by altering the fMRI pulse sequence so that EEG can be sampled during times when GA is known to be negligible. However, Stepping Stone Sampling has been largely superseded because newer post-processing methods allow for equivalent or better (28) recovery of neuronal activity from continuous scanning using conventional fMRI pulse sequences.

4.1.1. EEG-fMRI Setup

If not avoiding GA using Stepping Stone Sampling or another method, the EEG equipment must have sufficient dynamic range to record both the GA and the underlying EEG to facilitate subsequent post-processing to separate these signals. Newer amplifiers that are wireless and can adapt amplification depending on MR gradient sequences are in development (29) but are not currently available. One problem with recording EEG in the MR environment is that EEG leads can form large loops, which increase the prominence of induced current from GA, and may be dangerous if heating occurs (30). To reduce the size of EEG cable loops in the MR environment and to reduce the magnitude of GA being recorded, EEG cables should be twisted (22, 30–32), as short as possible (32, 33), and located centrally

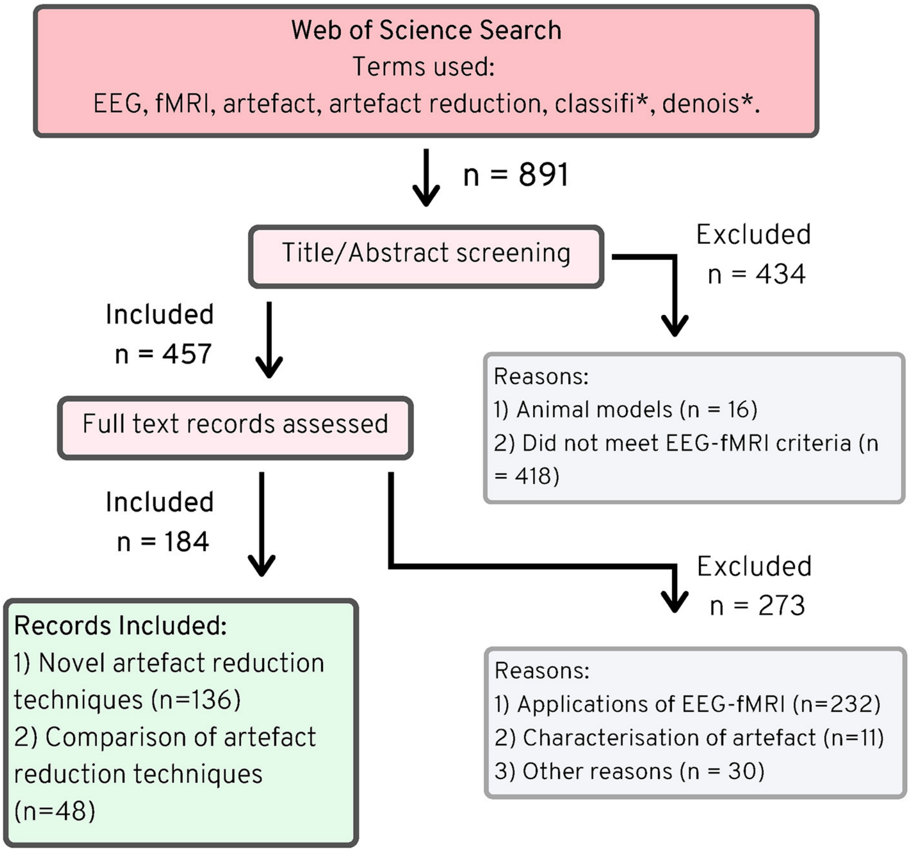

FIGURE 2 | PRISMA chart (25), EEG-fMRI novel artifact reduction methods, 1998–2019.

on the EEG cap (34). Re-wiring the EEG cables based on scanner specific artifact recordings may further reduce the amount of GA recorded in the EEG (35). Also by optimizing the setup of EEG equipment, positioning the subject with nasian 4 cm posterior to isocenter (36) may reduce GA contamination of EEG.

4.1.2. Post-processing

Template methods, such as AAS can be used to remove GA, and blind source separation (BSS) methods, as well as other filtering methods, have been proposed as alternatives.

4.1.2.1. Template Methods

Template methods are techniques that create an estimate of the artifact, which is removed from the noisy data, to obtain clean EEG. GA is assumed to be repetitive and time-locked to each repetition time (TR) during fMRI scanning, whereas the neuronal EEG of interest is assumed to be random and fluctuating without regard to TR. Template methods average the signal over many TRs, leveraging the fact that the neuronal EEG signal, which is not time locked to the TR, will average out toward zero, leaving the GA signal, which can be subtracted from the recording to give the cleaned EEG (37). Providing that the assumption of GA stability and EEG fluctuation, with regard to TR timing, throughout the recording is valid, template methods can provide a relatively easy and reliable way to clean the EEG.

Temporal jitter of EEG and MRI scanner clocks leads to slight differences in the calculation of templates, resulting in residual GA contamination of EEG after artifact removal by template methods. Therefore, to accurately sample the GA and use template methods most effectively, MR and EEG clocks should be synchronized (27, 38–40), preferably using a synchronization hardware device (38). For studies where synchronization hardware is not available, post-processing methods, such as interpolation (41), auto-correlation (42), time continuous cubic spline model (43), or least across squares variance (44), can be used to realign EEG and fMRI data. However, the use of synchronization hardware, available with many commercial EEG-fMRI systems, remains the optimal approach.

The template methods for GA removal described in the literature differ from each other by the way that the template is generated, as well as how the template is subtracted from the recording. The earliest template method, AAS, considers GA at each TR epoch in the temporal domain, and applies a moving average filter (over some number of immediately preceding TR epochs) to remove GA, leaving the cleaned EEG data (15). Other template methods, such as template sets based

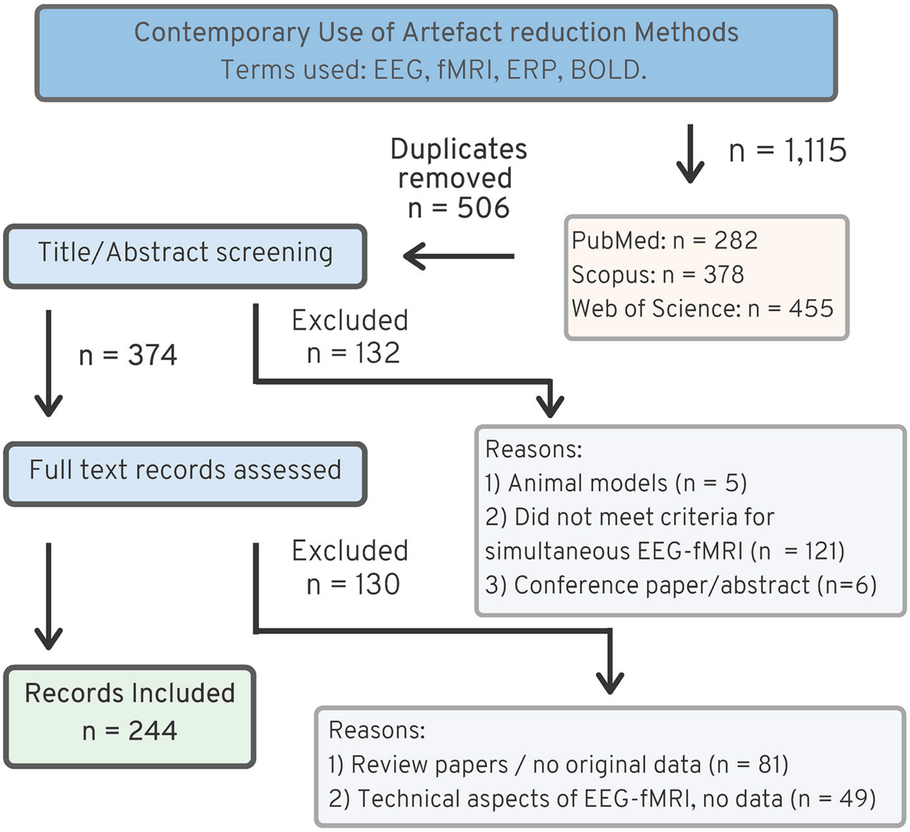

FIGURE 3 | PRISMA chart (25), showing search strategy for recent EEG-fMRI papers, 2016–2019.

on cubic spline interpolation (45) and hierarchical clustering (46) use templates derived from the whole recording rather than temporally preceding, and filter data based on these clusters, or sets, of templates.

There have been few comparisons of template methods available in the literature. However, even in the original paper that describes it, cubic spline interpolation did not outperform AAS, unless additional motion parameters from an MR compatible camera (or, it was suggested head displacement parameters from fMRI analysis could possibly be substituted) were also incorporated into the algorithm (45). The addition of head displacement parameters gives an additional information to the cubic spline model, and it is unclear if using AAS with this additional information would have produced comparable results. Hierarchical clustering showed improved performance compared with a pipeline of AAS and interpolation of EEG and MR data, but was not implemented on a dataset where EEG and MR timing were synchronized (46). It is therefore questionable whether hierarchical clustering could improve the performance of AAS if adequate synchronization was employed, and it is difficult to suggest this method without appropriate independent validation. The literature search showed that of the three template methods described above, only AAS has been independently scrutinized, and many papers have built on or suggested additional factors for its implementation.

AAS, when used for removing GA, can be prone to residual artifact due to fluctuations in GA over the course of the recording, such as from head motion (47), drift in EEG sampling rates (12, 38), or from contamination due to BCG artifact (48). Methods to reduce the resultant residual artifact present after AAS include using extra steps such as pre-processing template data (49), or improving the template estimation by weighting templates based on proximity (50), linear regression (51), cross-correlation (52), or adaptive filtering (53). However, these methods that describe extra steps for removing residual artifact with AAS are dealing with the residual artifact from non-synchronization of clocks, and if they compare their method with AAS, it is AAS without synchronization (49, 51, 53). One paper [cross-correlation (52)] considered how synchronization of EEG and MRI would affect their method, and stated that their method would likely provide a similar magnitude of GA reduction compared to using AAS with synchronization. Weighting templates based on proximity (50) was tested using synchronized EEG and MRI data, but the protocol for MR acquisition was Stepping Stone Sampling (27), an uncommon MRI sequence. The paper was aimed toward retaining high-frequency signatures of EEG, rather than reducing GA (50), and therefore, the findings of this paper will be more relevant to those working in the field of high-frequency EEG.

The biggest issue with using AAS to remove GA is that BCG and motion artifact affect the accurate calculation of AAS templates (47), with these inaccurate templates often causing the residual artifact seen in recordings (48). In 2009, two groups independently published methods showing that motion information, obtained from fMRI head displacement parameters, can be added to the calculation of AAS templates to improve GA removal (12, 54). The addition of head displacement parameters to AAS is particularly suited to cohorts such as children where motion is unavoidable, and is particularly beneficial when head displacement during the time of the scan exceeds 1 mm. The addition of motion parameters to AAS showed an experimental increase event-related potential (ERP) power of 10–40%, (12), as well as a reduction in residual GA of 20–50% (54). Recently, it has been suggested that information from hardware that directly records head motion, rather than fMRI head motion parameters, could also be used to improve the calculation of AAS templates (55, 56). A discussion of direct motion hardware is given later in section 4.2.3. Finally, a recent study capitalized on the fact that the GA is stable, and using a model of the GA and the principles of Faraday's law enable us to determine which volumes were affected by head motion, and thus adjust the AAS templates accordingly (47).

4.1.2.2. Blind Source Separation Methods

BSS techniques are a group of data-driven methods that aim to decompose a mixed signal (input signal) into its multiple original sources (57). In EEG-fMRI, the noisy signal (EEG and artifact) is the input, with output components ideally being separated into components representing neuronal signal or sources of noise. BSS typically uses statistical properties, such as Gaussianity, variance, or correlation to identify these sources, even when no prior information is given (58). As such, BSS methods can be preferable to template methods when information about the signal, such as MR slice timing, is unknown.

Popular BSS methods employed to reduce GA in EEG-fMRI studies include independent components analysis (ICA) (59), principal components analysis (PCA) (60), canonical correlation analysis (CCA) (61), and blind source extraction (BSE) (62). Variations of these main methods for GA reduction include the optimal basis set (OBS) method (63), which uses template methods alongside PCA, independent vector analysis (IVA) (64), which employs ICA over multiple EEG channels, and single value decomposition (SVD) (65), a subset of PCA.

Of the BSS methods described, ICA and OBS have been independently compared for removal of GA from EEG-fMRI data, with ICA showing good results in simulated data, but OBS outperforming ICA in experimental data (66). A difficulty with using BSS methods is the challenge of correctly choosing the components that represent artifact and those which represent neuronal activity, especially if no prior knowledge about the signal is available. There is a chance that by rejecting too many components, neuronal signal, as well as artifact, is removed from the recording and important information is lost (67).

4.1.2.3. Other Methods

4.1.2.3.1. Frequency Filtering. Frequency filtering uses algorithms such as the Fourier transform (FT) to represent the EEG signal in the frequency domain, where frequencies corresponding to GA can be removed (26). However, given that some GA occurs at frequencies corresponding to neural activity, frequency filtering is not suitable for accurately reducing GA without losing important neuronal information (26). Frequency filtering using the FT has been suggested as an option for real-time removal of GA, where computational speed of the algorithm is more important than a potential loss of neuronal signal (68). The Taylor–Fourier transform expands the FT by allowing for fluctuations in harmonics during each temporal segment of data, regardless of how small, (69), allowing it to capture amplitude and phase variations that would not be possible with the FT alone. For EEG-fMRI, the Taylor–Fourier transform method creates a dynamic template at each individual TR, and was shown to improve removal of residual artifact, but was not validated against AAS or any other GA removal technique (70).

4.1.2.3.2. Dictionary Learning. Another approach to GA reduction, dictionary learning, is a computationally expensive way of separating the GA and EEG, which has shown an ability to remove GA from contaminated EEG, but has not been tested against other commonly used GA removal methods, either in the original paper or independently (71). Therefore, we cannot recommend the dictionary learning model for removing GA until further validation of the method is available.

4.1.2.4. Comparison of Methods

Few papers independently compare GA removal methods for post-processing of EEG-fMRI data. In 2007, Grouiller et al. (66) published a study that compared AAS, OBS, ICA, and FT in both simulated and experimental EEG-fMRI data. Results showed that while ICA performed well for simulated data under 30 Hz, AAS and OBS performed better in experimental data, and FT had the poorest results. Other studies have compared AAS and OBS only, especially in their commonly used software, with AAS often being implemented from commercial software Brain Vision Analyser, and OBS implemented by an open source plug in through EEGLAB (63). Comparisons of AAS and OBS suggest that OBS may be more adept at removing artifact (67, 72), although it has been suggested that the increase in artifact removal seen from OBS is due to additional BCG removal as well as GA removal, and which may have been removed during other post-processing steps for removing BCG later (72, 73). Overall, the methods of AAS and OBS appear similar for cleaning of GA from EEG-fMRI, provided that adequate synchronization of MR and EEG clocks occur. OBS may clean additional BCG from the data during the GA cleaning step, and therefore should conservative artifact removal be required, AAS with synchronization may be preferred. Future studies that independently compare some of the less known methods, such as dictionary learning, and template methods (not AAS), would help to improve guidance for GA removal from EEG-fMRI studies.

4.1.3. Recommendations for Removing Gradient Artifact

Recommendations for Removing Gradient Artifact from EEG-fMRI:

- EEG cable length (from cap to amplifier) as short as possible.
- EEG cables (cap and cable bundle to amplifier) twisted to reduce loop areas, minimizing magnetic field effects.
- EEG cable position central to the bore and patient cap.
- Patient nasian 4 cm from isocenter.
- Synchronization of EEG and MR clocks, preferably using hardware rather than interpolation methods.
- Post-processing removal of GA with either AAS (conservative, possible residual artifact) or OBS (rigorous, possible loss of neuronal information).
    - Additions to these algorithms (e.g., including head motion parameters) may remove GA more accurately.

4.1.4. Contemporary Use of GA Removal Methods

The results of the review of contemporary EEG-fMRI studies show that AAS (15) is still overwhelmingly the most widely used technique for removing GA from EEG acquired during fMRI studies (61%, **Figure 4**). The OBS method [48] is used in only 10% of studies, while filtering, hardware and all other methods make up only 7% of GA removal methods. Despite there being a number of published papers outlining extensions to the AAS method to make it more accurate (for a full list, see the **Supplementary Material**), 6% of papers published between 2016 and 2019 report using an extended AAS method. In 17% of papers, the GA removal method was either unclear (9%), or there was no indication of GA removal at all (8%). GA removal method was considered "unclear" if the paper mentioned removing GA but did not state a specific method, or the paper commented on the commercial software used to remove artifact but did not outline method or steps taken within that software.

A surprising result from this review is that despite the many reported benefits of synchronizing EEG and MR clocks for later artifact removal (38, 39), less than 50% of the EEG-fMRI papers included in this review reported using synchronization hardware (for full data, see the **Supplementary Material**). The low percentage of synchronization hardware use may be partially due to the inadequate reporting of methods in the literature. Regardless, the low number of papers reporting use of synchronization is concerning given that effective GA removal using template methods such as AAS (the most commonly used method) relies heavily on adequate synchronization (38). We recommend that synchronization hardware be used in all EEG-fMRI studies so that GA can be accurately removed from EEG, and also recommend that authors include synchronization use in their methodology when publishing research.

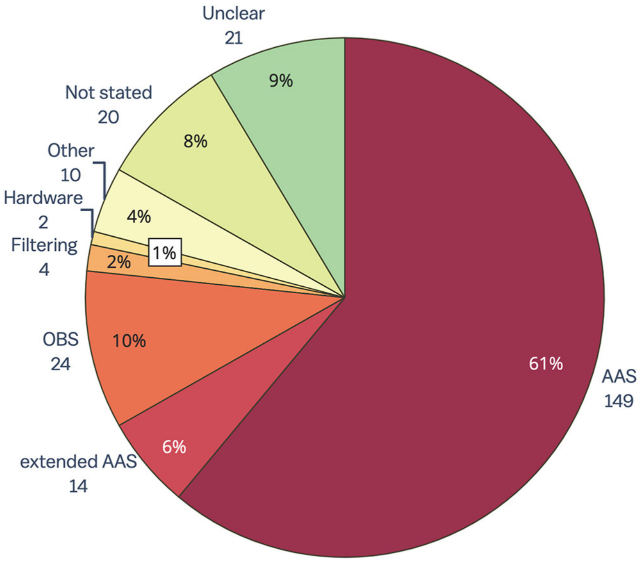

FIGURE 4 | Gradient artifact removal in EEG-fMRI papers, published between 2016 and 2019 (*n* = 244). AAS, average artifact subtraction; OBS, optimal basis set.

4.2. Ballistocardiogram Artifact

The BCG, pulse, or cardio-ballistic artifact, refers to contamination of the EEG due to pulsatile motion associated with cardiac output (65). BCG voltage has been measured at around 50 μV, which is in the physiological range of typical EEG signals of interest (19), and therefore is a considerable confound that cannot easily be avoided. A technique known as pulse triggered scanning (74) has been proposed as a way to avoid the main source of BCG artifact, but is only practical for task-based fMRI and requires specific technical expertise to set up. Therefore, most studies opt to use standard fMRI sequences, and rely on accurate recording of pulse and physiological signals during EEG-fMRI to estimate and remove BCG artifact during post-processing of EEG data.

4.2.1. Measurement of BCG

Monitoring physiological signals such as heart and breathing rate can give a baseline estimate of BCG artifact and enable better removal during post-processing of EEG. Common methods to measure physiological signals include using an additional electrode to measure ECG (19, 30), as well as the use of photoplethysmography (PPG) or a respiratory band, which is sometimes included with the MRI scanner setup (39). Choice of measurement may depend on the post-processing methods chosen, and the researcher needs to ensure that any additional signals measured can be accurately synchronized with EEG and MR timings.

4.2.2. Post-processing

From a post-processing perspective, BCG artifact removal is arguably more difficult than GA removal because BCG varies throughout the recording (46, 75, 76). BCG artifact differs across scalp electrodes, and may be contributed to by pulsation motion of the scalp, electromagnetic effects of blood flow under the scalp (Hall voltage), and movement related to respiration (17). BCG can be removed with various post-processing methods including template methods and BSS methods. Many of the methods outlined for GA removal in the previous section (section 4.1.2) have been adapted for BCG removal.

4.2.2.1. Template Methods

Template methods can be used to remove BCG artifact from EEG-fMRI data in a similar way to GA methods described in section 4.1.2. However, unlike for GA, where the beginning of each template is defined by MR trigger events at the beginning of each TR, the beginning of each BCG template is usually determined based on the peaks seen during simultaneous recording of physiological signals, such as ECG, alongside EEG-fMRI.

BCG removal from EEG recorded inside the MR environment was first proposed by Allen et al. (19) in 1998, using the AAS template method with QRS complexes from ECG used to mark the beginning of each BCG template. An issue with using AAS method for removing BCG artifact is that it assumes that all BCG will be of the same or similar shape, and only slowly vary across the whole recording, whereas evidence from literature has shown that BCG is highly variable across the recording and has many different shapes (46, 77). Because of this problem, adaptations of AAS for BCG removal have been proposed, including using exponential weights for previous BCG instances to account for the variability of BCG artifact (30), data warping the AAS template to account for shape differences (77), as well as additional steps such as wavelet decomposition to help remove residual BCG artifact left by inaccurate BCG templates (78). These methods, while shown to improve the correlation of EEG from outside scanner with filtered inside scanner recordings compared to AAS alone (77, 78), still do not account for all the dynamic changes that occur in BCG between subsequent heart beats. The dynamic time warping approach goes some way to account for shape changes that occur between BCG instances, but still uses previous iterations of BCG to determine the general shape of the waveform (77).

One of the problems associated with AAS is that BCG artifact can continue longer than a single heartbeat event, and therefore might overlap with the next BCG event in the recording. In fact, a study showed that when recorded at 3T, BCG artifact that overlapped into the next BCG template accounted for up to 30% of all recorded BCG (46). Several methods to overcome this overlapping of BCG artifacts has been proposed: the moving General Linear Model (mGLM) (79) and hierarchical clustering (46). The mGLM method uses a Fourier series to model each BCG template, and therefore does not cut off the template at the beginning of the following heartbeat. The mGLM model is similar to AAS in that the BCG template is updated temporally and relies on information from previous templates in its generation. In fact, if there is no overlapping of BCG, then mGLM will act identically to AAS (79). Clustering algorithms, such as hierarchical clustering (41, 46) and k-means clustering (80), account for overlapping BCG components by dividing all BCG instances from the entire recording into groups of similar templates, which can then be removed. Hierarchical clustering was tested on EEG-fMRI data from a sample of 29 healthy people at 1.5 T, as well as 15 epilepsy patients and one healthy person at 3 T. Results showed that BCG template duration was longer for higher magnetic field MRI (3 T) compared with 1.5 T recordings, and that the BCG templates not only vary between subjects, but within the recording, with clusters not ordered throughout the recording (46). This implies that techniques such as AAS-based methods and even mGLM may work sub-optimally, due to relying on information from previous BCG for determining the shape of the BCG template. By using the whole recording and clustering all BCG instances, the hierarchical clustering method is able to overcome the limitations of overlapping BCG as well as the variability of BCG. When compared to AAS and OBS, k-means clustering has showed slightly less BCG attenuation, but better neuronal preservation, compared with OBS—and vice versa compared with AAS—during an EEG-fMRI visual task at 7 T (80). Therefore, it has been suggested that clustering algorithms may be a good trade off for both attenuating BCG and preserving neuronal activity, compared with AAS and OBS (80).

Template methods for BCG removal typically require an accurate recording of physiological signals, particularly QRS complexes from ECG, that are used to generate BCG templates. While the AAS method uses amplitude information to detect the R peak of the QRS complex, other algorithms have been described for detecting R peaks. These algorithms include a modified Pan–Tompkins algorithm, which uses width and slope measurements as well as amplitude to detect R peaks (81), and k-Teager Energy Operator algorithm, which determines the total energy of the signal in a particular frequency range to identify R peaks (63, 78, 82, 83). Other methods for detecting R peaks have also been suggested, such as using the amplitude of the difference between the positive R peak and negative peak between S and T waves to determine the location of the R peak, as well as using a window of intervals based on expected heart rates to determine approximate location of peaks (84). We did not find any direct comparisons of the methods for R peak detection for BCG artifact recorded during EEG-fMRI. The most commonly cited R peak detector, k-Teager Energy Operator, was proposed for the specific purpose of finding peaks for BCG that occurs during EEG-fMRI (78), and therefore may be a better fit than older algorithms such as Pan–Thompkins, which was initially developed with the purpose of identifying peaks during ambulatory ECG (85). A potential issue with using the k-Teager Energy Operator is identifying the best value of k (the expected frequency of peaks). The default value, which is calculated based on the sampling rate of data, may identify too many false positive peaks (83), so heuristic customization may be required. An incentive for using k-Teager Energy Operator is that it can be used with other physiological recordings of BCG, such as from electrooculogram (EOG) electrodes attached to the side of the head, rather than using an ECG electrode (78). In this way, motion aspects of BCG may be better represented in EOG electrodes, without requiring direct motion recording from additional hardware, and without lag between QRS complexes recorded in ECG leads and BCG artifact seen on the head.

4.2.2.2. Blind Source Separation Methods

Blind source separation techniques, ICA, PCA, CCA, as well as OBS, have also been applied to removing BCG artifact from EEG-fMRI (for all methods, see **Supplementary Material**). BSS techniques offer a data-driven way to remove BCG, regardless of the variability of the BCG artifact, and without the necessity of measuring physiological signals.

4.2.2.2.1. Principal Components Analysis. PCA was first described alongside ICA, for BCG removal by (86). While, PCA was shown to be capable of removing BCG and improving the detection of epileptic spikes, it was concluded that ICA performed better (86). Since then, research into blind source separation methods for BCG removal in EEG-fMRI has focused on ICA rather than PCA, unless some extension or modification of the PCA algorithm was used.

One such algorithm that builds on PCA is the maximum noise fraction, which uses similar processes to PCA, but differs in that it derives two matrices—one for the signal (which is assumed to have a degree of smoothness) and one for estimated noise (which is assumed orthogonal to the signal). For the purpose of separating BCG from neuronal electrical activity, the BCG is assumed the temporally smoother "signal" and neuronal activity the "noise." The algorithm generates output components based on maximizing signal to noise ratio (SNR) between these matrices (87). In this way, the maximum noise fraction approach can be considered superior to ICA or PCA, because the components generated from the maximum noise fraction are automatically sorted into BCG and likely neuronal activity components (87). In a test of four subjects, with BCG removal compared between ICA and maximum noise fraction, the maximum noise fraction components chosen to represent BCG were more specific to the actual BCG artifact in comparison with the independent components from ICA (87).

Another method that builds on PCA is to precede it with empirical mode decomposition (EMD) (88, 89). Empirical mode decomposition first decomposes the signal into intrinsic mode functions with various frequencies and amplitudes, and then PCA is undertaken on each of the intrinsic mode functions (89). The combination of EMD and PCA is more sensitive to temporal variation that occurs in BCG, compared to application of PCA or ICA alone (89). EMD-PCA has been tested for many different EEG-fMRI paradigms, and has shown better removal of BCG from ERP task EEG-fMRI compared with OBS and AAS (88–90). In resting state EEG-fMRI, EMD-PCA removal of BCG improved the detection of most parameters measured from the EEG and was shown to be a useful technique when a reference signal such as ECG is not available to estimate BCG onset (91).

4.2.2.2.2. Optimal Basis Set. The OBS method (63), section 4.1.2, uses PCA in conjunction with a template method to remove artifact. Like AAS, OBS for BCG removal relies on accurate generation of templates and can benefit from techniques to precisely identify QRS complexes from physiological data. Adaptations of OBS include real-time monitoring of EEG data during fMRI (92) and correlation between PCA components and ECG signal, which helps to reduce the issues with temporal variation of BCG (93). The original OBS method used three main principal components (PCs) to represent the BCG from a recording. However, independent studies have shown conflicting data, with some suggesting that altering PC number for each individual dataset alters the outcome (73), whilst others show that OBS is relatively stable regardless of PC number chosen (76). A study using high-field 9.4 T MRI showed that OBS was not successful in extracting ERPs, unless ICA, with specific methods for choosing ICs, was used alongside it (94). Therefore, the evidence suggests that for removing BCG artifact, OBS is best used in conjunction with ICA, provided that IC selection is carefully monitored.

4.2.2.2.3. Independent Components Analysis. The main advantage of ICA, compared with template methods, is the ability to combine spatial and temporal information about BCG, without the need to record physiological signals, in a process which is fully data driven (95). However, there is a risk one may remove independent components (ICs), which relate to neuronal activity rather than artifact. Common methods for sorting BCG ICs include correlation (95, 96) variance (97), auto-correlation, frequency sorting, or peak to peak measures, all of which rely on the ECG channel as a reference [for a full overview, see review in (76)]. More recent methods of sorting BCG ICs include using Mutual Information algorithm (65, 98), clustering the results of multiple ICA runs (99), using a Magnitude Squared Coherence Function (100), and finally using a projection of QRS complexes from ECG into the IC space, followed by k-means clustering of all ICs (101). In addition, a variation of ICA, constrained ICA (cICA), may improve on ICA alone by using a prior estimation of BCG artifact to help derive ICs which are likely to closely match the BCG artifact (102–105). A comparison study of common IC sorting methods showed that peak to peak sorting of BCG ICs outperformed sorting by variance measures (76). However, this is in contrast to a second comparison study that showed that depending on the weight given to artifact removal or neuronal activity retention, the effectiveness of each of the IC sorting method differed (101). In this second study, sorting ICs by frequency showed the best overall reduction of BCG regardless of neuronal activity loss, while sorting ICs using auto-correlation showed the best outcomes for preserving neuronal activity and removing BCG, tested on 7 T data (101). When taken together, these results suggest that sorting of ICs is difficult, and may be confounded by scanner setup, magnetic field, as well as the study requirements that prioritize either full BCG removal, or neuronal activity preservation.

4.2.2.2.4. Canonical Correlation Analysis. CCA is a technique that takes two sets of basis vectors and computes linear sets of vectors from each set (106). CCA was adapted for removing BCG from EEG-fMRI by temporally segmenting the data based on BCG artifact timing, followed by employing CCA on consecutive epochs of BCG instances, to determine the underlying sources responsible for common signal between the segmented epochs (106). It was argued that CCA would be superior to ICA or PCA, as it is able to take into account temporal (periodicity) and spatial (topography) aspects of the BCG due to taking consecutive BCG instances into account (106). Originally requiring manual identification of BCG artifacts on EEG (106), later implementations of CCA used ECG and R peak detection for determining BCG onset (107). CCA performance has been observed to be better than AAS for some subjects, whereas for others the performance can be quite similar to AAS (108). In ERP studies, CCA appears to perform similarly to OBS or AAS when trial number is high, and better when trial number is relatively low (107). Results of these studies suggest that CCA may be a useful post-processing technique for studies where BCG variability within a subject is high, and recording time of the EEG-fMRI study is short.

4.2.2.3. Other Methods

Other methods for BCG removal include techniques that filter BCG based on some of its characteristics such as its spatial (109), spectral (110, 111), or morphological (112, 113) features. In addition, several papers outline the application of advanced filters such as Kalman filtering (114, 115), for BCG removal during EEG-fMRI. Finally, Abolghasemi and Ferdowsi (116) used dictionary learning for removal of BCG from EEG data, where a sparse dictionary is able to model the BCG data from EEG-fMRI data.

Removal of BCG by its spatial characteristics (109) was shown to be adequate compared with AAS, but only improved on AAS in the instance when BCG effects were temporally and spatially locked with EEG events of interest. Source Extraction (CSE), based on the spectral components of BCG, has been shown to be able to remove BCG from signals and result in good SNR and visual evoked potential (VEP) recovery, in comparison to AAS and OBS (110). Harmonic regression (111), another technique which is based on removing the spectral features of BCG, has shown similar or better results compared with AAS and OBS in experimental data. Morphological BCG removal (112, 113), which uses a Discrete Hermite Transform to model BCG shape, was shown to be superior to AAS and comparable to ICA, in the original paper in which it is described. Kalman filtering has been shown to be comparable to AAS, and may be preferred for real-time monitoring (114), but is unlikely to supersede AAS for post-processing, due to its computational complexity. Dictionary learning is able to model BCG well, but experimental data show that BCG removal was not significantly improved compared to the more common methods of AAS and OBS (116). Of all other methods for BCG removal, spectral and morphological methods appear to carry the most promise; however, all these approaches have not been validated independently outside of the group that first described them, making it difficult to recommend them given the current evidence.

4.2.2.4. Comparisons of Post-processing Methods

The most commonly compared processes are AAS, OBS, and ICA, and to a lesser extent, clustering and CCA methods. Individual comparisons of OBS and AAS have shown conflicting results, with some favoring AAS (66, 107, 117), and others favoring OBS (28, 73), although the consensus is that it may depend on the research question or EEG correlate of interest, as to which method will provide the best reduction in BCG artifact, without losing possible EEG information of interest (118). A recent 7 T study showed that a k-means clustering algorithm may be a good trade-off between neuronal preservation and BCG attenuation compared with AAS and OBS (80), but no other studies have independently compared clustering algorithms. Considering that AAS is OBS with a PC number of 1, altering the number of PCs chosen as BCG artifact has been a source of investigation, with one study showing that OBS with a default PC number of 3 provides better BCG removal compared with AAS (76), while a later study showed no significant differences between AAS and OBS (PC = 3), unless the PC number chosen was optimized for each individual participant, case in which OBS outperformed AAS (73). Research has shown that for task-based EEG-fMRI studies involving high numbers of trials, use of AAS, OBS, or CCA is adequate for removing BCG (107), while for studies looking at fewer trials, or when EEG correlates are small and difficult to detect, BSS methods such as OBS (28) or CCA (107) may improve removal of BCG, and thus, detection of the underlying EEG correlate. Most studies show that ICA is best used after either AAS or OBS, because the difficulty of correctly choosing the number of components and ensuring stability of the algorithm means that the outcome might otherwise be more likely to involve erroneous results for little gain in BCG removal (76, 94, 119). Other methods, such as spatial, morphological, wavelet, dictionary, and spectral methods for reducing BCG have not been independently compared with OBS, AAS, or ICA outside of the original papers that introduced them, making it impossible to judge the quality and reliability of these methods.

4.2.3. Direct Artifact Recording

There is evidence that the biggest contributor to BCG is pulse driven head motion, which obviously cannot be avoided during EEG-fMRI in human subjects (17, 75, 97). Options for measuring this physiological head motion artifact include methods to directly measure artifact at the head, such as altering the EEG cap, or using additional hardware connected to the cap. The benefits of these systems is that they are able to directly record any artifact occurring at the head, including small and large head motion, as well as monitoring environmental artifact such as vibration (120). However, higher costs and technical skill is required to ensure that any new and modified hardware is used safely and accurately.

Alterations to the EEG cap can include isolating some electrodes from the scalp using plastic (121–123), artificially joining electrodes using a gel bridge (124), or altering the position of some electrodes and bundling cables so that neuronal signals and motion can be adequately distinguished (125). The above options, however, result in sacrificing some electrodes for motion detection purposes, and may not be suitable for all EEG-fMRI setups, especially where electrode number is small or electrode number is important for the study outcome. Another method is to increase the number of EEG leads to provide an over-complete set of measurements that can be subsequently analyzed to distinguish between voltages arising from neuronal activity and those arising from motion of the sensors in a magnetic field (126). Further methods for alteration of the EEG cap include the creation of an entirely new electrode reference layer, isolated from scalp potentials, and located either underneath the EEG cap (127), on top of the EEG cap (128), or between EEG electrodes (129). For researchers not wanting to alter the EEG cap itself, additional sensors, such as extra electrodes (130), motion sensors (131), and carbon wire loops (55, 132–134), can be used to directly measure artifact from any sources including motion, without requiring alterations to the EEG cap itself. Signals obtained from direct artifact sensors can be successfully removed from the EEG with the aid of, for example, a multi-channel least squares fitting algorithm (55).

A study comparing the reference layer cap, wire loops, and AAS showed that while all methods adequately reduced BCG, using additional hardware (loops or reference cap) to filter data acquired during periods of deliberate motion, led to lower RMS values compared to AAS (120). This study suggested that the reference layer cap may be preferable to wire loops, but this was not shown definitively, as data obtained from the two methods were measured at different time points (120). While direct recording of artifact is preferable for all EEG-fMRI studies, implementation of this will depend on the research group's preferences and technical skill level.

4.2.4. Recommendations for Removing Ballistocardiogram Artifact

Recommendations for Reducing Ballistocardiogram Artifact in EEG-fMRI:

- Additional hardware, such as carbon wire loops, additional sensors, or a reference layer cap, to directly measure BCG and motion:
    - Adaptive filtering to remove BCG based on direct recordings.
- Where additional hardware is not available, use of AAS, OBS or CCA or clustering methods with:
    - Recording of physiological signals (ECG, PPG, or respiration).
    - Precise recording and detection of QRS complexes using k Teager Energy Operator or Pan-Tompkins algorithm.
    - ICA post-processing of data to remove residual BCG if using AAS or OBS.

4.2.5. Contemporary Use of BCG Removal Methods

The main methods used to remove BCG artifact from EEG-fMRI studies between 2016 and 2019 consisted of AAS, OBS, ICA and PCA, as well as hardware methods such as direct recording of BCG by wire loops or modified EEG cap (**Figure 5**). Like GA removal, the most common method of reducing BCG was AAS, with around one-third of studies using AAS alone for removing BCG, compared to almost two-thirds using AAS for removing GA. Use of OBS was the second most common BCG removal technique, with 14% of studies, a slightly higher percentage than for GA removal (10%). ICA rivaled OBS as a popular form of BCG removal at 13%, with a further 2% of studies using either ICA and OBS, or ICA and another technique. Hardware (4%), PCA (5%), and other methods (4%) were less frequently adopted. BCG removal method was either unclear, or not stated, in 18% of studies.

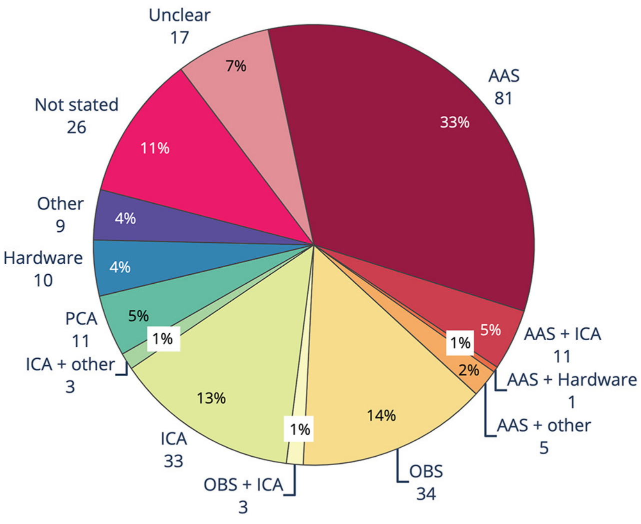

FIGURE 5 | Ballistocardiogram (BCG) artifact removal method in literature using EEG-fMRI published between 2016 and 2019 (*n* = 244). AAS, average artifact subtraction; OBS, optimal basis set; ICA, independent components analysis; PCA, principle components analysis.

The biggest difference seen between the methods for GA and BCG removal is the large uptake of BSS methods, particularly ICA and to a lesser extent PCA, for BCG removal (**Figure 5**). When ICA was used in conjunction with another method, total reported use of ICA was over 15%. Our guidelines recommend use of ICA only in conjunction with, and after, another method, due to the likelihood of either under- or over-removal of BCG (76, 94, 119).

BCG artifact is most commonly measured by separate ECG channel, with around two-thirds of studies included in the review reporting collection of ECG data (see **Supplementary Material**). In comparison, only 11% of studies reported using physiological monitoring such as a respiratory band or pulse. Nine percent of studies used external hardware, such as modified EEG caps, wire loops, and/or external sensors such as cameras, for measuring artifact occurring at the head (see **Supplementary Material**), yet of those, only 5% of studies reported using hardware for removing BCG (**Figure 5**). These results show that easy to implement techniques such as measuring ECG are more widely adopted than unique measures such as physiological monitoring and external hardware, despite the benefits of using external hardware. The technical expertise, money, time or skill in implementing additional artifact reduction hardware may be beyond the capacity of many researchers using EEG-fMRI.

Incorrectly removing artifact can lead to erroneous reporting of EEG results, incorrect mark-up of EEG events, and inaccurate

EEG-fMRI outcomes (135). Eighteen percent of studies are unclear or do not state the BCG reduction method used. Considering the importance of reproducibility in science and the need to be able to replicate studies, it is important that artifact reduction methods are implemented and fully described in the Methods section.

4.3. Motion Artifact

Gross head motion is that which involves potentially large, sudden head movements as well as slow changes to head position. Reducing gross head motion can be achieved by using restraints such as foam padding or a vacuum cushion around the subject's head (86). Foam padding or vacuum cushions are readily available with most MR systems and should be used when available.

In subject populations where gross head motion is expected (such as children), the use of additional monitors for motion could be useful. During post-processing, these measurements of head motion can be used to filter out motion artifact or exclude periods of data if motion is considerable. Motion monitoring can be in the form of an Optical Motion Tracking system for whole head movement (45, 136) or indirect measurement of motion using an MR compatible camera (137). In addition, techniques used to directly measure BCG-related artifact (as outlined in section 4.2.3) can also be used to filter out gross head motion. A recent study (138) compared an Optical Motion Tracking system (MPT) (139) and two direct artifact recording methods: a reference layer cap (129) and isolation of electrodes from the scalp (123). The direct artifact recording measures both outperformed the MPT in reducing artifact during different tasks and different types of motion (138). Therefore, hardware to directly record artifact may be a good investment, as it is able to reduce both BCG and gross head motion artifact with greater accuracy than many data-driven methods (132, 136), and it may provide more accurate artifact estimation compared with motion detection hardware such as Optical Motion Tracking systems (138).

For studies where the subject has their eyes open, recording the EOG may be helpful for measuring eye movement (137). In the literature search conducted, no papers specifically dealt with removal techniques for EOG artifact from EEG-fMRI datasets. There are, however, many papers that describe removal techniques for EOG artifact from datasets recorded outside the MRI environment [for a recent review, see (138)]. These methods are likely also suitable for within-MRI recording, provided that GA and BCG artifact are adequately removed in previous steps. In the MRI scanner, the electrodes positioned near the orbits may exhibit additional localized motion artifact due to eye movement, as well as the concomitant EOG signal, potentially aiding in detection of such events.

4.3.1. Recommendations for Reducing Motion Artifact

Recommendations for Reducing Motion Artifact in EEG-fMRI:

- Use of head restraints such as foam pads or vacuum cushion for all studies
- Additional hardware to measure motion should be considered:
    - In eyes open studies, use of EOG electrode to measure eye blink movement.
    - In all studies, direct artifact measurements, such as EEG cap alterations or additional sensors such as carbon fiber loops (see section 4.2.3), are recommended as they can deal with head motion, BCG, and residual GA. Indirect methods such as MR-compatible camera recordings or Optical Motion Tracking may also be useful for dealing with motion-related artifact.

4.3.2. Contemporary Use of Motion Artifact Removal Methods

Almost 70% of contemporary studies mentioned removal of motion, or residual artifact that might be still present in EEG, even after GA and BCG removal (for all data, see **Supplementary Material**). Residual artifact, including motion, was dealt with by using some form of ICA, in around one-third of studies, while other data-driven post-processing methods for reducing motion were used in 15 % of studies. For reducing motion artifact exclusively, the most reported method, as seen in 23% of studies, was using head restraints such as foam pillows or a vacuum cushion. Also popular was the technique of removing artifact from studies by visual inspection of motion-related time points and excluding data during post-processing, which was reported in 16% of studies. The most common form of additional hardware reported was MR compatible cameras or video systems (4%), followed by motion loops and modified EEG caps (5% combined). A small percentage of studies used an external calibration of eye blinks to reduce artifact from eye movement in their studies. It is also worth noting that 5 studies, or 2%, reported that the subjects were sedated during the EEG-fMRI study, and therefore did not record motion. However, sedation does not remove BCG artifact or potential environmental sources of motion (see section 4.4), so we would recommend direct recording of head motion artifact even when subjects are sedated.

Compared with our recommendations, less than a quarter of studies have reported reducing motion through simple measures such as head restraints, for example, foam padding or vacuum cushions. Additionally, the uptake of hardware such as motion loops or modified EEG caps for recording motion are very limited, at only 5% of all studies. While a camera or video monitoring system (4% of all studies) can be good for indirectly measuring motion and therefore excluding periods of high motion, direct motion monitoring systems allow the user to directly record, and remove artifact directly occurring at the head. A greater uptake of direct recording systems in the future could allow an improvement in EEG-fMRI studies through reduction of motion artifact.

TABLE 1 | Examples of commonly cited toolboxes for removing artifact from EEG recorded during fMRI.

Toolbox	Manufacturer	Cost	Web link	Notes
Brain Vision Analyzer	Brain Products	Paid software, requires license	https://www.brainproducts.com/analyzer2_release.php	Standalone software for processing EEG. Typically purchased together with BrainProducts hardware.
Netstation	Magstim EGI	Paid software, requires license	https://www.egi.com/research-division/net-station-eeg-software	Standalone software for processing EEG. Typically purchased together with Magstim EGI hardware.
Curry	Compumedics Neuroscan	Paid Software, requires license	https://www.compumedics.com.au/en/products/curry/	Standalone software for processing EEG. Typically purchased together with Compumedics hardware.
EEGLAB	Swartz Center for Computational Neuroscience, University of California	Free and open source, requires Matlab (see below)	https://sccn.ucsd.edu/eeglab	Free toolbox for MATLAB, contains many useful EEG filtering tools, as well as additional plug ins specific to filtering fMRI artifact from EEG. Toolboxes include: • FMRIB plug in (http://fsl.fmrib.ox.ac.uk/eeglab/fmribplugin/) • BERGEN (may no longer be supported, still listed on the EEGLAB plug-in site).
MATLAB	Mathworks	Paid software, requires license	https://au.mathworks.com/products/matlab.html	General analysis software environment. User can write their own code for filtering the EEG, or combine custom code with the output from EEGLAB toolbox (see above).

4.4. Environmental Artifact

While the noise from gradient, cardio-ballistic, and subject motion are the main sources of artifact in EEG-fMRI, noise from the MRI environment such as power line noise, lights, and ventilation are also a problem that few studies have addressed (18). Of all the possible environmental sources of noise, the ventilation system and helium cooling pump have been shown produce the most noise (33), which is thought to be mainly due to small vibrations that induce motion, and therefore voltage, in EEG electrodes. Environmental artifact can be avoided by turning off electrical equipment which is unnecessary during scanning, if possible and safe to do so (18). Artifacts can also be reduced by altering the setup of some equipment, specifically by reducing the vibration artifact on EEG cabling. EEG leads and amplifiers should be isolated from the scanner bore in order to reduce direct transfer of vibration, and methods such as using sand or rice bags (86, 140), or a cantilever beam (141), will improve stability and restrict the motion of the EEG cables connecting the EEG cap and amplifiers.

For setups where the helium pump and ventilation cannot be turned off for the duration of the study (e.g., due to safety concerns or the length of the scan), and environmental artifact is shown to negatively affect the quality of the EEG, the use of direct artifact recording, or post-processing methods for removing environmental artifact should be considered. Template measures such as AAS have been shown to reduce ventilation and helium cooling pump noise compared with no intervention (142), while another study has shown that a BSS algorithm, recursive, Segmented PCA (rsPCA), is able to reduce MRI helium pump noise (14). Alternatively, direct artifact recording measures, such as carbon wire loops (section 4.2.3), have also been shown to adequately remove helium pump artifacts, with filtering using carbon wire loops showing less residual helium pump artifact in comparison to AAS, OBS, or OBS-ICA artifact reduction pipelines (132).

While altering the setup of the EEG-fMRI study to reduce vibrational artifact is relatively easy to implement, the choice to include additional hardware or post-processing steps for reducing MR helium pump and ventilation noise will depend on the residual artifact seen in the individual scanner setup, and whether it is likely to adversely affect the outcome of the study.

4.4.1. Recommendations for Reducing Environmental Artifact

Recommendations for Reducing Environmental Artifact in EEG-fMRI:

- EEG leads and amplifiers should be secured along the center of the bore using one of:
    - Sand or rice bags, or
    - Cantilever beam (141)
- If safe to do so, MR helium cooling pump and scanner ventilation could be turned off for the duration of the scan.
- If environmental artifact is expected to interfere with the EEG of interest, using carbon wire loops (55, 132) will directly record this artifact, enabling its removal via adaptive filtering.
    - If carbon wire loops are not available, using AAS or PCA methods during post-processing may help reduce residual environmental artifact.

4.4.2. Contemporary Use of Environmental Artifact Reduction Methods

In contemporary literature of EEG-fMRI studies, consideration of environmental artifact was reported in only 22% of studies (see **Supplementary Material**), with the few studies reporting mitigation of environmental artifact using methods to reduce

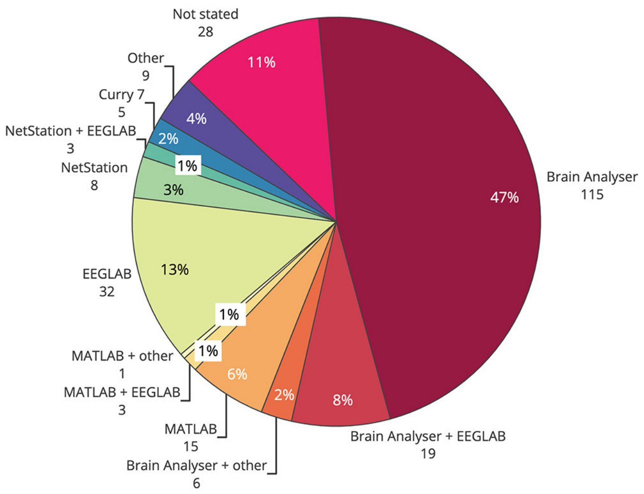

FIGURE 6 | Use of software toolboxes for filtering artifact from EEG collected during fMRI, papers published 2016–2019 (*n* = 244).

EEG cable vibrations (7 %) and either: optimizing amplifier placement, or turning off lights during the experiment (11%). Despite literature suggesting that the helium cooling pump and scanner ventilation system may affect EEG-fMRI recordings (18), only around 5% of studies report taking steps to turn off, measure, or reduce, the effects of these artifacts, respectively. Only one study in the cohort reported use of a post-processing method (13) for removing helium pump artifact. Although environmental artifact may be reduced during other post-processing methods for removal of GA and BCG, and environmental artifact may not interfere with the EEG correlate of interest in the study, there appears to be a lack of awareness of this potential artifact within the wider research community.

4.5. Artifact Removal Toolboxes: Contemporary Usage

Commercial EEG-fMRI systems may influence the choice of artifact reduction method used in any particular study. An overview of common toolboxes, and where to find them, is presented in **Table 1**. Brain Vision Analyser, from Brain Products, was the most widely used single toolbox for removal of artifact in EEG-informed fMRI (**Figure 6**), with over half of studies published using the software for at least part of the filtering. EEGLAB, a toolbox requiring MATLAB, was the second most used software, with over 20% of all studies reporting its use in some part of their processing. Given that Brain Vision Analyzer as standard employs AAS for gradient and BCG correction, and that OBS is available as a plug in for EEGLAB (FMRIB plug in), the results of toolbox use show a similarity between the use of methods and their software. Given that most researchers are time poor and may not have the technical expertise to test different artifact reduction methods, the most commonly used methods are the ones that are readily available and easy to access. Therefore, it is crucial that developers of new EEG-fMRI artifact removal algorithms consider the functionality and ease of use for the end users of any new software or algorithms.

4.6. Overall Recommendations for Artifact Reduction in EEG-fMRI

Figure 7 provides an overview of the recommendations for EEG-fMRI artifact removal based on the current literature review. These recommendations include steps that all EEG-fMRI users should take to avoid artifacts in the recording, as well as 3–4 questions that users can ask to make the best possible decisions for removing artifact during post-processing, depending on the study design and hardware available. These recommendations represent the combination of all recommendations from previous sections of this review (gradient, BCG, motion, and environmental artifact).

A limitation of the current study is that there is no distinction between the so-called "online" and "offline" artifact reduction techniques. Online artifact reduction refers to the filtering of artifact from EEG recording during fMRI in as close to real time as possible, whereas offline artifact removal undertaken at the conclusion of the data collection. For this review, it is assumed that the EEG-fMRI study is designed in such a way that the researcher has ample time to filter and interpret EEG (offline artifact removal), gaining results from the study well after the subject has left the room. However, for certain study designs, such as neurofeedback studies (143), clean EEG is required with as little lag time as possible, so that data are available during the study, and therefore, online reduction is required. Several studies have adapted common artifact reduction methods for real-time use, including AAS (144, 145), OBS (92), and FT (68). Online artifact reduction prioritizes computational efficiency and speed over accuracy of the artifact reduction on EEG, and therefore, some recommendations given in this review will not be relevant for studies of this design.

Another aspect of the current review not yet discussed is that the EEG measure of interest varies between different studies. In our survey of contemporary EEG-fMRI literature, the most popular EEG measurements were epilepsy-related EEG events, event-related potentials, and EEG power bands (see section 6.5 in **Supplementary Material** for more detailed information). This creates a question as to whether there is a need for high level artifact removal in all studies, or whether basic removal of artifacts may be enough to see the EEG measure of interest. There is, however, always a risk that using sub-optimal artifact removal will result in false positive EEG features being reported. Evidence from literature shows, for example, that marking motion in EEG as though it is an effect of interest may lead to plausible looking networks in the subsequent fMRI analysis (135). We recommend that EEG-fMRI users should employ the best possible EEG setup and artifact removal possible to reduce the chances of false positive EEG features being reported. While not all scientists will have access to the hardware components mentioned in **Figure 7**, we have endeavored to include alternative methods, so that all users of EEG-fMRI can have the best chance of producing accurate and reproducible results.

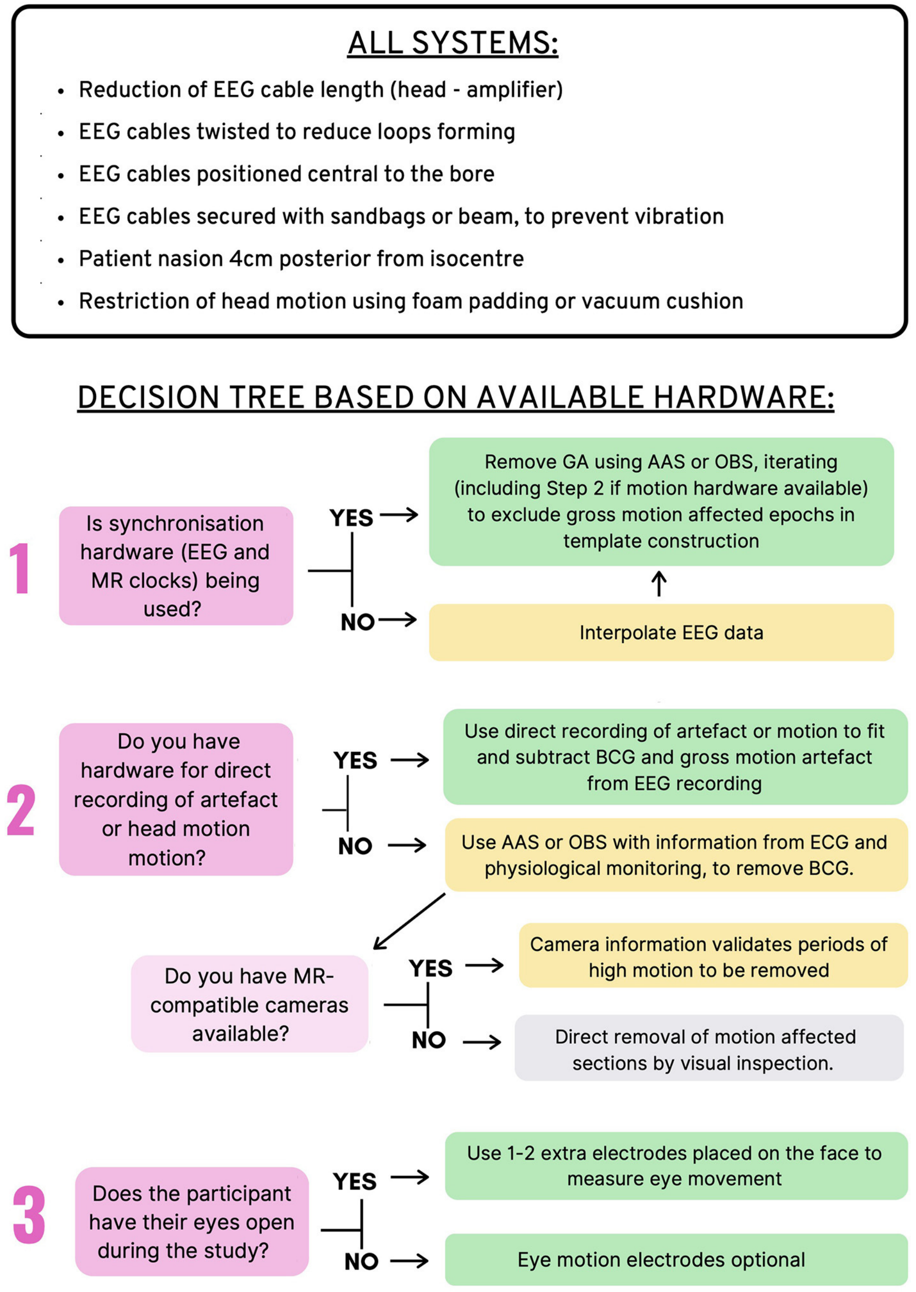

ALL SYSTEMS:

- Reduction of EEG cable length (head - amplifier)
- EEG cables twisted to reduce loops forming
- EEG cables positioned central to the bore
- EEG cables secured with sandbags or beam, to prevent vibration
- Patient nasion 4cm posterior from isocentre
- Restriction of head motion using foam padding or vacuum cushion

FIGURE 7 | Recommendations for Removal of artifact in EEG-fMRI studies. **Top:** Recommendations for all EEG-fMRI setups; **Bottom:** Recommendations based on hardware available and study design.

5. CONCLUSIONS

There are many published artifact removal methods for EEG-fMRI, however, uptake of newer methods in contemporary studies is limited. In addition, many novel methods have been proposed that have not been adequately compared with the currently available methods on independent datasets. Our review provides a comprehensive overview of all artifact reduction methods available since 1998 (see **Supplementary Material**), and there is an opportunity for future studies to compare these different methods in one comprehensive data set to independently validate the best pipeline for artifact reduction in EEG-fMRI.

Best practice EEG-fMRI artifact reduction relies largely on using additional hardware to synchronize clocks, and to directly record artifact at the head, including motion, vibration, and eye blinks. Without monitoring from hardware during EEG-fMRI studies, the researcher is making assumptions as to which aspects of the recording represent artifact, and which represent plausible neuronal activity. However, our review of the contemporary literature showed that reported use of synchronization hardware cited in less than 50% of studies, and reported use of hardware to directly measure artifact was even less frequently cited (less than 10% of studies, see **Supplementary Material**). Actual use may be higher in practice, but cannot be included in these statistics due to lack of reporting in the literature. Software used for filtering EEG showed a preference for BrainVision Analyser and EEGLAB, and it is likely that the ease of use of these packages played a role in their wide use. Therefore, it can be hypothesized that the lack of accessibility of direct artifact recording measures is hampering their use in contemporary studies, despite literature showing that their use may result in more accurate EEG-fMRI studies (120). Compared with synchronization hardware, which is included in some commercial EEG-fMRI setups, direct artifact recording has not been available commercially, leaving it up to researchers to bear the cost should they wish to directly record artifact using hardware.

Overall, there appears to be a basic understanding in contemporary EEG-fMRI studies about the importance of reducing artifact, especially for gradient and BCG artifacts. However, there was almost 15% of contemporary studies that did not adequately report artifact reduction methods for GA and BCG, and very few studies reported methods to avoid or reduce motion and environmental artifacts at all. A review such as this, and indeed reproducible science, is limited by the extent to which researchers accurately and completely report their methods. We would encourage authors publishing EEG-fMRI results to fully report all measures taken to reduce artifact to help make their research as reproducible as possible. We recommend authors consider the recommendations from the Organization for Human Brain Mapping's Committee on Best Practices in Data Analysis and Sharing (COBIDAS) for reproducible EEG and MEG research (146). If a journal word-count limit makes this difficult in a main manuscript, then authors should consider including detailed methods in **Supplementary Information**.

This review provides recommendations for artifact reduction in EEG-fMRI in an easy to understand way for all users of EEG-fMRI (see **Figure 7**). We suggest that wider use of hardware methods such as clock synchronization and direct artifact recording is the easiest way to improve data accuracy in EEG-fMRI studies, but seeing adoption of hardware methods requires input from all EEG-fMRI stakeholders—from methods developers, vendors, and end users.

DATA AVAILABILITY STATEMENT

The original contributions generated for the study are included in the article/**Supplementary Material**, further inquiries can be directed to the corresponding author/s.

AUTHOR CONTRIBUTIONS

MB conducted the literature search. MB and DA contributed to the manuscript preparation. MB, DA, and GJ revised the manuscript. All authors read and approved the final manuscript.

FUNDING

This work was supported by the National Health and Medical Research Council of Australia (Program Grant 1091593). MB was supported by a Commonwealth Government Research Training Program scholarship, and Fay Marles Scholarship from the University of Melbourne. DA was supported by fellowship funding from the Australian National Imaging Facility. The Florey Institute of Neuroscience and Mental Health acknowledges the strong support from the Victorian Government and in particular the funding from the Operational Infrastructure Support Grant.

SUPPLEMENTARY MATERIAL

The Supplementary Material for this article can be found online at: https://www.frontiersin.org/articles/10.3389/fneur.2021.622719/full#supplementary-material

REFERENCES

1. Ives JR, Warach S, Schmitt F, Edelman RR, Schomer DL. Monitoring the patient's EEG during echo planar MRI. *Electroencephalogr Clin Neurophysiol*. (1993) 87:417–20. doi: 10.1016/0013-4694(93)90156-P
2. Warach S, Ives JR, Schlaug G, Patel MR, Darby DG, Thangaraj V, et al. EEG-triggered echo-planar functional MRI in epilepsy. *Neurology*. (1996) 47:89–93. doi: 10.1212/WNL.47.1.89
3. Ritter P, Villringer A. Simultaneous EEG-fMRI. *Neurosci Biobehav Rev*. (2006) 30:823–38. doi: 10.1016/j.neubiorev.2006.06.008
4. Manganas S, Bourbakis N. A Comparative survey on simultaneous EEG-fMRI methodologies. In: *2017 IEEE 17th International Conference on Bioinformatics and Bioengineering (BIBE)*. New York, NY: IEEE (2017). p. 1–8. doi: 10.1109/BIBE.2017.00-87
5. Baenninger A, Diaz Hernandez L, Rieger K, Ford JM, Kottlow M, Koenig T. Inefficient preparatory fMRI-BOLD network activations predict working memory dysfunctions in patients with schizophrenia. *Front. Psychiatry*. (2016) 7:29. doi: 10.3389/fpsyt.2016.00029
6. Ford JM, Roach BJ, Palzes VA, Mathalon DH. Using concurrent EEG and fMRI to probe the state of the brain in schizophrenia. *Neuroimage Clin*. (2016) 12:429–41. doi: 10.1016/j.nicl.2016.08.009
7. Pisauro MA, Fouragnan E, Retzler C, Philiastides MG. Neural correlates of evidence accumulation during value-based decisions revealed via simultaneous EEG-fMRI. *Nat Commun*. (2017) 8:15808. doi: 10.1038/ncomms15808
8. Muraskin J, Brown TR, Walz JM, Tu T, Conroy B, Goldman RI, et al. A multimodal encoding model applied to imaging decision-related neural cascades in the human brain. *Neuroimage*. (2018) 180:211–22. WOS:000443268900021. doi: 10.1016/j.neuroimage.2017.06.059
9. Bagshaw AP, Hale JR, Campos BM, Rollings DT, Wilson RS, Alvim MKM, et al. Sleep onset uncovers thalamic abnormalities in patients with idiopathic generalised epilepsy. *Neuroimage Clin*. (2017) 16:52–7. doi: 10.1016/j.nicl.2017.07.008
10. Hsiao FC, Tsai PJ, Wu CW, Yang CM, Lane TJ, Lee HC, et al. The neurophysiological basis of the discrepancy between objective and subjective sleep during the sleep onset period: an EEG-fMRI study. *Sleep*. (2018) 41:zsy056. doi: 10.1093/sleep/zsy056

11. Abreu R, Leal A, Lopes da Silva F, Figueiredo P. EEG synchronization measures predict epilepsy-related BOLD-fMRI fluctuations better than commonly used univariate metrics. *Clin Neurophysiol*. (2018) 129:618–35. doi: 10.1016/j.clinph.2017.12.038
12. Moosmann M, Schonfelder VH, Specht K, Scheeringa R, Nordby H, Hugdahl K. Realignment parameter-informed artefact correction for simultaneous EEG-fMRI recordings. *Neuroimage*. (2009) 45:1144–50. doi: 10.1016/j.neuroimage.2009.01.024
13. Rothlubbers S, Relvas V, Leal A, Murta T, Lemieux L, Figueiredo P. Characterisation and reduction of the EEG artefact caused by the helium cooling pump in the MR environment: validation in epilepsy patient data. *Brain Topogr*. (2015) 28:208–20. doi: 10.1007/s10548-014-0408-0
14. Kim HC, Yoo SS, Lee JH. Recursive approach of EEG-segment-based principal component analysis substantially reduces cryogenic pump artifacts in simultaneous EEG-fMRI data. *Neuroimage*. (2015) 104:437–51. doi: 10.1016/j.neuroimage.2014.09.049
15. Allen PJ, Josephs O, Turner R. A method for removing imaging artifact from continuous EEG recorded during functional MRI. *Neuroimage*. (2000) 12:230–9. doi: 10.1006/nimg.2000.0599
16. Yan WX, Mullinger KJ, Brookes MJ, Bowtell R. Understanding gradient artefacts in simultaneous EEG/fMRI. *Neuroimage*. (2009) 46:459–71. doi: 10.1016/j.neuroimage.2009.01.029
17. Yan WX, Mullinger KJ, Geirsdottir GB, Bowtell R. Physical modeling of pulse artefact sources in simultaneous EEG/fMRI. *Hum Brain Mapp*. (2010) 31:604–20. doi: 10.1002/hbm.20891
18. Nierhaus T, Gundlach C, Goltz D, Thiel SD, Pleger B, Villringer A. Internal ventilation system of MR scanners induces specific EEG artifact during simultaneous EEG-fMRI. *Neuroimage*. (2013) 74:70–6. doi: 10.1016/j.neuroimage.2013.02.016
19. Allen PJ, Polizzi G, Krakow K, Fish DR, Lemieux L. Identification of EEG events in the MR scanner: the problem of pulse artifact and a method for its subtraction. *Neuroimage*. (1998) 8:229–39. doi: 10.1006/nimg.1998.0361
20. Abreu R, Leal A, Figueiredo P. EEG-informed fMRI: a review of data analysis methods. *Front Hum Neurosci*. (2018) 12:29. doi: 10.3389/fnhum.2018.00029
21. Mullinger KJ, Castellone P, Bowtell R. Best current practice for obtaining high quality EEG data during simultaneous fMRI. *J Visual Exp*. (2013) 76:e50283. doi: 10.3791/50283
22. Jorge J, Grouiller F, Ipek Z, Stoermer R, Michel CM, Figueiredo P, et al. Simultaneous EEG-fMRI at ultra-high field: Artifact prevention and safety assessment. *Neuroimage*. (2015) 105:132–44. doi: 10.1016/j.neuroimage.2014.10.055
23. Thornton RC, Graan LAv, Powell RH, Lemieux L. fMRI in epilepsy. In: Filippi M, editor. *fMRI Techniques and Protocols. Neuromethods*. New York, NY: Humana Press (2016). p. 741–99. doi: 10.1007/978-1-4939-5611-1_24
24. Schrooten M, Vandenberghe R, Peeters R, Dupont P. Quantitative analyses help in choosing between simultaneous vs. separate EEG and fMRI. *Front Neurosci*. (2019) 12:1009. doi: 10.3389/fnins.2018.01009
25. Moher D, Liberati A, Tetzlaff J, Altman DG. Preferred reporting items for systematic reviews and meta-analyses: the PRISMA statement. *BMJ*. (2009) 339:b2535. doi: 10.1136/bmj.b2535
26. Hoffmann A, Jager L, Werhahn KJ, Jaschke M, Noachtar S, Reiser M. Electroencephalography during functional echo-planar imaging: detection of epileptic spikes using post-processing methods. *Magnet Reson Med*. (2000) 44:791–98. doi: 10.1002/1522-2594(200011)44:5<791::AID-MRM17>3.0.CO;2-2
27. Anami K, Mori T, Tanaka F, Kawagoe Y, Okamoto J, Yarita M, et al. Stepping stone sampling for retrieving artifact-free electroencephalogram during functional magnetic resonance imaging. *Neuroimage*. (2003) 19(2 Pt 1):281–95. doi: 10.1016/S1053-8119(03)00048-X
28. Warbrick T, Bagshaw AP. Scanning strategies for simultaneous EEG-fMRI evoked potential studies at 3 T. *Int J Psychophysiol*. (2008) 67:169–77. doi: 10.1016/j.ijpsycho.2007.05.014
29. Mandal R, Babaria N, Cao J, Liu Z. Adaptive and wireless recordings of electrophysiological signals during concurrent magnetic resonance imaging. *IEEE Trans Biomed Eng*. (2019) 66:1649–57. doi: 10.1109/TBME.2018.2877640
30. Goldman RI, Stern JM, Engel J, Cohen MS. Acquiring simultaneous EEG and functional MRI. *Clin Neurophysiol*. (2000) 111:1974–80. doi: 10.1016/S1388-2457(00)00456-9
31. Allen EA, Damaraju E, Eichele T, Wu L, Calhoun VD. EEG signatures of dynamic functional network connectivity states. *Brain Topogr*. (2018) 31:101–16. doi: 10.1007/s10548-017-0546-2
32. Chowdhury MEH, Mullinger KJ, Bowtell R. Simultaneous EEG-fMRI: evaluating the effect of the cabling configuration on the gradient artefact. *Phys Med Biol*. (2015) 60:N241–50. doi: 10.1088/0031-9155/60/12/N241
33. Assecondi S, Lavallee C, Ferrari P, Jovicich J. Length matters: Improved high field EEG-fMRI recordings using shorter EEG cables. *J Neurosci Methods*. (2016) 269:74–87. doi: 10.1016/j.jneumeth.2016.05.014
34. Mullinger KJ, Chowdhury MEH, Bowtell R. Investigating the effect of modifying the EEG cap lead configuration on the gradient artifact in simultaneous EEG-fMRI. *Front Neurosci*. (2014) 8:226. doi: 10.3389/fnins.2014.00226
35. Chowdhury MEH, Khandakar A, Mullinger KJ, Al-Emadi N, Bowtell R. Simultaneous EEG-fMRI: evaluating the effect of the EEG cap-cabling configuration on the gradient artifact. *Front Neurosci*. (2019) 13:90. doi: 10.3389/fnins.2019.00690
36. Mullinger KJ, Yan WX, Bowtell R. Reducing the gradient artefact in simultaneous EEG-fMRI by adjusting the subject's axial position. *Neuroimage*. (2011) 54:1942–50. doi: 10.1016/j.neuroimage.2010.09.079
37. Laufs H, Daunizeau J, Carmichael DW, Kleinschmidt A. Recent advances in recording electrophysiological data simultaneously with magnetic resonance imaging. *Neuroimage*. (2008) 40:515–28. doi: 10.1016/j.neuroimage.2007.11.039
38. Mandelkow H, Halder P, Boesiger P, Brandeis D. Synchronization facilitates removal of MRI artefacts from concurrent EEG recordings and increases usable bandwidth. *Neuroimage*. (2006) 32:1120–6. doi: 10.1016/j.neuroimage.2006.04.231
39. Mullinger KJ, Morgan PS, Bowtell RW. Improved artifact correction for combined electroencephalography/functional MRI by means of synchronization and use of vectorcardiogram recordings. *J Magnet Reson Imaging*. (2008) 27:607–16. doi: 10.1002/jmri.21277
40. Gebhardt H, Blecker CR, Bischoff M, Morgen K, Oschmann P, Vaitl D, et al. Synchronized measurement of simultaneous EEG-fMRI: a simulation study. *Clin Neurophysiol*. (2008) 119:2703–11. doi: 10.1016/j.clinph.2008.09.018
41. Goncalves SI, Pouwels PJW, Kuijer JPA, Heethaar RM, de Munck JC. Artifact removal in co-registered EEG/fMRI by selective average subtraction. *Clin Neurophysiol*. (2007) 118:2437–50. doi: 10.1016/j.clinph.2007.08.017
42. Mandelkow H, Brandeis D, Boesiger P. Good practices in EEG-MRI: The utility of retrospective synchronization and PCA for the removal of MRI gradient artefacts. *Neuroimage*. (2010) 49:2287–303. doi: 10.1016/j.neuroimage.2009.10.050
43. Koskinen M, Vartiainen N. Removal of imaging artifacts in EEG during simultaneous EEG/fMRI recording: reconstruction of a high-precision artifact template. *Neuroimage*. (2009) 46:160–7. doi: 10.1016/j.neuroimage.2009.01.061
44. Tan A, Tu Y, Fu Z, Huang G, Hung YS, Zhang Z. A least across-segment variance (LASV) method for the correction of EEG-fMRI desynchronization. In: *2017 8th International IEEE/EMBS Conference on Neural Engineering (NER)*. New York, NY: IEEE (2017). p. 5–8. doi: 10.1109/NER.2017.8008278
45. LeVan P, Zhang S, Knowles B, Zaitsev M, Hennig J. EEG-fMRI gradient artifact correction by multiple motion-related templates. *IEEE Trans Biomed Eng*. (2016) 63:2647–53. doi: 10.1109/TBME.2016.2593726
46. de Munck JC, van Houdt PJ, Goncalves SI, van Wegen E, Ossenblok PPW. Novel artefact removal algorithms for co-registered EEG/fMRI based on selective averaging and subtraction. *Neuroimage*. (2013) 64:407–15. doi: 10.1016/j.neuroimage.2012.09.022
47. Zhang S, Hennig J, LeVan P. Direct modelling of gradient artifacts for EEG-fMRI denoising and motion tracking. *J Neural Eng*. (2019) 16:056010. doi: 10.1088/1741-2552/ab2b21
48. Steyrl D, Mueller-Rutz GR. Artifacts in EEG of simultaneous EEG-fMRI: pulse artifact remainders in the gradient artifact template are a source of

artifact residuals after average artifact subtraction. *J Neural Eng*. (2019) 16:016011. doi: 10.1088/1741-2552/aaec42

49. Ferreira JL, Aarts RM, Cluitmans PJM. Optimized moving-average filtering for gradient artefact correction during simultaneous EEG-fMRI. In: *5th ISSNIP-IEEE Biosignals and Biorobotics Conference. Biosignals and Robotics for Better and Safer Living*. New York, NY: IEEE (2014). p. 1–6. doi: 10.1109/BRC.2014.6880955
50. Freyer F, Becker R, Anami K, Curio G, Villringer A, Ritter P. Ultrahigh-frequency EEG during fMRI: pushing the limits of imaging-artifact correction. *Neuroimage*. (2009) 48:94–108. doi: 10.1016/j.neuroimage.2009.06.022
51. Sartori E, Formaggio E, Storti SF, Bertoldo A, Manganotti P, Fiaschi A, et al. Gradient artifact removal in co-registration EEG/fMRI. In: Dossel O, Schlegel WC, editors. *World Congress on Medical Physics and Biomedical Engineering*. New York, NY: Springer (2010). p. 1143-46. doi: 10.1007/978-3-642-03882-2_304
52. Huang CH, Ju MS, Lin CCK. A robust algorithm for removing artifacts in EEG recorded during FMRI/EEG study. *Comput Biol Med*. (2012) 42:458–67. doi: 10.1016/j.compbiomed.2011.12.014
53. Wan X, Iwata K, Riera J, Ozaki T, Kitamura M, Kawashima R. Artifact reduction for EEG/fMRI recording: nonlinear reduction of ballistocardiogram artifacts. *Clin Neurophysiol*. (2006) 117:668–80. doi: 10.1016/j.clinph.2005.12.015
54. Sun L, Hinrichs H. Simultaneously recorded EEG-fMRI: removal of gradient artifacts by subtraction of head movement related average artifact waveforms. *Hum Brain Mapp*. (2009) 30:3361–77. doi: 10.1002/hbm.20758
55. Abbott DF, Masterton RAJ, Archer JS, Fleming SW, Warren AEL, Jackson GD. Constructing carbon fiber motion-detection loops for simultaneous EEG-fMRI. *Front Neurol*. (2014) 5:260. doi: 10.3389/fneur.2014.00260
56. Chowdhury MEH, Khandakar A, Mullinger K, Hossain B, Al-Emadi N, Antunes A, et al. Reference layer artefact subtraction (RLAS): electromagnetic simulations. *IEEE Access*. (2019) 7:17882–95. doi: 10.1109/ACCESS.2019.2892766
57. Borga M, Knutsson H. *A Canonical Correlation Approach to Blind Source Separation*. (2001). p. 12. Available online at: https://www.researchgate.net/publication/239744723_A_Canonical_Correlation_Approach_to_Blind_Source_Separation.
58. Cichocki A, Rutkowski T, Siwek K. Blind signal extraction of signals with specified frequency band. In: *Proceedings of the 12th IEEE Workshop on Neural Networks for Signal Processing*. Bourlard H, Adali T, Bengio S, Larsen J, Douglas S, editors. New York, NY: IEEE (2002).
59. Ryali S, Glover GH, Chang C, Menon V. Development, validation, and comparison of ICA-based gradient artifact reduction algorithms for simultaneous EEG-spiral in/out and echo-planar fMRI recordings. *Neuroimage*. (2009) 48:348–61. doi: 10.1016/j.neuroimage.2009.06.072
60. Negishi M, Abildgaard M, Nixon T, Constable RT. Removal of time-varying gradient artifacts from EEG data acquired during continuous fMRI. *Clin Neurophysiol*. (2004) 115:2181–92. doi: 10.1016/j.clinph.2004.04.005
61. Li J, Chen Y, Taya F, Lim J, Wong K, Sun Y, et al. A unified canonical correlation analysis-based framework for removing gradient artifact in concurrent EEG/fMRI recording and motion artifact in walking recording from EEG signal. *Med Biol Eng Comput*. (2017) 55:1669–81. doi: 10.1007/s11517-017-1620-3
62. Jing M, Sanei S. Scanner artifact removal in simultaneous EEG-fMRI for epileptic seizure prediction. In: Tang YY, Wang SP, Lorette G, Yeung DS, Yan H, editors. *18th International Conference on Pattern Recognition*. Los Alamitos, CA: IEEE Computer Soc (2006). p. 722.
63. Niazy RK, Beckmann CF, Iannetti GD, Brady JM, Smith SM. Removal of FMRI environment artifacts from EEG data using optimal basis sets. *Neuroimage*. (2005) 28:720–37. doi: 10.1016/j.neuroimage.2005.06.067
64. Acharjee PP, Phlypo R, Wu L, Calhoun VD, Adali T. Independent vector analysis for gradient artifact removal in concurrent EEG-fMRI data. *IEEE Trans Biomed Eng*. (2015) 62:1750–8. doi: 10.1109/TBME.2015.2403298
65. Liu Z, de Zwart JA, van Gelderen P, Kuo LW, Duyn JH. Statistical feature extraction for artifact removal from concurrent fMRI-EEG recordings. *Neuroimage*. (2012) 59:2073–87. doi: 10.1016/j.neuroimage.2011.10.042
66. Grouiller F, Vercueil L, Krainik A, Segebarth C, Kahane P, David O. A comparative study of different artefact removal algorithms for EEG signals acquired during functional MRI. *Neuroimage*. (2007) 38:124–37. doi: 10.1016/j.neuroimage.2007.07.025
67. Ritter P, Becker R, Graefe C, Villringer A. Evaluating gradient artifact correction of EEG data acquired simultaneously with fMRI. *Magnet Reson Imaging*. (2007) 25:923–32. doi: 10.1016/j.mri.2007.03.005
68. Shaw SB. Real-time filtering of gradient artifacts from simultaneous EEG-fMRI data. In: *2017 International Workshop on Pattern Recognition in Neuroimaging (PRNI)*. New York, NY: IEEE (2017). doi: 10.1109/PRNI.2017.7981510
69. Platas-Garza MA, de la O Serna JA. Dynamic harmonic analysis through Taylor-Fourier transform. *IEEE Trans Instrument Meas*. (2011) 60:804–13. doi: 10.1109/TIM.2010.2064690
70. Frigo G, Narduzzi C. *EEG Gradient Artifact Removal by Compressive Sensing and Taylor-Fourier Transform*. New York, NY: IEEE (2014). doi: 10.1109/MeMeA.2014.6860079
71. Xu P, Chen H, Liu Z, Yao D. A new method based on sparse component decomposition to remove MRI artifacts in the continuous EEG recordings. In: *2005 27th Annual International Conference of the IEEE Engineering in Medicine and Biology Society*. New York, NY: IEEE (2005). p. 2006–8. WOS:000238998401248.
72. Glaser J, Beisteiner R, Bauer H, Fischmeister FPS. FACET - a "Flexible Artifact Correction and Evaluation Toolbox" for concurrently recorded EEG/fMRI data. *BMC Neurosci*. (2013) 14:138. doi: 10.1186/1471-2202-14-138
73. Shams N, Alain C, Strother S. Comparison of BCG artifact removal methods for evoked responses in simultaneous EEG-fMRI. *J Neurosci Methods*. (2015) 245:137–146. doi: 10.1016/j.jneumeth.2015.02.018
74. Ertl M, Kirsch V, Leicht G, Karch S, Olbrich S, Reiser M, et al. Avoiding the ballistocardiogram (BCG) artifact of EEG data acquired simultaneously with fMRI by pulse-triggered presentation of stimuli. *J Neurosci Methods*. (2010) 186:231–41. doi: 10.1016/j.jneumeth.2009.11.009
75. Mullinger KJ, Havenhand J, Bowtell R. Identifying the sources of the pulse artefact in EEG recordings made inside an MR scanner. *Neuroimage*. (2013) 71:75–83. doi: 10.1016/j.neuroimage.2012.12.070
76. van derperren K, De Vos M, Ramautar JR, Novitskiy N, Mennes M, Assecondi S, et al. Removal of BCG artifacts from EEG recordings inside the MR scanner: a comparison of methodological and validation-related aspects. *Neuroimage*. (2010) 50:920–34. doi: 10.1016/j.neuroimage.2010.01.010
77. Kustra AJL, Fernandes JM, Cunha JPS. EEG-fMRI ballistocardiogram removal: a new non-linear dynamic time warping approach. In: Katashev A, Dekhtyar Y, Spigulis J, editors. *14th Nordic-Baltic Conference on Biomedical Engineering and Medical Physics*. New York, NY: Springer (2008). p. 278–81. doi: 10.1007/978-3-540-69367-3_75
78. Kim KH, Yoon HW, Park HW. Improved ballistocardiac artifact removal from the electroencephalogram recorded in fMRI. *J Neurosci Methods*. (2004) 135:193–203. doi: 10.1016/j.jneumeth.2003.12.016
79. Vincent JL, Larson-Prior LJ, Zempel JM, Snyder AZ. Moving GLM ballistocardiogram artifact reduction for EEG acquired simultaneously with fMRI. *Clin Neurophysiol*. (2007) 118:981–98. doi: 10.1016/j.clinph.2006.12.017
80. Jorge J, Bouloc C, Brechet L, Michel CM, Gruetter R. Investigating the variability of cardiac pulse artifacts across heartbeats in simultaneous EEG-fMRI recordings: a 7T study. *Neuroimage*. (2019) 191:21–35. doi: 10.1016/j.neuroimage.2019.02.021
81. Ellingson ML, Liebenthal E, Spanaki MV, Prieto TE, Binder JR, Ropella KM. Ballistocardiogram artifact reduction in the simultaneous acquisition of auditory ERPS and fMRI. *Neuroimage*. (2004) 22:1534–42. doi: 10.1016/j.neuroimage.2004.03.033
82. Oh SS, Chung JY, Yoon HW, Park H. An accurate heart beat detection method in the EKG recorded in fMRI system. In: *2007 Annual International Conference of the IEEE Engineering in Medicine and Biology Society*. New York, NY: IEEE (2007). p. 656. doi: 10.1109/IEMBS.2007.4352375
83. Wen X, Kang M, Yao L, Zhao X. Real-time ballistocardiographic artifact reduction using the k-teager energy operator detector and multi-channel referenced adaptive noise cancelling. *Int J Imaging Syst Technol*. (2016) 26:209–15. doi: 10.1002/ima.22178
84. Oh SS, Han Y, Lee J, Yun SD, Kang JK, Lee EM, et al. A pulse artifact removal method considering artifact variations in the simultaneous

recording of EEG and fMRI. *Neurosci Res*. (2014) 81–82:42–50. doi: 10.1016/j.neures.2014.01.008

85. Pan J, Tompkins WJ. A real-time QRS detection algorithm. *IEEE Trans Biomed Eng*. (1985) 32:230–6. doi: 10.1109/TBME.1985.325532
86. Benar CG, Aghakhani Y, Wang Y, Izenberg A, Al-Asmi A, Dubeau F, et al. Quality of EEG in simultaneous EEG-fMRI for epilepsy. *Clin Neurophysiol*. (2003) 114:569–80. doi: 10.1016/S1388-2457(02)00383-8
87. Sun L, Rieger J, Hinrichs H. Maximum noise fraction (MNF) transformation to remove ballistocardiographic artifacts in EEG signals recorded during fMRI scanning. *Neuroimage*. (2009) 46:144–53. doi: 10.1016/j.neuroimage.2009.01.059
88. Javed E, Faye I, Malik AS, Abdullah JM. A Hybrid method to improve the reduction of ballistocardiogram artifact from EEG data. In: Loo CK, Yap KS, Wong KW, Teoh A, Huang K, editors. *Neural Information Processing (ICONIP 2014)*. Cham: Springer International Publishing Ag (2014). p. 186–93. doi: 10.1007/978-3-319-12640-1_23
89. Javed E, Faye I, Malik AS, Abdullah JM. *An EMD based Method for Reduction of Ballistocardiogram Artifact from EEG Studies of Evoked Potentials*. Amsterdam: Elsevier Science (2015). doi: 10.1109/ICMLA.2015.81
90. Javed E, Faye I, Malik AS, Abdullah JM. Reference-free reduction of ballistocardiogram artifact from EEG data using EMD-PCA. In: *2014 5th International Conference on Intelligent and Advanced Systems (ICIAS 2014)*. New York, NY: IEEE (2014). doi: 10.1109/ICIAS.2014.6869512
91. Javed E, Faye I, Malik AS, Abdullah JM. Removal of BCG artefact from concurrent fMRI-EEG recordings based on EMD and PCA. *J Neurosci Methods*. (2017) 291:150–65. doi: 10.1016/j.jneumeth.2017.08.020
92. Wu X, Wu T, Zhan Z, Yao L, Wen X. A real-time method to reduce ballistocardiogram artifacts from EEG during fMRI based on optimal basis sets (OBS). *Comput Methods Prog Biomed*. (2016) 127:114–25. doi: 10.1016/j.cmpb.2016.01.018
93. Marino M, Liu Q, Koudelka V, Porcaro C, Hlinka J, Wenderoth N, et al. Adaptive optimal basis set for BCG artifact removal in simultaneous EEG-fMRI. *Sci Rep*. (2018) 8:8902. doi: 10.1038/s41598-018-27187-6
94. Arrubla J, Neuner I, Dammers J, Breuer L, Warbrick T, Hahn D, et al. Methods for pulse artefact reduction: experiences with EEG data recorded at 9.4 T static magnetic field. *J Neurosci Methods*. (2014) 232:110–7. doi: 10.1016/j.jneumeth.2014.05.015
95. Srivastava G, Crottaz-Herbette S, Lau KM, Glover GH, Menon V. ICA-based procedures for removing ballistocardiogram artifacts from EEG data acquired in the MRI scanner. *Neuroimage*. (2005) 24:50–60. doi: 10.1016/j.neuroimage.2004.09.041
96. Mantini D, Perrucci MG, Cugini S, Ferretti A, Romani GL, Del Gratta C. Complete artifact removal for EEG recorded during continuous fMRI using independent component analysis. *Neuroimage*. (2007) 34:598–607. doi: 10.1016/j.neuroimage.2006.09.037
97. Debener S, Mullinger KJ, Niazy RK, Bowtell RW. Properties of the ballistocardiogram artefact as revealed by EEG recordings at 1.5, 3 and 7 T static magnetic field strength. *Int J Psychophysiol*. (2008) 67:189–99. doi: 10.1016/j.ijpsycho.2007.05.015
98. Abbasi O, Dammers J, Arrubla J, Warbrick T, Butz M, Neuner I, et al. Time-frequency analysis of resting state and evoked EEG data recorded at higher magnetic fields up to 9.4 T. *J Neurosci Methods*. (2015) 255:1–11. doi: 10.1016/j.jneumeth.2015.07.011
99. Briselli E, Garreffa G, Bianchi L, Bianciardi M, Macaluso E, Abbafati M, et al. An independent component analysis-based approach on ballistocardiogram artifact removing. *Magnet Reson Imaging*. (2006) 24:393–400. doi: 10.1016/j.mri.2006.01.008
100. Silva de Souza AC, Rodrigues GF, Callan D, Yehia HC. Analysis of the ballistocardiographic artifact removal in simultaneous EEG-fMRI recording using independent component analysis and coherence function. In: Herencsar N, Molnar K, editors. *2013 36th International Conference on Telecommunications and Signal Processing (TSP)*. New York, NY: IEEE (2013). p. 552–56. doi: 10.1109/TSP.2013.6613994
101. Abreu R, Leite M, Leal A, Figueiredo P. Objective selection of epilepsy-related independent components from EEG data. *J Neurosci Methods*. (2016) 258:67–78. doi: 10.1016/j.jneumeth.2015.10.003
102. Rasheed T, In MH, Lee YK, Lee S, Lee SY, Kim TS. Constrained ICA based ballistocardiogram and electro-oculogram artifacts removal from visual evoked potential EEG signals measured inside MRI. In: King I, Wang J, Chan L, Wang DL, editors. *Neural Information Processing, Pt 1, Proceedings*. Berlin: Springer-Verlag (2006). p. 1088-97. doi: 10.1007/11893028_121
103. Rasheed T, Lee YK, Lee SY, Kim TS. Attenuation of artifacts in EEG signals measured inside an MRI scanner using constrained independent component analysis. *Physiol Meas*. (2009) 30:387–404. doi: 10.1088/0967-3334/30/4/004
104. Leclercq Y, Balteau E, Dang-Vu T, Schabus M, Luxen A, Maquet P, et al. Rejection of pulse related artefact (PRA) from continuous electroencephalographic (EEG) time series recorded during functional magnetic resonance imaging (fMRI) using constraint independent component analysis (cICA). *Neuroimage*. (2009) 44:679–91. doi: 10.1016/j.neuroimage.2008.10.017
105. Wang K, Li W, Dong L, Zou L, Wang C. Clustering-constrained ICA for ballistocardiogram artifacts removal in simultaneous EEG-fMRI. *Front Neurosci*. (2018) 12:59. doi: 10.3389/fnins.2018.00059
106. Assecondi S, Van Hese P, Hallez H, D'Asseler Y, Lemahieu I, Bianchi AM, et al. *Ballistocardiographic Artifact Removal from Simultaneous EEG/FMRI Recording by Means of Canonical Correlation Analysis*. Setubal: Insticc-Inst Syst Technologies Information Control & Communication (2008).
107. Assecondi S, Vanderperren K, Novitskiy N, Ramautar JR, Fias W, Staelens S, et al. Effect of the static magnetic field of the MR-scanner on ERPs: evaluation of visual, cognitive and motor potentials. *Clin Neurophysiol*. (2010) 121:672–85. doi: 10.1016/j.clinph.2009.12.032
108. Assecondi S, Hallez H, Staelens S, Bianchi AM, Huiskamp GM, Lemahieu I. Removal of the ballistocardiographic artifact from EEG-fMRI data: a canonical correlation approach. *Phys Med Biol*. (2009) 54:1673–89. doi: 10.1088/0031-9155/54/6/018
109. Siniatchkin M, Moeller F, Jacobs J, Stephani U, Boor R, Wolff S, et al. Spatial filters and automated spike detection based on brain topographies improve sensitivity of EEG-fMRI studies in focal epilepsy. *Neuroimage*. (2007) 37:834–43. doi: 10.1016/j.neuroimage.2007.05.049
110. Ghaderi F, Nazarpour K, McWhirter JG, Sanei S. Removal of ballistocardiogram artifacts using the cyclostationary source extraction method. *IEEE Trans Biomed Eng*. (2010) 57:2667–76. doi: 10.1109/TBME.2010.2060334
111. Krishnaswamy P, Bonmassar G, Poulsen C, Pierce ET, Purdon PL, Brown EN. Reference-free removal of EEG-fMRI ballistocardiogram artifacts with harmonic regression. *Neuroimage*. (2016) 128:398–412. doi: 10.1016/j.neuroimage.2015.06.088
112. Mahadevan A, Acharya S, Sheffer DB, Mugler DH. Ballistocardiogram artifact removal in EEG-fMRI signals using discrete hermite transforms. *IEEE J Select Top Signal Process*. (2008) 2:839–53. doi: 10.1109/JSTSP.2008.2008367
113. Mahadevan A, Mugler DH, Acharya S. Adaptive filtering of ballistocardiogram artifact from EEG signals using the dilated discrete hermite transform. In: *2008 30th Annual International Conference of the IEEE Engineering in Medicine and Biology Society*. New York, NY: IEEE (2008). p. 2630. doi: 10.1109/IEMBS.2008.4649740
114. In MH, Lee SY, Park TS, Kim TS, Cho MH, Ahn YB. Ballistocardiogram artifact removal from EEG signals using adaptive filtering of EOG signals. *Physiol Meas*. (2006) 27:1227–40. doi: 10.1088/0967-3334/27/11/014
115. Sameni R, Shamsollahi MB, Jutten C. Model-based Bayesian filtering of cardiac contaminants from biomedical recordings. *Physiol Meas*. (2008) 29:595–613. doi: 10.1088/0967-3334/29/5/006
116. Abolghasemi V, Ferdowsi S. EEG-fMRI: Dictionary learning for removal of ballistocardiogram artifact from EEG. *Biomed Signal Process Control*. (2015) 18:186–94. doi: 10.1016/j.bspc.2015.01.001
117. Hoffmann S, Labrenz F, Themann M, Wascher E, Beste C. Crosslinking EEG time-frequency decomposition and fMRI in error monitoring. *Brain Struct Funct*. (2014) 219:595–605. doi: 10.1007/s00429-013-0521-y
118. Debener S, Kranczioch C, Gutberlet I. *EEG Quality: Origin and Reduction of the EEG Cardiac-Related Artefact*. Berlin: Springer-Verlag (2010). doi: 10.1007/978-3-540-87919-0_8
119. Debener S, Strobel A, Sorger B, Peters J, Kranczioch C, Engel AK, et al. Improved quality of auditory event-related potentials recorded simultaneously with 3-T fMRI: removal of the ballistocardiogram artefact. *Neuroimage*. (2007) 34:587–97. doi: 10.1016/j.neuroimage.2006.09.031

120. Hermans K, Munck JCD, Verdaasdonk R, Boon P, Krausz G, Prueckl R, et al. Effectiveness of reference signal-based methods for removal of EEG artifacts due to subtle movements during fMRI scanning. *IEEE Trans Biomed Eng*. (2016) 63:2638–46. doi: 10.1109/TBME.2016.2602038
121. Xia H, Ruan D, Cohen MS. Removing ballistocardiogram (BCG) artifact from full-scalp EEG acquired inside the MR scanner with Orthogonal Matching Pursuit (OMP). *Front Neurosci*. (2014) 8:218. doi: 10.3389/fnins.2014.00218
122. Xia H, Ruan D, Cohen MS. Separation and reconstruction of BCG and EEG signals during continuous EEG and fMRI recordings. *Front Neurosci*. (2014) 8:163. doi: 10.3389/fnins.2014.00163
123. Jorge J, Grouiller F, Gruetter R, van der Zwaag W, Figueiredo P. Towards high-quality simultaneous EEG-fMRI at 7T: detection and reduction of EEG artifacts due to head motion. *Neuroimage*. (2015) 120:143–53. doi: 10.1016/j.neuroimage.2015.07.020
124. Cohen N, Tsizin E, Fried I, Fahoum F, Hendler T, Gazit T, et al. Conductive gel bridge sensor for motion tracking in simultaneous EEG-fMRI recordings. *Epilepsy Res*. (2019) 149:117–22. doi: 10.1016/j.eplepsyres.2018.12.008
125. Klovatch-Podlipsky I, Gazit T, Fahoum F, Tsirelson B, Kipervasser S, Kremer U, et al. Dual array EEG-fMRI: an approach for motion artifact suppression in EEG recorded simultaneously with fMRI. *NeuroImage*. (2016) 142:674–86. doi: 10.1016/j.neuroimage.2016.07.014
126. Dyrholm M, Goldman R, Sajda P, Brown TR. Removal of BCG artifacts using a non-Kirchhoffian overcomplete representation. *IEEE Trans Biomed Eng*. (2009) 56:200–4. doi: 10.1109/TBME.2008.2005952
127. Luo Q, Huang X, Glover GH. Ballistocardiogram artifact removal with a reference layer and standard EEG cap. *J Neurosci Methods*. (2014) 233:137–49. doi: 10.1016/j.jneumeth.2014.06.021
128. Chowdhury MEH, Mullinger KJ, Glover P, Bowtell R. Reference layer artefact subtraction (RLAS): a novel method of minimizing EEG artefacts during simultaneous fMRI. *Neuroimage*. (2014) 84:307–19. doi: 10.1016/j.neuroimage.2013.08.039
129. Steyrl D, Krausz G, Koschutnig K, Edlinger G, Muller-Putz GR. Reference layer adaptive filtering (RLAF) for EEG artifact reduction in simultaneous EEG-fMRI. *J Neural Eng*. (2017) 14:026003. doi: 10.1088/1741-2552/14/2/026003
130. Iannotti GR, Pittau F, Michel CM, Vulliemoz S, Grouiller F. Pulse artifact detection in simultaneous EEG-fMRI recording based on EEG map topography. *Brain Topogr*. (2015) 28:21–32. doi: 10.1007/s10548-014-0409-z
131. Bonmassar G, Purdon PL, Jaaskelainen IP, Chiappa K, Solo V, Brown EN, et al. Motion and ballistocardiogram artifact removal for interleaved recording of EEG and EPs during MRI. *Neuroimage*. (2002) 16:1127–41. doi: 10.1006/nimg.2002.1125
132. van der Meer JN, Pampel A, Van Someren EJW, Ramautar JR, van der Werf YD, Gomez-Herrero G, et al. Carbon-wire loop based artifact correction outperforms post-processing EEG/fMRI corrections–A validation of a real-time simultaneous EEG/fMRI correction method. *Neuroimage*. (2016) 125:880–94. doi: 10.1016/j.neuroimage.2015.10.064
133. van der Meer JN, Pampel A, van Someren E, Ramautar J, van der Werf Y, Gomez-Herrero G, et al. "Eyes Open–Eyes Closed" EEG/fMRI data set including dedicated "Carbon Wire Loop" motion detection channels. *Data Brief*. (2016). 7:990–4. doi: 10.1016/j.dib.2016.03.001
134. Masterton RAJ, Abbott DF, Fleming SW, Jackson GD. Measurement and reduction of motion and ballistocardiogram artefacts from simultaneous EEG and fMRI recordings. *Neuroimage*. (2007) 37:202–11. doi: 10.1016/j.neuroimage.2007.02.060
135. Flanagan D, Abbott DF, Jackson GD. How wrong can we be? The effect of inaccurate mark-up of EEG/fMRI studies in epilepsy. *Clin Neurophysiol*. (2009) 120:1637–47. doi: 10.1016/j.clinph.2009.04.025
136. LeVan P, Maclaren J, Herbst M, Sostheim R, Zaitsev M, Hennig J. Ballistocardiographic artifact removal from simultaneous EEG-fMRI using an optical motion-tracking system. *Neuroimage*. (2013) 75:1–11. doi: 10.1016/j.neuroimage.2013.02.039
137. Ruggieri A, Vaudano AE, Benuzzi F, Serafini M, Gessaroli G, Farinelli V, et al. Mapping (and modeling) physiological movements during EEG-fMRI recordings: The added value of the video acquired simultaneously. *J Neurosci Methods*. (2015) 239:223–37. doi: 10.1016/j.jneumeth.2014.10.005
138. Daniel AJ, Smith JA, Spencer GS, Jorge J, Bowtell R, Mullinger KJ. Exploring the relative efficacy of motion artefact correction techniques for EEG data acquired during simultaneous fMRI. *Hum Brain Mapp*. (2019) 40:578–96. doi: 10.1002/hbm.24396
139. Maziero D, Velasco TR, Hunt N, Payne E, Lemieux L, Salmon CEG, et al. Towards motion insensitive EEG-fMRI: correcting motion-induced voltages and gradient artefact instability in EEG using an fMRI prospective motion correction (PMC) system. *Neuroimage*. (2016) 138:13–27. doi: 10.1016/j.neuroimage.2016.05.003
140. Kruggel F, Wiggins CJ, Herrmann CS, von Cramon DY. Recording of the event-related potentials during functional MRI at 3.0 Tesla field strength. *Magnet Reson Med*. (2000) 44:277–82. doi: 10.1002/1522-2594(200008)44:2<277::AID-MRM15>3.0.CO;2-X
141. Mullinger KJ, Brookes M, Stevenson C, Morgan P, Bowtell R. Exploring the feasibility of simultaneous electroencephalography/functional magnetic resonance imaging at 7 T. *Magnet Reson Imaging*. (2008) 26:968–77. doi: 10.1016/j.mri.2008.02.014
142. Rothluebbers S, Relvas V, Leal A, Figueiredo P. Characterization and reduction of MR-environment-related EEG artefacts. In: Sanches JM, Mico L, Cardoso JS, editors. *Pattern Recognition and Image Analysis, IBPRIA 2013*. Berlin: Springer-Verlag Berlin (2013). p. 808–18. doi: 10.1007/978-3-642-38628-2_96
143. Mano M, Lecuyer A, Bannier E, Perronnet L, Noorzadeh S, Barillot C. How to build a hybrid neurofeedback platform combining EEG and fMRI. *Front Neurosci*. (2017) 11:140. doi: 10.3389/fnins.2017.00140
144. Garreffa G, Carni M, Gualniera G, Ricci GB, Bozzao L, De Carli D, et al. Real-time MR artifacts filtering during continuous EEG/fMRI acquisition. *Magnet Reson Imaging*. (2003) 21:1175–189. doi: 10.1016/j.mri.2003.08.019
145. Gualniera G, Garreffa G, Morasso P, Carni M, Granozio G, Repetti A, et al. A method for real-time artifact filtering during simultaneous EEG/fMRI acquisition: preliminary results. *Neurocomputing*. (2004) 58:1171–9. doi: 10.1016/j.neucom.2004.01.182
146. Pernet C, Garrido MI, Gramfort A, Maurits N, Michel CM, Pang E, et al. Issues and recommendations from the OHBM COBIDAS MEEG committee for reproducible EEG and MEG research. *Nat Neurosci*. (2020) 23:1473–83. doi: 10.1038/s41593-020-00709-0

Conflict of Interest: The Florey Institute of Neuroscience and Mental Health acknowledges a partnership with Brain Products GmbH toward development of commercially available carbon wire loops (CWL) for direct artifact detection and correction. This includes work that was in part supported by an Australian Government Global Connections Fund Bridging Grant (Application number 279313678, awarded to DA).

The authors declare that the research was conducted in the absence of any other commercial or financial relationships that could be construed as a potential conflict of interest.

frontiers in Neurology

ORIGINAL RESEARCH
published: 26 April 2021
doi: 10.3389/fneur.2021.644874

Blind Visualization of Task-Related Networks From Visual Oddball Simultaneous EEG-fMRI Data: Spectral or Spatiospectral Model?

René Labounek[1]*, Zhuolin Wu[1,2], David A. Bridwell[3], Milan Brázdil[4], Jiří Jan[5] and Igor Nestrašil[1,6]*

[1] Division of Clinical Behavioral Neuroscience, Department of Pediatrics, University of Minnesota, Minneapolis, MN, United States, [2] Department of Biomedical Engineering, University of Minnesota, Minneapolis, MN, United States, [3] Mind Research Network, Albuquerque, NM, United States, [4] Central European Institute of Technology, Masaryk University, Brno, Czechia, [5] Department of Biomedical Engineering, Brno University of Technology, Brno, Czechia, [6] Center for Magnetic Resonance Research, Department of Radiology, University of Minnesota, Minneapolis, MN, United States

OPEN ACCESS

Edited by:
Brunno Machado De Campos,
State University of Campinas, Brazil

Reviewed by:
Elias Ebrahimzadeh,
Institute for Research in Fundamental Sciences (IPM), Iran
Jonas Vibell,
University of Hawaii, United States

***Correspondence:**
René Labounek
rlaboune@umn.edu
Igor Nestrašil
nestr007@umn.edu

Specialty section:
This article was submitted to Applied Neuroimaging, a section of the journal Frontiers in Neurology

Received: *22 December 2020*
Accepted: *22 March 2021*
Published: *26 April 2021*

Citation:
Labounek R, Wu Z, Bridwell DA, Brázdil M, Jan J and Nestrašil I (2021) Blind Visualization of Task-Related Networks From Visual Oddball Simultaneous EEG-fMRI Data: Spectral or Spatiospectral Model? Front. Neurol. 12:644874. doi: 10.3389/fneur.2021.644874

Various disease conditions can alter EEG event-related responses and fMRI-BOLD signals. We hypothesized that event-related responses and their clinical alterations are imprinted in the EEG spectral domain as event-related (spatio)spectral patterns (ERSPat). We tested four EEG-fMRI fusion models utilizing EEG power spectra fluctuations (i.e., absolute spectral model - ASM; relative spectral model - RSM; absolute spatiospectral model - ASSM; and relative spatiospectral model - RSSM) for fully automated and blind visualization of task-related neural networks. Two (spatio)spectral patterns (high δ_4 band and low β_1 band) demonstrated significant negative linear relationship ($p_{\mathrm{FWE}} < 0.05$) to the frequent stimulus and three patterns (two low δ_2 and δ_3 bands, and narrow θ_1 band) demonstrated significant positive relationship ($p < 0.05$) to the target stimulus. These patterns were identified as ERSPats. EEG-fMRI F-map of each δ_4 model showed strong engagement of insula, cuneus, precuneus, basal ganglia, sensory-motor, motor and dorsal part of fronto-parietal control (FPCN) networks with fast HRF peak and noticeable trough. ASM and RSSM emphasized spatial statistics, and the relative power amplified the relationship to the frequent stimulus. For the δ_4 model, we detected a reduced HRF peak amplitude and a magnified HRF trough amplitude in the frontal part of the FPCN, default mode network (DMN) and in the frontal white matter. The frequent-related β_1 patterns visualized less significant and distinct suprathreshold spatial associations. Each θ_1 model showed strong involvement of lateralized left-sided sensory-motor and motor networks with simultaneous basal ganglia co-activations and reduced HRF peak and amplified HRF trough in the frontal part of the FPCN and DMN. The ASM θ_1 model preserved target-related EEG-fMRI associations in the dorsal part of the FPCN. For δ_4, β_1, and θ_1 bands, all models provided high local F-statistics in expected regions. The most robust EEG-fMRI associations were observed for ASM and RSSM.

Keywords: simultaneous EEG-fMRI, task-related network visualization, spectral and spatiospectral models, visual oddball paradigm, general linear model, GLM, independent component analysis

INTRODUCTION

Ives et al. and Huang-Hellinger et al. optimized initial simultaneous EEG-fMRI data acquisition (1, 2) and Allen et al. and Goldman et al. implemented first algorithms suppressing gradient MR artifacts induced in the simultaneous EEG recordings (3, 4). The development of various multimodal data fusion strategies has taken off driven by the motivation to gain the most information from EEG high temporal resolution and fMRI high spatial resolution. The first published data fusion approach cross-correlated EEG α band power fluctuations with the fMRI-BOLD signals of the resting-state paradigm (5, 6), followed by the general linear model (GLM) implementation (7, 8). The GLM became a prominent method frequently applied in the field and not only for the EEG spectra integration with resting-state (9–14) or task induced (15–20) datasets. GLMs inducing event-related potential (ERP) amplitudes or timings (21, 22), and spike-informed GLMs (23–25) have been proposed and optimized.

The voxelwise GLM results self-organize into large scale brain network (LSBN) structures (19). Concurrent fusion strategy often rotates fMRI data into space of linearly mixtured spatially independent components, i.e., the LSBNs, with their representative clusterwise induced BOLD fluctuations, which are compared to various EEG dynamics (26–31). In parallel, regression or correlation approaches inferring EEG and fMRI dynamics, joint independent component analysis (32), graph build approach (33), dynamic functional connectivity (34), or multimodal dynamic causal modeling (35) have been proposed to fuse EEG-fMRI data with various result interpretations. Many regression or deconvolution approaches reported that EEG-fMRI hemodynamic response function (HRF) demonstrates varying timings and shapes (10, 19, 20, 36–42). In physiologic situations, the BOLD signal is delayed to EEG events but an extreme example is the epileptic spike EEG-fMRI where BOLD signal peaks can precede the EEG spikes (41, 42). Thus, it is a preferable approach to model variable HRF than to use fixed canonical HRF, which has still been dominating in the common practice (5–9, 11–18, 21–26, 28–33, 43).

Over various existing EEG-fMRI data fusion techniques, the ability to blindly and automatically visualize and quantify robust task-related functional networks and their EEG-fMRI associations (e.g., *via* variable HRF) is lacking. We have focused on the simple GLM fusion approach with variable HRF aggregating automatically induced EEG spectra (19, 20) and tested whether we can identify fusion settings that blindly visualizes task-related networks. This automated method may offer high reproducibility with tremendous potential in the clinical research or even clinical practice applications to quantitatively measure cognitive dysfunction.

Cognitive dysfunction may occur in various neurologic and psychiatric conditions including epilepsy and can be estimated from EEG, e.g., by measuring cognitive event-related responses such as P300 potential. The P300 response is time-locked to an event and is elicited by a task/event when a tested individual is requested to respond to a single stimulus or a set of stimuli as in the oddball paradigm. The P300 has been increasingly investigated as a marker of cognitive processing. Specifically, the P300 response represents a neural signature of the processing of stimulus context depending on the attention and state of arousal leading to an appropriate response (44). Although the P300 has been almost exclusively assessed in the temporal domain *via* ERPs (45, 46), the characterization in the frequency/spectral domain, since time and frequency are fully complementary domains, may provide additional insight into the data. Spectral (Equation 1) (16, 17, 43, 47) and spatiospectral (Equation 2) (19, 43) models have already been proposed for the blind visualization of task-related networks from simultaneous EEG-fMRI data. The 1st model (Equation 1) assumes that local fMRI BOLD signal fluctuations (b) are proportional to fluctuations of the frequency-specific (ω) weighted EEG absolute/relative power spectra (p) with modeled between-signal delay *via* HRF convolution kernel (h). The weighting function $g(\omega)$ can be considered a frequency specific filter modulating the power spectra and final power fluctuations are often estimated as an average over channels (16, 17, 43, 47). The 2nd model (Equation 2) is similar but considers the filtering property to be channel (c) specific. The identification of a robust task-related weighting function $g(\omega)$ or $g(c,\omega)$, i.e., event-related (spatio)spectral patterns (ERSPat) in EEG spectra, remains a not fully optimized challenge in the fusion process.

$$b \propto \left(\int g(\omega)p(\omega)\, d\omega \right) * h \tag{1}$$

$$b \propto \left(\int \int g(c,\omega)p(c,\omega)\, dc\, d\omega \right) * h \tag{2}$$

The EEG absolute/relative power spectra consist of a linear mixture of *stable* spatiospectral patterns [i.e., different stable $g(c,\omega)$ functions in Equation (2)] with temporal fluctuations that were more task-related for the relative power rather than the absolute power (48, 49). Absolute EEG power identified 14 stable patterns with highly significant EEG-fMRI associations at visual oddball dataset (19, 48). Relative EEG power identified 10 stable patterns similar to the absolute power patterns and two other relative power specific stable patterns, for which the EEG-fMRI relationships have not been investigated yet (49).

Several studies utilized the spectral model for the visualization of task-related neuronal networks from EEG-fMRI data (15–18) or the spatiospectral model (19, 43) with few mutual discrepancies: (i) the response function was fixed or variable; (ii) different tasks were used. Therefore, a direct and fair comparison between models still needs to be investigated.

Within the current study, we are presenting the full comparison between absolute/relative power based spectral (Equation 1) and spatiospectral (Equation 2) models for fully automatic EEG-fMRI fusion. The goal is to optimize the automatic visualization and quantification of task-related neuronal networks. The robustness over models was objectively assessed.

MATERIALS AND METHODS

Experimental Design

The identical simultaneous EEG-fMRI dataset of visual oddball paradigm was used as previously described (18, 19, 48, 49). The event-related designed visual oddball task was performed by 21 healthy subjects (13 right-handed men, one left-handed man, seven right-handed women; age 23 ± 2 years). Three stimulus types were presented randomly to each subject. Each stimulus consisted of a single yellow uppercase letter shown for 500 ms on a black background. Inter-stimulus intervals were either 4, 5, or 6 s (drawn uniformly and randomly). A total of 336 stimuli (divided into four consequential sessions) were presented, consisting of targets (letter X, 15%), frequents (letter O, 70%), and distractors (letters other than X and O, 15%). Subjects were instructed to press a button on the box held in their right hand whenever the target stimulus appeared and not to respond to distractor or frequent stimuli.

This study was approved by and carried out in accordance with the recommendations of the Masaryk University Ethics committee guidelines and all subjects signed the approved written informed consent in accordance with the Declaration of Helsinki.

Simultaneous EEG-fMRI Data Acquisition

The scalp EEG data, with reference between Cz and Fz electrodes, were acquired with an MR compatible 32-channel 10/20 EEG system (*BrainProducts, Germany*) and a sampling frequency of 5 kHz. Two channels were used for ECG and EOG. *Via* the BrainVision Recorder system (*BrainProducts, Germany*), the EEG data were synchronized and acquired simultaneously with fMRI data during gradient echo imaging sequences [1.5 T Siemens Symphony scanner equipped with Numaris 4 System (*Mrease*)]. Gradient echo, echo-planar functional imaging sequence was acquired with following parameter setting: TR = 1,660 ms; TE = 45 ms; FOV = 250 × 250 mm; FA = 80°; matrix size = 64 × 64 (3.9 × 3.9 mm); slice thickness = 6 mm; 15 transverse slices covering the whole brain except the inferior part of the cerebellum. The task was divided into four equal runs of 256 scans and 84 stimuli.

Following simultaneous EEG-fMRI acquisition, high-resolution anatomical T1-weighted images were acquired using an MPRAGE sequence with 160 sagittal slices, matrix size 256 × 256 resampled to 512 × 512; TR = 1,700 ms; TE = 3.96 ms; FOV = 246 mm; FA = 15°; and slice thickness = 1.17 mm.

EEG Data Preprocessing

The EEG data were preprocessed as described in (19, 48) using BrainVision Analyzer 2.02 (*BrainProducts, Germany*) with the implemented manufacturer's pipeline. Gradient artifacts were removed using average artifact subtraction (used sliding window with window length=21*TR) at the acquisition sampling rate 5 kHz (3) and filtered with a Butterworth zero phase 1–40 Hz band-pass filter. Then, EEG signals were resampled to 250 Hz (antialiasing filter included). Ballistocardiogram (BCG) artifacts were removed by average artifact subtraction (used sliding window with window length = 21*BCG epochs) waveform from each channel (50) and signals were re-referenced to the average. Eye-blinking artifacts were removed by conducting a temporal ICA decomposition and removing eye-blink artifacts from the back-reconstructed time course.

EEG Spatiospectral Decomposition

The decomposition was the same as implemented and previously described (48, 49). The preprocessed EEG signal from each lead and session was normalized to 0 mean and variance 1, and divided into 1.66 s (repetition time of fMRI scanning TR) epochs without overlap. Each epoch was transformed to a spectral domain with the fast Fourier transform (FFT), generating a vector (length = 67) of complex valued spectral coefficients between 0 and 40 Hz. Complex values were converted to absolute power by taking the absolute value and squaring, or converted to relative power value by dividing the squared value by the power of the whole epoch. The output vector of 67 real absolute/relative power values comprised a 3D matrix $\boldsymbol{E}$ with dimensions n_t, n_c, and n_ω. The dimension n_t represents the number of spatiospectral epochs ($n_t = 256$), the dimension n_c is the total number of leads ($n_c = 30$), the dimension n_ω is the total number of spectral coefficients ($n_\omega = 67$). The EEG spatiospectral decomposition (Equation 3) decomposes the matrix of spatiospectral maps $\boldsymbol{E}$ into a source matrix $\boldsymbol{S}$ of dimensions $\boldsymbol{S}(m,n_c^* n_\omega)$ containing independent spatiospectral patterns and a mixing matrix $\boldsymbol{W}$ of dimensions $\boldsymbol{W}(n_t,m)$ containing the patterns' dynamics. Dimension m is the number of decomposed independent spatiospectral components ($m = 20$).

$$\mathbf{E} = \mathbf{WS} \tag{3}$$

Using the GIFT toolbox (http://mialab.mrn.org/software/gift/) (51), the matrix $\boldsymbol{E}$ was dimensionally reduced using PCA (single-subject reduction to 50 principle components and group-based reduction to 20 components), followed by INFOMAX group-ICA (52) with 10 ICASSO runs (53).

Only spatiospectral patterns, which were reported to be stable and observed in both absolute/relative power spectra (48, 49), i.e., 10 patterns, have been selected from output source matrices $\boldsymbol{S}$ of separate group-ICA runs for absolute/relative powers.

Individual subject's time courses were generated by PCA based back-reconstruction (i.e., the individual partition of the PCA reducing matrix is matrix multiplied by the individual partition of the aggregate reducing matrix) (51) of the group spatiospectral patterns on the individual subject spatiospectral maps and time-courses.

Selection of Stable EEG Spatiospectral Patterns With Relationship to the Task

For each subject and session, we have one matrix $\boldsymbol{W}$ with dimensions $\boldsymbol{W}(n_t, 20)$ containing the back-reconstructed time course of each spatiospectral component. Let a matrix $\boldsymbol{U}$ of dimensions $\boldsymbol{U}$ $(4^* n_t,10)$ to be a single-subject matrix of fluctuations of stable spatiospectral patterns over all four sessions. Relationships between these dynamics and stimulus vector timings (in matrix $\boldsymbol{X}$) were assessed with a single-subject general linear model (Equation 4, GLM) (54) solved with the least mean square algorithm (Equation 5) and a continuous group one-sample t-test for the *k-th* stimulus vector (Equation 6) (48). Variable c is the vector of binary positive contrast at the stimulus vector of interest, the brackets <> characterize the expectation over subjects, variable σ is the standard deviation and variable s is the total number of subjects. Model matrix $\boldsymbol{X}$ contained frequent, target and distractor timings in 12 separate binary vectors for each stimulus and session and four vectors for the DC component in each session.

$$\mathbf{U} = \mathbf{X}\beta + \epsilon \tag{4}$$

$$\beta = (\mathbf{X}^T\mathbf{X})^{-1}\mathbf{X}^T\mathbf{U} \tag{5}$$

$$t_k = \sqrt{s}\frac{\langle \mathbf{c}_k^T \beta_k \rangle}{\sigma_{\langle \mathbf{c}_k^T \beta_k \rangle}} \tag{6}$$

These spatiospectral patterns, where any |t|-value was higher than 3.25 (critical value at $p_{\mathrm{FWE}} < 0.05$ for 10 multiple comparisons, i.e., 10 selected stable patterns, and 16 degrees of freedom, i.e., 16 variables in model matrix $\boldsymbol{X}$) for any stimulus type in absolute or relative power, were considered as a pattern with task-related EEG power fluctuations. Second selection criteria was to demonstrate mean |t|-value averaged over all spatiospectral/spectral models with $p < 0.05$ ($\sim|t| > 2.0$) with relatively small standard deviation in the averaged |t|-value over models, i.e., $\mathrm{STD}_{|t|} < 0.5$.

Task-Related EEG Spectral Patterns

All 10 stable spatiospectral patterns observed in both power types were averaged over leads and provided 10 spectral filters $g(\omega)$ (Equation 1). The filters were used for filtering of power spectra of matrix $\boldsymbol{E}$ reshaped at dimensions $\boldsymbol{E}(n_t, n_c, n_\omega)$. Separate for each filter, time point and channel, the absolute/relative power value $p(t,c)$ was filtered as Equation 7. Time-course $p(t)$ of each channel c was normalized to mean 0 and variance 1, and final absolute/relative power fluctuation $\bar{p}(t)$ was estimated as an average over channels for each specific spectral pattern.

$$p(t,c) = \sum_{\omega=1}^{n_\omega} g(\omega)E(t,c,\omega) \tag{7}$$

Task-related spectral patterns were evaluated and identified with the same methodology as described in sub-chapter Selection of Stable EEG Spatiospectral Patterns With Relationship to the Task, but matrix $\bar{\boldsymbol{U}}$ (Equations 4, 5) consisted of 10 pattern-specific averaged $\bar{p}(t)$ fluctuations.

fMRI Data Preprocessing

The fMRI data were preprocessed with SPM8 (*Wellcome Trust Center for Neuroimaging, London, UK*) software library. Motion artifacts were minimized by alignment of all functional scans, followed by co-registration with the subject's anatomical image and normalization into standardized MNI space (*Montreal Neurological Institute* template) (55). Functional scans were spatially smoothed with an isotropic 3D Gaussian filter (FWHM = 8 mm) to increase the signal to noise ratio (SNR) and to make the random errors more normally distributed. Periods longer than 128 s were linearly detrended to remove slow drifts and physiological noise.

EEG-fMRI General Linear Modeling With Variable HRFs

Relationships between fMRI voxel time-courses ($\boldsymbol{Y}$) and EEG task-related spectral/spatiospectral pattern time-courses were examined using the individual GLMs (Equation 8) (54) with the EEG time course convolved with the canonical HRF ($\boldsymbol{x}_1$), convolved with the 1st temporal derivative of the HRF ($\boldsymbol{x}_2$) or convolved with the 2nd temporal derivative of the HRF ($\boldsymbol{x}_3$) (19, 20). In addition to the three EEG regressors $\boldsymbol{x}_1$-$\boldsymbol{x}_3$, the model matrix $\boldsymbol{X}$ contained a DC component. Regression matrices $\boldsymbol{\beta}$ were estimated over all GLMs with the ReML algorithm (Restricted Maximum Likelihood) implemented in SPM12 software (*Wellcome Trust Center for Neuroimaging, London, UK*) in the MATLAB programing environment (*MathWorks, Natick, USA*).

$$\mathbf{Y} = \mathbf{X}\beta + \epsilon \tag{8}$$

Group-averaged EEG-fMRI results were estimated with a one-way ANOVA test (implemented in SPM12) of three EEG-derived single-subject spatial β-maps for each of three EEG regressors. The β weights served as dependent variables in separate ANOVA tests conducted for each spectral/spatiospectral pattern, generating group-averaged spatial EEG-fMRI F-maps. The final F-maps were thresholded for objective evaluations at $p < 0.001$ uncorrected for multiple statistical tests (i.e., with a critical absolute F-value of 5.7), and the criteria that clusters contain 100 voxels or more. For visualizations, the F-maps were thresholded at $p < 0.0001$ (i.e., $F > 8.1$) due to high result robustness.

Group-averaged EEG-fMRI HRFs ($\boldsymbol{h}_i$) in each voxel i were estimated from group-averaged regression coefficients $\boldsymbol{\beta}$ (estimated within Equation 8) with Equation 9 where $\boldsymbol{r}$ is the canonical HRF and numbers 1–3 are indexes of regressors $\boldsymbol{x}_1$-$\boldsymbol{x}_3$ (19, 56).

$$\mathbf{h}_i = \beta_{i,1}\mathbf{r} + \beta_{i,2}\frac{d\mathbf{r}}{dt} + \beta_{i,3}\frac{d^2\mathbf{r}}{dt^2} \tag{9}$$

Assessment of EEG-fMRI Results

Group-averaged EEG-fMRI F-maps and HRFs were visually inspected for a subjective similarity/dissimilarity evaluation over the similar spectral/spatiospectral patterns. For the objective assessment, volume, mean F-value, median F-value, and maximal F-value were automatically extracted from the suprathreshold voxels ($p < 0.001$) of the final group-averaged EEG-fMRI F-maps of every stable task-related spectral/spatiospectral pattern. The spectral/spatiospectral model with the highest objective metrics was considered as the most successful one in blind visualization of a task-related neural network.

RESULTS

Task-Related EEG Spectral/Spatiospectral Patterns

Significant negative linear relationship between EEG fluctuations and frequent stimulus was observed in two

TABLE 1 | Group *t*-values of linear relationship between stable EEG pattern fluctuations and stimuli vectors.

		Spectral		Spatiospectral		Mean	STD
		Absolute	Relative	Absolute	Relative		
Frequent	δ_1	−0.09	0.46	−1.13	−0.58	−0.34	0.59
	δ_2	**−5.24**	−2.42	−0.81	−0.92	−2.35	1.79
	δ_3	**−3.71**	−1.71	−1.45	−1.45	−2.08	0.95
	δ_4	**−3.44**	**−4.70**	−2.09	**−4.32**	**−3.64**	1.00
	θ_1	−1.76	−0.87	−0.34	−2.03	−1.25	0.68
	θ_4	−2.54	−1.95	0.39	−1.01	−1.28	1.10
	α_1	1.65	**3.54**	1.72	2.59	2.38	0.77
	α_3	0.62	2.03	2.48	0.12	1.31	0.97
	β_1	**−3.64**	**−3.25**	−3.23	**−3.28**	**−3.35**	0.17
	β_2	−1.89	−0.64	−0.17	**−3.74**	−1.61	1.38
Target	δ_1	2.80	**3.35**	−0.40	−1.86	0.97	2.18
	δ_2	2.53	2.93	1.77	2.63	2.46	0.43
	δ_3	2.26	2.20	2.43	2.46	2.34	0.11
	δ_4	1.08	0.35	0.24	1.04	0.68	0.39
	θ_1	2.18	1.49	2.37	2.17	2.05	0.33
	θ_4	1.93	0.65	0.39	1.45	1.11	0.62
	α_1	2.05	0.51	2.62	1.73	1.73	0.77
	α_3	0.93	0.17	0.58	0.21	0.47	0.31
	β_1	−0.11	−2.30	−0.52	−1.44	−1.09	0.85
	β_2	−0.82	−2.06	−0.06	−1.40	−1.08	0.74
Distractor	δ_1	−0.19	0.30	0.56	0.21	0.22	0.27
	δ_2	−1.30	−0.40	0.31	1.30	−0.02	0.95
	δ_3	−1.05	−0.56	0.21	−0.35	−0.44	0.45
	δ_4	−3.11	−2.76	−2.24	−1.46	−2.39	0.62
	θ_1	−0.58	1.45	−0.25	0.01	0.16	0.77
	θ_4	−2.06	−2.52	−1.00	−0.43	−1.50	0.83
	α_1	−0.23	1.17	0.56	1.65	0.79	0.70
	α_3	−0.39	0.60	−0.34	0.40	0.07	0.44
	β_1	−0.79	0.19	−0.61	−0.97	−0.55	0.44
	β_2	−1.06	−1.00	0.12	−1.31	−0.81	0.55

Bold highlighted t-values demonstrated significant relationship with $p_{FWE} < 0.05$. Green-color highlighted rows indicate the patterns with significant task-related relationships. These patterns demonstrated $p_{FWE} < 0.05$ or a mean over models of $p < 0.05$ (i.e., mean $|t| > 2.0$) with t-value standard deviation of $STD_{|t|} < 0.5$.

spectral/spatiospectral patterns (i.e., δ_4 with inter-model *t*-value −3.64 ± 1.00, β_1 with *t*-value −3.35 ± 0.17, **Table 1**, **Figure 1A**, $p_{\mathrm{FWE}} < 0.05$). The negative linear relationship can be interpreted as the EEG pattern power decrease during the frequent stimulus onset. Other three patterns (i.e., δ_2 with *t*-value 2.46 ± 0.43, δ_3 with *t*-value 2.34 ± 0.11, θ_1 with *t*-value 2.05 ± 0.33) demonstrated a significant positive linear relationship between the EEG power fluctuations and target stimulus (**Table 1**, **Figure 1B**, $p < 0.05$ and $STD_{|t|} < 0.5$). The positive linear relationship can be interpreted as the EEG pattern power increase during the target stimulus onset. The δ_4 pattern fluctuations with *t*-value −2.39 ± 0.62 may also be sensitive to distractor stimulus with similar negative linear relationship (**Table 1**, **Figure 1A**, $p < 0.05$) as observed for the frequent stimulus. Lower robustness of relationships between EEG patterns and target or distractor stimuli might be caused by lower stimulus amounts. Five of 10 analyzed stable EEG patterns demonstrated potentially significant relationship to stimuli vectors of the visual oddball task (**Table 1**, **Figure 1**).

Frequent-Related EEG-fMRI Networks

As the δ_4 pattern demonstrated the highest level of relationship between pattern fluctuations and frequent stimulus, the EEG-fMRI F-maps also visualized the highest *F*-values and largest amounts of supra-threshold voxels over all four investigated EEG patterns (**Table 2**, **Figure 2**). The absolute spectral model (ASM) provided the largest and the most significant EEG-fMRI associations in comparison to other models (**Table 2**). Still, statistical measures are very high and robust in all investigated models for the δ_4 pattern (**Table 2**).

Positive δ_4 pattern demonstrated significant ($p_{\mathrm{FWE}} < 0.05$) bilateral EEG-fMRI associations in cuneus, precuneus, insula, basal ganglia, and in sensory-motor network, somatosensory network and dorsal parts of the fonto-parietal control network

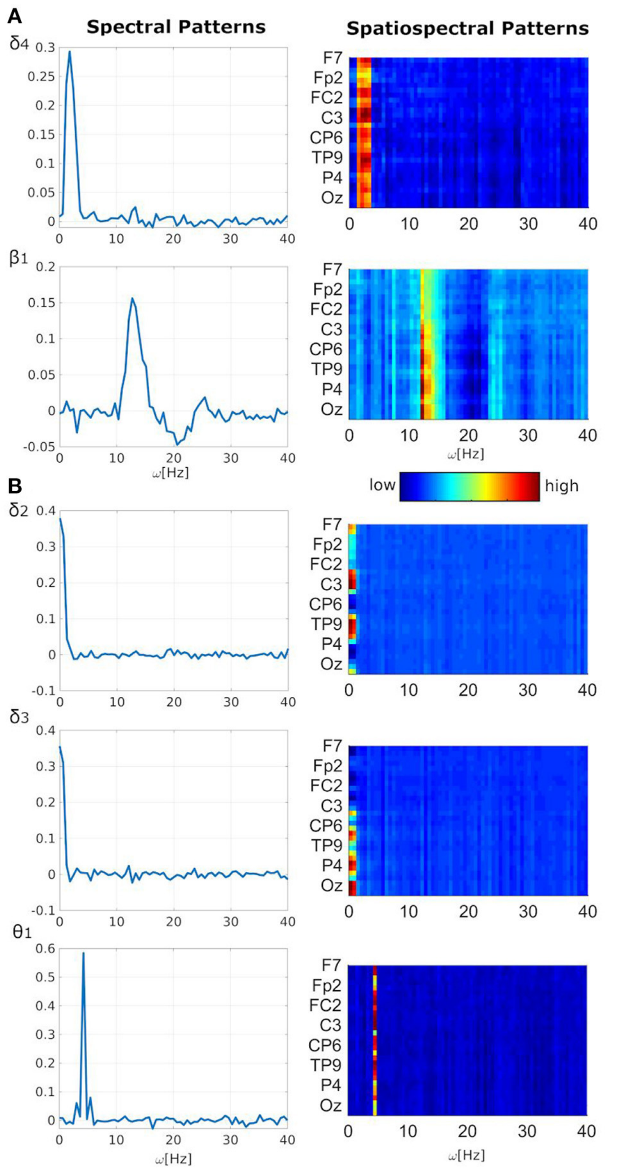

FIGURE 1 | Task-related EEG spectral or spatiospectral patterns. **(A)** Frequent related; **(B)** target related. Pattern shortcuts and indexes (e.g., δ_4) are the same as used in (19) for consistency purposes. All spectral patterns are averages over electrodes of both absolute or relative spatiospectral patterns. Patterns' amplitudes (i.e., y-axis for spectral patterns and color-coding for spatiospectral patterns) are in arbitrary units. For spatiospectral patterns, the dark blue color is an approximate minimum value in the y-axis of the corresponding spectral pattern. The dark red color is an approximate maximum value in the y-axis of the corresponding spectral pattern.

(FPCN) (57–60) (**Figure 2**). Putamen, pallidum, thalamus, and brainstem were involved within subcortical gray matter structures (**Figure 2**). The dorsal parts of the FPCN overlap with the dorsal attention network (DAN) (57) and may be no discernable one from the other in a lower spatial resolution (**Figure 2**). Spatial distribution in **Figure 2B** represents the same result, which was presented in (19) with absolute spatiospectral model (ASSM) and variable HRF modeling. Here, we proposed that the ASM with variable HRF modeling or relative spatiospectral model (RSSM) with variable HRF modeling increased the statistical power and the robustness (**Table 2**, **Figure 2**). All models demonstrated a positive HRF peak faster than a peak timing of widely used canonical HRF (**Figure 2**) and noticeable HRF trough (**Figure 2**) in the insula, sensory-motor network, somatosensory network, dorsal part of the FPCN and basal ganglia. Except this expected response (i.e., red HRFs in **Figure 2**), every model detected brain areas with reduced HRF peak followed by larger HRF trough amplitude (i.e., the blue HRFs in **Figure 2**). Trough peaks in both detected HRFs were again faster than an expected trough timing for the canonical HRF (**Figure 2**). The HRF with a reduced peak and an amplified trough was observed in areas of superior frontal cortex and parietal cortex (**Figure 2A**), which might belong to the frontal parts of the FPCN (57–60) or default mode network (DMN) (57). Inferiorly, we noticed significant ($p_{\mathrm{FWE}} < 0.05$) bilateral cluster spots in frontal white matter areas (**Figure 2A**) where forceps minor, anterior thalamic radiation and inferior fronto-occipital fasciculus might pass [evaluated by a visual inspection of EEG-fMRI F-maps overlaid with the JHU white-matter atlas (61–63) in the MNI space].

As the β_1 pattern demonstrated similar negative linear relationship between its power fluctuation and the frequent stimulus (**Table 1**), the EEG-fMRI F-maps demonstrated similar locations of association spots (**Figure 3**) where maximal $|F|$ values were observed in the δ_4 EEG-fMRI F-maps (**Figure 2**), and similar HRF properties (**Figure 3**). The β_1 EEG-fMRI F-maps demonstrated a lower statistical robustness for all models (**Figure 3**, **Table 2**) when compared to the δ_4 F-map robustness (**Figure 2**, **Table 2**). Again, the ASM provided the most robust statistics at the inter-model comparison level (**Table 2**). The relative spectral model (RSM) did not demonstrate any significant EEG-fMRI associations, which is analogical to the previous observation of no relative β associations with the fixed canonical HRF at the same dataset (18). Again, the RSSM was more robust than the ASSM (**Table 2**). Overall, the lower robustness, the β_1 EEG-fMRI associations might appear more spatially specific. As interpreted from the ASM EEG-fMRI β_1 F-map (**Figure 3**). From the basal ganglia, the bilateral putamen demonstrated EEG-fMRI associations with normal HRF peak. From the sensory-motor network, bilateral EEG-fMRI associations with normal HRF peak were observed in primary sensoric, premotor, somatosensory cortices, supramarginal gyrus, left lateralized Brodmann area 7 (BA7), and premotor BA6. The reduced HRF peak properties were observed for lateralized BA9, BA10, BA46, and right hand primary motor cortex. The RSSM emphasized somatosensory BA6 associations compared to the ASM results (**Figure 3**). In regards to the mentioned spatial specificity, it is important to note that one can get similar spatial distribution for the δ_4 EEG-fMRI F-map if stricter threshold than $p < 0.0001$ is set in the **Figure 2** visualization where local spatial statistics exceeded the β_1 pattern results (**Table 2**).

TABLE 2 | Spatial statistics of task-related EEG-fMRI F-maps.

			Spectral		Spatiospectral	
			Absolute	**Relative**	**Absolute**	**Relative**
Frequent related	δ_4	Volume [mm^3]	**937,845**	431,865	571,266	656,910
		Mean *F*-value	**14.08**	9.96	10.65	13.05
		Median *F*-Value	**12.48**	9.04	9.57	11.4
		Max *F*-value	**53.83**	27.35	32.19	45.27
	β_1	Volume [mm^3]	**282,555**	-	40,797	106,704
		Mean *F*-value	**8.37**	-	7.4	7.61
		Median *F*-Value	**7.76**	-	7.19	7.23
		Max *F*-value	**22.39**	-	12.17	15.31
Target related	δ_2	Volume [mm^3]	**524,205**	26,271	58,185	26,865
		Mean *F*-value	**10.14**	7.34	7.68	7.35
		Median *F*-Value	**9.14**	7.00	7.26	6.96
		Max *F*-value	**28.86**	13.76	16.12	14.97
	δ_3	Volume [mm^3]	**658,557**	15,525	2,646	17,118
		Mean *F*-value	**10.64**	7.54	7.01	7.45
		Median *F*-Value	**9.45**	7.05	6.81	6.98
		Max *F*-value	**36.09**	16.5	9.57	14.03
	θ_1	Volume [mm^3]	**852,930**	140,994	236,844	334,746
		Mean *F*-value	**12.44**	7.94	8.92	9.02
		Median *F*-Value	**11.08**	7.41	8.25	8.19
		Max *F*-value	**47.32**	17.1	21.24	29.78

The values were estimated from all supra-thresholded voxels with $p < 0.001$ (i.e., $|F| > 5.7$). Bold highlighted numbers are the highest obtained values over investigated models per metric. Values $|F| > 8.1$ met the condition $p < 0.0001$, values $|F| > 12.1$ met the condition $p_{FWE} < 0.05$.

Target-Related EEG-fMRI Neworks

Although δ_2, δ_3, and θ_1 patterns demonstrated all the positive relationship ($p < 0.05$ and $\text{STD}_{|t|} < 0.5$) between EEG pattern fluctuations and target stimulus, the EEG-fMRI data fusion visualized the largest and most robust F-maps for the θ_1 pattern over all investigated models (**Table 2**, **Figure 4**). The most robust statistics was yielded by ASM, followed by RSSM, ASSM, and RSM (**Table 2**). All models emphasized left lateralized EEG-fMRI associations in the sensory-motor network (corresponding to the push on the right hand held button box and the target push button response) with smaller amounts of the basal ganglia associations, which were somewhat preserved for the ASM and partly for the RSSM (**Figure 4**). The ASM preserved significant EEG-fMRI associations in the dorsal parts of the FPCN overlapping with DAN (**Figure 4**). These EEG-fMRI associations presented a non-reduced HRF peak and a noticeable HRF trough again with timing faster than classic canonical HRF (**Figure 4**). The ASM still visualized a significant ($p_{\mathrm{FWE}} < 0.05$) reduced HRF peak and an amplified HRF trough in areas of the frontal parts of the FPCN, DMN and superior frontal white matter but in smaller amounts than observed for the frequent-related δ_4 pattern (**Figures 2**, **4**). The RSM, ASSM, and RSSM revealed a comparably smaller amount of significant clusters in locations as ASM (**Figure 4**).

The RSM, ASSM and RSSM did not demonstrate almost any significant EEG-fMRI associations for δ_2 and δ_3 patterns (**Figures 5**, **6**, **Table 2**). The ASM for δ_2 and δ_3 patterns showed similar spatial and HRF observation as for the θ_1 ASM (**Figures 4A**, **5A**, **6A**). The similarity in EEG-fMRI results between δ_2 and δ_3 ASMs was expected as both use almost the same spectral filtering properties over all leads (**Figure 1**).

Distractor-Related EEG-fMRI Networks

The evidence of a negative relationship between EEG power fluctuations and distractor stimulus was only noticed for the δ_4 pattern. The δ_4 EEG-fMRI F-maps might then represent both frequent-related or distractor-related associations (**Figure 2**).

DISCUSSION

Novelty and Neuroimaging Impact

Our results on visual oddball task data represent the systematic objective comparison of spectral (i.e., ASM, RSM) and spatiospectral (i.e., ASSM, RSSM) EEG-fMRI data fusion methods with the variable HRF permitting the variable delay between the immediate EEG following the BOLD signal changes. The automatically quantified effect of the variable HRF in the EEG-fMRI data fusion was remarkable. Both ASM and RSM results gained from the same dataset with fixed canonical HRF were far from reaching $p_{\mathrm{FWE}} < 0.05$ in EEG-fMRI statistical parametric maps (18, 43). In contrast, large numbers of voxels in δ_4 and θ_1 EEG-fMRI F-maps for all models met the statistical significance condition $p_{\mathrm{FWE}} < 0.05$. While accounting for the obtained EEG-fMRI map robustness and due to the involvement of insula, sensory-motor cortex, somatosensory

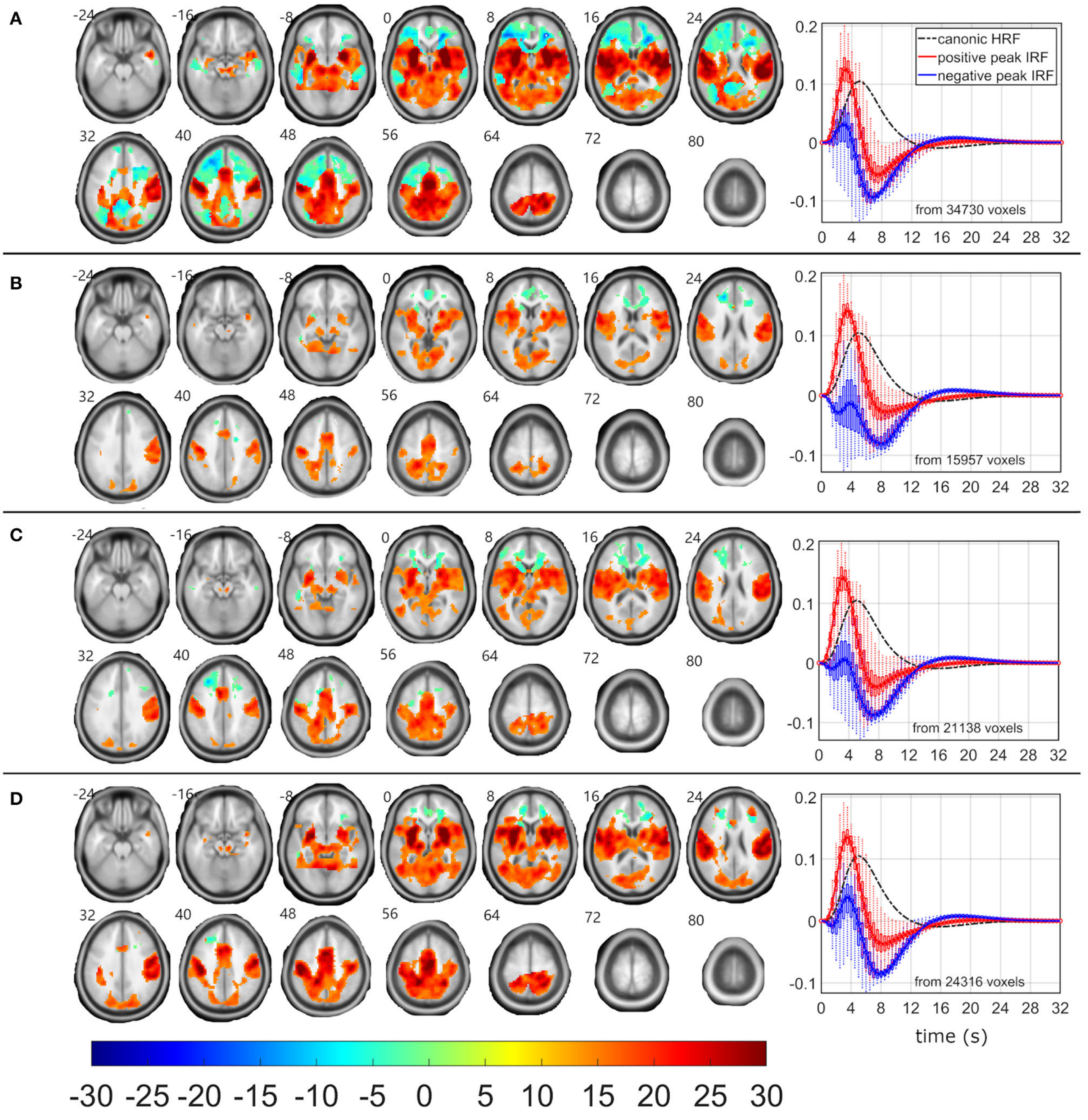

FIGURE 2 | EEG-fMRI F-maps and estimated hemodynamic response functions for all investigated models of the δ_4 pattern. The EEG-fMRI F-map colorbar is the same over all models. HRF, hemodynamic response function; IRF, impulse response function. If HRF demonstrated a reduced peak and an amplified trough (i.e., blue color-coded HRFs) the *F*-values were assigned with a negative sign. The F-maps were threholded with $p < 0.0001$, i.e., $|F| > 8.1$. The voxels with $|F| > 12.1$ met the condition $p_{FWE} < 0.05$. The red color coded HRFs were derived from voxels with positive signed suprathreshold *F*-values. All F-maps are shown following the neurological convention, i.e., left hemisphere on the left side of the axial slice. **(A)** Absolute spectral. **(B)** Relative spectral. **(C)** Absolute spatiospectral. **(D)** Relative spatiospectral.

cortex, cuneus, precuneus, basal ganglia, and FPCN (also known as central executive network) in the oddball/P300 tasks (64–73), we recommend using variable HRF and absolute spectral (ASM) or relative spatiospectral model (RSSM) for blind and fully automatic visualization of task-related networks from simultaneous EEG-fMRI data.

The current approach is fully automated, blind, and robust. It overcomes EEG-fMRI fusion *via* event related potential (ERP,

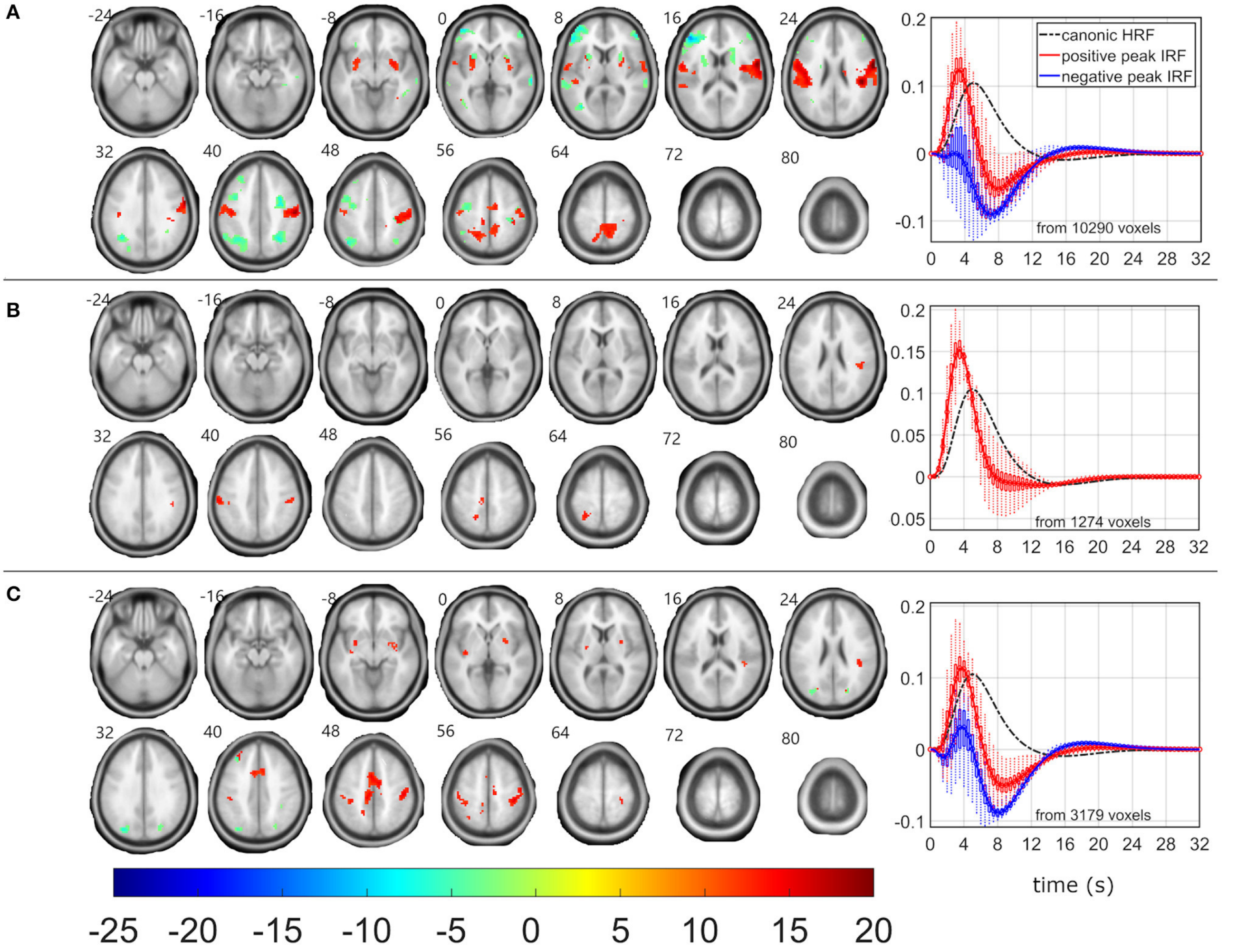

FIGURE 3 | EEG-fMRI F-maps and estimated hemodynamic response functions for all investigated models of the β_1 pattern. The EEG-fMRI F-map colorbar is the same over all models. HRF, hemodynamic response function; IRF, impulse response function. If HRF demonstrated a reduced peak and an amplified trough (i.e., blue color-coded HRFs) the *F*-values were assigned with a negative sign. The F-maps were threholded with $p < 0.0001$, i.e., $|F| > 8.1$. The voxels with $|F| > 12.1$ met the condition $p_{FWE} < 0.05$. The red color coded HRFs were derived from voxels with positive signed suprathreshold *F*-values. All F-maps are shown following the neurological convention, i.e., left hemisphere on the left side of the axial slice. **(A)** Absolute spectral. **(B)** Relative spectral. **(C)** Absolute spatiospectral. **(D)** Relative spatiospectral.

e.g., the P300) analysis of amplitudes or latencies (22, 74–76) and is without a need of supplying an input information about stimuli timings. Manpower expertise and efforts are required for the visual identification in the ERP analysis. In the proposed analysis approach, quantitative EEG-fMRI task-related networks are generated automatically. The potential neuroimaging impact of this methodology is in a quantitative measurement of local data-driven determinants of cognitive deficit in patients suffering with epilepsy or other conditions with a cognitive impairment. The specific outcome determinants may be subject/group-specific *F*-value magnitudes or variable HRF amplitudes and latencies. High variance in local HRF latencies has been recently reported in patients with refractory focal epilepsy (40). This observation underlines the importance of variable HRF models for future clinical EEG-fMRI applications.

We demonstrated local EEG-fMRI response functions with the reduced HRF peak and the amplified HRF trough with the most robust location in the center of white matter bundles. These bundles may convey information related to execution and goal-directed tasks (77–79). Although the white matter BOLD signal was considered as a nuisance signal that was usually regressed out from the dataset during the preprocessing (80), several studies have reported the white matter fMRI-BOLD signal and disregarded its previous categorization as a blind spot in the functional imaging (81–85). Our robust white matter EEG-fMRI associations with the reduced HRF peak and the amplified HRF trough corroborate this recent blind spot hypothesis.

Task-related δ_4 and θ_1 EEG-fMRI associations might be considered controversial but we are convinced that they represent the bands of major event-related fingerprints in the

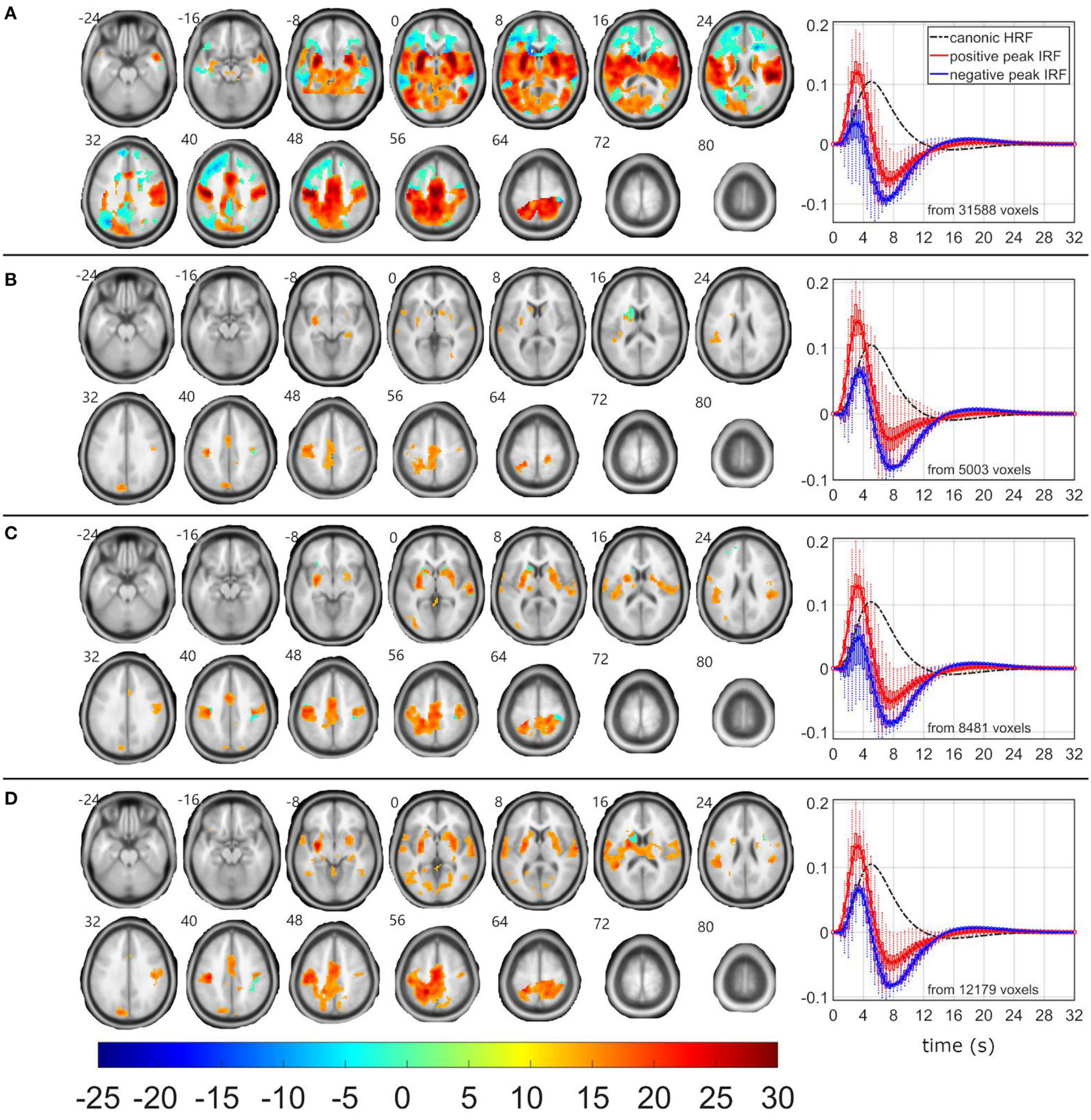

FIGURE 4 | EEG-fMRI F-maps and estimated hemodynamic response functions for all investigated models of the θ_1 pattern. The EEG-fMRI F-map colorbar is the same over all models. HRF, hemodynamic response function; IRF, impulse response function. If HRF demonstrated a reduced peak and an amplified trough (i.e., blue color-coded HRFs) the *F*-values were assigned with a negative sign. The F-maps were thresholded with $p < 0.0001$, i.e., $|F| > 8.1$. The voxels with $|F| > 12.1$ met the condition $p_{FWE} < 0.05$. The red color coded HRFs were derived from voxels with positive signed suprathreshold *F*-values. All F-maps are shown following the neurological convention, i.e., left hemisphere on the left side of the axial slice. **(A)** Absolute spectral. **(B)** Relative spectral. **(C)** Absolute spatiospectral. **(D)** Relative spatiospectral.

simultaneously recorded EEG spectra. The postulated event-related fingerprint hypothesis is described in more detail in the following sub-chapter and supported by previous ERP findings.

Event-Related Fingerprints in EEG Spectra Hypothesis

The oddball paradigm elicits ERPs in EEG recordings (22, 67, 74–76, 86). The averaged ERP can be decomposed

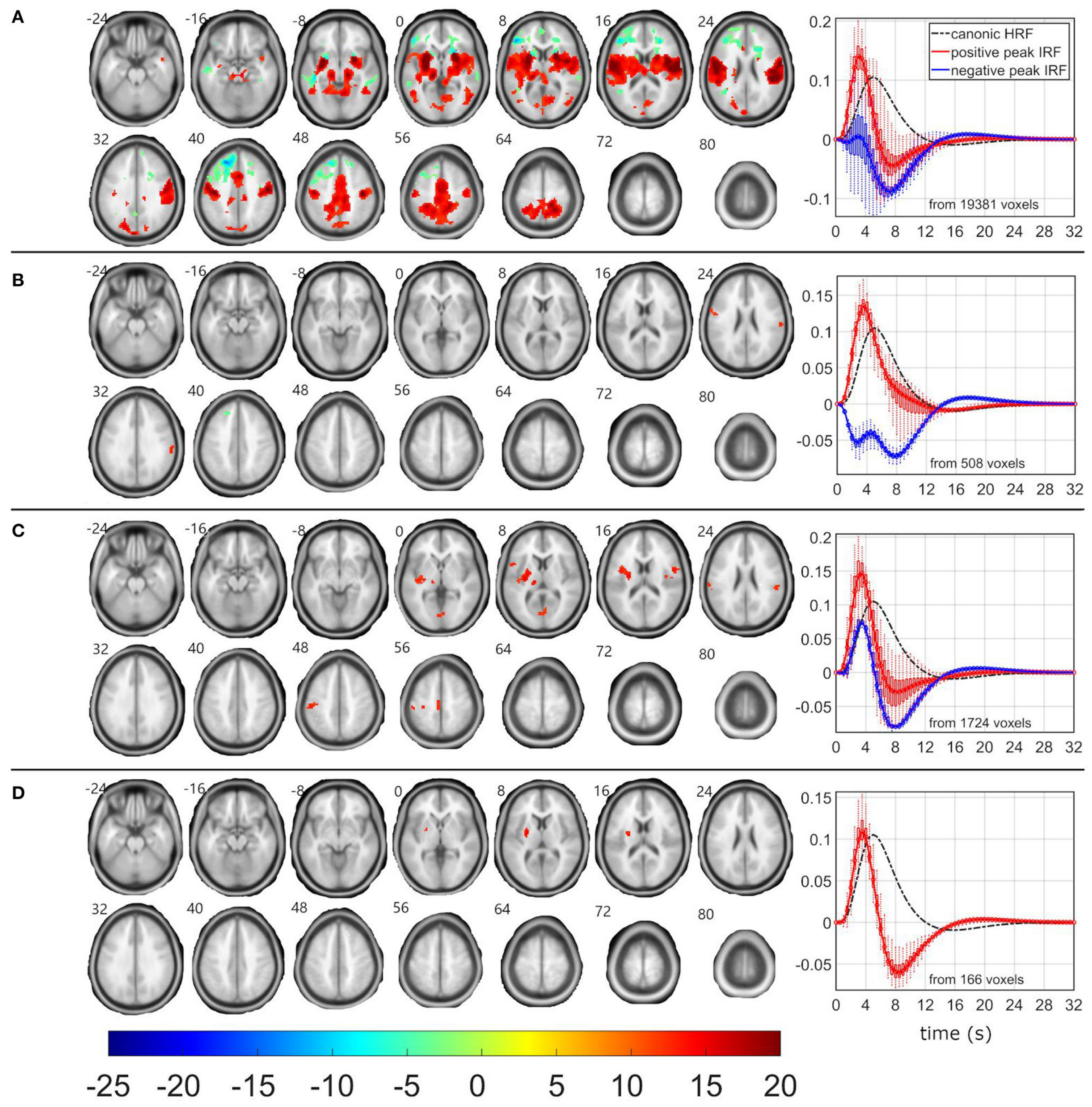

FIGURE 5 | EEG-fMRI F-maps and estimated hemodynamic response functions for all investigated models of the δ_2 pattern. The EEG-fMRI F-map colorbar is the same over all models. HRF, hemodynamic response function; IRF, impulse response function. If HRF demonstrated a reduced peak and an amplified trough (i.e., blue color-coded HRFs) the *F*-values were assigned with a negative sign. The F-maps were threholded with $p < 0.0001$, i.e., $|F| > 8.1$. The voxels with $|F| > 12.1$ met the condition $p_{FWE} < 0.05$. The red color coded HRFs were derived from voxels with positive signed suprathreshold *F*-values. All F-maps are shown following the neurological convention, i.e., left hemisphere on the left side of the axial slice. **(A)** Absolute spectral. **(B)** Relative spectral. **(C)** Absolute spatiospectral. **(D)** Relative spatiospectral.

at several components of different frequency bands with major contributions of δ oscillations to P300 wave and θ oscillations to P300, P1, and N1 waves (87). Generally, δ and θ oscillations, which underline the P300 wave (88–93), reconfigure and enhance functional connectivity architecture from the baseline resting-state condition to the P300 task condition (73).

Temporal and spectral domains are fully complementary spaces. Therefore, each single event-related change of each oddball stimulus recorded in the EEG temporal domain

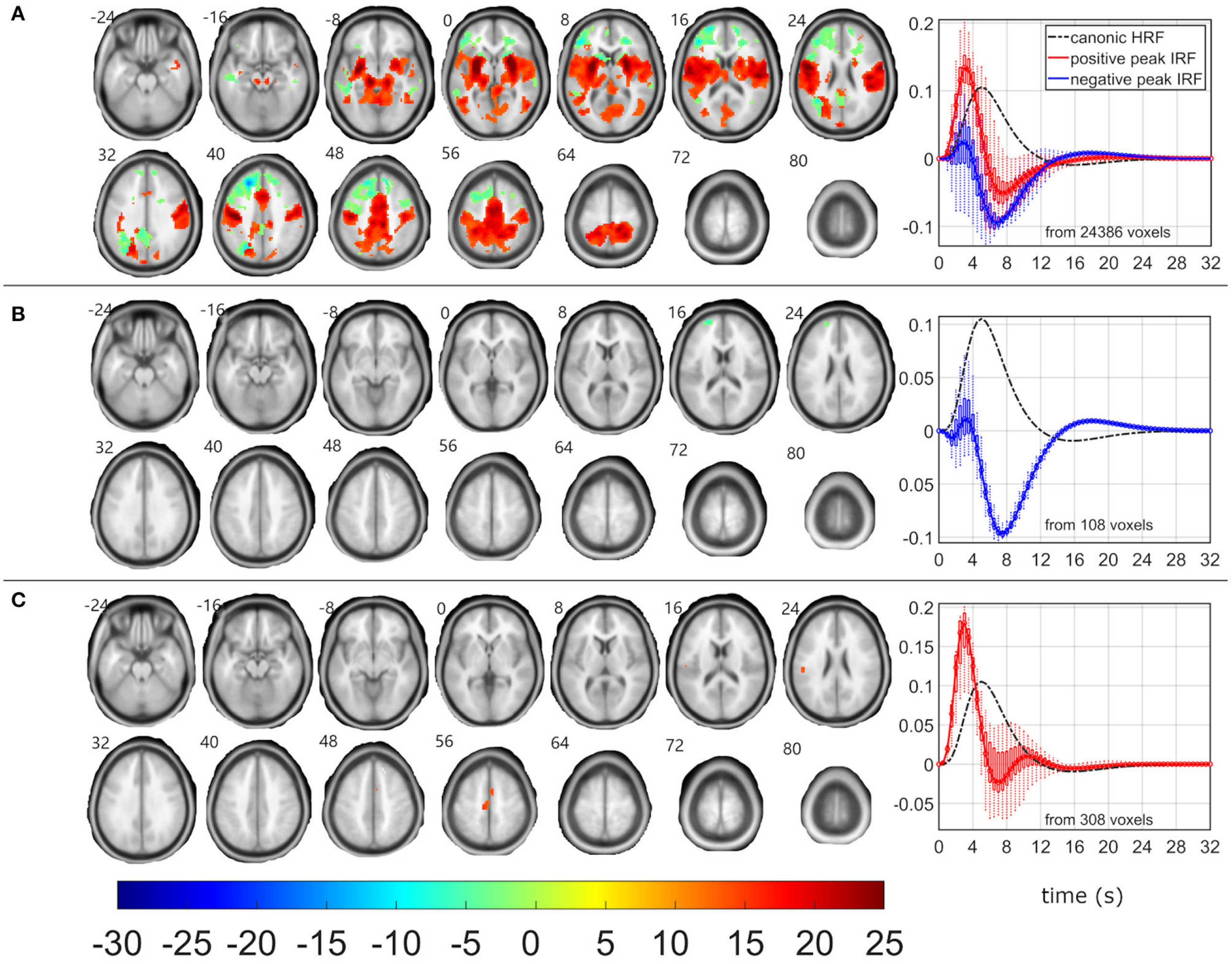

FIGURE 6 | EEG-fMRI F-maps and estimated hemodynamic response functions for all investigated models of the δ_3 pattern. The EEG-fMRI F-map colorbar is the same over all models. HRF, hemodynamic response function; IRF, impulse response function. If HRF demonstrated a reduced peak and an amplified trough (i.e., blue color-coded HRFs) the *F*-values were assigned with a negative sign. The F-maps were threholded with $p < 0.0001$, i.e., $|F| > 8.1$. The voxels with $|F| > 12.1$ met the condition $p_{\mathrm{FWE}} < 0.05$. The red color coded HRFs were derived from voxels with positive signed suprathreshold *F*-values. All F-maps are shown following the neurological convention, i.e., left hemisphere on the left side of the axial slice. **(A)** Absolute spectral. **(B)** Relative spectral. **(C)** Absolute spatiospectral. **(D)** Relative spatiospectral.

fingerprints into the spectral domain such as power change in the ERSPat. Then, the task-related networks can be visualized while utilizing power spectral or spatiospectral models in the fully automated approach that is fully blind to the external stimulus timings. Our results demonstrated that the δ_4 and θ_1 ERSPats might be key filtering properties, i.e., $g(\omega)$ in Equation 1 or $g(c,\omega)$ in Equation 2, which appear to be in correspondence with the spectral properties of the P300 ERP (87–93). Our observation expands beyond the original hypothesis that was simply monitoring changes in the EEG mean root square frequency characterizing a signal roughness increase after stimuli (16, 47). These global EEG spectra changes are tiny and hard to detect in the event-related paradigm design. The ERSPat approach may be beneficial for the assessment of the event-related changes in EEG signal.

We have shortened the term, "event-related (spatio)spectral patterns" to an acronym, "ERSPat" and not "ERSP" to avoid confusion with the ERSP acronym. The "ERSP" acronym is used in the field for the event-related spectral perturbation (94), which are estimated from EEG segments that are apriori time-locked to the stimulus on-sets. Thus, ERSP has a slightly different meaning and interpretation than proposed ERSPats.

Comparison With Concurrent Brain Network and Early Visual Components

Our results corroborate the previous findings of δ and θ oscillations representing the major operating rhythms in P300 (87–93). Detected β oscillations underlying P300 were likely related to directed attention and cognitive activity (95). The earliest components in ERP with visual sensory input are positive and negative peaks reflecting P1 and N1 potentials and are likely generated in lateral extrastriate occipital cortex, temporoparietal junction, and fusiform gyrus, respectively (96–98). These components may be linked to visual perceptual processing, especially visuospatial attention. Within the latency window of P1-N1 complex (90–120 ms for P1; and 150–190 ms for N1), the suggested superposition of α and θ evoked oscillations (99) was corroborated with the oscillatory activity detected in α and θ bands in the frequency decomposition of P300 response (87). In our findings, the activity in the α_1 band approached the borderline of significance for the frequent stimulus and, thus, was not associated with fMRI signals. We believe that the θ activity was likely dominated by the P300-related oscillatory response and the discernibility of the rhythms linked to a minute P1-N1 complex is rather challenging.

The detection and discrimination between stimuli initiate a frontal lobe activity underlying attention-demanding task. The frontal activation interplays with an activation in temporal-parietal areas that promote memory operations. At rest, DMN (hippocampal-cingular-temporal-parietal network) is characterized by high activity. During attention-demanding task DMN activity is suppressed. FPCN is often found to be reciprocally anti-correlated with DMN, which is one of the examples of the functional antagonism (100–103). The involvement (δ_4 and θ_1 oscillation related) of the insula, the central node of the salience-detection system, represents an expected "switch" between the DMN and the FPCN (57–60). Observed δ_4 oscillation related EEG-fMRI associations in the DMN regions are speculative. Predominantly, α oscillation related DMN deactivation has been present within the oddball task (18, 19, 60, 73) or resting-state (13). The involvement of the posterior cingulate cortex has been proposed as a potential regulatory modulator of the DMN in the task-negative state (104, 105).

Comparison With Concurrent Methods Applicable for EEG-fMRI Fusion

Temporal ICA of EEG data can isolate time-locked oscillations, artifacts (e.g., EKG, eye-blinking, etc.) (106) and epileptogenic spikes (if present) (25, 107, 108). The task specific activity represents only a small portion of signal variance, such as high frequency gamma band activity or ERPs. In addition, the present approach isolates EEG responses over large windows (e.g., 1.66 s in the present study), which discards the time-locked activity present with conventional ERP analysis. The time-locked activity preservation, e.g., with group temporal ICA, may also be a promising approach for task data (48).

Yet, considering the hypothesis that event-related changes (i.e., the small portion of signal variance) fingerprints into several distinct spectral patterns (87), then the temporal ICA appears less well-suited at decomposing distinct EEG oscillations (i.e., decompose EEG signal from EEG signal) compared to alternative approaches including (but not limited to) second-order blind identification (109–111), approximate joint diagonalization of cospectra (112, 113), and spectral ICA (114, 115).

The presented GLM EEG-fMRI fusion approach with variable HRF significantly increased robustness of obtained results for all investigated models compared to the same dataset observations proposed with ASM/RSM with the fixed HRF (18). The dominating fixed HRF GLM approach (5–9, 11–18, 21–26, 28–33, 43) may be revisited to gain an increased robustness of the results enabling variable HRF timings or utilizing an EEG-fMRI deconvolution approach (36–38). Similarly, this approach can be adopted for epileptogenic focus localization (25, 107, 108) due to the fact that the deconvolution approach demonstrated that delay timings between ictal EEG-fMRI associations does not fit to canonical HRF timings and often the local BOLD signal even precedes the EEG spike (41, 42).

The voxel-wise GLM approach is not the only data processing strategy to compare and fuse the EEG and fMRI data. The spatial ICA can rotate fMRI data into a space of spatially independent large scale brain networks (116, 117) with a representative component-specific time-course, which can be associated with simultaneously acquired EEG signal transformed into a comparable signal form (i.e., undersampled to fMRI timings, power fluctuations, spike timings/delays, etc.) (27, 30). Utilizing sliding windows over both EEG and fMRI-BOLD time-courses can be applied in the estimation of dynamic functional connectivity associations (34). A graph matrix between EEG and fMRI measures may be build *via* correlation measures or other similarity criteria (33). EEG-fMRI mixing parameters can be estimated through joint analysis approaches such as the joint-ICA (32, 118–120).

Over various existing EEG-fMRI data fusion strategies, we have demonstrated a fully automated GLM approach for robust lateralized task-related network visualization from local fMRI-BOLD signals and spectrally distinct task-related EEG patterns. In our approach, the variable HRF significantly improved the final robustness as the modeled EEG-fMRI peak delay did not overlap with the canonical HRF peak delay for the most task-related spectral patterns. Therefore, we propose this method for future clinical research applications in patients with neurocognitive deficits. These outcomes may also derive objective disease specific markers through local F-statistics or HRF changes that can be potentially used for the diagnostics, disease severity and treatment effect evaluations.

Limitations and Future Work

From the set of tested models, the ASM and RSSM were the most promising and robust for the blind visualization of task-related networks derived from simultaneous EEG-fMRI data. Several similar spectral models (16, 17, 47) considered Equation 10 instead of using Equation 1 for the EEG-fMRI fusion formulation, sometimes not-using the function $g(\omega)$. Comparison to the Equation 10 spectral model was not addressed here. All investigated EEG patterns were narrow band-pass filters and the effect of the non-linear ω^2 modulation were considered minimal. The ASM and RSSM have also not been directly compared to the concurrent recent data-driven EEG spectra decomposition approaches such as parallel factor analysis (PARAFAC) (20, 30, 121), coupled matrix-tensor factorization (40, 122), coupled tensor-tensor decomposition (123), or source-space ICA (124, 125). A full comparison to the most recent EEG-spectra fusion strategies should be addressed in the future research. Yet the variability in HRF yielded more significant effects with all four models than in our previous work (18).

$$b \propto \left(\int \omega^2 g(\omega) p(\omega)\, d\omega \right) * h \tag{10}$$

The robust task-related EEG-fMRI F-maps might be an effect of the active push-button response to the target stimuli. The maps' robustness may decrease using target count or passive responses (126) but such investigation was beyond the investigation of the current dataset and the study scope. The F-maps can be interpreted as data-driven functional connectivity maps (127, 128) where the EEG pattern's fluctuations emphasize the common relationships with local variable HRFs. The effective connectivity (127, 128) has not been quantified and evaluated here. Dynamic causal modeling (DCM), mostly between pre-selected regions of interest (ROIs), belongs to one of the most actively developed procedures quantifying the effective connectivity in fMRI or EEG data (129–132). Recently, the Bayesian fusion and multimodal EEG-fMRI DCM substantially improved the best effective connectivity model evidence (35). Future test-retest at ROIs of robust visual oddball data can provide important evidence of the DCM applicability.

Although the ASM provided the most robust spatial results, there are two weaknesses in the current ASM approach: (i) All ASM filtering properties were derived as an spectral average of the ASSM and RSSM patterns. Therefore, there would not be any optimized spectral filtering property without prior EEG ASSM and RSSM data-driven estimation *via* the spatiospectral ICA. Still, it appears that simple band-pass filters might be a sufficient approximation for the most promising δ_4 and θ_1 patterns. (ii) Thresholded ASM spatial F-maps appeared very similar over different EEG patterns. That might be an effect of a reported broadband component in the absolute EEG spectra resulting in lower spatial specificity of the ASM. On the other hand, high spatial specificity might be obtained with stricter statistical threshold, e.g., $p_{\mathrm{FWE}} < 0.01$ or even more stricter, which, however, would not be applicable for other fusion models.

Several EEG patterns demonstrated similar spatial EEG-fMRI F-maps while variable HRF was modeled in each voxel of each EEG band. It was not optimized and tested whether a weighted ($w_i \in$ <-1,1>) mixture of N EEG patterns ($\boldsymbol{u}_i$) would increase a linear dependence (i.e., |t|-values) between the final EEG pattern and the stimulus vector ($\boldsymbol{x}$), see Equation 11. Then, a general linear mixture EEG-fMRI fusion model with one global but still variable HRF would appear as Equation 12. Similar model analogy has been tested on hand-grip task data and compared to a single band EEG pattern with variable HRF (39). The results demonstrated more significant and specific blind task-related network visualizations for single δ and θ bands with band-specific variable HRFs. It is basically the same result presented here on the visual oddball dataset. Considering a linear mixture of EEG patterns with pattern specific HRFs maximizing relationships to the task, the Equation 12 would change to Equation 13. The optimization of the right side of the Equation 13 regarding the maximized linear dependence to the stimulus vector is challenging. Such EEG-fMRI fusion model alterations (i.e., Equations 12, 13) require a further investigation and testing on visual oddball data within the future research.

$$\mathbf{w} = \arg\max t\left(\sum_{i=1}^{N} w_i \mathbf{u}_i, \mathbf{x} \right) \tag{11}$$

$$\mathbf{b} \propto \sum_{i=1}^{N} w_i \mathbf{u}_i * \mathbf{h} \tag{12}$$

$$\mathbf{b} \propto \sum_{i=1}^{N} w_i \mathbf{u}_i * \mathbf{h}_i \tag{13}$$

Although temporal and spectral domains are considered fully complementary, the phase information of the spectral domain in all implemented EEG-fMRI fusion models was omitted here. It is a common procedure in the field to only utilize the magnitude information (5, 7, 10, 16, 17, 26). We suggest that the phase coupling effect should not be neglected in the future research. The phase coupling can separate different sources of similar magnitude/power profiles and it has already been successfully implemented in several EEG spectra blind source separation techniques (112–114, 133–136) including the used spatiospectral ICA (37, 137).

Our proposed experiments and the comparison of the fully automated and blind methodological approaches were tested in healthy subjects. The clinical impact needs to be determined in future studies of the electrical neural and neurovascular associations measured by simultaneous EEG-fMRI. The P300 ERP has been extensively investigated in studies of cognition in healthy individuals and in a wide range of neurological or psychiatric disorders. The lower amplitude and longer latency are measures indicative of slowing of general cognitive ability due to the disease condition (100, 138). We propose that local F-map or HRF changes may discern patients with a specific cognitive dysfunction and improve spatial specificity of dysfunction focus as a benefit of the fMRI resolution in future applications.

DATA AVAILABILITY STATEMENT

The data analyzed in this study is subject to the following licenses/restrictions: Data are property of the 1st Department of Neurology, St. Anne's University Hospital Brno, Czech Republic. Data can be made available upon request by email. Requests to access these datasets should be directed to Milan Brázdil, milan.brazdil@fnusa.cz.

ETHICS STATEMENT

The studies involving human participants were reviewed and approved by Masaryk University Ethics Committee, Brno, Czech Republic. The patients/participants provided their written informed consent to participate in this study.

AUTHOR CONTRIBUTIONS

RL implemented ASSM and RSSM and wrote the first draft of the manuscript. ZW implemented ASM and RSM, compared all models, designed manuscript graphics and tables, and revised the manuscript. DB supervised the blind source separation of EEG spectra and revised the manuscript. MB led the EEG-fMRI data acquisition and preprocessing, approved the neurophysiological validity of the results, and revised the manuscript. JJ supervised the EEG-fMRI data fusion method implementation, confirmed signal processing validity of implemented methods, and revised the manuscript. IN supervised the current model comparison research, approved the neurophysiological validity of the results, and significantly revised the first draft of the manuscript. All authors contributed to the article and approved the submitted version.

ACKNOWLEDGMENTS

All EEG-fMRI measurements were performed at the 1st Department of Neurology, St. Anne's University Hospital Brno, Czech Republic. Authors thanks to Drs. R. Mareček and M. Mikl for the data preprocessing work.

REFERENCES

1. Ives JR, Warach S, Schmitt F, Edelman RR, Schomer DL. Monitoring the patient's EEG during echo planar MRI. *Electroencephalogr Clin Neurophysiol.* (1993) 87:417–20. doi: 10.1016/0013-4694(93)90156-P
2. Huang-Hellinger FR, Breiter HC, McCormack G, Cohen MS, Kwong KK, Sutton JP, et al. Simultaneous functional magnetic resonance imaging and electrophysiological recording. *Hum Brain Mapp.* (1995) 3:13–23. doi: 10.1002/hbm.460030103
3. Allen PJ, Josephs O, Turner R. A method for removing imaging artifact from continuous EEG recorded during functional MRI. *Neuroimage.* (2000) 12:230–9. doi: 10.1006/nimg.2000.0599
4. Goldman RI, Stern JM, Engel J Jr, Cohen MS. Acquiring simultaneous EEG and functional MRI. *Clin Neurophysiol.* (2000) 111:1974–80. doi: 10.1016/S1388-2457(00)00456-9
5. Goldman RI, Stern JM, Engel J Jr, Cohen MS. Simultaneous EEG and fMRI of the alpha rhythm. *Neuroreport.* (2002) 13:2487–92. doi: 10.1097/00001756-200212200-00022
6. Moosmann M, Ritter P, Krastel I, Brink A, Thees S, Blankenburg F, et al. Correlates of alpha rhythm in functional magnetic resonance imaging and near infrared spectroscopy. *Neuroimage.* (2003) 20:145–58. doi: 10.1016/S1053-8119(03)00344-6
7. Laufs H, Kleinschmidt A, Beyerle A, Eger E, Salek-Haddadi A, Preibisch C, et al. EEG-correlated fMRI of human alpha activity. *Neuroimage.* (2003) 19:1463–76. doi: 10.1016/S1053-8119(03)00286-6
8. Laufs H, Krakow K, Sterzer P, Eger E, Beyerle A, Salek-Haddadi A, et al. Electroencephalographic signatures of attentional and cognitive default modes in spontaneous brain activity fluctuations at rest. *Proc Natl Acad Sci USA.* (2003) 100:11053–8. doi: 10.1073/pnas.1831638100
9. Gonçalves SI, de Munck JC, Pouwels PJW, Schoonhoven R, Kuijer JPA, Maurits NM, et al. Correlating the alpha rhythm to BOLD using simultaneous EEG/fMRI: inter-subject variability. *Neuroimage.* (2006) 30:203–13. doi: 10.1016/j.neuroimage.2005.09.062
10. de Munck JC, Gonçalves SI, Mammoliti R, Heethaar RM, Lopes da Silva FH. Interactions between different EEG frequency bands and their effect on alpha–fMRI correlations. *Neuroimage.* (2009) 47:69–76. doi: 10.1016/j.neuroimage.2009.04.029
11. Scheeringa R, Bastiaansen MCM, Petersson KM, Oostenveld R, Norris DG, Hagoort P. Frontal theta EEG activity correlates negatively with the default mode network in resting state. *Int J Psychophysiol.* (2008) 67:242–51. doi: 10.1016/j.ijpsycho.2007.05.017
12. Scheeringa R, Petersson KM, Kleinschmidt A, Jensen O, Bastiaansen MCM. EEG α power modulation of fMRI resting-state connectivity. *Brain Connect.* (2012) 2:254–64. doi: 10.1089/brain.2012.0088
13. Rusiniak M, Wróbel A, Cieśla K, Pluta A, Lewandowska M, Wójcik J, et al. The relationship between alpha burst activity and the default mode network. *Acta Neurobiol Exp.* (2018) 78:92–113. doi: 10.21307/ane-2018-010
14. Portnova GV, Tetereva A, Balaev V, Atanov M, Skiteva L, Ushakov V, et al. Correlation of BOLD signal with linear and nonlinear patterns of EEG in resting state EEG-informed fMRI. *Front Hum Neurosci.* (2017) 11:654. doi: 10.3389/fnhum.2017.00654
15. Sammer G, Blecker C, Gebhardt H, Bischoff M, Stark R, Morgen K, et al. Relationship between regional hemodynamic activity and simultaneously recorded EEG-theta associated with mental arithmetic-induced workload. *Hum Brain Mapp.* (2007) 28:793–803. doi: 10.1002/hbm.20309
16. Rosa MJ, Kilner J, Blankenburg F, Josephs O, Penny W. Estimating the transfer function from neuronal activity to BOLD using simultaneous EEG-fMRI. *Neuroimage.* (2010) 49:1496–509. doi: 10.1016/j.neuroimage.2009.09.011
17. Sclocco R, Tana MG, Visani E, Gilioli I, Panzica F, Franceschetti S, et al. EEG-informed fMRI analysis during a hand grip task: estimating the relationship between EEG rhythms and the BOLD signal. *Front Hum Neurosci.* (2014) 8:186. doi: 10.3389/fnhum.2014.00186
18. Labounek R, Lamoš M, Mareček R, Brázdil M, Jan J. Exploring task-related variability in fMRI data using fluctuations in power spectrum of simultaneously acquired EEG. *J Neurosci Methods.* (2015) 245:125–36. doi: 10.1016/j.jneumeth.2015.02.016
19. Labounek R, Bridwell DA, Mareček R, Lamoš M, Mikl M, Bednařík P, et al. EEG spatiospectral patterns and their link to fMRI BOLD signal *via* variable hemodynamic response functions. *J Neurosci Methods.* (2019) 318:34–46. doi: 10.1016/j.jneumeth.2019.02.012
20. Marecek R, Lamos M, Mikl M, Barton M, Fajkus J, Rektor I, et al. What can be found in scalp EEG spectrum beyond common frequency bands. EEG–fMRI study. *J Neural Eng.* (2016) 13:046026. doi: 10.1088/1741-2560/13/4/046026
21. Mulert C, Jäger L, Schmitt R, Bussfeld P, Pogarell O, Möller H-J, et al. Integration of fMRI and simultaneous EEG: towards a comprehensive understanding of localization and time-course of brain activity in target detection. *Neuroimage.* (2004) 22:83–94. doi: 10.1016/j.neuroimage.2003.10.051
22. Bénar C-G, Schön D, Grimault S, Nazarian B, Burle B, Roth M, et al. Single-trial analysis of oddball event-related potentials in simultaneous EEG-fMRI. *Hum Brain Mapp.* (2007) 28:602–13. doi: 10.1002/hbm.20289
23. Lemieux L, Salek-Haddadi A, Josephs O, Allen P, Toms N, Scott C, et al. Event-related fMRI with simultaneous and continuous EEG: description of the method and initial case report. *Neuroimage.* (2001) 14:780–7. doi: 10.1006/nimg.2001.0853
24. Vulliemoz S, Rodionov R, Carmichael DW, Thornton R, Guye M, Lhatoo SD, et al. Continuous EEG source imaging enhances analysis of EEG-fMRI in focal epilepsy. *Neuroimage.* (2010) 49:3219–29. doi: 10.1016/j.neuroimage.2009.11.055
25. Ebrahimzadeh E, Shams M, Fayaz F, Rajabion L, Mirbagheri M, Nadjar Araabi B, et al. Quantitative determination of concordance in localizing epileptic focus by component-based EEG-fMRI. *Comput Methods Programs Biomed.* (2019) 177:231–41. doi: 10.1016/j.cmpb.2019.06.003
26. Mantini D, Perrucci MG, Del Gratta C, Romani GL, Corbetta M. Electrophysiological signatures of resting state networks in the human brain. *Proc Natl Acad Sci USA.* (2007) 104:13170–5. doi: 10.1073/pnas.0700668104
27. Mantini D, Marzetti L, Corbetta M, Romani GL, Del Gratta C. Multimodal integration of fMRI and EEG data for high spatial and temporal resolution analysis of brain networks. *Brain Topogr.* (2010) 23:150–8. doi: 10.1007/s10548-009-0132-3
28. Omata K, Hanakawa T, Morimoto M, Honda M. Spontaneous slow fluctuation of EEG alpha rhythm reflects activity in deep-brain structures: a simultaneous EEG-fMRI study. *PLoS ONE.* (2013) 8:e66869. doi: 10.1371/journal.pone.0066869

29. Hiltunen T, Kantola J, Abou Elseoud A, Lepola P, Suominen K, Starck T, et al. Infra-slow EEG fluctuations are correlated with resting-state network dynamics in fMRI. *J Neurosci.* (2014) 34:356–62. doi: 10.1523/JNEUROSCI.0276-13.2014
30. Mareček R, Lamoš M, Labounek R, Barton M, Slavíček T, Mikl M, et al. Multiway array decomposition of EEG spectrum: implications of its stability for the exploration of large-scale brain networks. *Neural Comput.* (2017) 29:968–89. doi: 10.1162/NECO_a_00933
31. Keinänen T, Rytky S, Korhonen V, Huotari N, Nikkinen J, Tervonen O, et al. Fluctuations of the EEG-fMRI correlation reflect intrinsic strength of functional connectivity in default mode network. *J Neurosci Res.* (2018) 96:1689–98. doi: 10.1002/jnr.24257
32. Moosmann M, Eichele T, Nordby H, Hugdahl K, Calhoun VD. Joint independent component analysis for simultaneous EEG–fMRI: principle and simulation. *Int J Psychophysiol.* (2008) 67:212–21. doi: 10.1016/j.ijpsycho.2007.05.016
33. Yu Q, Wu L, Bridwell DA, Erhardt EB, Du Y, He H, et al. Building an EEG-fMRI multi-modal brain graph: a concurrent EEG-fMRI study. *Front Hum Neurosci.* (2016) 10:476. doi: 10.3389/fnhum.2016.00476
34. Lamoš M, Mareček R, Slavíček T, Mikl M, Rektor I, Jan J. Spatial-temporal-spectral EEG patterns of BOLD functional network connectivity dynamics. *J Neural Eng.* (2018) 15:036025. doi: 10.1088/1741-2552/aab66b
35. Wei H, Jafarian A, Zeidman P, Litvak V, Razi A, Hu D, et al. Bayesian fusion and multimodal DCM for EEG and fMRI. *Neuroimage.* (2020) 211:116595. doi: 10.1016/j.neuroimage.2020.116595
36. de Munck JC, Gonçalves SI, Huijboom L, Kuijer JPA, Pouwels PJW, Heethaar RM, et al. The hemodynamic response of the alpha rhythm: an EEG/fMRI study. *Neuroimage.* (2007) 35:1142–51. doi: 10.1016/j.neuroimage.2007.01.022
37. Wu L, Eichele T, Calhoun VD. Reactivity of hemodynamic responses and functional connectivity to different states of alpha synchrony: a concurrent EEG-fMRI study. *Neuroimage.* (2010) 52:1252–60. doi: 10.1016/j.neuroimage.2010.05.053
38. Bridwell DA, Wu L, Eichele T, Calhoun VD. The spatiospectral characterization of brain networks: fusing concurrent EEG spectra and fMRI maps. *Neuroimage.* (2013) 69:101–11. doi: 10.1016/j.neuroimage.2012.12.024
39. Prokopiou PC, Xifra-Porxas A, Kassinopoulos M. Modeling the hemodynamic response function using motor task and eyes-open resting-state EEG-fMRI. *bioRxiv.* (2020). doi: 10.1101/2020.06.29.178483v1
40. Van Eyndhoven S, Dupont P, Tousseyn S, Vervliet N, Van Paesschen W, Van Huffel S, et al. Augmenting interictal mapping with neurovascular coupling biomarkers by structured factorization of epileptic EEG and fMRI data. *NeuroImage.* (2021) 228:117652. doi: 10.1016/j.neuroimage.2020.117652
41. Jacobs J, Levan P, Moeller F, Boor R, Stephani U, Gotman J, et al. Hemodynamic changes preceding the interictal EEG spike in patients with focal epilepsy investigated using simultaneous EEG-fMRI. *Neuroimage.* (2009) 45:1220–31. doi: 10.1016/j.neuroimage.2009.01.014
42. LeVan P, Tyvaert L, Moeller F, Gotman J. Independent component analysis reveals dynamic ictal BOLD responses in EEG-fMRI data from focal epilepsy patients. *Neuroimage.* (2010) 49:366–78. doi: 10.1016/j.neuroimage.2009.07.064
43. Labounek R, Janeček D, Mareček R, Lamoš M, Slaviček T, Mikl M, et al. Generalized EEG-FMRI spectral and spatiospectral heuristic models. In: *2016 IEEE 13th International Symposium on Biomedical Imaging (ISBI).* Prague (2016). p. 767–70. doi: 10.1109/ISBI.2016.7493379
44. Polich J. Theoretical overview of P3a and P3b. In: *Detection of Change: Event-Related Potential and fMRI Findings*, Polich J, editor. Boston, MA: Springer US (2003). p. 83–98. doi: 10.1007/978-1-4615-0294-4_5
45. Tueting P, Sutton S, Zubin J. Quantitative evoked potential correlates of the probability of events. *Psychophysiology.* (1970) 7:385–94. doi: 10.1111/j.1469-8986.1970.tb01763.x
46. Kok A. Event-related-potential (ERP) reflections of mental resources: a review and synthesis. *Biol Psychol.* (1997) 45:19–56. doi: 10.1016/S0301-0511(96)05221-0
47. Kilner JM, Mattout J, Henson R, Friston KJ. Hemodynamic correlates of EEG: a heuristic. *Neuroimage.* (2005) 28:280–6. doi: 10.1016/j.neuroimage.2005.06.008
48. Labounek R, Bridwell DA, Mareček R, Lamoš M, Mikl M, Slavíček T, et al. Stable scalp EEG spatiospectral patterns across paradigms estimated by group ICA. *Brain Topogr.* (2018) 31:76–89. doi: 10.1007/s10548-017-0585-8
49. Labounek R, Bridwell DA, Mareček R, Lamoš M, Mikl M, Brázdil M, et al. Stable EEG spatiospectral sources using relative power as group-ICA input. In: *World Congress on Medical Physics and Biomedical Engineering 2018.* Singapore: Springer Singapore (2019). p. 125–8. doi: 10.1007/978-981-10-9038-7_22
50. Allen PJ, Polizzi G, Krakow K, Fish DR, Lemieux L. Identification of EEG events in the MR scanner: the problem of pulse artifact and a method for its subtraction. *Neuroimage.* (1998) 8:229–39. doi: 10.1006/nimg.1998.0361
51. Calhoun VD, Adali T, Pearlson GD, Pekar JJ. A method for making group inferences from functional MRI data using independent component analysis. *Hum Brain Mapp.* (2001) 14:140–51. doi: 10.1002/hbm.1048
52. Bell AJ, Sejnowski TJ. An information-maximization approach to blind separation and blind deconvolution. *Neural Comput.* (1995) 7:1129–59. doi: 10.1162/neco.1995.7.6.1129
53. Himberg J, Hyvärinen A, Esposito F. Validating the independent components of neuroimaging time series *via* clustering and visualization. *Neuroimage.* (2004) 22:1214–22. doi: 10.1016/j.neuroimage.2004.03.027
54. Friston KJ, Holmes AP, Worsley KJ, Poline J-P, Frith CD, Frackowiak RSJ. Statistical parametric maps in functional imaging: a general linear approach. *Hum Brain Mapp.* (1994) 2:189–210. doi: 10.1002/hbm.460020402
55. Friston KJ, Ashburner J, Frith CD, Poline J-B, Heather JD, Frackowiak RSJ. Spatial registration and normalization of images. *Hum Brain Mapp.* (1995) 3:165–89. doi: 10.1002/hbm.460030303
56. Friston KJ, Fletcher P, Josephs O, Holmes A, Rugg MD, Turner R. Event-related fMRI: characterizing differential responses. *Neuroimage.* (1998) 7:30–40. doi: 10.1006/nimg.1997.0306
57. Uddin LQ, Yeo BTT, Spreng RN. Towards a universal taxonomy of macro-scale functional human brain networks. *Brain Topogr.* (2019) 32:926–42. doi: 10.1007/s10548-019-00744-6
58. Menon V, Uddin LQ. Saliency, switching, attention and control: a network model of insula function. *Brain Struct Funct.* (2010) 214:655–67. doi: 10.1007/s00429-010-0262-0
59. Uddin LQ. Salience processing and insular cortical function and dysfunction. *Nat Rev Neurosci.* (2015) 16:55–61. doi: 10.1038/nrn3857
60. Sridharan D, Levitin DJ, Menon V. A critical role for the right fronto-insular cortex in switching between central-executive and default-mode networks. *Proc Natl Acad Sci USA*. (2008) 105:12569–74. doi: 10.1073/pnas.0800005105
61. Mori S,Wakana S, van Zijl PCM, Nagae-Poetscher LM. *MRI Atlas of Human White Matter*. Amsterdam: Elsevier (2005). Available online at: https://www.elsevier.com/books/mri-atlas-of-human-white-matter/mori/978-0-444-51741-8
62. Wakana S, Caprihan A, Panzenboeck MM, Fallon JH, Perry M, Gollub RL, et al. Reproducibility of quantitative tractography methods applied to cerebral white matter. *Neuroimage.* (2007) 36:630–44. doi: 10.1016/j.neuroimage.2007.02.049
63. Hua K, Zhang J, Wakana S, Jiang H, Li X, Reich DS, et al. Tract probability maps in stereotaxic spaces: analyses of white matter anatomy and tract-specific quantification. *Neuroimage.* (2008) 39:336–47. doi: 10.1016/j.neuroimage.2007.07.053
64. Linden DE, Prvulovic D, Formisano E, Völlinger M, Zanella FE, Goebel R, et al. The functional neuroanatomy of target detection: an fMRI study of visual and auditory oddball tasks. *Cereb Cortex.* (1999) 9:815–23. doi: 10.1093/cercor/9.8.815
65. Stevens AA, Skudlarski P, Gatenby JC, Gore JC. Event-related fMRI of auditory and visual oddball tasks. *Magn Reson Imaging.* (2000) 18:495–502. doi: 10.1016/S0730-725X(00)00128-4
66. Kiehl KA, Laurens KR, Duty TL, Forster BB, Liddle PF. An event-related fMRI study of visual and auditory oddball tasks. *J. Psychophysiol.* (2001) 15:221–40. doi: 10.1027//0269-8803.15.4.221
67. Brázdil M, Dobsík M, Mikl M, Hlustík P, Daniel P, Pazourková M, et al. Combined event-related fMRI and intracerebral

ERP study of an auditory oddball task. *Neuroimage.* (2005) 26:285–93. doi: 10.1016/j.neuroimage.2005.01.051

68. Brázdil M, Mikl M, Marecek R, Krupa P, Rektor I. Effective connectivity in target stimulus processing: a dynamic causal modeling study of visual oddball task. *Neuroimage.* (2007) 35:827–35. doi: 10.1016/j.neuroimage.2006.12.020
69. Chen C-C, Syue K-S, Li K-C, Yeh S-C. Neuronal correlates of a virtual-reality-based passive sensory P300 network. *PLoS ONE.* (2014) 9:e112228. doi: 10.1371/journal.pone.0112228
70. Li F, Chen B, Li H, Zhang T, Wang F, Jiang Y, et al. The time-varying networks in P300: a task-evoked EEG study. *IEEE Trans Neural Syst Rehabil Eng.* (2016) 24:725–33. doi: 10.1109/TNSRE.2016.2523678
71. Li F, Yi C, Jiang Y, Liao Y, Si Y, Yao D, et al. The construction of large-scale cortical networks for P300 from scalp EEG. *IEEE Access.* (2018) 6:68498–506. doi: 10.1109/ACCESS.2018.2879487
72. Zhang Y, Tang AC, Zhou X. Synchronized network activity as the origin of a P300 component in a facial attractiveness judgment task. *Psychophysiology.* (2014) 51:285–9. doi: 10.1111/psyp.12153
73. Li F, Yi C, Liao Y, Jiang Y, Si Y, Song L, et al. Reconfiguration of brain network between resting-state and P300 task. *IEEE Trans Cogn Dev Syst.* (2020). doi: 10.1109/TCDS.2020.2965135. [Epub ahead of print].
74. Liebenthal E, Ellingson ML, Spanaki MV, Prieto TE, Ropella KM, Binder JR. Simultaneous ERP and fMRI of the auditory cortex in a passive oddball paradigm. *Neuroimage.* (2003) 19:1395–404. doi: 10.1016/S1053-8119(03)00228-3
75. O'Connell RG, Balsters JH, Kilcullen SM, Campbell W, Bokde AW, Lai R, et al. A simultaneous ERP/fMRI investigation of the P300 aging effect. *Neurobiol Aging.* (2012) 33:2448–61. doi: 10.1016/j.neurobiolaging.2011.12.021
76. Campanella S, Bourguignon M, Peigneux P, Metens T, Nouali M, Goldman S, et al. BOLD response to deviant face detection informed by P300 event-related potential parameters: a simultaneous ERP–fMRI study. *Neuroimage.* (2013) 71:92–103. doi: 10.1016/j.neuroimage.2012.12.077
77. Altieri R, Melcarne A, Junemann C, Zeppa P, Zenga F, Garbossa D, et al. Inferior Fronto-Occipital fascicle anatomy in brain tumor surgeries: from anatomy lab to surgical theater. *J Clin Neurosci.* (2019) 68:290–4. doi: 10.1016/j.jocn.2019.07.039
78. Dalrymple-Alford JC, Harland B, Loukavenko EA, Perry B, Mercer S, Collings DA, et al. Anterior thalamic nuclei lesions and recovery of function: relevance to cognitive thalamus. *Neurosci Biobehav Rev.* (2015) 54:145–60. doi: 10.1016/j.neubiorev.2014.12.007
79. Schepers IM, Beck A-K, Bräuer S, Schwabe K, Abdallat M, Sandmann P, et al. Human centromedian-parafascicular complex signals sensory cues for goal-oriented behavior selection. *Neuroimage.* (2017) 152:390–9. doi: 10.1016/j.neuroimage.2017.03.019
80. Barton M, Mareček R, Krajčovičová L, Slavíček T, Kašpárek T, Zemánková P, et al. Evaluation of different cerebrospinal fluid and white matter fMRI filtering strategies—quantifying noise removal and neural signal preservation. *Hum Brain Mapp.* (2019) 40:1114–38. doi: 10.1002/hbm.24433
81. Mazerolle EL, Beyea SD, Gawryluk JR, Brewer KD, Bowen CV, D'Arcy RCN. Confirming white matter fMRI activation in the corpus callosum: co-localization with DTI tractography. *Neuroimage.* (2010) 50:616–21. doi: 10.1016/j.neuroimage.2009.12.102
82. Gawryluk JR, Mazerolle EL, D'Arcy RCN. Does functional MRI detect activation in white matter? A review of emerging evidence, issues, and future directions. *Front Neurosci.* (2014) 8:239. doi: 10.3389/fnins.2014.00239
83. Ding Z, Huang Y, Bailey SK, Gao Y, Cutting LE, Rogers BP, et al. Detection of synchronous brain activity in white matter tracts at rest and under functional loading. *Proc Natl Acad Sci USA.* (2018) 115:595–600. doi: 10.1073/pnas.1711567115
84. Grajauskas LA, Frizzell T, Song X, D'Arcy RCN. White matter fMRI activation cannot be treated as a nuisance regressor: overcoming a historical blind spot. *Front. Neurosci.* (2019) 13:1024. doi: 10.3389/fnins.2019.01024
85. Li M, Newton AT, Anderson AW, Ding Z, Gore JC. Characterization of the hemodynamic response function in white matter tracts for event-related fMRI. *Nat Commun.* (2019) 10:1140. doi: 10.1038/s41467-019-09076-2
86. Rektor I, Brázdil M, Nestrasil I, Bares M, Daniel P. Modifications of cognitive and motor tasks affect the occurrence of event-related potentials in the human cortex: cognitive and motor task modifications of event-related potentials. *Eur J Neurosci.* (2007) 26:1371–80. doi: 10.1111/j.1460-9568.2007.05713.x
87. Başar E, Düzgün A. The CLAIR model: extension of Brodmann areas based on brain oscillations and connectivity. *Int J Psychophysiol.* (2016) 103:185–98. doi: 10.1016/j.ijpsycho.2015.02.018
88. Başar-Eroglu C, Başar E, Demiralp T, Schürmann M. P300-response: possible psychophysiological correlates in delta and theta frequency channels. A review. *Int J Psychophysiol.* (1992) 13:161–79. doi: 10.1016/0167-8760(92)90055-G
89. Bernat EM, Malone SM, Williams WJ, Patrick CJ, Iacono WG. Decomposing delta, theta, and alpha time-frequency ERP activity from a visual oddball task using PCA. *Int J Psychophysiol.* (2007) 64:62–74. doi: 10.1016/j.ijpsycho.2006.07.015
90. Harper J, Malone SM, Bernat EM. Theta and delta band activity explain N2 and P3 ERP component activity in a go/no-go task. *Clin Neurophysiol.* (2014) 125:124–32. doi: 10.1016/j.clinph.2013.06.025
91. Peng W, Hu L, Zhang Z, Hu Y. Causality in the association between P300 and alpha event-related desynchronization. *PLoS ONE.* (2012) 7:e34163. doi: 10.1371/journal.pone.0034163
92. Bender S, Banaschewski T, Roessner V, Klein C, Rietschel M, Feige B, et al. Variability of single trial brain activation predicts fluctuations in reaction time. *Biol Psychol.* (2015) 106:50–60. doi: 10.1016/j.biopsycho.2015.01.013
93. Başar-Eroglu C, Demiralp T. Event-related theta oscillations: an integrative and comparative approach in the human and animal brain. *Int J Psychophysiol.* (2001) 39:167–95. doi: 10.1016/S0167-8760(00)00140-9
94. Makeig S. Auditory event-related dynamics of the EEG spectrum and effects of exposure to tones. *Electroencephalogr Clin Neurophysiol.* (1993) 86:283–93. doi: 10.1016/0013-4694(93)90110-H
95. Güntekin B, Emek-Savaş DD, Kurt P, Yener GG, Başar E. Beta oscillatory responses in healthy subjects and subjects with mild cognitive impairment. *Neuroimage Clin.* (2013) 3:39–46. doi: 10.1016/j.nicl.2013.07.003
96. Lin Y-Q, Cui S-S, Du J-J, Li G, He Y-X, Zhang P-C, et al. N1 and P1 components associate with visuospatial-executive and language functions in normosmic Parkinson's disease: an event-related potential study. *Front Aging Neurosci.* (2019) 11:18. doi: 10.3389/fnagi.2019.00018
97. Luck SJ, Heinze HJ, Mangun GR, Hillyard SA. Visual event-related potentials index focused attention within bilateral stimulus arrays. II. Functional dissociation of P1 and N1 components. *Electroencephalogr Clin Neurophysiol.* (1990) 75:528–42. doi: 10.1016/0013-4694(90)90139-B
98. Novitskiy N, Ramautar JR, Vanderperren K, De Vos M, Mennes M, Mijovic B, et al. The BOLD correlates of the visual P1 and N1 in single-trial analysis of simultaneous EEG-fMRI recordings during a spatial detection task. *Neuroimage.* (2011) 54:824–35. doi: 10.1016/j.neuroimage.2010.09.041
99. Klimesch W, Schack B, Schabus M, Doppelmayr M, Gruber W, Sauseng P. Phase-locked alpha and theta oscillations generate the P1–N1 complex and are related to memory performance. *Cogn Brain Res.* (2004) 19:302–16. doi: 10.1016/j.cogbrainres.2003.11.016
100. Bledowski C, Prvulovic D, Hoechstetter K, Scherg M, Wibral M, Goebel R, et al. Localizing P300 generators in visual target and distractor processing: a combined event-related potential and functional magnetic resonance imaging study. *J Neurosci.* (2004) 24:9353–60. doi: 10.1523/JNEUROSCI.1897-04.2004
101. Anticevic A, Cole MW, Murray JD, Corlett PR, Wang X-J, Krystal JH. The role of default network deactivation in cognition and disease. *Trends Cogn Sci.* (2012) 16:584–92. doi: 10.1016/j.tics.2012.10.008
102. Fox MD, Snyder AZ, Vincent JL, Corbetta M, Van Essen DC, Raichle ME. The human brain is intrinsically organized into dynamic, anticorrelated functional networks. *Proc Natl Acad Sci USA.* (2005) 102:9673–8. doi: 10.1073/pnas.0504136102
103. Li Y, Wang L-Q, Hu Y. Localizing P300 generators in high-density event-related potential with fMRI. *Med Sci Monit.* (2009) 15:MT47–53. Available online at: https://www.medscimonit.com/download/index/idArt/869569
104. Wang RWY, Chang W-L, Chuang S-W, Liu I-N. Posterior cingulate cortex can be a regulatory modulator of the default mode network in task-negative state. *Sci Rep.* (2019) 9:7565. doi: 10.1038/s41598-019-43885-1

105. Leech R, Sharp DJ. The role of the posterior cingulate cortex in cognition and disease. *Brain.* (2014) 137:12–32. doi: 10.1093/brain/awt162
106. Winkler I, Haufe S, Tangermann M. Automatic classification of artifactual ICA-components for artifact removal in EEG signals. *Behav Brain Funct.* (2011) 7:30. doi: 10.1186/1744-9081-7-30
107. Ebrahimzadeh E, Soltanian-Zadeh H, Araabi BN, Fesharaki SSH, Habibabadi JM. Component-related BOLD response to localize epileptic focus using simultaneous EEG-fMRI recordings at 3T. *J Neurosci Methods.* (2019) 322:34–49. doi: 10.1016/j.jneumeth.2019.04.010
108. Ebrahimzadeh E, Shams M, Rahimpour Jounghani A, Fayaz F, Mirbagheri M, Hakimi N, et al. Localizing confined epileptic foci in patients with an unclear focus or presumed multifocality using a component-based EEG-fMRI method. *Cogn Neurodyn.* (2020) 15:207–22. doi: 10.1007/s11571-020-09614-5
109. Belouchrani A, Abed-Meraim K, Cardoso J, Moulines E. A blind source separation technique using second-order statistics. *IEEE Trans Signal Process.* (1997) 45:434–44. doi: 10.1109/78.554307
110. Tang AC, Sutherland MT, McKinney CJ. Validation of SOBI components from high-density EEG. *Neuroimage.* (2005) 25:539–53. doi: 10.1016/j.neuroimage.2004.11.027
111. Tang A. Applications of second order blind identification to high-density EEG-based brain imaging: a review. In: *Advances in Neural Networks - ISNN 2010* (Heidelberg: Springer Berlin) (2010). p. 368–77. doi: 10.1007/978-3-642-13318-3_46
112. Congedo M, Gouy-Pailler C, Jutten C. On the blind source separation of human electroencephalogram by approximate joint diagonalization of second order statistics. *Clin Neurophysiol.* (2008) 119:2677–86. doi: 10.1016/j.clinph.2008.09.007
113. Congedo M, John RE, De Ridder D, Prichep L. Group independent component analysis of resting state EEG in large normative samples. *Int J Psychophysiol.* (2010) 78:89–99. doi: 10.1016/j.ijpsycho.2010.06.003
114. Hyvärinen A, Ramkumar P, Parkkonen L, Hari R. Independent component analysis of short-time Fourier transforms for spontaneous EEG/MEG analysis. *Neuroimage.* (2010) 49:257–71. doi: 10.1016/j.neuroimage.2009.08.028
115. Bridwell DA, Rachakonda S, Silva RF, Pearlson GD, Calhoun VD. Spatiospectral decomposition of multi-subject EEG: evaluating blind source separation algorithms on real and realistic simulated data. *Brain Topogr.* (2018) 31:47–61. doi: 10.1007/s10548-016-0479-1
116. Allen EA, Erhardt EB, Damaraju E, Gruner W, Segall JM, Silva RF, et al. A baseline for the multivariate comparison of resting-state networks. *Front Syst Neurosci.* (2011) 5:2. doi: 10.3389/fnsys.2011.00002
117. Spadone S, Della Penna S, Sestieri C, Betti V, Tosoni A, Perrucci MG, et al. Dynamic reorganization of human resting-state networks during visuospatial attention. *Proc Natl Acad Sci USA.* (2015) 112:8112–7. doi: 10.1073/pnas.1415439112
118. Calhoun VD, Liu J, Adali T. A review of group ICA for fMRI data and ICA for joint inference of imaging, genetic, and ERP data. *Neuroimage.* (2009) 45:S163–72. doi: 10.1016/j.neuroimage.2008.10.057
119. Edwards BG, Calhoun VD, Kiehl KA. Joint ICA of ERP and fMRI during error-monitoring. *Neuroimage.* (2012) 59:1896–903. doi: 10.1016/j.neuroimage.2011.08.088
120. Mangalathu-Arumana J, Beardsley SA, Liebenthal E. Within-subject joint independent component analysis of simultaneous fMRI/ERP in an auditory oddball paradigm. *Neuroimage.* (2012) 60:2247–57. doi: 10.1016/j.neuroimage.2012.02.030
121. Martínez-Montes E, Valdés-Sosa PA, Miwakeichi F, Goldman RI, Cohen MS. Concurrent EEG/fMRI analysis by multiway Partial Least Squares. *Neuroimage.* (2004) 22:1023–34. doi: 10.1016/j.neuroimage.2004.03.038
122. Van Eyndhoven S, Vervliet N, De Lathauwer L, Van Huffel S. Identifying stable components of matrix/tensor factorizations via lowrank approximation of inter-factorization similarity. In: *2019 27th European Signal Processing Conference (EUSIPCO)* (A Coruña: IEEE) (2019). p. 1–5. doi: 10.23919/EUSIPCO.2019.8902954
123. Jonmohamadi Y, Muthukumaraswamy S, Chen J, Roberts J, Crawford R, Pandey A. Extraction of common task features in EEG-fMRI data using coupled tensor-tensor decomposition. *Brain Topogr.* (2020) 33:636–50. doi: 10.1007/s10548-020-00787-0
124. Jonmohamadi Y, Poudel G, Innes C, Jones R. Source-space ICA for EEG source separation, localization, and time-course reconstruction. *Neuroimage.* (2014) 101:720–37. doi: 10.1016/j.neuroimage.2014.07.052
125. Jonmohamadi Y, Forsyth A, McMillan R, Muthukumaraswamy SD. Constrained temporal parallel decomposition for EEG-fMRI fusion. *J Neural Eng.* (2019) 16:16017. doi: 10.1088/1741-2552/aaefda
126. Warbrick T, Reske M, Shah NJ. Do EEG paradigms work in fMRI? Varying task demands in the visual oddball paradigm: implications for task design and results interpretation. *Neuroimage.* (2013) 77:177–85. doi: 10.1016/j.neuroimage.2013.03.026
127. Friston KJ. Functional and effective connectivity in neuroimaging: a synthesis. *Hum Brain Mapp.* (1994) 2:56–78. doi: 10.1002/hbm.460020107
128. Friston KJ. Functional and effective connectivity: a review. *Brain Connect.* (2011) 1:13–36. doi: 10.1089/brain.2011.0008
129. Friston KJ, Harrison L, Penny W. Dynamic causal modelling. *Neuroimage.* (2003) 19:1273–302. doi: 10.1016/S1053-8119(03)00202-7
130. Friston KJ, Preller KH, Mathys C, Cagnan H, Heinzle J, Razi A, et al. Dynamic causal modelling revisited. *Neuroimage.* (2019) 199:730–44. doi: 10.1016/j.neuroimage.2017.02.045
131. Havlicek M, Roebroeck A, Friston K, Gardumi A, Ivanov D, Uludag K. Physiologically informed dynamic causal modeling of fMRI data. *Neuroimage.* (2015) 122:355–72. doi: 10.1016/j.neuroimage.2015.07.078
132. Stephan KE, Tittgemeyer M, Knösche TR, Moran RJ, Friston KJ. Tractography-based priors for dynamic causal models. *NeuroImage.* (2009) 47:1628–38. doi: 10.1016/j.neuroimage.2009.05.096
133. Anemüller J, Sejnowski TJ, Makeig S. Complex independent component analysis of frequency-domain electroencephalographic data. *Neural Netw.* (2003) 16:1311–23. doi: 10.1016/j.neunet.2003.08.003
134. Bernat EM, Williams WJ, Gehring WJ. Decomposing ERP time–frequency energy using PCA. *Clin Neurophysiol.* (2005) 116:1314–34. doi: 10.1016/j.clinph.2005.01.019
135. Kauppi J-P, Parkkonen L, Hari R, Hyvärinen A. Decoding magnetoencephalographic rhythmic activity using spectrospatial information. *Neuroimage.* (2013) 83:921–36. doi: 10.1016/j.neuroimage.2013.07.026
136. Shou G, Ding L, Dasari D. Probing neural activations from continuous EEG in a real-world task: time-frequency independent component analysis. *J Neurosci Methods.* (2012) 209:22–34. doi: 10.1016/j.jneumeth.2012.05.022
137. Ramkumar P, Parkkonen L, Hari R, Hyvärinen A. Characterization of neuromagnetic brain rhythms over time scales of minutes using spatial independent component analysis. *Hum Brain Mapp.* (2012) 33:1648–62. doi: 10.1002/hbm.21303
138. Zhong R, Li M, Chen Q, Li J, Li G, Lin W. The P300 event-related potential component and cognitive impairment in epilepsy: a systematic review and meta-analysis. *Front Neurol.* (2019) 10:943. doi: 10.3389/fneur.2019.00943

Conflict of Interest: The authors declare that the research was conducted in the absence of any commercial or financial relationships that could be construed as a potential conflict of interest.

frontiers in Neurology

REVIEW
published: 27 April 2021
doi: 10.3389/fneur.2021.645594

Localization of Epileptic Foci Based on Simultaneous EEG–fMRI Data

Seyyed Mostafa Sadjadi[1], *Elias Ebrahimzadeh*[1,2], *Mohammad Shams*[3], *Masoud Seraji*[4,5] *and Hamid Soltanian-Zadeh*[1,2,6]*

[1] Control and Intelligent Processing Center of Excellence (CIPCE), School of Electrical and Computer Engineering, College of Engineering, University of Tehran, Tehran, Iran, [2] Neuroimage Signal and Image Analysis Group, School of Cognitive Sciences, Institute for Research in Fundamental Sciences (IPM), Tehran, Iran, [3] Neural Engineering Laboratory, Department of Electrical and Computer Engineering, George Mason University, Fairfax, VA, United States, [4] Center for Molecular and Behavioral Neuroscience, Rutgers University, Newark, NJ, United States, [5] Behavioral and Neural Sciences Graduate Program, Rutgers University, Newark, NJ, United States, [6] Medical Image Analysis Laboratory, Departments of Radiology and Research Administration, Henry Ford Health System, Detroit, MI, United States

Combining functional magnetic resonance imaging (fMRI) and electroencephalography (EEG) enables a non-invasive investigation of the human brain function and evaluation of the correlation of these two important modalities of brain activity. This paper explores recent reports on using advanced simultaneous EEG–fMRI methods proposed to map the regions and networks involved in focal epileptic seizure generation. One of the applications of EEG and fMRI combination as a valuable clinical approach is the pre-surgical evaluation of patients with epilepsy to map and localize the precise brain regions associated with epileptiform activity. In the process of conventional analysis using EEG–fMRI data, the interictal epileptiform discharges (IEDs) are visually extracted from the EEG data to be convolved as binary events with a predefined hemodynamic response function (HRF) to provide a model of epileptiform BOLD activity and use as a regressor for general linear model (GLM) analysis of the fMRI data. This review examines the methodologies involved in performing such studies, including techniques used for the recording of EEG inside the scanner, artifact removal, and statistical analysis of the fMRI signal. It then discusses the results reported for patients with primary generalized epilepsy and patients with different types of focal epileptic disorders. An important matter that these results have brought to light is that the brain regions affected by interictal epileptic discharges might not be limited to the ones where they have been generated. The developed methods can help reveal the regions involved in or affected by a seizure onset zone (SOZ). As confirmed by the reviewed literature, EEG–fMRI provides information that comes particularly useful when evaluating patients with refractory epilepsy for surgery.

Keywords: EEG-fMRI, epilepsy, localization, seizure onset zone, epileptic foci, BOLD response, IED

Edited by:
Fernando Cendes,
State University of Campinas, Brazil

Reviewed by:
Umair Javaid Chaudhary,
Queen Elizabeth Hospital Birmingham,
United Kingdom
Gerhard Drenthen,
Maastricht University Medical
Centre, Netherlands

***Correspondence:**
Hamid Soltanian-Zadeh
hszadeh@ut.ac.ir;
hsoltan1@hfhs.org

Specialty section:
This article was submitted to
Applied Neuroimaging,
a section of the journal
Frontiers in Neurology

Received: *23 December 2020*
Accepted: *11 March 2021*
Published: *27 April 2021*

Citation:
Sadjadi SM, Ebrahimzadeh E,
Shams M, Seraji M and
Soltanian-Zadeh H (2021) Localization
of Epileptic Foci Based on
Simultaneous EEG–fMRI Data.
Front. Neurol. 12:645594.
doi: 10.3389/fneur.2021.645594

INTRODUCTION

Localization of the epileptic generators is one of the striking topics in the treatment of epilepsy. It is still a challenge to find the precise brain regions of epileptic foci. Simultaneous EEG and fMRI data recordings are two modalities that can expose the brain regions with changes in metabolism and blood flow in response to epileptic spikes seen in the EEG, which are presumably accordant to the origin of epileptic discharges. fMRI which has a relatively poor temporal resolution but excellent spatial resolution is proper for localizing the brain regions with neuronal activity changes compared to the sham. This change is accompanied by a modification of the ratio of the concentration of oxy- and deoxy-hemoglobin in the blood, measured through the blood oxygen level-dependent (BOLD) effect (1, 2). In contrast, EEG has a high temporal resolution that makes it capable of measuring the neuronal currents directly from the scalp in the range of milliseconds but poor spatial resolution, which causes difficulty in determining the exact location of the current sources. The limitations of EEG are the deficiency in precise information of individual geometry and conductivity and the limited number of recording channels. Therefore, simultaneous recording of EEG and fMRI data provides a useful tool in using the two techniques' complementary features and overcoming the spatial limitations of EEG and fMRI's temporal boundaries.

An area where EEG and fMRI modalities have considerable clinical relevance is the pre-surgical evaluation in patients with epilepsy. In many patients with drug-resistant focal epilepsy undergoing surgery, standard magnetic resonance imaging (MRI) scans cannot visualize an exact source of epileptic seizures. Therefore, an invasive stereo-EEG analysis is required. However, simultaneous EEG and fMRI recordings offer a non-invasive alternative that can be a valuable approach for the localization of brain regions generating interictal epileptiform activity. This recording approach has become a useful tool for exploring ictal and interictal epileptic activity to reveal the epileptic foci and specify the relationship between hemodynamic changes and epileptic activity (3–6). EEG and fMRI are complementary for the localization of epileptic spike areas, but they can indicate different activity regions. Also, SEEG measures confirm EEG and fMRI results, although the concordance of simultaneous EEG–fMRI is not as good as the concordance between either one and SEEG (7). Unlike the general fMRI studies involving sensory, motor, and cognitive functions, the control and experimental conditions are determined based on the task. In epilepsy studies, these conditions are determined based on the absence and presence of epileptic discharges on the baseline of the EEG signal. So, in this context, the EEG signal is necessary for the analysis of fMRI data. The epileptic analysis of EEG–fMRI data is conventionally based on the identification of IEDs on EEG to create a regressor representing the effects of interest for a GLM analysis. Also, the model of epileptic activity is generally obtained by the convolution of EEG events as the stick functions of unitary amplitude with a predefined model of the event-related fMRI response, represented by the HRF. Finally, the activity maps showing the regions of significant IED-related change are obtained through the voxel-wise fitting of the model and application of appropriate statistical thresholds (3, 6, 8–10). Generally, BOLD responses are much less visible in patients with focal epilepsy compared to patients with generalized epilepsy (11, 12). Also, the posterior head regions are almost as involved as frontal regions in the BOLD response of patients with generalized epilepsy (11).

This paper reviews majority of the interictal studies presented with the aim of epileptic focus localization. For this purpose, the articles were classified based on their analysis method and reviewed in each part sorted by their publication date to reveal the trend of works in all the covered methods. First, we will present the primary concepts of epileptic source localization and analyze EEG inside the MRI scanner covered by associated studies. We will then review the localization methods and their clinical results obtained from patients with various types of epilepsy, showing the capability of each method for the pre-surgical evaluation of patients with epilepsy in comparison with the other methods. Finally, we discuss the complex issue of interpreting the result of EEG–fMRI in epilepsy studies. In this review, we tried to strike a balance between method-based studies and clinical outcomes. The Preferred Reporting Items for Systematic Reviews and Meta-Analyses (PRISMA) flowchart below shows the organization of the extracted articles (**Figure 1**). This review includes all EEG–fMRI studies focused on epileptic focus localization, which we have found by searching the related keywords in Google Scholar, PubMed dataset, Scopus, and ResearchGate. All studies are done interictally.

PRIMARY CONCEPTS

Signal Quality and Pre-processing

Recording EEG in the MR scanner requires non-magnetic electrodes and an MR-compatible amplifier system that transmits the amplified EEG outside the scanner. The patient must be as immobile as possible during the session. The magnetic gradient of the MR scanner induces large artifacts in the EEG. After the scanning session is finished, the artifacts will be removed by software to retrieve an EEG of reasonable quality (to retrieve a "clean" EEG); consequently, it allows us to mark the time of epileptic events. The next step is to build a mathematical model of what the BOLD signal should be at the voxels involved in the event. Voxels that took part in the event should have changes in their time courses as a result of each event in a predictable manner (in concordance with the HRF). Finally, the time course of every voxel is analyzed, and the voxels that have a correlative time course with the model are identified. Such voxels are either involved in the generation of the marked epileptic events in the EEG or a consequence of the event (3–6, 8–11).

Although the simultaneous recording of EEG–fMRI is one of the most valuable non-invasive tools for studying brain activity, it remains challenging to reach a high-quality signal of EEG and fMRI recorded simultaneously. Generally, simultaneous EEG–fMRI data are affected by various confounding factors and artifacts. The most important effective factor on the quality of the EEG and MRI recording is the immobilization of the head and electrode wires that can be reached by a plastic bag full of small polystyrene spheres. Besides, MRI-compatible sandbags are well-suited to immobilize the electrode wires on the way to the amplifiers (13).

Among the various artifacts, the artifact of MR gradient switching and ballistocardiogram (BCG) remain the major challenges in simultaneous EEG–fMRI study that make the EEG signal hard to interpret. Removing the fMRI scanner artifact is essential for the successful EEG–fMRI analysis. On the other hand, the presence of the BCG artifact does not necessarily lead

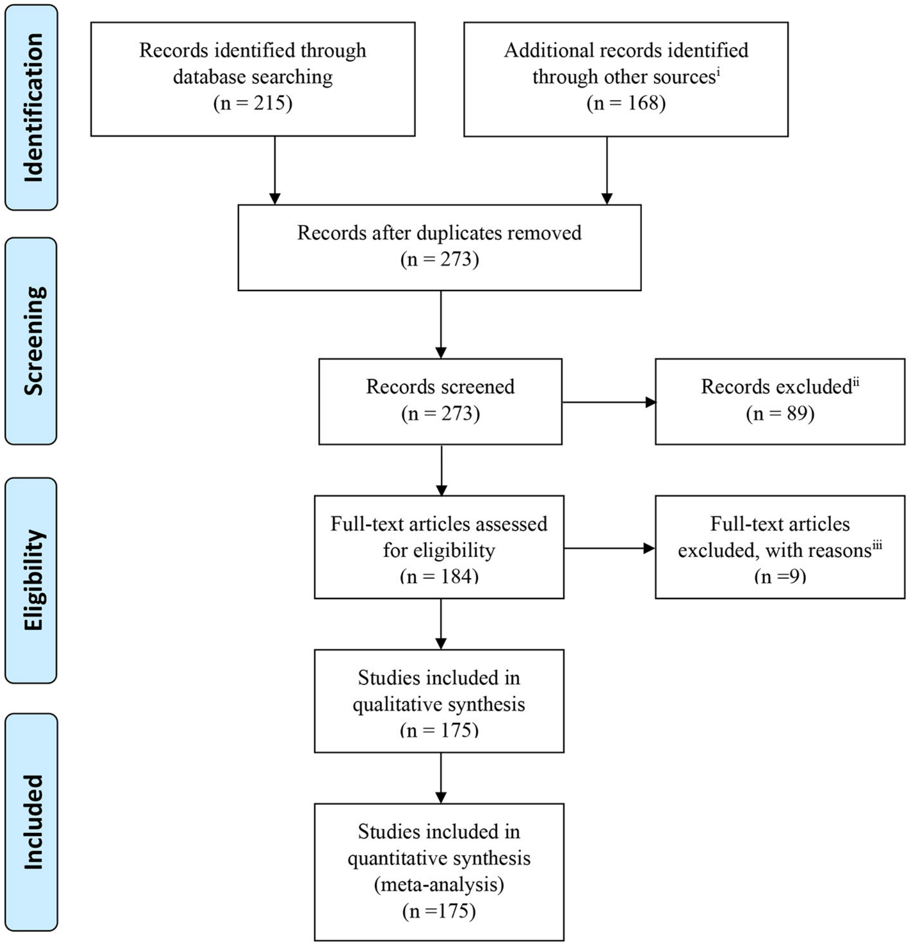

FIGURE 1 | PRISMA flowchart showing the classification of the extracted articles related to the epileptic focus localization through simultaneous EEG–fMRI recording. [i]Web of Science, Google Scholar, Pub Med, Scopus dataset, and ResearchGate websites and the references of the research and review articles. [ii]Not relevant to research question, aims and objectives, or old articles. [iii]Intracranial or ictal studies.

to a complete failure in identifying epileptic events (13–16). Yet, eliminating the BCG artifact improves the readability of the EEG and is useful for detecting subtle events like small epileptic discharges (13, 17).

To reduce the MR artifacts, one of the effective ways is the blind source extraction (BSE) algorithm followed by the averaging-and-subtraction method (18). Also, Amini et al. (19) proposed an approach based on generalized eigenvalue decomposition (GEVD) and median filtering, which demonstrated a considerable improvement in reducing MR artifacts compared to the conventional methods.

For eliminating BCG artifacts, two well-known methods are independent component analysis (ICA) and principal component analysis (PCA) which keep the spikes intact. However, ICA usually makes a better distinction between artifact and non-artifact components and performs stronger in artifact removal while preserving the spikes (13). Also, for a significant number of events, the subtraction filter is better than the Fourier filter in producing distortion but impairs the readability of EEG because of leaving large remaining artifacts inside the frames (13). Another approach for BCG artifact correction is multiple-source correction (MSC) (20). First, the source of IEDs is extracted from the EEG data collected outside the scanner to avoid the distortion of EEG data during the correction of BCG artifacts. Then, the topographies of the BCG artifacts defined based on the EEG data acquired inside the scanner are added to the alternative model of IED sources. The combined source model is applied inside the EEG data. Lastly, the artifact signal is subtracted from the EEG without considerable distortion of the IED topography. Compared with the traditional averaged artifact subtraction (AAS) method, the MSC approach has improved the ability of IED detection, especially when the BCG artifact is correlated and time-locked with the EEG signal produced by the focal brain activity of interest (20).

In the study of Körbl et al. (21), 18 patients with epilepsy were studied with the common methods of BCG removal and the conventional method of using marked IEDs to perform event-related analysis. Besides, nine patients used the moiré phase tracking (MPT) marker to discard suspicious IEDs synchronous with the BCG before the event-related analysis. The results demonstrated no significant difference between the two groups. However, the IED timing distribution was significantly related to the cardiac cycle in 11 of the 18 patients recorded without the MPT marker, but only two of the nine patients with the marker. In patients recorded without the marker, failing to discard suspicious IEDs led to more distant activations and more inaccurate fMRI maps.

In some of our previous works (22–24), the MRI gradient switching artifact was removed by using the fMRIb algorithm (https://fsl.fmrib.ox.ac.uk/eeglab/fmribplugin), which first increases the sampling rate to 20 kHz and then applies a low-pass filter at 60 Hz. The fMRIb toolbox also removed the BCG artifact associated with cardiac pulsations. **Figure 2** shows the EEG signals inside the scanner before and after the artifact removal procedure.

One of the other factors that affect the quality of the BOLD images is the signal loss due to variations in magnetic susceptibility, which alters the local magnetic field experienced by the subject's brain. For reducing this signal loss and increasing the ability to detect significant regions of BOLD signal changes, z-shimming is a practical technique. However, the question is whether this signal loss will be a limiting factor to identify the spike-related BOLD signal changes in patients with epilepsy. To find the actual effect of z-shimming in the results of identifying the spike-related BOLD responses, Bagshaw et al. (25) designed an experiment in which eight patients with temporal lobe epilepsy (TLE) underwent an EEG–fMRI session, and z-shimming was applied to their BOLD images. After comparing the intensities between z-shimmed and standard images and creating BOLD activation maps from the two sets of functional images using the times of spikes extracted from the EEG, it was found that the mean signal of the temporal lobes (TLs) increased $45.9 \pm 4.5\%$ as a result of z-shimming. Also, the percentage of the TL voxels above the brain intensity threshold increased from $66.1 \pm 7.6\%$ to $77.6 \pm 5.7\%$. However, this increase in the signal did not make any significant differences in the statistical maps. So, the signal loss is not a limiting factor for identifying the spike-related BOLD responses in patients with TLE.

The magnetic field strength of the MRI scanners could be an effective factor for the reproducibility of the EEG–fMRI results, which makes the results reliable as a clinically valuable method. This issue was addressed by Gholipour et al. (26). Fifteen epilepsy patients, including seven who had one 1.5T and one 3T EEG–fMRI scans and eight who had two 3T EEG–fMRI scans were studied. Then, the IED-related BOLD responses acquired from equal numbers of the IED events were compared between the scans of each patient. In four of the 15 patients, the results of the comparison between two sets of scans acquired from 1.5T and 3T scanners showed more significant responses in 3T scans just because of the higher magnetic field strength. Also, for the eight patients, the results of comparisons between two consecutive 3T scans showed reproducible responses in five cases with similarity in the visual pattern of activation and partly differences in terms of maximum *t*-score and cluster size in some cases.

Reduction of motion interference has been considered in some studies. In a study of Klovatch-Podlipsky et al. (27), a method based on MR-compatible dual-array EEG (daEEG) was proposed to reduce the motion interference in the EEG–fMRI recordings. The EEG electrodes were organized into two sets of nearly orthogonally intersecting wire bundles, and virtual bipolar measurements were obtained both along and across the bundles. By applying ICA on the EEG data and using the fact that only motion interference is influenced by the cable orientation and is more prominent in across-bundle measurements, daEEG allows suppression of both BCG and non-BCG interference from the data. Testing this method in 10 patients with epilepsy and comparing the results with those of the Optimal Basis Set (OBS) (28–30) showed more detected spikes after using daEEG than after OBS in nine of the 10 patients.

In the GLM analysis, settings and preprocesses are also important for the localization of the epileptic sources and can be optimized. For instance, considering some video-EEG physiological confounds like eye blinks and swallowing as additional regressors can reveal further IED-related BOLD clusters which might be part of the epileptic networks (31). Mikl et al. in (32) used the EEG–fMRI data of 13 patients with pharmacoresistant epilepsy and an excellent surgical outcome and performed 240 statistical analyses for each patient including all possible combinations of the used preprocessing and GLM settings. The results showed that preprocessing type, i.e., mainly the basic pipeline, or cardiac artifact correction does not affect GLM-based analysis results. The IED stimulation time course shifted 2 s earlier than positions from the EEG description, and also the massive filtering of artifact (24 movement regressors, signals from white matter and CSF, and global signal) are considered as the optimal preprocessing pipeline. Also, they reported that the canonical HRF as the basis function led to the best results of GLM analysis in agreement with some previous studies like (33, 34). However, its superiority over more flexible basis functions may be due to the used concordance measure. It is noticeable that in another study, Lemieux et al. (35) used a more flexible model of the event-related response, a Fourier basis set, to identify regions of activation corresponding to non-canonical responses associated with individual IED in 30 experiments of patients with focal epilepsy. They reported that non-canonical activations were almost always remote from the presumed generator of epileptiform activity. Thus, the BOLD response to IED is primarily canonical and the non-canonical responses may represent a number of phenomena, including artifacts and propagated epileptiform activity.

HRF and Spike Characteristics

In the common methods of EEG–fMRI analysis, a particular HRF is usually used for all patients. For example, the GLM framework models a prior knowledge of hemodynamic response in the design matrix and then explains the measured data by parameter estimation (10, 36–38). However, the real BOLD response to IEDs for each patient can be significantly different from the healthy controls (6, 39, 40). Even in a specific patient, the shape of HRF

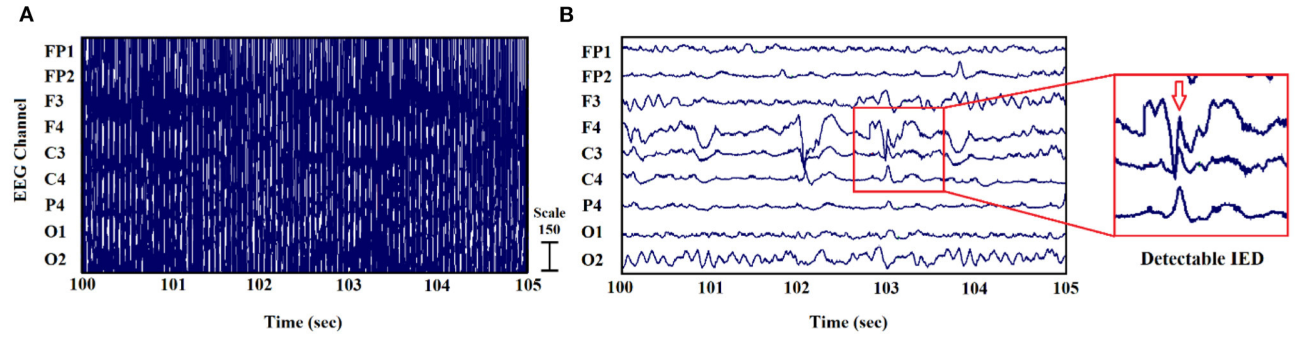

FIGURE 2 | EEG signal recorded inside the MR scanner: **(A)** before and **(B)** after the elimination of gradient and BCG artifacts (24).

varies with different brain areas and also is time-variant in each area (41, 42). The delay of the estimated function in a patient is different from those of the common theoretical models (43, 44). Using patient-specific HRF increases the detection sensitivity of epileptic spikes in EEG–fMRI (40). For instance, van Houdt et al. (17) used a finite impulse response approach for estimating the HRF from a dataset including 42 IED sets acquired in 29 patients and observed that more brain regions were active consistent with the EEG focus compared to the classical approach supposing a fixed HRF for each voxel in the brain (26 vs. 16).

Using multiple HRFs with peaks ranging from 3 to 9 s increases the BOLD response compared with using the standard HRF alone (11, 45). It was shown that the standard HRF that peaked at 5.4 s was more proper in detecting positive BOLD responses, and the HRFs that peaked later than the standard were more accurate for negative BOLD responses (45).

It has been observed that the results of EEG–fMRI analysis are influenced by the evaluation of the EEG signal and the scanning techniques more than the HRF model. Thus, although the HRF model influences the results of EEG–fMRI analysis, it may not be the main parameter in clinical practice (46).

Regarding the epileptic spikes in the EEG signal, it is revealed that the activation in BOLD response from EEG–fMRI analysis depends on the number of IEDs occurring during data acquisition (11, 17). However, the spiking rate is not the only influencing factor in the presence of the BOLD response. BOLD responses were seen in patients who had very few spikes, and a lack of response was noted in patients who had a high spiking rate (11).

Another issue is the spike identification that can be done automatically (20, 47) or by an expert. According to the study of Pedreira et al. (48), the automated spike-sorting algorithms for the classification of IEDs increase the value of EEG–fMRI analysis and mapping of IED-related BOLD responses (**Figure 3**). However, there is uncertainty in the results of spike identification because of the false detections and missed events. Huiskamp et al. (49) evaluated the impact of these two errors on the significance of the expected fMRI activation and revealed that the effect of missed events is larger in deteriorating the expected results. According to this study, although the uncertain spikes cause errors in IED-related BOLD responses, if they are considered as the events and included in the analysis, the responses will be closer to the expected results.

In the same direction, the aim of Flanagan et al. (50) was to find the influence of inexact or unreliable marking of EEG epileptiform events on the result of statistical parametric mapping (SPM) analysis in EEG–fMRI studies of patients with epilepsy. In this paper, the EEG–fMRI data of 10 patients with epilepsy were analyzed, and epileptiform events were marked. Then, the effect of omitting, mislabeling, and inconsistent timing of events was observed separately, considering the numbers of voxels above the threshold in the resulting SPM analysis. The results showed that omitting true epileptiform events decreased the number of above-threshold voxels. Mixing epileptiform and non-epileptiform events usually (but not always) caused a similar decrease. Inconsistent timing of events for small (<200 ms) and large (>500 ms) inconsistencies had small and large effects on the results, respectively. This suggests that accurate marking up of epileptiform events in EEG is still one of the most important factors for obtaining reliable results from EEG–fMRI analysis.

Besides, multiple fast fMRI sequences have been recently developed, one of which is magnetic resonance encephalography (MREG). Comparing MREG with the traditional sequence of echo-planar imaging (EPI) has revealed that MREG gives higher maximum *t*-values than EPI (49). However, Safi-Harb et al. in (51) reported that EPI yielded a better true positive rate and larger cluster size than MREG using a proper threshold. Also, it was shown that the HRF shape had a larger effect on MREG detection than EPI. Additional studies are needed to make a definitive judgment on their relative sensitivity. In terms of localizing the epileptic network, Jäger et al. (52) state that high-density EEG and fast fMRI seem to improve EEG–fMRI analysis results.

Pre-spike BOLD Signal Changes

Hemodynamic changes that are time-locked to spikes may reflect the propagation of neuronal activity from a focus, or conversely the activation of a network linked to spike generation (53). That is why pre-spike concordant BOLD signal changes may contain information about the epileptic networks. In a study of Jacobs et al. (54), five patients with idiopathic focal epilepsy and six patients with symptomatic focal epilepsy were studied. Spike timing was identified, and HRFs were calculated as the most focal

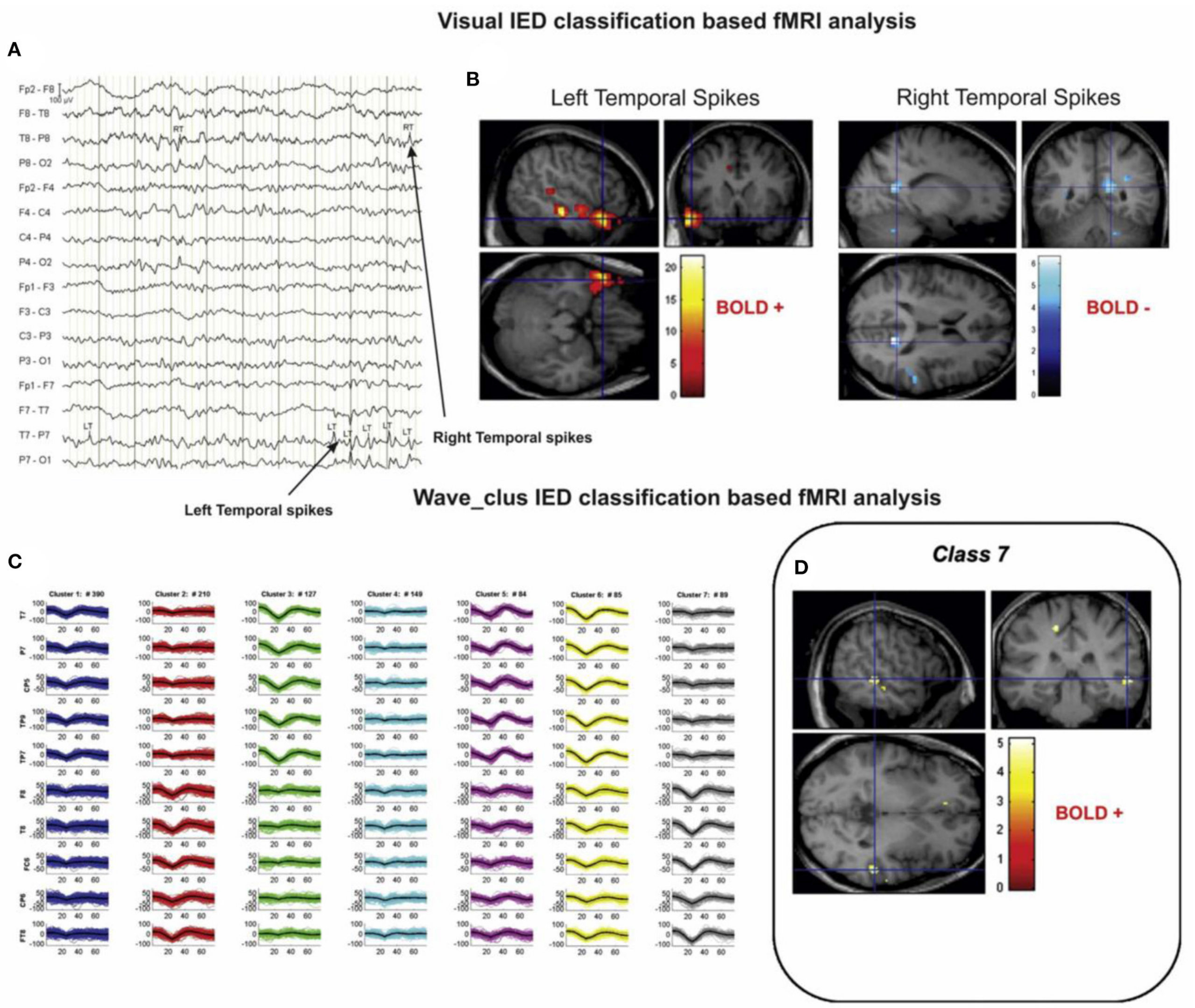

FIGURE 3 | A sample of visual and algorithmic classification of the IEDs. **(A)** The result of visual classification from the bipolar montage (64 channels) of EEG recorded inside the scanner is performed by an expert. **(B)** The results of EEG–fMRI analysis, based on visual-IED labeling. **(C)** The seven classes identified using the algorithmic classification. **(D)** The result of EEG–fMRI analysis, associated with class 7 of identified IEDs. All the fMRI results are overlaid on the subject's T1-weighted image (48).

BOLD response to model the regressors of statistical analysis with the timing of spike events convolved to HRFs peaking at −9 to +9 s around the spike. The results showed pre-spike BOLD responses in 11 of the 13 studies which were more focal and related to the spike field than post-spike responses (**Figure 4**).

The question of whether these pre-spike BOLD responses were the result of a synchronized neuronal discharge was yet to be investigated. In another study (55), four patients with pharmacoresistant focal epilepsy were selected by showing both pre- and post-spike BOLD responses concordant with the EEG focus during the session of EEG–fMRI recording. Then, they underwent stereo-EEG (SEEG) as part of their pre-surgical evaluation to specify the origin of pre-spike BOLD signal changes. Pre-spike BOLD signal changes in the spike field area were analyzed using HRFs with peaks ranging from −9 to +9 s around the spike. After that, SEEG signals were analyzed for detecting electrographic changes consistent with the time and location of the early HRF responses. The results showed that only one of the patients had a consistent SEEG interictal discharge. No electrographic changes were detected in the rest of the patients, consistent with the early HRF responses in period and location. Therefore, the early BOLD signal change usually reflects a metabolic event that does not seems to be the result of a synchronized neuronal discharge.

BOLD Response to IEDs

There may be a direct relationship between the BOLD signal changes and overall synaptic activity (56, 57). The generation mechanisms of interictal discharges are unknown in humans,

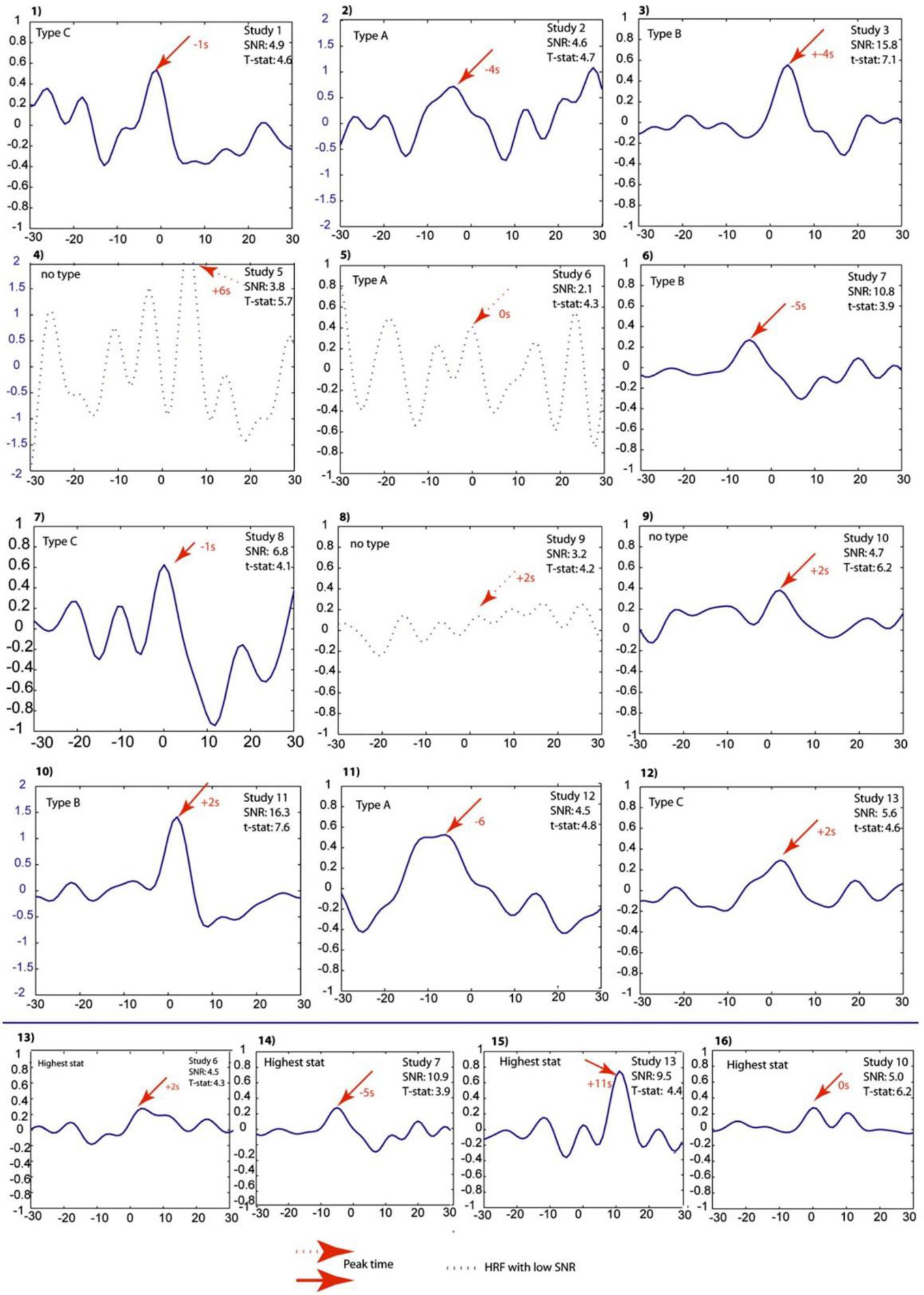

FIGURE 4 | Projected HRFs illustrated according to a sequence of patients. The bottom row shows HRFs calculated over the area with the highest t-statistic. The HRFs which presented with dotted lines are those that did not pass the SNR criterion of 4.5. The Blue scales had to be adjusted to obtain visibility of the HRF and thus differ from the rest. The HRF shape differences and their sporadic early peak times are obvious (54).

but the cortical development abnormalities have distinctive interictal discharges (56). For a reliable localization of epileptic foci using EEG–fMRI, we need IEDs correlated with the BOLD signals recorded simultaneously. However, the epileptogenic regions with correlated signals have not yet been thoroughly understood (58). Thus, a considerable part of the literature is centered on the behavior of BOLD signal changes associated with interictal discharges.

Federico et al. (56) focused on the BOLD signal changes associated with interictal discharges in six patients with malformations of cortical development and seizures using spike-triggered fMRI 3T. They revealed four positive changes in the lesion and four negative changes surrounding the lesion, five changes at distant cortical sites, and three subcortical sites (basal ganglia, reticular formation, or thalamic). Waites et al. (33) studied two patients with frequent epileptiform events and concluded that interictal discharges result in BOLD responses distinctly different from those obtained by examining random events. Besides, Bonaventura et al. (59) investigated BOLD responses related to epileptic EEG abnormalities in 31 partial and 12 generalized epilepsy patients and revealed that there are obvious associations between BOLD results and EEG abnormalities in 21 cases with 18 concordant to electro-clinical findings.

Another strand of literature focuses on idiopathic generalized epilepsy (IGE). For instance, Briellmann et al. in (60) analyzed the data from 17 patients with IGE and frequent, stereotypical generalized discharges that were present in 14 of them during scanning. As reported, the cortical changes were found in all patients, and subcortical changes were found in only seven of the patients who had bursts of rhythmic discharges during scanning. Fifty-five percent of the patients showed deactivation in the posterior cingulate, and two of the patients who had marked activation and electro-clinical absences during scanning showed thalamic signal change.

Tyvaert et al. (61) analyzed the EEG–fMRI data from 10 patients with IGE during generalized spike-and-wave discharges (GSWDs). The HRFs were calculated in four ROIs related to the left and right thalamic structures and were compared within and between them. The results pointed to an activation of the centromedian and parafascicular (CM-Pf) nuclei and then of the anterior nucleus during GSWDs. This suggests that the early propagation and maintenance of epileptic discharges may belong to the posterior intralaminar nuclei and anterior nucleus, respectively.

In another study (62), the EEG–fMRI data of 83 patients with medication-refractory IGE (R-IGE) were analyzed, and statistical parametric maps concerning the BOLD response were generated. Thirty-six patients were identified as cases with absence seizures. It was inferred that when thalamic BOLD changes peaked at ∼6 s after the onset of absence seizures, the other areas, including the prefrontal and dorsolateral cortices, showed brief and non-sustained peaks at ∼2 s earlier than the thalamic peak. Also, TL peaks occurred at the same time as the thalamic peak, with a cerebellar peak occurring ∼1 s later. Thus, the origin of absence seizures may be the widespread cortical (frontal and parietal) regions and sustained in subcortical (thalamic) areas, representing the cortical onset of epileptic seizures with propagation to the thalamus.

In a study of Benuzzi et al. (63), 18 patients with IGE and absence seizure (AS) were studied, and the event-related analysis was performed using the onset and duration of GSWD as one regressor and GSWD offset as another. The results pointed to a thalamic activation and a deactivation in pre-cuneus/posterior cingulate related to the GSWD onset and a BOLD signal decrease over the bilateral dorsolateral frontal cortex GSWD termination.

For a 28-year-old focal epilepsy patient with left frontal seizures who were treated with oxcarbazepine (1,200 mg/d), two sessions 1 month apart of continuous EEG–fMRI with two different runs for each session were held. The IEDs were extracted using the location of the electrodes with the maximum amplitude of the epileptiform activity, and the colocalization of fMRI clusters was established based on the anatomical lesion and IEDs. In both runs of the first session, a unique left frontal main cluster was identified in the left opercular region colocalized to IEDs and near the posttraumatic lesion. However, in the second session, two main clusters were detected in the inferior frontal gyrus of both hemispheres. Therefore, EEG activity did not considerably change within each session, whereas the spatial distribution of interictal events showed significant variations between the sessions (64).

In another study, Flanagan et al. (65) reviewed the EEG–fMRI data of 27 patients with focal epilepsy in terms of the location and extent of the IEDs and the resulting pattern of significant BOLD responses. This study characterized important features of the BOLD responses associated with the IEDs and confirmed that the piriform cortex is a common node underlying IEDs and suggests a purpose for further study and potential therapy.

Fahoum et al. (66) studied 32 patients with TLE, 14 patients with frontal lobe epilepsy (FLE), and 20 patients with posterior quadrant epilepsy (PQE) and acquired the patterns of cortical and subcortical BOLD responses related to focal IEDs using a group analysis. The patients with TLE showed activations in the midcingulate gyri bilaterally, ipsilateral mesial and neocortical temporal regions, insula, and cerebellar cortex, and also the most widespread deactivations in the default mode network (DMN) areas. The patients with FLE showed activations in the midcingulate gyri bilaterally, ipsilateral frontal operculum, thalamus, internal capsule, and the contralateral cerebellum, and also deactivations in the DMN areas. Lastly, the patients with PQE showed only deactivations in the DMN area.

Negative BOLD Signals

For the cases of negative BOLD signals, the epileptogenic regions with correlated signals are not also completely understood (58). For explaining the negative BOLD signals, three different scenarios could be as follows: An overcompensating cerebral blood flow decrease could accompany a decreased metabolism as a "normal" negative BOLD response; the epileptic activity could produce an increased metabolism without adequate blood flow change resulting in a negative BOLD effect; and the oxygen consumption could stay constant throughout the IED event while at the same time, a reduced local blood flow is induced (58).

The study of Rathakrishnan et al. (67) aimed to explain the negative BOLD responses seen in the source of epileptiform discharges by the undershoot of an antecedent positive response. In analyzing the EEG–fMRI data of 82 patients with focal epilepsy, only eight patients showed a focal negative BOLD response in the spike field area using models with HRFs peaking from −9 to +9 s around the spike. Thus, the origin of negative BOLD responses in the epileptic foci is not an initial positive BOLD response and remains unexplained in most patients.

To determine the origin of BOLD negative response to the IEDs, Pittau et al. (68) studied two groups of patients, each including 15 patients with significant positive and negative BOLD responses within the IED region, and explored the relationship between the type of response (activation/deactivation) and several IED characteristics. The results denoted that the IEDs of patients with deactivation were more frequently of long duration with larger involved cortical areas and more focused in the posterior quadrant. Also, the IEDs accompanied by a slow wave were present in 87% of the deactivation group and only in 33% of the activation group which is the critical feature reliable for focal deactivations.

LOCALIZATION APPROACHES

Localization of Epileptic Focus Using EEG–fMRI

The EEG–fMRI analysis has been widely used for the localization of epileptic foci. However, the respective approaches need more refinement to be reliable for pre-surgical decision making (69). In the following section, the results of applying various analysis methods are reported.

Conventional Analysis

Simultaneous EEG and fMRI recordings can reveal the source of spiking activity that is highly correlated with epileptic foci and epileptogenic lesions in a large number of patients. However, many of the patients have no significant activation for unknown reasons (12). In the study of Al-Asmi et al. (12), the EEG–fMRI data of 38 patients with focal epilepsy and frequent spikes were analyzed in terms of fMRI activation using two methods: (1) the significance of the t-statistic value at every single voxel and (2) the significance in the clusters of contiguous voxels based on random field theory (70). The concordance between the spike location of EEG and anatomic abnormalities of MRI and other EEG and clinical measures were taken into consideration. From the analyzable ones, activation regions were obtained in 39% that were concordant with EEG source localization in nearly all of them. Forty percent showed activation without any MRI lesion, and 37.5% showed activation near or inside the lesion.

In a study of Zijlmans et al. (71), the EEG–fMRI data of 29 patients with epilepsy were studied, and 46 sets of IEDs were identified in the agreement between two experts. The BOLD response related to each type of IEDs was modeled in an event-related design using a canonical HRF with a temporal derivative, and statistical maps of activity were created. The results showed an improvement in the localization of epileptic focus and opened new prospects for surgery. For instance, at least one significant positive BOLD response topographically concordant with the IEDs was found in eight patients who were rejected for surgery due to reasons like unclear focus or multifocality. This is, therefore, a valuable tool in the pre-surgical evaluation of patients with epilepsy.

Besides, in the study of De Tiège et al. (72), the IEDs were extracted and segregated into separate regressors applying a half-maximum amplitude cutoff in six children with pharmacoresistant focal epilepsy. The regressors were then convolved with the canonical HRF and its temporal derivative for an event-related fMRI analysis. The results showed significant activations in four children, colocalized with the presumed epileptic focus, activation and deactivation in one child, and a widespread deactivation in another.

In another study, Grova et al. (73) evaluated the level of consistency between EEG source localization and BOLD responses using two comparison strategies: (1) MEM concordance, which is the comparison between EEG sources detected using Maximum Entropy on the Mean (MEM) and fMRI clusters of significant BOLD response and (2) fMRI relevance: if sources located in an fMRI cluster could explain some scalp EEG data, the assessment of the fMRI-relevance index α would measure when this fMRI cluster was used to constrain the EEG inverse problem. For this purpose, seven patients with focal epilepsy underwent EEG–fMRI and an EEG recording outside the scanner. The results of combining two mentioned strategies to report the concordance between BOLD response and EEG sources showed that from 62 fMRI clusters assessed by standard event-related analysis, 15 were highly concordant with EEG according to both strategies, five were concordant only according to the fMRI-relevance index, 30 were not concordant, and 10 clusters had a significantly negative α index suggesting EEG–fMRI discordance.

Avesani et al. (74) analyzed the EEG–fMRI data of a patient with symptomatic epilepsy to find the linkage between the "epileptogenic" zone and the "irritative" zone, which is the meticulous cortical distribution of spikes. They used EEG signals as paradigms in the fMRI study and compared the EEG interictal slow-spiked wave with the normal EEG conditions. The results showed a BOLD signal increase around the epileptogenic area in the left neocortical temporal region, laterally and posteriorly to the porencephalic cavity, representing a connection between "epileptogenic" and "irritative" areas.

In a study of Jackson (75), Jackson extracted 46 IED sets from 29 patients with epilepsy who were excluded for surgery on unclear foci. Also, he analyzed the fMRI data to identify BOLD, significant responses, and topographical concordance with IEDs. Fifteen patients showed significant positive or negative BOLD responses. Eight patients showed IED-related positive BOLD responses. Four of the five patients with presumed multifocality showed multiple epileptic foci. Four of six patients with unclear foci showed a confined focus, opening new predictions for surgery.

Besides, in the study of Liu et al. (76), the EEG–fMRI analysis for the localization of partial epilepsy includes extracting and convolving the spike times with a two gamma-variate canonical HRF and adding the result as a task regressor to the SPM design matrix. This approach was applied to the data of eight EEG–fMRI sessions acquired from six patients with partial epilepsy and showed six with activation and deactivation, one with activation only, and one with deactivation only. Seven of the observations corresponded to electroclinical localization of epileptic focus. As reported in this study, the concordance seems to be more associated with positive BOLD responses, and the response to deactivation seems less associated with IEDs. Such studies generally demonstrate that IEDs may be revealed in the brain regions well beyond the presumed area in which they are generated (77). In the study of Moeller et al. (78), the EEG–fMRI data was acquired from nine patients with non-lesional frontal lobe epilepsy (FLE). Using four HRFs, IED-related BOLD responses were obtained and compared to the spike topography determined by BESA as a voltage activation map. The results showed a concordance between the positive BOLD response and the spike localization in eight of nine patients.

Borelli et al. in (79) studied a patient of focal cryptogenic epilepsy with speech arrest seizures and bilateral synchronous spike and wave scalp EEG pattern (secondary bilateral synchrony). Following the conventional analysis of EEG–fMRI data, the IEDs were identified, convolved with a two-gamma canonical HRF, and added to a single-subject GLM. The statistical map of significantly activated voxels showed an explicit BOLD response over the left supplementary motor area (SMA) and, to a lesser degree, over the homolateral motor strip. Forty-three patients with focal epilepsy were studied in (80), and BOLD responses associated with IEDs, including at least five significant contiguous voxels, were extracted and labeled as consistent and inconsistent with the EEG spike field and contributory or not contributory, based on whether or not they provided additional information to EEG about the epileptic foci. The main analysis included convolving a regressor developed using the time and duration of each IED-type event with four HRF peaking at 3, 5, 7, and 9 s and adding all the regressors to GLM. Thirty-three patients who had more than two IEDs during recording were shown to have significant BOLD changes, among which 29 were considered consistent, and 21 were contributory. The BOLD responses were validated in 12 of 14 patients having intracerebral EEG or a focal lesion on MRI.

Ten patients with atypical benign partial epilepsy (ABPE) underwent simultaneous EEG–fMRI, and several types of IEDs were extracted from their data in (81). The analysis of BOLD signal changes associated with each IED type showed distant significant responses in cortical and subcortical structures for 31 cases out of 33 among which 21 were concordant with the spike field. Also, to find the responses across the patients, group analysis was performed and showed a thalamic activation. It is noteworthy that the revealed activation in ABPE was analogous to the outlines showed in studies of rolandic epilepsy and continuous spike-wave during slow sleep (CSWS). Zhang et al. (82) investigated the results of pre-surgical EEG–fMRI analysis and iEEG monitoring in a patient with seizure recurrence after epilepsy surgery. They suggested that EEG–fMRI is a useful tool for pre-surgical evaluation but requires caution. Also, the intact seizure foci in the remaining brain may cause the non-seizure-free outcome.

In previous studies of improvement in the localization of epileptic foci, Tousseyn et al. (83) used the conventional GLM-based approach for the localization of epileptic focus in a semi-automated manner by proposing a spike identification method as an alternative for the challenging and time-consuming visual spike detection. In this method, a patient-specific spike template was generated by averaging the spikes observed on the EEG outside the scanner, and the cross-correlations were calculated between the template and the EEG inside the scanner. Then, the result was binarized by a threshold determined from healthy controls and convolved with a canonical HRF to be used as the regressor of GLM. Examining this semi-automatic method on the EEG–fMRI data of 21 patients with refractory focal epilepsy yielded a good performance with the optimal area under the ROC curve of 0.77.

Sandhya et al. (84) studied three patients with drug-resistant reflex epilepsy, including eating, startle myoclonus, and hot water epilepsy using conventional analysis. The results showed frontoparietal network activation pattern in the patient with startle myoclonus epilepsy concordant with SPECT, fronto-temporo-parietal involvement in the patient with eating epilepsy concordant with SPECT, and fronto-parietal-occipital involvement in the patient with hot water epilepsy. In research conducted by Tousseyn et al. (85), 28 patients with refractory focal epilepsy underwent EEG–fMRI and subtraction ictal SPECT co-registered to MRI (SISCOM). Comparing the perfusion changes during seizures obtained from SISCOM and spike-related BOLD signal changes obtained from EEG–fMRI revealed a concordance between the BOLD responses and EEG spikes in 27 cases, a significant spatial overlap between hyperperfusion on SISCOM and hemodynamic changes on EEG–fMRI in 20 cases, and significant overlay between ictal hypoperfusion and interictal deactivation in 22 cases.

Dipole-Based Analysis

The spike source reconstruction of EEG is generally consistent with the BOLD localization (86). It can therefore be used for the localization of epileptic focus. Some of the source localization methods are fixed dipoles, moving dipoles, LCMV (linearly constrained minimum variance), spatial filtering, MUSIC (multiple-signal classification) dipole scans, and LORETA (low-resolution tomography) (87).

Lemieux et al. (86) recorded a 12-channel EEG inside a 1.5T MRI scanner in six epilepsy patients with partial seizures. A T1-weight volume scan and a 64-channel scalp EEG outside the scanner were obtained from each patient. Having extracted spikes from the EEG signals, they performed the source reconstruction using three generator models consisting of multiple moving dipoles, MUSIC dipole scan, and current density reconstruction (Curry 3.0 software) to localize spike generators and compared its results with the spike-triggered fMRI activation maps (SPM96 software). They concluded that the spike generator was located inside or in the same fMRI activation lobe. Therefore, source reconstruction was generally consistent in EEG generator models and fMRI individual clusters.

Bagshaw et al. (88) showed that EEG–fMRI results should not constrain MEG and EEG inverse solutions for equivalent current dipole approaches in epilepsy and that the use of distributed source modeling would be a more appropriate way of combining EEG–fMRI results with source localization techniques. They analyzed the EEG–fMRI data from 17 patients with focal epilepsy and compared the results of spatiotemporal dipole modeling with the peak and closest EEG–fMRI activations and deactivations. They reported that, generally, the distance from the dipoles to the voxel with the highest positive *t*-value and nearest activated voxel was 58.5 and 32.5 mm, respectively, and also that for deactivations was 60.8 and 34.0 mm, respectively. It is obvious that these values are significantly higher than what is generally observed with ERPs, possibly due to a comparatively broad field that could lead to deep artificial dipoles and also the prevalence of EEG–fMRI responses away from the focus of the epileptic activity hypothesis.

Recently, a new method has been proposed for measuring the physical distance between the BOLD clusters and selected component dipoles to improve the identification of epilepsy-related components in the EEG–fMRI analysis (22).

In a study of Secca et al. (89), two patients with idiopathic occipital lobe epilepsy (OLE) were studied in terms of the source analysis using instantaneous regional dipoles at the peak of averaged detected spikes with a three-layer boundary element model (BEM) of volume conduction. Relating the BOLD effect with interictal spikes using a standard Gamma HRF with derivatives, the authors were able to detect BOLD clusters and compared them with the malformative lesion and diagnosed seizure symptomatology, which was moving the right hand, which yielded a very good concordance for each patient between the BOLD clusters, malformative lesion, and the seizure symptomatology.

In another study (90), three patients with idiopathic childhood occipital lobe epilepsy (OLE) underwent EEG–fMRI. EEG source analysis was conducted using prompt moving dipoles at the peak of averaged spikes, which were detected visually, with a standard three-layer boundary element model (BEM). Next, the BOLD activation map was acquired coupled with the incidence of EEG spikes. The results showed no changes in the BOLD activation in the cortex adjoining to the source analysis dipoles. Deactivation analysis showed several clusters with more consistency to the localization of EEG source analysis over the right parietal area. Therefore, the spatial overlap between EEG source analysis results and the BOLD activation map was not quite acceptable. However, the fMRI results were more consistent with the clinical advents.

In our works, we used a dipole-based method for the evaluation of our localization method (22). This study revealed that BOLD responses were related to epileptic spikes in various brain regions of patients with refractory focal epilepsy (**Figure 5**). So, dipole-based analysis can help in the localization of epileptic focus in patients with focal epilepsy and is comprised as part of the pre-surgical evaluation for patients with pharmacoresistant epilepsy.

Component-Involved Analysis

Besides the SPM that is a hypothesis-driven method, ICA is a data-driven method (91) that can be used to find independent components of epileptic sources and add them to the simultaneous EEG–fMRI analysis. The component-involved approaches can also corroborate a negative decision concerning surgical candidacy in some cases (24).

In the study of Penney et al. (92), the EEG–fMRI data of a patient with refractory right TLE were studied. Applying spatial ICA (sICA) to the BOLD fMRI measurements, a hemodynamic response model signal derived from the task-related spatial ICs and used as a regressor in SPM to generate the significant BOLD activity maps. The results of this approach were compared to the same results using a conventional regressor generated from a canonical hemodynamic model and revealed a concordance between the activated regions. So, this sICA-based model may improve the accuracy of localizing epileptic focus.

Also, in the study of Rodionov et al. (93), the findings of sICA compared to the EEG-based GLM analysis in eight patients with focal epilepsy. The spatiotemporal concordance was assessed between the BOLD-related ICs and GLM-derived results to find one IC related to IED-based GLM results. So, the remaining candidate BOLD-related ICs may include the IEDs which were not apparent on the EEG. So, the sICA-based approach can be used to recognize the SOZ and may be helpful when the epileptic activities are not evident on the EEG signal.

Sercheli et al. in (94) used the EEG dipole modeling analysis to ICA components for the localization of epileptic focus in a patient with right mesial TLE before and after a successful resecting of the epileptic region. With this aim, the same dipole source localization of ICs was performed within a three-shell boundary element model of MNI standard brain using DIPFIT2 plug-in of the EEGLAB toolbox. The conventional approach was also performed to evaluate the results of ICA dipole modeling analysis, which used the fMRI statistical analysis with a regressor of IEDs convolved to a gamma HRF. The results of the conventional analysis showed a right hippocampus induction of the large interictal activity in the left hemisphere. However, the results of dipole modeling analysis showed a widespread distribution of activity, and almost only a quarter of the dipoles were near the right hippocampus region. Using just the EEG analysis to precisely identify the epileptic sources is too weak even by a sophisticated method like ICA.

Marques et al. (4) suggested a technique based on the ICA and applied it to the EEG–fMRI data of nine patients with epilepsy. In this method, after using ICA on the EEG data, the candidate ICs were one or two components that were most powerfully related to IED activity considering only the signal, which is over three standard deviations from the mean of the respective channel. The candidate components were convolved with the canonical HRF and added as the regressor to GLM of the BOLD signals. The results of this method were compared with the conventional method and showed concordance in six patients with more significance and extent in most of them, compared to the conventional method results. The rest of the three patients showed no significant activation using the conventional method to be comparable.

In another study (95), various IED types were classified using ICA and temporal correlation of ICs with the raw EEG channel. Then, the time pulse of each IED type was convolved with a

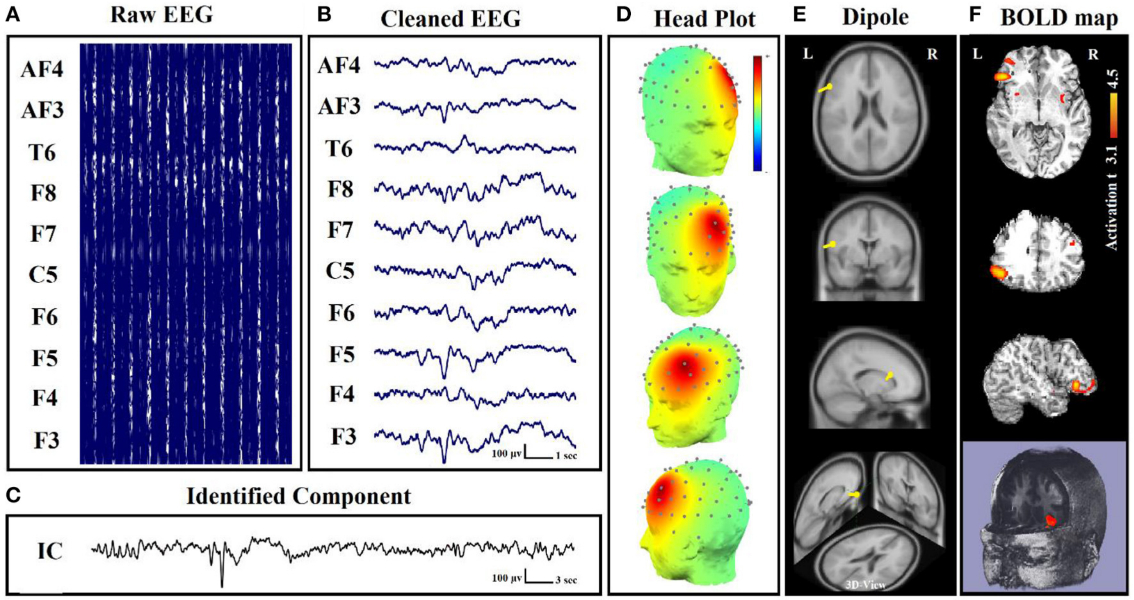

FIGURE 5 | Dipole-related BOLD response showed a focal activation in the left frontal lobe. **(A)** Raw EEG data acquired inside the MR scanner. **(B)** Cleaned EEG after removing the gradient artifact. **(C)** Identified component time series. **(D)** The component identified on scalp EEG located in the left lateral frontal lobe. The active area is marked by yellow-red color. **(E)** Dipole localization of the identified generator in deep brain structures. **(F)** Localization of the generator applying simultaneous analysis of EEG–fMRI (22).

canonical HRF and added separately to GLM for finding the focus of each identified IED type. This method was used in 10 patients with epilepsy including two cases with unknown sources of activity using the conventional method. The results of the proposed method on two patients with unknown source of activity showed some foci consistent with electroclinical data, and those on the rest of the eight patients showed significant activity from at least one type of IED consistent with the conventional method that proves the efficacy of this method for the localization of epileptic focus.

In a study of LeVan (96), 15 patients with focal epilepsy underwent simultaneous EEG–fMRI, and ICA was applied to each of their fMRI data. Then, matching a canonical HRF to the ICs time series in the IEDs' time, the components associated with the seizures were found, and the matched HRFs were used to regulate the sign and delay of the actual HRF peaks. HRFs with an obvious peak were used to create the activation maps of significant BOLD signal changes and compared with the results of a common GLM method. Evaluating the concordance of results with the presumed epileptic foci determined by clinical history, EEG, and MRI abnormalities revealed that the ICA maps were correlated with the GLM maps for all the patients with an activation network that always included the presumed epileptic foci, but more widespread, as much as 20.3% of the brain volume averagely.

Besides, in the study of Leite et al. (97), five metrics including total power, un-normalized root mean square frequency, un-normalized mean frequency, root mean square frequency, and mean frequency were calculated and added to GLM using the performed ICA on the EEG data. For calculating these metrics, the power spectrum was acquired from time-frequency analysis using Morlet wavelets. The metrics were calculated for only the component spectrums presenting spectral alterations during the events identified by the neurophysiologist. In a practical case, applying this method to the EEG–fMRI data of one patient with epilepsy produced wider and more significant activation maps compared to the conventional method using a standard square waveform regressor. Furthermore, the EEG metrics with a frequency content were better predictors of the BOLD signal than global power metrics, supporting previous theoretical predictions and experimental evidence. This method was also tested in (98) for four patients with epilepsy and again revealed more significant activations compared to the conventional analysis.

In another experiment (99), a 10-year-old male patient with epilepsy underwent simultaneous EEG–fMRI for investigating the dynamic responses of epileptic networks. ICA was used in fMRI data, and IED-related ICs were detected fitting an HRF to their time courses at the time of the IED event. Then, the epileptic source of the EEG signals was identified by convolving a canonical HRF with the time pulse function of IEDs as a regressor of a GLM analysis. Comparing IED-related ICs with the EEG source imaging of IEDs in terms of HRF peak delay and spatial consistency using minimum norm estimation (MNE), the fMRI ICs were classified into spatially consistent and inconsistent ones. So, the spatially compatible ICs with early HRF peaks which resulted from spatial-temporal EEG–fMRI fusion (STEFF) would be the possible indicators of the epileptic focus.

Formaggio et al. in (100) presented a novel automatic approach for simultaneous EEG–fMRI to identify the epileptic focus based on ICA and wavelet analysis. This method consists of four steps: (1) applying ICA and selecting components related to IEDs based on their power using a wavelet time-frequency representation because of higher amplitude in IED activity than background activity and the non-stationarity of the signal; (2) eliminating unselected components and reconstructing the EEG signal with only the IED-related components; (3) calculating the cross-correlation between the reconstructed EEG and the original signal to compare and find the IED channel with the highest correlation coefficient, and also building the power signal using a partial maximum of the estimated time-frequency power spectrum of IED channel for each epoch of 3.7 s by wavelet analysis; and (4) convolving the power time series with the canonical two-gamma HRF as the regressor of GLM. After validating this method on simulated data and applying it on real EEG–fMRI data, including five patients with partial epilepsy and two normal subjects, the results showed an extension in current knowledge on epileptic focus localization and suggested that BOLD activation related to slow activity might contribute to the localization of epileptic foci even in the absence of clear interictal spikes.

Franchin et al. (101) presented a method to classify the ICs of fMRI using an elevated algorithm to distinguish the sources of interest from noisy signals. Applying this method for estimating the BOLD activations related to epilepsy and comparing its results with the conventional GLM approach showed that the activations resulted using this method comprised subareas of the those resulted from the conventional analysis, even with partial discordant patterns of the activated areas, and also consists of additional negative regions implicated in a default mode of brain activity, and not clearly identified by GLM.

In our previous study (24), we attempted to localize the focus of epileptic seizures by identifying the neural behavior of the seizures and detecting the related components as a regressor and the input of a GLM model. For this aim, 28 sets of IEDs from nine patients who were excluded for surgery because of unclear focus in four, presumed multifocality in three, and a combination condition in two cases were analyzed. The result of localization showed an improvement in localization of foci using the component-based approach, which includes five of six patients with unclear foci, advocating one of the foci in five patients with assumed multifocality, confirming multifocality in one of them, opening new prospects for surgery in seven of the patients. Also, in two of the patients, intracranial EEG supported the EEG–fMRI results.

In a study of Hunyadi et al. (102), the ICA was used in the fMRI time series collected from 28 patients with refractory focal epilepsy. For reducing the number of ICs to an optimal number by the minimum description length (MDL) criteria, the temporal dimension of the time series was reduced using principal component analysis (PCA). Then, the component activation maps were generated with Z-scoring the component voxel values and using the threshold of $Z > 5$. The results showed that the selected ICs, regardless of the spike presence during EEG recording, truly correspond to the epileptic activity. Considering only one of the ICs as the epileptic IC according to the overlap with the already known SOZ, the component activation maps were ordered. The average overlap between the epileptic IC and the SOZ was 10.6% ± 7.2.

Rummel et al. (103) analyzed the ordinal patterns and revealed that the BOLD responses to EEG-ICA predictors involved the brain region whose resection led to seizure freedom. In the study of Panda et al. (104), the EEG microstates were considered as the regressor in the GLM design to reveal the epileptic resting-state network. The EEG microstates were obtained from the maxima of the global field power (GFP) due to the stability in topography around the peaks of the GFP using sLORETA software. Considering each EEG microstate as an event, an input function was modeled based on the timing of each microstate and convolved with three columns customized gamma HRF. This model was added as the regressor in the GLM design for the ICA of fMRI data. The results of this method on five patients with epilepsy showed that using EEG microstate and ICA of fMRI data may examine the brain areas involved in resting-state brain discharge.

In another study (105), eight patients with epilepsy and known epileptogenic zone from the outcome of surgery were studied for the association between the ICs of fMRI epochs during the presence and absence of the IEDs. The fMRI data were divided into two epochs according to the EEG signal with visible IEDs and without IEDs. Then, spatial ICA was applied to each epoch separately, and IC maps were compared to the resection area and the EEG–fMRI correlation pattern by calculating a spatial correlation coefficient for identifying the epilepsy-related IC. The results showed a high similarity between the epilepsy-related ICs of the epochs with IEDs and those without IEDs. So, the epilepsy-related components are not contingent on the existence of the IEDs in the EEG signals.

Hunyadi et al. (106) studied 12 patients with refractory epilepsy and good surgical outcomes. The epilepsy-related independent components (eICs) were obtained from temporal ICA applied to EEG and spatial ICA applied to fMRI. After convolving the time courses of EEG ICs with the canonical HRF and upsampling the time courses of fMRI ICs to match the sampling rate of the EEG, Pearson's correlation coefficient was calculated for all possible pairs of EEG–fMRI ICs and labeled as matched for the correlation coefficient > 0.1. The results showed matching EEG-eIC for a single fMRI-eIC in four patients with three overlapped to the epileptic zone and matching EEG-eIC for at least two fMRI-eICs in six further patients.

Carnì et al. (107) compared two data-driven methods based on sICA and semi-blind ICA with the conventional GLM-based method using the EEG–fMRI data of 10 patients with epilepsy. A cross-correlation analysis was then completed between the epilepsy-related ICs and a GLM regressor. The results showed a concordance of the BOLD activation areas in response to synchronized epileptic activity obtained from sICA and semi-blind ICA with the GLM analysis and presumed electroclinical hypothesis. Semi-blind ICA showed more power against the noise and a higher correlation with the GLM regressor.

In our study (22), to measure the physical distance between BOLD clusters and selected component dipole location using patient-specific high-resolution anatomical images, we recommended a component-based EEG–fMRI method. The EEG–fMRI data of 17 patients with refractory focal epilepsy underwent this method for the localization of epileptic focus, determination of quantitative concordance, and comparison of the maximum BOLD cluster with the recognized component dipole. For the concordance level, the distance from the voxel with maximal z-score of maximum BOLD response to the center of the extracted component dipole was measured. This improved the localization accuracy to 97% that marks a significant rise compared to conventional works. **Figure 6** illustrates a graphic illustration of the recommended technique in (22) to identify the components. The results of the implementation of the proposed method are shown in **Table 1**.

Also, in our recent work (23), we found and obtained the time series of components associated with epileptic foci from EEG and added them to the GLM analysis. Twenty patients with refractory epilepsy and 20 age- and gender-matched healthy controls were studied, and the identified components were examined statistically to find the epilepsy-related components. The threshold of localization accuracy was determined as 86% using receiver operating characteristic (ROC) curve analysis, and the accuracy, sensitivity, and specificity were found to be 88, 85, and 95%, respectively. Also, the contribution of EEG–fMRI and concordance between the location of maximal BOLD response and the spike field were evaluated. The result confirmed the concordance in 19 patients and contribution in 17. Besides, considering the spatial correlation between the spike template and candidate components as well as the patients' medical records makes it possible to predict the behavior of epileptic generators. **Figure 7** shows the results of the method proposed in (23), comparing three different methods. In this study, the epileptic focus localization can be viewed through the ICA algorithm, dipole, and on the MR images.

Dynamic Causal Modeling Analysis

Dynamic causal modeling (DCM) is another useful tool that can be used for estimating the synaptic drivers of cortical dynamics during an epileptic seizure. However, it has a costly computation in the requisite Bayesian inversion procedure (108).

In the study of Hamandi et al. (109), the EEG–fMRI data was acquired from a 23-year-old patient with refractory TLE. The EEG spikes were detected and convolved with an HRF and its temporal derivative to be used as the onsets of GLM. The results showed activation related to the left anterior temporal interictal discharges, in the left temporal, parietal, and occipital lobes. For determining the functional relationship between the IED-related activation areas, DCM was used and the deployment of neural activity from the focus of temporal to the region of occipital activation was suggested. Also, for tractography analysis, the probabilistic index of connectivity (PICo) algorithm was used to detect the anatomical connections of TL activation and showed connections from this origin to the site of occipital activation, which delineate the pathways of deployment of epileptic activity.

In a study of Murta et al. (110), the EEG–fMRI data from five patients with focal epilepsy were analyzed for detecting the focus of epileptic seizures. For this purpose, three different methods were used, and the outcomes were compared with the clinical outlook: (1) the classic method based on GLM at different neurophysiology regressor lags (LasgM) considering 19 regressors by lags ranging from −16 to +20 s in 2-s steps around the events which were convolved with four types of HRF including single gamma with its temporal derivative, canonical HRF with its temporal derivative, gamma bases functions, and FIR basis functions. In this method, the activation map was obtained using GLM analysis for each lag, and the lags with the maximum number of activated voxels for each VOI were selected to detect the focus of activity propagation; (2) the DCM method, which is a suitable model-based method for studying effective connectivity and has been used several times in the fMRI data of epilepsy patients (109, 111); and (3) the Granger causality (GC) which is a data-driven statistical hypothesis test to analyze effective connectivity in fMRI data with the primary precondition of stationary covariance for the data variables (62, 112–114). Evaluating the results of three methods revealed that DCM analysis, although suffering from generally poor SNR, provides meaningful results in a sufficient number of seizure events. Also, the LagsM results were concordant with the clinical anticipation as much as to be a useful complementary approach. However, the CG results showed that this method seems to be not appropriated to use in the cases like this effective connectivity analysis, at least with the situation of SNR and time resolution of the data used in this study.

In epilepsy associated with hypothalamic hamartomas (HH), although the origin of seizures is known to be in HH, diffusion pathways are not known specifically. Murta et al. in (115) employed the DCM approach to estimate these diffusion pathways from the fMRI data acquired from an HH patient. Examination evaluating a set of clinically possible network connectivity models of discharge diffusion, the most likely model to explain the data showed a diffusion pathway from the HH to the temporal–occipital lobe followed by the frontal lobe. Therefore, this method makes it possible to find the diffusion pathway of seizures, which is helpful in the surgical procedure of epilepsy treatment (**Figure 8**).

Vaudano et al. in (116) studied a patient with reading epilepsy (RE) to identify the network of seizures. The BOLD, significant changes were obtained in 21 s around each seizure corresponding to various linear combinations of a set of Fourier basis functions to find a range of possible HRF shapes. Then, using the results of this analysis, four ROIs were selected, and four linear models were constructed using DCM to analyze the effective connectivity between ROIs. It was eventually revealed that the dominant premotor cortex (BA6) is the origin of seizures in RE, but also an area in the left deep PFC is closely linked to the beginning of the epileptic activity.

For the localization of epileptic focus, IED-related fMRI maps acquired from common analysis methods often show a network including multiple regions of the signal change instead of a highly focal region that drives the generation of seizures within the epileptic network. Vaudano et al. in (117) used the DCM approach to identify the SOZ on the EEG–fMRI data of one patient with FLE. Although pre-surgical EEG–fMRI showed two distinct clusters of IED-related BOLD activation in the left frontal

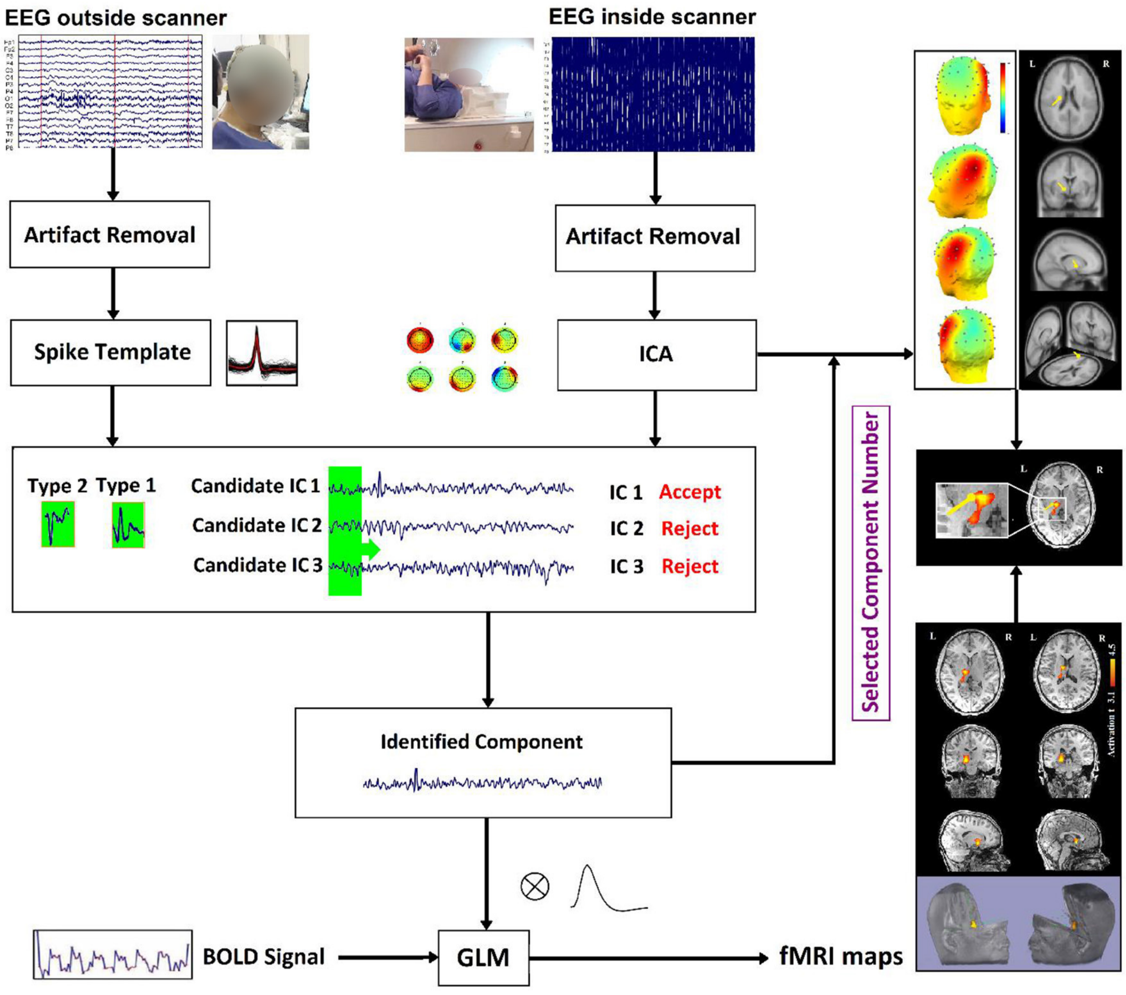

FIGURE 6 | The model of the proposed approach in (22) to identify the components.

pole and the ipsilateral dorsolateral frontal cortex, the DCM approach revealed the left dorsolateral frontal cortex as the driver of changes in the frontopolar area, and An et al. in (118) generated the BOLD activation maps and linearly registered them to postoperative anatomic MRI images for 35 patients with focal epilepsy who later had a surgical resection. The results showed 10 fully concordant patients with maximum *t*-value inside the resection area, nine partially concordant patients with maximum *t*-value near to resection area and overlapped results, five partially discordant patients with a less significant cluster inside the resection area, and 11 fully discordant patients with no response related to the resection area.

Functional Connectivity Analysis

Functional connectivity is a perfect technique for epilepsy to detect the complex brain effects because of dysfunctional and maladaptive networks produced by seizures (119).

Preti et al. in (120) recommended a new way to reveal the connectivity changes associated with an epileptic activity using the information of EEG and dynamic functional connectivity (dFC). Applying this method to the EEG–fMRI data of two patients with epilepsy revealed the specific patterns of connections and disconnections successfully associated with the epileptic activity.

Omidvarnia et al. (121) studied seven patients with focal epilepsy who underwent EEG–fMRI to identify the relationship between the interictal EEG power and local fMRI connectivity. The wavelet coherence was developed between dynamic regional phase synchrony (DRePS, calculated from fMRI) and band amplitude fluctuation (BAF) of a target EEG electrode with dominant IEDs. This approach revealed the regions with a concordance between EEG power and local fMRI connectivity that were near the suspected SOZ in some of the cases. Also, the found regions had a little overlap with the results of conventional EEG–fMRI analysis more in medial posterior cortices, perhaps because of reflecting different aspects of the epileptic network.

In a study of Dong et al. (122), 18 patients with juvenile myoclonic epilepsy (JME) were studied to identify discharge-affecting networks using eigenspace maximal information

TABLE 1 | Summary of IED studies which indicated a significant component-related BOLD response to consensus IEDs (22).

Pt.-type	Ictal EEG	Interictal EEG	IED	Activation	Deactivation
1-1	Temporal left	Temporal right/left	14	Temporal right/left (++)	–
1-2	Frontocentral bilateral	Frontal left	9	Frontocentral bilateral (*)	
2-1	Unclear	Frontal right	11	–	Frontal right (++)
3-1	Parietal left/right	Parietal left	13	–	Parietal right (+)
3-2	Temporal left	Parietotemporal left	8	Parietotemporal left (++)	Frontotemporal left-right (*)
4-1	Bilateral generalized	Bilateral generalized	9	Thalamus (++)	–
5-1	Unclear	Temporal right–left	15	Temporal right (*)	Temporofrontal (+)
5-2	Frontal right/left	Frontal right	6	–	–
5-3	Frontal left	Frontocentral left	7	Frontal left (++)	–
6-1	Left hemisphere	Frontotemporal left	17	Frontotemporal left (++)	–
7-1	Occipitotemporal right	Occipitotemporal right	12	–	Occipital right (++)
7-2	Bitemporal	Bilateral temporal	7	Bilateral temporal (++)	Bilateral temporal (++)
7-3	Left parietal/post temporal	Left parietal/post temporal	11	Paritotemporal bilateral (*)	Frontal right (–)
8-1	Frontopolar right	Frontocentral right	14	Frontal right–left (+)	Central right (–)
9-1	Unclear	Temporal right	12	Temporoparietal right (*)	Temporal right (++)
9-2	Parieto-occipital left	Parietal left	9	Parietal left (++)	Occipital right (–)

In the superscript, the topographical concordance between clinical localization and BOLD response is given: (++): same area, ipsilateral; (+): same area, contralateral; (*): ipsilateral but a different area; (–): no concordance (22).

canonical correlation analysis (emiCCA) and functional network connectivity (FNC) analysis (**Figure 9**). emiCCA is a data-driven method to detect the linear and non-linear relationships between two datasets, which can be the EEG discharges and fMRI networks in JME, and tackle the multivariate problem in the comparison of two datasets (123). Also, the FNC is an approach to identify the interactions between resting-state networks (RSNs) and the effects of epileptic discharges on them (124–127). The results showed a relationship of the epileptic discharges with the discharge-affecting networks in the DMN, self-reference (SRN), basal ganglia (BGN), and frontal networks. Also, a significant increase was found in FNCs between the salience network (SN) and resting-state networks.

In the study of Siniatchkin et al. (128), the EEG–fMRI data recorded from 33 children with focal and multifocal epilepsy during sleep and resting-state functional connectivity were acquired using 15 ROIs. For the focal epilepsy patients, some strong correlations were found between the corresponding interhemispheric homotopic regions with a short-distance and weak long-distance functional connectivity similar to the healthy children. However, for the multifocal epilepsy patients, significantly stronger correlations were found among several regions of DMN, thalamus, and brainstem with longer-distance functional connectivity and not dependent on the presence of Lennox-Gastaut syndrome in patients.

In another study (129), a total of 261 IED events from 21 patients with unilateral left and right TLE were identified, and a 20-s period around them was used in the dynamic FC analysis for left and right hippocampus and amygdala separately. The results showed that the left IEDs had more effect on the hippocampus-seeded networks and caused FC changes in the reward–emotion network (more of the prefrontal-limbic system) and visual network, but the right IEDs had more effect on amygdala-seeded networks and caused a coactivation in the reward-emotion network (more of the reward system).

Su et al. (130) identified the different types of IEDs according to the spatial distributions from 38 patients with focal epilepsy and were used separately in the analysis of IED-related BOLD responses. The concordance between the maximal BOLD responses and the SOZ was found using iEEG, and then the functionally connected zone was determined for each one using the maximal BOLD as a seed (**Figure 10**). Lastly, IED rates in iEEG channels inside and outside the functional connectivity zone (FCZ) were examined. The results of 36 studies from 25 patients revealed that IED rates inside the FCZ were considerably greater than outside in concordant cases.

In a study of Iannotti et al. (131), 10 patients with pharmacoresistant focal epilepsy were studied, and the regions involved in epileptic network generation were identified by GLM analysis using the time course of fMRI-defined focus acquired from the IED-related BOLD maps as the main regressor. Then, using a sliding-window approach, the dFC time courses were assessed between the involved regions and correlated with the sliding-window variance of the IED signal (VarIED) to identify connections whose dynamics related to the epileptic activity. This method's results revealed the epileptic network in nine patients with dynamic subnetwork connections proximate to the epileptic focus (**Figure 11**).

Electrical Source Imaging

Electrical source imaging (ESI) is a non-invasive, low-cost method of localizing the sources of the EEG signals recorded with scalp electrodes (132). So, it also can be used in the EEG–fMRI analysis of localizing the epileptic sources.

In the study of Vulliemoz et al. (133), 13 IED types detected from nine patients with focal epilepsy were used as the separate

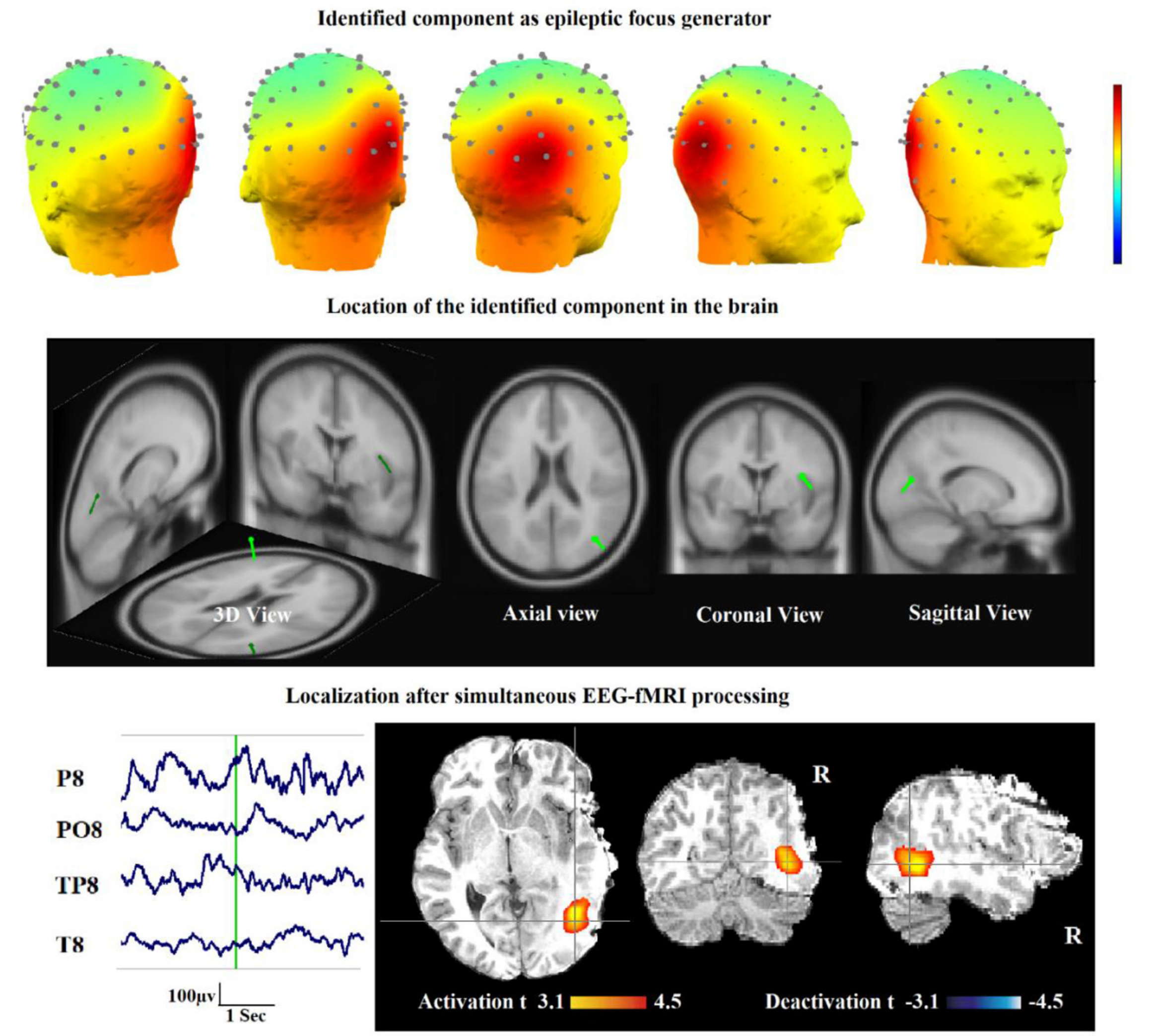

FIGURE 7 | A sample of component-related BOLD response illustrates a neocortical activation in the first occipito-temporal cortex concordant with the spike field. Also, the marked events are in P8, PO8, and TP8 with referential montage. Top: The identified epilepsy-related component located in the right occipito-temporal lobe. Middle: The result of dipole-based localization of the identified component. Bottom: The localization of the epileptic generator acquired from simultaneous EEG–fMRI analysis (23).

regressors in the GLM to obtain the map of IED-related BOLD signal changes. Also, in 12 cases, the electrical source imaging (ESI) could be performed successfully on the IEDs using a realistic head model (SMAC) and a distributed linear inverse solution (LAURA). The results showed that in 10/12 studies, ESI at IED onset (ESIo) was anatomically close to one BOLD cluster in which, for 4/12, it was most relative to the maximally significant positive BOLD cluster, and for 4/12, it was closest to the negative BOLD responses. Furthermore, in 6/12, ESI at a later time frame (ESIp) revealed a diffusion to remote sources co-localized with other BOLD clusters. So, this study showed that analyzing ESI and EEG–fMRI simultaneously can discriminate areas of BOLD response related to the initiation of IED from propagation areas.

In another similar study of Vulliemoz et al. (134), the maps of BOLD responses explained by continuous activity of the estimated IED sources (cESI) were compared to the results of the conventional IED-related analysis. The comparison showed a concordance between the results in 13/15 different types of IED. The cESI model showed other major BOLD alterations in the concordant regions for 10/15, better detection of the IED-related BOLD responses in 4/7, and contaminated diffusion pattern due to the incompletely corrected artifacts of the source signal in four IED types.

Brodbeck et al. (135) performed the ESI using LAURA on the IEDs of 10 operated patients with non-lesional MRI, and at postsurgical follow-up of at least 1 year five had extratemporal lobe epilepsy. The results showed localization of the SOZ in

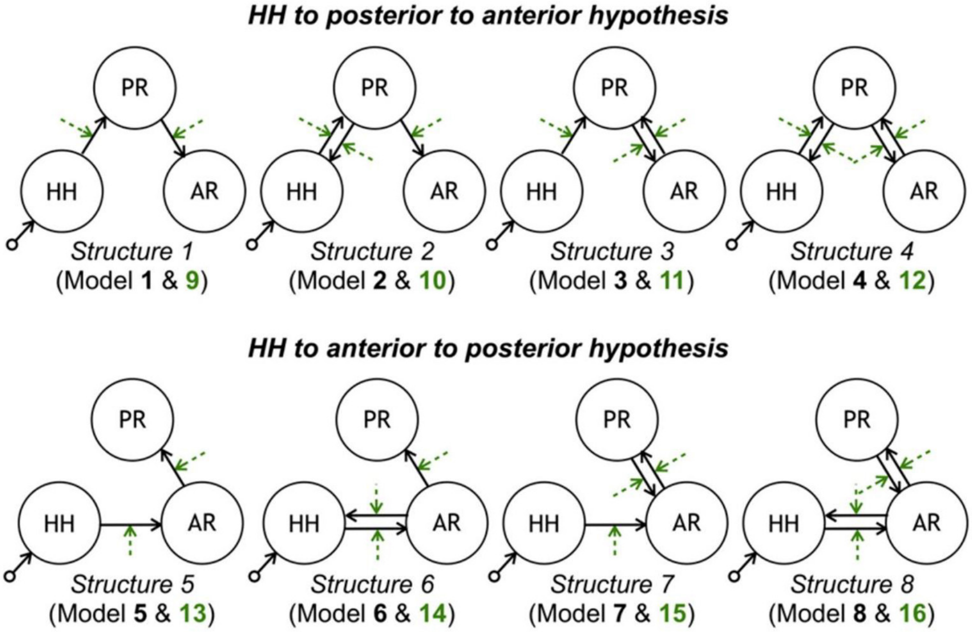

FIGURE 8 | Model space tested with DCM. Each row contains eight models consistent with each propagation hypothesis. Each column corresponds to a different latent connectivity structure. For each latent connectivity structure, the linear model is presented with solid arrows and the bilinear model is presented with solid arrows (intrinsic connections) and dashed arrows (connections' modulation). Seizure activity is fed into the HH network node (115).

eight patients correctly, and it means that ESI reflects the definite source of the epileptic activity. However, the spike peak comprises the diffusion areas.

In another study (136), nine children with refractory focal epilepsy undergoing pre-surgical evaluation were studied. The resected area was compared with three analyses for the localization of epileptic foci, which were, respectively, the conventional method, the analysis of IED-related BOLD changes using spike-specific voltage maps of average IED acquired from long-standing monitoring outside the scanner, and the ESI approach using LAURA. The concordant results of activation within the resection area using the mentioned analysis were revealed in three, four, and all the nine patients, respectively. Therefore, the ESI method is a more valid approach to localize the epileptic foci in children with refractory focal epilepsy.

Also, Centeno et al. (137), studied 53 children with drug-resistant epilepsy, and the localization map of the epileptic focus was performed using BOLD responses, ESI, and the combination of both maps. Comparing the results with the presumed epileptic focus and the postsurgical outcome revealed significant maps in 52 patients, which included 47 for EEG–fMRI, 44 for ESI, and 34 for both. Also, the epileptogenic zone was concordant with the results of 29 patients, which included 11 for EEG–fMRI, 17 for ESI, and 11 for both (**Figure 12**).

Long-Term EEG Recording

In conventional methods, an experienced neurophysiologist reviews the EEG obtained from within the scanner and identified and marked the timing of epileptiform discharges. Spikes were modeled as zero-duration events, convolved with a standard HRF, and used as a regressor for the GLM model and fMRI analysis (138). Given that it is difficult to detect spikes inside the scanner due to artifacts, many studies have suggested automatic detection methods. These methods require long-term EEG recording outside the scanner (139, 140). In many studies, to extract the spike pattern inside the scanner, it is necessary to identify the spike pattern of the same subject outside the scanner in order to extract the spikes inside the scanner through computational methods and detection algorithms (22, 24, 83). To this end, IED-related spikes distinguished on the EEG collected outside the MRI scanner are averaged to build a patient-specific spike template, and their similarity is then examined through methods such as cross-correlation (23, 141, 142). In these studies, all patients undergo a preoperative assessment at the hospital, including long-term monitoring (143). To evaluate the extracted results from source localization algorithms, the results obtained need to be compared with the medical results obtained from different modalities. For the localization of SOZ and irritative zone (IZ) in the pre-surgical evaluation of each patient, all the available data such as the comprehensive clinical record, full neurological examination, long-term video-EEG monitoring (144), structural MRI (145), neuropsychological assessment, and other non-invasive investigations such as PET and ictal SPECT (146) are usually reviewed.

An important study by Grouiller et al. (139) benefited from long-term EEG recording to localize seizure foci in patients without inside scanner IEDs. To this end, the correlation of epilepsy-specific EEG voltage maps with the hemodynamic

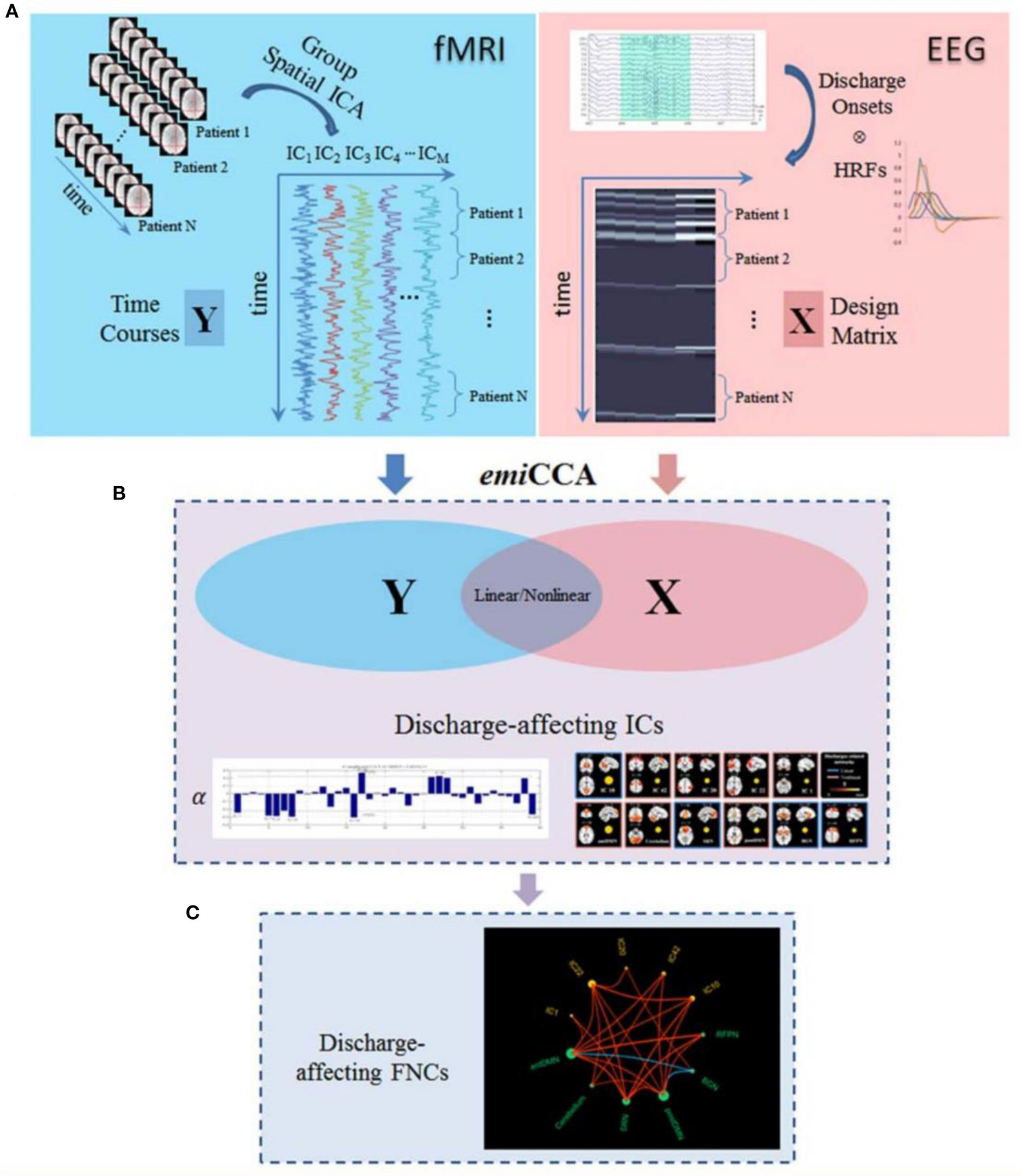

FIGURE 9 | The framework of discharge-affecting network analysis using emiCCA. **(A)** Dataset Y was defined by applying group ICA to fMRI data and concatenating the ICs across the patients. Also, after identifying the onsets of GSWDs by neurologists and convolving with four SPM canonical HRFs peaking at 3–9 s, one Glover HRF, and one single Gamma HRF, a design matrix containing all of them formed the dataset X. **(B)** The emiCCA was applied for identifying significant linear and non-linear discharge affecting ICs with weights (α) exceeding the 1.5 standard deviations of weight values corresponding to the significant maximal information Eigen coefficients (MIECs). **(C)** For examining the possible functional network connectivity between the networks identified by emiCCA, the maximal time-lagged correlation method was used (122).

changes was investigated in 23 patients with focal epilepsy. An epilepsy-specific EEG voltage map was built by averaging IEDs acquired from long-term clinical EEG recording outside the scanner. Then, for each time frame, the correlation between the voltage maps of the EEG signals outside and inside the scanner was calculated. Next, the time course of the correlation coefficient convolved with a standard HRF was used as a regressor for fMRI analysis. The results of this technique were like those of the conventional analysis in all five patients who had significant BOLD changes associated with IEDs. More importantly, the

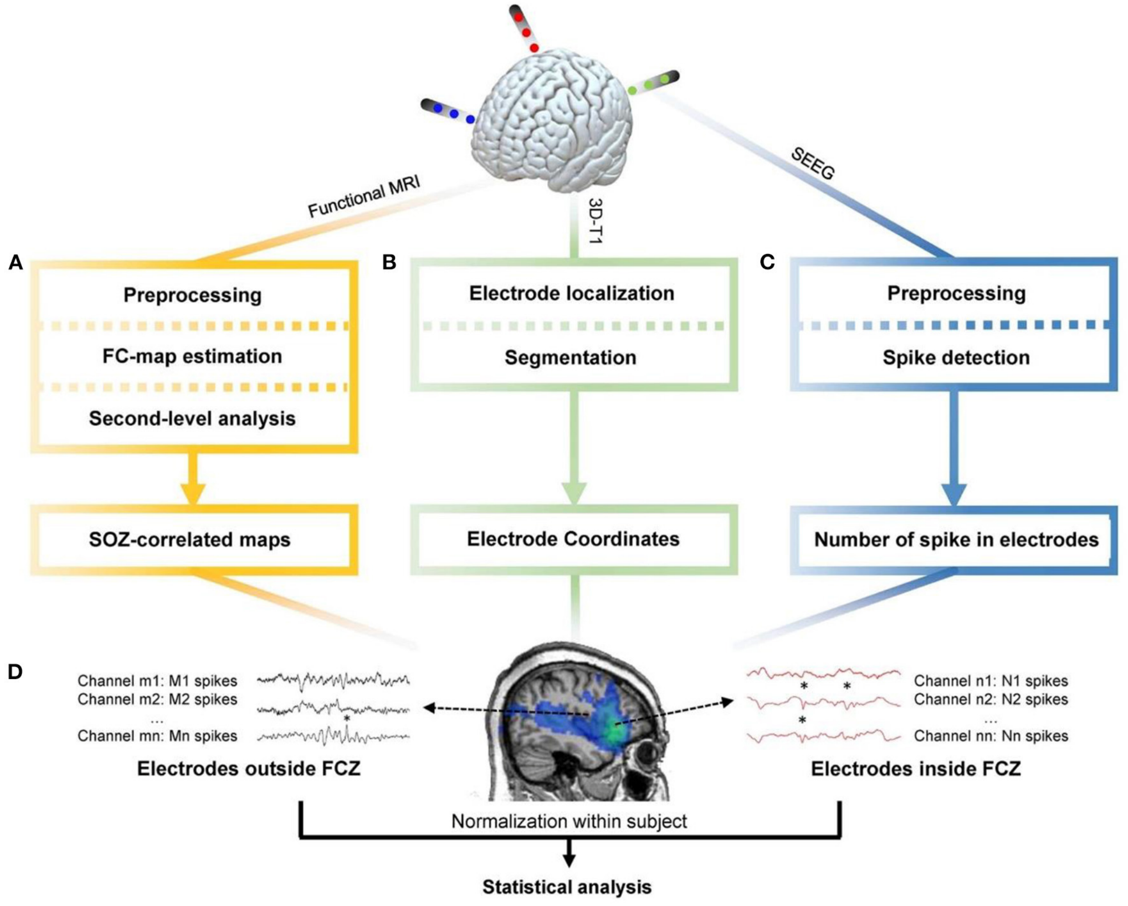

FIGURE 10 | The general pipeline of the research (130). **(A)** Functional MRI data were preprocessed through realignment, slice timing, outlier detection, coregistration, segmentation, spatial smoothing, and noise regression. Then the maximal BOLD response and its neighboring 26 voxels were used as seed regions to calculate the seed-based functional connectivity maps. One-sample *t*-test was applied to determine regions with significant functional connectivity. **(B)** Preimplantation 3D-T1 images were segmented to obtain the brain region. The postimplantation 3D-T1 images were first coregistered to the pre-implantation images, and then the location of electrodes was determined. **(C)** The iEEG data were resampled to 200 Hz, band-pass-filtered between 10 and 60 Hz, and notch-filtered at 60 Hz to eliminate noise. Spike detection based on signal envelope distribution modeling was applied afterward. **(D)** The number of IEDs in each channel was normalized by the median number of IEDs in each subject. Statistical analysis was performed to determine group difference of IED rates between channels inside and outside the FCZ (130).

method correlated BOLD responses with the scalp maps of epileptic activity in 14 out of the remaining 18 patients who had inconclusive simultaneous EEG–fMRI study using conventional analysis due to the absence of IEDs in the inside scanner EEG recording.

In another study (147), 30 patients with drug-resistant TLE and undergoing TL resection were monitored. The IEDs were visually identified by experts on the intra-MRI EEG, and the average topography map of IEDs recorded during long-term video-EEG outside the scanner was computed. Then, both of them were used as the regressors of a GLM analysis, and the results of BOLD responses in TL were divided into two groups of Concordant and Discordant compared to the surgical resection areas. So, it was revealed that 13 of the patients with good surgical outcomes were in the concordant group (16 patients), and only three of them were in the Discordant group (14 patients).

In our previous study (24), we extracted the IED template from the outside of the scanner for computing the correlation. To this end, IED-related spikes were detected in the outside of the scanner and were averaged to build a patient-specific spike template. After band-pass filtering, the template was ultimately outlined by a significant spike deflection on the EEG channels, beginning from the onset at baseline to the negative peak of the following slow wave. The objective was to identify the neural behavior of epileptic generators by detecting the components-of-interest and using the GLM analysis substituting in the classical linear regressor. The general pipeline of this study is shown in **Figure 13**. This method applied 28 IED sets from nine patients who were excluded for surgery because of the unclear focus in four, presumed multifocality in three, and a combination of the two conditions in two of them. The results revealed at least one BOLD response, which was significant, positive, and topographically related to the IEDs in eight patients.

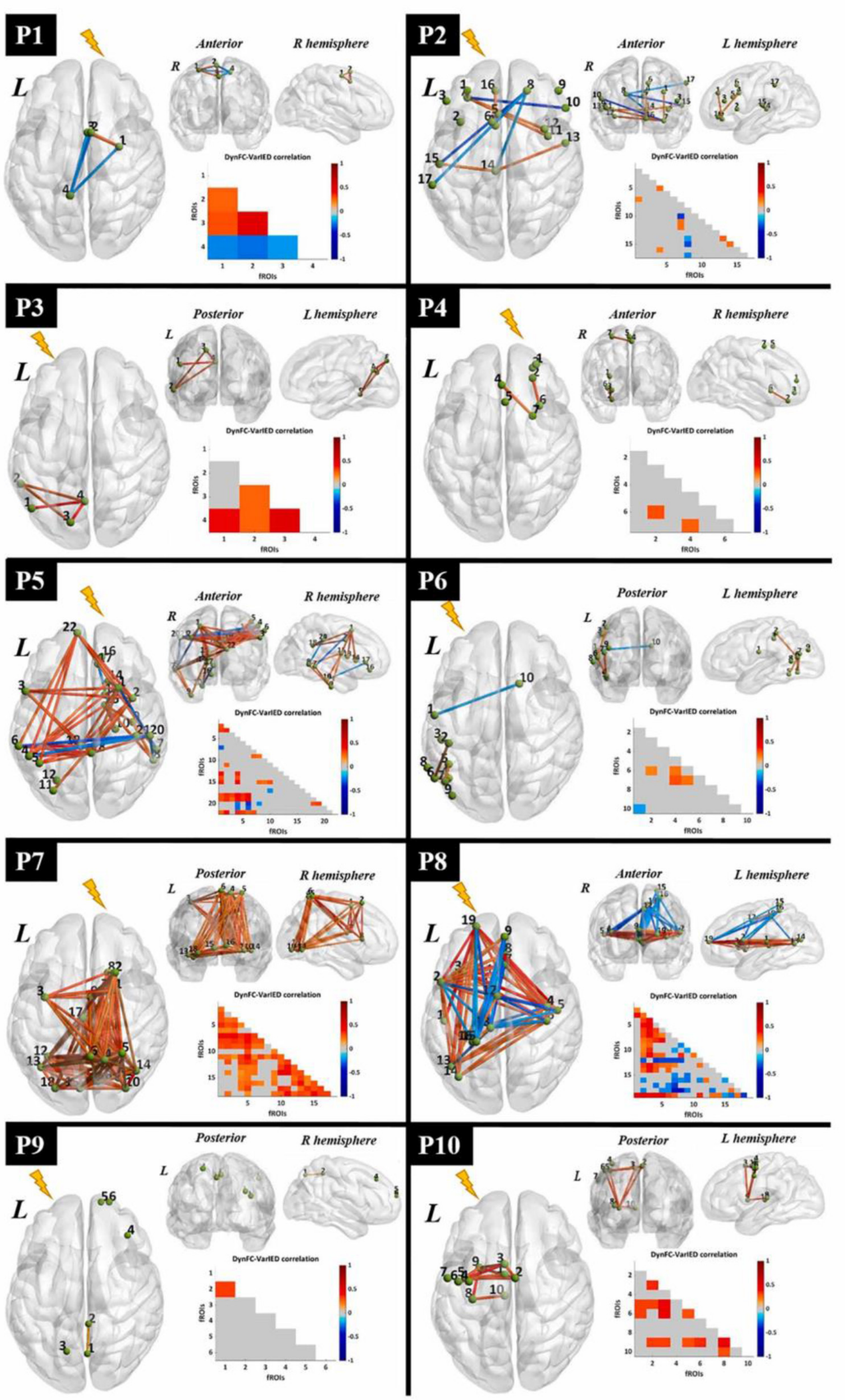

FIGURE 11 | Visualization of dynamic epileptic subnetwork. For each patient, the dynamic epileptic subnetwork is shown in the form of a brain graph in axial, coronal, and sagittal views. Green spheres of equal size represent fROIs, labeled with a number indicating their statistical relevance in the epileptic network. The strength of significant connections is color-coded according to a global color bar scaled in the range [−1, 1]. The dynamic epileptic subnetwork is also reported in the form of a lower triangular correlation matrix with equivalent color-code. The lightning bolt indicates the epileptogenic hemisphere for each patient. L, left; R, right (131).

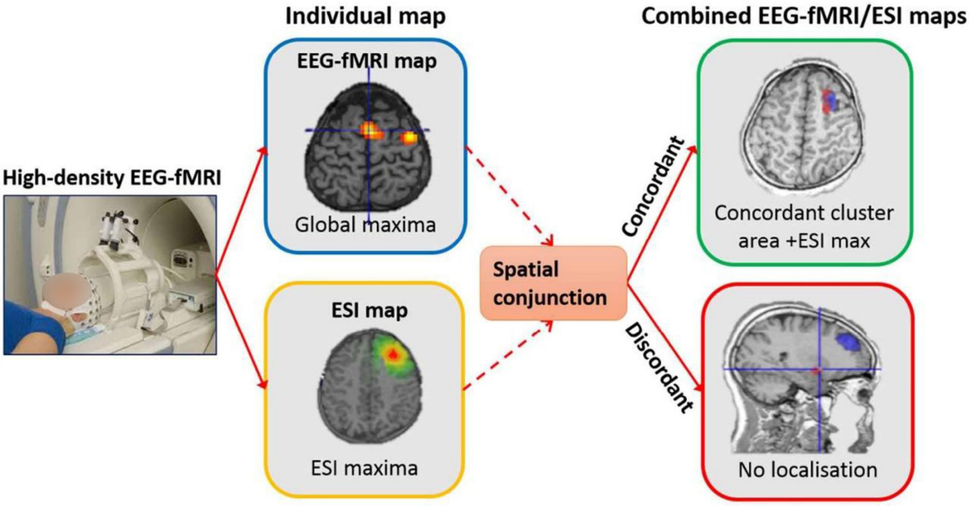

FIGURE 12 | Localization extraction procedure from left to right. For the individual map of EEG–fMRI, the result of localization based on global maxima is shown. Also, for the individual map of ESI, the same result based on maxima in the map from the 50% rising phase of the IED is shown. For the combined test, the spatial conjunction of both maps was used for the localization. Only for the concordant maps, the result of combined localization was extracted from the region encompassing the ESI max and the closest significant EEG–fMRI cluster located in the same sub-lobe (137).

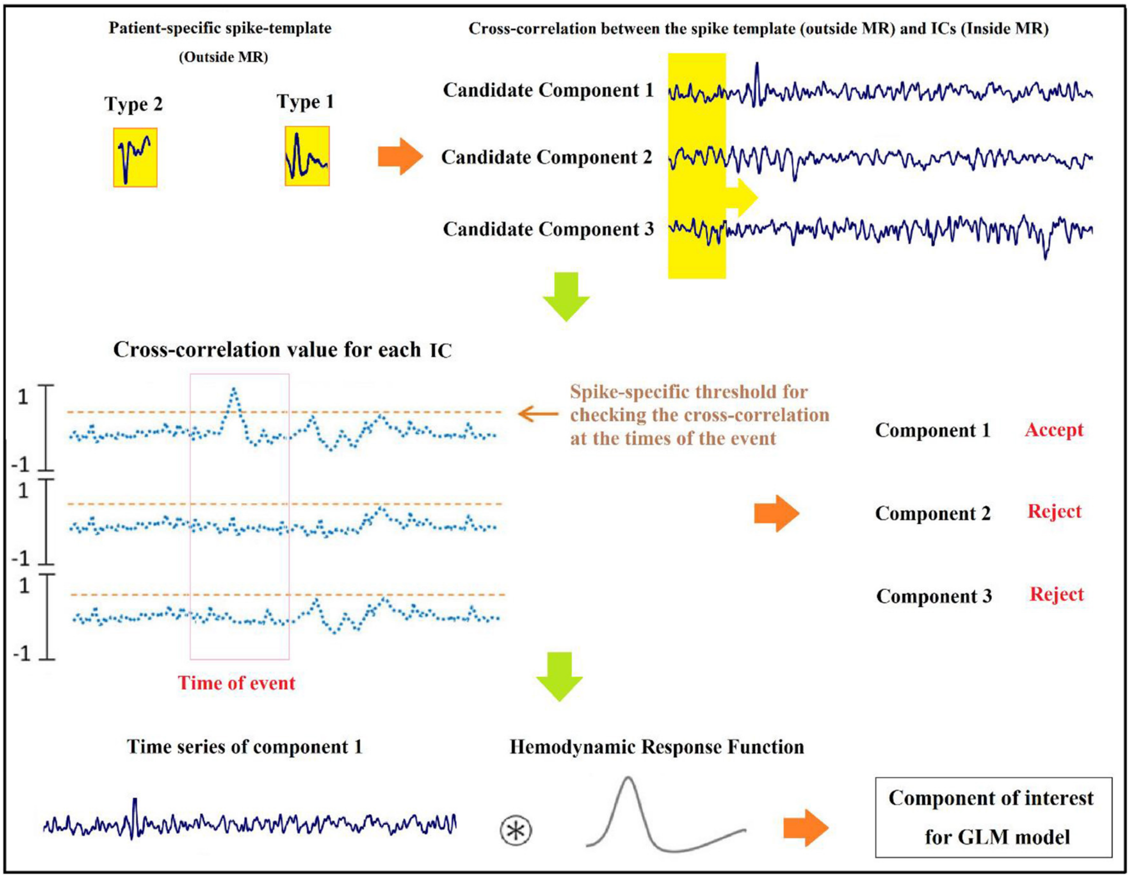

FIGURE 13 | Graphic illustration of the suggested method for identification of components (24).

Localization of Epileptic Focus Using Other Approaches

EEG Slow-Wave Discharges

In the study of Laufs et al. (148), a patient with refractory epilepsy was studied using continuous EEG–fMRI, characterizing the seizures by head turning to the left and clonic jerking of the left arm that suggests a right mesial frontal onset zone. The routine interictal EEG showed symmetrical post-central alpha rhythm and occasional runs of independent, non-lateralized slow activity in the delta band with right frontocentral dominance. Although long-term scalp EEG, structural MRI, and the EEG during simultaneous EEG–fMRI showed no clear significance, the observed slow activity suggests a role for seizure localization with EEG–fMRI even in the absence of clear interictal discharges.

Manganotti et al. in (149) compared the BOLD signal changes on fMRI in two states of rest and activation in terms of EEG focal interictal slow-wave discharges. In all the eight volunteered patients with partial epileptic seizures, the EEG activation of focal slow-wave discharges caused a significant BOLD activation in the related brain region. This significant concordance showed that focal BOLD activation provides useful information for the pre-surgical process even in partial epilepsy patients whose standard EEGs demonstrate focal interictal slow-wave discharges without spikes.

Additional EEG Measures

In the recent EEG–fMRI studies for identifying epileptic focus, some patients have shown poor sensitivity and inconsistency between EEG epileptic foci and BOLD activation patterns. That said, using additional measures may be helpful for better localization of epileptic focus. Moehring et al. (150) studied 11 children with focal epilepsy. Then, the sleep-specific activities such as sleep spindles, k-complexes, and vertex sharp waves were extracted, characterized as a twig function, convolved with a canonical HRF peaking at 6 s, and considered in the GLM as the additional separate regressors. The results showed that considering these regressors increased the significance of activated voxels inside the anticipated IED source area and decreased the number of significantly activated voxels outside of it. So, using the sleep-specific activities in the statistical model is useful to achieving better sensitivity and results of identifying seizure foci in epilepsy.

Also, in the study of R. Abreu et al. (151), the phase synchronization index (PSI) and global field synchronization (GFS) within the frequency bands of 1–45 and 3–10 Hz along with the root mean square frequency (RMSF), total power (TP), and conventional unitary regressors were computed and used to reveal the associated epileptic networks on nine EEG–fMRI datasets including IEDs. After cross-validating the results through ESI, the best performance was revealed using the average PSI within 3–10 Hz across several measures in all datasets (**Figure 14**). Also, testing the PSI in three patients with no IEDs during EEG recording showed partially reasonable networks in all patients.

Mutual Information Maps

The most outstanding feature of using mutual information (MI) for the EEG–fMRI analysis is the balance of involving both imaging modalities, not requiring any prior model of HRF or relationship between EEG spikes and BOLD responses (152).

In the study of Caballero Gaudes et al. (153), five patients with epilepsy underwent EEG–fMRI and electroclinical localization of epileptic focus. For each IED onset, a period with TR duration was defined, and the result was downsampled to the temporal resolution of BOLD signals. Then, the voxel-wise MI was computed between the EEG–fMRI score and the fMRI data, and MI maps were thresholded using a non-parametric wavelet resampling approach. Comparison of the results with the electroclinical localization and conventional GLM-based analysis revealed a concordance of focal BOLD responses in four patients.

Caballero-Gaudes et al. (154) investigated the MI between the IEDs on EEG and BOLD signal on fMRI to generate the MI maps and validate its performance for the localization of epileptic focus (**Figure 15**). The EEG–fMRI data of 14 patients with pharmacoresistant focal epilepsy were used to generate the MI maps based on the four-dimensional wavelet packet resampling method. Comparing the results with the statistical maps obtained from two conventional GLM methods showed the same concordance of ∼57% with the epileptogenic area defined electro-clinically or surgically.

Voxel-Based Morphometry

In the study of Salek-Haddadi et al. (155), nine patients with reading epilepsy underwent simultaneous EEG–fMRI with an extra recording of voice, electromyography (EMG), and electrocardiography (ECG), and six of them experienced reading-induced seizures during recording. Also, 30 neurologically normal control subjects with a similar age range and gender distribution were scanned for comparison. Voxel-based morphometry (VBM) was used for the structural brain analysis. However, as the result of VBM analysis, no significant differences in gray matter density were detected comparing the epilepsy patients with the control group.

Non-linear Hemodynamic Responses

Pouliot et al. (34) studied the EEG–fMRI data recorded from three patients with refractory focal epilepsy for quantifying non-linear hemodynamic responses using the second-order expansion of the Volterra kernel. In the Volterra expansion, which is a functional Taylor expansion, the time-dependent inputs were epileptic spikes, and the outputs were BOLD, oxyhemoglobin (HbO), and deoxyhemoglobin (HbR) time series at a certain fMRI voxel. The results showed significant non-linearities in all the patients with a good concordance to the epileptic focus and negative BOLD response regions. Furthermore, this method identified the epileptic focus in one patient who had shown nothing while common analyses.

Two-Dimensional Temporal Clustering Analysis

The two-dimensional temporal clustering analysis (2dTCA) is a data-driven approach for the localization of epileptic networks using fMRI data. Maziero et al. in (156) used the EEG–fMRI data

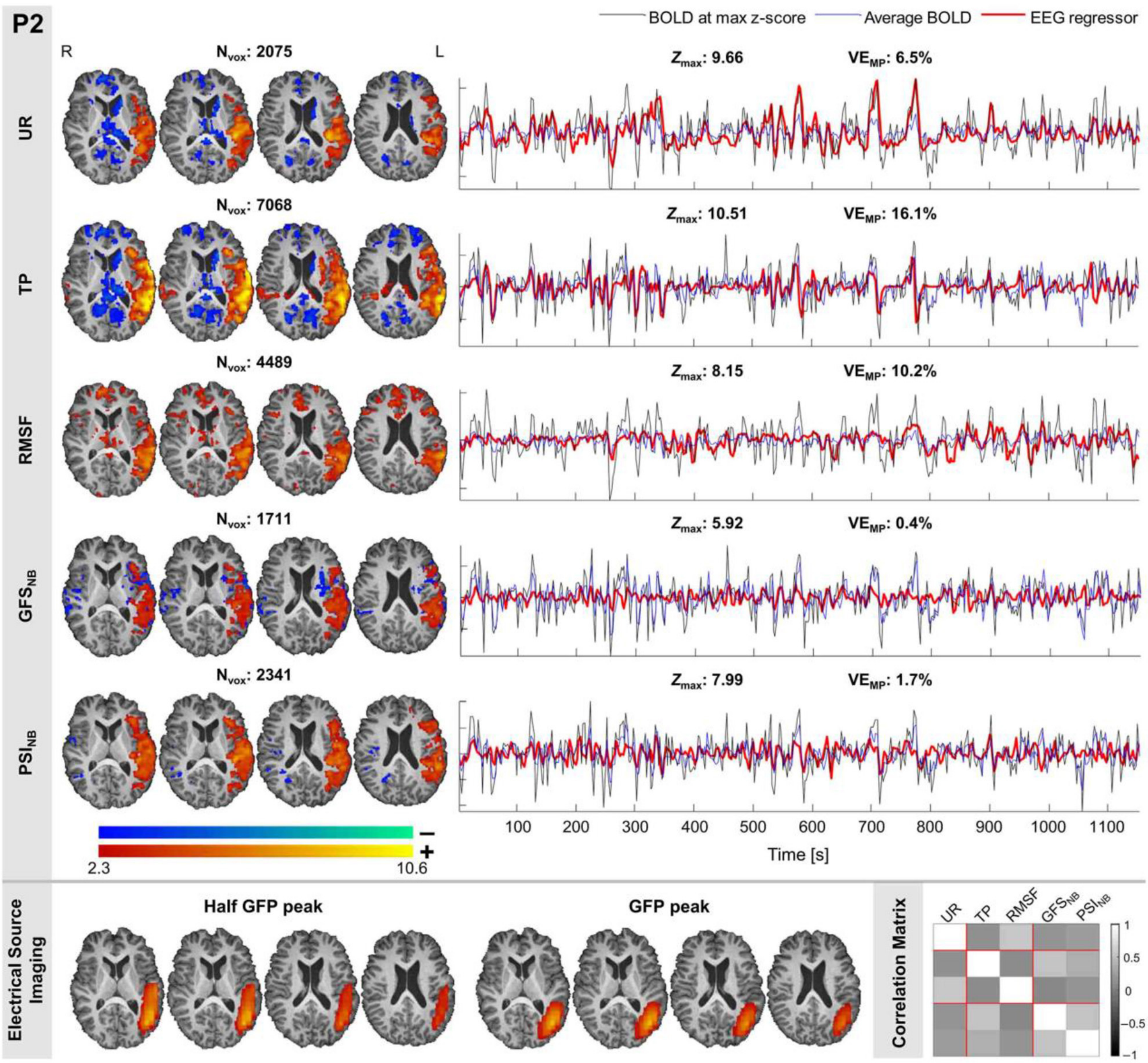

FIGURE 14 | The results of epileptic network mapping for a patient. (Top–Left) The epileptic networks obtained using the EEG regressors UR, TP, RMSF, $\mathrm{GSF}_{\mathrm{NB}}$, and $\mathrm{PSI}_{\mathrm{NB}}$, together with the number of voxels (Nvox); the color codes red-yellow and blue-green depict positive and negative BOLD responses, respectively. (Top–Right) The BOLD signal measured at the maximum Z-score voxel (black trace), the average BOLD signal within the activation cluster (blue trace), and EEG regressor (thicker red trace), together with the maximum Z-score (Zmax) and the variance explained by the motion parameters (VEMP). (Bottom–Left) ESI solution maps at IED onset and propagation, obtained at half the maximum of the first rising phase of GFP and its associated peak, respectively, for validation of the GLM-derived epileptic networks. Consistent results with the ESI solutions were obtained for all patients with clear IEDs only when using the $\mathrm{PSI}_{\mathrm{NB}}$ metric. (Bottom–Right) Correlation matrix between all metrics of interest (151).

of 14 patients with epilepsy as inputs to the 2dTCA for generating the histograms and adding to GLM as predictors. The results showed success in eight patients, not confined to the presence of IEDs, while the conventional analysis identified coherent maps in only six patients who had at least one IED during recording.

Maziero et al. (157) also used the 2dTCA to map the seizure onset zone in 18 patients with focal epilepsy (12 presenting IEDs). The results of this method, along with the conventional method, were compared to the region of surgical resection. The concordant results showed that 2dTCA was successful in localizing the EZ in 13 patients (3 of the cases with no IEDs), but the conventional method was successful in only five of the patients who presented IEDs.

Lateralization Index

Mangalore et al. in (158) used the EEG–fMRI data of 10 patients with refractory epilepsy who showed well-formed IEDs in a proposing method to lateralize the seizure focus in an ROI

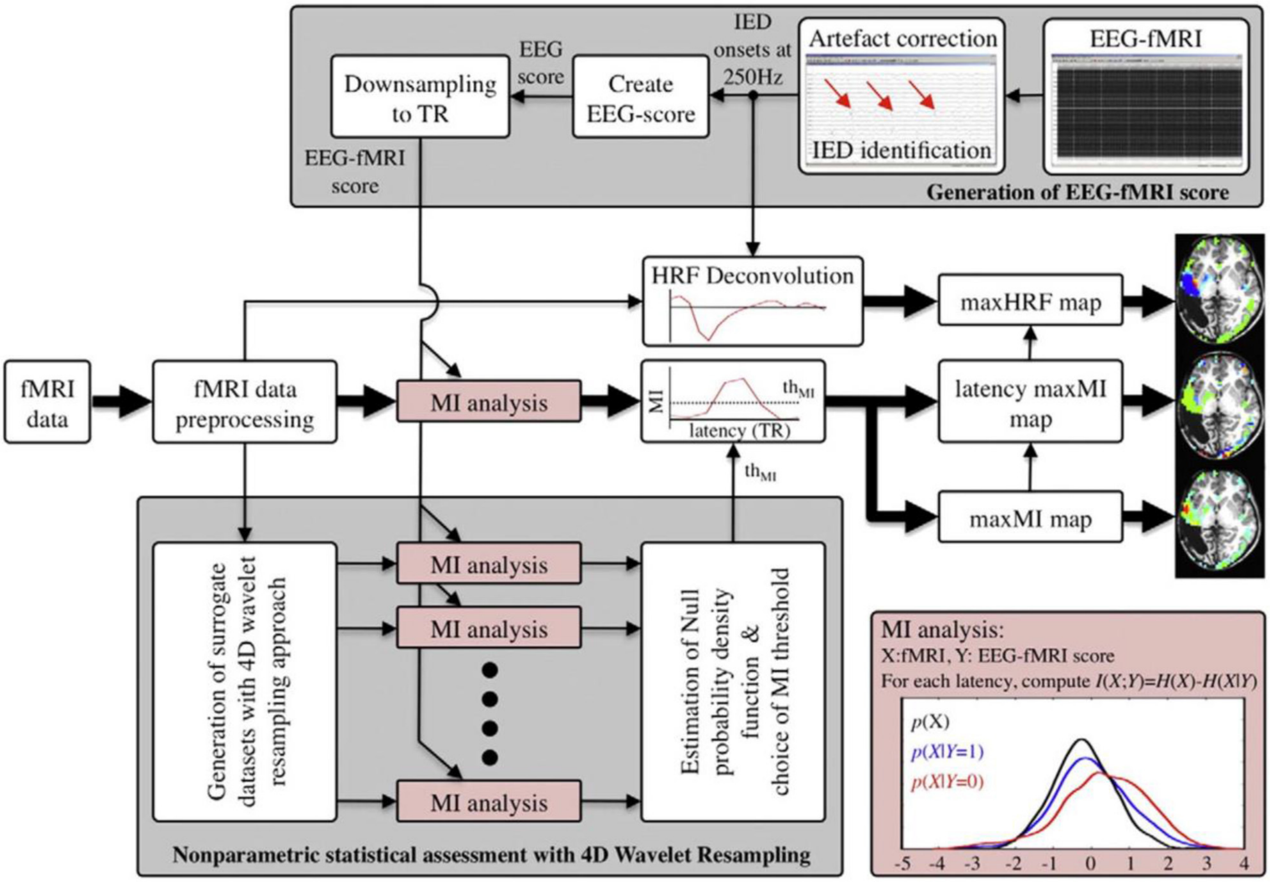

FIGURE 15 | Schematic diagram of the information-theoretic approach. The EEG recorded in the MR scanner is corrected for gradient and pulse artifacts. The time of occurrence of IED peaks is marked, and the EEG score indicating the existence of epileptic activity is created and finally downsampled to the temporal resolution of fMRI (TR) to generate the EEG–fMRI score (top gray-shaded square). The fMRI data is first preprocessed (rigid-body registration for motion correction, spatially smoothed, high-pass filtered, and z-normalized). The MI between the fMRI voxel time series and the EEG–fMRI score is computed based on the entropy and conditional entropy (bottom-right red-shaded square) at multiple latencies by shifting the EEG–fMRI score, resulting in an MI time course. The shape of the HRF is deconvolved based on the IED timing. Significant MI statistics are those exceeding a thresholded th_{MI}, which is chosen according to the non-parametric statistical procedure where 19 surrogate datasets created with a 4D wavelet resampling approach are analyzed in the same way as the original dataset and the PDF of the MI statistics under the null is estimated (bottom gray-shaded square). To summarize the results, three maps are generated: a maximum MI map, a latency map showing the latency at which the maximum MI occurs, and a map plotting the amplitude of the HRF at the latency of the maximum MI (154).

with the aid of the peak BOLD signals. For each patient, the lateralization index was computed from the significant clusters of different ROIs using the following formula: the number of activated voxels multiplied by the Z-scored intensity of activation in the given ROI. Then, the seizure focus was determined by thresholding the lateralization index. Compared with the output of other modalities, the results of this method were successful in temporal and extratemporal lobe epilepsy, reflex epilepsy, and lesional epilepsy. The only disadvantage of EEG–fMRI in this work was if irrelevant BOLD changes were correlated with the specified IED or not.

Adapted Directed Transfer Function

In the study of Qin et al. (159), 18 patients with juvenile myoclonic epilepsy (JME) underwent simultaneous EEG–fMRI. Between EEG electrodes, the adapted directed transfer function (ADTF) values were computed to describe the time-varying network, and its information within sliding windows were used as a temporal regressor in GLM analysis (**Figure 16**). The outcomes demonstrated that BOLD activations allied with high network variation were mostly placed in the thalamus, cerebellum, precuneus, inferior TL, and sensorimotor-related areas, including the middle cingulate cortex (MCC), supplemental motor area (SMA), and paracentral lobule. Also, the deactivations related to medium network alternative were originated in the frontal, parietal, and occipital areas.

Four-Stage Localization Method

Wan et al. (160) proposed a four-stage method for the localization of SOZ that includes identifying events of interest using

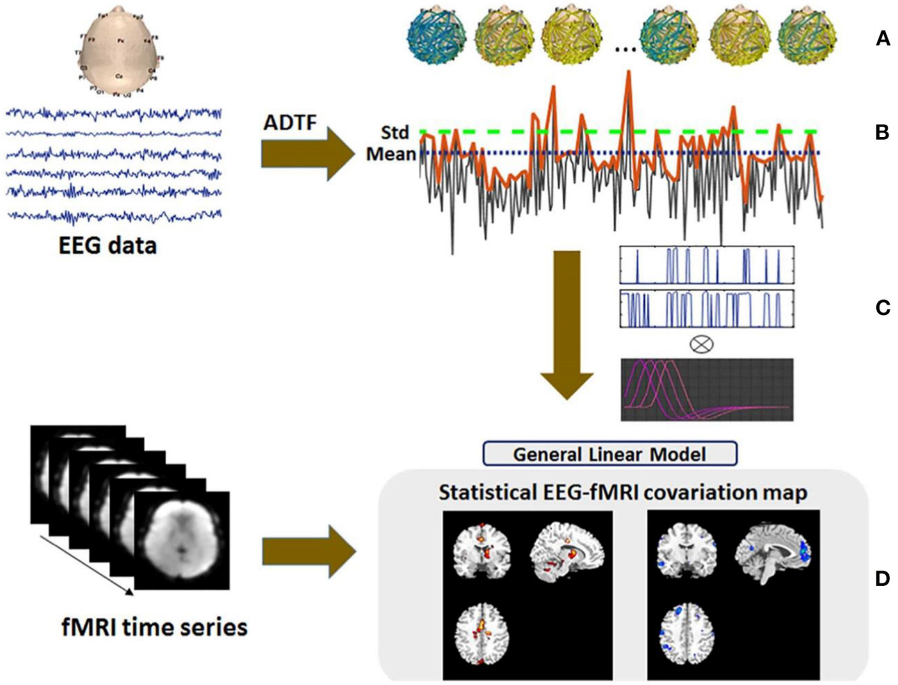

FIGURE 16 | An overview of the suggested EEG–fMRI analysis. **(A)** After preprocessing the EEG signal, the time-varying scalp network was constructed using ADTF. **(B)** The variation of the ADTF information flow between electrodes in each 2-s time window was extracted for the generation of network variation time series. **(C)** The significant values of network variation time series exceeding one standard deviation and the mean were selected as the regressors and added to the GLM analysis, respectively. **(D)** The results were acquired from the GLM analysis (159).

Hilbert transform, acquiring channels of interest (CoIs) using the Shannon-entropy-based complex Morlet wavelet transform (SE-CMWT)-based power spectral density, detecting high-frequency oscillations (HFOs) on CoIs with the combination of adaptive-genetic-algorithm-based matching pursuit (AGA-MP) and Morlet wavelets, and localizing SOZs based on the half-maximum method using characteristics of HFOs. This approach showed the highest sensitivity and specificity compared to the four existing methods of SE-CMWT, AGA-MP, RMS, and CMWT.

Ancillary Issues

The Relation Between rCBF and Epileptogenic Areas

Studies have shown that seizures induced by musical stimulation, especially in temporal epilepsy, cause a rise of regional cerebral blood flow (rCBF) in putative epileptogenic foci and the other brain regions. However, this is a virtual temporal relation between epileptic discharges and rCBF changes due to the offline EEG recordings (161). In the study of Marrosu et al. (161), simultaneous EEG–fMRI recording of musicogenic elicited seizures was studied in a patient with partial epilepsy. The statistical maps obtained from the GLM technique showed that EEG features extracted from epileptogenic areas are largely coupled with rCBF increase. Also, the rCBF changes in other areas may suggest further aspects of musicogenic seizures. For instance, this physiological activation induced by music in several brain areas may initiate musicogenic seizures in predisposed subjects.

Validation of EEG–fMRI Results Using a Gold Standard

For the validation of EEG–fMRI outcomes with a gold standard to figure out the actual role of this multimodal approach in pre-surgical evaluation, Houdt et al. (162) compared the correlation patterns of EEG–fMRI data acquired from 16 surgical candidates with the involved brain areas of ECoG IEDs, the SOZ, resected area, and degree of seizure freedom (**Figure 17**). The results of the comparison revealed a concordance between at least one of the EEG–fMRI areas and an interictally active ECoG area for all patients. Also, the EEG–fMRI areas covered the whole SOZ in 83% and resected area in 93% of the dataset.

The Relations Between IEDs and SOZ

Regarding the relations between IEDs and SOZ, Yamazoe et al. (163) hypothesized that the number of IEDs and their spatial extent could contribute to revealing the SOZ. To test this hypothesis, 157 types of IED grouped by spatial distribution were extracted clinically from the EEG–fMRI data of 64 patients with refractory localization-related epilepsy. Then, each IED was convolved with four HRFs peaking at 3, 5, 7, and 9 s to construct four regressors, and a combined *t*-map was created with the most significant *t*-value at each voxel. Two levels of significance were defined to observe reliable activation in the combined t-maps. The first level was defined by any set of five contiguous voxels with the *t*-value $\geq$ 3.1, and the second level was the *t*-values being higher than the whole-brain topological false discovery rate (FDR) of 0.05 for multiple-cluster comparisons. For each type of

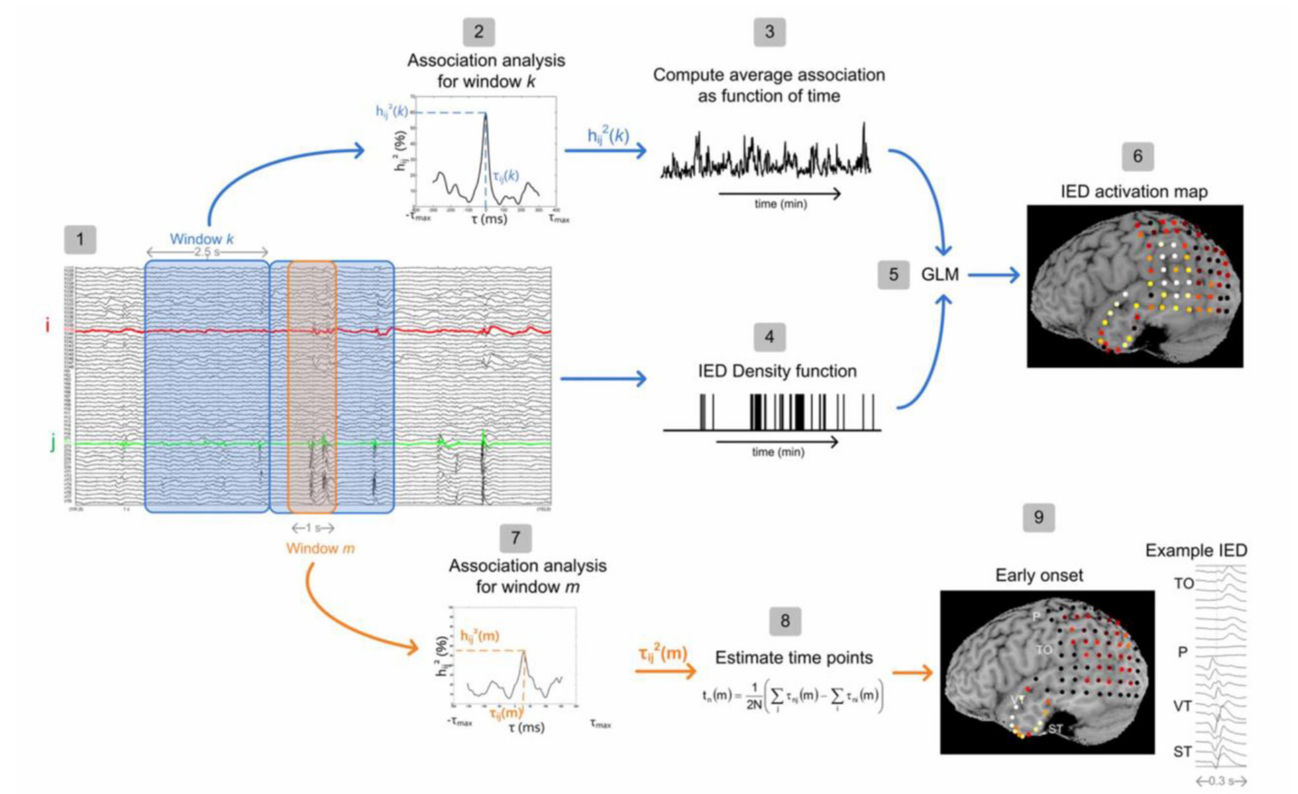

FIGURE 17 | Flowchart of ECoG analysis consisting of two steps: estimation of interictally active ECoG areas (steps 1–6) and the estimation of an onset area (steps 7–9) (162).

IED, the primary cluster was referred to as the cluster with the highest absolute *t*-value at a peak located in the cerebral cortex compared to the thresholds defined in significance levels. Finally, the presumed seizure onset zone (pSOZ) of the patients that were determined using SEEG findings or the other comprehensive evaluations (164) was compared to the primary cluster in EEG–fMRI to measure their concordance at the sublobar level. The result of this study confirmed the initial hypothesis and revealed the significance in the number of IEDs in the types with *t*-value above FDR that was higher than below FDR and in the extent of IED types concordant with the SOZ that was larger than IED types discordant with the SOZ. The complex pathophysiology of epileptic cerebral structures, types of seizures, and frequency features have not been studied as the authoritative factor for precise detection of epileptic foci using EEG–fMRI (22).

CONCLUSIONS

Recording EEG and fMRI simultaneously is a non-invasive method identifying cerebral hemodynamic changes related to IEDs on scalp EEG. Several studies revealed the capacity of EEG–fMRI to distinguish various forms of generalized and focal epilepsy. In patients with epilepsy, especially those who are pharmacoresistant and surgical candidates, the significant clinical matter of how BOLD changes relate to IEDs can contribute to localizing the epileptic focus. The BOLD signal usually rises in regions causing focal IEDs, but often in the context of more extensive, or even distant, responses.

The simultaneous EEG–fMRI recording is an effective non-invasive method to study the brain regions associated with the epileptic discharges. The neuronal discharges that occur through interictal spikes or spike-wave bursts cause an increase in metabolism and blood flow, redirected in the BOLD signal measured by fMRI. Although this increase has the highest intensity in generating discharges, it can be revealed in areas only affected by the discharges. Also, the epileptic discharges can lead to a decrease in metabolism that the origin of which is not completely understood. It has been shown that EEG–fMRI applied to patients with focal epilepsy results in maxima of the BOLD signal most often concordant with other localization methods and helped to localize the epileptic focus in non-lesional frontal-lobe epilepsy. It has also been revealed that the thalamus is an active region in generalized epileptic discharges. These can be used to investigate the location and extent of the brain regions intricate during epileptic discharges and evaluate the disease progression.

Simultaneous recording of EEG and fMRI provides a great potential to find the pathophysiological mechanisms of the discharges (165). The most capable method of acquiring data is probably continuous scanning followed by EEG artifact removal. Some cases have shown inconsistent fMRI results with EEG. However, we cannot imagine a one-to-one correspondence between EEG and fMRI findings. These inconsistencies may be due to the fMRI data analysis problems. Some of the responses shown in the fMRI results are "noises" caused by practical artifacts such as movement, an erroneous HRF model, or inappropriate statistical methods. Despite the noise, most responses can be considered valid since they make sense in the context of our understanding of an epileptic condition.

It is also essential to consider the natural differences between the two modalities. First, in fMRI, the BOLD response is measured everywhere, but EEG records only superficial cortical layer activity. Secondly, two different types of activities are evaluated: one is electrical, and the other is based on the changes in deoxyhemoglobin in the veins. EEG and fMRI are considered complementary since each measures an activity that the other one does not.

Although the ideal approach of data analysis remains undefined, the majority of focal and generalized epilepsy patients had a consistent BOLD effect with the spikes. Instead of using techniques developed for functional activation in the future, there should be a focus on adapting fMRI analysis techniques to the specific requirements of the epileptic activity. Friston et al. (166) proposed a method that does not depend on linear assumption. Other approaches such as temporal clustering try to analyze the BOLD signal independently of the EEG event (167, 168). The deconvolution approach makes assumptions with regard to HRF (169, 170). Finally, the ICA approach decomposes the data sets into spatially independent components. Using some of these methods, we may be able to discover epileptic discharges anywhere in the brain, regardless of seeing spikes on the scalp EEG.

The importance of the diverse BOLD response is another issue that should be assessed. In epilepsy studies, the fact that we see both activation and deactivation is considered perplexing, where it is expected to see activation (increased BOLD) as a result of extreme neural activity. Moreover, it is important to assess particular responses in different types of epileptogenic structural abnormalities such as mesial temporal sclerosis, brain tumors, and malformations of cortical development (MCDs), which are commonly complicated by intractable focal epilepsy (171).

The presence of both positive and negative BOLD responses in generalized epilepsy patients may be interpreted differently, also indicating the explanation of deactivation. Bilateral activations were observed in the thalamus, mesial mid-frontal region, insulae, and cerebellum. Deactivations were found bilaterally in the anterior frontal and parietal regions, in a global pattern resembling the default state of the brain (98). This finding suggests that the default state of the brain is suspended during an epileptic discharge. Deactivation occurs as a result of the indirect effect of the discharges on attention mechanisms. Performing these studies on experimental animals provides further insight into human results (172, 173).

When the BOLD responses are found in multiple regions, particularly in focal epilepsy, this possibility arises that the regions are related to the propagation of the interictal discharge, or distant sites particularly sensitive to the effect of epileptic discharges. However, the temporal resolution of fMRI is not able to measure the propagation times of a few milliseconds. So, the EEG source modeling can help to assess the propagation of epileptic discharges if the model includes EEG sources in the same regions as BOLD responses. BOLD response patterns may be different in the primary epileptogenic region and in the region in which the activity propagated (42). It would be interesting to assess functional connectivity using the fMRI data (174).

In the past, most studies used a 1.5-T scanner, although a few studies used 3 T. Using a 3-T scanner may create the expectation of better recognition of hemodynamic changes and deteriorating some difficulties such as higher signal loss as a result of susceptibility artifact, the pulse artifact, and movements that cause worse artifacts in the EEG. Fortunately, with suitable artifact removal methods, studies in a 3-T scanner would be more efficient (26).

Finally, an important study of Markoula et al. (175) assessed the impact of EEG–fMRI on the clinical decision-making process and showed the actual capability of this approach to be applied prospectively in localization of seizure focus during the pre-surgical evaluation. They studied 16 patients with refractory extra-temporal focal epilepsy, referred for pre-surgical evaluation in a period of 18 months. Interpretable EEG–fMRI results which were available in 13 patients made a modification of the initial surgical plan in 10 (77%), suggesting a significant influence of EEG–fMRI on epilepsy surgery planning.

In conclusion, combining EEG and fMRI seems to be a potential method in the source localization of epileptic foci. This complicated technique is quite practical and offers a new view in the study of epileptic disorders. Although applying it to individual patients (subjects) to localize epileptic foci is not yet justified, it can present potential areas for further research, for instance, focused anatomical MRI analysis or electrode implantation.

All in all, the works reviewed in this paper can bring us closer to the localization of focal epileptic activity and, afterward, to real-life applications. Applying simultaneous EEG–fMRI for combining EEG temporal resolution and fMRI spatial resolution recommends more excellent diagnoses of precise epileptic source localization. This allows for providing more patients with the option of surgery while increasing the likelihood of a successful and life-improving operation.

AUTHOR CONTRIBUTIONS

SS, EE, and HS-Z jointly designed the study. SS, EE, and MSh did the literature survey and wrote the initial version of the manuscript. HS-Z edited the draft and submitted the manuscript. All authors participated in the revision process and approved the final version of the manuscript.

ACKNOWLEDGMENTS

The authors thank the publishers for providing permission to use some of their published illustrations.

REFERENCES

1. Kwong KK, Belliveau JW, Chesler DA, Goldberg IE, Weisskoff RM, Poncelet BP, et al. Dynamic magnetic resonance imaging of human brain activity during primary sensory stimulation. *Proc Natl Acad Sci USA*. (1992) 89:5675–9. doi: 10.1073/pnas.89.12.5675
2. David W, Ogawa S, Tank DW, Menon R, Ellermann JM, Kim SG, et al. Intrinsic signal changes accompanying sensory stimulation: functional brain mapping with magnetic resonance imaging. *Proc Natl Acad Sci USA*. (1992) 89:5951–5. doi: 10.1073/pnas.89.13.5951
3. Salek-Haddadi A, Diehl B, Hamandi K, Merschhemke M, Liston A, Friston K, et al. Hemodynamic correlates of epileptiform discharges: an EEG-fMRI study of 63 patients with focal epilepsy. *Brain Res.* (2006) 1088:148–66. doi: 10.1016/j.brainres.2006.02.098
4. Marques JP, Rebola J, Figueiredo P, Pinto A, Sales F, Castelo-Branco M. ICA decomposition of EEG signal for fMRI processing in epilepsy. *Hum Brain Mapp.* (2009) 30:2986–96. doi: 10.1002/hbm.20723
5. Moeller F, LeVan P, Gotman J. Independent component analysis (ICA) of generalized spike wave discharges in fMRI: comparison with general linear model-based EEG-fMRI. *Hum Brain Mapp.* (2011) 32:209–17. doi: 10.1002/hbm.21010
6. LeVan P, Tyvaert L, Gotman J. Modulation by EEG features of BOLD responses to interictal epileptiform discharges. *Neuroimage.* (2010) 50:15–26. doi: 10.1016/j.neuroimage.2009.12.044
7. Bénar CG, Grova C, Kobayashi E, Bagshaw AP, Aghakhani Y, Dubeau F, et al. EEG-fMRI of epileptic spikes: concordance with EEG source localization and intracranial EEG. *Neuroimage.* (2006) 30:1161–70. doi: 10.1016/j.neuroimage.2005.11.008
8. Bénar CG, Gross DW, Wang Y, Petre V, Pike B, Dubeau F, et al. The BOLD response to interictal epileptiform discharges. *Neuroimage.* (2002) 17:1182–92. doi: 10.1006/nimg.2002.1164
9. Hamandi K, Salek-Haddadi A, Fish DR, Lemieux L. EEG/functional MRI in epilepsy: the queen square experience. *J Clin Neurophysiol.* (2004) 21:241–8. doi: 10.1097/00004691-200407000-00002
10. Gotman J, Kobayashi E, Bagshaw AP, Bénar CG, Dubeau F. Combining EEG and fMRI: a multimodal tool for epilepsy research. *J Magn Reson Imaging.* (2006) 23:906–20. doi: 10.1002/jmri.20577
11. Gotman J, Bénar CG, Dubeau F. Combining EEG and fMRI in epilepsy: methodological challenges and clinical results. *J Clin Neurophysiol.* (2004) 21:229–40. doi: 10.1097/01.WNP.0000139658.92878.2A
12. Al-Asmi A, Bénar CG, Gross DW, Agha Khani Y, Andermann F, Pike B, et al. fMRI activation in continuous and spike-triggered EEG-fMRI studies of epileptic spikes. *Epilepsia.* (2003) 44:1328–39. doi: 10.1046/j.1528-1157.2003.01003.x
13. Bénar CG, Aghakhani Y, Wang Y, Izenberg A, Al-Asmi A, Dubeau F, et al. Quality of EEG in simultaneous EEG-fMRI for epilepsy. *Clin Neurophysiol.* (2003) 114:569–80. doi: 10.1016/S1388-2457(02)00383-8
14. Goldman RI, Stern JM, Engel J, Cohen MS. Acquiring simultaneous EEG and functional MRI. *Clin Neurophysiol.* (2000) 111:1974–80. doi: 10.1016/S1388-2457(00)00456-9
15. Allen PJ, Polizzi G, Krakow K, Fish DR, Lemieux L. Identification of EEG events in the MR scanner: the problem of pulse artifact and a method for its subtraction. *Neuroimage.* (1998) 8:229–39. doi: 10.1006/nimg.1998.0361
16. Bonmassar G, Anami K, Ives J, Belliveau JW. Visual evoked potential (VEP) measured by simultaneous 64-channel EEG and 3T fMRI. *Neuroreport.* (1999) 10:1893–7. doi: 10.1097/00001756-199906230-00018
17. van Houdt PJ, de Munck JC, Zijlmans M, Huiskamp G, Leijten FSS, Boon PAJM, et al. Comparison of analytical strategies for EEG-correlated fMRI data in patients with epilepsy. *Magn Reson Imaging.* (2010) 28:1078–86. doi: 10.1016/j.mri.2010.03.022
18. Jing M, Sanei S. Scanner artifact removal in simultaneous EEG-fMRI for epileptic seizure prediction. In: *Proceedings - International Conference on Pattern Recognition*. (2006). p. 722–725.
19. Amini L, Sameni R, Jutten C, Hossein-Zadeh GA, Soltanian-Zadeh H. MR artifact reduction in the simultaneous acquisition of EEG and fMRI of epileptic patients. In: *European Signal Processing Conference* (IEEE). (2008). p. 1–5.
20. Siniatchkin M, Moeller F, Jacobs J, Stephani U, Boor R, Wolff S, et al. Spatial filters and automated spike detection based on brain topographies improve sensitivity of EEG-fMRI studies in focal epilepsy. *Neuroimage.* (2007) 37:834–43. doi: 10.1016/j.neuroimage.2007.05.049
21. Körbl K, Jacobs J, Herbst M, Zaitsev M, Schulze-Bonhage A, Hennig J, et al. Marker-based ballistocardiographic artifact correction improves spike identification in EEG-fMRI of focal epilepsy patients. *Clin Neurophysiol.* (2016) 127:2802–11. doi: 10.1016/j.clinph.2016.05.361
22. Ebrahimzadeh E, Shams M, Fayaz F, Rajabion L, Mirbagheri M, Nadjar Araabi B, et al. Quantitative determination of concordance in localizing epileptic focus by component-based EEG-fMRI. *Comput Methods Programs Biomed.* (2019) 177:231–41. doi: 10.1016/j.cmpb.2019.06.003
23. Ebrahimzadeh E, Soltanian-Zadeh H, Araabi BN, Fesharaki SSH, Habibabadi JM. Component-related BOLD response to localize epileptic focus using simultaneous EEG-fMRI recordings at 3T. *J Neurosci Methods.* (2019) 322:34–49. doi: 10.1016/j.jneumeth.2019.04.010
24. Ebrahimzadeh E, Shams M, Rahimpour Jounghani A, Fayaz F, Mirbagheri M, Hakimi N, et al. Localizing confined epileptic foci in patients with an unclear focus or presumed multifocality using a component-based EEG-fMRI method. *Cogn Neurodyn.* (2020) 5:207–22. doi: 10.1007/s11571-020-09614-5
25. Bagshaw AP, Torab L, Kobayashi E, Hawco C, Dubeau F, Pike GB, et al. EEG-fMRI using z-shimming in patients with temporal lobe epilepsy. *J Magn Reson Imaging.* (2006) 24:1025–32. doi: 10.1002/jmri.20744
26. Gholipour T, Moeller F, Pittau F, Dubeau F, Gotman J. Reproducibility of interictal EEG-fMRI results in patients with epilepsy. *Epilepsia.* (2011) 52:433–42. doi: 10.1111/j.1528-1167.2010.02768.x
27. Klovatch-Podlipsky I, Gazit T, Fahoum F, Tsirelson B, Kipervasser S, Kremer U, et al. Dual array EEG-fMRI: an approach for motion artifact suppression in EEG recorded simultaneously with fMRI. *Neuroimage.* (2016) 142:674–86. doi: 10.1016/j.neuroimage.2016.07.014
28. Wu X, Wu T, Zhan Z, Yao L, Wen X. A real-time method to reduce ballistocardiogram artifacts from EEG during fMRI based on optimal basis sets (OBS). *Comput Methods Programs Biomed.* (2016) 127:114–25. doi: 10.1016/j.cmpb.2016.01.018
29. Harrison AH, Noseworthy MD, Reilly JP, Connolly JF. Ballistocardiogram correction in simultaneous EEG/ fMRI recordings: a comparison of average artifact subtraction and optimal basis set methods using two popular software tools. *Crit Rev Biomed Eng.* (2014) 42:95–107. doi: 10.1615/CritRevBiomedEng.2014011220
30. Niazy RK, Beckmann CF, Iannetti GD, Brady JM, Smith SM. Removal of FMRI environment artifacts from EEG data using optimal basis sets. *Neuroimage.* (2005) 28:720–37. doi: 10.1016/j.neuroimage.2005.06.067
31. Chaudhary UJ, Rodionov R, Carmichael DW, Thornton RC, Duncan JS, Lemieux L. Improving the sensitivity of EEG-fMRI studies of epileptic activity by modelling eye blinks, swallowing and other video-EEG detected physiological confounds. *Neuroimage.* (2012) 61:1383–93. doi: 10.1016/j.neuroimage.2012.03.028
32. Mikl M, Mareček R, Janoušová E, Slavíček T, Barton M, Brázdil M. Influence of data processing pipelines on EEG-fMRI results in patients with epilepsy. *Clin Neurophysiol.* (2015) 126:e42–3. doi: 10.1016/j.clinph.2014.10.195
33. Waites AB, Shaw ME, Briellmann RS, Labate A, Abbott DF, Jackson GD. How reliable are fMRI-EEG studies of epilepsy? A nonparametric approach to analysis validation and optimization. *Neuroimage.* (2005) 24:192–9. doi: 10.1016/j.neuroimage.2004.09.005
34. Pouliot P, Tremblay J, Robert M, Vannasing P, Lepore F, Lassonde M, et al. Nonlinear hemodynamic responses in human epilepsy: a multimodal analysis with fNIRS-EEG and fMRI-EEG. *J Neurosci Methods.* (2012) 204:326–40. doi: 10.1016/j.jneumeth.2011.11.016
35. Lemieux L, Laufs H, Carmichael D, Paul JS, Walker MC, Duncan JS. Noncanonical spike-related BOLD responses in focal epilepsy. *Hum Brain Mapp.* (2008) 29:329–45. doi: 10.1002/hbm.20389
36. Friston KJ, Holmes AP, Worsley J-P, Frith CD, Frackowiak RS. Statistical parametric maps in functional imaging: a general linear approach. *Hum Brain Mapp.* (1995) 2:189–210. doi: 10.1002/hbm.460020402
37. Jacobs J, Kobayashi E, Boor R, Muhle H, Stephan W, Hawco C, et al. Hemodynamic responses to interictal epileptiform discharges in children with symptomatic epilepsy. *Epilepsia.* (2007) 48:2068–78. doi: 10.1111/j.1528-1167.2007.01192.x

38. Laufs H, Hamandi K, Salek-Haddadi A, Kleinschmidt AK, Duncan JS, Lemieux L. Temporal lobe interictal epileptic discharges affect cerebral activity in "default mode" brain regions. *Hum Brain Mapp.* (2007) 28:1023–32. doi: 10.1002/hbm.20323
39. Bagshaw AP, Hawco C, Bénar CG, Kobayashi E, Aghakhani Y, Dubeau F, et al. Analysis of the EEG-fMRI response to prolonged bursts of interictal epileptiform activity. *Neuroimage.* (2005) 24:1099–112. doi: 10.1016/j.neuroimage.2004.10.010
40. Kang JK, Bénar CG, Al-Asmi A, Khani YA, Pike GB, Dubeau F, et al. Using patient-specific hemodynamic response functions in combined EEG-fMRI studies in epilepsy. *Neuroimage.* (2003) 20:1162–70. doi: 10.1016/S1053-8119(03)00290-8
41. Aguirre G, Zarahn E, D'Esposito M. The variability of human BOLD hemodynamic responses. *Neuroimage.* (1998) 7:S574. doi: 10.1016/S1053-8119(18)31407-1
42. Menz MM, Neumann J, Müller K, Zysset S. Variability of the BOLD response over time: An examination of within-session differences. *Neuroimage.* (2006) 32:1185–94. doi: 10.1016/j.neuroimage.2006.06.003
43. Xue K, Tang X. Hemodynamic response function in absence epilepsy: an EEG-fMRI study. In: *2016 5th International Conference on Measurement, Instrumentation and Automation (ICMIA 2016)*. Atlantis Press (2016). p. 366–9.
44. Xue K, Luo C, Yao Z, Yao D. Hemodynamic response function in temporal lobe epilepsy with interictal regional slow wave: an EEG-fMRI study. In: *2010 International Conference on Medical Image Analysis and Clinical Application, MIACA 2010.* (2010). p. 30–33.
45. Bagshaw AP, Aghakhani Y, Bénar CG, Kobayashi E, Hawco C, Dubeau F, et al. EEG-fMRI of focal epileptic spikes: analysis with multiple haemodynamic functions and comparison with gadolinium-enhanced MR angiograms. *Hum Brain Mapp.* (2004) 22:179–92. doi: 10.1002/hbm.20024
46. van Houdt P, Zijlmans M. Different ways to analyze EEG-fMRI in focal epilepsy: does it matter? *Clin Neurophysiol.* (2013) 124:2070–2. doi: 10.1016/j.clinph.2013.06.007
47. Omidvarnia A, Kowalczyk MA, Pedersen M, Jackson GD. Towards fast and reliable simultaneous EEG-fMRI analysis of epilepsy with automatic spike detection. *Clin Neurophysiol.* (2019) 130:368–78. doi: 10.1016/j.clinph.2018.11.024
48. Pedreira C, Vaudano AE, Thornton RC, Chaudhary UJ, Vulliemoz S, Laufs H, et al. Classification of EEG abnormalities in partial epilepsy with simultaneous EEG-fMRI recordings. *Neuroimage.* (2014) 99:461–76. doi: 10.1016/j.neuroimage.2014.05.009
49. Huiskamp GJ, Hersevoort M, Zijlmans M, Leijten F. The impact of uncertain spike identification in event related EEG-fMRI in epilepsy. In: *Proc. of 2007 Joint Meet. of the 6th Int. Symp. on Noninvasive Functional Source Imaging of the Brain and Heart and the Int. Conf. on Functional Biomedical Imaging, NFSI and ICFBI 2007*. (2017). p. 148–50.
50. Flanagan D, Abbott DF, Jackson GD. How wrong can we be? The effect of inaccurate mark-up of EEG/fMRI studies in epilepsy. *Clin Neurophysiol.* (2009) 120:1637–47. doi: 10.1016/j.clinph.2009.04.025
51. Safi-Harb M, Proulx S, von Ellenrieder N, Gotman J. Advantages and disadvantages of a fast fMRI sequence in the context of EEG-fMRI investigation of epilepsy patients: a realistic simulation study. *Neuroimage.* (2015) 119:20–32. doi: 10.1016/j.neuroimage.2015.06.039
52. Jäger V, Dümpelmann M, LeVan P, Ramantani G, Mader I, Schulze-Bonhage A, et al. Concordance of epileptic networks associated with epileptic spikes measured by high-density EEG and fast fMRI. *PLoS ONE.* (2015) 10:e0140537. doi: 10.1371/journal.pone.0140537
53. Faizo NL, Burianová H, Gray M, Hocking J, Galloway G, Reutens D. Identification of pre-spike network in patients with mesial temporal lobe epilepsy. *Front Neurol.* (2014) 5:222. doi: 10.3389/fneur.2014.00222
54. Jacobs J, LeVan P, Moeller F, Boor R, Stephani U, Gotman J, et al. Hemodynamic changes preceding the interictal EEG spike in patients with focal epilepsy investigated using simultaneous EEG-fMRI. *Neuroimage.* (2009) 45:1220–31. doi: 10.1016/j.neuroimage.2009.01.014
55. Pittau F, Levan P, Moeller F, Gholipour T, Haegelen C, Zelmann R, et al. Changes preceding interictal epileptic EEG abnormalities: comparison between EEG/fMRI and intracerebral EEG. *Epilepsia.* (2011) 52:1120–9. doi: 10.1111/j.1528-1167.2011.03072.x
56. Federico P, Archer JS, Abbott DF, Jackson GD. Cortical/subcortical BOLD changes associated with epileptic discharges: an EEG-fMRI study at 3 T. *Neurology.* (2005) 64:1125–30. doi: 10.1212/01.WNL.0000156358.72670.AD
57. Ekstrom A. How and when the fMRI BOLD signal relates to underlying neural activity: the danger in dissociation. *Brain Res Rev.* (2010) 62:233–44. doi: 10.1016/j.brainresrev.2009.12.004
58. Volz S, Lengler U, Krakow K, & Wibral M. Feasibility of fully simultaneous EEG / PASL / BOLD-fMRI for characterisation of hemodynamic responses to pathophysiologic and physiologic neuronal activation in epilepsy patients. *Proc Intl Soc Mag Reson Med.* (2007) 15:544.
59. Bonaventura C Di, Vaudano AE, Carnì M, Pantano P, Nucciarelli V, Garreffa G, et al. EEG/fMRI study of ictal and interictal epileptic activity: methodological issues and future perspectives in clinical practice. *Epilepsia.* (2006) 47:52–8. doi: 10.1111/j.1528-1167.2006.00878.x
60. Briellmann RS, Waites AB, Labate A, Abbott DF, Federico P, Harvey AS, et al. Simultaneous fMRI/EEG in idiopathic generalized epilepsy (IGE). *Ann Neurol.* (2005) 13:2005.
61. Tyvaert L, Chassagnon S, Sadikot A, Levan P, Dubeau F, Gotman J. Thalamic nuclei activity in idiopathic generalized epilepsy: an EEG-fMRI study. *Neurology.* (2009) 73:2018–22. doi: 10.1212/WNL.0b013e3181c55d02
62. Szaflarski JP, DiFrancesco M, Hirschauer T, Banks C, Privitera MD, Gotman J, et al. Cortical and subcortical contributions to absence seizure onset examined with EEG/fMRI. *Epilepsy Behav.* (2010) 18:404–13. doi: 10.1016/j.yebeh.2010.05.009
63. Benuzzi F, Ballotta D, Mirandola L, Ruggieri A, Vaudano AE, Zucchelli M, et al. An EEG-fMRI study on the termination of generalized spike-and-wave discharges in absence epilepsy. *PLoS ONE.* (2015) 10:1–16. doi: 10.1371/journal.pone.0130943
64. Cosottini M, Pesaresi I, Maritato P, Belmonte G, Taddei A, Sartucci F, et al. EEG topography-specific BOLD changes: a continuous EEG-fMRI study in a patient with focal epilepsy. *Magn Reson Imaging.* (2010) 28:388–93. doi: 10.1016/j.mri.2009.11.011
65. Flanagan D, Badawy RAB, Jackson GD. EEG-fMRI in focal epilepsy: local activation and regional networks. *Clin Neurophysiol.* (2014) 125:21–31. doi: 10.1016/j.clinph.2013.06.182
66. Fahoum F, Lopes R, Pittau F, Dubeau F, Gotman J. Widespread epileptic networks in focal epilepsies: EEG-fMRI study. *Epilepsia.* (2012) 53:1618–27. doi: 10.1111/j.1528-1167.2012.03533.x
67. Rathakrishnan R, Moeller F, Levan P, Dubeau F, Gotman J. BOLD signal changes preceding negative responses in EEG-fMRI in patients with focal epilepsy. *Epilepsia.* (2010) 51:1837–45. doi: 10.1111/j.1528-1167.2010.02643.x
68. Pittau F, Fahoum F, Zelmann R, Dubeau F, Gotman J. Negative BOLD response to interictal epileptic discharges in focal epilepsy. *Brain Topogr.* (2013) 26:627–40. doi: 10.1007/s10548-013-0302-1
69. Gupta A, Ashalatha R, Sujesh S, Anakha GL, James J, Thomas B. *Statistical Parametric Mapping of EEG correlated fMRI data to detect Epileptic foci*. Madras: Indian Institute of Technology (2012).
70. Cao J. The size of the connected components of excursion sets of $\chi 2$, t and F fields. *Adv Appl Probab.* (1999) 31:579–95. doi: 10.1239/aap/1029955192
71. Zijlmans M, Huiskamp G, Hersevoort M, Seppenwoolde JH, Van Huffelen AC, Leijten FSS. EEG-fMRI in the preoperative work-up for epilepsy surgery. *Brain.* (2007) 130:2343–53. doi: 10.1093/brain/awm141
72. De Tiège X, Laufs H, Boyd SG, Harkness W, Allen PJ, Clark CA, et al. EEG-fMRI in children with pharmacoresistant focal epilepsy. *Epilepsia.* (2007) 48:385–9. doi: 10.1111/j.1528-1167.2006.00951.x
73. Grova C, Daunizeau J, Kobayashi E, Bagshaw AP, Lina JM, Dubeau F, et al. Concordance between distributed EEG source localization and simultaneous EEG-fMRI studies of epileptic spikes. *Neuroimage.* (2008) 39:755–74. doi: 10.1016/j.neuroimage.2007.08.020
74. Avesani M, Formaggio E, Milanese F, Baraldo A, Gasparini A, Cerini R, et al. Continuous EEG-fMRI in pre-surgical evaluation of a patient with symptomatic seizures: bold activation linked to interictal epileptic discharges caused by Cavernoma. *Neuroradiol J.* (2008) 21:183–91. doi: 10.1177/197140090802100205

75. Jackson G. EEG-fMRI in the presurgical work-up of patients with partial epilepsy and unclear seizure focus: commentary. *Nat Clin Pract Neurol.* (2008) 4:128–9. doi: 10.1038/ncpneuro0738
76. Liu Y, Yang T, Yang X, Liu I, Liao W, Lui S, et al. EEG-fMRI study of the interictal epileptic activity in patients with partial epilepsy. *J Neurol Sci.* (2008) 268:117–23. doi: 10.1016/j.jns.2007.11.019
77. Gotman J. Epileptic networks studied with EEG-fMRI. *Epilepsia.* (2008) 49:42–51. doi: 10.1111/j.1528-1167.2008.01509.x
78. Moeller F, Tyvaert L, Nguyen DK, Levan P, Bouthillier A, Kobayashi E, et al. EEG-fMRI: adding to standard evaluations of patients with nonlesional frontal lobe epilepsy. *Neurology.* (2009) 73:2023–30. doi: 10.1212/WNL.0b013e3181c55d17
79. Borelli P, Avesani M, Formaggio E, Storti SF, Zanoni T, Moretto G, et al. EEG-fMRI as an useful tool to detect epileptic foci associated with secondary bilateral synchrony. *Seizure.* (2010) 19:605–8. doi: 10.1016/j.seizure.2010.09.001
80. Pittau F, Dubeau F, Gotman J. Contribution of EEG/fMRI to the definition of the epileptic focus. *Neurology.* (2012) 78:1479–87. doi: 10.1212/WNL.0b013e3182553bf7
81. Moeller F, Moehring J, Ick I, Steinmann E, Wolff S, Jansen O, et al. EEG-fMRI in atypical benign partial epilepsy. *Epilepsia.* (2013) 54:103–8. doi: 10.1111/epi.12243
82. Zhang J, Liu Q, Mei S, Zhang X, Wang X, Liu W, et al. Presurgical EEG-fMRI in a complex clinical case with seizure recurrence after epilepsy surgery. *Neuropsychiatr Dis Treat.* (2013) 9:1003–10. doi: 10.2147/NDT.S47099
83. Tousseyn S, Dupont P, Robben D, Goffin K, Sunaert S, Van Paesschen W. A reliable and time-saving semiautomatic spike-template-based analysis of interictal EEG-fMRI. *Epilepsia.* (2014) 55:2048–58. doi: 10.1111/epi.12841
84. Sandhya M, Bharath RD, Panda R, Chandra SR, Kumar N, George L, et al. Understanding the pathophysiology of reflex epilepsy using simultaneous EEG-fMRI. *Epileptic Disord.* (2014) 16:19–29. doi: 10.1684/epd.2014.0632
85. Tousseyn S, Dupont P, Goffin K, Sunaert S, Van Paesschen W. Correspondence between large-scale ictal and interictal epileptic networks revealed by single photon emission computed tomography (SPECT) and electroencephalography (EEG)-functional magnetic resonance imaging (fMRI). *Epilepsia.* (2015) 56:382–92. doi: 10.1111/epi.12910
86. Lemieux L, Krakow K, Scott C, Allen P, Fish D. The localization of epileptic spikes based on spike-triggered fMRI is consistent with EEG source reconstruction. *Neuroimage.* (2000) 11:S118. doi: 10.1016/S1053-8119(00)91051-6
87. Fontanarosa JB, Lasky RE, Lee HC, Van Drongelen W. Localization of brainstem auditory evoked potentials in primates: a comparison of localization techniques applied to deep brain sources. *Brain Topogr.* (2004) 17:99–108. doi: 10.1007/s10548-004-1007-2
88. Bagshaw AP, Kobayashi E, Dubeau F, Pike GB, Gotman J. Correspondence between EEG-fMRI and EEG dipole localisation of interictal discharges in focal epilepsy. *Neuroimage.* (2006) 30:417–25. doi: 10.1016/j.neuroimage.2005.09.033
89. Secca MF, Fernandes HM, Cabral JR, Leal A. Optimization of fMRI processing parameters for simutaneous acquisition of EEG/fMRI in focal epilepsy. *IFMBE Proc.* (2008) 20:505–8. doi: 10.1007/978-3-540-69367-3_135
90. Forjaz Secca M, Leal A, Cabral J, Fernandes H. Comparison of methods and co-registration maps of EEG and fMRI in occipital lobe epilepsy. *IFMBE Proc.* (2007) 16:505–8. doi: 10.1007/978-3-540-73044-6_129
91. Hu D, Yan L, Liu Y, Zhou Z, Friston KJ, Tan C, et al. Unified SPM-ICA for fMRI analysis. *Neuroimage.* (2005) 25:746–55. doi: 10.1016/j.neuroimage.2004.12.031
92. Penney TJM, Goodyear B, Pittman D, Federico P, Koles ZJ. Comparison of hemodynamic response models in a combined EEG-fMRI study of an epileptic patient. In: *Proc. of 2007 Joint Meet. of the 6th Int. Symp. on Noninvasive Functional Source Imaging of the Brain and Heart and the Int. Conf. on Functional Biomedical Imaging, NFSI and ICFBI 2007.* (2007). p. 155–8.
93. Rodionov R, De Martino F, Laufs H, Carmichael DW, Formisano E, Walker M, et al. Independent component analysis of interictal fMRI in focal epilepsy: comparison with general linear model-based EEG-correlated fMRI. *Neuroimage.* (2007) 38:488–500. doi: 10.1016/j.neuroimage.2007.08.003
94. Sercheli MS, Bilevicius E, Alessio A, Ozelo H, Pereira FRS, Rondina JM, et al. EEG spike source localization before and after surgery for temporal lobe epilepsy: a BOLD EEG-fMRI and independent component analysis study. *Brazilian J Med Biol Res.* (2009) 42:582–7. doi: 10.1590/S0100-879X2009000600017
95. Luo C, Yao Z, Li Q, Lei X, Zhou D, Qin Y, et al. Imaging foci of epileptic discharges from simultaneous EEG and fMRI using the canonical HRF. *Epilepsy Res.* (2010) 91:133–42. doi: 10.1016/j.eplepsyres.2010.07.003
96. LeVan P, Tyvaert L, Moeller F, Gotman J. Independent component analysis reveals dynamic ictal BOLD responses in EEG-fMRI data from focal epilepsy patients. *Neuroimage.* (2010) 49:366–78. doi: 10.1016/j.neuroimage.2009.07.064
97. Leite M, Leal A, Sanches J, Figueiredo P. "Improved EEG-fMRI integration in epilepsy," in *Proceedings of RecPad 2010 - 16th Portuguese Conference on Pattern Recognition*. Vila Real (2010) 15:2–3. Available online at: https://welcome.isr.tecnico.ulisboa.pt/
98. Leite M, Figueiredo P, Leal. A. Estimation of the haemodynamic response to epileptic activity in EEG-fMRI data. In: *IEEE 2nd Portuguese Meeting in Bioengineering (ENBENG), IEEE*. (2012). p. 3–8.
99. Lei X, Luo C, Yao D. Imaging epileptic networks using spatial-temporal EEG-fMRI fusion. *Int J.* (2011) 13:249–54.
100. Formaggio E, Storti SF, Bertoldo A, Manganotti P, Fiaschi A, Toffolo GM. Integrating EEG and fMRI in epilepsy. *Neuroimage.* (2011) 54:2719–31. doi: 10.1016/j.neuroimage.2010.11.038
101. Franchin T, Tana MG, Cannata V, Cerutti S, Bianchi AM. Independent component analysis of EEG-fMRI data for studying epilepsy and epileptic seizures. In: *Proceedings of the Annual International Conference of the IEEE Engineering in Medicine and Biology Society, EMBS*. (2013). p. 6011–4.
102. Hunyadi B, Tousseyn S, Mijović B, Dupont P, Van Huffel S, Van Paesschen W, et al. ICA extracts epileptic sources from fMRI in EEG-negative patients: a retrospective validation study. *PLoS ONE.* (2013) 8:e78796. doi: 10.1371/journal.pone.0078796
103. Rummel C, Abela E, Hauf M, Wiest R, Schindler K. Ordinal patterns in epileptic brains: analysis of intracranial EEG and simultaneous EEG-fMRI. *Eur Phys J Spec Top.* (2013) 222:569–85. doi: 10.1140/epjst/e2013-01860-9
104. Panda R, Bharath RD, Mangalore S, Upadhyay N, Thamodharan A, Kanungo S. Resting state networks analysis using simultaneous EEG-fMRI for epilepsy patient. *Lect Notes Electr Eng.* (2013) 222:607–17. doi: 10.1007/978-81-322-1000-9_56
105. van Houdt PJ, Ossenblok PPW, Colon AJ, Hermans KHM, Verdaasdonk RM, Boon PAJM, et al. Are epilepsy-related fMRI components dependent on the presence of interictal epileptic discharges in scalp EEG? *Brain Topogr.* (2015) 28:606–18. doi: 10.1007/s10548-014-0407-1
106. Hunyadi B, De Vos M, Van Paesschen W, Van Huffel S. Exploring the epileptic network with parallel ICA of interictal EEG-fMRI stadius. In: *22nd European Signal Processing Conference*. (2015). p. 429–433.
107. Carnì M, Di Bonaventura C, Borrazzo C, Fattouch J, Giallonardo AT, Casciato S, et al. Analysis of simultaneous EEG/FMRI data acquisition in epileptic patients: comparison of semi-blind ICA, spatial ICA and GLM based methods. *Phys Med.* (2016) 32:126. doi: 10.1016/j.ejmp.2016.01.434
108. Cooray GK, Sengupta B, Douglas PK, Friston K. Dynamic causal modelling of electrographic seizure activity using Bayesian belief updating. *Neuroimage.* (2016) 125:1142–54. doi: 10.1016/j.neuroimage.2015.07.063
109. Hamandi K, Powell HWR, Laufs H, Symms MR, Barker GJ, Parker GJM, et al. Combined EEG-fMRI and tractography to visualise propagation of epileptic activity. *J Neurol Neurosurg Psychiatry.* (2008) 79:594–7. doi: 10.1136/jnnp.2007.125401
110. Murta T, Figueiredo P, Leal A. EEG-fMRI measures of functional brain connectivity in epilepsy. In: *1st Portuguese Meeting in Biomedical Engineering, ENBENG* (2011).
111. Vaudano AE, Laufs H, Kiebel SJ, Carmichael DW, Hamandi K, Guye M, et al. Causal hierarchy within the thalamo-cortical network in spike and wave discharges. *PLoS ONE.* (2009) 4:e6475. doi: 10.1371/journal.pone.0006475
112. David O, Guillemain I, Saillet S, Reyt S, Deransart C, Segebarth C, et al. Identifying neural drivers with functional MRI: an electrophysiological validation. *PLoS Biol.* (2008) 6:e315. doi: 10.1371/journal.pbio.0060315
113. Cadotte AJ, DeMarse TB, Mareci TH, Parekh MB, Talathi SS, Hwang DU, et al. Granger causality relationships between local field potentials in an

animal model of temporal lobe epilepsy. *J Neurosci Methods.* (2010) 189:121–9. doi: 10.1016/j.jneumeth.2010.03.007

114. Cadotte AJ, Mareci TH, DeMarse TB, Parekh MB, Rajagovindan R, Ditto WL, et al. Temporal lobe epilepsy: anatomical and effective connectivity. *IEEE Trans Neural Syst Rehabil Eng.* (2009) 17:214–23. doi: 10.1109/TNSRE.2008.2006220
115. Murta T, Leal A, Garrido MI, Figueiredo P. Dynamic causal modelling of epileptic seizure propagation pathways: a combined EEG-fMRI study. *Neuroimage.* (2012) 62:1634–42. doi: 10.1016/j.neuroimage.2012.05.053
116. Vaudano AE, Carmichael DW, Salek-Haddadi A, Rampp S, Stefan H, Lemieux L, et al. Networks involved in seizure initiation a reading epilepsy case studied with EEG-fMRI and MEG. *Neurology.* (2012) 79:249–53. doi: 10.1212/WNL.0b013e31825fdf3a
117. Vaudano AE, Avanzini P, Tassi L, Ruggieri A, Cantalupo G, Benuzzi F, et al. Causality within the epileptic network: an EEG-fMRI study validated by intracranial EEG. *Front Neurol.* (2013) 4:1–12. doi: 10.3389/fneur.2013.00185
118. An D, Fahoum F, Hall J, Olivier A, Gotman J, Dubeau F. Electroencephalography/functional magnetic resonance imaging responses help predict surgical outcome in focal epilepsy. *Epilepsia.* (2013) 54:2184–94. doi: 10.1111/epi.12434
119. Tracy JI, Doucet GE. Resting-state functional connectivity in epilepsy: growing relevance for clinical decision making. *Curr Opin Neurol.* (2015) 28:158–65. doi: 10.1097/WCO.0000000000000178
120. Preti MG, Leonardi N, Karahanoılu FI, Grouiller F, Genetti M, Seeck M, et al. Epileptic network activity revealed by dynamic functional connectivity in simultaneous EEG-fMRI. In: *2014 IEEE 11th International Symposium on Biomedical Imaging, ISBI 2014.* (2014). p. 9–12.
121. Omidvarnia A, Pedersen M, Vaughan DN, Walz JM, Abbott DF, Zalesky A, et al. Dynamic coupling between fMRI local connectivity and interictal EEG in focal epilepsy: a wavelet analysis approach. *Hum Brain Mapp.* (2017) 38:5356–74. doi: 10.1002/hbm.23723
122. Dong L, Luo C, Zhu Y, Hou C, Jiang S, Wang P, et al. Complex discharge-affecting networks in juvenile myoclonic epilepsy: a simultaneous EEG-fMRI study. *Hum Brain Mapp.* (2016) 37:3515–29. doi: 10.1002/hbm.23256
123. Dong L, Zhang Y, Zhang R, Zhang X, Gong D, Valdes-Sosa PA, et al. Characterizing nonlinear relationships in functional imaging data using eigenspace maximal information canonical correlation analysis (emiCCA). *Neuroimage.* (2015) 109:388–401. doi: 10.1016/j.neuroimage.2015.01.006
124. Luo C, Qiu C, Guo Z, Fang J, Li Q, Lei X, et al. Disrupted functional brain connectivity in partial epilepsy: a resting-state fMRI study. *PLoS ONE.* (2012) 7:e28196. doi: 10.1371/journal.pone.0028196
125. Centeno M, Carmichael DW. Network connectivity in epilepsy: resting state fMRI and EEG-fMRI contributions. *Front Neurol.* (2014) 5:93. doi: 10.3389/fneur.2014.00093
126. Salsabilian S, Zhu L, Lee CR, Margolis DJ and Najafizadeh L. Identifying Task-Related Brain Functional States Via Cortical Networks. In: *2020 IEEE International Symposium on Circuits and Systems (ISCAS).* (2020). p. 1–4. doi: 10.1109/ISCAS45731.2020.9180913
127. Li Q, Cao W, Liao X, Chen Z, Yang T, Gong Q, et al. Altered resting state functional network connectivity in children absence epilepsy. *J Neurol Sci.* (2015) 354:79–85. doi: 10.1016/j.jns.2015.04.054
128. Siniatchkin M, Moehring J, Kroeher B, Galka A, von Ondarza G, Moeller F, et al. Multifocal epilepsy in children is associated with increased long-distance functional connectivity: an explorative EEG-fMRI study. *Eur J Paediatr Neurol.* (2018) 22:1054–65. doi: 10.1016/j.ejpn.2018.07.001
129. Tong X, An D, Xiao F, Lei D, Niu R, Li W, et al. Real-time effects of interictal spikes on hippocampus and amygdala functional connectivity in unilateral temporal lobe epilepsy: an EEG-fMRI study. *Epilepsia.* (2019) 60:246–54. doi: 10.1111/epi.14646
130. Su J, Khoo HM, von Ellenrieder N, Zeng LL, Hu D, Dubeau F, et al. fMRI functional connectivity as an indicator of interictal epileptic discharges. *NeuroImage Clin.* (2019) 24:102038. doi: 10.1016/j.nicl.2019.102038
131. Iannotti GR, Preti MG, Grouiller F, Carboni M, De Stefano P, Pittau F, et al. Modulation of epileptic networks by transient interictal epileptic activity: a dynamic approach to simultaneous EEG-fMRI. *NeuroImage Clin.* (2020) 28:102467. doi: 10.1016/j.nicl.2020.102467
132. Kaiboriboon K, Lüders HO, Hamaneh M, Turnbull J, Lhatoo SD. EEG source imaging in epilepsyg€"practicalities and pitfalls. *Nat Rev Neurol.* (2012) 8:498–507. doi: 10.1038/nrneurol.2012.150
133. Vulliemoz S, Thornton R, Rodionov R, Carmichael DW, Guye M, Lhatoo S, et al. The spatio-temporal mapping of epileptic networks: combination of EEG-fMRI and EEG source imaging. *Neuroimage.* (2009) 46:834–43. doi: 10.1016/j.neuroimage.2009.01.070
134. Vulliemoz S, Rodionov R, Carmichael DW, Thornton R, Guye M, Lhatoo SD, et al. Continuous EEG source imaging enhances analysis of EEG-fMRI in focal epilepsy. *Neuroimage.* (2010) 49:3219–29. doi: 10.1016/j.neuroimage.2009.11.055
135. Brodbeck V, Spinelli L, Lascano AM, Pollo C, Schaller K, Vargas MI, et al. Electrical source imaging for presurgical focus localization in epilepsy patients with normal MRI. *Epilepsia.* (2010) 51:583–91. doi: 10.1111/j.1528-1167.2010.02521.x
136. Elshoff L, Groening K, Grouiller F, Wiegand G, Wolff S, Michel C, et al. The value of EEG-fMRI and EEG source analysis in the presurgical setup of children with refractory focal epilepsy. *Epilepsia.* (2012) 53:1597–606. doi: 10.1111/j.1528-1167.2012.03587.x
137. Centeno M, Tierney TM, Perani S, Shamshiri EA, StPier K, Wilkinson C, et al. Combined EEG-fMRI and ESI improves localisation of paediatric focal epilepsy. *Ann Neurol.* (2017) 82:278–87. doi: 10.1002/ana.25003
138. Kowalczyk MA, Omidvarnia A, Dhollander T, Jackson GD. Dynamic analysis of fMRI activation during epileptic spikes can help identify the seizure origin. *Epilepsia.* (2020) 61:2558–71. doi: 10.1111/epi.16695
139. Grouiller F, Thornton RC, Groening K, Spinelli L, Duncan JS, Schaller K, et al. With or without spikes: localization of focal epileptic activity by simultaneous electroencephalography and functional magnetic resonance imaging. *Brain.* (2011) 134:2867–86. doi: 10.1093/brain/awr156
140. Ebrahimzadeh E, Shams M, Rahimpour Jopungha A, Fayaz F, Mirbagheri M, Hakimi N, et al. Epilepsy presurgical evaluation of patients with complex source localization by a novel component-based EEG-fMRI approach. *Iran J Radiol.* (2019) 16:18–9. doi: 10.5812/iranjradiol.99134
141. Bast T, Oezkan O, Rona S, Stippich C, Seitz A, Rupp A, et al. EEG and MEG source analysis of single and averaged interictal spikes reveals intrinsic epileptogenicity in focal cortical dysplasia. *Epilepsia.* (2004) 45:621–31. doi: 10.1111/j.0013-9580.2004.56503.x
142. Ebrahimzadeh E, Soltanian-Zadeh H, Araabi BN, Fesharaki SSH, Habibabadi JM. Localizing epileptic focus through simultaneous EEG-fMRI recording and automated detection of IED from inside-scanner EEG. *Iran J Biomed Eng.* (2019) 13:135–45. doi: 10.22041/IJBME.2019.103479.1447
143. Ebrahimzadeh E, Soltanian-Zadeh H, Araabi BN, Fesharaki SSH, Habibabadi JM. Localizing epileptic focus through simultaneous EEG-fMRI recording and automated detection of interictal epileptiform discharges (IED) from EEG in inside MRI. In: *25th National and 3th International Iranian Conference on Biomedical Engineering (ICBME 2018).* (2018). p. 1–6.
144. Raeisi Kh, Mohebbi M, Khazaei M, Seraji M, Yoonessi A. Phase-synchrony evaluation of EEG signals for Multiple Sclerosis diagnosis based on bivariate empirical mode decomposition during a visual task. *Comput Biol Med.* (2020) 117:103596. doi: 10.1016/j.compbiomed.2019.103596
145. Ebrahimzadeh E, Nikravan M, Nikravan M, Manuchehri MS, Amoozegar S, Rahimi Dolatabad MJ, et al. Simultaneous EEG-fMRI: A Multimodality Approach to Localize the Seizure Onset Zone in Patients with Epilepsy. *Int J Biol Med.* (2019) 1:130–9. doi: 10.36811/ijbm.2019.110017
146. Ebrahimzadeh E, Soltanian-Zadeh H, Nadjar Araabi B. Localization of epileptic focus using simultaneously acquired EEG-FMRI data. *Comput Intell Electr Eng.* (2018) 9:15–28.
147. Coan AC, Chaudhary UJ, Grouiller F, Campos BM, Perani S, De Ciantis A, et al. EEG-fMRI in the presurgical evaluation of temporal lobe epilepsy. *J Neurol Neurosurg Psychiatry.* (2016) 87:642–9. doi: 10.1136/jnnp-2015-310401
148. Laufs H, Hamandi K, Walker MC, Scott C, Smith S, Duncan JS, et al. EEG-fMRI mapping of asymmetrical delta activity in a patient with refractory epilepsy is concordant with the epileptogenic region determined by intracranial EEG. *Magn Reson Imaging.* (2006) 24:367–71. doi: 10.1016/j.mri.2005.12.026
149. Manganotti P, Formaggio E, Gasparini A, Cerini R, Bongiovanni LG, Storti SF, et al. Continuous EEG-fMRI in patients with partial epilepsy and

focal interictal slow-wave discharges on EEG. *Magn Reson Imaging.* (2008) 26:1089–100. doi: 10.1016/j.mri.2008.02.023

150. Moehring J, Coropceanu D, Galka A, Moeller F, Wolff S, Boor R, et al. Improving sensitivity of EEG-fMRI studies in epilepsy: the role of sleep-specific activity. *Neurosci Lett.* (2011) 505:211–5. doi: 10.1016/j.neulet.2011.10.028
151. Abreu R, Leal A, Lopes da Silva F, Figueiredo P. EEG synchronization measures predict epilepsy-related BOLD-fMRI fluctuations better than commonly used univariate metrics. *Clin Neurophysiol.* (2018) 129:618–35. doi: 10.1016/j.clinph.2017.12.038
152. Fuhrmann Alpert G, Sun FT, Handwerker D, D'Esposito M, Knight RT. Spatio-temporal information analysis of event-related BOLD responses. *Neuroimage.* (2007) 34:1545–61. doi: 10.1016/j.neuroimage.2006.10.020
153. Caballero Gaudes C, Vulliemoz S, Grouiller F, Seeck M, Van De Ville D, Lazeyras F. Spatio-temporal mapping of interictal epileptic discharges based on mutual information of concurrent {EEG} and {FMRI}. In: *Proceedings of the ISMRM 19th Annual Meeting and Exhibition*. (2011). p. 4139.
154. Caballero-Gaudes C, Van de Ville D, Grouiller F, Thornton R, Lemieux L, Seeck M, et al. Mapping interictal epileptic discharges using mutual information between concurrent EEG and fMRI. *Neuroimage.* (2013) 68:248–62. doi: 10.1016/j.neuroimage.2012.12.011
155. Salek-Haddadi A, Mayer T, Hamandi K, Symms M, Josephs O, Fluegel D, et al. Imaging seizure activity: a combined EEG/EMG-fMRI study in reading epilepsy. *Epilepsia.* (2009) 50:256–64. doi: 10.1111/j.1528-1167.2008.01737.x
156. Maziero D, Velasco TR, Salmon CEG. EEG-fMRI in focal epilepsy patients : comparison of classical analysis and 2d- temporal clustering analysis. In: *Conference: 20th Annual Meeting of the Organization for Human Brain Mapping (OHBM)*. (2014). p. 2–6.
157. Maziero D, Velasco TR, Salmon CEG, Morgan VL. Two-dimensional temporal clustering analysis for patients with epilepsy: detecting epilepsy-related information in EEG-fMRI concordant, discordant and spike-less patients. *Brain Topogr.* (2018) 31:322–36. doi: 10.1007/s10548-017-0598-3
158. Mangalore S, Bharath RD, Upadhyay N, Chaitanya G, Panda R, Gupta A, et al. The relevance of interictal bold changes to lateralize seizure focus using simultaneous EEG-fMRI. *J Epilepsy Res.* (2015) 5:60–9. doi: 10.14581/jer.15011
159. Qin Y, Jiang S, Zhang Q, Dong L, Jia X, He H, et al. BOLD-fMRI activity informed by network variation of scalp EEG in juvenile myoclonic epilepsy. *NeuroImage Clin.* (2019) 22:101759. doi: 10.1016/j.nicl.2019.101759
160. Wan T, Wu M, Lai X, Wan X, She J, Du Y. A four-stage localization method for epileptic seizure onset zones. *IFAC PapersOnLine.* (2017) 50:4412–7. doi: 10.1016/j.ifacol.2017.08.915
161. Marrosu F, Barberini L, Puligheddu M, Bortolato M, Mascia M, Tuveri A, et al. Combined EEG/fMRI recording in musicogenic epilepsy. *Epilepsy Res.* (2009) 84:77–81. doi: 10.1016/j.eplepsyres.2008.11.019
162. van Houdt PJ, de Munck JC, Leijten FSS, Huiskamp GJM, Colon AJ, Boon PAJM, et al. EEG-fMRI correlation patterns in the presurgical evaluation of focal epilepsy: a comparison with electrocorticographic data and surgical outcome measures. *Neuroimage.* (2013) 75:238–48. doi: 10.1016/j.neuroimage.2013.02.033
163. Yamazoe T, von Ellenrieder N, Khoo HM, Huang YH, Zazubovits N, Dubeau F, et al. Widespread interictal epileptic discharge more likely than focal discharges to unveil the seizure onset zone in EEG-fMRI. *Clin Neurophysiol.* (2019) 130:429–38. doi: 10.1016/j.clinph.2018.12.014
164. Chowdhury RA, Pellegrino G, Aydin Ü, Lina JM, Dubeau F, Kobayashi E, et al. Reproducibility of EEG-MEG fusion source analysis of interictal spikes: relevance in presurgical evaluation of epilepsy. *Hum Brain Mapp.* (2018) 39:880–901. doi: 10.1002/hbm.23889
165. Detre JA, Crino PB. A multilayered approach to studying cortical malformations EEG-fMRI. *Neurology.* (2005) 64:1108–10. doi: 10.1212/01.WNL.0000161078.53641.12
166. Friston KJ, Josephs O, Rees G, Turner R. Nonlinear event-related responses in fMRI. *Magn Reson Med.* (1998) 39:41–52. doi: 10.1002/mrm.1910390109
167. Gao JH, Yee SH. Iterative temporal clustering analysis for the detection of multiple response peaks in fMRI. *Magn Reson Imaging.* (2003) 21:51–3. doi: 10.1016/S0730-725X(02)00627-6
168. Morgan VL, Price RR, Arain A, Modur P, Abou-Khalil B. Resting functional MRI with temporal clustering analysis for localization of epileptic activity without EEG. *Neuroimage.* (2004) 21:473–81. doi: 10.1016/j.neuroimage.2003.08.031
169. Lu Y, Bagshaw AP, Grova C, Kobayashi E, Dubeau F, Gotman J. Using voxel-specific hemodynamic response function in EEG-fMRI data analysis. *Neuroimage.* (2006) 32:238–47. doi: 10.1016/j.neuroimage.2005.11.040
170. Lu Y, Grova C, Kobayashi E, Dubeau F, Gotman J. Using voxel-specific hemodynamic response function in EEG-fMRI data analysis: an estimation and detection model. *Neuroimage.* (2007) 34:195–203. doi: 10.1016/j.neuroimage.2006.08.023
171. Tyvaert L, Hawco C, Kobayashi E, LeVan P, Dubeau F, Gotman J. Different structures involved during ictal and interictal epileptic activity in malformations of cortical development: an EEG-fMRI study. *Brain.* (2008) 131:2042–60. doi: 10.1093/brain/awn145
172. Tenney JR, Duong TQ, King JA, Ludwig R, Ferris CF. Corticothalamic modulation during absence seizures in rats: a functional MRI assessment. *Epilepsia.* (2003) 44:1133–40. doi: 10.1046/j.1528-1157.2003.61002.x
173. Tenney JR, Marshall PC, King JA, Ferris CF. FMRI of generalized absence status epilepticus in conscious marmoset monkeys reveals corticothalamic activation. *Epilepsia.* (2004) 45:1240–7. doi: 10.1111/j.0013-9580.2004.21504.x
174. Karl JF. Functional and effective connectivity in neuroimaging: a synthesis. *Hum Brain Mapp.* (1994) 2:56–78. doi: 10.1002/hbm.460020107
175. Markoula S, Chaudhary UJ, Perani S, De Ciantis A, Yadee T, Duncan JS, et al. The impact of mapping interictal discharges using EEG-fMRI on the epilepsy presurgical clinical decision making process: a prospective study. *Seizure.* (2018) 61:30–7. doi: 10.1016/j.seizure.2018.07.016

Conflict of Interest: The authors declare that the research was conducted in the absence of any commercial or financial relationships that could be construed as a potential conflict of interest.

frontiers in Neurology

ORIGINAL RESEARCH
published: 28 May 2021
doi: 10.3389/fneur.2021.668856

Different Functional Network Connectivity Patterns in Epilepsy: A Rest-State fMRI Study on Mesial Temporal Lobe Epilepsy and Benign Epilepsy With Centrotemporal Spike

Cong Fu[1], *Aikedan Aisikaer*[2], *Zhijuan Chen*[1], *Qing Yu*[3], *Jianzhong Yin*[2]* *and Weidong Yang*[1]*

[1] Department of Neurosurgery, Tianjin Medical University General Hospital, Tianjin, China, [2] Department of Radiology, Tianjin First Central Hospital, Tianjin, China, [3] Department of Neurology, Tianjin Medical University General Hospital, Tianjin, China

Edited by:
Brunno Machado De Campos,
State University of Campinas, Brazil

Reviewed by:
Azeez Adebimpe,
University of Pennsylvania,
United States
Sandrine de Ribaupierre,
Western University, Canada

***Correspondence:**
Weidong Yang
yangweidongshine@sina.com
Jianzhong Yin
jianzhongyin@gmail.com

Specialty section:
This article was submitted to
Epilepsy,
a section of the journal
Frontiers in Neurology

Received: *17 February 2021*
Accepted: *06 May 2021*
Published: *28 May 2021*

Citation:
Fu C, Aisikaer A, Chen Z, Yu Q, Yin J and Yang W (2021) Different Functional Network Connectivity Patterns in Epilepsy: A Rest-State fMRI Study on Mesial Temporal Lobe Epilepsy and Benign Epilepsy With Centrotemporal Spike.
Front. Neurol. 12:668856.
doi: 10.3389/fneur.2021.668856

The stark discrepancy in the prognosis of epilepsy is closely related to brain damage features and underlying mechanisms, which have not yet been unraveled. In this study, differences in the epileptic brain functional connectivity states were explored through a network-based connectivity analysis between intractable mesial temporal lobe epilepsy (MTLE) patients and benign epilepsy with centrotemporal spikes (BECT). Resting state fMRI imaging data were collected for 14 MTLE patients, 12 BECT patients and 16 healthy controls (HCs). Independent component analysis (ICA) was performed to identify the cortical functional networks. Subcortical nuclei of interest were extracted from the Harvard-Oxford probability atlas. Network-based statistics were used to detect functional connectivity (FC) alterations across intranetworks and internetworks, including the connectivity between cortical networks and subcortical nuclei. Compared with HCs, MTLE patients showed significant lower activity between the connectivity of cortical networks and subcortical nuclei (especially hippocampus) and lower internetwork FC involving the lateral temporal lobe; BECT patients showed normal cortical-subcortical FC with hyperconnectivity between cortical networks. Together, cortical-subcortical hypoconnectivity in MTLE suggested a low efficiency and collaborative network pattern, and this might be relevant to the final decompensatory state and the intractable prognosis. Conversely, cortical-subcortical region with normal connectivity remained well in global cooperativity, and compensatory internetwork hyperconnectivity caused by widespread cortical abnormal discharge, which might account for the self-limited clinical outcome in BECT. Based on the fMRI functional network study, different brain network patterns might provide a better explanation of mechanisms in different types of epilepsy.

Keywords: resting state networks, mesial temporal lobe epilepsy, benign epilepsy with centrotemporal spikes, BOLD fMRI, functional network connectivity

INTRODUCTION

Epilepsy derives from the long-term spontaneous abnormal discharge of neurons in the brain, resulting in hypersynchronization of the cortical-cortical and subcortical-cortical regions, thus leading to brain dysfunction and behavioral abnormalities. About 25% epilepsy patients with a dissatisfied clinical control of seizure even with the optimal anti-epileptic drugs (AEDs) (1). The most common drug-resistant epilepsy in adults is mesial temporal lobe epilepsy (MTLE) (2), accounting for 80% of temporal lobe onset seizures (3). Inversely, some of the epilepsy patients have a good response to AEDs and even achieve a seizure-free result, such as benign epilepsy with centrotemporal spikes (BECT). BECT is the most common form of childhood focal epilepsy and is usually idiopathic without structural brain abnormalities (4).

The drug-resistance epilepsy might relate to brain decompensatory processes (5) and self-limited epilepsy might contribute to compensatory cortical reorganization (6, 7). Therefore, patients with MTLE and BECT might mark different prognosis by different brain compensatory patterns. The two patterns manifest brain networks abnormalities usually caused by epileptic discharges in widespread brain areas in MTLE and BECT. Thus, resting state functional connectivity (RSFC) could be used to detect the network -level epileptic effect.

Routine EEG examination and different imaging methods drive the conclusion that epilepsy is a network disease that is not only confined to the epileptogenic zones but also involved in widespread cortical and subcortical disturbances (8, 9). Ictal EEG performance suggests that MTLE primarily involves the temporal lobes, and the abnormal network is known to have widespread extratemporal connectivity, such as the lateral temporal, insular, and frontal regions (2, 10, 11). Imaging observations have suggested the presence of one or more common subcortical sources of widespread network dysfunction in MTLE. Hippocampal sclerosis is very significant and the most common pathological feature of MTLE. Moreover, the thalamus directly connected to the hippocampus has been shown to suffer atrophy (12, 13). In addition, chronic network changes associated with MTLE have been identified by impaired RSFC within the hippocampus and enhanced RSFC within the medial temporal lobe with extensions to the lateral temporal lobes (10, 14).

In the same vein, patients with BECT were found to have bilateral frontal and parieto-occipital regions that showed spectral changes in a resting-state EEG study (15). A growing body of literature examining cognitive and behavioral outcomes by imaging methods suggests that BECTS children perform less well-than their peers (16), including worse attention and visuomotor performance (17, 18) and reversible speech and cognitive dysfunction (19, 20).

MTLE and BECT both suffer from neural abnormal discharges while their prognosis is obviously different. Moreover, alterations in the brain functional networks related to epileptic prognosis remain to be fully clarified, especially in the state of epileptic compensation. Thus, the fMRI approach was used to find the changes in functional networks and probably pathological mechanisms. We speculated that the network-based approach would be promising for revealing the complex network patterns to explain the mechanisms underlying the different prognosis in epilepsy.

MATERIALS AND METHODS

Participants

Fourteen MTLE patients and twelve BECT patients were recruited from the Epilepsy Clinic of Neurology and Neurosurgery Departments in Tianjin Medical University General Hospital. The diagnoses of MTLE and BECT were established by history, clinical symptoms, magnetic resonance imaging (MRI), and video electroencephalogram (VEEG) by 2 senior epileptologists (Q.Y. and Z.C.). The inclusion criteria for patients with MTLE and BECT were as follows: (1) typical clinical manifestations and specific EEG characteristics according to International League Against Epilepsy (ILAE) (21); (2) the presence of routine clinical scans, including high-resolution 3D T1-weighted and FLAIR MRI and high in-plane resolution 2D coronal T2-weighted MRI according to the Harmonized Neuroimaging Of Epilepsy Structural Sequences (HARNESS) (22); (3) no evidence of other structural brain abnormalities due to hypoplasia of brain parenchyma, brain trauma, tumor, etc; and (4) MTLE patients should be diagnosed as the drugs resistance epilepsy (23) and the patients with BECT should respond well to AEDs. Patients in both groups received oxcarbazepine/carbamazepine for seizures treatment.

For the lesion lateralization, there were 2 on right MTL and 3 on left MTL, and the rest of our drug-resistant MTLE patients were failed to detect the epileptogenic focus. And all of the BECT patients were bilateral abnormal discharges in EEG and we could not find the stationary focus on one side. Patient demographics and a clinical summary are shown in **Table 1**. A healthy control group ($n = 16$) was matched by demographic characteristics from the local community. None of the HCs had a history of neurological or mental illness. The study was approved by the ethics committee of Tianjin Medical University General Hospital and completed according to the standards established in the Helsinki Declaration. Each subject gave written informed consent in accordance with the Hospital Research Ethics Committee.

MRI Acquisition

All MRI scanning data were obtained on a 3-Tesla MRI scanner (Siemens Trio Tim). High-resolution T1-weighted data images were acquired using a magnetization-prepared rapid gradient echo (MPRAGE) sequence (repetition time (TR) = 1,900 ms, echo time (TE) = 2.52 ms, field of view (FOV) = 256 mm × 256 mm, matrix 256 × 256, slice thickness 1 mm, 176 volumes). Resting-state functional blood oxygen level-dependent (12) data images were acquired using an echo planar imaging sequence (TR = 2,000 ms, TE = 30 ms, flip angle 90°, FOV = 220 mm × 220 mm, matrix 80 × 80, slice thickness 5 mm, 300 volumes). The patients were asked to not move and to stay with eyes closed and resting. Headphones and cushions were used to reduce noise interference and prevent excessive head movement.

Network-Based Functional MRI (fMRI) Analysis

Resting-State fMRI Preprocessing

Preprocessing of the data was performed according to the Graph-theoretical Network Analysis Toolkit (GRETNA) (http://www.nitrc.org/projects/gretna/) fMRI preprocessing pipeline. The first 10 volumes were removed, and then slice-timing correction and head motion correction were performed. The data from patients with head motion exceeding 2 mm or head rotations <2° were excluded from further calculations, while head motion in controls was limited 1 mm or 1°,The motion-corrected functional images were normalized to the standard Montreal Neurological Institute (MNI) space by applying an EPI template at a 3 × 3 × 3 mm^3 resolution, which led to our data showing a better match with the EPI template (24). Subsequently, to avoid mixing white matter and gray matter signals, the normalized images were spatially smoothed using a 4-mm full-width half-maximum Gaussian kernel. The acquired smoothed data were utilized in independent component analysis (ICA).

The following denoising steps were performed with the unsmoothed images (25): (1) removing the linear trends of time courses; (2) bandpass filtration (0.01–0.08 Hz) to minimize the influence of low-frequency drifts and high-frequency physiological noise; (3) linear regressing out the confounding signals that were unlikely to reflect neural activity, including the head motion effect (26) (Friston 24 parameter), white matter and cerebrospinal fluid signals; and (4) an indispensable "scrubbing" procedure (27). Concretely, in terms of the criteria of framewise displacement (FD) above 0.5 mm, functional imaging data presenting sudden head motion were discarded, together with one volume before and two volumes after the bad volume (28). No patient had fewer than 200 volumes. BOLD signal

TABLE 1 | Demographic and clinical characteristic of all participants.

Characteristics	**Groups**			***p***
	HCs *n* = 16	**MTLE *n* = 14**	**BECT *n* = 12**	
Male: Female (*n*)	6:10	5:9	5:7	0.95
Age (years)				
Mean ± SD	27.1 ± 4.8	35.36 ± 17.2	10.42 ± 4.5	<0.001
Epilepsy Duration (years)				
Mean ± SD		17.28 ± 8.16	4.62 ± 4.1	<0.001
Seizure type (*n*)				
SPS: CPS: SGTCS		1:12:1	2:5:5	0.06
Interictal EEG (*n*)				
BCT: +CFT: +CPT		–	7:3:2	
Sph1: Sph2		7:7	–	

HCs, healthy controls; MTLE, mesial temporal lobe epilepsy; BECT, benign epilepsy with centrotemporal spikes; SPS, simple partial seizure; CPS, complex partial seizure; SGTCS, secondary generalized tonic-clonic seizure; BCT, bilateral centro-temporal; +CPT, BCT and centro-parieto-temporal; +CFT, BCT and centro-fronto-temporal; Sph1, left sphenoid electrode; Sph2, right sphenoid electrode.

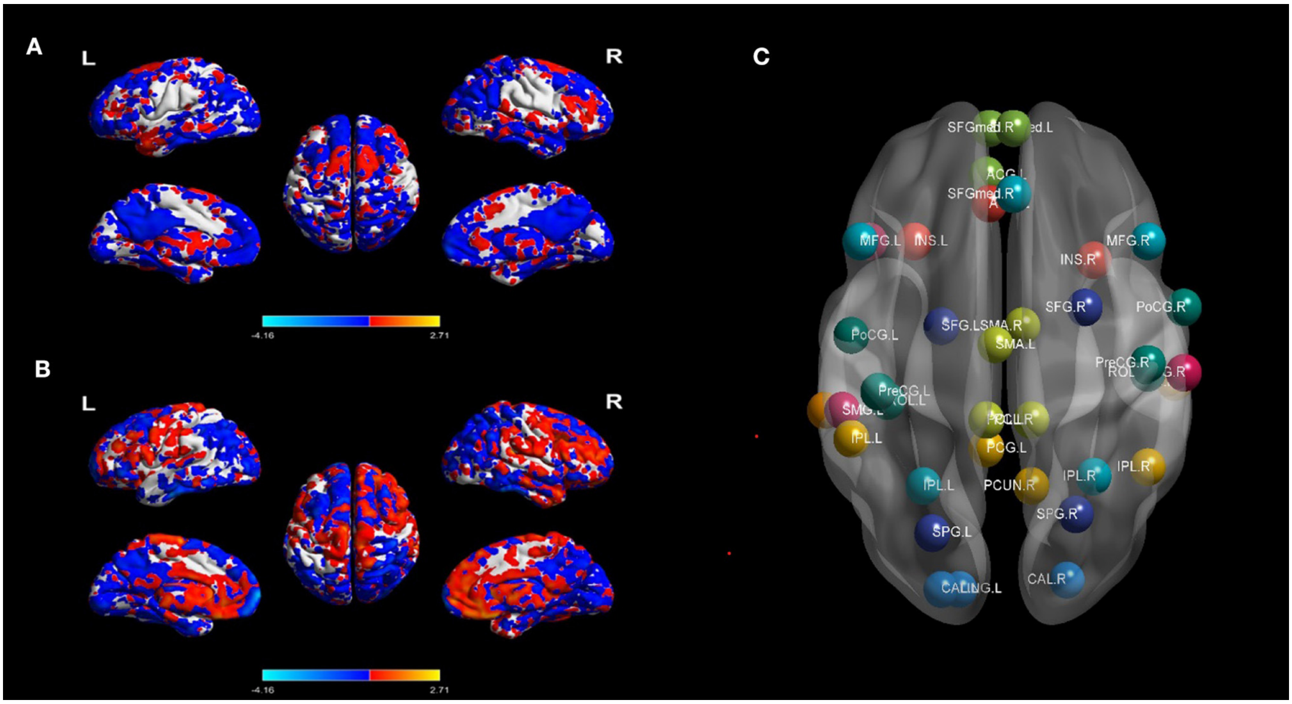

FIGURE 1 | BOLD signal contrasts and seed regions from the 10 RSNs. BOLD signal of HC and MTLE was compared in **(A)**, and BECT-HC contrast in **(B)** ($p < 0.05$, cluster sizes: 50 voxels). Spatial maps of the 10 independent components computed across the entire samples. The color scale represents t values in each spatial component of RSN (maps thresholded at $p < 0.01$, FDR corrected). For networks construction, nodes of interest in the RSNs were extracted according to the peak coordinates of thresholding maps. Different RSNs were depicted as different colors in **(C)**.

differences of MTLE-HC and BECT-HC pair-wise contrasts were depicted by REST 18 toolbox (29) to under two simple *t*-test ($p < 0.05$) with cluster sizes as 50 voxels, shown in **Figure 1**.

Cortical Network Identification

Regions that exhibit correlated BOLD fluctuations, i.e., functional connectivity (FC), are regarded as the same functional network (30). According to this theory, we used the group ICA (GICA) method to extract the spatial components of 10 defined resting state networks (RSNs). The Group ICA Of fMRI Toolbox was used for all participants for the group spatial ICA. The data were decomposed into 61 components that were estimated by GIFT, including data reduction by PCA, ICA separation, and back-reconstruction. Two-step PCA was used for data reduction. The maximum likelihood algorithm was used for group-level spatial ICA. A regular algorithm was used for stability analysis, and GICA was used for back-reconstruction. Each subject obtained a spatial component and the corresponding time-series component, and correlation coefficients were converted to a normal distribution by Fishers r-to-z transformation. For each component selection, we obeyed the selection criterion. In particular, ICA selection was independently completed by 2 senior neuroimaging physicians (J.Y. and A.A.) and referred to corresponding templates (31). The spatial maps of each RSN were gathered across all the subjects by the intranetwork connectivity maximum for each cluster of voxels ($p < 0.01$, FDR corrected). The 10 statistic maps were T-value connectivity maps. We selected the total 38 ROIs in 10 RSNs based on where was the highest T-value in the bilateral sides. The methodology was according to King BR et al. (32). For each local maximum, 38 regions of interest (ROIs) with a 6-mm radius sphere centered on the peak voxel were built with the xjView toolbox (http://www.alivelearn.net/xjview, version 9.6) and REST in MATLAB (**Supplementary Figure 1**).

Subcortical Nucleus Identification

We defined three core subcortical ROIs, the bilateral hippocampi, thalamus and putamen, based on the Harvard-Oxford subcortical atlas in MNI space (33, 34). The subcortial ROIs selection criteria: hippocampus is crucial for MTLE pathological mechanism (35) and putamen and thalamus are all key nuclei for patients with epilepsy. For local motor seizures, epileptogenic networks include thalamocortical circus (36). And putamen is a core nucleus for basal ganglia neuromodulation for motor seizures treatment (37). Therefore, we chose the 3 ROIs in subcortical. Because we did not focus on effects from particular sides of the ROIs, we regarded bilateral ROIs as one seed. In the current study, the hippocampus, putamen and thalamus are abbreviated Hip, Put and Tha, respectively. The selected subcortical ROIs are shown in **Supplementary Figure 2**. Finally, we obtained 41 spatial mappings of RSNs and 41 average time series of ROIs. The brain networks were visualized with BrainNet Viewer (http://www.nitrc.org/projects/bnv, version 1.6).

Intranetwork and Internetwork Analyses

The corresponding time series of the ROI seeds were extracted with REST software, and RSFC in the BECT group, TLE group and HC group was calculated. We obtained three 41 × 41 RSFC matrices and performed Fishers z transformation. For completeness, plots depicting seed-level connectivity (i.e., 41 × 41 matrices) are provided in **Supplementary Figure 3**. The significance level was set at $p < 0.05$ and corrected for multiple comparisons using network-based statistic (NBS) method (38) (NBS, edge significance: $p < 0.001$, component significance: $p < 0.05$, iterations: 1,000). RSN matrices were acquired by averaging the NBS-corrected FC value ($p < 0.05$) in each group to generate 13 × 13 RSN matrices (32). Cortical internetworks and cortical-subcortical interactions are shown in the off-diagonal line of the 13 × 13 RSN matrices. Intranetwork analysis results were revealed in the diagonal line and indicated the interaction between the inner seeds of each cortical network.

Statistical Analysis

Demographic information, including age and sex, was compared among the BECT, MTLE and HC groups. Seizure type and duration of epilepsy were compared between BECT and MTLE patients. One-way analysis of variance (ANOVA) was used to test discrepancies in age among the three groups. Chi-square tests were used to compare categorical data, such as sex among the three groups and seizure type distribution between the BECT and TLE groups.

Two-sample *t*-test was used to test the differences of duration between two patient groups. All the above analyses were performed in SPSS 25.0, and $p < 0.05$ was statistically significant.

Ten spatial components of thirty-eight seeds were chosen based on a one-sided one-sample *t*-test ($p < 0.01$, FDR corrected). Correlation maps for each seed in each RSN were computed by correlating regional time series (averaged over all voxels within the seed region) with every voxel in the brain. The 41 time courses, including 3 pairs of subcortical nuclei, were extracted to generate RSFC maps of the 41 × 41 matrix in the three groups. Correlation maps were converted to z maps using Fisher's r-to-z transformation (**Supplementary Figure 4**). Then, comparisons within each group were performed using one-sided one-sample *t*-tests ($p < 0.05$, NBS corrected) in GRETNA. For detecting intergroups differences, two sample *t*-test was used between MTLE/BECT and HC. And the age differences were taken into account in pairwise comparisons, and the level of significance for group differences was set at $p < 0.05$ (edge $p < 0.001$, NBS corrected).

RESULTS

Demographic and Clinical Data

No differences were found among the 3 groups in terms of gender ($p = 0.951$) and seizure type ($p = 0.056$) between the BECT and MTLE groups. For the analysis of duration, BECT shows significant different with MTLE group ($p < 0.001$). One-way ANOVA revealed a significant difference in age among the three groups ($p < 0.001$). A *post hoc* test was performed to find that the BECT-HC contrast ($p < 0.001$) and BECT-MTLE contrast ($p < 0.001$) were significant. The demographic and clinical information of the study participants is presented in **Table 1**.

BOLD Signal Contrast and Resting State Networks

The differences of BOLD signal between BECT-HC and MTLE-HC were shown in **Figures 1A,B** ($p < 0.05$, cluster size: 50 voxels). A total of 61 components were identified by ICA. After selection by visual inspection and templates, 10 valuable components were identified. One-sample t-test showed a typical spatial pattern in each RSN and ROIs in each RSN are shown **Figure 1C** and **Table 2**. Spatial location of 38 ROIs were detailed in **Supplementary Figure 1**.

Functional Connectivity Analysis

Internetwork Connectivity

Our findings showed different aberrations in network-based interactions in the MTLE (**Figure 2A**) and BECT (**Figure 2B**) groups. Compared with the HC group, the MTLE group had lower connectivity between the subcortical hippocampus and task-positive RSNs (ECN and DAN) and sensory RSN (SMN). Notably, the auditory network showed widespread abnormal connectivity with other functional networks, excluding the SMN (**Figure 2C**), which has been associated with impaired interictal connectivity with the temporal neocortex.

The BECT group showed increased connectivity in the frontoparietal cortex, including the intrinsic RSNs, task-positive RSNs and sensory RSNs ($p < 0.05$, NBS corrected). The SMN showed an increased negative (farther from zero) connectivity with the attention networks (DAN and VAN) and VN (**Figure 2D**), indicating a relationship to visual attention deficit. Importantly, no particular differences in connectivity were revealed between the cortical networks and the subcortical ROIs, but a trend toward higher interconnectivity was observed ($p >$ 0.05, NBS corrected).

Intranetwork Connectivity

No differences were found between the MTLE and BECT patients and the HC participants through a two-sample t-test. Some critical trends in intranetwork connectivity were revealed in each group. In the MTLE group, intranetwork connectivity was not different from that in the HC group, with the exception of the AN in the lateral temporal lobe. The BECT group showed higher levels of connectivity within most RSNs, such as the SN, pDMN, ECN and DAN (**Figure 4**).

DISCUSSION

A comparative study of epilepsy compensatory and decompensatory prognosis was conducted in this research. We recruited the patients with BECT and MTLE, the most common types of benign and drug-resistant epilepsies. With the utility of a network-based approach, we demonstrated the different network pattern changes caused by compensation and decompensation, and we also uncovered meaningful networks in a wide range of brain areas with implications for cognitive function.

TABLE 2 | Resting state functional connectivity networks.

Brain network and label	Abbreviation	MNI Coordinates			t
		X	Y	Z	
Salience network	**SN**				
Left insula	INS.L	−30	21	−6	16.10
Right insula	INS.R	30	−15	−18	15.66
Anterior cingulum	ACG.L	−5	33	30	15.26
Post default modal network	**pDMN**				
Left inferior parietal	IPL.L	−51	−42	42	9.48
Right inferior parietal	IPL.R	48	−51	39	6.45
Post cingulum	PCG.L	−6	−45	30	20.79
Right precuneus	PCUN.R	9	−57	27	23.50
Anterior default modal network	**aDMN**				
Anterior cingulum	ACG.L	−6	42	−3	12.16
Left medial prefrontal cortex	SFGmed.L	−5	57	6	16.59
Right medial prefrontal cortex	SFGmed.R	3	57	18	18.32
Executive control network	**ECN**				
Left dorsal lateral prefrontal cortex	MFG.L	−48	21	33	16.12
Right dorsal lateral prefrontal cortex	MFG.R	48	21	33	19.03
Medial prefrontal cortex	SFGmed.R	3	36	39	10.63
Left post parietal cortex	IPL.L	−27	−57	39	9.42
Right post parietal cortex	IPL.R	30	−54	45	6.91
Dorsal attention network	**DAN**				
Left intraparietal sulcus	SPG.L	−24	−72	51	18.88
Right intraparietal sulcus	SPG.R	24	−66	51	17.73
Left frontal eye field	SFG.L	−21	−6	57	9.04
Right frontal eye field	SFG.R	27	0	57	9.05
Ventral attention network	**VAN**				
Left temporoparietal junction	SMG.L	−54	−33	27	11.72
Right temporoparietal junction	SMG.R	60	−21	24	15.53
Ventral frontal cortex	ORBsupmed.L	−45	21	−9	8.27
Auditory network	**AN**				
Left superior temporal	STG.L	−60	−33	9	14.81
Right superior temporal	STG.R	57	−24	−3	18.14
Medial somatomotor network	**mSMN**				
Left support motor area	SMA.L	−3	−12	63	13.39
Right support motor area	SMA.R	6	−6	48	15.56
Left paracentral lobule	PCL.L	−6	−36	54	16.04
Right paracentral lobule	PCL.R	9	−36	54	15.33
Lateral somatomotor network	**lSMN**				
Left precentral gyrus	PreCG.L	−42	−27	51	16.37
Right precentral gyrus	PreCG.R	48	−18	45	17.65
Left postcentral gyrus	ProCG.L	−51	−9	30	15.73
Right postcentral gyrus	ProCG.R	60	0	24	17.87
Left Rolandic operculum	ROL.L	−39	−30	15	21.32
Right Rolandic operculum	ROL.R	48	−21	15	13.32
Visual network	**VN**				
Left lingual	LING.L	−15	−90	−9	17.11
Right lingual	LING.R	21	−87	−3	16.46
Left calcarine	CAL.L	−21	−90	−6	15.67
Right calcarine	CAL.R	21	−87	6	14.82

MNI coordinates and peak connectivity t value for the 38 seed regions extracted from the 10 networks of interest and labels and abbreviations based on the AAL template in MNI space. Ten RSNs were belonged to the following three types of intrinsic functional connectivity pattern: (1) task-positive RSNs (ECN, DAN and VAN); (2) intrinsic RSNs (DMN, SAN); (3) sensory RSNs (SMN, AN and VN). The DMN was subdivided into the anterior DMN (aDMN) and the posterior DMN (pDMN) in our outcomes. And SMN was divided into the medial SMN (mSMN) and the lateral SMN (lSMN).

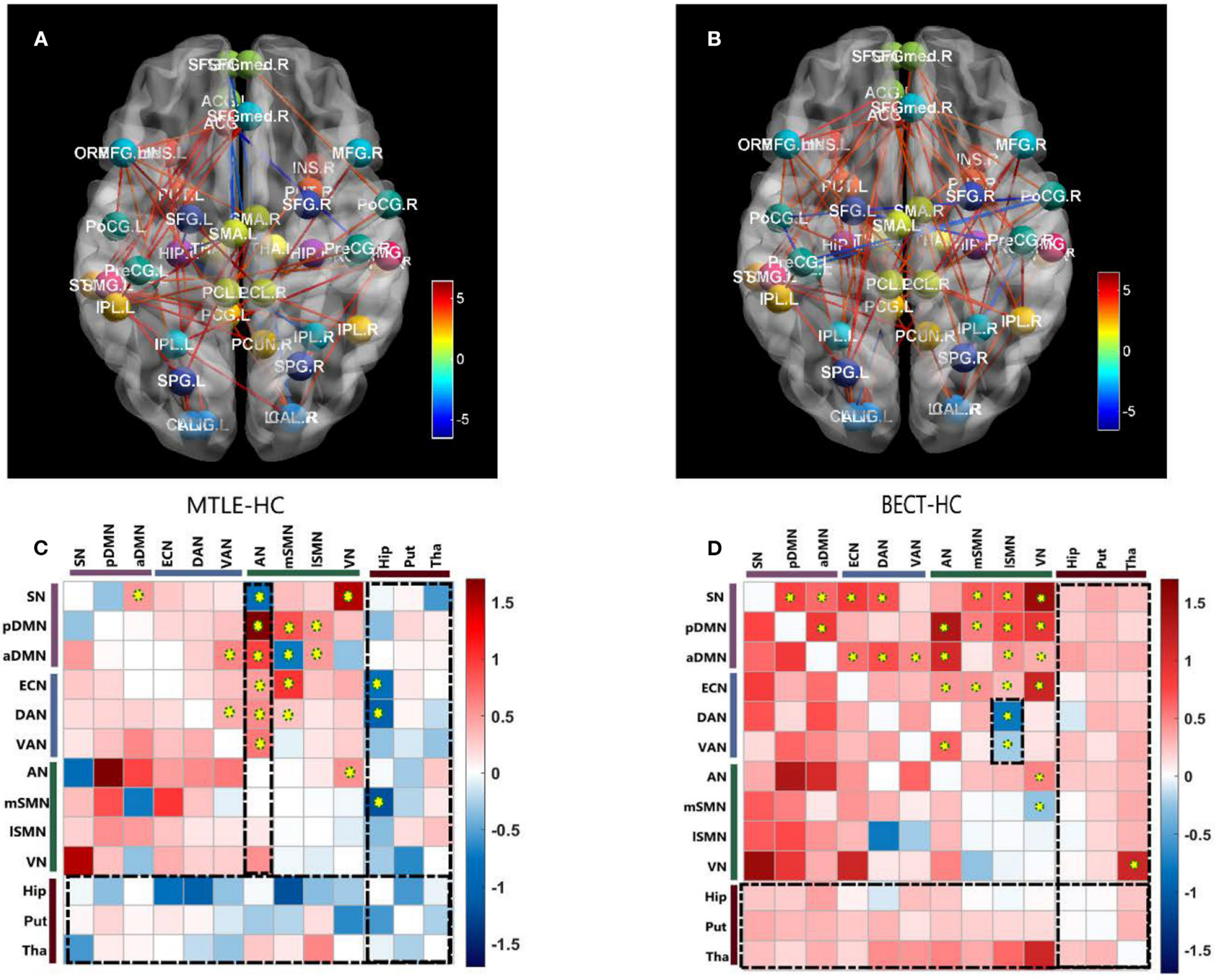

FIGURE 2 | Pairwise comparisons of Internetwork connectivity aberration. Values represented t-statistics between 10 networks and 3 subcortical regions of interest (ROIs: bilateral hippocampus, putamen and thalamus) in the pairwise comparisons of MTLE- HC (**A, C**) and BECT- HC **(B, D)**. Tests of statistical significance were based on two-sample *t*-test corrected for multiple comparisons with a network-based statistic (NBS) threshold set to 0.05. Thredsholded edges and nodes corresponded results of internetwork connectivity **(A, B)**. Specially, we used AAL coordinates to symbolically depict the subcortical ROIs. To better elucidate the general trend, matrix maps were used **(C, D)**. Significant differences are also marked by yellow circuses in the connectivity matrices. The black rectangular box highlighted the characteristic networks, AN in MTLE-HC and lSMN in BECT-HC (details as shown in **Figure 3**).

RSN Alterations in Patients With MTLE

The current study found that RSNs in the MTLE patients compared with the HCs had lower connectivity with subcortical ROIs, especially the hippocampus, which plays a core role in MTLE. The abnormal connectivity patterns of these networks with the hippocampus were related to functional and structural impairments in the hippocampus. Deactivation compared to the control condition corresponded to decreased synaptic activity, such as that caused by reduced neuronal input from the hippocampus (35). In current study, the condition of impaired consciousness in most patients with MTLE (13/14) might have been caused by subcortical networks with extensive impairments in connectivity with the cortical functional networks (39). These abnormal connections occurred with both task-positive networks and sensory networks. Task-positive networks (e.g., ECN, DAN, and VAN) are dominant in executive control and external attention. Sensory networks are primarily involved in primary somatomotor, somatosensory, visual and auditory processes. Our findings accorded with earlier observations, which showed that MTLE patients demonstrated diffuse neocortical hypometabolism and multitudinous brain connectivity perturbations (40).

The AN showed higher connectivity with other widespread RSNs, including the DMN, which could be explained by the reconfiguration in the lateral temporal area in MTLE patients (41). Blumenfeld and his colleagues used SPECT (39) and found that ictal TLE patients had increased cerebral blood flow (CBF) in the temporal lobe, as well as an increase in CBF in

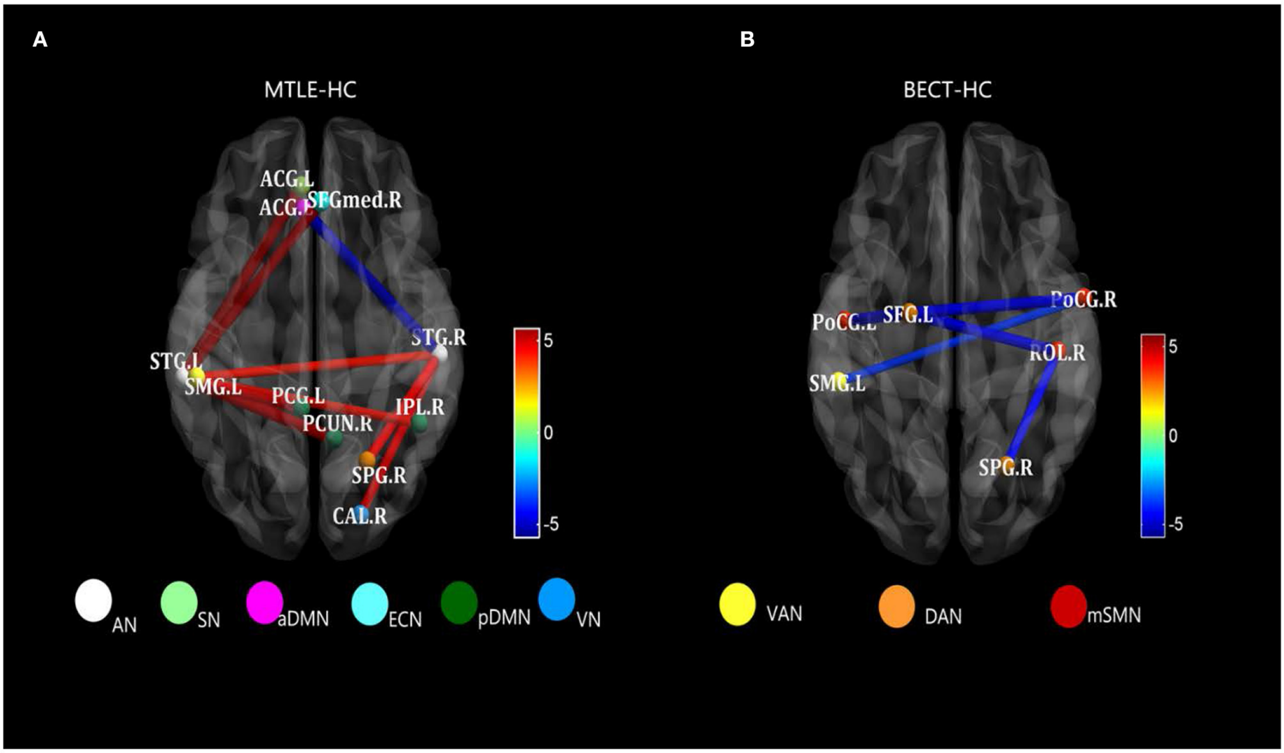

FIGURE 3 | Strongly characteristic networks in MTLE and BECT. We detailed the black rectangular boxes in **Figures 2C,D**, AN in MTLE-HC and lSMN in BECT-HC. In the analysis of pairwise seed connectivity, bilateral superior temporal gyrus (STG) were found hyperconnectivity with almost functional networks in MTLE-HC **(A)**. Bilateral postcentral gyrus (ProCG.L and ProCG.R) and right Rolandic operculum (ROL.R) showed hypoconnectivity with right intraparietal sulcus (SPG.R within DAN) and left temporoparietal junction (SMG.L within VAN) **(B)**. Tests of statistical significance were based on two-sample *t*-tests ($p < 0.05$, NBS corrected).

bilateral midline subcortical structures. CBF activity coherence was interpreted as a BOLD signal effect between the lateral temporal and midline areas, manifested as a higher connectivity compared with HCs (see **Figure 3A**). Thus, damage to lateral temporal lobes, one of the functional network hubs, will affect the sets of functional brain areas at large (42).

RSN Alterations in Patients With BECT

A resting-state BOLD response was demonstrated to be consistent with interictal seizure discharges in the rolandic region in an EEG-fMRI study (43). Initial studies have shown that the areas of increased connectivity and activity are usually the sensorimotor cortex and immediate regions surrounding the zone. Therefore, a network-based approach may expand our traditional knowledge about the organization of the sensorimotor cortex, especially the interaction between the motor system and the rest of the networks.

The network we refer to as "rolandic" has usually been recognized as a sensorimotor network (SMN) in large-scale RSNs. Effective connectivity studies have suggested that the rolandic area is the key region for the spread of interictal epileptic spikes to distal cortical regions. However, the effect of the rolandic regions is based on the regional distribution of its connectivity among the sets of functional brain areas. Consistent with the research, several studies have found that participants who reported using functional near-infrared spectroscopy (fNIRS) and fMRI also detected a decreased oxyhaemoglobin (HbO) response and an increased deoxyhaemoglobin (HbR) response in the frontal and parieto-occipital lobes, indicating a widespread effect across distributed networks (44, 45).

Similar findings of discrepant intranetwork connectivity have been previously reported (18, 46), although the current results were not significant compared with the HC group (**Figure 4**). It was difficult to explain this result, but it might be related to a stronger regional integration (47) in BECT patients. Regardless, there was higher internetwork connectivity among an extensive range of networks, such as the DMN and SAN with other sensory networks ($p < 0.05$, NBS corrected), which corresponded to the loss of cortical global processing (48). In the network-based analysis, excitatory local and global networks indicated that the small-world functional topology was disrupted in BECT patients (49). Notably, no marked lower or higher FC was found between cortical RSNs and subcortical ROIs, which indicated that subcortical core nuclei were not involved in the alterations.

In addition, we uncovered a decreased RSFC between the SMN and attention networks in the hyperconnectivity setting (see **Figure 2D**) ($p < 0.05$, NBS corrected). The SMN is a motor network as demonstrated in previous studies but is also partially integrated into a multimodal network associated with motor systems and cognitive hubs (50). Impacts on cognition were

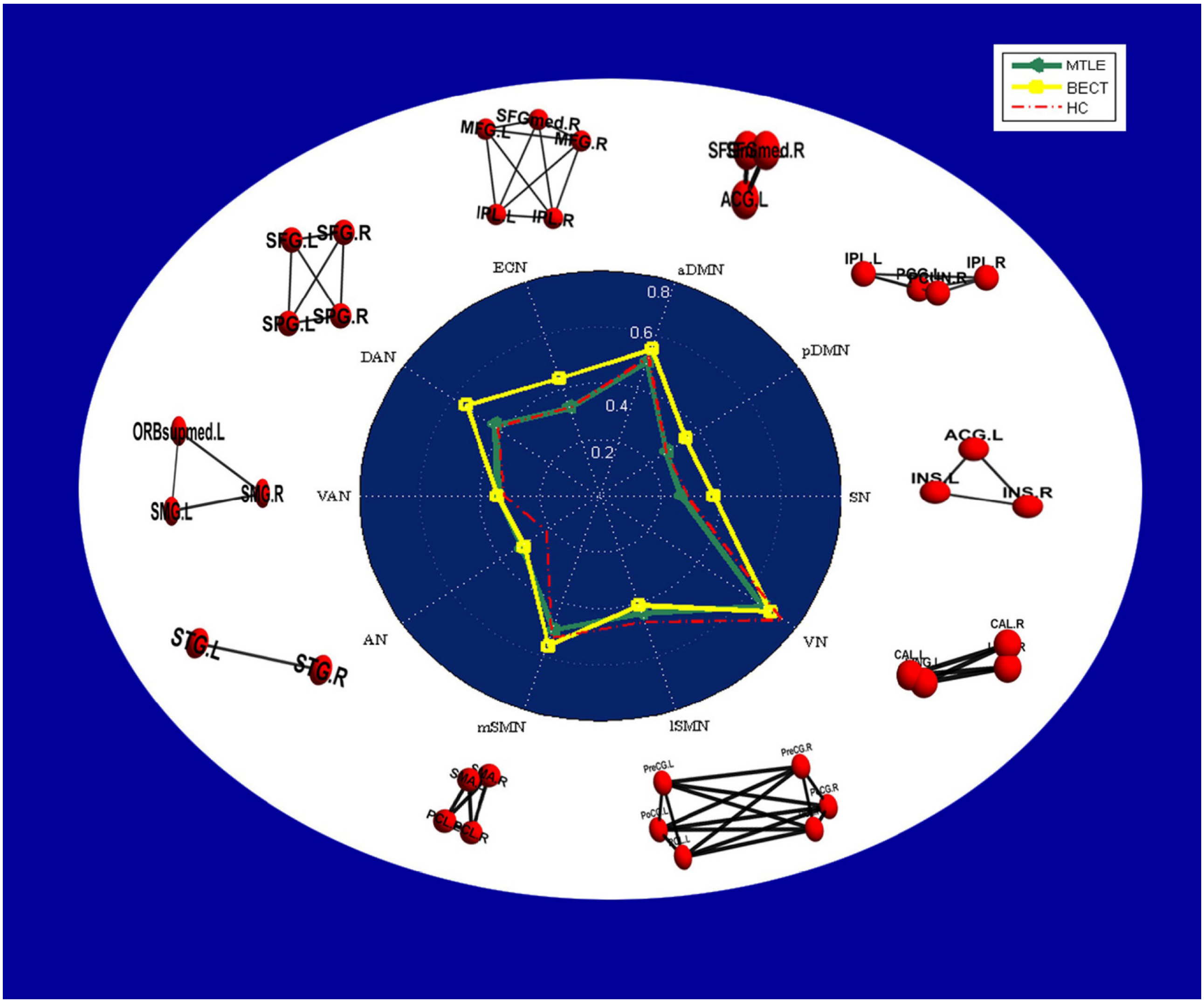

FIGURE 4 | Radar plots showing intranetwork RSFC differences in each group. The values displayed by the dots in the radar plots are the Fisher z-transformed values of Pearson's correlation in each group, and a table of the values is provided in **Supplementary Table 1**. In the white area, node-edge graphs of 10 RSNs were showed according to **Table 2**.

shown by Caterina et al., who found that BECT patients had impairments in attention (51). Attention control deficits have been related to alterations in the DAN and VAN. A previous study showed increased FC within the VAN in patients when compared with controls (46). This finding was also supported by Jiang et al., who found that children newly diagnosed with BECT showed alterations in brain activity in the attention networks, and the unmedicated group showed increased RSFC in the rolandic network and decreased RSFC in the DAN (52). These findings were in line with attention dysfunction in BECT patients (see **Figure 3B**). Moreover, the decreased connectivity between the VN and SMN can explain the poor visual spatial memory observed in BECT children (49, 53), which manifests as a loss in integration of the motor network and visual network that forms a multimodal network (54). Moreover, the VN was shown to have a strong correlation with the DMN, indicating that BECT was characterized by possible functional compensatory mechanisms (55) and related to attention-deficit/hyperactivity disorder (ADHD).

Considering the age differences between BECT group (10.42 ± 4.5) and HC group (27.1 ± 4.8), characteristics of RSNs in heathy children and adults were also needed to be discussed as it might influence the results' interpretation to some degree. Resting state studies have shown that children have the same RSNs as adults' and children round 8 years old have strong functional organization, but exhibit immature characteristics (56, 57). Compared with adults, this immature performance was characterized by the functional segregation and the insufficient integration (58, 59). And structure network studies suggested that the approach of network interaction changed from local anatomically regions in children to long-distance cortical interaction in young adults (59, 60). A study of the size of functional networks was found that the number of voxels were more than adults in the majority RSNs and also more widespread (57). In conclusion, it is demonstrated that this kind of segregative pattern in children is less efficient or specialized than adult (61). However, a principle finding in RSNs development was that SMN increased the efficiency of local and global functional connectivity with aging (57, 62). In the current study, BECT patients suffered from the epileptic neural activity in Rolandic area, which could be the reason why healthy adult subjects showed a lower connectivity compared with BECT children. Hence, our primary result was not be interrupted by the age differences.

Differences in RSNs in Patients With MTLE and BECT

In the internetwork analysis, it was notable that network state differences between the MTLE and BECT patients showed hypoconnectivity between cortical networks and subcortical ROIs in a general setting of lower connectivity in MTLE contrasted against normal cortical-subcortical connectivity and extensive hyperconnectivity among the majority of networks in BECT. This suggested that the two types of epilepsy have completely different brain network patterns that impact clinical outcomes. In our study, patients with MTLE and BECT have totally different severity of clinical manifestations. One of the critical reasons is because the different pathological mechanism. Generally, patients with MTLE have the most common etiology and pathological performance, hippocampus sclerosis, which is irreversible in the course of epilepsy (3). By comparison, BECT is an idiopathic epilepsy without brain structural abnormality and recently research have shown a strong correlation between genetics and BECT development (63). Moreover, different durations of two patient groups were also contributed to different clinical response. Long-term epileptiform discharges would be able to interrupt the brain normal functional activity and also induced structural damage in MTLE (64) while majority of BECT patients remit spontaneously before adolescence.

Connectivity patterns seem to be correlated with the duration and severity of the disease, indicating progressive connectivity reorganization in the context of recurrent seizure activity. BECT was more reflective of a state of increased synchronization in functional network activities, which could be understood as synchronous activity of these related regions that did not stop during the interictal period. Hence, it could conceivably be regarded as a compensatory state of higher synchronization. Moreover, normal cortical-subcortical interactions suggested disruptions confined to cortical functional regions in BECT. In contrast, the MTLE patients showed a widespread state of lower connectivity between RSNs and subcortical ROIs compared with the HCs, which meant a lower global cooperativity that should have relevant functional consequences due to the loss of their normal FC. It could be concluded that MTLE results in more significant disruptions throughout brain networks, and this may help to explain the longer course of the disease, more severe symptoms and worse prognosis of MTLE than BECT through a pathological network mechanism.

We provide new evidence for brain network pattern abnormalities in different epilepsy compensatory states. And we expect that future studies will focus more on the lateral temporal lobes in MTLE and the attention networks in BECT. Furthermore, it seems feasible to use different neuromodulation approaches, for example, transcranial magnetic stimulation (TMS), to investigate these underpinning mechanisms. Michael D. Fox and his colleagues (65) suggested the potential to balance abnormal activity based on RSFC in psychiatric and neurological diseases, including epilepsy (66, 67). Network-based cortical modulation in BECT and MTLE, as typical focal epilepsies, might have the potential to investigate the substrate. Concretely, our findings suggested that the lateral temporal lobes and attention networks are probably valid TMS targets for MTLE and BECT. In addition, transcranial direct current stimulation (tDCS) and other network-based neuromodulation methods, which take these variables into account, will need to be undertaken.

LIMITATIONS

In the current study, our primary focus was on the discrepant state and characteristics of brain functional networks in patients with MTLE and BECT. However, the study findings should be interpreted in the context of their limitations. Firstly, a potential limitation of our study was the small sample size in both epilepsy groups. A larger sample size may produce significant results when the MTLE and BECT groups are compared with the HC group in the intranetwork analysis. Secondly, in our future study, the age discrepancy between BECT and HC needed to be further solved. Thirdly, cognitive state evaluation, such as attention, motion, audition and visual function, is necessary as a Supplementary to verify these dysfunctions. Finally, there is more detailed and related work that could be performed, including effective connectivity and global property analysis in future studies. Future work is required for a full consideration of the above factors.

DATA AVAILABILITY STATEMENT

The original contributions generated for the study are included in the article/**Supplementary Material**, further inquiries can be directed to the corresponding authors.

AUTHOR CONTRIBUTIONS

JY and CF: conceptualization. CF: methodology and writing—original draft preparation. ZC, AA, and QY: validation. AA and QY: resources. AA and ZC: data curation. JY and WY: writing—review editing, and supervision. WY: funding acquisition. All authors contributed to the article and approved the submitted version.

FUNDING

This work was supported by the Natural Science Foundation of Tianjin City (grants number 12JCYBJC16900).

ACKNOWLEDGMENTS

We thank all the authors for their work on this study. We also thank the patients and healthy controls who contributed their time and effort to this study.

SUPPLEMENTARY MATERIAL

The Supplementary Material for this article can be found online at: https://www.frontiersin.org/articles/10.3389/fneur.2021.668856/full#supplementary-material

REFERENCES

1. Shorvon SD, Goodridge DM. Longitudinal cohort studies of the prognosis of epilepsy: contribution of the national general practice study of epilepsy and other studies. *Brain.* (2013) 136(Pt 11):3497–510. doi: 10.1093/brain/awt223
2. Karunakaran S, Rollo MJ, Kim K, Johnson JA, Kalamangalam GP, Aazhang B, et al. The interictal mesial temporal lobe epilepsy network. *Epilepsia.* (2018) 59:244–58. doi: 10.1111/epi.13959
3. Tatum IV, WO. Mesial temporal lobe epilepsy. *J Clin Neurophysiol.* (2012) 29:356–65. doi: 10.1097/WNP.0b013e31826b3ab7
4. Bourel-Ponchel E, Mahmoudzadeh M, Adebimpe A, Wallois F. Functional and structural network disorganizations in typical epilepsy with centro-temporal spikes and impact on cognitive neurodevelopment. *Front Neurol.* (2019) 10:809. doi: 10.3389/fneur.2019.00809
5. Halász P, Rásonyi G. Neuroprotection and epilepsy. *Adv Exp Med Biol.* (2004) 541:91–109. doi: 10.1007/978-1-4419-8969-7_6
6. Datta AN, Oser N, Bauder F, Maier O, Martin F, Ramelli GP, et al. Cognitive impairment and cortical reorganization in children with benign epilepsy with centrotemporal spikes. *Epilepsia.* (2013) 54:487–94. doi: 10.1111/epi.12067
7. Prince DA. Benign focal epilepsies of childhood: genetically determined pathophysiology–epilepsy that comes and goes. *Epilepsia.* (2000) 41:1085–7. doi: 10.1111/j.1528-1157.2000.tb00310.x
8. Englot DJ, Konrad PE, Morgan VL. Regional and global connectivity disturbances in focal epilepsy, related neurocognitive sequelae, and potential mechanistic underpinnings. *Epilepsia.* (2016) 57:1546–57. doi: 10.1111/epi.13510
9. Holmes MD, Tucker DM. Identifying the epileptic network. *Front Neurol.* (2013) 4:84. doi: 10.3389/fneur.2013.00084
10. Bartolomei F, Chauvel P, Wendling F. Epileptogenicity of brain structures in human temporal lobe epilepsy: a quantified study from intracerebral EEG. *Brain.* (2008) 131(Pt 7):1818–30. doi: 10.1093/brain/awn111
11. Ebersole JS, Pacia SV. Localization of temporal lobe foci by ictal EEG patterns. *Epilepsia.* (1996) 37:386–99. doi: 10.1111/j.1528-1157.1996.tb00577.x
12. Bonilha L, Edwards JC, Kinsman SL, Morgan PS, Fridriksson J, Rorden C, et al. Extrahippocampal gray matter loss and hippocampal deafferentation in patients with temporal lobe epilepsy. *Epilepsia.* (2010) 51:519–28. doi: 10.1111/j.1528-1167.2009.02506.x
13. Coan AC, Appenzeller S, Bonilha L, Li LM, Cendes F. Seizure frequency and lateralization affect progression of atrophy in temporal lobe epilepsy. *Neurology.* (2009) 73:834–42. doi: 10.1212/WNL.0b013e3181b783dd
14. Haneef Z, Lenartowicz A, Yeh HJ, Engel Jr J, Stern JM. Effect of lateralized temporal lobe epilepsy on the default mode network. *Epilepsy Behav.* (2012) 25:350–7. doi: 10.1016/j.yebeh.2012.07.019
15. Adebimpe A, Aarabi A, Bourel-Ponchel E, Mahmoudzadeh M, Wallois F. EEG resting state analysis of cortical sources in patients with benign epilepsy with centrotemporal spikes. *Neuro Image Clin.* (2015) 9:275–82. doi: 10.1016/j.nicl.2015.08.014
16. Bouma PA, Bovenkerk AC, Westendorp RG, Brouwer OF. The course of benign partial epilepsy of childhood with centrotemporal spikes: a meta-analysis. *Neurology.* (1997) 48:430–37. doi: 10.1212/WNL.48.2.430
17. Croona C, Kihlgren M, Lundberg S, Eeg-Olofsson O, Eeg-Olofsson KE. Neuropsychological findings in children with benign childhood epilepsy with centrotemporal spikes. *Dev Med Child Neurol.* (1999) 41:813–8. doi: 10.1017/S0012162299001620
18. Xiao F, Lei D, An D, Li L, Chen S, Chen F, et al. Functional brain connectome and sensorimotor networks in rolandic epilepsy. *Epilepsy Res.* (2015) 113:113–25. doi: 10.1016/j.eplepsyres.2015.03.015
19. Besseling RM, Jansen JF, Overvliet GM, van der Kruijs SJ, Vles JS, Ebus SC, et al. Reduced functional integration of the sensorimotor and language network in rolandic epilepsy. *Neuroimage Clin.* (2013) 2:239–46. doi: 10.1016/j.nicl.2013.01.004
20. Bulgheroni S, Franceschetti S, Vago C, Usilla A, Pantaleoni C, D'Arrigo S, et al. Verbal dichotic listening performance and its relationship with EEG features in benign childhood epilepsy with centrotemporal spikes. *Epilepsy Res.* (2008) 79:31–8. doi: 10.1016/j.eplepsyres.2007.12.016
21. Proposal for revised classification of epilepsies and epileptic syndromes. *Epilepsia.* (1989) 30:389–99. doi: 10.1111/j.1528-1157.1989.tb05316.x
22. Bernasconi A, Cendes F, Theodore WH, Gill RS, Koepp MJ, Hogan RE, et al. Recommendations for the use of structural magnetic resonance imaging in the care of patients with epilepsy: a consensus report from the international league against epilepsy neuroimaging task force. *Epilepsia.* (2019) 60:1054–68. doi: 10.1111/epi.15612
23. Schmidt D, Löscher W. Drug resistance in epilepsy: putative neurobiologic and clinical mechanisms. *Epilepsia.* (2005) 46:858–77. doi: 10.1111/j.1528-1167.2005.54904.x
24. Calhoun VD, Wager TD, Krishnan A, Rosch KS, Seymour KE, Nebel MB, et al. The impact of T1 versus EPI spatial normalization templates for fMRI data analyses. *Hum Brain Mapp.* (2017) 38:5331–42. doi: 10.1002/hbm.23737
25. Wang J, Wang X, Xia M, Liao X, Evans A, He Y. GRETNA: A graph theoretical network analysis toolbox for imaging connectomics. *Front Hum Neurosci.* (2015) 9:386. doi: 10.3389/fnhum.2015.00386
26. Friston KJ, Williams S, Howard R, Frackowiak RS, Turner R. Movement-related effects in fMRI time-series. *Magn Reson Med.* (1996) 35:346–55. doi: 10.1002/mrm.1910350312
27. Power JD, Barnes KA, Snyder AZ, Schlaggar BL, Petersen SE. Spurious but systematic correlations in functional connectivity MRI networks arise from subject motion. *Neuroimage.* (2012) 59:2142–54. doi: 10.1016/j.neuroimage.2011.10.018
28. Power JD, Schlaggar BL, Petersen SE. Recent progress and outstanding issues in motion correction in resting state fMRI. *Neuroimage.* (2015) 105:536–51. doi: 10.1016/j.neuroimage.2014.10.044
29. Song XW, Dong Z-Y, Long X-Y, Li S-F, Zuo X-N, Zhu C-Z, et al. REST: a toolkit for resting-state functional magnetic resonance imaging data processing. *PLoS ONE.* (2011) 6:e25031. doi: 10.1371/journal.pone.0025031
30. Greicius MD, Krasnow B, Reiss AL, Menon V. Functional connectivity in the resting brain: a network analysis of the default mode hypothesis. *Proc Natl Acad Sci USA.* (2003) 100:253–8. doi: 10.1073/pnas.0135058100
31. Mantini D, Perrucci MG, Del Gratta C, Romani GL, Corbetta M. Electrophysiological signatures of resting state networks in the human brain. *Proc Natl Acad Sci USA.* (2007) 104:13170–5. doi: 10.1073/pnas.0700668104
32. King BR, van Ruitenbeek P, Leunissen I, Cuypers K, Heise KF, Santos Monteiro T, et al. Age-related declines in motor performance are associated with decreased segregation of large-scale resting state brain networks. *Cereb Cortex.* (2018) 28:4390–402. doi: 10.1093/cercor/bhx297
33. Desikan RS, Segonne F, Fischl B, Quinn BT, Dickerson BC, Blacker D, et al. An automated labeling system for subdividing the human cerebral cortex on MRI scans into gyral based regions of interest. *Neuroimage.* (2006) 31:968–80. doi: 10.1016/j.neuroimage.2006.01.021
34. Diedrichsen J, Balsters JH, Flavell J, Cussans E, Ramnani N. A probabilistic MR atlas of the human cerebellum. *Neuroimage.* (2009) 46:39–46. doi: 10.1016/j.neuroimage.2009.01.045
35. Gotman J. Epileptic networks studied with EEG-fMRI. *Epilepsia.* (2008) 49(Suppl. 3):42–51. doi: 10.1111/j.1528-1167.2008.01509.x
36. Yeterian EH, Pandya DN. Corticothalamic connections of paralimbic regions in the rhesus monkey. *J Comp Neurol.* (1988) 269:130–46. doi: 10.1002/cne.902690111

37. Vuong J, Devergnas A. The role of the basal ganglia in the control of seizure. *J Neural Transm.* (2018) 125:531–45. doi: 10.1007/s00702-017-1768-x
38. Zalesky A, Fornito A, Bullmore ET. Network-based statistic: identifying differences in brain networks. *Neuroimage.* (2010) 53:1197–207. doi: 10.1016/j.neuroimage.2010.06.041
39. Blumenfeld H, McNally KA, Vanderhill SD, Paige AL, Chung R, Davis K, et al. Positive and negative network correlations in temporal lobe epilepsy. *Cerebral Cortex*. (2004) 14:892–902. doi: 10.1093/cercor/bhh048
40. Alvim MK, Coan AC, Campos BM, Yasuda CL, Oliveira MC, Morita ME, et al. Progression of gray matter atrophy in seizure-free patients with temporal lobe epilepsy. *Epilepsia*. (2016) 57:621–9. doi: 10.1111/epi.13334
41. Vaughan DN, Rayner G, Tailby C, Jackson GD. MRI-negative temporal lobe epilepsy: a network disorder of neocortical connectivity. *Neurology*. (2016) 87:1934–42. doi: 10.1212/WNL.0000000000003289
42. Warren DE, Power JD, Bruss J, Denburg NL, Waldron EJ, Sun H, et al. Network measures predict neuropsychological outcome after brain injury. *Proc Natl Acad Sci USA*. (2014) 111:14247–52. doi: 10.1073/pnas.1322173111
43. Masterton RAJ, Harvey AS, Archer JS, Lillywhite LM, Abbott DF, Scheffer IE, et al. Focal epileptiform spikes do not show a canonical BOLD response in patients with benign rolandic epilepsy (BECTS). *Neuroimage.* (2010) 51:252–60. doi: 10.1016/j.neuroimage.2010.01.109
44. Archer JS, Briellman RS, Abbott DF, Syngeniotis A, Wellard RM, Jackson GD. Benign epilepsy with centro-temporal spikes: spike triggered fMRI shows somato-sensory cortex activity. *Epilepsia*. (2003) 44:200–4. doi: 10.1046/j.1528-1157.2003.02502.x
45. Boor S, Vucurevic G, Pfleiderer C, Stoeter P, Kutschke G, Boor R. EEG-related functional MRI in benign childhood epilepsy with centrotemporal spikes. *Epilepsia*. (2003) 44:688–92. doi: 10.1046/j.1528-1157.2003.27802.x
46. Xiao F, Li L, An D, Lei D, Tang Y, Yang T, et al. Altered attention networks in benign childhood epilepsy with centrotemporal spikes (BECTS): a resting-state fMRI study. *Epilepsy Behav*. (2015) 45:234–41. doi: 10.1016/j.yebeh.2015.01.016
47. Zeng H, Ramos CG, Nair VA, Hu Y, Liao J, La C, et al. Regional homogeneity (ReHo) changes in new onset versus chronic benign epilepsy of childhood with centrotemporal spikes (BECTS): a resting state fMRI study. *Epilepsy Res.* (2015) 116:79–85. doi: 10.1016/j.eplepsyres.2015.06.017
48. Asadi-Pooya AA, Xiao F, Zhou D. Real-time effects of centrotemporal spikes on cognition in rolandic epilepsy: An EEG-fMRI study. *Neurology*. (2016) 87:551–2. doi: 10.1212/WNL.0000000000002967
49. Azeez A, Ardalan A, Emilie BP, Mahdi M, Fabrice W, He B. Functional brain dysfunction in patients with benign childhood epilepsy as revealed by graph theory. *PLoS ONE.* (2015) 10:e0139228. doi: 10.1371/journal.pone.0139228
50. Sepulcre J, Sabuncu MR, Yeo TB, Liu H, Johnson KA. Stepwise connectivity of the modal cortex reveals the multimodal organization of the human brain. *J Neurosci*. (2012) 32:10649–61. doi: 10.1523/JNEUROSCI.0759-12.2012
51. Cerminara C, D'Agati E, Lange KW, Kaunzinger I, Tucha O, Parisi P, et al. Benign childhood epilepsy with centrotemporal spikes and the multicomponent model of attention: a matched control study. *Epilepsy Behav.* (2010) 19:69–77. doi: 10.1016/j.yebeh.2010.07.008
52. Jiang Y, Song L, Li X, Zhang Y, Chen Y, Jiang S, et al. Dysfunctional white-matter networks in medicated and unmedicated benign epilepsy with centrotemporal spikes. *Hum Brain Mapp.* (2019) 40:3113–24. doi: 10.1002/hbm.24584
53. Cohen M. Auditory/verbal and visual/spatial memory in children with complex partial epilepsy of temporal lobe origin. *Brain Cogn.* (1992) 20:315–26. doi: 10.1016/0278-2626(92)90024-G
54. Sepulcre J. Integration of visual and motor functional streams in the human brain. *Neurosci Lett.* (2014) 567:68–73. doi: 10.1016/j.neulet.2014.03.050
55. Cortese S, Kelly C, Chabernaud C, Proal E, Di Martino A, Milham MP, et al. Toward systems neuroscience of ADHD: a meta-analysis of 55 fMRI studies. *Am J Psychiatry.* (2012) 169:1038–55. doi: 10.1176/appi.ajp.2012.11101521
56. Fair DA, Cohen AL, Power JD, Dosenbach NU, Church JA, Miezin FM, et al. Functional brain networks develop from a "local to distributed" organization. *PLoS Comput Biol.* (2009) 5:e1000381. doi: 10.1371/journal.pcbi.1000381
57. JollesDD, van Buchem MA, Crone EA, Rombouts SA. A comprehensive study of whole-brain functional connectivity in children and young adults. *Cereb Cortex.* (2011) 21:385–91. doi: 10.1093/cercor/bhq104
58. Fair DA, Dosenbach NU, Church JA, Cohen AL, Brahmbhatt S, Miezin FM, et al. Development of distinct control networks through segregation and integration. *Proc Natl Acad Sci USA*. (2007) 104:13507–12. doi: 10.1073/pnas.0705843104
59. Vogel AC, Power JD, Petersen SE, Schlaggar BL. Development of the brain's functional network architecture. *Neuropsychol Rev*. (2010) 20:362–75. doi: 10.1007/s11065-010-9145-7
60. Power JD, Fair DA, Schlaggar BL, Petersen SE. The development of human functional brain networks. *Neuron.* (2010) 67:735–48. doi: 10.1016/j.neuron.2010.08.017
61. Johnson MH, Munakata Y. Processes of change in brain and cognitive development. *Trends Cogn Sci.* (2005) 9:152–8. doi: 10.1016/j.tics.2005.01.009
62. Kelly AM, Di Martino A, Uddin LQ, Shehzad Z, Gee DG, Reiss PT, et al. Development of anterior cingulate functional connectivity from late childhood to early adulthood. *Cereb Cortex.* (2009) 19:640–57. doi: 10.1093/cercor/bhn117
63. Guerrini R, Pellacani S. Benign childhood focal epilepsies. *Epilepsia.* (2012) 53(Suppl. 4):9–18. doi: 10.1111/j.1528-1167.2012.03609.x
64. Liao W, Zhang Z, Pan Z, Mantini D, Ding J, Duan X, et al. Default mode network abnormalities in mesial temporal lobe epilepsy: a study combining fMRI and DTI. *Hum Brain Mapp.* (2011) 32:883–95. doi: 10.1002/hbm.21076
65. Fox MD, Buckner RL, Liu H, Chakravarty MM, Lozano AM, Pascual-Leone A. Resting-state networks link invasive and noninvasive brain stimulation across diverse psychiatric and neurological diseases. *Proc Natl Acad Sci USA*. (2014) 111:E4367–75. doi: 10.1073/pnas.1405003111
66. Brighina F, Daniele O, Piazza A, Giglia G, Fierro B. Hemispheric cerebellar rTMS to treat drug-resistant epilepsy: case reports. *Neurosci Lett*. (2006) 397:229–33. doi: 10.1016/j.neulet.2005.12.050
67. Sun W, Mao W, Meng X, Wang D, Qiao L, Tao W, et al. Low-frequency repetitive transcranial magnetic stimulation for the treatment of refractory partial epilepsy: a controlled clinical study. *Epilepsia*. (2012) 53:1782–9. doi: 10.1111/j.1528-1167.2012.03626.x

Conflict of Interest: The authors declare that the research was conducted in the absence of any commercial or financial relationships that could be construed as a potential conflict of interest.

frontiers
in Neurology

BRIEF RESEARCH REPORT
published: 03 June 2021
doi: 10.3389/fneur.2021.658239

Interictal Epileptiform Discharge Dynamics in Peri-sylvian Polymicrogyria Using EEG-fMRI

Noa Cohen[1,2*†], *Yoram Ebrahimi*[1†], *Mordekhay Medvedovsky*[3], *Guy Gurevitch*[1,2], *Orna Aizenstein*[1,4], *Talma Hendler*[1,2,5,6], *Firas Fahoum*[2,7] and *Tomer Gazit*[1,2]

[1] Sagol Brain Institute, Wohl Institute for Advanced Imaging, Sourasky Medical Center, Tel Aviv, Israel, [2] Sackler School of Medicine, Tel Aviv University, Tel Aviv, Israel, [3] Department of Neurology, Agnes Ginges Center of Neurogenetics, Hadassah-Hebrew University Medical Center, Jerusalem, Israel, [4] Department of Diagnostic Imaging, Sourasky Medical Center, Tel Aviv, Israel, [5] School of Psychological Science, Tel Aviv University, Tel Aviv, Israel, [6] Sagol School of Neuroscience, Tel Aviv University, Tel Aviv, Israel, [7] Electroencephalography and Epilepsy Unit, Sourasky Medical Center, Tel Aviv, Israel

Polymicrogyria (PMG) is a common malformation of cortical development associated with a higher susceptibility to epileptic seizures. Seizures secondary to PMG are characterized by difficult-to-localize cerebral sources due to the complex and widespread lesion structure. Tracing the dynamics of interictal epileptiform discharges (IEDs) in patients with epilepsy has been shown to reveal the location of epileptic activity sources, crucial for successful treatment in cases of focal drug-resistant epilepsy. In this case series IED dynamics were evaluated with simultaneous EEG-fMRI recordings in four patients with unilateral peri-sylvian polymicrogyria (PSPMG) by tracking BOLD activations over time: before, during and following IED appearance on scalp EEG. In all cases, focal BOLD activations within the lesion itself preceded the activity associated with the time of IED appearance on EEG, which showed stronger and more widespread activations. We therefore propose that early hemodynamic activity corresponding to IEDs may hold important localizing information potentially leading to the cerebral sources of epileptic activity. IEDs are suggested to develop within a small area in the PSPMG lesion with structural properties obscuring the appearance of their electric field on the scalp and only later engage widespread structures which allow the production of large currents which are recognized as IEDs on EEG.

Keywords: epilepsy, interictal epileptiform discharges, polymicrogyria, EEG-fMRI, interictal dynamics

Edited by:
Ana Carolina Coan,
State University of Campinas, Brazil

Reviewed by:
Umit Aydin,
King's College London,
United Kingdom
Jacopo Lanzone,
Sant'Isidoro Hospital Ferb Onlus
Trescore Balneario, Italy

***Correspondence:**
Noa Cohen
noahcohen@tauex.tau.ac.il

† These authors have contributed equally to this work

Specialty section:
This article was submitted to Epilepsy,
a section of the journal
Frontiers in Neurology

Received: *25 January 2021*
Accepted: *05 May 2021*
Published: *03 June 2021*

Citation:
Cohen N, Ebrahimi Y, Medvedovsky M, Gurevitch G, Aizenstein O, Hendler T, Fahoum F and Gazit T (2021) Interictal Epileptiform Discharge Dynamics in Peri-sylvian Polymicrogyria Using EEG-fMRI. Front. Neurol. 12:658239. doi: 10.3389/fneur.2021.658239

INTRODUCTION

Recent findings point to both ictal (during seizures) and interictal (between seizures) epileptic event types as arising from a common cortical source, termed the epileptogenic zone [EZ; (1, 2)]. Though the precise relationship between these epileptic phenomena and their cerebral origins is still not sufficiently understood (3, 4), interictal activity is often utilized in order to identify the generators of seizure activity. This is particularly relevant for patients with drug-resistant epilepsy for which achieving seizure control highly depends on correct EZ localization and its removal by surgical resection. Such patients undergo extensive pre-surgical testing including neuroimaging, electrophysiology and neuropsychological examinations for identifying their seizure sources. In most cases, no single method is sufficient for reliably assessing this area's location and extent and even after exhaustive testing, many surgical procedures are unsuccessful (5, 6). When possible, seizure semiology and neurophysiology are used to study the sources of seizure activity, however in many cases seizures are difficult to capture in a clinical setting. Interictal activity, however, may be captured non-invasively and in an outpatient setting, providing more accessible options for EZ identification and adding crucial localizing information (7).

PMG is a common malformation of cortical development, characterized by an excessively folded cortical ribbon of miniature, individually thin convolutions (8). PMG, including the most common peri-sylvian (PSPMG) subtype, has been associated with a wide range of clinical manifestations such as cognitive impairment (9), focal neurological deficits (10) and intractable epilepsy (11). Contradicting findings have been reported regarding the areas generating ictal and interictal events in patients with PMG, which include areas within the PMG (12) and outside of it (13). In the latter study, Jacobs and colleagues suggested that aberrant synaptic connectivity develops around the microgyri and produces a focal epileptogenic zone whose capacity to generate epileptiform activity does not depend on connections with the malformation itself. Intralesional recordings in humans with PMG demonstrated a large epileptic network involving both the lesion and non-malformed cortex (14), while intracranial electroencephalography (iEEG) studies have shown that the seizure onset zone may only partially overlap with the PMG cortex (15). Surgical resection of sub-portions of the malformed cortex have been shown to result in positive surgical outcomes (16, 17), suggesting that a region within the PMG may be the source of abnormal electrical activity.

In many cases, fast propagation and dynamic distribution of IEDs confound the localization of their cerebral sources (18, 19), leading to misinterpretation of pre-surgical testing and mis-localization of the EZ. Using high resolution imaging methods, studies have shown that source localization may be improved when focusing on the early phases of the interictal discharge, as the later stages are associated with more widespread activity (1, 18). The simultaneous measurement of electroencephalography (EEG) and functional magnetic resonance imaging (fMRI) is a non-invasive neuroimaging method which provides valuable information concerning the localization of regions generating IEDs (20, 21). It is a useful diagnostic tool to guide pre-surgical evaluation of refractory epilepsy, assisting in depth electrode implantation (22) and consistent with epileptogenic tissue (23). EEG-fMRI had also been successfully used for localizing the EZ in patients with cortical and subcortical malformations such as focal cortical dysplasia (24), cortical tubers (25) and polymicrogyria [PMG; (26)]. Notwithstanding, the efficacy of this method is still under investigation and its sensitivity to epileptic sources is reportedly equal to or lower than other diagnostic methods (27). Recent work suggests the sensitivity of EEG-fMRI may be enhanced by taking into account the temporal dynamics of epileptic activity (28). Epileptogenic lesions such as PMG may affect IED dynamics in predictable ways (29), allowing to test the ability of EEG-fMRI to map IED pathways over time.

IED dynamics in PSPMG have been studied in animal models but are difficult to assess in humans non-invasively. This may be due to source epileptic structures being located deep in the brain in unorganized cortical structures not able to produce sufficiently strong dipoles as to be observed from the scalp (30). Thus, it is not always clear whether the fields observed by scalp EEG and MEG are related to the source of the activity or due to its spread to neighboring superficial and more organized cortical structures. The purpose of the current study was to examine the dynamics of IEDs as reflected in EEG-fMRI BOLD activations correlated with observed IEDs on the scalp of patients with PSPMG. We hypothesized that IEDs observed on the scalp would correspond to IED spread to superficial cortical structures while BOLD activity within the PMG could be observed in the time preceding IED appearance on scalp recordings and reveal their focal sources.

METHODS

Patients

Included in this study are all four patients diagnosed with PSPMG and refractory epileptic seizures which underwent an EEG-fMRI scan at the Tel Aviv Sourasky Medical Center between March 2014 and June 2019. Patients' clinical and imaging findings are detailed below and summarized in **Table 1**. Neuroimaging results include scalp EEG seizure onset, main MRI finding, major dipole concentration on MEG, significant PET results and peak BOLD activations observed during EEG-fMRI. Activations are reported at two time points: 2.25 s after IED appearance on scalp EEG, corresponding to pre-IED activity; and 5.25 s after IED appearance on scalp EEG, corresponding to IED initiation according to the standard hemodynamic response function [HRF; (31)].

Patient 1 is a right-handed female aged 24 suffering from epilepsy since the age of 13 involving frequent complex partial seizures. Ictal EEG shows right frontotemporal onset with fast contralateral spread. Neurological deficits include memory loss and difficulties with word retrieval, concentration and motivation. MRI shows a right PSPMG with pre-central and post-central involvement and right hemispheric atrophy. Interictal PET scan showed diffuse hypometabolism. Interictal MEG sources were found in right temporo-parietal areas.

Patient 2 is a right-handed female aged 19 suffering from epilepsy since the age of 10. Ictal semiology is concordant with right hemisphere onset with or without secondary generalization. She suffers from left sided hemiparesis from childhood. MRI shows diffuse right PSPMG including pre and post central areas with loss of volume in the right hemisphere. PET shows right temporo-parietal hypometabolism and left temporal hypometabolism. MEG shows right fronto-temporal dipoles.

Patient 3 is a right-handed female aged 26 suffering from epilepsy since the age of 16. She has a mild left hemiparesis and focal seizures originating from the right antero-mid temporal areas. Right PSPMG is seen on MRI with loss of volume in the right hemisphere and specifically in right hippocampus. MEG reveals right temporal dipole concentration and PET shows right temporo-parieto-occipital and left temporal hypometabolism.

Patient 4 is a right-handed female aged 42 suffering from early onset epilepsy which subsided for several years. At the age of 19 seizures reappeared characterized as focal seizures with impaired consciousness accompanied by right temporal

TABLE 1 | Summary of patient details and main neuroimaging findings.

Patient	Age (years)	Onset (years)	Hand-edness	Ictal EEG onset	MRI	MEG	PET	Pre-IED peak activity	IED peak activity
1	24	13	R	R FT	R PSPMG	R TP	Diff (HM)	R In	R IFG R In
2	19	10	R	R F	R PSPMG	R FT	L T (HM)	R SFG R Op	R SFG
3	26	16	R	R FT	R PSPMG	R T	R TPO L T (HM)	R In*	R MTG R STG
4	40	19**	R	R T	R PSPMG R Schize- ncephaly	–	RT (HM)	R TOp	R TOp

R, right; L, left; PSPMG, perisylvian polymicrogyria; T, temporal; O, occipital; P, parietal; F, frontal; In, insula; Op, operculum; IFG, inferior frontal gyrus; SFG, superior frontal gyrus; MTG, medial temporal gyrus; STG, superior temporal gyrus; HM, hypometabolism; Diff, diffuse.

**Not significant after FWE correction.*

***Onset age of typical seizures. Patient reported childhood absence seizures as well.*

sharp and slow waves on EEG. MRI shows right sided PSPMG and schizencephaly, and a PET scan points to right lateral temporal hypometabolism.

Data Acquisition

The study was approved by the Tel-Aviv Sourasky Medical Center Ethical Review Board. Written informed consent for participation in the study was obtained from all patients.

All patients underwent EEG-fMRI scans using the dual array EEG (daEEG) method for improved EEG signal artifact identification and removal. EEG was performed using a 64-channel recording system (**Figure 1**) based on an in-house adaptation of an MR compatible 64-electrode EEG cap (Brain Products GmbH, Gilching, Germany). For a full description of the adapted system see (32).

MRI scans for patients 1–3 *(4)* were performed in a 3.0 T MRI scanner [GE Signa EXCITE *(Siemens Prisma system)*] using a body transmitter coil and an eight *(twenty)* channel head receiver coil. The EEG-fMRI recordings were performed in 20 *(10)* m sessions of scanning; 3–5 *(8)* such sessions were recorded during each patient scan. Patients were instructed to lie still and remain at rest. The helium pump was turned off during the recording as well as air conditioning inside the bore. A T2*- weighted, gradient echo, echo planar imaging (EPI) sequence was used for recording the fMRI images (TR/TE/flip angle: 3000/35/90). Thirty-nine *(forty)* axial slices (thickness/gap: 3/0) were collected (FOV: 22 × 22 cm; matrix size: 128 × 128). In addition, a high resolution T1-weighted 3D (1 × 1 × 1 mm) volume was obtained using spoiled gradient echo [SPGR *(MPRAGE)*] sequence.

EEG Evaluation

EEG data analysis was performed using EEGLAB software (33). Initial EEG processing included gradient interference suppression (FMRIB plug-in for EEGLAB, provided by the University of Oxford Centre for Functional MRI of the Brain), down-sampling from 5,000 to 250 Hz and band-pass filtering to 0.5–40 Hz. After recalculating the data according to the daEEG method, ICA was applied in order to identify and separate components which are differently distributed between the channels. The effect of motion artifacts is larger in data corresponding to measurements between electrodes connected to different bundles in comparison to electrodes connected to the same bundle (**Figure 1**). The ICA components considered as artifact-affected were removed (32). In order to account for signal changes associated with cardiac activity, the components with high correlation to the recorded ECG trace were removed as well.

Detection of IEDs from the EEG traces after artifact removal was performed manually by a neurologist experienced in EEG interpretation. IEDs of predominant topography and morphology were selected for further analysis. Epochs concurrent with large EEG artifacts were regressed out of the fMRI analysis using the Artifact Detection Tools (ART) toolbox (nitrc.org/projects/artifact_detect/).

fMRI Analysis

Data analysis was performed using SPM12 software (34). Preprocessing included slice timing correction, 3D motion correction and co-registration to the anatomical image. No normalization to an anatomical atlas was performed. The data was spatially smoothed with an 8 mm full width at half maximum (FWHM) Gaussian kernel. For each session, the first six functional volumes were excluded from analysis. Functional EPI data were automatically aligned and co-registered with 3D anatomical data and manually corrected if necessary. Standard SPM event related fMRI analysis was performed with a general linear model, using the timing of the detected EEG epileptiform waveforms as events. To follow the dynamics of the epileptic events, predictors were modeled with three delays: the standard delay (HRF peak at 5.25 s after the event, corresponding to IED appearance), −3 s delay (HRF peak at 2.25 s after event, corresponding to pre-IED activity) and +3 s delay (HRF peak at 8.25 s after event, corresponding to post-IED activity). In each analysis voxel clusters were significantly active at $p < 0.05$ after Family-Wise Error correction (FWE) and a minimum cluster size of 50 adjacent voxels. Earlier peaks showed weaker and more focal activations as expected, thus any cluster of activation composed of over 10 adjacent significant voxels was reported. If no clusters were found significant for standard or early peaks, clusters of >50 adjacent voxels at an uncorrected $p < 0.005$ threshold are reported. Sub-threshold clusters within white matter regions were not reported.

RESULTS

See **Supplementary Material** for full details of all detected activation clusters (**Table A1** in **Supplementary Material**) and

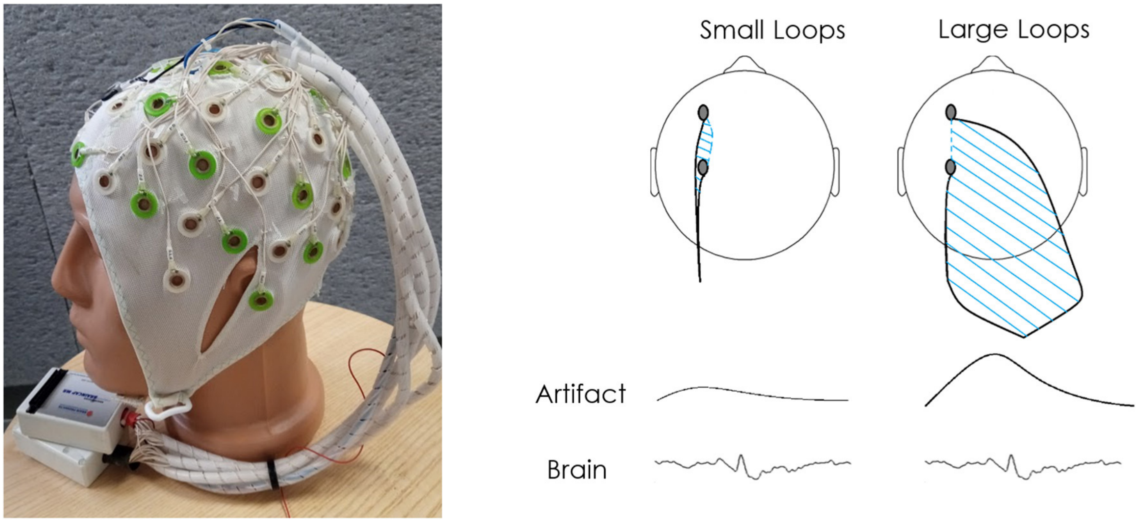

FIGURE 1 | Dual array design and concept. **(A)** The electrode cables are arranged into bundles according to two sets of intersecting lines: longitudinal and transverse. The bundles are grouped into two braids of cables so that the bundles from two neighboring lines travel to the different braids. Each braid is connected to a separate 32 channel referential MR-compatible EEG amplifier. In the dual array arrangement applied in this study, adjacent bundles were sent to a distal amplifier location to cause an increase in the area between electrode cables. A comparison of the bundles is used to differentiate motion artifact from brain signal. **(B)** This wire arrangement is used in order to reduce as much as possible the area within the loop created by two adjacent electrode wires along a single bundle (along bundles) and increase the area within the loop created by adjacent electrodes of different bundles (across bundles). Thus, while the true brain signal should be recorded similarly by adjacent electrodes, motion artifacts should differ depending on the loop created by the bundle each electrode is connected to, allowing separation between signal and noise. For a more detailed explanation of this setup see Klovatch-Podlipsky et al. (32).

for representative IED traces of each patient (**Figure A1** in **Supplementary Material**).

Patient 1

During the 40-min recording, 28 spike-and-wave complexes, 11 poly-spike clusters lasting up to 3.5 s and 180 slow waves lasting up to 8 s (1.13 ± 1.36) were detected over right and left fronto-centro-parietal areas. Only spike complexes and clusters were used for the subsequent analyses. Standard delay generated peak activation ($T = 8.37$) at the right inferior frontal gyrus, anterior to the malformation (**Figure 2**, P1). The FWE corrected BOLD map included the inferior frontal gyrus and insula (areas within the malformation). At −3 s delay the peak activation ($T = 5.51$) was at the right anterior insula (within the malformation, **Figure 2**, P1) which survived FWE correction. At +3 s delay no significant activation was found, but five clusters of deactivations were observed within the malformation (right pre-central area, right posterior insula) and outside of it in the left temporal operculum, left post central gyrus and left posterior insula all with a peak T-score between 5 and 5.6.

Patient 2

In the 40-min recording 16 spike-and-wave complexes and 25 poly-spike clusters lasting up to 94 s were detected over right fronto-centro-parietal areas. Standard delay generated peak activation at the right anterior superior frontal gyrus ($T = 6.2$). The related FWE corrected BOLD map included this cluster only (**Figure 2**, P2). Peak deactivation was found in a bilateral occipital cluster ($T = 7.0$). FWE corrected deactivation maps included additional clusters within the malformation (**Table A1** in **Supplementary Material**). At −3 s delay the peak activation ($T = 6.3$) was at the right superior frontal gyrus and a second cluster in the right parietal operculum cortex within the malformation. The related FWE corrected BOLD map consisted of the described clusters. Two deactivation clusters were found in the right and left occipital lobes. At +3 s delay no significant activation was found, five clusters of deactivations were observed.

Patient 3

In the 20-min recording 108 spike-and-wave complexes were detected over right centroparietal areas. Standard delay generated peak activation ($T = 6.21$) outside the lesion at the right middle temporal gyrus (**Figure 2**, P3) along with a superior temporal gyrus activation with similar statistics ($T = 6.19$) and both survived FWE correction. No additional activation or deactivations were found. At −3 s delay the peak activation ($T = 3.76$) was at the right anterior insula. No cluster survived FWE correction, but at $p = 0.005$ without correction this cluster could be observed along with three additional clusters in the right posterior insula, right posterior temporal cortex and a small left occipital cluster. No significant deactivations were found. At +3 s delay no significant activations or deactivations were found.

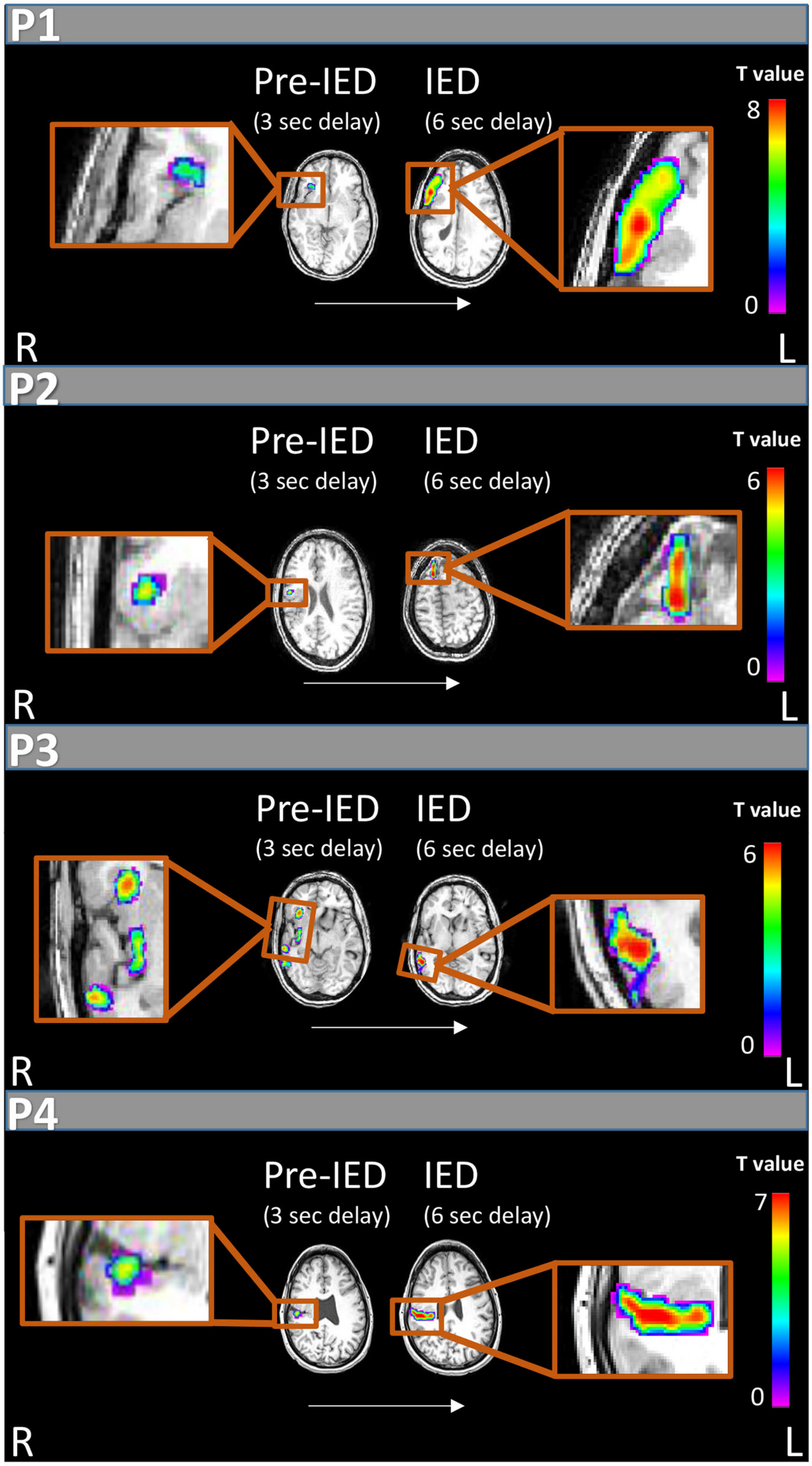

FIGURE 2 | IED and pre-IED correlated fMRI maps for patients 1-4. For each patient areas of peak activation are marked at two time points: 6 s after IED appearance on scalp EEG, showing activity correlated with IEDs according to the standard delay of the HRF peak (right), and 3 s after scalp IED appearance on EEG which shows pre-IED activity (left). All patients show weaker and earlier pre-IED activations within the PMG and later stronger activations on the border of the malformation or outside of it correlated with IED appearance.

Patient 4

In the 60-min recording 62 spike-and-wave complexes were detected over right temporal areas. Standard delay after FWE correction generated peak activation ($T = 7.9$) at the right temporal operculum within a widespread cluster extending to parietal and frontal operculum (**Figure 2**, P4). Three seconds earlier a peak activation ($T = 5.61$) appeared within a smaller cluster within the temporal operculum. Deactivations correlated with a standard delay were seen in bilateral frontal areas. At +3 s delay one activation was seen at the right post-central gyrus and several deactivation clusters were detected mostly around bilateral frontal areas (**Table A1** in **Supplementary Material**).

DISCUSSION

The origin of both ictal and interictal activity in PMG has been debated in the literature with findings pointing to an electrophysiological source within the PMG (12) or outside of it (13). In the current study, we set out to evaluate this disagreement by analyzing the simultaneous EEG-fMRI scan results of four patients with unilateral PSPMG, before, during and after the appearance of IED on scalp EEG. All four patients presented BOLD activations within and surrounding the lesion. When applying the HRF with the standard delay, the maximum BOLD activation was found outside or on the borders of the cortical malformation (premotor cortex, superior frontal gyrus, middle temporal gyrus and parietal operculum for patients 1,2,3, and 4, respectively, **Figure 2**) and corresponded to the maximum BOLD activation overall, considering all evaluated time shifts. Interestingly, we found focal activations correlated with an HRF peak shifted by −3 s in relation to the standard HRF model, and these activations were within the PMG in all four patients (insula in patients 1 and 3, and operculum in patients 2 and 4).

Stutterd and Leventer (35) illustrated that polymicrogyria is highly heterogeneous and the most poorly-delineated among the more common malformations of cortical development. The initial result with the standard HRF seems to support the line of both animal and human studies placing the source of epileptic activity outside of the anatomical malformation. For example, Jacobs et al. (13) proposed that cortical afferents are unable to find appropriate targets within the malformed region and may instead synapse in the adjacent paramicrogyral area, thus suggesting that there is an increase in the number of functional excitatory synapses in the paramicrogyral cortex causing seizures. One previous study evaluated EEG-fMRI in patients with PMG (26) and reported variable maximum BOLD locations: of the 13 analyses showing activations in nine patients, four were inside the lesion, four on the edge and five outside the lesion's boundaries. This discrepancy may stem from the heterogeneity of pathologies evaluated including bilateral, unilateral, frontal and parieto-occipital PMG. The reported variability may have also resulted from the grouping of multiple time delays: at each voxel, the maximum t value was taken from four t-maps created using four hemodynamic response functions with peaks at 3, 5, 7, and 9 s. Such an analysis has the potential to obscure earlier and possibly weaker activations.

In this work, we thus concentrated on a homogenous group of patients with unilateral PSPMG. Indeed, we found focal activations in the analysis correlated with an HRF peak shifted by −3 s in relation to the standard HRF model, and these activations were within the PMG in all four patients (insula in patients 1 and 3, and operculum in patients 2 and 4). On this basis, we propose that IEDs in PSPMG initiate in a relatively small cortical structure within the lesion itself. The stronger activations observed with the standard delay are suggested to represent the shift and expansion of the interictal generators to adjacent, more organized or superficial cortical structures, as these structures are more capable of producing currents detected on the scalp. BOLD responses preceding interictal activity have been previously observed and discussed (36–39). These studies point to the significance of such early, often weaker BOLD responses and their potential clinical relevance. Jacobs et al. (36) suggested that early hemodynamic activity seen in the spike field prior to scalp EEG result from neuronal activity invisible to scalp EEG which is more focal and which systematically leads to a more widespread response. This early activity has also been associated with other metabolic events preceding the IED and suggested to be associated with its generation (36, 38).

Several models have been proposed for the epileptogenicity of the PMG cortex. Takano (12) found reduced parvalbumin-immunoreactive interneurons within the medial parts of the PMG compared to more lateral parts. Stouffer et al. (40) report malfunction of the cytoskeleton caused by mutations of neural migration genes leading to an excitatory-inhibitory imbalance. Our study does not allow the evaluation of such hypotheses and further research, primarily with animal models, is necessary to improve our understanding of these mechanisms. Moreover, our study only examines IED related activity, which may be governed by a divergent neuro-electrical circuit as compared to that which governs ictal phenomena (41). Nevertheless, this result implies several mechanistic traits of the processes underlying epileptic seizures secondary to PSPMG. From the spread of both activations and deactivations we observed (with the standard delay and +3 s delays), it appears that a complex interaction of network nodes within the PMG and outside it is involved during IEDs. Such a heterogeneous network of cortical activation has also been reported in human intracranial studies. Ramantani (42) found a network of interictal and ictal activity including the PMG and medial temporal cortex and Chassoux et al. (14) reported epileptogenicity in the PMG cortex extending beyond the visible abnormality.

Our work further suggests that the focal activity preceding later widespread interictal events may be overlooked using standard EEG-fMRI. Such activity may also be undetected with iEEG as shown in one study which explored the area of early BOLD activation with depth electrodes. In this study the early focal activity was correlated with interictal events on iEEG in only one of four patients examined (38). The authors suggest this finding may point to the early BOLD activations reflecting non-synchronized neuronal activity or non-neuronal mechanisms. In addition, while intracranial recordings offer an opportunity to directly record local fields, they have the disadvantage of under-sampling relevant areas. As resective surgery was not performed on these patients, this study cannot verify whether the reported initial areas of activation indeed identify the epileptogenic zone. Further studies using intracranial recordings and clinical outcomes of surgery are needed to address this question. Notwithstanding, these results support the exploration of interictal dynamics at the timescale of BOLD activity for inferring patterns of epileptic spread from the source areas.

When considering the presented results and their interpretation it is important to note several limitations of the applied methodology. Primarily, the hemodynamic response itself may vary within and between patients, reflecting differences in the BOLD signal among brain areas and conditions, as suggested by previous studies (43, 44). Such differences could also account for the activity associated with the different HRF peaks, perhaps pointing to sources of several interictal event types and not the shift of a specific IED source. In addition, the averaged IEDs may themselves carry information regarding the location of earlier activity as suggested in studies which use high resolution source imaging with MEG or EEG data (1, 18). In future studies it may thus be interesting to compare the sources of averaged IEDs recorded by EEG or MEG to the hemodynamic activations seen with fMRI. In these cases, the appearance of early focal activation clusters within the PMG may still be indicative of relevant treatment targets as previously discussed. Our finding of preceding activations within the PSPMG support the notion that IEDs initiate inside the PMG and propagate to neighboring cortex. As well as improving our understanding of epilepsy related processes in PMG, this finding has the potential to assist in tailoring invasive treatments: from directing depth electrode implantation, to guiding resection and neuro-stimulation probes. Finally, this finding supports the use of EEG-fMRI for tracing IED dynamics with potential benefits for improved localization of epileptogenic areas.

DATA AVAILABILITY STATEMENT

The raw data supporting the conclusions of this article will be made available by the authors, without undue reservation.

ETHICS STATEMENT

The studies involving human participants were reviewed and approved by Tel-Aviv Sourasky Medical Center Ethical Review Board. The patients/participants provided their written informed consent to participate in this study. Written informed consent was obtained from the individual(s) for the publication of any potentially identifiable images or data included in this article.

AUTHOR CONTRIBUTIONS

NC, TG, and YE carried out data analysis and wrote the manuscript. TG suggested the project. MM, FF, TH, NC, and TG supervised the work. OA, MM, and FF provided clinical and diagnostic information. FF, TG, OA, TH, and GG revised the manuscript. All authors contributed to the article and approved the submitted version.

SUPPLEMENTARY MATERIAL

The Supplementary Material for this article can be found online at: https://www.frontiersin.org/articles/10.3389/fneur.2021.658239/full#supplementary-material

REFERENCES

1. Plummer C, Vogrin SJ, Woods WP, Murphy MA, Cook MJ, Liley DTJ. Interictal and ictal source localization for epilepsy surgery using high-density EEG with MEG: a prospective long-term study. *Brain.* (2019) 142:932–51. doi: 10.1093/brain/awz015
2. Wilke C, Drongelen W van, Kohrman M, He B. Identification of epileptogenic foci from causal analysis of ECoG interictal spike activity. *Clin Neurophysiol.* (2009) 120:1449–56. doi: 10.1016/j.clinph.2009.04.024
3. Karoly PJ, Freestone DR, Boston R, Grayden DB, Himes D, Leyde K, et al. Interictal spikes and epileptic seizures: their relationship and underlying rhythmicity. *Brain.* (2016) 139:1066–78. doi: 10.1093/brain/aww019
4. De Curtis M, Avanzini G. Interictal spikes in focal epileptogenesis. *Prog Neurobiol.* (2001) 63:541–67. doi: 10.1016/S0301-0082(00)00026-5
5. Jobst BC, Cascino GD. Resective epilepsy surgery for drug-resistant focal epilepsy: a review. *J Am Med Assoc.* (2015) 313:285–93. doi: 10.1001/jama.2014.17426
6. Vakharia VN, Duncan JS, Witt JA, Elger CE, Staba R, Engel J. Getting the best outcomes from epilepsy surgery. *Ann Neurol.* (2018) 83:676–90. doi: 10.1002/ana.25205
7. Khoo HM, Hao Y, von Ellenrieder N, Zazubovits N, Hall J, Olivier A, et al. The hemodynamic response to interictal epileptic discharges localizes the seizure-onset zone. *Epilepsia.* (2017) 58:811–23. doi: 10.1111/epi.13717
8. Sisodiya SM. Malformations of cortical development: burdens and insights from important causes of human epilepsy. *Lancet Neurol.* (2004) 3:29–38. doi: 10.1016/S1474-4422(03)00620-3
9. Guerrini R, Parrini E. Neuronal migration disorders. *Neurobiol Dis.* (2010) 38:154–66. doi: 10.1016/j.nbd.2009.02.008
10. Caraballo R, Cersósimo R, Fejerman N. A particular type of epilepsy in children with congenital hemiparesis associated with unilateral polymicrogyria. *Epilepsia.* (1999) 40:865–71. doi: 10.1111/j.1528-1157.1999.tb00792.x
11. Takano T, Matsuwake K, Yoshioka S, Takeuchi Y. Congenital polymicrogyria including the perisylvian region in early childhood. *Congenit Anom.* (2010) 50:64–7. doi: 10.1111/j.1741-4520.2009.00253.x
12. Takano T. Seizure susceptibility in polymicrogyria: clinical and experimental approaches. *Epilepsy Res.* (2011) 96:1–10. doi: 10.1016/j.eplepsyres.2011.06.010
13. Jacobs KM, Hwang BJ, Prince DA. Focal epileptogenesis in a rat model of polymicrogyria. *J Neurophysiol.* (1999) 81:159–73. doi: 10.1152/jn.1999.81.1.159
14. Chassoux F, Landre E, Rodrigo S, Beuvon F, Turak B, Semah F, et al. Intralesional recordings and epileptogenic zone in focal polymicrogyria. *Epilepsia.* (2008) 49:51–64. doi: 10.1111/j.1528-1167.2007.01267.x
15. Maillard L, Ramantani G. Epilepsy surgery for polymicrogyria: a challenge to be undertaken. *Epileptic Disord.* (2018) 20:319–38. doi: 10.1684/epd.2018.1004
16. Cossu M, Pelliccia V, Gozzo F, Casaceli G, Francione S, Nobili L, et al. Surgical treatment of polymicrogyria-related epilepsy. *Epilepsia.* (2016) 57:2001–10. doi: 10.1111/epi.13589

17. Maillard LG, Tassi L, Bartolomei F, Catenoix H, Dubeau F, Szurhaj W, et al. Stereoelectroencephalography and surgical outcome in polymicrogyria-related epilepsy: a multicentric study. *Ann Neurol.* (2017) 82:781–94. doi: 10.1002/ana.25081
18. Lantz G, Spinelli L, Seeck M, De Peralta Menendez RG, Sottas CC, Michel CM. Propagation of interictal epileptiform activity can lead to erroneous source localizations: a 128-channel EEG mapping study. *J Clin Neurophysiol.* (2003) 20:311–9. doi: 10.1097/00004691-200309000-00003
19. Conrad EC, Tomlinson SB, Wong JN, Oechsel KF, Shinohara RT, Litt B, et al. Spatial distribution of interictal spikes fluctuates over time and localizes seizure onset. *Brain.* (2020) 143:554–69. doi: 10.1093/brain/awz386
20. Abreu R, Leal A, Figueiredo P. EEG-informed fMRI: a review of data analysis methods. *Front Hum Neurosci.* (2018) 12:29. doi: 10.3389/fnhum.2018.00029
21. Bénar CG, Gross DW, Wang Y, Petre V, Pike B, Dubeau F, et al. The BOLD response to interictal epileptiform discharges. *Neuroimage.* (2002) 17:1182–92. doi: 10.1006/nimg.2002.1164
22. Zijlmans M, Huiskamp G, Hersevoort M, Seppenwoolde JH, Van Huffelen AC, Leijten FSS. EEG-fMRI in the preoperative work-up for epilepsy surgery. *Brain.* (2007) 130:2343–53. doi: 10.1093/brain/awm141
23. van Houdt PJ, de Munck JC, Leijten FSS, Huiskamp GJM, Colon AJ, Boon PAJM, et al. EEG-fMRI correlation patterns in the presurgical evaluation of focal epilepsy: a comparison with electrocorticographic data and surgical outcome measures. *Neuroimage.* (2013) 75:238–48. doi: 10.1016/j.neuroimage.2013.02.033
24. Pittau F, Ferri L, Fahoum F, Dubeau F, Gotman J. Contributions of EEG-fMRI to assessing the epileptogenicity of focal cortical dysplasia. *Front Comput Neurosci.* (2017) 11:8. doi: 10.3389/fncom.2017.00008
25. Jacobs J, Rohr A, Moeller F, Boor R, Kobayashi E, LeVan Meng P, et al. Evaluation of epileptogenic networks in children with tuberous sclerosis complex using EEG-fMRI. *Epilepsia.* (2008) 49:816–25. doi: 10.1111/j.1528-1167.2007.01486.x
26. Kobayashi E, Bagshaw AP, Jansen A, Andermann F, Andermann E, Gotman J, et al. Intrinsic epileptogenicity in polymicrogyric cortex suggested by EEG-fMRI BOLD responses. *Neurology.* (2005) 64:1263–6. doi: 10.1212/01.WNL.0000154640.23656.A3
27. Rossi Sebastiano D, Tassi L, Duran D, Visani E, Gozzo F, Cardinale F, et al. Identifying the epileptogenic zone by four non-invasive imaging techniques versus stereo-EEG in MRI-negative pre-surgery epilepsy patients. *Clin Neurophysiol.* (2020) 131:1815–23. doi: 10.1016/j.clinph.2020.05.015
28. Iannotti GR, Preti MG, Grouiller F, Carboni M, De Stefano P, Pittau F, et al. Modulation of epileptic networks by transient interictal epileptic activity: a dynamic approach to simultaneous EEG-fMRI. *NeuroImage Clin.* (2020) 28:102467. doi: 10.1016/j.nicl.2020.102467
29. Tyvaert L, Hawco C, Kobayashi E, LeVan P, Dubeau F, Gotman J. Different structures involved during ictal and interictal epileptic activity in malformations of cortical development: an EEG-fMRI study. *Brain.* (2008) 131:2042–60. doi: 10.1093/brain/awn145
30. Lopes Da Silva F. Functional localization of brain sources using EEG and/or MEG data: volume conductor and source models. *Magn Reson Imaging.* (2004) 22:1533–8. doi: 10.1016/j.mri.2004.10.010
31. Glover GH. Deconvolution of impulse response in event-related BOLD fMRI. *Neuroimage.* (1999) 9:416–29. doi: 10.1006/nimg.1998.0419
32. Klovatch-Podlipsky I, Gazit T, Fahoum F, Tsirelson B, Kipervasser S, Kremer U, et al. Dual array EEG-fMRI: an approach for motion artifact suppression in EEG recorded simultaneously with fMRI. *Neuroimage.* (2016) 142:674–86. doi: 10.1016/j.neuroimage.2016.07.014
33. Delorme A, Makeig S. EEGLAB: an open-source toolbox for analysis of single-trial EEG dynamics. *J Neurosci Methods.* (2004) 134:9–21. doi: 10.1016/j.jneumeth.2003.10.009
34. Kiebel SJ, Friston KJ. Statistical parametric mapping for event-related potentials: I. Generic considerations. *Neuroimage.* (2004) 22:492–502. doi: 10.1016/j.neuroimage.2004.02.012
35. Stutterd CA, Leventer RJ. Polymicrogyria: a common and heterogeneous malformation of cortical development. *Am J Med Genet C Semin Med Genet.* (2014) 166C:227–39. doi: 10.1002/ajmg.c.31399
36. Jacobs J, LeVan P, Moeller F, Boor R, Stephani U, Gotman J, et al. Hemodynamic changes preceding the interictal EEG spike in patients with focal epilepsy investigated using simultaneous EEG-fMRI. *Neuroimage.* (2009) 45:1220–31. doi: 10.1016/j.neuroimage.2009.01.014
37. Hawco CS, Bagshaw AP, Lu Y, Dubeau F, Gotman J. BOLD changes occur prior to epileptic spikes seen on scalp EEG. *Neuroimage.* (2007) 35:1450–8. doi: 10.1016/j.neuroimage.2006.12.042
38. Pittau F, Levan P, Moeller F, Gholipour T, Haegelen C, Zelmann R, et al. Changes preceding interictal epileptic EEG abnormalities: comparison between EEG/fMRI and intracerebral EEG. *Epilepsia.* (2011) 52:1120–9. doi: 10.1111/j.1528-1167.2011.03072.x
39. Rollings DT, Assecondi S, Ostwald D, Porcaro C, McCorry D, Bagary M, et al. Early haemodynamic changes observed in patients with epilepsy, in a visual experiment and in simulations. *Clin Neurophysiol.* (2016) 127:245–53. doi: 10.1016/j.clinph.2015.07.008
40. Stouffer MA, Golden JA, Francis F. Neuronal migration disorders: focus on the cytoskeleton and epilepsy. *Neurobiol Dis.* (2016) 92:18–45. doi: 10.1016/j.nbd.2015.08.003
41. Jensen MS, Yaari Y. The relationship between interictal and ictal paroxysms in an in vitro model of focal hippocampal epilepsy. *Ann Neurol.* (1988) 24:591–8. doi: 10.1002/ana.410240502
42. Ramantani G, Koessler L, Colnat-Coulbois S, Vignal JP, Isnard J, Catenoix H, et al. Intracranial evaluation of the epileptogenic zone in regional infrasylvian polymicrogyria. *Epilepsia.* (2013) 54:296–304. doi: 10.1111/j.1528-1167.2012.03667.x
43. Kang JK, Bénar CG, Al-Asmi A, Khani YA, Pike GB, Dubeau F, et al. Using patient-specific hemodynamic response functions in combined EEG-fMRI studies in epilepsy. *Neuroimage.* (2003) 20:1162–70. doi: 10.1016/S1053-8119(03)00290-8
44. Bagshaw AP, Aghakhani Y, Bénar CG, Kobayashi E, Hawco C, Dubeau F, et al. EEG-fMRI of focal epileptic spikes: analysis with multiple haemodynamic functions and comparison with gadolinium-enhanced MR angiograms. *Hum Brain Mapp.* (2004) 22:179–92. doi: 10.1002/hbm.20024

Conflict of Interest: FF, TH, and MM are authors of patent: Device for use in electro-biological signal measurement in the presence of a magnetic field, WO2012046237, 12.04.2012.

The remaining authors declare that the research was conducted in the absence of any commercial or financial relationships that could be construed as a potential conflict of interest.

frontiers in Neurology

ORIGINAL RESEARCH
published: 10 June 2021
doi: 10.3389/fneur.2021.671890

Altered Relationship Between Heart Rate Variability and fMRI-Based Functional Connectivity in People With Epilepsy

Michalis Kassinopoulos[1,2]*, Ronald M. Harper*[3,4]*, Maxime Guye*[5,6]*, Louis Lemieux*[1,2] *and Beate Diehl*[1,2]*

[1] Department of Clinical and Experimental Epilepsy, Institute of Neurology, University College London, London, United Kingdom, [2] Epilepsy Society, Buckinghamshire, United Kingdom, [3] Brain Research Institute, University of California, Los Angeles, Los Angeles, CA, United States, [4] Department of Neurobiology, David Geffen School of Medicine, University of California, Los Angeles, Los Angeles, CA, United States, [5] Aix Marseille Univ, CNRS, CRMBM, Marseille, France, [6] APHM, Hôpital Universitaire Timone, CEMEREM, Marseille, France

Edited by:
Maria Centeno,
University College London,
United Kingdom

Reviewed by:
Piergiorgio Salvan,
University of Oxford, United Kingdom
Friederike Moeller,
Great Ormond Street Hospital for
Children NHS Foundation Trust,
United Kingdom

***Correspondence:**
Beate Diehl
b.diehl@ucl.ac.uk

Specialty section:
This article was submitted to
Applied Neuroimaging,
a section of the journal
Frontiers in Neurology

Received: *24 February 2021*
Accepted: *18 May 2021*
Published: *10 June 2021*

Citation:
Kassinopoulos M, Harper RM, Guye M, Lemieux L and Diehl B (2021) Altered Relationship Between Heart Rate Variability and fMRI-Based Functional Connectivity in People With Epilepsy. Front. Neurol. 12:671890. doi: 10.3389/fneur.2021.671890

Background: Disruptions in central autonomic processes in people with epilepsy have been studied through evaluation of heart rate variability (HRV). Decreased HRV appears in epilepsy compared to healthy controls, suggesting a shift in autonomic balance toward sympathetic dominance; recent studies have associated HRV changes with seizure severity and outcome of interventions. However, the processes underlying these autonomic changes remain unclear. We examined the nature of these changes by assessing alterations in whole-brain functional connectivity, and relating those alterations to HRV.

Methods: We examined regional brain activity and functional organization in 28 drug-resistant epilepsy patients and 16 healthy controls using resting-state functional magnetic resonance imaging (fMRI). We employed an HRV state-dependent functional connectivity (FC) framework with low and high HRV states derived from the following four cardiac-related variables: 1. RR interval, 2. root mean square of successive differences (RMSSD), 4. low-frequency HRV (0.04–0.15 Hz; LF-HRV) and high-frequency HRV (0.15–0.40 Hz; HF-HRV). The effect of group (epilepsy vs. controls), HRV state (low vs. high) and the interactions of group and state were assessed using a mixed analysis of variance (ANOVA). We assessed FC within and between 7 large-scale functional networks consisting of cortical regions and 4 subcortical networks, the amygdala, hippocampus, basal ganglia and thalamus networks.

Results: Consistent with previous studies, decreased RR interval (increased heart rate) and decreased HF-HRV appeared in people with epilepsy compared to healthy controls. For both groups, fluctuations in heart rate were positively correlated with BOLD activity in bilateral thalamus and regions of the cerebellum, and negatively correlated with BOLD activity in the insula, putamen, superior temporal gyrus and inferior frontal gyrus. Connectivity strength in patients between right thalamus and ventral attention network (mainly insula) increased in the high LF-HRV state compared to low LF-HRV; the opposite trend appeared in healthy controls. A similar pattern emerged for connectivity between the thalamus and basal ganglia.

Conclusion: The findings suggest that resting connectivity patterns between the thalamus and other structures underlying HRV expression are modified in people with drug-resistant epilepsy compared to healthy controls.

Keywords: state-dependent functional connectivity, sympathovagal balance, SUDEP, thalamic connectivity, ventral attention network, insula cortex

INTRODUCTION

Heart rate varies on a moment-to-moment basis in response to changing physiological demands, and is regulated by sympathetic and parasympathetic components of the autonomic nervous system (ANS). Evaluation of the momentary changes in heart rate variability (HRV) can provide insights into the interplay of central mechanisms controlling sympathetic and parasympathetic (vagal) activity (1, 2). A shift toward parasympathetic dominance is typically accompanied by heart rate declines and increased HRV; whereas, increased sympathetic dominance is typically associated with an accelerated heart rate and decreased HRV [although deviations from this generality occur (3)]. Considerable evidence exists that HRV provides an indication of sympathovagal balance and can be useful as a marker for certain cardiovascular diseases (4), mortality, and sudden death (5).

Epilepsy is accompanied by significantly different patterns of HRV (6). A lower interictal HRV is often reported in drug-resistant epilepsy, suggesting a shift toward sympathetic predominance (6–9). In addition, a link between peri-ictal HRV and major motor seizure severity (10) has been outlined, as well as an indication of seizure reduction following vagal nerve stimulation in patients with drug-resistant epilepsy (11). HRV determination of low parasympathetic activity and increased risk of sudden unexpected death in epilepsy SUDEP has been described (12, 13), as well as altered circadian rhythms of HRV in epilepsy (14, 15); the latter finding may explain the larger number of night-time SUDEP cases (16). However, a poor understanding of the mechanisms underlying expression of cardiac functions in epilepsy hampers interpretation of alterations in brain regulatory sites controlling HRV and the potential to gain insights into dysfunctions within those processes.

Functional magnetic resonance imaging (fMRI), a non-invasive tool for probing brain activity and functional connectivity (FC), has been used to study the neural substrates of autonomic regulation (17–20). Initial studies primarily relied on tasks to excite the ANS (21–26), while subsequent studies have used resting-state fMRI (27–29), which has a benefit of not being confounded by task-related changes in local brain activity and FC. Differences in HRV across participants as well as fluctuations in HRV within-individuals have been related to spontaneous regional blood-oxygen-level-dependent (BOLD) fluctuations and connectivity between distinct regions (27–29). Regions found in fMRI studies to be associated with autonomic regulation, such as the anterior cingulate (ACC), medial prefrontal (mPFC) and insular cortices, form part of the central autonomic network (CAN) described in preclinical studies, a system of brain structures involved in ANS functions (30, 31).

Functional connectivity measures between brain sites are altered in people with epilepsy (32–36); however, it is unclear whether these alterations are linked to impaired cardiac regulation. Here, we investigated alterations in brain functional organization in relation to cardiac rhythms in people with epilepsy. We employed an HRV state-dependent FC framework with two levels of variability states estimated from electrocardiogram (ECG) recorded during resting-state fMRI. Given the association between HRV measures and time-varying FC reported in the literature (27), a state-dependent FC framework informed by concurrent cardiac recordings appeared more suitable for studying cardiac dysfunction than static FC approaches that do not utilize physiological recordings. Moreover, we examined whole-brain FC in a data-driven manner rather than restricting the analysis to interactions between regions of the CAN, as recent studies suggested that the neural correlates of cardiac regulation are more widespread than initially thought (17, 29, 37).

MATERIALS AND METHODS

Subjects

Thirty-two (32) patients with drug-resistant epilepsy were selected from an ongoing investigation into the localization of epileptic activity in the brain using simultaneous EEG-fMRI with ECG (38), with a case ascertainment period between 2005 and 2014. The inclusion criteria were: (1) the availability of a resting-state EEG-fMRI scan; and (2) a high-resolution T1-weighted scan. The exclusion criteria were: (1) large brain lesion or previous neurosurgery [we considered large to be anything greater than a small area of focal cortical dysplasia (FCD) or sclerosis – e.g., tumors, cavernomas] (2) incomplete clinical or imaging data (e.g., abandoned scans). Sixteen (16) healthy controls were also considered with comparable age and sex characteristics; the group demographics and clinical details are shown in **Supplementary Tables 1, 2**. The study was approved by the National Research Ethics Committee (United Kingdom; 04/Q0502/89) and all patients gave written informed consent.

Simultaneous EEG-fMRI Acquisition

Scanning was performed at the Epilepsy Society (Chalfont St Peter, Buckinghamshire, UK) on a 3.0 Tesla GE (Signa excite HDX) scanner. A 20-min (400 vol) T_2^*-weighted fMRI scan was collected from each subject except for two patients that were scanned for 10-min instead. The fMRI scan was done using a gradient-echo echo-planar-imaging with the following characteristics: repetition time (TR) = 3,000 ms, echo time (TE) = 30 ms, flip angle = 90, matrix size = 64 × 64, field of view (FOV) = 24 × 24 cm^2, slice thickness = 2.4 mm with 0.6 mm gap, 44 slices, and voxel size = 3.75 × 3.75 × 3 mm^3. Subjects were instructed to keep their eyes closed, avoid falling asleep, and not think about anything in particular. A T_1-weighted image was also acquired using an FSPGR (fast spoiled gradient recalled echo) sequence, with the following parameters: matrix size = 256 × 256, FOV = 24 × 24 cm^2, slice thickness = 1.5 mm, 150 slices, and voxel size = 0.94 × 0.94 × 1.5 mm^3.

Scalp EEG signals and an ECG signal were simultaneously acquired during fMRI scanning at 5 kHz using a 64 channel MR-compatible EEG system with ring Ag/AgCl electrodes (BrainAmp MR+; Brain Products GmbH, Munich, Germany). The electrodes were placed according to the 10/20 system and referenced to electrode FCz.

Preprocessing of fMRI Data

As described previously (38), preprocessing of fMRI data was conducted using the Statistical Parametric Mapping software (SPM12, Welcome Trust Centre for Neuroimaging, London, UK, http://www.fil.ion.ucl.ac.uk/spm) (39) in a Matlab environment (R2020a; Mathworks, Natick, Massachusetts, USA). The first five functional volumes were discarded to allow steady-state magnetization to be established, and the remaining volumes were realigned to correct for head movements. The structural image of each subject was co-registered to the mean realigned functional volume and, subsequently, underwent tissue segmentation into gray matter, white matter and cerebrospinal fluid tissue compartments. The functional images as well as the coregistered structural images and tissue compartment masks were spatially normalized to the Montreal Neurological Institute (MNI) reference space using non-linear transformation.

To account for anatomical variability across participants and reduce thermal noise, all individual functional volumes were smoothed using a 5 mm full-width half-maximum (FWHM) Gaussian kernel. Subsequently, the Brainnetome atlas was used to extract mean fMRI time-series from 210 cortical and 36 subcortical parcels (40). The parcel time-series were high-pass filtered at 0.008 Hz to avoid spurious correlations that arise from low-frequency fluctuations (41).

We used the framewise displacement (FD) as defined in Power et al. (42) to identify and exclude subjects with high levels of motion, as motion can obscure neural-related BOLD activity (43, 44) and lead to systematic biases in FC studies (45–47). FD is calculated from the six motion realignment parameters and reflects the extent of motion at each timepoint. Subjects that were characterized by mean FD larger than 0.25 mm were excluded. In addition, for the remaining of the subjects that were considered in the study, timepoints with FD larger than 0.2 mm were disregarded.

Finally, to further mitigate the effects of motion as well as reduce the effects of physiological processes and scanner artifacts, we regressed out the following nuisance regressors from all parcel time-series: the first ten principal components from voxel time-series within the white matter (48), six regressors related to cardiac pulsatility artifacts obtained with the convolution model proposed in Kassinopoulos and Mitsis (45), and the mean fMRI time-series averaged across all voxels within the gray matter.

Preprocessing of ECG and Calculation of HRV Measures

The ECG was corrected for gradient artifacts using adaptive template subtraction (49) implemented in BrainVision Analyzer 2 software (Brain Products GmbH, Munich, Germany), and band-pass filtered from 0.5 to 40 Hz. The R-waves were detected using Matlab's function findpeaks with a minimum peak distance varying between 0.5 and 0.9 s depending on the subject's average RR interval (time between successive R-waves).

The RR intervals were used to obtain time-series of the root mean square of successive differences in RR intervals (RMSSD), and the normalized low (0.04–0.15 Hz) and high (0.15–0.40 Hz) frequency components of HRV. The aforementioned three HRV measures were computed in adjacent time windows of 100 s each, and a timestep of 1 s, to probe changes in sympathetic and parasympathetic activity during the 20-min resting-state scan. RMSSD is a time-domain HRV measure that is believed to reflect parasympathetic activity (50), the low-frequency HRV (LF-HRV) is a frequency-domain measure presumably sensitive to both branches of the ANS, and the high-frequency HRV (HF-HRV) is a frequency-domain measure that, similar to RMSSD, reflects parasympathetic activity. To derive the normalized LF- and HF-HRV measures, the time-series of successive differences in RR intervals was uniformly resampled at 10 Hz before estimating the Welch power spectral density. Subsequently, the power within the frequency ranges 0.04–0.15 Hz (LF-HRV) and 0.15–0.40 Hz (HF-HRV) was divided by the power within the range 0.04–0.50 Hz and multiplied by 100%. Apart from the three HRV measures, the moving average of RR intervals was also computed across the time windows. Before the calculation of an HRV measure or mean RR interval within a time window, outliers of RR values, defined as three median absolute deviations (MAD) away from the median, were linearly interpolated. To disentangle fluctuations in HRV from fluctuations in RR interval, the three HRV measures were orthogonalized with respect to fluctuations in RR interval. Furthermore, heart rate was estimated as the inverse of instantaneous RR interval multiplied by 60. The heart rate was preferred over the instantaneous RR interval to facilitate comparison with the activation maps shown in Valenza et al. (29) that link regional BOLD fluctuations to heart rate.

Relationship Between BOLD Fluctuations and Cardiac Dynamics

The three HRV measures (RMSSD, LF-HRV and HF-HRV), moving-average RR interval and instantaneous heart rate were convolved with the canonical hemodynamic response function (HRF) from SPM12 (39) prior to resampling at the fMRI acquisition rate. The association between the obtained time-series and voxel-wise fMRI time-series within the gray matter was quantified using one-sample t-test on the associated beta parameters derived from the general linear model. Differences in the activation maps between epilepsy patients and healthy controls were assessed with a second-level, mixed-effects analysis with subjects as the random-effects factor, using a two-sample *t*-test on the associated beta parameters. To control for potential effects, sex, age and levels of head motion (i.e., mean FD) were treated as covariates. Moreover, to account for false positives, the statistical maps were thresholded with a voxel-wise threshold of family-wise error (FWE) rate $p < 0.05$ corrected for multiple comparisons using the random-field theory (51) and an extent threshold ≥ 10 voxels.

Whole-Brain HRV State-Dependent Functional Connectivity

To investigate the effects of HRV state on brain functional organization, a whole-brain state-dependent FC analysis was performed on the parcellation of the Brainnetome atlas that includes 246 parcels covering the neocortex and sub-cortical regions (40). The connectivity strength between parcel pairs was determined based on the pairwise Pearson correlation coefficient of the parcel time-series. Cortical parcels were grouped into the following seven large-scale functional networks described in Yeo et al. (52): visual (34 parcels), somatomotor (33 parcels), dorsal attention (30 parcels), ventral attention (22 parcels), limbic (26 parcels), frontoparietal (26 parcels) and default mode (36 parcels), using the mapping provided on the Brainnetome atlas' website (https://atlas.brainnetome.org/), and the subcortical parcels were grouped into the following four networks: amygdala (four parcels), hippocampus (four parcels), basal ganglia (12 parcels) and thalamus (16 parcels) (three cortical parcels were excluded from the analysis as they were not assigned to any of the networks). To better understand how FC depends on the state of autonomic activity, we estimated FC in each individual considering low or high HRV states separately. The low and high HRV states were defined as the timepoints in a scan at which an HRV measure (e.g., RMSSD) had values in the lowest and highest quartile range for that given scan, respectively.

A mixed analysis of variance (ANOVA) was conducted with the group (epilepsy patients / healthy controls) as a between-subject factor and HRV state (low/high) as a within-subject factor, which allowed us to examine the effect of the group and HRV state on FC within and between networks as well as their interactions. Potential effects of sex, age and levels of head motion on FC were regressed out through linear regression at the group level before conducting the mixed ANOVA. The levels of head motion for the low and high HRV state were determined separately considering only the timepoints corresponding to each state. The connectivity strength between pairs of networks that was used in the mixed ANOVA was defined as the mean correlation averaged across all pairs of parcels that belonged to the two corresponding networks. The HRV state-dependent FC analysis was performed for the three HRV measures and the moving-average RR interval. Statistical significance was set at $p < 0.0125$ (i.e., 0.05/4) adjusted for multiple comparison with respect to pairs of networks using false discovery rate (FDR).

RESULTS

Data from four patients were excluded due to excessive motion (mean FD > 0.25 mm). The sex and age distributions were similar between the epilepsy patients ($n = 28$, mean age of 28.7, 14 women) and healthy controls ($n = 16$, mean age of 30.6, seven women;) ($p > 0.48$; two-sample permutation test; number of permutations $q = 10{,}000$; **Supplementary Table 2**). Motion-contaminated fMRI volumes (FD > 0.2 mm) were also excluded, resulting in an average of 353 ± 65 volumes per subject. Based on a two-sample permutation test ($q = 10{,}000$) there were no significant differences in the number of volumes between healthy controls and epilepsy patients ($p > 0.10$), and the two groups exhibited similar levels of motion during the fMRI scan ($p > 0.10$; **Supplementary Figure 1**). The consideration of a subset of volumes for the low and high HRV states (average 88 volumes per state) did not have any apparent effects on the estimates of whole-brain FC as compared to the FC matrices obtained from the entire scan (**Supplementary Figure 2**).

Heart Rate and HRV Measures

Comparisons of cardiac dynamic metrics between patients and healthy controls were performed using a two-sample permutation test ($q = 10{,}000$) after regressing out potential effects of sex and age. The mean RR interval during the 20-min scan was significantly lower in patients compared to healthy controls (950 ± 100 ms vs. 1,100 ± 200 ms; $p < 0.003$; equivalently, the mean heart rate was significantly higher) (**Figure 1**). HF-HRV was also lower in epilepsy compared to controls (71 ± 11% vs. 78 ± 8 %; $p < 0.05$) whereas RMSSD and LF-HRV were similar in the two groups. The LF-HRV (0.04–0.15 Hz) and HF-HRV (0.15–0.40 Hz) measures demonstrated a strong negative inter-correlation ($r = -0.56$; **Supplementary Figure 3**) whereas the correlations between the remaining pairs of RR interval and HRV measures were relatively low (<0.26; **Supplementary Figure 3**).

Relationship Between BOLD Fluctuations and Cardiac Dynamics

Across all subjects, BOLD signal fluctuations were associated ($p < 0.05$; FWE-corrected) with only one of the cardiac dynamic metrics, namely instantaneous heart rate, in the following regions: positive correlations in the thalamus and several regions of the cerebellum (culmen, declive, uvula, nodulus and inferior semilunar lobule); negative correlations in the bilateral inferior frontal gyrus, orbitofrontal cortex, middle temporal gyrus, precentral gyrus and claustrum, as well as right insula and putamen (**Figure 2**). A more liberal threshold of $p < 0.001$ uncorrected indicated positive correlations of heart rate in bilateral caudate, and negative correlations in left insula and putamen, as well as bilateral superior temporal gyrus (**Supplementary Figure 4**). We did not find significant differences in correlations between the two groups.

HRV State-Dependent Functional Connectivity

When comparing whole-brain connectivity between patients and healthy controls, for all cardiac dynamic metrics, the strongest differences were observed in the connectivity strength between the frontoparietal, limbic and default mode networks, albeit these did not reach statistical significance (**Figure 3** left column). The connectivity strength of the thalamus with the ventral attention

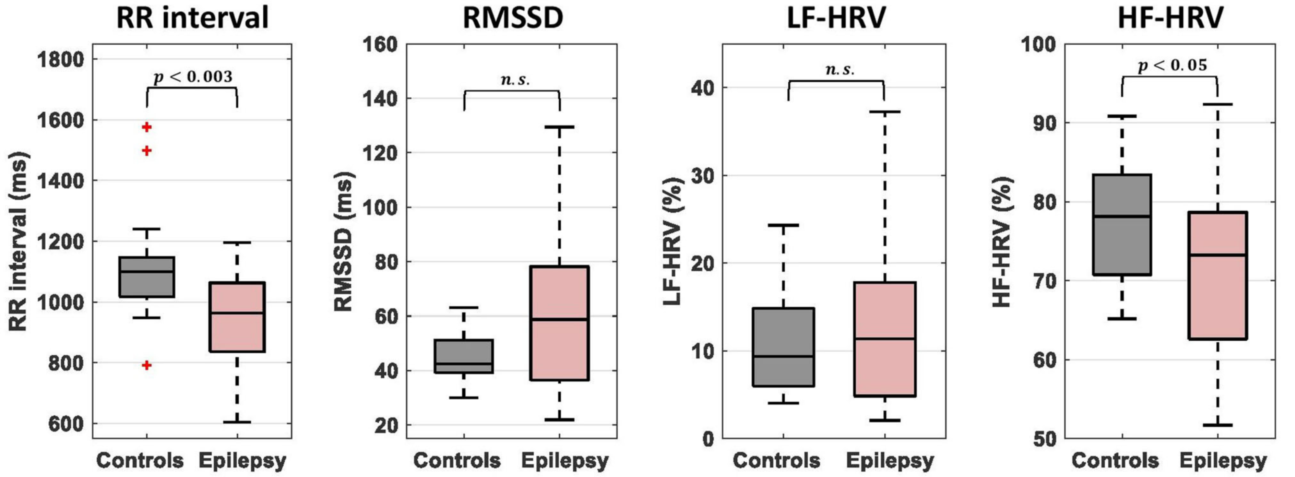

FIGURE 1 | Comparison of mean RR interval and heart rate variability (HRV) measures between epilepsy patients and healthy controls. The bottom and top of each box correspond to the 25th and 75th percentiles of the sample distribution, the line in the box corresponds to the median and the crosses indicate outliers, defined as values that are more than 1.5 times the interquartile range away from the edges of the box. The epilepsy patients showed significantly lower values of mean RR interval and HR-HRV than healthy controls. n.s., not significant.

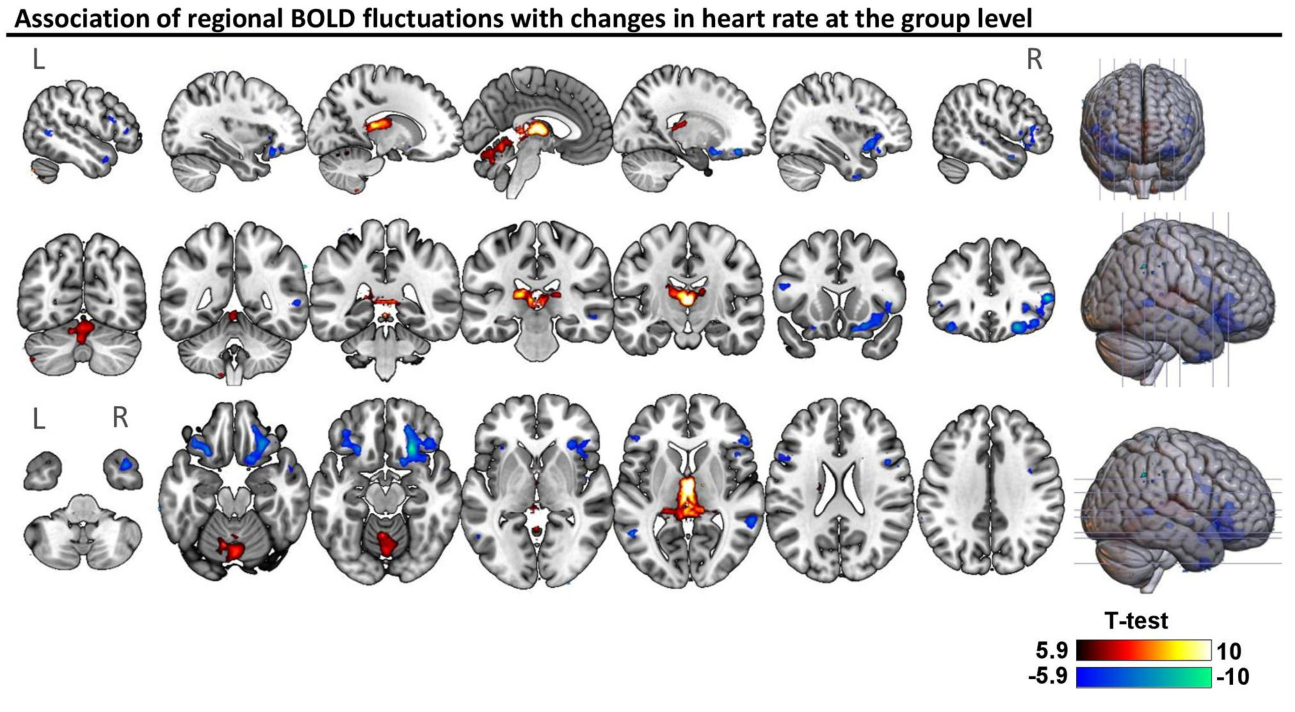

FIGURE 2 | Association of regional BOLD fluctuations with changes in heart rate at the group level. Statistical map of one-sample *t*-test considering patients and controls ($n = 44$), thresholded with a voxel-wise threshold of family-wise error (FWE) rate $p < 0.05$ corrected for multiple comparisons using the random-field theory (51). The unthresholded statistical map is available at https://neurovault.org/collections/9452/.

network and basal ganglia had strong interactions of group and LF-HRV state ($p < 0.0125$, FDR corrected; **Figure 3** right column). The connectivity between the thalamus and ventral attention network demonstrated also strong interactions of group and RMSSD state.

To shed further light on the interactions of group and HRV state in the connectivity of thalamus with the ventral attention network and basal ganglia, we performed a *post-hoc* analysis on the connectivity between the pairs of parcels of the associated networks with the strongest interactions. Specifically, we investigated the connectivity between the right caudal temporal thalamus and left dorsal granular insula (parcel of the ventral attention network; f-test for interactions = 17.5) and the connectivity between the left posterior parietal thalamus

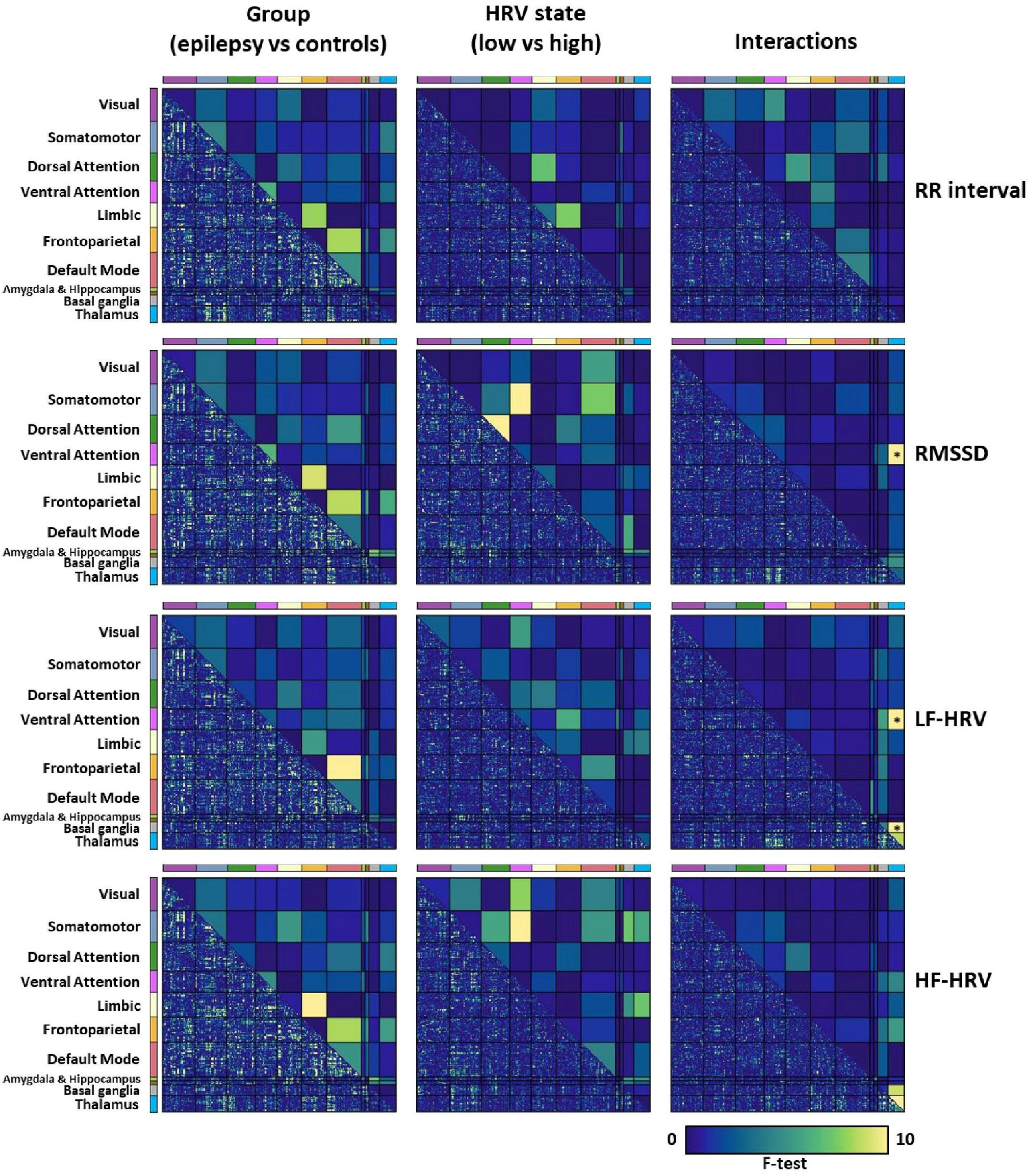

FIGURE 3 | Mixed analysis of variance (ANOVA) for evaluating the effects of the group (epilepsy vs. controls; 1st column) and HRV state (low vs. high, patients and healthy controls; 2nd column) on whole-brain connectivity, and their interactions (3rd column). The lower triangular matrix corresponds to the *f*-test for pairs of parcels whereas the upper triangular matrix corresponds to the *f*-test for pairs of the eleven networks. The connectivity strength between pairs of networks that was used in the mixed ANOVA was defined as the mean correlation averaged across all pairs of parcels that belonged to the two corresponding networks. Pairs of networks with $p < 0.0125$ after FDR correction are indicated with an asterisk (*). Note that the lower triangular matrices are only shown to provide a qualitative description of the interactions of networks at the parcel level, and that their significance levels are not assessed. We observe that the connectivity strength of the thalamus with the ventral attention network and basal ganglia has strong interactions between the group and the LF-HRV state, which led us to examine thalamic connectivity with the ventral attention network and basal ganglia more carefully.

and left ventromedial putamen (parcel of the basal ganglia; f-test for interactions $= 17.7$). For both connections of the thalamus, healthy controls exhibited a lower (toward negative values) connectivity strength in the high LF-HRV state compared to the low LF-HRV state, whereas epilepsy patients exhibited the opposite trend (**Figure 4**).

Figure 5 shows the degree to which the voxel-level connectivity profile of the right caudal temporal and left posterior parietal thalamus differs between low and high LF-HRV state (red color corresponds to higher correlations in high LF-HRV compared to low LF-HRV, and vice versa for blue color), for both controls and patients as well as the differences between the two groups. When comparing high with low HRV-state, in controls we observe a decrease in the connectivity of the caudal temporal thalamus with the bilateral anterior insula cortex (AIC), the anterior cingulate cortex (ACC), middle frontal gyrus (MFG) and supramarginal gyrus (SMG); whereas, in patients, we observe a small decrease in the connectivity with MFG and an increase with ACC. When examining the effect of LF-HRV state in the connectivity of the posterior parietal thalamus, in controls, a decrease in connectivity with the bilateral AIC, putamen and caudate appears, and in patients, an increase in connectivity with left putamen and AIC as well as bilateral caudate.

DISCUSSION

We examined the association of autonomic cardiac regulation with spontaneous fluctuations in fMRI and whole-brain FC in people with drug-resistant epilepsy, compared to healthy controls. In both groups, heart rate was positively correlated with fMRI signal intensity in bilateral thalamus and regions of the cerebellum, and negatively correlated with lateral regions, including bilateral inferior frontal gyrus, orbitofrontal cortex, middle temporal gyrus and right insula and putamen (**Figure 2**; **Supplementary Figure 4**). In addition, fluctuations in RMSSD and LF-HRV exhibited strong associations with changes in FC (**Figure 3**), despite the absence of correlation with brain activity in individual regions. Importantly, these relations differed between healthy controls and epilepsy patients. In controls, increased levels of RMSSD and LF-HRV were associated with declines in connectivity between thalamus and ventral attention network, whereas in patients, similar HRV changes accompanied increases in connectivity. The different patterns between the two groups were more pronounced for the connectivity between right caudal temporal thalamus and left dorsal granular insula (**Figure 4**). Note, however, that the interactions between ipsilateral regions [left (right) caudal temporal thalamus with left (right) dorsal granular insula] were also statistically significant, albeit with slightly higher p-values ($p < 0.01$). Therefore, it is unclear whether the stronger interactions observed between the right caudal temporal thalamus and left dorsal granular insula compared to ipsilateral interactions have some biological significance. Similar altered interactions emerged for changes in LF-HRV levels and connectivity between the thalamus and basal ganglia, with more pronounced effects for the connectivity of left posterior parietal thalamus and ventromedial putamen.

These findings support the role of thalamus, insula and putamen in autonomic control, as shown in previous studies (17, 20, 30, 53), and add roles for the temporal gyrus whose role in cardiac regulation has been recently suggested (29, 37). Despite the well-established association of activity in amygdala with heart rate fluctuations in task-based experiments (17, 54), no association was observed here. Valenza et al. (29), who also investigated the neural substrates of heart rate in task-free fMRI, found no association of amygdala activity with heart rate either, which may indicate that recruitment of amygdala activity with heart rate occurs mainly during emotional processing tasks rather than the neutral conditions studied; the amygdala traditionally serves affective roles. The neural correlates of heart rate found in our work and in Valenza et al. (29) were not entirely consistent, which may result from the more aggressive physiological correction applied in our work. Artifacts due to cardiac pulsatility were removed using the newly proposed cardiac pulsatility model (55) and systemic low-frequency oscillations were removed through gray matter signal regression (47, 56).

In healthy controls, a seed-to-voxel connectivity analysis revealed that thalamic activity was anticorrelated with core regions of the ventral attention network such as the insula, anterior cingulate cortex (ACC) and supramarginal gyrus, and this anti-correlation was enhanced during elevated levels of HRV (**Figure 5**). However, the HRV-dependent interplay between the thalamus and ventral attention network was absent in epilepsy. Burianová et al. (57) previously demonstrated a disturbed (static) connectivity between thalamus and the ventral attention network (also referred to as the salience network) in patients with mesial temporal lobe epilepsy which is consistent with our findings (i.e., the insula exhibited increased connectivity with the thalamus and decreased connectivity with the dorsal ACC). However, the present study also shows a strong relationship within healthy individuals between autonomic cardiac regulation and thalamus – ventral attention network connectivity, in line with findings of Chang et al. (27), which is altered in epilepsy.

The thalamus consists of a series of nuclei which are responsible, among others, for the relay of information from cardiovascular receptors to the insular cortex (31). In turn, the insular cortex integrates this information with inputs from ACC, amygdala and high-order polysensory cortex, providing interoceptive awareness. Stimulation of the insula (58, 59), basal ganglia or thalamus (60) lead to marked changes in heart rate and blood pressure. Any impairment in connectivity between these regions, such as found here, may be involved in cardiac rate and variability dysfunction.

A growing body of evidence from functional and structural studies suggests thalamic dysfunction in epilepsy which may underlie the abnormal connectivity of the thalamus with the ventral attention network and the basal ganglia observed in our study (**Figures 4**, **5**). Allen et al. (32), using resting-state fMRI, showed that the nodal participation of thalamus, a measure that reflects the connectivity strength of a region with regions from separate large-scale networks, was increased in epilepsy patients compared to healthy controls, and particularly in patients that succumbed to SUDEP or were at high-risk. Similarly, two recent studies reported altered thalamocortical

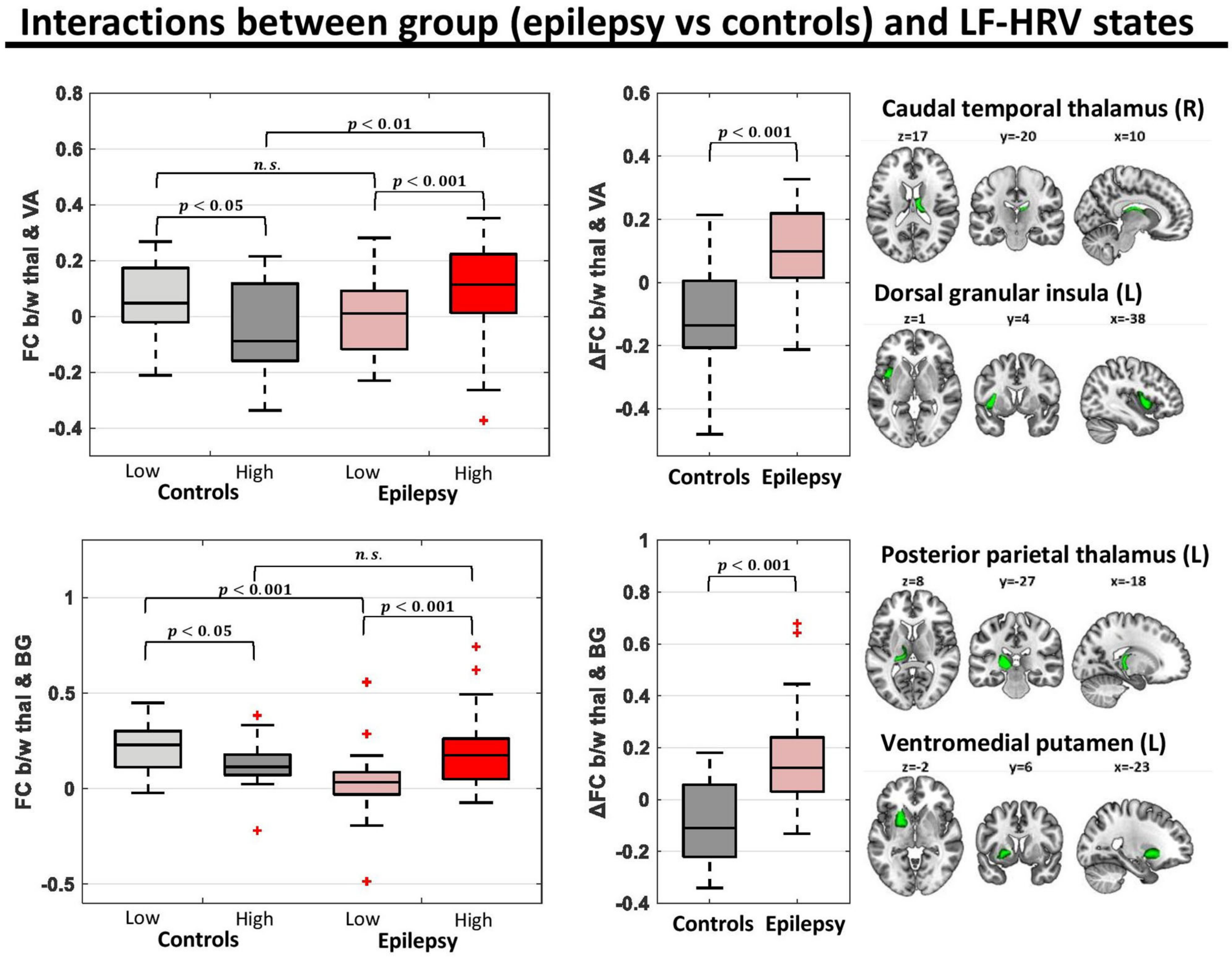

FIGURE 4 | Functional connectivity (FC) for pairs of parcels with strong group (epilepsy vs. controls)-LF-HRV interactions. In the healthy controls ($n = 16$), the connectivity strength between the right caudal temporal thalamus and left dorsal granular insula [region of ventral attention (VA) network] was lower in times with high levels of LF-HRV (i.e., levels of LF-HRV in the highest quartile of a scan) compared to times with low levels of LF-HRV (i.e., levels of LF-HRV in the lowest quartile of a scan), whereas in people with epilepsy ($n = 28$) the connectivity strength was higher in times with high levels of LF-HRV. Similar results were observed for the connectivity strength between the left posterior parietal thalamus and the left ventromedial putamen [region of the basal ganglia (BG)].

connectivity (61) as well as impaired connectivity between thalamus and basal ganglia (62) in individuals with focal to bilateral tonic-clonic seizures (FBTCS), a group of epilepsy patients associated with increased risk of seizure-related injuries and sudden unexpected death. Structural studies have revealed association of thalamic volume loss with SUDEP and high-risk patients (63) as well as with patients that present severe hypoxia during generalized tonic-clonic seizures (64). Moreover, electrical stimulations of the anterior nucleus of the thalamus has been shown in clinical trials to reduce seizure frequency even when seizures are remote from the stimulation site (65–67). The body of thalamic evidence on mediating seizure processes, and especially the altered FC between the thalamus and ventral attention network in epilepsy suggest a target for intervention. Specialized regions within the thalamus can be modified by peripheral somatosensory stimulation; activation of those thalamic sites by active stimulation has the potential to modify these FC networks, and thus alter the dysfunction patterns we found here.

RR intervals and, to a less extent, the high frequency component of HRV (i.e., HF-HRV), were on average lower in patients compared to controls (**Figure 1**) which is consistent with the increased interictal heart rate and decreased HRV reported in several studies (6–9). A major component of HF-HRV (0.15–0.40 Hz) is respiratory sinus arrhythmia, a phenomenon where heart rate fluctuates in synchrony with the breathing cycle at around 0.3 Hz, and is often considered to reflect parasympathetic influences on heart rate (68). Therefore, the findings may indicate reduced parasympathetic influences on the heart in the patients of our cohort. Interestingly, although RMSSD and LF-HRV had similar levels in the two groups, when state-dependent FC was assessed based on these two metrics it revealed different connectivity patterns between the groups, suggesting that HRV-state dependent FC has the potential to lead to more

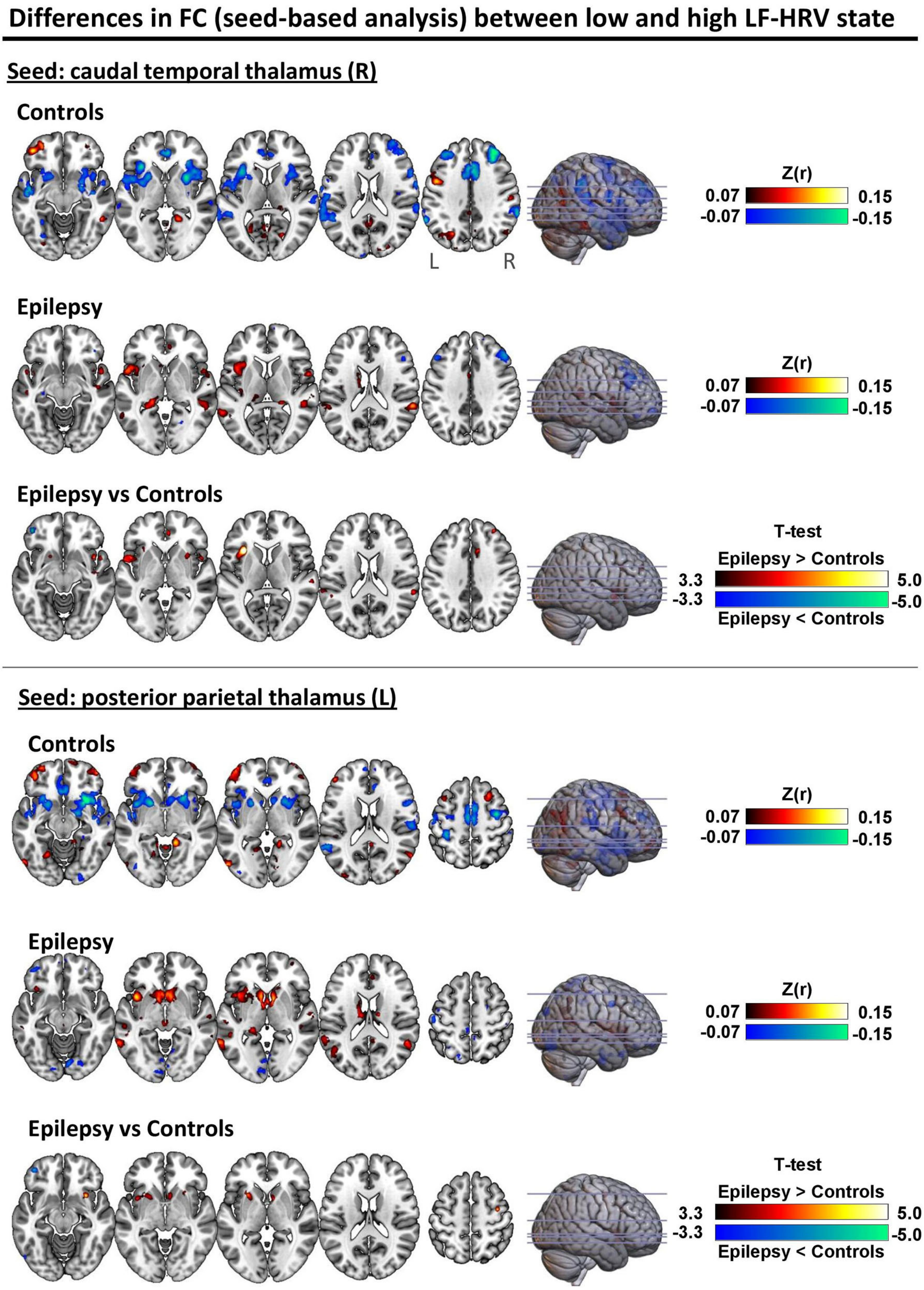

FIGURE 5 | Differences in seed-based FC between low and high LF-HRV state with seeds placed in the (top) right caudal temporal thalamus and (bottom) left posterior parietal thalamus. The first and second rows of each panel show the fisher-transformed correlations average across all healthy controls and epilepsy

(Continued)

FIGURE 5 | patients, respectively. Red color indicates higher (toward positive values) connectivity with the seed region in high LF-HRV state whereas blue color indicates lower connectivity. The last row of each panel shows the two-sample *t*-test thresholded at $p < 0.001$ (uncorrected). Even though no significant differences were found between the two groups after correcting for multiple comparison (FWE; $p < 0.05$), the differences observed with $p < 0.001$ (uncorrected) are consistent with the results obtained with the analysis in the atlas space (**Figures 3**, **4**) where the spatial autocorrelation between voxels of the same parcel are implicitly taken into account. The unthresholded statistical maps are available at https://neurovault.org/collections/9452/.

sensitive biomarkers for cardiac dysfunction processes than HRV quantification alone.

This study has limitations that should be considered. While cardiovascular mechanisms are likely impaired in epilepsy and contribute to SUDEP (69), breathing disturbances also appear (70), and may contribute to alterations in FC. Cardiorespiratory arrests monitored via video-electroencephalogram (VEEG) suggest that terminal cardiac arrest was preceded by central apnea in the majority of the cases (71), indicating a potential mediator role for disturbed breathing in cardiac dysfunction. To obtain a more holistic understanding of the neural processes underlying autonomic dysregulation in epilepsy, recognition of the close coupling of respiratory and autonomic control mechanisms should be incorporated in the analysis which was not possible in the present study, as breathing was not monitored during the fMRI scans. Respiratory measures would also be helpful in distinguishing parasympathetic from sympathetic activity in frequency-based HRV measures. HRV parasympathetic activity, lying within the high-frequency range (0.15–0.40 Hz) and associated with respiratory sinus arrhythmia, can decline below 0.15 Hz during periods with low breathing rate, and apnea can completely disrupt respiratory sinus arrhythmia measures. As a consequence, HRV-based measures of parasympathetic and sympathetic activity may be blurred when considering solely cardiac recordings (72).

Several studies describe an inverse relationship between heart rate and HRV measures (73–76). However, as this relationship is not well-understood and heart rate (or RR interval) is already a good measure of ANS activity that can be easily measured, further research is needed to understand the additional information provided with HRV compared to heart rate (73, 77). To this end, in this study, the power spectral density of the HRV that the LF-HRV and HF-HRV measures were derived from, was estimated using the successive difference in RR intervals rather than the RR intervals as this was found to yield HRV measures less correlated with fluctuations in RR interval. In addition, to further disentangle fluctuations in HRV from fluctuations in RR interval, the three HRV measures were orthogonalized with respect to fluctuations in RR interval.

An important caveat of this study in the use of fMRI as a means to study the neural correlates of ANS activity is that there are not well-established methods for disentangling neuronal from physiological effects of autonomic activity (18, 19). While the BOLD (T_2*) contrast mechanism used in fMRI is a measure sensitive to changes in blood oxygenation induced by local neuronal activity (78), it is also prone to sources of noise that can be categorized to scanner artifacts, motion artifacts, high-frequency physiological artifacts and systemic low-frequency oscillations (79–81). Sources from the first three categories, including fast effects of cardiac pulsatility (∼1.0 Hz) and breathing motion (∼0.3 Hz), can be mitigated to a large degree using advanced pulse sequences (e.g., multi-echo fMRI) and noise correction techniques (43–45, 47, 79, 82, 83). However, systemic low-frequency (<0.1 Hz) oscillations which typically refer to BOLD fluctuations driven by changes in heart rate, breathing patterns and blood pressure can be difficult to be separated from neuronal fluctuations as they share the same mechanism; i.e., both neuronal (in an attempt to satisfy increased demands in oxygen) and physiological processes (e.g., heart rate) influence the levels of blood oxygenation (56, 84–87). When studying the neural substrates of the ANS, this is particularly problematic as brain regions not involved in autonomic regulation may share similar BOLD activity with core regions of the CAN due to effects of heart rate in global cerebral blood flow, and therefore the physiological effects of autonomic activity (e.g., fluctuations in heart rate) may lead to artificial connectivity. In this study, to mitigate the effects of systemic low-frequency oscillations, we employed gray matter signal regression which outperforms alternative preprocessing strategies (45, 47, 88, 89). Note that the effects of systemic oscillations are more prominent in visual and sensorimotor areas (85, 89), regions that did not appear to be correlated with heart rate variations in the present study (**Figure 2**), suggesting that the preprocessing strategy employed here successfully removed the effects of systemic oscillations. However, we cannot exclude the possibility that gray matter regression removed signal of interest as well.

HRV impairment in epilepsy is more pronounced during nocturnal periods (14, 15) and risk for SUDEP is increased during night hours (16). These observations raise the question whether alterations in FC are also enhanced by sleep or during particular phases of the HRV circadian cycles. Note that even though participants often fall asleep during resting-state fMRI and, thus, there might be segments of fMRI data corresponding to sleep in our dataset, the low sample size ($N = 44$) impedes investigations in relation to sleep effects. The potential for more exaggerated changes in FC during sleep mandates further studies on this issue.

This study represents an exploratory, data-driven approach to investigate whether large-scale networks are involved in cardiac regulation, and is hampered by potential sleep, breathing, and circadian interactions that could interfere with understanding of important brain interactions. A hypothesis-driven analysis, controlling for these interactions may elucidate more precisely the key disruptions in autonomic processes found in epilepsy.

CONCLUSION

In healthy controls and people with drug-resistant epilepsy, fluctuations in heart rate covaried with brain activity in key regions of the central autonomic network and in regions associated with cardiac regulation. Functional connectivity of the thalamus with the basal ganglia, a major autonomic regulatory site, and the ventral attention network was strongly linked to levels of LF-HRV, and that relationship differed between healthy controls and epilepsy patients. These findings support a significant role for thalamic contributions to cardiovascular impairments in epilepsy which may lead to cardiac rhythm and blood pressure failings implicated in SUDEP. Because activity in regional thalamic structures can be so readily modified by somatosensory peripheral stimulation, we speculate that the findings suggest a means to interfere with the deficient functional connectivity patterns in epilepsy.

DATA AVAILABILITY STATEMENT

The datasets presented in this article are not readily available because there is not written informed consent from the patients/participants to share their data with external investigators. Requests to access the datasets should be directed to LL, louis.lemieux@ucl.ac.uk.

ETHICS STATEMENT

The studies involving human participants were reviewed and approved by the National Research Ethics Committee (United Kingdom; 04/Q0502/89). The patients/participants provided their written informed consent to participate in this study.

AUTHOR CONTRIBUTIONS

MK preprocessed and analyzed data, interpreted the findings, and drafted the initial manuscript. RH interpreted the findings, revised the manuscript, and refined the clinical and physiological interpretation of findings. MG advised on methodological aspects of the study and revised the manuscript. LL and BD designed and conceptualized study, interpreted the findings, and revised the manuscript. All authors contributed to the article and approved the submitted version.

FUNDING

This work was funded by Epilepsy Research UK (Grant No. P1905; MK, LL, and BD). Funding by the NIH — National Institute of Neurological Disorders and Stroke U01-NS090407 (The Center for SUDEP Research) is acknowledged (BD and RH). This work was supported by the National Institute for Health Research University College London Hospitals Biomedical Research Centre.

ACKNOWLEDGMENTS

Thanks to Dr. Luke Allen for help. We are grateful to the Epilepsy Society for supporting the Epilepsy Society MRI scanner.

SUPPLEMENTARY MATERIAL

The Supplementary Material for this article can be found online at: https://www.frontiersin.org/articles/10.3389/fneur.2021.671890/full#supplementary-material

REFERENCES

1. Acharya UR, Joseph KP, Kannathal N, Lim CM, Suri JS. Heart rate variability: a review. *Med Biol Eng Comput.* (2006) 44:1031–51. doi: 10.1007/s11517-006-0119-0
2. Katona PG, Jih F. Respiratory sinus arrhythmia: noninvasive measure of parasympathetic cardiac control. *J Appl Physiol.* (1975) 39:801–5. doi: 10.1152/jappl.1975.39.5.801
3. Goldberger JJ, Challapalli S, Tung R, Parker MA, Kadish AH. Relationship of heart rate variability to parasympathetic effect. *Circulation.* (2001) 103:1977–83. doi: 10.1161/01.CIR.103.15.1977
4. Haensel A, Mills PJ, Nelesen RA, Ziegler MG, Dimsdale JE. The relationship between heart rate variability and inflammatory markers in cardiovascular diseases. *Psychoneuroendocrinology.* (2008) 33:1305–12. doi: 10.1016/j.psyneuen.2008.08.007
5. Malik M, Camm AJ, Bigger JT, Breithardt G, Cerutti S, Cohen RJ, et al. Heart rate variability. Standards of measurement, physiological interpretation, clinical use. *Eur Heart J.* (1996) 17:354–81. doi: 10.1111/j.1542-474X.1996.tb00275.x
6. Myers KA, Sivathamboo S, Perucca P. Heart rate variability measurement in epilepsy: how can we move from research to clinical practice? *Epilepsia.* (2018) 59:2169–78. doi: 10.1111/epi.14587
7. Ericson M, Ihrman C, Lindblad LE. Heart rate variability in patients with epilepsy. *Epilepsy Res.* (1998) 30:77–83. doi: 10.1016/S0920-1211(97)00094-6
8. Massetani R, Strata G, Galli R, Gori S, Gneri C, Limbruno U, et al. Alteration of cardiac function in patients with temporal lobe epilepsy : different roles of EEG-ECG monitoring and spectral analysis of RR variability. *Epilepsia.* (1997) 38:363–9. doi: 10.1111/j.1528-1157.1997.tb01129.x
9. Mativo P, Anjum J, Pradhan C, Sathyaprabha TN, Raju TR, Satishchandra P. Study of cardiac autonomic function in drug-naïve, newly diagnosed epilepsy patients. *Epileptic Disord.* (2010) 12:212–6. doi: 10.1684/epd.2010.0325
10. Arbune AA, Jeppesen J, Conradsen I, Ryvlin P, Beniczky S. Peri-ictal heart rate variability parameters as surrogate markers of seizure severity. *Epilepsia.* (2020) 61:S55–60. doi: 10.1111/epi.16491
11. Liu H, Yang Z, Meng F, Guan Y, Ma Y, Liang S. Preoperative heart rate variability as predictors of vagus nerve stimulation outcome in patients with drug-resistant epilepsy. *Sci Rep.* (2018) 8:3856. doi: 10.1038/s41598-018-21669-3
12. DeGiorgio CM, Miller P, Meymandi S, Chin A, Epps J, Gordon S, et al. RMSSD, a measure of vagus-mediated heart rate variability, is associated with risk factors for SUDEP: The SUDEP-7 Inventory. *Epilepsy Behav.* (2010) 19:78–81. doi: 10.1016/j.yebeh.2010.06.011
13. Novak JL, Miller PR, Markovic D, Meymandi SK, DeGiorgio CM. Risk assessment for sudden death in epilepsy: the SUDEP-7 inventory. *Front Neurol.* (2015) 6:1–5. doi: 10.3389/fneur.2015.00252
14. Persson H, Kumlien E, Ericson M, Tomson T. Circadian variation in heart-rate variability in localization-related epilepsy. *Epilepsia.* (2007) 48:917–22. doi: 10.1111/j.1528-1167.2006.00961.x
15. Ronkainen E, Ansakorpi H, Huikuri HV, Myllyl,ä VV, Isojärvi JIT, Korpelainen JT. Suppressed circadian heart rate dynamics in temporal lobe epilepsy. *J Neurol Neurosurg Psychiatry.* (2005) 76:1382–6. doi: 10.1136/jnnp.2004.053777

16. Purnell BS, Thijs RD, Buchanan GF. Dead in the night: sleep-wake and time-of-day influences on sudden unexpected death in epilepsy. *Front Neurol.* (2018) 9:5–8. doi: 10.3389/fneur.2018.01079
17. Beissner F, Meissner K, Bar K-J, Napadow V. The autonomic brain: an activation likelihood estimation meta-analysis for central processing of autonomic function. *J Neurosci.* (2013) 33:10503–11. doi: 10.1523/JNEUROSCI.1103-13.2013
18. Chang C, Raven EP, Duyn JH. Brain–heart interactions: challenges and opportunities with functional magnetic resonance imaging at ultra-high field. *Philos Trans R Soc A Math Phys Eng Sci.* (2016) 374:20150188. doi: 10.1098/rsta.2015.0188
19. Mulcahy JS, Larsson DEO, Garfinkel SN, Critchley HD. Heart rate variability as a biomarker in health and affective disorders: a perspective on neuroimaging studies. *Neuroimage.* (2019) 202:116072. doi: 10.1016/j.neuroimage.2019.116072
20. Thayer JF, Åhs F, Fredrikson M, Sollers JJ, Wager TD. A meta-analysis of heart rate variability and neuroimaging studies: implications for heart rate variability as a marker of stress and health. *Neurosci Biobehav Rev.* (2012) 36:747–56. doi: 10.1016/j.neubiorev.2011.11.009
21. Critchley HD, Mathias CJ, Josephs O, O'Doherty J, Zanini S, Dewar BK, et al. Human cingulate cortex and autonomic control: converging neuroimaging and clinical evidence. *Brain.* (2003) 126:2139–52. doi: 10.1093/brain/awg216
22. Gianaros PJ, Van der Veen FM, Jennings JR. Regional cerebral blood flow correlates with heart period and high-frequency heart period variability during working-memory tasks: implications for the cortical and subcortical regulation of cardiac autonomic activity. *Psychophysiology.* (2004) 41:521–30. doi: 10.1111/1469-8986.2004.00179.x
23. Harper RM, Bandler R, Spriggs D, Alger JR. Lateralized and widespread brain activation during transient blood pressure elevation revealed by magnetic resonance imaging. *J Comp Neurol.* (2000) 417:195–204. doi: 10.1002/(SICI)1096-9861(20000207)417:2<195::AID-CNE5>3.0.CO;2-V
24. Harper RM, Gozal D, Bandler R, Spriggs D, Lee J, Alger J. Regional brain activation in humans during respiratory and blood pressure challenges. *Clin Exp Pharmacol Physiol.* (1998) 25:483–6. doi: 10.1111/j.1440-1681.1998.tb02240.x
25. Macey PM, Ogren JA, Kumar R, Harper RM. Functional imaging of autonomic regulation: methods and key findings. *Front Neurosci.* (2016) 9:1–23. doi: 10.3389/fnins.2015.00513
26. Napadow V, Dhond R, Conti G, Makris N, Brown EN, Barbieri R. Brain correlates of autonomic modulation: combining heart rate variability with fMRI. *Neuroimage.* (2008) 42:169–77. doi: 10.1016/j.neuroimage.2008.04.238
27. Chang C, Metzger CD, Glover GH, Duyn JH, Heinze H-JJ, et al. Association between heart rate variability and fluctuations in resting-state functional connectivity. *Neuroimage.* (2013) 68:93–104. doi: 10.1016/j.neuroimage.2012.11.038
28. Jennings JR, Sheu LK, Kuan DCH, Manuck SB, Gianaros PJ. Resting state connectivity of the medial prefrontal cortex covaries with individual differences in high-frequency heart rate variability. *Psychophysiology.* (2016) 53:444–54. doi: 10.1111/psyp.12586
29. Valenza G, Sclocco R, Duggento A, Passamonti L, Napadow V, Barbieri R, et al. The central autonomic network at rest: uncovering functional MRI correlates of time-varying autonomic outflow. *Neuroimage.* (2019) 197:383–90. doi: 10.1016/j.neuroimage.2019.04.075
30. Benarroch EE. The central autonomic network: functional organization, dysfunction, and perspective. *Mayo Clin Proc.* (1993) 68:988–1001. doi: 10.1016/S0025-6196(12)62272-1
31. Palma J-A, Benarroch EE. Neural control of the heart: recent concepts and clinical correlations. *Neurology.* (2014) 83:261–71. doi: 10.1212/WNL.0000000000000605
32. Allen LA, Harper RM, Guye M, Kumar R, Ogren J, Vos S, et al. Altered brain connectivity in sudden unexpected death in epilepsy (SUDEP) revealed using resting-state fMRI. *NeuroImage Clin.* (2019) 24:102060. doi: 10.1016/j.nicl.2019.102060
33. Liao W, Zhang Z, Pan Z, Mantini D, Ding J, Duan X, et al. Altered functional connectivity and small-world in mesial temporal lobe epilepsy. *PLoS ONE.* (2010) 5:27–9. doi: 10.1371/journal.pone.0008525
34. Pereira FRS, Alessio A, Sercheli MS, Pedro T, Bilevicius E, Rondina JM, et al. temporal lobe epilepsy: evidence from resting state fMRI. *BMC Neurosci.* (2010) 11:66. doi: 10.1186/1471-2202-11-66
35. Pittau F, Grova C, Moeller F, Dubeau F, Gotman J. Patterns of altered functional connectivity in mesial temporal lobe epilepsy. *Epilepsia.* (2012) 53:1013–23. doi: 10.1111/j.1528-1167.2012.03464.x
36. Waites AB, Briellmann RS, Saling MM, Abbott DF, Jackson GD. Functional connectivity networks are disrupted in left temporal lobe epilepsy. *Ann Neurol.* (2006) 59:335–43. doi: 10.1002/ana.20733
37. Valenza G, Passamonti L, Duggento A, Toschi N, Barbieri R. Uncovering complex central autonomic networks at rest: a functional magnetic resonance imaging study on complex cardiovascular oscillations. *J R Soc Interface.* (2020) 17:20190878. doi: 10.1098/rsif.2019.0878
38. Coan AC, Chaudhary UJ, Grouiller F, Campos BM, Perani S, De Ciantis A, et al. EEG-fMRI in the presurgical evaluation of temporal lobe epilepsy. *J Neurol Neurosurg Psychiatry.* (2016) 87:642–9. doi: 10.1136/jnnp-2015-310401
39. Friston KJ, Ashburner J, Kiebel SJ, Nichols TE, Penny WD, (editors). *Statistical Parametric Mapping: The Analysis of Functional Brain Images*. Academic Press (2007). Available online at: https://www.elsevier.com/books/statistical-parametric-mapping-the-analysis-of-functional-brain-images/penny/978-0-12-372560-8
40. Fan L, Li H, Zhuo J, Zhang Y, Wang J, Chen L, et al. The human brainnetome atlas : a new brain atlas based on connectional architecture. *Cereb Cortex.* (2016) 26:3508–26. doi: 10.1093/cercor/bhw157
41. Leonardi N, Van De Ville D. On spurious and real fluctuations of dynamic functional connectivity during rest. *Neuroimage.* (2015) 104:430–6. doi: 10.1016/j.neuroimage.2014.09.007
42. Power JD, Barnes KA, Snyder AZ, Schlaggar BL, Petersen SE. Spurious but systematic correlations in functional connectivity MRI networks arise from subject motion. *Neuroimage.* (2012) 59:2142–54. doi: 10.1016/j.neuroimage.2011.10.018
43. Lemieux L, Salek-Haddadi A, Lund TE, Laufs H, Carmichael D. Modelling large motion events in fMRI studies of patients with epilepsy. *Magn Reson Imaging.* (2007) 25:894–901. doi: 10.1016/j.mri.2007.03.009
44. Salek-Haddadi A, Diehl B, Hamandi K, Merschhemke M, Liston A, Friston K, et al. Hemodynamic correlates of epileptiform discharges: an EEG-fMRI study of 63 patients with focal epilepsy. *Brain Res.* (2006) 1088:148–66. doi: 10.1016/j.brainres.2006.02.098
45. Kassinopoulos M, Mitsis GD. A multi-measure approach for assessing the performance of fMRI preprocessing strategies in resting-state functional connectivity. *bioRxiv.* (2021) 1–61. doi: 10.1101/837609
46. Power JD, Schlaggar BL, Petersen SE. Recent progress and outstanding issues in motion correction in resting state fMRI. *Neuroimage.* (2015) 105:536–51. doi: 10.1016/j.neuroimage.2014.10.044
47. Xifra-Porxas A, Kassinopoulos M, Mitsis GD. Physiological and head motion signatures in static and time-varying functional connectivity and their subject discriminability. *bioRxiv.* (2020). doi: 10.1101/2020.02.04.934554
48. Behzadi Y, Restom K, Liau J, Liu TT. A component based noise correction method (CompCor) for BOLD and perfusion based fMRI. *Neuroimage.* (2007) 37:90–101. doi: 10.1016/j.neuroimage.2007.04.042
49. Allen PJ, Josephs O, Turner R. A method for removing imaging artifact from continuous EEG recorded during functional MRI. *Neuroimage.* (2000) 12:230–9. doi: 10.1006/nimg.2000.0599
50. Shaffer F, Ginsberg JP. An overview of heart rate variability metrics and norms. *Front Public Heal.* (2017) 5:1–17. doi: 10.3389/fpubh.2017.00258
51. Worsley KJ, Marrett S, Neelin P, Vandal AC, Friston KJ, Evans AC. A unified statistical approach for determining significant signals in images of cerebral activation. *Hum Brain Mapp.* (1996) 4:58–73. doi: 10.1002/(SICI)1097-0193(1996)4:1<58::AID-HBM4>3.0.CO;2-O
52. Yeo TBT, Krienen FM, Sepulcre J, Sabuncu MR, Lashkari D, Hollinshead M, et al. The organization of the human cerebral cortex estimated by intrinsic functional connectivity. *J Neurophysiol.* (2011) 106:1125–65. doi: 10.1152/jn.00338.2011
53. Chapman WP, Livingston RB, E LK. Frontal lobotomy and electrical stimulation of orbital surface of frontal lobes; effect on respiration and on blood pressure in man. *Arch Neurol Psychiatry.* (1949) 62:701. doi: 10.1001/archneurpsyc.1949.02310180002001

54. Yang TT, Simmons AN, Matthews SC, Tapert SF, Bischoff-Grethe A, Frank GKW, et al. Increased amygdala activation is related to heart rate during emotion processing in adolescent subjects. *Neurosci Lett.* (2007) 428:109–14. doi: 10.1016/j.neulet.2007.09.039
55. Kassinopoulos M, Mitsis GD. Physiological noise modeling in fMRI based on the pulsatile component of photoplethysmograph. *bioRxiv*. (2020). doi: 10.1101/2020.06.01.128306
56. Tong Y, Hocke LM, Frederick BB. Low frequency systemic hemodynamic "noise" in resting state BOLD fMRI: characteristics, causes, implications, mitigation strategies, and applications. *Front Neurosci*. (2019) 13:787. doi: 10.3389/fnins.2019.00787
57. Burianová H, Faizo NL, Gray M, Hocking J, Galloway G, Reutens D. Altered functional connectivity in mesial temporal lobe epilepsy. *Epilepsy Res.* (2017) 137:45–52. doi: 10.1016/j.eplepsyres.2017.09.001
58. Oppenheimer S. Cerebrogenic cardiac arrhythmias. *Clin Auton Res.* (2006) 16:6–11. doi: 10.1007/s10286-006-0276-0
59. Oppenheimer SM, Gelb A, Girvin JP, Hachinski VC, Med D. Cardiovascular effects of human insular cortex stimulation. *Neurology*. (1992) 42:1727–32. doi: 10.1212/WNL.42.9.1727
60. Thornton JM, Aziz T, Schlugman D, Paterson DJ. Electrical stimulation of the midbrain increases heart rate and arterial blood pressure in awake humans. *J Physiol*. (2002) 539:615–21. doi: 10.1113/jphysiol.2001.014621
61. Caciagli L, Allen LA, He X, Trimmel K, Vos SB, Centeno M, et al. Thalamus and focal to bilateral seizures: a multiscale cognitive imaging study. *Neurology.* (2020) 95:e2427–41. doi: 10.1212/WNL.0000000000010645
62. He X, Chaitanya G, Asma B, Caciagli L, Bassett DS, Tracy JI, et al. Disrupted basal ganglia-thalamocortical loops in focal to bilateral tonic-clonic seizures. *Brain.* (2020) 143:175–90. doi: 10.1093/brain/awz361
63. Allen LA, Vos SB, Kumar R, Ogren JA, Harper RK, Winston GP, et al. Cerebellar, limbic, and midbrain volume alterations in sudden unexpected death in epilepsy. *Epilepsia*. (2019) 60:718–29. doi: 10.1111/epi.14689
64. Allen LA, Harper RM, Vos SB, Scott CA, Lacuey N, Vilella L, et al. Peri-ictal hypoxia is related to extent of regional brain volume loss accompanying generalized tonic-clonic seizures. *Epilepsia.* (2020) 61:1570–80. doi: 10.1111/epi.16615
65. Cooper IS, Upton ARM, Amin I. Reversibility of chronic neurologic deficits. Some effects of electrical stimulation of the thalamus and internal capsule in man. *Stereotact. Funct Neurosurg.* (1980) 43:244–58. doi: 10.1159/000102263
66. Fisher R, Salanova V, Witt T, Worth R, Henry T, Gross R, et al. Electrical stimulation of the anterior nucleus of thalamus for treatment of refractory epilepsy. *Epilepsia.* (2010) 51:899–908. doi: 10.1111/j.1528-1167.2010.02536.x
67. Upton AR, Amin I, Garnett S, Springman M, Nahmias C, Cooper IS. Evoked metabolic responses in the limbicstriate system produced by stimulation of anterior thalamic nucleus in man. *Pacing Clin Electrophysiol.* (1987) 10:217–25. doi: 10.1111/j.1540-8159.1987.tb05952.x
68. Angelone A, Coulter NA. Respiratory sinus arrhythmia: a frequency dependent phenomenon. *J Appl Physiol.* (1964) 19:479–82. doi: 10.1152/jappl.1964.19.3.479
69. Devinsky O, Hesdorffer DC, Thurman DJ, Lhatoo S, Richerson G. Sudden unexpected death in epilepsy: epidemiology, mechanisms, and prevention. *Lancet Neurol.* (2016) 15:1075–88. doi: 10.1016/S1474-4422(16)30158-2
70. Manni R, Terzaghi M, Arbasino C, Sartori I, Galimberti CA, Tartara A. Obstructive sleep apnea in a clinical series of adult epilepsy patients: frequency and features of the comorbidity. *Epilepsia.* (2003) 44:836–40. doi: 10.1046/j.1528-1157.2003.55702.x
71. Ryvlin P, Nashef L, Lhatoo SD, Bateman LM, Bird J, Bleasel A, et al. Incidence and mechanisms of cardiorespiratory arrests in epilepsy monitoring units (MORTEMUS): a retrospective study. *Lancet Neurol.* (2013) 12:966–77. doi: 10.1016/S1474-4422(13)70214-X
72. García-González MA, Vázquez-Seisdedos C, Pallàs-Areny R. Variations in breathing patterns increase low frequency contents in HRV spectra. *Physiol Meas.* (2000) 21:417–23. doi: 10.1088/0967-3334/21/3/307
73. Kazmi SZH, Zhang H, Aziz W, Monfredi O, Abbas SA, Shah SA, et al. Inverse correlation between heart rate variability and heart rate demonstrated by linear and nonlinear analysis. *PLoS ONE.* (2016) 11:1–10. doi: 10.1371/journal.pone.0157557
74. Mangin L, Swynghedauw B, Benis A, Thibault N, Lerebours G, Carré F. Relationships between heart rate and heart rate variability: study in conscious rats. *J Cardiovasc Pharmacol*. (1998) 32:601–7. doi: 10.1097/00005344-199810000-00012
75. Monfredi O, Lyashkov AE, Johnsen AB, Inada S, Schneider H, Wang R, et al. Biophysical characterization of the underappreciated and important relationship between heart rate variability and heart rate. *Hypertension.* (2014) 64:1334–43. doi: 10.1161/HYPERTENSIONAHA.114.03782
76. Yu L, De Mazancourt M, Hess A, Ashadi FR, Klein I, Mal H, et al. Functional connectivity and information flow of the respiratory neural network in chronic obstructive pulmonary disease. *Hum Brain Mapp.* (2016) 37:2736–54. doi: 10.1002/hbm.23205
77. Coumel P, Maison-Blanche P, Catuli D. Heart rate and heart rate variability in normal young adults. *J Cardiovasc Electrophysiol.* (1994) 5:899–911. doi: 10.1111/j.1540-8167.1994.tb01130.x
78. Attwell D, Iadecola C. The neural basis of functional brain imaging signals. *Trends Neurosci.* (2002) 25:621–5. doi: 10.1016/S0166-2236(02)02264-6
79. Caballero-Gaudes C, Reynolds RC. Methods for cleaning the BOLD fMRI signal. *Neuroimage.* (2017) 154:128–49. doi: 10.1016/j.neuroimage.2016.12.018
80. Liu TT. Noise contributions to the fMRI signal: an overview. *Neuroimage.* (2016) 143:141–51. doi: 10.1016/j.neuroimage.2016.09.008
81. Murphy K, Birn RM, Bandettini PA. Resting-state fMRI confounds and cleanup. *Neuroimage.* (2013) 80:349–59. doi: 10.1016/j.neuroimage.2013.04.001
82. Kundu P, Brenowitz ND, Voon V, Worbe Y, Vértes PE, Inati SJ, et al. Integrated strategy for improving functional connectivity mapping using multiecho fMRI. *Proc Natl Acad Sci USA.* (2013) 110:16187–92. doi: 10.1073/pnas.1301725110
83. Liston AD, Lund TE, Salek-Haddadi A, Hamandi K, Friston KJ, Lemieux L. Modelling cardiac signal as a confound in EEG-fMRI and its application in focal epilepsy studies. *Neuroimage.* (2006) 30:827–34. doi: 10.1016/j.neuroimage.2005.10.025
84. Birn RM, Diamond JB, Smith MA, Bandettini PA. Separating respiratory-variation-related fluctuations from neuronal-activity-related fluctuations in fMRI. *Neuroimage.* (2006) 31:1536–48. doi: 10.1016/j.neuroimage.2006.02.048
85. Kassinopoulos M, Mitsis GD. Identification of physiological response functions to correct for fluctuations in resting-state fMRI related to heart rate and respiration. *Neuroimage.* (2019) 202:116150. doi: 10.1016/j.neuroimage.2019.116150
86. Shmueli K, van Gelderen P, de Zwart J, a., Horovitz SG, Fukunaga M, et al. Low-frequency fluctuations in the cardiac rate as a source of variance in the resting-state fMRI BOLD signal. *Neuroimage.* (2007) 38:306–20. doi: 10.1016/j.neuroimage.2007.07.037
87. Whittaker JR, Driver ID, Venzi M, Bright MG, Murphy K, Chen J, et al. Cerebral autoregulation evidenced by synchronized low frequency oscillations in blood pressure and resting-state fMRI. *Front Neurosci.* (2019) 13:433. doi: 10.3389/fnins.2019.00433
88. Power JD, Plitt M, Gotts SJ, Kundu P, Voon V, Bandettini PA, et al. Ridding fMRI data of motion-related influences: removal of signals with distinct spatial and physical bases in multiecho data. *Proc Natl Acad Sci USA.* (2018) 115:E2105–14. doi: 10.1073/pnas.1720985115
89. Power JD, Plitt M, Laumann TO, Martin A. Sources and implications of whole-brain fMRI signals in humans. *Neuroimage.* (2017) 146:609–25. doi: 10.1016/j.neuroimage.2016.09.038

Conflict of Interest: The authors declare that the research was conducted in the absence of any commercial or financial relationships that could be construed as a potential conflict of interest.

ORIGINAL RESEARCH
published: 08 July 2021
doi: 10.3389/fneur.2021.644278

Deep Learning-Based Localization of EEG Electrodes Within MRI Acquisitions

*Caroline Pinte, Mathis Fleury and Pierre Maurel**

Univ Rennes, Inria, CNRS, Inserm, Empenn ERL U1228, Rennes, France

The simultaneous acquisition of electroencephalographic (EEG) signals and functional magnetic resonance images (fMRI) aims to measure brain activity with good spatial and temporal resolution. This bimodal neuroimaging can bring complementary and very relevant information in many cases and in particular for epilepsy. Indeed, it has been shown that it can facilitate the localization of epileptic networks. Regarding the EEG, source localization requires the resolution of a complex inverse problem that depends on several parameters, one of the most important of which is the position of the EEG electrodes on the scalp. These positions are often roughly estimated using fiducial points. In simultaneous EEG-fMRI acquisitions, specific MRI sequences can provide valuable spatial information. In this work, we propose a new fully automatic method based on neural networks to segment an ultra-short echo-time MR volume in order to retrieve the coordinates and labels of the EEG electrodes. It consists of two steps: a segmentation of the images by a neural network, followed by the registration of an EEG template on the obtained detections. We trained the neural network using 37 MR volumes and then we tested our method on 23 new volumes. The results show an average detection accuracy of 99.7% with an average position error of 2.24 mm, as well as 100% accuracy in the labeling.

Keywords: EEG, fMRI, electrode detection, electrode labeling, deep learning, U-Net, ICP

Edited by:
Brunno Machado De Campos,
State University of Campinas, Brazil

Reviewed by:
Leonardo Abdala Elias,
State University of Campinas, Brazil
Georgios D. Mitsis,
McGill University, Canada

****Correspondence:***
Pierre Maurel
pierre.maurel@irisa.fr

Specialty section:
This article was submitted to Applied Neuroimaging, a section of the journal Frontiers in Neurology

Received: *20 December 2020*
Accepted: *07 June 2021*
Published: *08 July 2021*

Citation:
Pinte C, Fleury M and Maurel P (2021) Deep Learning-Based Localization of EEG Electrodes Within MRI Acquisitions. Front. Neurol. 12:644278. doi: 10.3389/fneur.2021.644278

1. INTRODUCTION

Functional magnetic resonance imaging (fMRI) is a technique that allows to visualize brain activity by detecting hemodynamic variations. It is a non-invasive method that is widely used for the study of brain function [see for example (1)]. Moreover, electroencephalography (EEG) is a technique for measuring the electrical activity of the brain by using electrodes placed on the scalp, which is also a non-invasive method, widely used for the diagnosis of brain disorders and the study of neurophysiological activity (2). These two techniques are complementary and can be very relevant in the study of many neurological disorders. In particular, recent studies have shown the contribution that simultaneous EEG-fMRI can make to the understanding and treatment of epilepsy, for example in identifying epileptogenic networks (3–5). Indeed, fMRI has an excellent spatial resolution, in the order of a millimeter, and a lower temporal resolution, in the order of a second, while EEG has a high temporal resolution (milliseconds), but has a lower spatial resolution (6). In fact, source localization in EEG requires the solving of an inverse problem that is sensitive to several parameters (7), one of the main ones being the forward head model used. Another important parameter for the inverse problem is the 3D position of the electrodes on the scalp (8). Indeed, the accuracy of the estimated coordinates of the EEG electrodes impacts the localization of the EEG sources. Position errors lead to inaccuracies in the estimation of the EEG inverse solution (9). This is an even more important issue in the case of studies involving simultaneous EEG/fMRI acquisitions, where several sessions and thus several EEG cap installations can be required. Furthermore, in order to take full advantage of these mixed acquisitions, the registration between EEG and MRI data must be optimal. It is therefore essential to be able to obtain the EEG electrode positions reliably and accurately.

Several methods have been proposed to address this question (10). To begin with, there are semi-automated methods that require manual measurements (11), which are therefore time-consuming and subject to human error. Then, there are methods that require additional material, such as electromagnetic or ultrasound digitizers (12, 13). Finally, in the context of simultaneous EEG/fMRI acquisitions, there are methods that use MR localization of electrodes. In that case, a measurement system external to the EEG, the MRI, is available, but with the following problem: MRI-compatible EEG systems are designed to be as invisible as possible on most MRI sequences. Therefore, some of these methods require manual measurements (14) as well, and others require special equipment (15, 16). More recent studies have proposed the use of an ultra-short echo-time (UTE) sequence in which the electrodes are more visible (17, 18). This type of recently proposed sequences (19, 20) allows to visualize the tissues with a very short T2 and T2⋆, such as cortical bone, tendons and ligaments, and has the side-effect of enabling imaging MR compatible electrode. The introduction of these new sequences opens the door to new methods, more automatic and more easily usable in the clinical routine. Indeed, no additional equipment is required, and the additional acquisition time is quite short, which does not overburden the corresponding EEG-fMRI studies. In (21), the authors proposed a fully automated method based on a segmentation step followed by a Hough transform in order to select the positions of MR-compatible electrodes in an MRI volume using the UTE sequence. This method does not require any additional hardware and is fully automatic, but can be sensitive to scalp segmentation error. Thus, our aim here is to keep the advantages of this method (i.e., generalization and automation) while simplifying the process, which means minimizing the preliminary steps, and improving performance. In this work, we therefore also use a type of UTE sequence to create an automatic method, but study the contribution of machine learning on the electrode detection task.

Therefore, we propose a new two-fold approach based on a combination of deep learning and template-based registration. In fact, our method starts by training a model to detect the position of the electrodes in an MRI volume. This model is based on the U-Net neural network, a fully convolutional neural network whose architecture allows to obtain accurate segmentations (22). As mentioned above, we use a type of UTE sequence: the PETRA (Pointwise Encoding Time reduction with Radial Acquisition) sequence (23), which is gradually becoming the new standard in applications of UTE sequences. Finally, we use the iterative closest point (ICP) (24) algorithm to take into account the geometrical constraints after the deep learning phase, and to obtain labeling of the electrodes.

2. MATERIALS

2.1. Simultaneous EEG/fMRI

EEG signals were acquired with an MR-compatible 64-channel cap (Brain Products, Gilching, Germany) of a circumference between 56 and 58 cm, with 64 Ag/AgCl electrodes placed in conformity with the extended international 10–20 EEG system, with one additional ground electrode as AFz. Two 32-channel MR-compatible amplifiers (actiCHamp, Brain Products, Gilching, Germany) were used, and the electrodes were attached to small cups of a diameter of 10 mm and a height of 4 mm, inserted in the cap with gel. A particular attention was given to the reduction of electrode impedance and the positioning of the electrodes according to standard fiducial points.

MRI was performed with a 3T Prisma Siemens scanner running VE11C with a 64-channel head coil (Siemens Healthineers, Erlangen, Germany). PETRA acquisitions were obtained using echo-planar imaging (EPI) with the following parameters: Repetition time (TR1)/(TR2) = 3.61/2,250 ms, Inversion Time (TI1)/(TI2) = 1,300/500 ms, Echo Time (TE) = 0.07 ms, Flip Angle 6°, FOV = 300 × 300 mm^2, 0.9 × 0.9 × 0.9 mm^3 voxel size, matrix size = 320 × 105, with 60,000 and 30,000 spokes. The acquisition lasted 6 min for the 60K quality and 3 min for the 30K quality. As a result, PETRA images that we used have a size of 320 × 320 × 320 mm and a voxel spacing of 0.9375 × 0.9375 mm. We also acquired a 1 mm isotropic 3D T1 MPRAGE structural scan.

2.2. Subjects

We acquired a set of 60 PETRA volumes that came from 20 different subjects, ranging from 2 to 5 images per subject acquired at different sessions (implying a new positioning of the EEG cap), all varying between two quality levels: 30k and 60k spokes. These volumes were divided into two datasets. The first one was used to train a segmentation model, and the second one was used to test the performance of this model. We decided to separate the data by taking 12 subjects for the training dataset and 8 subjects for the test dataset, resulting in 37 training volumes and 23 test volumes.

3. METHODS

Our two-fold method consists of a first step based on a deep neural network and a second based on a template registration. **Figure 1** shows an overview of the method's principles. We will begin by describing how to proceed to train a segmentation model, from data preparation to neural network training by deep learning. Then, we will detail our method for detecting and labeling EEG electrodes on MR images, by explaining how to use the previously trained

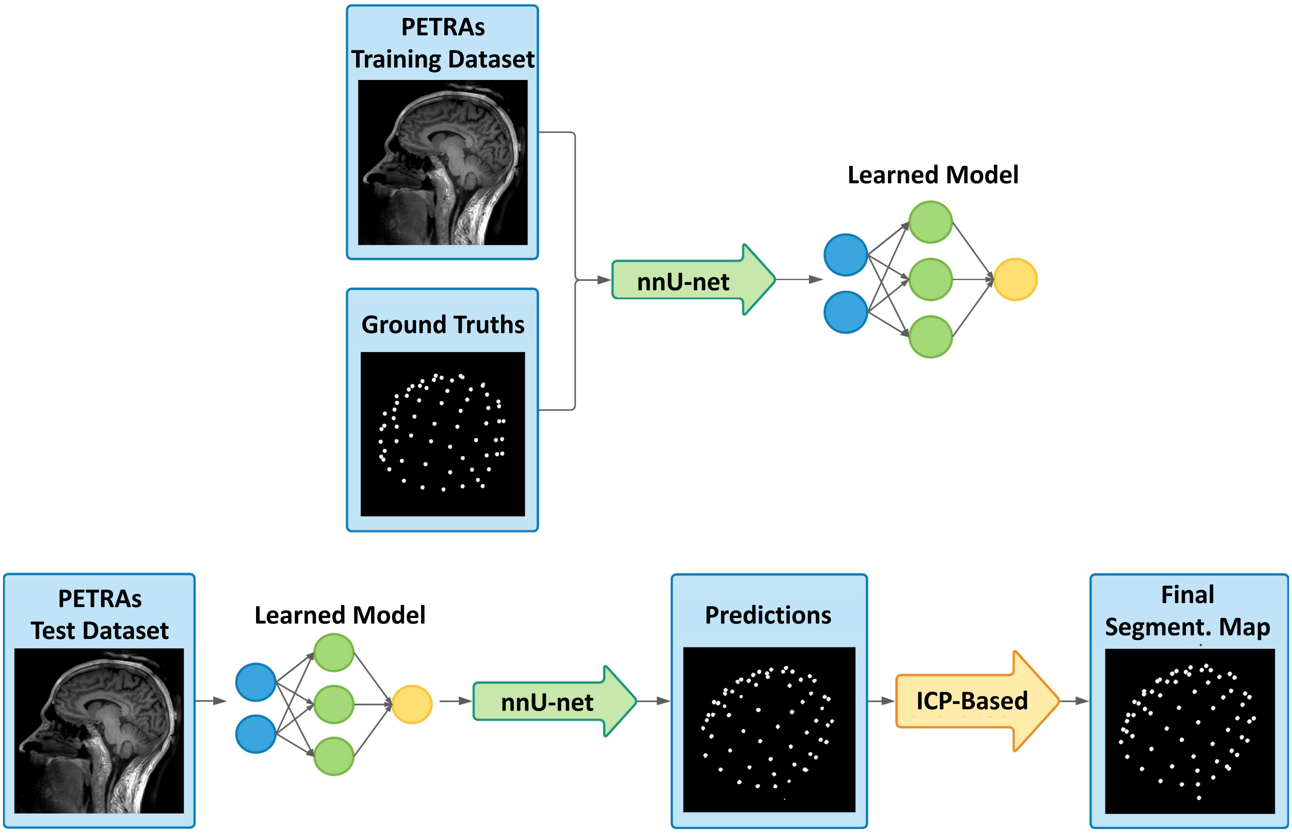

FIGURE 1 | Overview of the presented detection framework, with the learning process **(top)**, and then the deep learning-based prediction and the registration-based refinement step **(bottom)**. From the training dataset and the corresponding labeled ground truths, the deep learning model is trained using the nnU-Net framework. Secondly, our method consists of taking an image never seen by the model and making a predicted segmentation map of the electrodes. Then, template-based adjustments are carried out and the final labeled segmentation map is obtained.

model as well as the template registration step to obtain the electrode coordinates.

3.1. Ground Truth Estimation

To train our model, ground truth segmentation needs to be computed on the PETRA volumes in the training dataset. In our case, ground truths are segmentation maps of the same size and characteristics as the PETRA, with segmented spheres having a different value, also called "label," for the 65 EEG cap electrodes visible on the scalp and a value of 0 for the background.

To ease the manual creation of these ground truths, a scalp segmentation mask was first estimated. As T1 images have a higher quality than PETRA on the scalp area, this mask is obtained by firstly registering the T1 image on the corresponding PETRA image and then by segmenting the registered T1 image using the FSL library (25). These two inputs allow the use of a Matlab implementation, developed by Butler (26), of a method proposed by de Munck et al. (14) which displays a so-called "pancake" view of the scalp. This colorimetric 2D projection of the scalp region eases the manual selection of the electrode positions. As a result, a 3D labeled segmentation of each PETRA volume was created.

3.2. Training Framework

The training dataset thus consists of 37 PETRA images, and their associated ground truth, described above. We use the nnU-Net framework (27). This framework is a tool that can automate the choice of hyperparameters used to train a model from any dataset and for any segmentation task. This is very useful, especially since a large number of variations of neural network architectures have been proposed for segmentation, for example in the biomedical field, and the authors of (27) showed that slight design improvements hardly improve performance, while the choice of hyperparameters seems to be crucial. In fact, this framework with a basic U-Net architecture outperformed most of the specialized deep learning pipelines for 19 international competitions, and 49 segmentation tasks, demonstrating its efficiency but also its adaptability.

Among the different types of neural networks available, we chose the 3D U-Net (28) network whose operations such as convolutions and max pooling are replaced by their 3D counterparts. Once the neural network architecture is chosen, the framework automatically estimates the best training hyperparameters from the dataset provided as input. Here, our model is trained over 1,000 epochs (number of times each training data is considered) and 250 minibatches (number of samples considered before updating internal parameters), with a loss function which is the sum of cross-entropy and Dice loss and with a Stochastic Gradient Descent (SGD) optimizer. The patch used has a size of 128 × 128 × 128 and the default data augmentation scheme provided by nnU-net was used.

3.3. Deep Learning-Based Predictions and Template-Based Refinement

Once the model is trained, PETRA images from the test dataset can be provided as input and the model can then perform predictions. The method for making predictions, available in the nnU-net framework, consists of a sliding window approach, using the same patch size that has been used during training, overlapping half of the patch at each step. In order to increase performance, to avoid artifacts, and overall to have a good quality of segmentation, several strategies have been selected: a Gaussian importance weighting is used to reduce edge problems and stitching artifacts, and a so-called "test-time augmentation," which is data augmentation for test datasets, is used by generating slightly modified images from the tested image and averaging the detections made on them. This data augmentation step is quite time-consuming, so we will compare the results obtained with and without it in the following.

The deep network can take into account spatial information, as well as, naturally, the values present in the image. However, it has more difficulties to incorporate the rather strong geometrical constraint of our problem: the electrodes are all placed on a cap, certainly a little elastic, but the distances between electrodes are, for example, relatively steady. To take into account this geometric constraint, we propose a second step to improve the predictions provided by the neural network. The main objectives of this second step are therefore to force the number of detections to be exactly equal to 65, and to correctly label the electrodes. We start by registering the n detections (n is not necessarily equal to 65) to an average model of the EEG cap, using the Iterative Closest Point (ICP) algorithm. **Figure 2** illustrates the principles of this step.

This template used here is obtained by averaging the coordinates of 12 manually obtained ground truths point clouds from the training set (one per subject, to account for head shape variability). This step then consists of registering these two point clouds (the prediction from the deep learning step and the template) using the ICP algorithm with similarity transformation (rotation, translation, scaling). This registration algorithm (24), between two unpaired point clouds, iterates between two steps. First, each point of the moving set is associated with the nearest point in the fixed set. Then the geometric transformation that minimizes the distance between these pairs of corresponding points is estimated. We then apply this transformation and iterate until convergence.

Then, by comparing the distance between the prediction and the template points, a refinement of the detection is carried out. First, each prediction point is associated with its closest template point, and for each point of the template, only the closest prediction point is kept. As a result of this sub-step, a maximum of 65 predicted positions are conserved. Since only the predictions closest to the model were kept, outliers may have been removed from our initial detections. This is likely to improve the registration, which is why a new ICP is then performed. Finally, using this improved registration, and in the case where less than 65 predictions were kept, the missing positions are added as follows: each template point that is not associated with any prediction positions are added in the final result. Thus, our final result contains exactly 65 detections, each associated with a point of the template, which provides us with a label.

3.4. Validation on the Test Dataset

To evaluate the proposed method, and for the test dataset, we compared the detected electrodes to the ground truth coordinates obtained manually. We computed the connected components for the two images and the position of their center. Finally, for each prediction point, its distance to the nearest point of ground truth is computed. This distance is therefore considered a position error. A prediction presenting an error greater than 10 mm, corresponding to the diameter of an electrode cup, is considered as a wrong detection (false positive). Since we systematically consider the nearest ground truth electrode, we do not consider the labeling when estimating the position error. The quality of the final labeling, as well as that of the intermediate labeling, will be evaluated separately. Finally, the number of detections being exactly 65, the number of false positives is automatically equal to the number of missing points (false negatives).

3.5. Evaluation of the Robustness of the Method on a Different UTE Sequence

In order to evaluate the robustness of the method, as well as to compare our results with those of (21), we also applied it to images acquired according to a different UTE sequence, the one described in the mentioned article. First, we directly used the model learned from the PETRA images, to study the generalizability of the learned model to another MR sequence. Then, we learned a new model from the different UTE database, containing fewer images, allowing us to investigate the importance of the number of data in the learning set, but also to compare our results to the previously introduced method.

4. RESULTS

All the implementations were made on Nvidia Quadro M6000 24GB GPU (which was the most powerful graphics card in 2016 according to NVIDIA Corporation). The training then lasts between 1 and 2 weeks, depending on the number of processes launched on the GPU available. Classically in deep neural network methods, the prediction of one test data is much faster. The presented method predicts a segmentation map from a PETRA image in about 7 min on the above-mentioned GPU.

4.1. With Test-Time Augmentation

The results are assessed by measuring the position error as described in the validation section, for all volumes in the test dataset. **Table 1** presents the average results for all subjects in the PETRA test dataset. This test set consists of 23 volumes, from

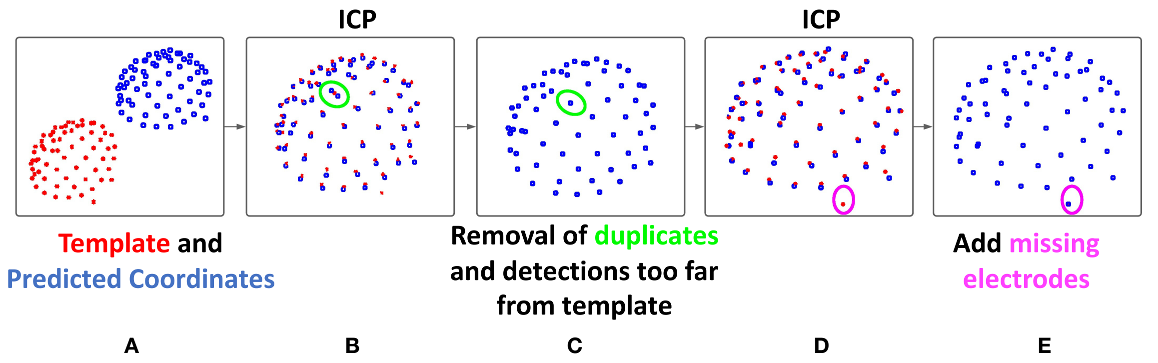

FIGURE 2 | Description of the registration-based refinement step. **(A)** In blue: the prediction points from the deep learning-based step, in red: the template obtained by averaging on the training set, **(B)** a first ICP is performed in order to register the two points cloud, **(C)** for each template point, only the closest detection is kept, **(D)** then, a second ICP is performed and the number of detections is now less than or equal to 65, **(E)** finally, the points in the model not associated with any predictions are added to our final result, which therefore contains exactly 65 detections.

TABLE 1 | Electrodes detection on the test dataset.

	Deep learning-based detection	Final results
Mean PE (mm)	2.12	2.24
Std PE (mm)	1.50	1.37
Max PE (mm)	8.84	7.99
Mean number of false positives	0.30	0.22
Mean number of true positives	65.0	64.8
PPV (%)	99.5	99.7

Rows 1,2,3: mean, standard deviation, and maximum values of Position Error (PE). Rows 4,5: mean number of false positives (PE $>$ 10 mm) and true positives (PE $\leq$ 10 mm). Second column: intermediate results after the deep learning step. Third column: our final results after registration-based refinement step.

8 different subjects not included in the learning data set, with sampling resolutions of either 30k or 60k spokes, corresponding to a more or less long acquisition time. The average position error is equal to 2.24 mm, to be compared with the diameter of one electrode cup, 10 mm. The number of good (true positive) and wrong (false positive) detections was also assessed, taking that distance of 10 mm as the threshold. As can be seen in the table, after the deep learning step, the number of detections was too high on average, and it was corrected after the registration step, resulting in a better Positive Predictive Value (PPV) defined as the percentage of detections that are true positive relative to the total number of detections.

The average total number of detections after the first step is 65.3 (65+0.3) and is therefore higher than the actual number of electrodes (65). This is totally logical since the neural network architecture used does not incorporate any constraint on the number of detections. The output of this first step is a simple volume, where, at each voxel, a label indicates whether it is considered to belong to the background or to a specific electrode. Note that, in this case, two detections associated with the same electrode can count as two good detections, as long as their distance to the said ground truth electrode is less than 10mm. After our registration-based refinement step, the final number of detections is, as expected, exactly equal to 65 (64.8+0.22). Twenty-three volumes were processed, corresponding to a total of 1,495 electrodes, out of which 1,490 were correctly detected and 5 were missed. These missing electrodes often corresponded to those located behind the ears and provoked few outliers in the output. These outliers are reflected in the value of the average maximum error, 8.84 mm. One can note a slight increase of the mean PE after registration. The refinement step indeed usually allows the recovering of some missing electrodes in the intermediate detections provided by the neural network. These new electrodes are therefore provided by the registered model. Although often considered as "true positives" because they are close enough to the ground truth, they are sometimes a little less accurate than the MRI-based detections and cause this relative increase of the mean PE. However, it can be noted that this increase in mean PE comes with a decrease in the standard deviation of position error.

Finally, regarding labeling, 100% of the electrodes were correctly labeled in our final results. As can be seen in the **Table 2**, this was not the case after the deep learning step. This explains our choice of ICP for the registration step: we cannot always rely on the labeling of intermediate results. Indeed, the number of labeling errors can be as many as 11 in a volume. In fact, these observed errors often correspond to a simple offset in labeling: an electrode is incorrectly labeled and all its neighbors are then likely to be contaminated by this error. We therefore decided to disregard the labeling information provided by the neural network and rely solely on the ICP result for this. It may seem a bit odd to include labels in the ground truth for the training step since we discard the resulting label afterward. Nevertheless, our experiences have interestingly shown that training a neural network with labeled ground truth improves detection results (in terms of position error) compared to a situation where the ground truths are simple binary maps. In particular, in the case where 65 different labels are provided during training, the network is

TABLE 2 | Electrodes labeling on the test dataset.

Number of labeling errors among true positives	Deep learning-based detection	Final results
Mean	1.87	0
Maximum	11	0

Number of labeling errors among the true positives, for the intermediate results from deep learning and for our final results.

TABLE 3 | Faster electrode detection on the test dataset.

	Faster deep learning-based detection	Final results
Mean PE (mm)	6.78	2.23
Std PE (mm)	25.4	1.40
Max PE (mm)	168.7	8.20
Mean number of false positives	2.57	0.13
Mean number of true positives	65.1	64.9
PPV (%)	96.3	99.8

Rows 1,2,3: mean, standard deviation, and maximum values of Position Error (PE). Rows 4,5: mean number of false positives (PE $>$ 10 mm) and true positives (PE $\leq$ 10 mm). Second column: intermediate results after the faster deep learning step. Third column: our final results after registration-based refinement step.

TABLE 4 | Electrodes labeling on the test dataset for the faster version.

Number of labeling errors among true positives	Deep learning-based detection	Final results
Mean	3.2	0
Maximum	13	0

Number of labeling errors among the true positives, for the intermediate results from deep learning and for our final results.

TABLE 5 | Electrodes detection on the UTE dataset, using the previous model, learned using the PETRA images.

	Deep learning-based detection	Final results
Mean PE (mm)	1.81	2.47
Std PE (mm)	1.67	1.64
Max PE (mm)	11.06	9.36
Mean number of false positives	0.33	0.72
Mean number of true positives	56.4	64.22
PPV (%)	99.4	98.89

Rows 1,2,3: mean, standard deviation, and maximum values of Position Error (PE). Rows 4,5: mean number of false positives (PE $>$ 10 mm) and true positives (PE $\leq$ 10 mm). Second column: intermediate results after the deep learning step. Third column: our final results after registration-based refinement step.

more likely to detect a number close to 65 also during the test phase.

4.2. Faster Predictions Without Test-Time Augmentation

For each new PETRA image provided, the method presented above allows us to make predictions in about 7 min on our GPU, almost all of this time being used by the first step, based on neural network. As a matter of fact, the ICP-based refinement step runs in few seconds. Therefore, we finally explored the possibility of reducing the computing time required by the neural network to obtain a prediction. To this end, we have removed the test-time augmentation, mentioned in section 3.3. The prediction time of an image was then significantly reduced to about 2 min. **Table 3** presents the results of this faster detection pipeline.

All of the indicators for intermediate results, after the deep learning-based step alone, show that they are clearly worse with this accelerated version: strong increase in Position Error (mean, standard deviation, and maximum values) and increase of the total number of detections. However, the associated detections contain enough valuable information so that the robustness brought by our refinement step allows us to finally obtain results as good as in the first version, as reported in **Table 1**. Counter-intuitively, some metric values are even slightly better. However, a statistical paired t-test showed that none of these changes were significant ($p > 0.5$ for all comparisons).

Finally, and as in the original version, the labeling contained some errors in the intermediate results, but is completely accurate in our final results, even with this faster version, as shown in **Table 4**. The second step, already important to improve the results in the previous version, turns out to be crucial when we want to accelerate the processing by the neural network, and allows us to obtain similar results.

4.3. Tests on a Different UTE Sequence

In order to evaluate the robustness of our method, we challenged it by testing it on a data set from another MRI sequence, the original UTE one (21). Eleven subjects were included in this new study. A 60k-spokes acquisition was done for all subjects and a 30k-spokes image was acquired for seven of them.

First, the previous model, learned using the PETRA images, was used to detect the electrode positions on these 18 new images, acquired with a different UTE sequence. Results are shown in **Table 5**. As expected, the detections estimated by the neural network were not as good as in the previous case. Indeed, the average number of electrodes provided was lower than 57. However, and very interestingly, these electrodes were mostly true detections. For this reason, and as can be seen in the table, the ICP-based registration step was able to retrieve almost all missing electrodes, leading once again to excellent performance results. Our registration-based refinement step thus brings robustness to the method, allowing to limits the risk of overfitting, and improving its generalizability.

Finally, in order to compare our results to (21), we learned a new neural network, using only this different UTE sequence, applied the refinement step, and evaluated the resulting performance. From the previously described UTE dataset, we built two groups: 9 MRI volumes in the training set and 9

TABLE 6 | Electrodes detection on the UTE dataset, using a new model, learned using images acquired with the same UTE sequence.

	Deep learning-based detection	Final results
Mean PE (mm)	1.70	2.42
Std PE (mm)	1.24	1.29
Max PE (mm)	8.02	8.19
Mean number of false positives	0.56	0.44
Mean number of true positives	60.0	64.6
PPV (%)	99.1	99.3

Rows 1,2,3: mean, standard deviation, and maximum values of Position Error (PE). Rows 4,5: mean number of false positives (PE > 10 mm) and true positives (PE ≤ 10 mm). Second column: intermediate results after the deep learning step. Third column: our final results after registration-based refinement step.

volumes in the test set, again ensuring that no subjects were present in both sets. **Table 6** shows the corresponding results. Training the model using the same type of images as in the tests slightly improves the quality of the detections, compared to when training the model on PETRA images. Moreover, and despite this smaller group size (compared to the PETRA study), our results are now better than those reported in (21). For example, the mean PPV is now 99.3% and was between 88 and 94% for 30k and 60k spokes images, respectively.

For both of these cases, all the detected electrodes were once again well-labeled: there was no mislabeling among the true positives.

5. DISCUSSION

We have introduced a new fully automatic method for the detection of EEG electrodes in an MRI volume during simultaneous EEG-MRI acquisition. This technique is easy to set up and use, and gives accurate and reliable results. Indeed, after the model has been learned once and for all, the method requires nothing more than acquiring a PETRA volume, after the installation of the EEG headset. No additional equipment is required, and the PETRA volume can be acquired in a few minutes. The computation time is, for the most part, used by the deep learning-based prediction. This can be accelerated up to 2 min and is the most important part of the proposed method. Nevertheless, as the results showed, the second registration-based step allows both to improve the final results and to make them more robust to possible outliers.

It is well-known that deep learning models are highly dependent on the quality and representativeness of the data in the learning set. Our first investigations in this direction, using a different UTE sequence, seem to indicate that the method can be generalized to other types of images, even keeping the model learned on the initial data, thanks to the robustness brought by the registration step. Another interesting question is the behavior of the method when the number of electrodes is not the same between the learning and testing phases. One can hope that the robustness brought by the second ICP-based step can provide a good detection, if the same sequence and the same type of electrodes are used, but this needs to be verified with a future investigation. Finally, this method has been tested on one type of EEG cap (Brain Products), but is valid for any detection problem of elements on the scalp. It will therefore also be interesting to test it on other EEG headsets, but also on other systems, for example, the near-infrared spectroscopy (NIRS) modality, which consists of a system of optodes placed on the scalp.

Finally, it should also be noted that our second study, on the original UTE sequence, had a smaller sample size, probably more consistent with a typical simultaneous EEG-MRI study (11 subjects were involved, corresponding to 18 volumes, and only 9 of these were used in the training phase). Despite the smaller amount of data, the results (**Table 6**) were only slightly less good than those obtained with a larger sample (**Table 1**).

6. CONCLUSION

We presented a new method for the detection and labeling of EEG electrodes in an MR volume acquired using PETRA sequence. The first step is to train a model from a set of training data and associated manual ground truths, then use this model to obtain a segmentation map, and finally to apply a step using the ICP registration algorithm to improve the detections and their labeling. This fully automatic method is easy to implement, requires very few steps, and gives excellent results. For all these reasons, we strongly believe that it can be very useful for all protocols with simultaneous EEG-fMRI acquisitions. In particular, when an EEG source localization is planned later, as is often the case when studying epilepsy, accurate information on the position of the electrodes is a definite advantage.

DATA AVAILABILITY STATEMENT

The datasets presented in this article are not readily available because of patient data. Requests to access the datasets should be directed to the corresponding author.

ETHICS STATEMENT

The studies involving human participants were reviewed and approved by Comite de Protection des Personnes Ouest V Rennes. The patients/participants provided their written informed consent to participate in this study.

AUTHOR CONTRIBUTIONS

CP, MF, and PM: conception of the method and manuscript writing. CP: implementation. All authors contributed to the article and approved the submitted version.

FUNDING

This project was supported by the National Research Agency in the Investing for 540 the Future program under reference ANR-10-LABX-07-0, and by the Fondation pour la Recherche Médicale under the convention #DIC20161236427.

ACKNOWLEDGMENTS

MRI data acquisition was partly supported by the Neurinfo MRI research facility from the University of Rennes I. Neurinfo is granted by the European Union (FEDER), the French State, the Brittany Council, Rennes Metropole, Inria, and the University Hospital of Rennes.

REFERENCES

1. Arthurs OJ, Boniface S. How well do we understand the neural origins of the fMRI BOLD signal? *Trends Neurosci*. (2002) 25:27–31. doi: 10.1016/S0166-2236(00)01995-0
2. Teplan M. Fundamentals of EEG measurement. *Meas Sci Rev*. (2002) 2:1–11.
3. Maloney TC, Tenney JR, Szaflarski JP, Vannest J. Simultaneous electroencephalography and functional magnetic resonance imaging and the identification of epileptic networks in children. *J Pediatr Epilepsy*. (2015) 4:174–83. doi: 10.1055/s-0035-1559812
4. Dong L, Luo C, Zhu Y, Hou C, Jiang S, Wang P, et al. Complex discharge-affecting networks in juvenile myoclonic epilepsy: a simultaneous EEG-fMRI study. *Hum Brain Mapp*. (2016) 37:3515–29. doi: 10.1002/hbm.23256
5. Omidvarnia A, Kowalczyk MA, Pedersen M, Jackson GD. Towards fast and reliable simultaneous EEG-fMRI analysis of epilepsy with automatic spike detection. *Clin Neurophysiol*. (2019) 130:368–78. doi: 10.1016/j.clinph.2018.11.024
6. Mele G, Cavaliere C, Alfano V, Orsini M, Salvatore M, Aiello M. Simultaneous EEG-fMRI for functional neurological assessment. *Front Neurol*. (2019) 10:848. doi: 10.3389/fneur.2019.00848
7. Pascual-Marqui RD, Michel CM, Lehmann D. Low resolution electromagnetic tomography: a new method for localizing electrical activity in the brain. *Int J Psychophysiol*. (1994). 18:49–65. doi: 10.1016/0167-8760(84)90014-X
8. Akalin Acar Z, Makeig S. Effects of forward model errors on EEG source localization. *Brain Topogr*. (2013) 26:378–96. doi: 10.1007/s10548-012-0274-6
9. Khosla D, Don M, Kwong B. Spatial mislocalization of EEG electrodes-effects on accuracy of dipole estimation. *Clin Neurophysiol*. (1999) 110:261–71. doi: 10.1016/S0013-4694(98)00121-7
10. Koessler L, Maillard L, Benhadid A, Vignal JP, Braun M, Vespignani H. Spatial localization of EEG electrodes. *Neurophysiol Clin*. (2007) 37:97–102. doi: 10.1016/j.neucli.2007.03.002
11. De Munck J, Vijn P, Spekreijse H. A practical method for determining electrode positions on the head. *Electroencephalogr Clin Neurophysiol*. (1991) 78:85–7. doi: 10.1016/0013-4694(91)90023-W
12. Le J, Lu M, Pellouchoud E, Gevins A. A rapid method for determining standard 10/10 electrode positions for high resolution EEG studies. *Electroencephalogr Clin Neurophysiol*. (1998) 106:554–8. doi: 10.1016/S0013-4694(98)00004-2
13. Steddin S, Bötzel K. A new device for scalp electrode localization with unrestrained head. *J Neurol*. (1995) 242:65.
14. de Munck JC, van Houdt PJ, Verdaasdonk RM, Ossenblok PP. A semi-automatic method to determine electrode positions and labels from gel artifacts in EEG/fMRI-studies. *Neuroimage*. (2012) 59:399–403. doi: 10.1016/j.neuroimage.2011.07.021
15. Adjamian P, Barnes G, Hillebrand A, Holliday I, Singh KD, Furlong PL, et al. Co-registration of magnetoencephalography with magnetic resonance imaging using bite-bar-based fiducials and surface-matching. *Clin Neurophysiol*. (2004) 115:691–8. doi: 10.1016/j.clinph.2003.10.023
16. Whalen C, Maclin EL, Fabiani M, Gratton G. Validation of a method for coregistering scalp recording locations with 3D structural MR images. *Hum Brain Mapp*. (2008) 29:1288–301. doi: 10.1002/hbm.20465
17. Butler R, Gilbert G, Descoteaux M, Bernier PM, Whittingstall K. Application of polymer sensitive MRI sequence to localization of EEG electrodes. *J Neurosci Methods*. (2017) 278:36–45. doi: 10.1016/j.jneumeth.2016.12.013
18. Marino M, Liu Q, Brem S, Wenderoth N, Mantini D. Automated detection and labeling of high-density EEG electrodes from structural MR images. *J Neural Eng*. (2016) 13:056003. doi: 10.1088/1741-2560/13/5/056003
19. Holmes JE, Bydder GM. MR imaging with ultrashort TE (UTE) pulse sequences: basic principles. *Radiography*. (2005) 11:163–74. doi: 10.1016/j.radi.2004.07.007
20. Keereman V, Fierens Y, Broux T, Deene YD, Lonneux M, Vandenberghe S. MRI-based attenuation correction for PET/MRI using ultrashort echo time sequences. *J Nuclear Med*. (2010) 351:812–8. doi: 10.2967/jnumed.109.065425
21. Fleury M, Barillot C, Mano M, Bannier E, Maurel P. Automated electrodes detection during simultaneous EEG/fMRI. *Front ICT*. (2019) 5:31. doi: 10.3389/fict.2018.00031
22. Ronneberger O, Fischer P, Brox T. U-net: convolutional networks for biomedical image segmentation. In: *International Conference on Medical Image Computing and Computer-Assisted Intervention*. Munich: Springer (2015) p. 234–41. doi: 10.1007/978-3-319-24574-4_28
23. Grodzki DM, Jakob PM, Heismann B. Ultrashort echo time imaging using pointwise encoding time reduction with radial acquisition (PETRA). *Magnet Reson Med*. (2012) 67:510–8. doi: 10.1002/mrm.23017
24. Besl PJ, McKay ND. A method for registration of 3-D shapes. *IEEE Trans Pattern Anal Mach Intell*. (1992) 14:239–56. doi: 10.1109/34.121791
25. Jenkinson M, Beckmann CF, Behrens TEJ, Woolrich MW, Smith SM. FSL. *Neuroimage*. (2012) 62:782–90. doi: 10.1016/j.neuroimage.2011.09.015
26. Butler R. *Electrode Hand Labeling and Segmentation Based off of UTE Image Intensity*. (2017). Available online at: https://github.com/russellu/ute_git/ (accessed August 19, 2020).
27. Isensee F, Jäger PF, Kohl SA, Petersen J, Maier-Hein KH. nnU-Net: a self-configuring method for deep learning-based biomedical image segmentation. *Nat Methods*. (2021) 18:203–11. doi: 10.1038/s41592-020-01008-z
28. Çiçek Ö, Abdulkadir A, Lienkamp SS, Brox T, Ronneberger O. 3D UNet: learning dense volumetric segmentation from sparse annotation. In: Ourselin S, Joskowicz L, Sabuncu M, Unal G, Wells W, editors. *Medical Image Computing and Computer-Assisted Intervention - MICCAI 2016*. Vol. 9901. Cham: Springer (2016). p. 424–32. doi: 10.1007/978-3-319-46723-8_49

Conflict of Interest: The authors declare that the research was conducted in the absence of any commercial or financial relationships that could be construed as a potential conflict of interest.

frontiers in Neurology

ORIGINAL RESEARCH
published: 02 August 2021
doi: 10.3389/fneur.2021.670881

Functional Connectivity of the Anterior Nucleus of the Thalamus in Pediatric Focal Epilepsy

Rory J. Piper[1,2,3]*, **Chayanin Tangwiriyasakul**[4,5], **Elhum A. Shamshiri**[6,7,8], **Maria Centeno**[9], **Xiaosong He**[10], **Mark P. Richardson**[4], **Martin M. Tisdall**[2] **and David W. Carmichael**[3]

[1] Department of Neurosurgery, John Radcliffe Hospital, Oxford, United Kingdom, [2] Department of Neurosurgery, Great Ormond Street Hospital for Children, UCL Great Ormond Street Institute of Child Health, London, United Kingdom, [3] Wellcome EPSRC Centre for Medical Imaging, Department of Biomedical Engineering, King's College London, London, United Kingdom, [4] Department of Basic and Clinical Neuroscience, Institute of Psychiatry Psychology and Neuroscience, King's College London, London, United Kingdom, [5] School of Biomedical Engineering and Imaging Sciences, King's College London, London, United Kingdom, [6] San Francisco Veterans Affairs Health Care System (SFVAHCS), San Francisco, CA, United States, [7] Department of Psychiatry, University of California, San Francisco, San Francisco, CA, United States, [8] Sierra Pacific Mental Illness Research Education and Clinical Centers, San Francisco, CA, United States, [9] Epilepsy Unit, Neurology Department, Hospital Clinic, Barcelona, Spain, [10] Department of Psychology, University of Science and Technology of China, Hefei, China

OPEN ACCESS

Edited by:
Jan Kassubek,
University of Ulm, Germany

Reviewed by:
Yann Quidé,
University of New South Wales, Australia
Eelco Van Duinkerken,
Hospital Universitário Gaffrée e Guinle, Brazil

***Correspondence:**
Rory J. Piper
rorypiper@doctors.org.uk

Specialty section:
This article was submitted to Applied Neuroimaging, a section of the journal Frontiers in Neurology

Received: 22 February 2021
Accepted: 27 May 2021
Published: 02 August 2021

Citation:
Piper RJ, Tangwiriyasakul C, Shamshiri EA, Centeno M, He X, Richardson MP, Tisdall MM and Carmichael DW (2021) Functional Connectivity of the Anterior Nucleus of the Thalamus in Pediatric Focal Epilepsy. Front. Neurol. 12:670881. doi: 10.3389/fneur.2021.670881

Objective: Whilst stimulation of the anterior nucleus of the thalamus has shown efficacy for reducing seizure frequency in adults, alterations in thalamic connectivity have not been explored in children. We tested the hypotheses that (a) the anterior thalamus has increased functional connectivity in children with focal epilepsy, and (b) this alteration in the connectome is a persistent effect of the disease rather than due to transient epileptiform activity.

Methods: Data from 35 children (7–18 years) with focal, drug-resistant epilepsy and 20 healthy children (7–17 years) were analyzed. All subjects underwent functional magnetic resonance imaging (fMRI) whilst resting and were simultaneously monitored with scalp electroencephalography (EEG). The fMRI timeseries were extracted for each Automated Anatomical Labeling brain region and thalamic subregion. Graph theory metrics [degree (DC) and eigenvector (EC) centrality] were used to summarize the connectivity profile of the ipsilateral thalamus, and its thalamic parcellations. The effect of interictal epileptiform discharges (IEDs) captured on EEG was used to determine their effect on DC and EC.

Results: DC was significantly higher in the anterior nucleus ($p = 0.04$) of the thalamus ipsilateral to the epileptogenic zone in children with epilepsy compared to controls. On exploratory analyses, we similarly found a higher DC in the lateral dorsal nucleus ($p = 0.02$), but not any other thalamic subregion. No differences in EC measures were found between patients and controls. We did not find any significant difference in DC or EC in any thalamic subregion when comparing the results of children with epilepsy before, and after the removal of the effects of IEDs.

Conclusions: Our data suggest that the anterior and lateral dorsal nuclei of the thalamus are more highly functionally connected in children with poorly controlled focal epilepsy. We did not detect a convincing change in thalamic connectivity caused by transient epileptiform activity, suggesting that it represents a persistent alteration to network dynamics.

Keywords: epilepsy, focal epilepsies, childhood epilepsies, deep brain stimulation, functional magnetic resonance imaging, electroencephaloagraphy, connectivity, thalamus

INTRODUCTION

Focal epilepsy is increasingly recognized as a disorder of brain connectivity (1–4), and both structural and functional connectome studies suggest that large-scale network alterations associate with epilepsy (5, 6). The thalamus has been implicated as a major "hub" in epilepsy since it integrates information across multiple functional cortical networks (7). Thalamo-cortical connectivity has long been implicated in the network-based pathogenesis of epileptic seizures (8–10), and has been shown to be a mechanism of interhemispheric seizure propagation, both in generalized (11, 12) and focal epilepsies (13).

Deep brain stimulation (DBS) has therefore become a potential surgical treatment for epilepsy and the SANTE trial in 2010 showed that bilateral stimulation of the anterior nuclei of the thalamus reduced seizure frequency in adults with both medically refractory, temporal lobe, and extratemporal lobe epilepsy (14). Mechanistic understanding of the alterations to thalamic connectivity that may be targeted by this therapy are invaluable for increasing, and potentially predicting efficacy. Thalamic DBS could be therapeutic in children but thus far has not yet been accepted as a therapeutic option to the same degree as in adults. In part this may be explained by the paucity of data on therapeutic outcomes of DBS in this group (15).

There have been a number of human neuroimaging studies in temporal lobe epilepsy (TLE) in adults that examined the significance of the thalamus in the functional and structural connectomes. Magnetic resonance imaging (MRI) currently offers the only non-invasive method of examining the role of thalamic connectivity within the whole-brain connectome. Graph theory has been increasingly used to analyze these structural and functional brain networks to understand the alterations posed by disease states such as epilepsy. Measures such as degree centrality (number of functional connections with other brain regions) and eigenvector centrality ("influence" of a node within a network) have commonly been used.

Studies from functional MRI (fMRI) have shown that the thalamus is a hub of functional connectivity in patients with TLE when compared to controls (16). The study by He et al. (16) demonstrated that the thalami of patients with TLE who were not seizure-free following temporal lobe resection had a higher degree and eigenvector centrality than compared to patients rendered seizure free and healthy controls. Studies of connectivity using diffusion tensor imaging (DTI) have shown findings suggestive of decreased structural connectivity between medial thalamic and temporal regions. Whilst this may seem paradoxical to findings from functional studies, this still strengthens the association of the abnormal connectivity between thalamus and the epileptogenic zone (17, 18). What is not clear from these imaging studies, however, is whether this altered thalamic connectivity is a result of the persistent effect of epilepsy or is instead due to transient interictal epileptiform activity. Interictal epileptiform discharges (IEDs) have been associated with significant thalamic or basal ganglia involvement in children with focal epilepsy (19, 20). This raises a question as to whether the differences in the functional connectivity seen in other studies may be driven by the transient epileptiform activity.

There has been notably less work on establishing the significance of the thalamus in the functional connectome in childhood focal epilepsies, particular in extratemporal epilepsy which has recently been reported to constitute 37.9% of all pediatric epilepsy surgeries (21). We therefore set out to test the hypothesis that the anterior nucleus of the thalamus has a higher level of functional connectivity in children with focal epilepsy than in those without epilepsy. We aimed to do this by using graph theory to measure connectiveness (degree and eigenvector centrality) of the anterior thalamus, as performed in prior studies (16). We additionally wished to test the hypothesis that these changes are not predominantly due to transient effects, but rather persisting alterations in the network.

METHODS

Our methodology and imaging pipeline is summarized in **Figure 1**.

Patients

This study examined data obtained from 35 children with drug-resistant, focal epilepsy undergoing evaluation for epilepsy surgery at Great Ormond Street Hospital (London, United Kingdom) (20/35 female, median age 15 years, age range 7–18 years), previously described in the work by Centeno et al. (19, 22). We excluded patients in whom there were large lesions that deformed brain architecture to ensure a reliable parcellation of brain regions would be possible in all subjects. The putative epileptogenic zone (determined by the epilepsy multidisciplinary team by means of clinical, neurophysiological, and neuroimaging data) was most commonly the frontal lobe (21/35 cases). The putative epileptogenic zone was lateralized to the left-side in 20/35 children. We summarize the patient details individually in **Table 1** and at a group level in **Table 2**. Our control group consisted of twenty children without epilepsy (13/20 female,

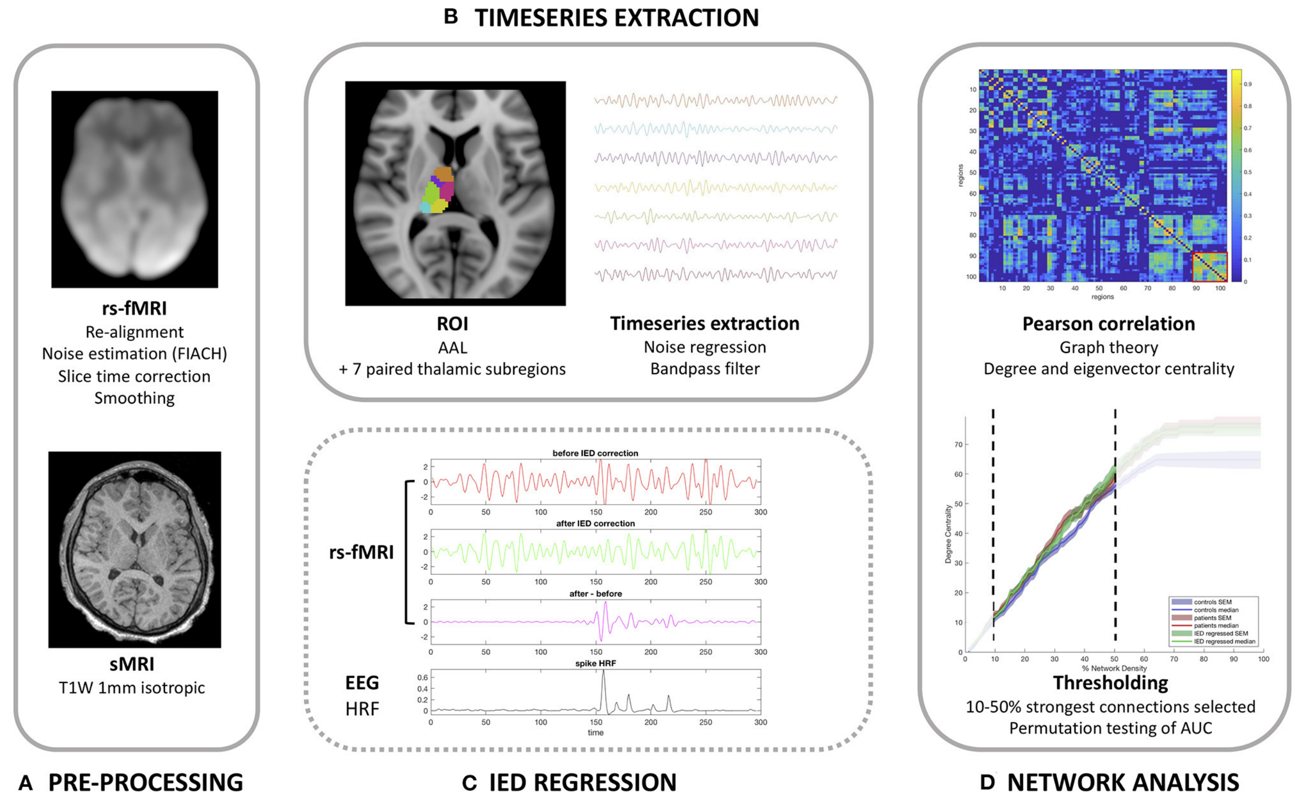

FIGURE 1 | Imaging analysis pipeline. **(A)** Pre-processing pipeline. **(B)** Timeseries extraction. **(C)** Demonstration of the correction method for interictal epileptiform discharges (IEDs) in the anterior nucleus of the thalamus for patients 13 (one spike type) as detailed in **Table 1**. **(D)** Functional network analysis.

median age 10 years, age range 7–17 years). Ethical approval was given by the NRES Committee London: Surrey Borders Research Ethics Committee London Center (REC reference: 11/LO/1421). The guardian of each participant provided informed and written consent on the participant's behalf.

Magnetic Resonance Imaging Acquisition

All subjects underwent simultaneous EEG-fMRI according to the protocol previously published Centeno et al. (22). Briefly, subjects were scanned at Great Ormond Street Hospital (London, United Kingdom) in a 1.5T Siemens Avanto scanner using a 12 channel receive head coil. One cubic millimeter isotropic T1-weighted images were acquired using a Fast Low Angle Single Shot (FLASH) gradient echo sequence. The fMRI acquisition consisted of echo planar imaging (EPI) with 3.3×3.3×4 mm resolution with a field of view of 210 mm, TR of 2,160 ms, TE of 30 ms and flip angle of 75 . There were 30 contiguous slices in each volume with a slice thickness of 3 mm, slice gap of 1 mm, and matrix of 64 × 64. There were 300 volumes per session but the first five volumes in each session were omitted. Each subject underwent up-to four fMRI sessions (each for 10 min and 48 s), based on their ability to tolerate all of the sessions. In two randomly allocated sessions the child watched a cartoon, and in the other two sessions the child was asked to rest with their eyes closed. We chose to include the first resting fMRI session, in which children were asked to rest with their eyes closed, since this session had reduced motion compared to the second on average (22).

Image Pre-processing

Image pre-processing was performed using Statistical Parametric Mapping (SPM; https://www.fil.ion.ucl.ac.uk/spm/software/spm12/). fMRI data was re-aligned and then the Functional Image Artifact Correction Heuristic (FIACH) method (23) was applied. This removes biophysically implausible signal jumps, and creates a parsimonious noise model from brain regions exhibiting high noise levels. This method has been shown to be highly effective when compared to a number of alternative pipelines (23, 24). The six noise regressors estimated by FIACH were added to the six re-alignment parameters generated by SPM. The fMRI data was then corrected for slice-timing and then registered to the 1 mm isotropic T1W volume. Image registration was visually verified for each subject. Each patient's T1W volumes were normalized to standard space (MNI 152 template) and then the fMRI was normalized using the derived transform. The fMRI volumes were then converted to a 2 mm isotropic resolution following the normalization step. A Gaussian kernel was used to smooth fMRI 8 mm in each direction.

TABLE 1 | Demographic, clinical, neurophysiological, and neuroradiological descriptions of each child.

ID	Age* (years)	Age of onset** (years)	Sex	Laterality of EZ	Location of EZ	MRI features	Focal vs. multifocal	No. of IEDs	Medications
1	8		Female	Left	Temporal	Tuberous sclerosis	Focal	2	NZP and ZNS
2	14	4	Female	Left	Frontal	Cryptogenic	Focal	2	LCM and LVT
3	11	0.25	Male	Left	Hypothalamus/temporal	Hypothalamic hamartoma	Focal	59	LVT
4	15	10	Male	Left	Posterior quadrant	Cryptogenic	Multifocal	31, 10	CBZ
5	17		Male	Right	Parietal	Focal cortical dysplasia	Multifocal	51, 37, 71, 28	LVT, CBZ, and VPA
6	15	10	Male	Right	Frontal-central	Cryptogenic	Focal	15	CBZ
7	17	3	Female	Left	Temporal	Cryptogenic	Multifocal	175, 30, 131	LVT
8	14	2.5	Female	Right	Temporal	Focal cortical dysplasia	Multifocal	206, 16	LVT and TOP
9	11	6	Female	Right	Frontal-temporal	Cryptogenic	Focal	132	CBZ and LTG
10	11	7	Female	Right	Frontal	Focal cortical dysplasia	Focal	141	OXC
11	17	10	Female	Right	Frontal	Cryptogenic	Focal	34	LTG and LEV
12	16	6	Female	Left	Frontal	Cryptogenic	Focal	7	VPA and CBZ
13	16	13	Female	Left	Insula	Focal cortical dysplasia	Focal	76	TPM and CBZ
14	11	3	Male	Right	Frontal	Cryptogenic	Multifocal	128, 29	CBZ
15	11	8	Male	Right	Frontal	Cryptogenic	Multifocal	25, 1	LVT and VPA
16	16	2	Female	Left	Temporal-parietal-occipital	Polymicrogyria	Multifocal	236, 62, 39	LEV and CLNZ
17	15	9	Male	Left	Temporo-occipital	Hippocampal sclerosis	Multifocal	83, 21	LMT 575 Zonasimne 200
18	15	8	Male	Left	Fronto-temporal	Focal cortical dysplasia	Focal	112	OXZC 1200 LVT
19	17	5	Female	Left	Frontal	Cryptogenic	Focal	82	OXC
20	8	4	Female	Left	Frontal	Middle cerebral artery stroke	Focal	150	VPA 1200, LEV 600, ETHX 1000
21	16		Male	Left	Frontal	Cryptogenic	Multifocal	129, 77	PMP
22	13	3	Male	Left	Frontal	Focal cortical dysplasia	Focal	26	OXC and CLBZ
23	10	3	Female	Left	Frontal	Cryptogenic	Multifocal	47, 4	LVT and CBZ
24	11	6	Male	Right	Posterior quadrant	Cryptogenic	Multifocal	25, 23, 5	OXC
25	17	8	Male	Left	Frontal	Cryptogenic	Multifocal	35, 13	LVT, OXC, and CLBZ
26	17		Male	Right	Occipital	Ischaemic perinatal insult	Focal	21	OXC, LMT, and LVT 2000
27	18		Female	Right	Frontal	Focal cortical dysplasia	Multifocal	148, 6	LTG
28	17	5	Female	Right	Fronto-temporal	Bilateral polymicrogyria	Multifocal	242, 43	LVT and VPA
29	11		Female	Right	Parietal	Cryptogenic	Focal	81	OXC, PHE, and CLBZ
30	17	5	Male	Left	Frontal	Cryptogenic	Focal	67	LVT and LAC
31	11	5	Female	Right	Parietal	Focal cortical dysplasia	Focal	450	OXC, CLBZ, and VPA
32	17	12	Female	Left	Frontal	Cryptogenic	Multifocal	62, 1, 75	VPA
33	13	7	Female	Left	Frontal	Focal cortical dysplasia	Multifocal	128, 23	VPA
34	15		Female	Right	Posterior cingulate	Dysembryoplastic neuroepithelial tumor	Focal	26	LVT and LTG
35	7		Male	Left	Frontal	Cryptogenic	Focal	145	LVT, OXC, and CLBZ

*The number of interictal epileptiform discharges (IEDs) are listed for each IED type within each patient. EZ, epileptogenic zone; IED, interictal epileptiform discharge; *Age rounded to nearest integer. **Age-of-onset (if known) is an approximate. CBZ, Carbamazepine; CLBZ, Clobazam; GAB, Gabapentin; LCM, Lacosamide; LTG, Lamotrigine; LVT, Levetiracetam; NZP, nitrazepam; OXC, Oxcarbazepine; PHE, Phenobarbital; PGB, Pregabalin; PMP, Perampanel; RUF, Rufinamide; TPM, Topiramate; VPA, Valproate; ZNS, Zonisamide.*

Electroencephalography (EEG) Acquisition and Analysis

Simultaneous scalp EEG data was acquired using a 64-channel, MRI-compatible cap (*EASYCAP*, Brain Products, Munich, Germany). The full EEG acquisition protocol is available in prior work (22). The onsets and durations of IEDs for each session were identified by a neurologist and neurophysiologist, as described in prior work (19, 22). Events onsets and durations were used to generate a temporal regressor by convolution with the standard canonical hemodynamic response, and its temporal and dispersion derivatives as implemented in SPM8.

Timeseries Analyses

Determination of the fMRI timeseries for each region within the brain had the following processing steps applied using MATLAB (MathWorks, Natick, MA, United States). This script is freely available to download (https://github.com/roryjpiper/rs-fMRI.git). A general linear model was applied to control noise

TABLE 2 | Summaries of the patient and control cohorts.

	Patients	Controls
Median age (range)	15 (7–18) years	10 (7–17) years
Male:female ratio	15:20	7:13
Median age of seizure onset (range)*	6 (0.25–13) years	–
Median duration of epilepsy*	7 (3–14) years	–

**Data missing for eight patients.*

according to the six re-alignment parameters aforementioned. We then took the mean timeseries signal from the voxels of each region of the brain according to the Automated Anatomical Labeling (AAL) template (25). The cerebellar regions were excluded to leave 90 cerebral regions. We investigated thalamic nuclei by removing the left and right thalami from the AAL atlas and replaced these with seven paired thalamic subregions, which instead parcellated the cerebrum into 102 regions. The sub-parcellations of the thalamus used here are described in previously published work by He et al. (26). These thalamic subregions included the anterior, medial dorsal, lateral dorsal, lateral posterior, ventral lateral posterior, medial pulvinar and lateral pulvinar subregions (shown in **Figure 1**). The timeseries signal for each region was then band-pass filtered to 0.04–0.07 Hz as per our previous work (27).

Correction for the Effects of Inter-ictal Epileptiform Discharges

Following the procedure described in detail by Shamshiri et al. (20), we used functions in R (Version 3.6.1) to remove the influence of IEDs from the fMRI signal. **Figure 2** demonstrates the effect of IED regression on fMRI signal. Briefly, IED signal changes are modeled by convolving the IEDs with the canonical hemodynamic response function, and its derivatives before projecting the data from each region into an orthogonal space. Following this correction, the "IED-corrected" timeseries' for each patient was determined using the identical pipeline as described above.

Graph Theory Analyses

We created a 102×102 adjacency matrix for each subject by calculating the Pearson correlation coefficient between each region using the *corcoeff.m* MATLAB function. We re-assigned the values in the diagonal of the adjacency matrix (self-correlation) to 0. All negative correlation values were re-assigned to 0. We used the Brain Connectivity Toolbox (29) (www.brain-connectivity-toolbox.net) in MATLAB to calculate the degree centrality (DC) (number of links connected to a node) and eigenvector centrality (EC) (self-referential measure of a node influence) for each region-of-interest (ROI) in every individual. These measures were selected to allow us to interpret our findings in the context of prior work in thalamic connectivity (16), but also are selected to test our hypothesis that brain activity will have greater synchrony in children with epilepsy when compared to those without.

Statistical Analyses

For the purpose of statistical analysis, we selected a range of 10–50% of the highest correlations found in the adjacency matrix. Fifty percent was used as the upper limit since after this point the number of connections (defined as positive correlation values) did not increase any further in some subjects. To determine the difference in DC and EC between groups that are relatively robust to our choice of network density and thresholds, we compared results derived from the thalamus ipsilateral to hemisphere of the epileptogenic focus in patients to the median results derived from the left and right thalami of controls. Using a MATLAB-based permutation test (30), we statistically compared the median area-under-the-curve (AUC) between 10 and 50% of the network density for each graph theory metric (see **Figure 2**) between the results for these subject groups. Statistical testing for measures of the anterior nucleus of the thalamus were performed with an established priori hypothesis, whereas those performed on the remaining thalamic subregions were exploratory, and the reported p-values should be interpreted as descriptive. Our statistical testing used 10,000 permutations and outputted a two-tailed p-value. The effect of IEDs on the graph theory measures were further examined by measuring the Spearman correlation of the residual AUC for each patient vs. the number of spikes per session. Effect size was determined using the Mann-Whitney-Wilcoxon test ($r = z / \sqrt{n_1 + n_2}$). Figure representation of data uses the median value ± standard error of the mean (SEM). Decimal places are rounded to two decimal points.

RESULTS

Degree and Eigenvector Centrality

The anterior nucleus of the thalamus ipsilateral to the EZ was found to have a significantly higher AUC for DC in children (1,516.5 ± 66.15) with epilepsy compared to controls (1,345 ± 56.41) ($r = 0.10$; $p = 0.04$) (**Figures 2**, **3**). We performed the same analysis on only the patients with a frontal EZ ($n = 17$) and found a similar trend in DC, but this did not reach statistical significance ($p = 0.38$).

We then performed an exploratory analysis of the medial dorsal, lateral dorsal, lateral posterior, ventral lateral posterior, medial pulvinar and lateral pulvinar thalamic subregions, on comparing these two groups again, the median AUC for DC was also significantly higher in the ipsilateral lateral dorsal nucleus ($p = 0.02$) (**Supplementary Figure 1**).

No significant difference was found, however, for the same analyses for the ipsilateral thalamus, taken as a whole (the AAL thalamus ROI) ($p = 0.30$), nor for any of the remaining five nuclei (**Supplementary Figure 2**). No significant differences were seen in EC between patients and controls (**Supplementary Figure 2**).

Effects of Interictal Epileptiform Activity

Total number of captured IEDs ranged from 2 to 450 per EEG-fMRI session, as detailed in **Table 1**. Nineteen patients had one spike type (focal) and 16 had more than one IED type. We did not detect significant differences in the median AUC for DC ($p = 0.62$) or EC ($p = 0.81$) in the anterior thalamic nucleus when comparing between the results from children with epilepsy

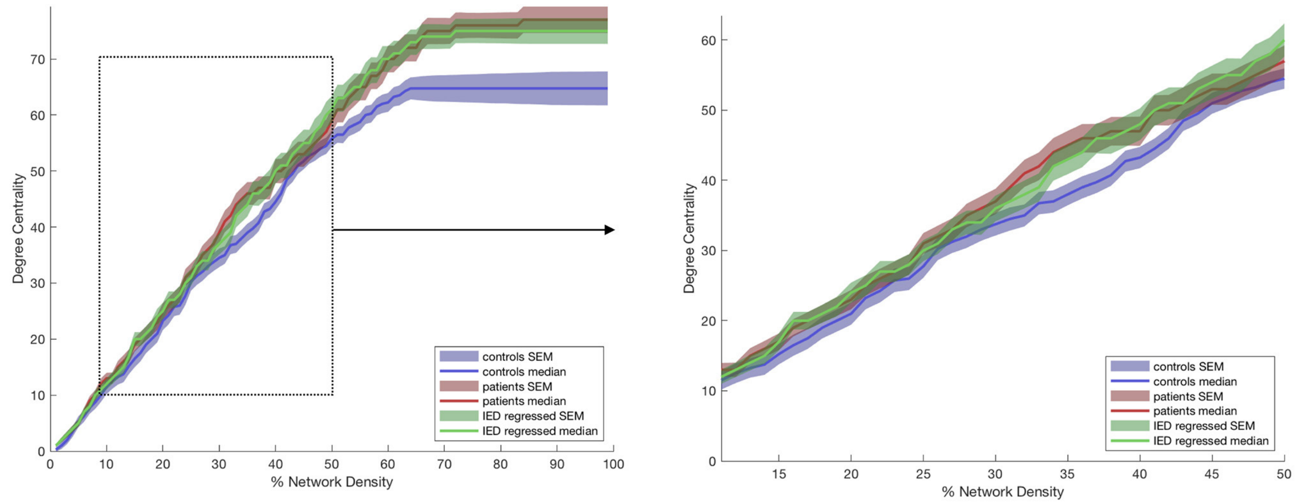

FIGURE 2 | Degree centrality of the anterior thalamic subregion ipsilateral to the epileptogenic zone (EZ). The lines represent controls (blue), patients before (red) and after (green) correction for interictal epileptiform discharges (IEDs). The left graphs show the full range of network densities from 0 to 100%. The dotted box shows the range selected for statistical analysis and shown in the right graph.

before, and after the effects of IEDs were removed. No other thalamic subregion showed these differences either.

When correlating between IED frequency and the AUC for DC in the ipsilateral anterior nucleus in children with epilepsy, we found a borderline, but non-significant negative correlation in DC [$\rho = -0.34$; $p = 0.05$ (rounded up to two decimal places)], and a significant negative correlation in EC ($\rho = -0.38$; $p = 0.03$).

DISCUSSION

The anterior nucleus of the thalamus has consistently been an area of clinical interest and a therapeutic target in patients with epilepsy. High-frequency stimulation of the anterior nucleus has been shown to desynchronize focal large-scale brain activity and reduce the number of IEDs in adults with TLE (31). The SANTE trial in 2010 is, to date, the largest randomized controlled trial of stimulation of the anterior nucleus of the thalamus significant reduction in seizure frequency for adults with both TLE and those with epileptogenic foci elsewhere (14).

Our study suggests that the number of connections (degree centrality [DC]), determined by fMRI, is higher in the anterior nucleus of the thalamus ipsilateral to the EZ in children with focal epilepsy when compared to age-matched controls. Our findings support the significance of these nuclei in the functional connectome of children with epilepsy, and add weight to the hypothesis that DBS to these regions could be therapeutic.

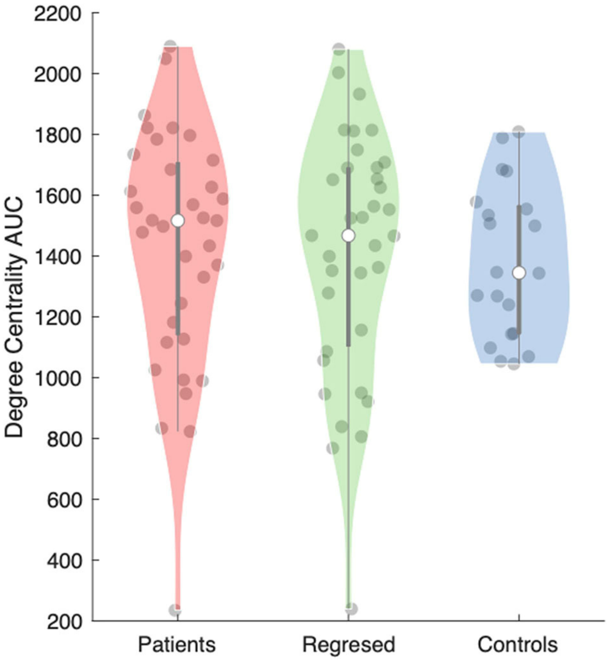

FIGURE 3 | Area under the curve (AUC) for the degree centrality of the anterior thalamic subregion ipsilateral to the epileptogenic zone (EZ). The violin plot (28) demonstrates the distributions of the AUC for degree centrality in patients before (red) and after (green) interictal epileptiform discharges (IEDs) and controls (blue). The clear dot shows the median.

The increased functional connectivity that we demonstrated in the anterior nucleus is in keeping with the aforementioned work, and also with a number of studies which have found the "midline thalamus" to be a key region involved in thalamo-temporal networks (32, 33). He et al. used resting state fMRI to study functional connectivity, and suggest that presurgical thalamic "hubness" (the thalamus being an important node in the network) is a biomarker for predicting seizure outcome in patients undergoing surgery for TLE (16). In patients not rendered seizure free, increased nodal hubness was seen in both the ipsilateral and contralateral thalami on account of an increased DC and EC. Furthermore, simulated lesioning of the thalami showed a greater reduction in network integration in the patients not rendered seizure free. In another study, Bonilha et al. (34), showed that a feature of the connectome after temporal lobectomy was reduced connectivity in thalamo-cortical circuits, and that patients were more likely to achieve seizure freedom if their preoperative network did not involve abnormal thalamic connectivity (35).

Furthermore, on exploratory analysis, we identified a higher functional connectivity of the lateral dorsal nucleus of the thalamus, but this in the context of a predominantly extra-temporal epilepsy cohort. The lateral dorsal nucleus has been shown to have connections with the limbic lobe (including cingulate gyrus), parietal and visual cortex (36). Furthermore, it has been postulated that the anterior and lateral dorsal nuclei, may represent a "higher order" set of thalamic nuclei that, rather than act as a "simple relay," have a more significant influence in the regulation of cortical-cortical interactions (37). It is important to note the limited spatial resolution and effects of co-registration that affect fMRI. It is possible that some of the effect seen in the lateral dorsal nucleus is a spillover of signal detected from the anterior nucleus.

The differences in functional connectivity we observed in this study, however, were of modest magnitude. In contradistinction to relatively homogeneous TLE cohort studies, this study included patients with an epileptic focus in various brain regions which is representative of the surgical population in pediatric practice. Additionally, thalamic connectivity in this cohort needs to be measured against a background of developmental changes. While both of these factors could dilute the effect in childhood epilepsy, we demonstrate a significant effect confirming our primary hypothesis. Our analysis of the patients in this dataset may have combined and averaged the results of distinct groups of children who either do or do not have the thalamus, or its subregions, as regions of higher connectivity within the functional network. It would be interesting to continue this work in this cohort by studying whether or not increased connectivity of the anterior thalamus is predictive of clinical outcome in children undergoing DBS.

Our secondary hypothesis was that altered functional connectivity of the anterior thalamic nuclei was not due to transient effects of IEDs, but instead to stable alterations in the network. We did not detect a significant difference in DC values in this region in patients after the effects of IEDs were corrected for. This study adds to the ongoing discussion regarding the effect of IEDs in the functional connectivity of the brain and the role of the thalamus. It could be that long-term alterations in thalamic connectivity facilitate the spread of IEDs and that thalamic DBS reduces seizure frequency by inhibiting this pathway of connectivity. This idea is supported by a study by Yu et al. (31) aforementioned, that showed that bilateral anterior thalamic nucleus stimulation reduces IEDs. An alternative hypothesis is that focal IEDs are the cause of increased thalamic connectivity, but our study did not show a significant difference between DC and EC in patients before, and after the effects of IEDs were removed, suggesting that the anterior and lateral dorsal thalamic regions have an intrinsically altered baseline. This is in keeping with prior work that suggests that increased connectivity within epileptogenic networks survives the regression of IED effects (38). A study by Shamshiri et al. (20) showed that IEDs can have a pervasive yet transient effect on the brain's functional organization using a seed-to-voxel analysis during a low level attention task. This is compatible with our study findings, where the anterior nucleus of the thalamus may facilitate a permissive state of increased connectivity whereby IEDs (from different brain regions in this heterogeneous group) can affect the coherence of "active" networks.

We acknowledge the following limitations of our study. Firstly, our patient group was heterogeneous in etiology and epileptogenic focus (with a frontal lobe predominance). This could, however, be observed as a strength since the findings we have detected have survived in this mixed cohort, which is somewhat reflective of the pool of patients referred for epilepsy surgery workup. Secondly, the AAL atlas was designed for the analysis of the adult MNI-registered brain. Although we have visually validated the registration of the AAL atlas in each case and used a kernel smoothing method for fMRI signal, there may be inaccuracies that are unavoidable when using this brain region atlas in children. Due to limited sample size and heterogeneous surgical management, we could not make meaningful correlations of clinical outcomes with our quantitative graph theory metrics. Lastly, we recognize the need to validate these findings in external cohorts, particularly in children with generalized epilepsy or those with focal seizures with secondary generalization.

DATA AVAILABILITY STATEMENT

The raw data supporting the conclusions of this article will be made available by the authors, without undue reservation.

ETHICS STATEMENT

The studies involving human participants were reviewed and approved by the NRES Committee London: Surrey Borders Research Ethics Committee London Center (REC reference: 11/LO/1421). Written informed consent to participate in this study was provided by the participants' legal guardian/next of kin.

AUTHOR CONTRIBUTIONS

All authors listed have made a substantial, direct and intellectual contribution to the work, and approved it for publication.

FUNDING

RP was supported by an NIHR Academic Clinical Fellowship. The study was in part funded by Epilepsy Research UK (PGE1402), Medical Research Council (MR/K013998/1), and Action Medical Research (grant number SP4646). This study was also supported by the King's College London Wellcome/EPSRC Centre for Medical Engineering (WT 203148/Z/16/Z). Writing of this manuscript was supported by the Department of Veterans

Affairs Office of Academic Affiliations, the Advanced Fellowship Program in Mental Illness Research and Treatment, and the Department of Veterans Affairs Sierra Pacific Mental Illness Research, Education, and Clinical Center (MIRECC) granted to ES.

SUPPLEMENTARY MATERIAL

The Supplementary Material for this article can be found online at: https://www.frontiersin.org/articles/10.3389/fneur.2021.670881/full#supplementary-material

REFERENCES

1. Centeno M, Carmichael DW. Network connectivity in epilepsy: resting state fMRI and EEG-fMRI contributions. *Front Neurol.* (2014) 5:93. doi: 10.3389/fneur.2014.00093
2. Spencer SS. Neural networks in human epilepsy: evidence of and implications for treatment. *Epilepsia.* (2002) 43:219–27. doi: 10.1046/j.1528-1157.2002.26901.x
3. Fisher RS, Cross JH, French JA, Higurashi N, Hirsch E, Jansen FE, et al. Operational classification of seizure types by the international league against epilepsy: position paper of the ILAE commission for classification and terminology. *Epilepsia.* (2017) 58:522–30. doi: 10.1111/epi.13670
4. Richardson MP. Large scale brain models of epilepsy: dynamics meets connectomics. *J Neurol Neurosurg Psychiatry.* (2012) 83:1238–48. doi: 10.1136/jnnp-2011-301944
5. Tavakol S, Royer J, Lowe AJ, Bonilha L, Tracy JI, Jackson GD, et al. Neuroimaging and connectomics of drug-resistant epilepsy at multiple scales: from focal lesions to macroscale networks. *Epilepsia.* (2019) 60:593–604. doi: 10.1111/epi.14688
6. Blumenfeld H. What is a seizure network? Long-range network consequences of focal seizures. *Adv Exp Med Biol.* (2014) 813:63–70. doi: 10.1007/978-94-017-8914-1_5
7. Hwang K, Bertolero MA, Liu WB, D'Esposito M. The human thalamus is an integrative hub for functional brain networks. *J Neurosci.* (2017) 37:5594–607. doi: 10.1523/JNEUROSCI.0067-17.2017
8. Blumenfeld H. The thalamus and seizures. *Arch Neurol.* (2002) 59:135–7. doi: 10.1001/archneur.59.1.135
9. Penfield W. Epileptic automatism and the centrencephalic integrating system. *Res Publ Assoc Res Nerv Ment Dis.* (1952) 30:513–28.
10. Paz JT, Davidson TJ, Frechette ES, Delord B, Parada I, Peng K, et al. Closed-loop optogenetic control of thalamus as a tool for interrupting seizures after cortical injury. *Nat Neurosci.* (2013) 16:64–70. doi: 10.1038/nn.3269
11. Gotman J, Grova C, Bagshaw A, Kobayashi E, Aghakhani Y, Dubeau F. Generalized epileptic discharges show thalamocortical activation and suspension of the default state of the brain. *Proc Natl Acad Sci USA.* (2005) 102:15236–40. doi: 10.1073/pnas.0504935102
12. Hamandi K, Salek-Haddadi A, Laufs H, Liston A, Friston K, Fish DR, et al. EEG–fMRI of idiopathic and secondarily generalized epilepsies. *Neuroimage.* (2006) 31:1700–10. doi: 10.1016/j.neuroimage.2006.02.016
13. Norden AD, Blumenfeld H. The role of subcortical structures in human epilepsy. *Epilepsy Behav.* (2002) 3:219–31. doi: 10.1016/S1525-5050(02)00029-X
14. Fisher R, Salanova V, Witt T, Worth R, Henry T, Gross R, et al. Electrical stimulation of the anterior nucleus of thalamus for treatment of refractory epilepsy. *Epilepsia.* (2010) 51:899–908. doi: 10.1111/j.1528-1167.2010.02536.x
15. Yan H, Toyota E, Anderson M, Abel TJ, Donner E, Kalia SK, et al. A systematic review of deep brain stimulation for the treatment of drug-resistant epilepsy in childhood. *J Neurosurg Pediatr.* (2018) 23:274–84. doi: 10.3171/2018.9.PEDS18417
16. He X, Doucet GE, Pustina D, Sperling MR, Sharan AD, Tracy JI. Presurgical thalamic "hubness" predicts surgical outcome in temporal lobe epilepsy. *Neurology.* (2017) 88:2285–93. doi: 10.1212/WNL.0000000000004035
17. Keller SS, O'Muircheartaigh J, Traynor C, Towgood K, Barker GJ, Richardson MP. Thalamotemporal impairment in temporal lobe epilepsy: a combined MRI analysis of structure, integrity, and connectivity. *Epilepsia.* (2014) 55:306–15. doi: 10.1111/epi.12520
18. Keller SS, Richardson MP, Schoene-Bake J-C, O'Muircheartaigh J, Elkommos S, Kreilkamp B, et al. Thalamotemporal alteration and postoperative seizures in temporal lobe epilepsy. *Ann Neurol.* (2015) 77:760–74. doi: 10.1002/ana.24376
19. Centeno M, Tierney TM, Perani S, Shamshiri EA, St Pier K, Wilkinson C, et al. Combined electroencephalography-functional magnetic resonance imaging and electrical source imaging improves localization of pediatric focal epilepsy. *Ann Neurol.* (2017) 82:278–87. doi: 10.1002/ana.25003
20. Shamshiri EA, Tierney TM, Centeno M, St Pier K, Pressler RM, Sharp DJ, et al. Interictal activity is an important contributor to abnormal intrinsic network connectivity in paediatric focal epilepsy. *Hum Brain Mapp.* (2017) 38:221–36. doi: 10.1002/hbm.23356
21. Barba C, Cross JH, Braun K, Cossu M, Klotz KA, De Masi S, et al. Trends in pediatric epilepsy surgery in Europe between 2008 and 2015: country-, center-, and age-specific variation. *Epilepsia.* (2020) 61:216–27. doi: 10.1111/epi.16414
22. Centeno M, Tierney TM, Perani S, Shamshiri EA, StPier K, Wilkinson C, et al. Optimising EEG-fMRI for localisation of focal epilepsy in children. *PLoS ONE.* (2016) 11:e0149048. doi: 10.1371/journal.pone.0149048
23. Tierney TM, Weiss-Croft LJ, Centeno M, Shamshiri EA, Perani S, Baldeweg T, et al. FIACH: a biophysical model for automatic retrospective noise control in fMRI. *Neuroimage.* (2016) 124:1009–20. doi: 10.1016/j.neuroimage.2015.09.034
24. De Blasi B, Caciagli L, Storti SF, Galovic M, Koepp M, Menegaz G, et al. Noise removal in resting-state and task fMRI: functional connectivity and activation maps. *J Neural Eng.* (2020) 17:046040. doi: 10.1088/1741-2552/aba5cc
25. Tzourio-Mazoyer N, Landeau B, Papathanassiou D, Crivello F, Etard O, Delcroix N, et al. Automated anatomical labeling of activations in SPM using a macroscopic anatomical parcellation of the MNI MRI single-subject brain. *Neuroimage.* (2002) 15:273–89. doi: 10.1006/nimg.2001.0978
26. He X, Chaitanya G, Asma B, Caciagli L, Bassett DS, Tracy JI, et al. Disrupted basal ganglia–thalamocortical loops in focal to bilateral tonic-clonic seizures. *Brain.* (2020) 143:175–90. doi: 10.1093/brain/awz361
27. Tangwiriyasakul C, Perani S, Centeno M, Yaakub SN, Abela E, Carmichael DW, et al. Dynamic brain network states in human generalized spike-wave discharges. *Brain.* (2018) 141:2981–94. doi: 10.1093/brain/awy223
28. Bechtold B. *Violin Plots for Matlab. GitHub.* (2016). doi: 10.5281/zenodo.4559847
29. Rubinov M, Sporns O. Complex network measures of brain connectivity: uses and interpretations. *Neuroimage.* (2010) 52:1059–69. doi: 10.1016/j.neuroimage.2009.10.003
30. Bassett DS, Nelson BG, Mueller BA, Camchong J, Lim KO. Altered resting state complexity in schizophrenia. *Neuroimage.* (2012) 59:2196–207. doi: 10.1016/j.neuroimage.2011.10.002
31. Yu T, Wang X, Li Y, Zhang G, Worrell G, Chauvel P, et al. High-frequency stimulation of anterior nucleus of thalamus desynchronizes epileptic network in humans. *Brain.* (2018) 141:2631–43. doi: 10.1093/brain/awy187
32. Bertram EH, Mangan PS, Zhang D, Scott CA, Williamson JM. The midline thalamus: alterations and a potential role in limbic epilepsy. *Epilepsia.* (2001) 42:967–78. doi: 10.1046/j.1528-1157.2001.042008967.x
33. Guye M, Régis J, Tamura M, Wendling F, McGonigal A, Chauvel P, et al. The role of corticothalamic coupling in human temporal lobe epilepsy. *Brain.* (2006) 129:1917–28. doi: 10.1093/brain/awl151

34. Bonilha L, Helpern JA, Sainju R, Nesland T, Edwards JC, Glazier SS, et al. Presurgical connectome and postsurgical seizure control in temporal lobe epilepsy. *Neurology*. (2013) 81:1704–10. doi: 10.1212/01.wnl.0000435306.95271.5f
35. Bonilha L, Jensen JH, Baker N, Breedlove J, Nesland T, Lin JJ, et al. The brain connectome as a personalized biomarker of seizure outcomes after temporal lobectomy. *Neurology*. (2015) 84:1846–53. doi: 10.1212/WNL.0000000000001548
36. Bezdudnaya T, Keller A. Laterodorsal nucleus of the thalamus: a processor of somatosensory inputs. *J Comp Neurol*. (2008) 507:1979–89. doi: 10.1002/cne.21664
37. Perry BAL, Mitchell AS. Considering the evidence for anterior and laterodorsal thalamic nuclei as higher order relays to cortex. *Front Mol Neurosci*. (2019) 12:167 doi: 10.3389/fnmol.2019.00167
38. Iannotti GR, Grouiller F, Centeno M, Carmichael DW, Abela E, Wiest R, et al. Epileptic networks are strongly connected with and without the effects of interictal discharges. *Epilepsia*. (2016) 57:1086–96. doi: 10.1111/epi.13400

Conflict of Interest: The authors declare that the research was conducted in the absence of any commercial or financial relationships that could be construed as a potential conflict of interest.

frontiers in Neurology

ORIGINAL RESEARCH
published: 21 September 2021
doi: 10.3389/fneur.2021.693504

Mapping Epileptic Networks Using Simultaneous Intracranial EEG-fMRI

Umair J. Chaudhary[1,2,3], Maria Centeno[1,2,4], David W. Carmichael[5], Beate Diehl[1,2,6], Matthew C. Walker[1,2], John S. Duncan[1,2] and Louis Lemieux[1,2]*

[1] Department of Clinical and Experimental Epilepsy, University College London (UCL) Institute of Neurology, National Hospital for Neurology and Neurosurgery, London, United Kingdom, [2] Magnetic Resonance Imaging (MRI) Unit, Epilepsy Society, Chalfont St. Peter, United Kingdom, [3] Neurology Department, University Hospital Coventry and Warwickshire, Coventry, United Kingdom, [4] Epilepsy Unit, Neurology Department, Hospital Clinic Barcelona, Barcelona, Spain, [5] Imaging and Biophysics Unit, University College London (UCL) Institute of Child Health, London, United Kingdom, [6] Clinical Neurophysiology, National Hospital for Neurology and Neurosurgery, London, United Kingdom

OPEN ACCESS

Edited by:
Clarissa Lin Yasuda,
State University of Campinas, Brazil

Reviewed by:
Umit Aydin,
King's College London,
United Kingdom
Marco Ciavarro,
Istituto Neurologico Mediterraneo
Neuromed (IRCCS), Italy
William B. Lo,
Birmingham Children's Hospital,
United Kingdom

***Correspondence:**
Louis Lemieux
louis.lemieux@ucl.ac.uk

Specialty section:
This article was submitted to
Epilepsy,
a section of the journal
Frontiers in Neurology

Received: *11 April 2021*
Accepted: *20 July 2021*
Published: *21 September 2021*

Citation:
Chaudhary UJ, Centeno M, Carmichael DW, Diehl B, Walker MC, Duncan JS and Lemieux L (2021) Mapping Epileptic Networks Using Simultaneous Intracranial EEG-fMRI. Front. Neurol. 12:693504. doi: 10.3389/fneur.2021.693504

Background: Potentially curative epilepsy surgery can be offered if a single, discrete epileptogenic zone (EZ) can be identified. For individuals in whom there is no clear concordance between clinical localization, scalp EEG, and imaging data, intracranial EEG (icEEG) may be needed to confirm a predefined hypothesis regarding irritative zone (IZ), seizure onset zone (SOZ), and EZ prior to surgery. However, icEEG has limited spatial sampling and may fail to reveal the full extent of epileptogenic network if predefined hypothesis is not correct. Simultaneous icEEG-fMRI has been safely acquired in humans and allows exploration of neuronal activity at the whole-brain level related to interictal epileptiform discharges (IED) captured intracranially.

Methods: We report icEEG-fMRI in eight patients with refractory focal epilepsy who had resective surgery and good postsurgical outcome. Surgical resection volume in seizure-free patients post-surgically reflects confirmed identification of the EZ. IEDs on icEEG were classified according to their topographic distribution and localization (Focal, Regional, Widespread, and Non-contiguous). We also divided IEDs by their location within the surgical resection volume [primary IZ (IZ1) IED] or outside [secondary IZ (IZ2) IED]. The distribution of fMRI blood oxygen level-dependent (BOLD) changes associated with individual IED classes were assessed over the whole brain using a general linear model. The concordance of resulting BOLD map was evaluated by comparing localization of BOLD clusters with surgical resection volume. Additionally, we compared the concordance of BOLD maps and presence of BOLD clusters in remote brain areas: precuneus, cuneus, cingulate, medial frontal, and thalamus for different IED classes.

Results: A total of 38 different topographic IED classes were identified across the 8 patients: Focal (22) and non-focal (16, Regional = 9, Widespread = 2, Non-contiguous = 5). Twenty-nine IEDs originated from IZ1 and 9 from IZ2. All IED classes were associated with BOLD changes. BOLD maps were concordant with the surgical resection volume for 27/38 (71%) IED classes, showing statistical global maximum BOLD cluster or another cluster in the surgical resection volume. The concordance of BOLD maps with surgical resection volume was greater ($p < 0.05$) for non-focal (87.5%, 14/16) as compared to Focal (59%, 13/22) IED classes. Additionally, BOLD clusters in remote cortical and deep brain areas were present in 84% (32/38) of BOLD maps, more commonly (15/16; 93%) for non-focal IED-related BOLD maps.

Conclusions: Simultaneous icEEG-fMRI can reveal BOLD changes at the whole-brain level for a wide range of IEDs on icEEG. BOLD clusters within surgical resection volume and remote brain areas were more commonly seen for non-focal IED classes, suggesting that a wider hemodynamic network is at play.

Keywords: intracranial EEG, EEG-fMRI, IED/spikes, BOLD, post-surgical outcome

INTRODUCTION

Intracranial electroencephalography (icEEG) recordings are performed during presurgical evaluation to localize irritative zone (IZ), seizure onset zone (SOZ), epileptogenic zone (EZ), and eloquent cortex for patients being considered for epilepsy surgery. icEEG has better spatial resolution and sensitivity compared to scalp EEG (1), which has low sensitivity (2, 3) and can provide inaccurate localization (4) and even lateralization (5), especially in patients with frontal lobe epilepsy. icEEG, however, has limited spatial sampling, only detecting electrical activity within a 1-cm core of tissue from recording site (6), and carries surgical risk (7, 8).

Simultaneous scalp EEG and functional magnetic resonance imaging (EEG-fMRI) can map interictal epileptiform discharges (IED) and seizure-related blood-oxygen-level-dependent (BOLD) changes (9–21). In patients with focal cortical dysplasia, IED-related BOLD changes distributed over multiple lobes are associated with poor postsurgical outcome (22). The interpretation of EEG-fMRI findings is often limited by the low sensitivity of scalp EEG, low rates of IED, and an incomplete understanding of the relationship between IED and BOLD changes (12, 13, 23–25). The sensitivity of EEG-fMRI can be increased by using topographical map correlation-based comparison of EEG recorded inside and outside the scanner (26). Simultaneous icEEG and fMRI (icEEG-fMRI) has been performed following extensive safety testing and locally adapted protocol (27–30) [see (31) for review], revealing IED-related BOLD changes local and remote from the relevant intracranial electrodes (32, 33).

We used icEEG-fMRI to explore BOLD changes and their distribution at the whole brain level for different IED classes on icEEG, in patients with refractory focal epilepsy who had good postsurgical outcome and well-characterized EZ. Surgical resection volume in this group of patients with good postsurgical represents confirmed identification of the EZ [where EZ is area of the brain deemed necessary to be resected to render patient seizure free (1, 34)].

Our hypotheses were as follows: (1) widespread BOLD networks, involving the surgical resection volume and remote brain areas, can be seen for IEDs on icEEG; (2) distribution of BOLD changes in surgical resection volume and remote brain areas is different for IED classes based on their topographic localization and their relationship with surgical resection volume. We investigated the anatomical localization and level of concordance of IED-related BOLD maps with the surgical resection volume. We also evaluated the relationship between different IED classes and level of concordance of BOLD maps with the surgical resection volume, and different IED classes and presence of BOLD changes in remote healthy cortex and other brain areas.

METHODS

Eight patients with refractory focal epilepsy had icEEG-fMRI during their invasive pre-surgical evaluation, who had subsequently undergone resective epilepsy surgery with a good postsurgical outcome, i.e., completely seizure free or only auras (ILAE class I or II outcome) for more than 2 years after surgery. All patients gave written informed consent. The study was approved by the joint research ethics committee of the National Hospital for Neurology and Neurosurgery, Queen Square, London (UCLH NHS Foundation Trust) and UCL Institute of Neurology, Queen Square, London, UK.

Clinical Background

Prior to implantation, all patients had undergone detailed clinical history and examination, a structural MRI as per protocol specifically designed for epilepsy (35), long-term scalp video-EEG monitoring, neuropsychological and neuropsychiatric assessments, and additional functional imaging tests including positron emission tomography (PET), magnetoencephalography (MEG), or ictal single photon emission computed tomography (ictal SPECT) as indicated (see **Table 1**).

In accordance with routine clinical practice at our center, implantation of intracranial electrodes was guided by a hypothesis-based consensus decision generated from the results of non-invasive investigations. The SOZ, EZ, and the extent of surgical resection (**Table 2**) were defined by experienced Clinical Neurophysiologists/Epileptologists (BD, TW, and MW) and members of the multidisciplinary team based on invasive (multiple grid/depth electrode contacts on icEEG) and non-invasive investigations. The implantation scheme for each patient is shown in **Supplementary Table 1**. Post-surgical outcome (**Table 2**) was assessed with the ILAE classification (36).

Intracranial EEG-fMRI Acquisition

After the clinical icEEG recordings were completed, the implanted electrodes (numbering between 56 and 128 contacts) were connected to magnetic resonance scanner-compatible cables and amplifier system (32) for icEEG-fMRI acquisition.

TABLE 1 | Clinical characteristics.

ID	Age	Sex	Age @ seizure onset	Epilepsy	Scalp EEG	MRI	Other non-invasive investigations
1	39	M	8	FLE	Sharp: R centro-parietal Seizure: central fast activity	*L HS	PET: R parietal and posterior frontal hypometabolism Ictal SPECT: bi frontocentral and R insular hyperperfusion MEG: R temporo-occipital and frontocentral spikes
2	28	M	12	FLE	Spike: L fronto-central Seizure: regional central	FCD L posterior SFG + MFG	PET: No focal hypometabolism Ictal SPECT: L frontal lobe
3	36	F	7	FLE	Spikes: L inferior frontal/orbito-frontal Seizure: regional L frontal	FCD L IFG	PET: L frontal hypometabolism
4	39	M	9	FLE	Spikes: Regional L temporal-frontal Seizure: Regional L fronto-central	FCD L posterior MFG	PET: No focal hypometabolism
5	32	M	16	FLE	Spikes: Regional R frontal, bi frontal and L fronto-temporal Seizure: Bi frontocentral	NL	PET: R frontal hypometabolism
6	27	F	3	FLE	Spikes: None Seizure: Regional L frontocentral frontocentral	FCD L superior frontal sulci	PET: L SFG hypometabolism Ictal SPECT: L frontal and insular hyperperfusion MEG: no spikes recorded
7	26	M	7	TLE	Spikes: Bi temporal regional Seizure: Regional L temporal	L HS	None
8	28	M	7	PLE	Spikes: Regional R anterior parietal Seizure: Focal R postcentral	FCD Right Supramarginal gyrus	None

*M, male; F, female; FLE, frontal lobe epilepsy; TLE, temporal lobe epilepsy; TOLE, Temporo-occipital lobe epilepsy; R, right; L, left; NL, nonlesional; HS, hippocampal sclerosis; FCD, focal cortical dysplasia; SFG, superior frontal gyrus; MFG, middle frontal gyrus; IFG, inferior frontal gyrus; SMC, sensori-motor cortex; HMC, hand motor cortex; *incidental finding.*

icEEG was recorded, processed online (to reduce the scanner-related artifacts), and displayed (BrainVision Recorder, Brain Products, Germany) during the fMRI scanning.

In accordance with our icEEG-fMRI protocol (29) echo planar images (EPI: TR/TE/flip angle = 3,000 ms/40 ms/90°, 64 × 64 acquisition matrix, 38 × 2.5 mm slices with a 0.5-mm gap) were acquired using a 1.5-T Siemens Avanto scanner (Erlangen, Germany) with a standard transmit/receive head coil and low specific absorption rate sequences ($\leq$ 0.1 W/kg, head average) to reduce the risk of health hazards. One (for patients #2 and 4) or two (for patients #1, 3, 5, 6, 7, and 8) 10-min resting-state EPI time series (depending on patient comfort inside the scanner and time constraints) and T1-weighted structural scans were acquired.

Intracranial EEG Pre-processing and IED Classification

icEEG recorded during fMRI was corrected offline for scanner-related artifact (37) and reviewed by expert users (UC and MC) to identify and classify all IED using BrainVision Analyzer2 (Brain Products GmbH, Germany) and compared with clinical long-term icEEG recording and reports.

The identified IEDs were classified for the purpose of fMRI modeling according to the topographic distribution and localization (**Table 2**). For this topographic scheme, IED were classified according to the number of electrodes involved, their spatial location, field extent, and propagation (38) (**Figure 1**, **Table 2**) as either Focal: if they involved 2–4 contiguous electrode contacts and had similar field; Regional: if they involved 5–10 contiguous electrode contacts that may span up to two gyri; Widespread: if they involved more than 10 contiguous electrode contacts; or Non-contiguous: if they had a focal or regional field but also propagated to non-contiguous electrode contacts. The Regional, Widespread, and Non-contiguous classes taken together formed the non-focal IED class.

Furthermore, to assess our second hypothesis, we divided IEDs for their relationship with the surgical resection volume (i.e., confirmed EZ): IED classes overlapping the surgical resection volume were identified as IZ1 (primary irritative zone) and IED classes outside the surgical resection volume were identified as IZ2 (secondary irritative zone) (39) (see **Table 2**).

For patients #3 and #7 one of the two icEEG-fMRI sessions had to be excluded: for patient #3, icEEG had scanning-related artifacts and patient #7 had a subclinical seizure during one of the sessions (40).

fMRI Processing and Modeling

The fMRI data were analyzed using Statistical Parametric Mapping 8 (www.fil.ion.ucl.ac.uk) after discarding the first two volumes to account for the T1-saturation effect. Functional

TABLE 2 | Invasive localization and post-surgical outcome.

ID	IED type (Number)	Spike classification		Seizure onset zone	Epileptogenic zone	Surgical resection	Histopathological diagnosis	Post-surgical outcome
		Topographic distribution	Irritative zone (IZ)					
1	PSMA1–3 (211)	Focal	IZ1: R SMA	R SMA	R SMA and SFG	R SMA and SFG	No FCD confirmed	ILAE II @ 5 years
	ASMA1–3 (46)							
	ASMA1–3 + PSMA1–3 (476)	Regional						
	PC5, 6 (150)	Focal	IZ2: R inferior parietal and MFG					
	PC5, 6 + AI5, 6 (150)	∼NC						
2	G4, 5 (72)	Focal	IZ1: L posterior SFG and MFG	L posterior SFG and MFG	L posterior SFG, MFG and SMA	L posterior SFG, MFG and SMA	FCD IIB (Balloon cells present)	ILAE I @ 6 years
	G12–15 (29)							
	G4–6 + G12, 13 + G22–24 + G28–30 (80)	Regional						
	G12–15 + G21–24 + DP2-4 (350)							
	G4–8 + G12–15 + G20–24 + G28–30 + DP2–4 (244)	Widespread						
3	DA3, 4 (770)	Focal	IZ1: L IFG and MFG	L anterior IFG and MFG	L anterior IFG and MFG	L anterior IFG and MFG	FCD IIB (Balloon cells present)	ILAE I @ 9 years
	DA3, 4 + G1 18, 27, 35, 43 (265)	Regional						
	G2 6, 14 (195)	Focal	IZ2: L lateral orbitofrontal					
4	DA3–6 (423)	Focal	IZ1: L IFG and MFG	L inferior MFG	L IFG, MFG and lateral orbitofrontal	L IFG, MFG and lateral orbitofrontal	FCD IIB (Balloon cells present)	ILAE I @ 2 years
	DA4, 5 + GA51 (261)							
	DA2–6 + GA49–54 (208)	Regional						
5	FP2–4 (140)	Focal	IZ1: R anterior inferior orbitofrontal	R anterior IFG and orbitofrontal	R anterior orbitofrontal	R anterior orbitofrontal	No FCD confirmed	ILAE I @ 7 years
	FP2–4 + AM2–4 (44)							
	AM2–4 + FP1–4 PMFG3–6 + IFG9-11 (36: runs of IED lasting 1–9 s)	∼NC	IZ2: R anterior inferior orbitofrontal, MFG, IFG, and SMA					
	AM1–4 + FP3–4 FP1–8 + AM1–14 + ASMA2–5+ PMFG3–10 + IFG5–10 (45: runs of IED lasting 3–12 s)							

(Continued)

TABLE 2 | Continued

ID	IED type (Number)	Spike classification		Seizure onset zone	Epileptogenic zone	Surgical resection	Histopathological diagnosis	Post-surgical outcome
		Topographic distribution	Irritative zone (IZ)					
	FP1–4 + AM1–6 FP1–8 + AM1–14 + FOF1–10 + ASMA2–7 + PMFG4–12 + IFG5–11 (90: runs of IED lasting 3–12 s)							
6	SF5–7 (168)	Focal	IZ1: L SFG (lateral and medial)	L SFG (lateral and medial)	L posterior SFG (lateral and medial)	L posterior SFG (lateral and medial)	FCD IIA (No Balloon cells)	ILAE I @ 7 years
	GB4-6 + 14–16 (90)	Regional						
	GC5–16 (474)							
	SF5–7 + GB5-8 + GC5, 10, 11, 12, 15, 16 (23)	~NC						
7	LAH1, 2 + LPH1, 2 + LA3, 4 (60)	Regional	IZ1: L temporal lobe	SOZ1: L hippocampus SOZ2: R amygdala	L anterior temporal lobe	L anterior temporal lobe	Hippocampal sclerosis No FCD	ILAE I @ 10 years
	LAH1–2 (359)	Focal						
	LA3–4 (57)	Focal						
	LPH 1–2 (96)	Focal	IZ2: R and L temporal lobe					
	RA1, 2 + RH1, 2 (624)	Focal						
	RA1, 2 + RAH1, 2 + LAH2, 3 + LPH2, 3 (10)	Regional						
8	D1+ D2 + G31 (62)	Widespread	IZ1: R supramarginal gyrus	SOZ: R supramarginal gyrus	R supramarginal gyrus extending to hand sensory cortex	R supramarginal gyrus extending to hand sensory cortex	FCD IIB (Balloon cells present)	ILAE I @ 7 years
	D1 3–4 (43)	Focal						
	D2 5–6 (2,481)	Focal						
	G23 (83)	Focal						
	G31 (72)	Focal						
	G36 (209)	Focal						
	G38 (226)	Focal						

R, right; L, left; NL, non-lesional; HS, hippocampal sclerosis; FCD, focal cortical dysplasia; SFG, superior frontal gyrus; MFG, middle frontal gyrus; IFG, inferior frontal gyrus; SMC, sensori-motor corte; HMC, hand motor cortex; SOZ, seizure onset zone.

~Focal/regional with non-contiguous spread.

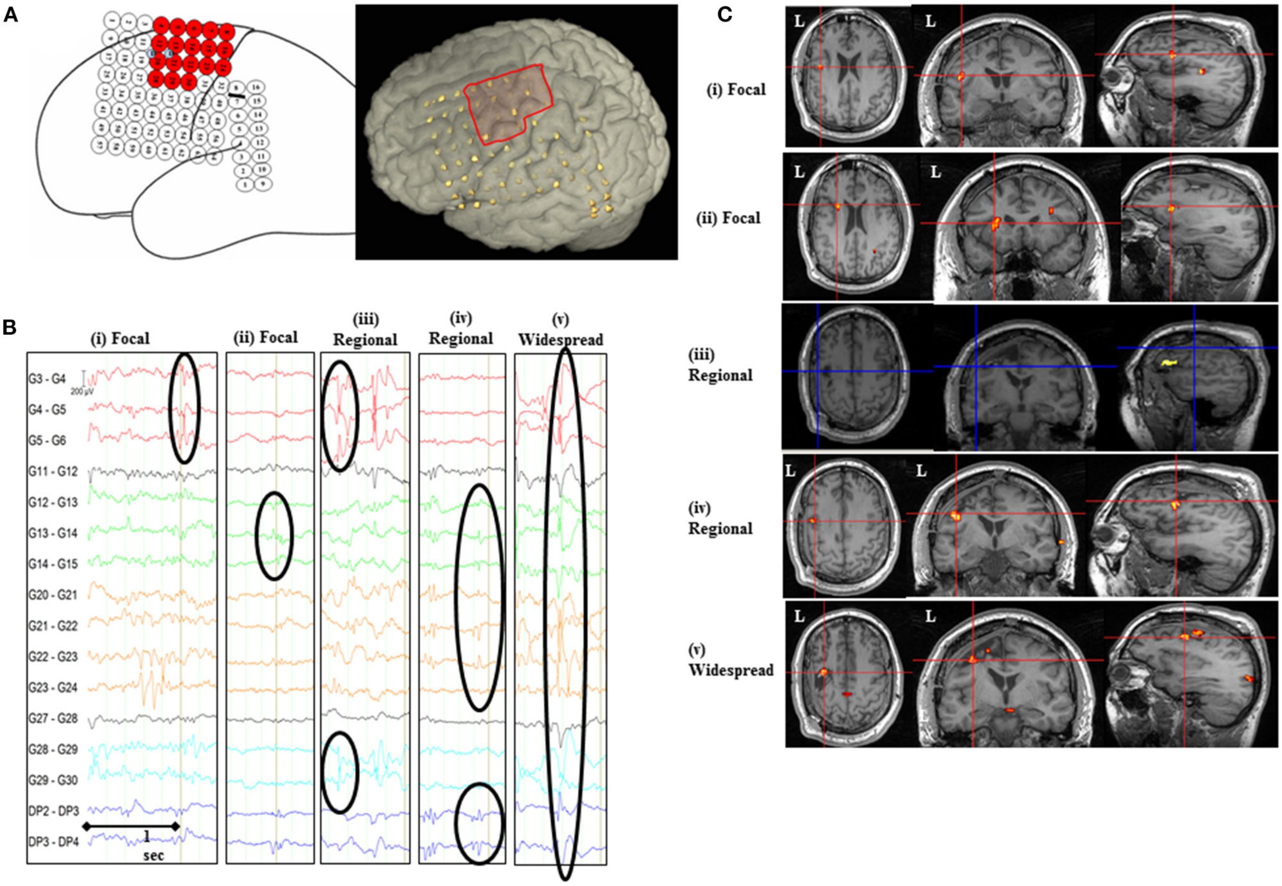

FIGURE 1 | IED-related BOLD changes for Patient #2. **(A)** Implantation scheme of intracranial grid, strip, and depth electrodes and the invasively defined EZ is highlighted as red-colored electrodes on the sketched diagram and red square on the 3D rendered brain. **(B)** Representative sample of icEEG showing different IED classes based on their topographic distribution and localization included in the general linear model. **(C)** SPM[F] maps ($p < 0.001$) for different IED types overlaid on co-registered postsurgical T1-volume. (i) Focal IED [G4, 5 ($n = 72$); Concordant plus BOLD map]: changes in left inferior/middle frontal gyrus (GM cluster, within 2 cm of the surgical resection volume), left posterior temporal, and cuneus/precuneus. (ii) Focal IED [G12–15 ($n = 29$); BOLD map with Some concordance]: changes in left medial occipital (GM cluster), left inferior/middle frontal gyrus (within 2 cm of the surgical resection volume), left parieto-temporal, and cingulate gyrus. (iii) Regional IED [G4–6 + G12, 13 + G22–24 + G28–30 ($n = 80$); Discordant BOLD map]: changes in left inferior frontal gyrus (GM cluster 2.6 cm from the surgical resection volume), medial superior frontal gyrus, left temporo-occipital, and left middle frontal gyrus. (iv) Regional IED [G12–15 + G21–24 + DP2–4 ($n = 350$); Concordant plus BOLD map]: changes in left middle/inferior frontal gyrus (GM cluster, within 2 cm of the surgical resection volume), medial superior frontal gyrus, and supplementary motor area. (v) Widespread IED [G4–8 + G12–15 + G20–24 + G28–30 + DP2–4 ($n = 244$); Concordant plus BOLD map]: changes in left middle frontal gyrus (GM cluster, within 2 cm of the surgical resection volume), right middle temporal gyrus, posterior supplementary motor area, and cingulate/precuneus.

imaging data were corrected for slice acquisition time, realigned to the mean, and spatially smoothed using an isotropic Gaussian kernel of 8-mm FWHM (41).

A general linear model (GLM) was built to map IED-related hemodynamic changes. For patients who underwent two EPI series, these were included in a single GLM as separate sessions. Each IED was represented either as a zero-duration stick function (individual IED) or blocks (runs of IED). Each IED class was modeled as a separate effect and the corresponding time series of stick functions or blocks convolved with the canonical hemodynamic response function and its temporal and dispersion derivatives. In line with previous analyses, 24 inter-scan realignment parameters [6 realignment parameters from image pre-processing and a Volterra-expansion of these (42)] were included in the GLM as confounds to account for motion-related effects similar to our previous work (40).

Assessment of IED-Related BOLD Changes

For each IED class, the presence of significant BOLD clusters was assessed over whole brain using SPM[F]-maps at a statistical threshold of $p < 0.001$ (uncorrected for family-wise error) and a cluster threshold of five contiguous voxels, as in previous studies from our group and others (15, 22, 26, 32, 40, 43). The resulting SPMs were co-registered with pre- and post-surgical T1-weighted MRI scans using rigid-body registration in SPM. The localization of BOLD clusters, for each IED class, was visually assessed in relation to the surgical resection volume. Clusters of activity were also assessed in remote areas including cuneus, precuneus, cingulate gyrus, medial frontal lobe, and other brain areas such as basal ganglia, thalamus. The fitted BOLD time course for each cluster was plotted and classified as increases, decreases, or biphasic (consisting of both increases and decreases) according to the sign of the peak change relative to baseline.

The concordance of BOLD maps with surgical resection volume (i.e., confirmed EZ) was assessed for each IED class on icEEG using a concordance classification scheme in line with our previous work (15, 22, 26, 40, 43) as either:

- Entirely concordant: All BOLD clusters overlapping with/or located within 2 cm of the surgical resection volume in the same lobe.
- Concordant plus: The global statistical maximum BOLD cluster (GM cluster) overlapping with/or located within 2 cm of the surgical resection volume in the same lobe and other clusters were remote (i.e., >2 cm away in different lobe or opposite hemisphere) from the surgical resection volume.
- Some concordance: The GM cluster was remote from the surgical resection volume and at least one of the other clusters overlapped with or located within 2 cm of the surgical resection volume in the same lobe.
- Discordant: all clusters were remote, i.e., more than 2 cm from the surgical resection volume in the same lobe or were in a different lobe or opposite hemisphere from the surgical resection volume.

BOLD clusters confined to the ventricular system, vascular tree, edges, and base of brain and cerebellum were not considered further in this analysis (20, 43–46).

We performed chi-square tests (χ^2) (SPSS Statistics) to assess the association between (1) topographic IED classes and level of concordance of BOLD maps/presence of BOLD clusters in remote brain areas/presence of balloon cells in patients with FCD; (2) IZ1/IZ2 IED classes and level of concordance of BOLD maps/presence of BOLD clusters in remote brain areas/presence of balloon cells in patients with FCD; (3) presence of balloon cells in FCD patients and level of concordance of BOLD maps.

RESULTS

The clinical details for eight patients fulfilling selection criteria are summarized in **Table 1**. There were six males; the median age at the time of icEEG-fMRI was 32 years and the median age at seizure onset was 7.5 years. Six patients had frontal lobe epilepsy, one had temporal lobe epilepsy, and one had parietal lobe epilepsy. The median follow-up time with ILAE class I/II postsurgical outcome was 6 years.

Classification of IED

All patients had a mixture of different topographic IED classes (**Table 2**). The number of IED classes in any given patient ranged between 3 and 7 (median 4.5). There was a total of 38 IED classes across the group. Out of these 38 IED classes, 22 were Focal, and 16 were non-focal: Regional = 9, Widespread = 2, and Non-contiguous = 5 according to topographic classification scheme (see **Table 2**). In terms of irritative zones, 29/38 IEDs originated from IZ1 (Focal = 18, Regional = 8, Widespread = 2, and Non-contiguous = 1) and 9/38 from IZ2 (Focal = 4, Regional = 1, Widespread = 0, and Non-contiguous = 4).

Distribution of IED-Related BOLD Changes for IED Classes

All IED classes were associated with significant BOLD clusters (**Table 3**) that were both co-located with recording electrodes but also in regions remote from them (**Figure 1**). BOLD clusters were seen within the surgical resection volume (Concordant) in 71% (27/38) of IED-related BOLD maps. The cluster of concordance corresponded to the statistical global maxima in 8 maps (Entirely Concordant = 1, Concordant plus = 7) and to the second or other significant cluster in 19 maps (Some concordance). At least two maps were concordant in every patient, with a mean of 70% of the maps per patient being concordant (range 50–100%).

All maps except one contained more than one BOLD cluster (see **Table 3**). Across the group, BOLD clusters were distributed in the ipsi/contralateral hemisphere remote cortical or other brain areas including precuneus, medial superior frontal gyrus, cingulate, basal ganglia, and thalamus in 32/38 (84%) of BOLD maps (see **Table 3**).

Relationship With IED Topographic Classification

BOLD maps for non-focal IEDs (Regional, Non-contiguous, and Widespread) were more commonly concordant with surgical resection volume (Entirely Concordant = 1, Concordant plus = 5, Some Concordance = 8; 14/16, 87.5%) than for Focal IEDs (Concordant plus = 2, Some Concordance = 11; 13/22, 59%), ($\chi^2 = 7.08$, $p < 0.05$). Presence of BOLD clusters in remote cortical and/or other brain areas, i.e., precuneus, medial frontal, cingulate, and thalamus, was more frequent for non-focal IED maps (15/16, 93%: Regional = 8, Non-contiguous = 5, and Widespread = 2) as compared to Focal IED maps (17/22, 77%) but the difference did not reach statistical significance.

Relationship With Irritative Zones

BOLD maps were concordant with the surgical resection volume for 20/29 (68%) IED classes from IZ1 (Entirely Concordant = 1; Concordant plus: 6; Some concordance: 13), and 7/9 (77%) IZ2 IED (Concordant plus: 1; Some concordance: 6). The map's level of concordance or presence of BOLD changes in remote cortical and/or other brain areas did not differ significantly between IZ1 and IZ2 IED classes.

Structural Abnormalities

Seven patients had structural abnormalities seen on MRI (**Table 1**). In six patients, these were in the *EZ* [focal cortical dysplasia (FCD) = 5, hippocampal sclerosis (HS) = 1], and one patient had an incidental finding of HS unrelated to the *EZ*.

In the subgroup of patients with FCD, four patients had FCD type IIB with balloon cells and one patient had FCD type IIA with no balloon cells (see **Table 2**). All patients with FCD showed at least one map with a BOLD cluster overlying the lesion. We did not find a statistically significant association between presence/absence of balloon cells and different IED classes and

TABLE 3 | BOLD changes for individual IED class.

Patient ID #	**IED type**	**BOLD clusters (↑ increase, ↓decrease, ↑↓biphasic)**									**Level of concordance**
		Neocortex								**Other Remote BOLD clusters**	
		Right				**Left**					
		Frontal	**Parietal**	**Temporal**	**Occipital**	**Frontal**	**Parietal**	**Temporal**	**Occipital**		
1	PSMA1–3	↓MFG	**↓Superior parietal**			↓IFG				**↑↓Medial SFG**	SC
	ASMA1–3	↓MFG, ↑**IFG**	↓Superior parietal			↓IFG	↓Superior parietal			↓SMA, Medial SFG, Precuneus/Cuneus. ↓Medial occipital	SC
	ASMA1–3 + PSMA1–3	↓SFG, MFG				↓**SFG**, MFG		↓ITG		↓Cuneus, Cingulate, Medial SFG/SMA	SC
	PC5, 6	↓MFG			↓Lateral superior					↓Medial SFG/SMA, Precuneus/Cuneus	SC
	PC5, 6 + AI5, 6	↓**SFG/MFG**,		↑Posterior temporal, MTG	↑Lateral superior	↓MFG		↑Posterior Temporal, MTG		↓Precuneus/Cuneus, Cingulate ↑SMA	C+
2	G4, 5					↓**IFG/MFG**		↑Posterior Temporal		↑Cuneus/Precuneus	C+
	G12–15					↓IFG/MFG	↓**Medial occipital**, Parieto-temporal			↓Cingulate, SMA	SC
	G4–6 + G12, 13 + G22–24 + G28–30					↓**IFG/**	↑MTG	↑Temporo-occipital		↑Medial SFG	D
	G12–15 + G21–24 + DP2–4					↓**MFG**/IFG				↑Medial SFG/SMA	C+
	G4–8 + G12–15 + G20–24 + G28–30 + DP2–4			↑MTG		↑**MFG**				↓SMA, Cingulate/Precuneus	C+
3	DA3, 4									↑**Thalamus**, ↓Cingulate	D
	G2 6, 14	↓OF	↓**Superior parietal**			↑MFG/IFG				↓Precuneus, Thalamus	SC
	DA3, 4 + G1 18, 27, 35, 43					↑**IFG**					EC
4	DA3–6	↓OF	↓Superior parietal	↓**ITG**, Temporo-occipital		↓IFG, OF			↓Medial occipital		SC
	DA4, 5 + GA51	↑IFG, SMC	↓**Superior parietal**	↑ITG, STG		↓OF/IFG			↑Medial occipital	↓Medial SFG	D
	DA2–6 + GA49–54	↑IFG	↓Inferior parietal	↑ITG		↓IFG				↓**Precuneus**	SC

(Continued)

TABLE 3 | Continued

Patient ID #	IED type	BOLD clusters (↑ increase, ↓decrease, ↑↓biphasic)									Level of concordance
		Neocortex								Other Remote BOLD clusters	
		Right				Left					
		Frontal	Parietal	Temporal	Occipital	Frontal	Parietal	Temporal	Occipital		
5	FP2–4						↑↓Inferior Parietal			**↑Cingulate**	D
	FP2–4 + AM2–4	↑↓**FP,** SFG	↑↓Superior parietal								C+
	AM2–4 + FP1–4 PMFG3–6 + IFG9–11	↑**MFG,** OF								↑↓Precuneus, Medial SFG	SC
	AM1–4 + FP3–4 FP1–8 + AM1–14 + ASMA2–5+ PMFG3–10 + IFG5–10	↓MFG, OF				↑↓FP				↑↓**Medial SFG, Cuneus/**Precuneus	SC
	FP1–4 + AM1–6 FP1–8 + AM1–14 + FOF1–10 + ASMA2–7 + PMFG4–12 + IFG5–11		↓Temporo-parietal			↓FP, OF		↓ITG		↓**Cingulate**, Basal ganglia, Medial OF	SC
6	SF5–7									**↑Cingulate**	D
	GB4–6 + 14–16				↓Medial occipital		↓Superior parietal		↓Medial occipital	↓**Precuneus,** Medial SFG	D
	GC5–16					**↑SFG/MFG**				↓Cingulate, Medial SFG	C+
	SF5–7 + GB5–8 + GC5, 10, 11, 12, 15, 16					↑↓MFG				↑↓**Cingulate**, Thalamus	SC
7	LAH1, 2 + LPH1, 2 + LA3, 4	↑MFG	↑Superior parietal			↑IFG, MFG, OF	↑Superior parietal	↑**Posterior temporal**, STG		↑Precuneus, Cingulate, Medial SFG	SC
	LAH1–2		↑Superior parietal, posterior temporal				↑Superior parietal	↑**Posterior temporal**, STG		↑Precuneus, Cingulate, Medial SFG	SC
	LA3–4	↑SFG		↑Posterior temporal				↑Posterior temporal		↓**Precuneus**	D
	LPH 1–2			↑Superior parietal		**↑MFG**				↑**Cingulate**	D
	RA1, 2 + RH1, 2		↓**Superior parietal**, Temporo-parietal, temporo-occipital				↓Superior parietal			↓Precuneus, cingulate	D
	RA1, 2 + RAH1, 2 + LAH2, 3 + LPH2, 3	↑MFG	↑Superior parietal	Temporal pole, Medial temporal		↑MFG, OF	↑Superior parietal	↑**Posterior temporal**, STG, ITG		↑Precuneus, Cingulate, Medial SFG	SC
8	D1 + D2 + G31	↑MFG	**↑SMG**, ↑Superior parietal				↑Superior parietal	↑Insula		↑Thalamus	C+

(Continued)

TABLE 3 | Continued

Patient ID #	IED type	BOLD clusters (↑ increase, ↓decrease, ↑↓biphasic)									Level of concordance
		Neocortex								Other Remote BOLD clusters	
		Right				Left					
		Frontal	Parietal	Temporal	Occipital	Frontal	Parietal	Temporal	Occipital		
	D1 3–4	↑MFG	↑SMG, ↑Deep parietal						↑Medial occipital	↑**Thalamus**	SC
	D2 5–6	↑IFG	↑SMG				↑**SMG**				SC
	G23	↓**IFG**									D
	G31	↓**Medial SFG**									D
	G36	↑MFG	↑SMG, ↑Superior parietal			↑MFG	↑SMG, ↑Superior parietal			↑**Medial SFG,** Thalamus	SC
	G38	↑MFG	↑SMG				↑**SMG**			↑Cingulate	SC

R, right; L, left; NAL, not-applicable; SFG, superior frontal gyrus; MFG, middle frontal gyrus; IFG, inferior frontal gyrus; MTG, middle temporal gyrus; FP, frontopolar; SMG, supramarginal gyrus; ITG, inferior temporal gyrus; SMC, sensori-motor cortex; STG, superior temporal gyrus; SMA, supplementary motor area; OF, orbitofrontal; EC, entirely concordant; C+, concordant plus; SC, some concordance; D, discordant.
Clusters shown in bold are global statistical maximum clusters.

level of concordance of BOLD maps in this small subgroup of patients.

The patient with hippocampal sclerosis (#7) did not show any BOLD cluster directly overlying HS; however, BOLD clusters were seen within 2 cm of the structural abnormality.

DISCUSSION

Scalp EEG-fMRI studies have shown that IED-related BOLD changes in EZ can predict good postsurgical outcome (9, 13, 14, 22–25, 47–49). One of the limiting factors for these studies has been low sensitivity of scalp EEG to capture the whole spectrum of epileptiform activity that can be revealed by invasive recordings (50, 51). Therefore, what is considered the baseline ("non-epileptic" state) in scalp EEG-fMRI studies must in fact contain a significant amount of epileptic discharges. Simultaneous icEEG-fMRI allows us to overcome this problem by exploring whole-brain changes for epileptiform discharges recorded directly from the cortex using icEEG. This study revealed significant BOLD signal changes for a wide range of IEDs using simultaneous icEEG-fMRI. Furthermore, we found that:

- Significant BOLD clusters for IEDs on icEEG were localized both within the surgical resection volume and remote cortical and other brain areas;
- More than 70% of IED classes showed BOLD maps concordant with the surgical resection volume, where BOLD clusters were seen within the surgical resection volume;
- IED with wider topographic distribution and localization: non-focal IED classes on icEEG were associated with the presence of BOLD clusters within the surgical resection volume.

Previous studies using icEEG-fMRI have shown BOLD changes related to IEDs and seizures (32, 33, 40, 52, 53). Comparison of visual and automated IED classification on icEEG (53) presented a more objective interpretation of icEEG, but there was no statistically significant difference in concordance of the BOLD maps for two IED classification techniques. The relationship of BOLD clusters in surgical resection volume and in remote brain areas for different IED classes has not been explored in previous studies. For this study, we think that visual classification of IEDs based on their topographic distribution and localization and IZs, which reflects clinical insight of the expert user, facilitates clinical interpretation of resulting BOLD maps. We compared distribution of BOLD clusters in surgical resection volume (i.e., level of concordance) and remote brain areas for different IED classes using icEEG-fMRI in the largest group of patients to date who had undergone epilepsy surgery and had a good postsurgical outcome with a long follow-up time (median: 6 years). The surgical resected volume can be rendered confirmed EZ considering long postsurgical seizure freedom.

Methodological Considerations

The feasibility and safety of simultaneous icEEG-fMRI has been established (27, 28, 30, 31). Signal degradation can be observed within up to 1 cm (often less at 1.5 T as in this study) of the electrode contacts and is orientation dependent (27), therefore limiting interpretation of the BOLD maps in the electrode contact's immediate vicinity. However, BOLD effects are generally more widespread (27, 54). BOLD maps revealed significant clusters for different IED classes on icEEG, which were concordant with the surgical resection volume (confirmed EZ) and other non-invasive and invasive investigations, and were also seen in distant areas known to be related to resting-state networks associated with interictal discharges (55, 56). Therefore, it is unlikely that these changes are false positive. Also, icEEG has high sensitivity to show IEDs from smaller generators as compared to scalp EEG (50, 51) and, thus, may be associated with relatively weaker BOLD changes from smaller brain regions; this is in line with previous icEEG-fMRI studies (29, 32, 33, 40).

IEDs were represented as single or series of events in separate regressors for each different class to evaluate specific BOLD pattern in a GLM framework (12, 22, 24, 32) using a standard hemodynamic response function and its derivatives as a hemodynamic kernel (41) to account for a degree of variability in hemodynamic peak delay and duration (12, 24).

In patients with a single seizure onset zone, there may be more than one IED class reflecting different topographic localization and distribution and IZs and not all of these require removal for good surgical outcome. Our interpretation of the IED classes took into account spatial localization, field distribution, propagation, and their relationship with the EZ (1, 38, 39).

In the concordance classification scheme, the first two levels of concordance—Entirely concordant and Concordant plus—are defined based on the location of GM cluster overlapping with or within 2 cm of the surgical resection volume ± presence of other BOLD clusters. For BOLD maps with Some concordance, a cluster other than GM cluster was overlapping with or within 2 cm of the surgical resection volume. In this retrospective study, confirmed EZ was known, and this other cluster in the surgical resection volume was identified. However, during prospective pre-surgical evaluation of patients with a presumed EZ, this cluster can be identified by a consensus agreement, for example, if it is concordant with the structural lesion such as FCD and/or other non-invasive/invasive localization techniques. Our choice of 2 cm as a distance threshold (within a single lobe) to ascertain concordant BOLD clusters reflects the uncertainties associated with implantation and co-registration-related brain shift and the anticipated spatial dislocation of two classes of signals due to neurovascular coupling (57, 58). We evaluated the level of concordance of IED-related BOLD maps irrespective of sign of BOLD change, as both BOLD increases and decreases can be found in the EZ (20, 22, 59, 60).

Neurophysiological and Neurobiological Significance

BOLD clusters were seen in multiple areas for all IEDs on icEEG, and these areas included surgical resection volume (i.e., confirmed EZ) and adjacent/remote apparently healthy cortex. This suggests the possibility of common underlying brain areas or networks recruited as propagation nodes or even generators for different IED classes (50, 51, 61–63), or these widespread BOLD changes may be secondary to extensive underlying pathology (64). We suggest that BOLD changes in cortex and other brain areas remote from the surgical resection volume (i.e., confirmed EZ) may represent propagated epileptic activity in agreement with scalp EEG-fMRI (16, 22, 24, 65, 66) and electric source imaging studies (67). Also, this propagated epileptic activity in remote cortical or other brain areas such as precuneus, medial frontal, cuneus, and thalamus may represent an interaction with resting-state networks in line with previous scalp EEG-fMRI studies (55, 56), which can have implications on level of cognition and consciousness (55, 68) at some level and grants further research. We noted that changes in these areas that are part of default mode network were deactivations, but activations were also seen for some IEDs (see **Table 3**). Though a complete picture of underlying neuronal activity for IEDs may not be seen on icEEG (48) due to its limited spatial sampling, it is difficult to further elucidate whether these activations represent propagation of epileptic activity and deactivations represent involvement of default mode network. Future investigations correlating IEDs on icEEG with topographic maps of IEDs on scalp EEG and their associated BOLD changes will be required to understand the full pathologic nature of such networks.

The presence of BOLD clusters in surgical resection volume (confirmed EZ), as reflected by level of concordance of BOLD maps, was associated with topographic and field distribution of IED on icEEG. Non-focal IEDs on icEEG with wider topographic and field distribution (Regional, Widespread, and Non-contiguous) showed BOLD clusters in surgical resection volume more commonly, compared to focal IEDs on icEEG. This finding is similar to a recent scalp EEG-fMRI study (66) in which widespread epileptic discharges were more likely to show BOLD activation in seizure onset areas. The significance of this finding raises interesting questions about the BOLD effect, for example: is there a spatial scale of neural activity below which the strength of the BOLD change reflects only the local intensity of that activity, in contrast to its spatial extent? Hemodynamic changes may be limited to the activation of a minimum neuronal volume and its synchronization on EEG (69); this may explain the more common presence of BOLD changes in surgical resection volume and remote areas for IEDs with more widespread field extent. It is possible that signal dropout in the local vicinity of icEEG contact (28, 29) can limit to show BOLD change for IED with a very focal field extent. Future imaging sequence development with less signal dropout around implanted electrodes may be able to localize BOLD changes for very focal IEDs on icEEG. In addition, duration of underlying field potentials for epileptic discharges reflected by the sharp wave width can also affect amplitude of the BOLD signal (70), and event parameterization (amplitude, frequency content and duration) may be a useful way forward to further investigate BOLD changes for IED on icEEG.

Clinical Significance

We found that icEEG-fMRI has greater sensitivity: all patients showed IED-related BOLD changes, whereas previously published scalp EEG-fMRI studies have shown IED-related BOLD changes in 30–78% of patients (12, 24, 26). We suggest that this partly reflects the high sensitivity, specificity, and spatial resolution of icEEG (when placed judiciously) compared to scalp EEG (1) and the possibility that this results in more accurate definition of the BOLD baseline. Also, there could possibly be selection bias; patients with a clear focus and IEDs on scalp EEG are more likely to proceed for invasive icEEG.

The strength of our data is that the surgical resection volume represents confirmed EZ as reflected by long seizure freedom after surgery (1). This level of confidence is lacking in previous studies. We found BOLD clusters located in the surgical resection volume in 70% of the maps for different IED classes on icEEG. As icEEG-fMRI can reveal BOLD network across the whole brain and does not suffer from limited spatial sampling of icEEG, it is possible that BOLD clusters remote from surgical resection volume may represent other generator or propagator areas of epileptic activity that are not covered by icEEG. Small sample size and heterogenous underlying pathology could be considered limitations of this study, restraining generalized application of these findings to all patients undergoing epilepsy surgery. It will be interesting to compare in the future, in larger sample size, if there is any difference of BOLD patterns for IEDs on icEEG between seizure-free patients and patients who did not achieve seizure freedom after epilepsy surgery, and if it can inform epilepsy surgery approach.

In conclusion, icEEG-fMRI studies constitute a significant step toward the better understanding of hemodynamic changes related to epileptic activity. It can provide localization of BOLD network at whole-brain level with high sensitivity for different classes of interictal discharges on icEEG originating from focal areas. In addition, BOLD clusters in surgical resection volume (confirmed EZ) were seen more commonly for non-focal epileptiform discharges on icEEG.

DATA AVAILABILITY STATEMENT

The datasets presented in this article are not readily available because subjects consent forms explicitly mention all information will be kept secure and strictly confidential, accessible only to those involved directly in this research. No information will be passed to any third parties or outside the EU for any reason without explicit consent of the subjects. Requests to access the datasets should be directed to Prof. Louis Lemieux, louis.lemieux@ucl.ac.uk.

ETHICS STATEMENT

The studies involving human participants were reviewed and approved by Joint research ethics committee of the National Hospital for Neurology and Neurosurgery, Queen Square, London (UCLH NHS Foundation Trust) and UCL Institute of Neurology, Queen Square, London, UK. The patients/participants provided their written informed consent to participate in this study.

AUTHOR CONTRIBUTIONS

UC, MC, and DC made substantial contributions to the conception, design, data collection, data analysis, interpretation of results, and writing the article. BD made substantial contributions to the recruitment of patients, data interpretation, and revising the manuscript critically for important intellectual content. MW made substantial contributions to the data interpretation and revising the manuscript critically for important intellectual content. JD made substantial contributions to the recruitment of patients, interpretation of results, and revising the manuscript critically for important intellectual content. LL made substantial contributions to the conception, design, data analysis, and revising the manuscript critically for important intellectual content. All authors contributed to the article and approved the submitted version.

FUNDING

This work was partly funded through grants and bursaries from the Medical Research Council (MRC Grant No. G0301067), Action Medical Research, Swiss National Science Foundation (SNF grant 320030-141165 and 33CM30-140332, SPUM Epilepsy), University of Modena, Reggio Emilia, and UCL Institute of Neurology. This work was undertaken at UCLH/UCL, which received a proportion of funding from the Department of Health's NIHR Biomedical Research Centers funding scheme.

ACKNOWLEDGMENTS

We are thankful to Dr. Tim Wehner (Neurophysiologist and Epileptologist), Catherine Scott (Electrophysiologist), and the Department of Clinical Neurophysiology, National Hospital for Neurology and Neurosurgery, Queen Square, London, UK for their expert help for obtaining intracranial EEG. We thank Prof. Maria Thom at the Department of Neuropathology, Institute of Neurology, Queen Square for her expert help with the interpretation of neuropathological diagnoses. We are grateful to the radiographers Lisa Strycharczuk, Bruce Metheringham, and Alison Duncan, and the MR physicists Mark White and Laura Mancini of the Lysholm Department of Neuroradiology and Neurophysics at the National Hospital for Neurology and Neurosurgery (UCLH NHS Foundation Trust), for their expert scanning assistance.

SUPPLEMENTARY MATERIAL

The Supplementary Material for this article can be found online at: https://www.frontiersin.org/articles/10.3389/fneur.2021.693504/full#supplementary-material

REFERENCES

1. Luders HO, Najm I, Nair D, Widdess-Walsh P, Bingman W. The epileptogenic zone: general principles. *Epileptic Disord*. (2006) 8(Suppl. 2):S1–9.
2. Binnie CD, Stefan H. Modern electroencephalography: its role in epilepsy management. *Clin Neurophysiol*. (1999) 110:1671–97. doi: 10.1016/S1388-2457(99)00125-X
3. Smith SJ. EEG in the diagnosis, classification, and management of patients with epilepsy. *J Neurol Neurosurg Psychiatry*. (2005) 76(Suppl. 2): ii2-ii7. doi: 10.1136/jnnp.2005.069245.0
4. Remi J, Vollmar C, de MA, Heinlin J, Peraud A, Noachtar S. Congruence and discrepancy of interictal and ictal EEG with MRI lesions in focal epilepsies. *Neurology*. (2011) 77:1383–90. doi: 10.1212/WNL.0b013e31823152c3
5. Catarino CB, Vollmar C, Noachtar S. Paradoxical lateralization of non-invasive electroencephalographic ictal patterns in extra-temporal epilepsies. *Epilepsy Res*. (2011) 99:147–55. doi: 10.1016/j.eplepsyres.2011.11.002
6. Lachaux JP, Rudrauf D, Kahane P. Intracranial EEG and human brain mapping. *J Physiol Paris*. (2003) 97:613–628. doi: 10.1016/j.jphysparis.2004.01.018
7. Wellmer J, von der GF, Klarmann U, Weber C, Elger CE, Urbach H, et al. Risks and benefits of invasive epilepsy surgery workup with implanted subdural and depth electrodes. *Epilepsia*. (2012) 53:1322–32. doi: 10.1111/j.1528-1167.2012.03545.x
8. Cardinale F, Rizzi M, Vignati E, Cossu M, Castana L, d'Orio P, et al. Stereoelectroencephalography: retrospective analysis of 742 procedures in a single centre. *Brain*. (2019) 142:2688–704. doi: 10.1093/brain/awz196
9. Caballero-Gaudes C, Van de Ville D, Grouiller F, Thornton R, Lemieux L, Seeck M, et al. Mapping interictal epileptic discharges using mutual information between concurrent EEG and fMRI. *Neuroimage*. (2013) 68:248–62. doi: 10.1016/j.neuroimage.2012.12.011
10. Donaire A, Capdevila A, Carreno M, Setoain X, Rumia J, Aparicio J, et al. Identifying the cortical substrates of interictal epileptiform activity in patients with extratemporal epilepsy: an EEG-fMRI sequential analysis and FDG-PET study. *Epilepsia*. (2013) 54:678–90. doi: 10.1111/epi.12091
11. Pittau F, Dubeau F, Gotman J. Contribution of EEG/fMRI to the definition of the epileptic focus. *Neurology*. (2012) 78:1479–87. doi: 10.1212/WNL.0b013e3182553bf7
12. Salek-Haddadi A, Diehl B, Hamandi K, Merschhemke M, Liston A, Friston K, et al. Hemodynamic correlates of epileptiform discharges: an EEG-fMRI study of 63 patients with focal epilepsy. *Brain Res*. (2006) 1088:148–66. doi: 10.1016/j.brainres.2006.02.098
13. Zijlmans M, Huiskamp G, Hersevoort M, Seppenwoolde JH, van Huffelen AC, Leijten FS. EEG-fMRI in the preoperative work-up for epilepsy surgery. *Brain*. (2007) 130:2343–53. doi: 10.1093/brain/awm141
14. Coan AC, Chaudhary UJ, Frederic G, Campos BM, Perani S, De CA, et al. EEG-fMRI in the presurgical evaluation of temporal lobe epilepsy. *J Neurol Neurosurg Psychiatry*. (2016) 87:642–9. doi: 10.1136/jnnp-2015-310401
15. Markoula S, Chaudhary UJ, Perani S, De CA, Yadee T, Duncan JS, et al. The impact of mapping interictal discharges using EEG-fMRI on the epilepsy presurgical clinical decision making process: a prospective study. *Seizure*. (2018) 61:30–7. doi: 10.1016/j.seizure.2018.07.016
16. Pittau F, Ferri L, Fahoum F, Dubeau F, Gotman J. Contributions of EEG-fMRI to assessing the epileptogenicity of focal cortical dysplasia. *Front Comput Neurosci*. (2017) 11:8. doi: 10.3389/fncom.2017.00008
17. Donaire A, Bargallo N, Falcon C, Maestro I, Carreno M, Setoain J, et al. Identifying the structures involved in seizure generation using sequential analysis of ictal-fMRI data. *Neuroimage*. (2009) 47:173–83. doi: 10.1016/j.neuroimage.2009.03.059
18. Thornton RC, Rodionov R, Laufs H, Vulliemoz S, Vaudano A, Carmichael D, et al. Imaging haemodynamic changes related to seizures: comparison of EEG-based general linear model, independent component analysis of fMRI and intracranial EEG. *Neuroimage*. (2010) 53:196–205. doi: 10.1016/j.neuroimage.2010.05.064
19. Tyvaert L, LeVan P, Dubeau F, Gotman J. Noninvasive dynamic imaging of seizures in epileptic patients. *Hum Brain Mapp*. (2009) 30:3993–4011. doi: 10.1002/hbm.20824
20. Chaudhary UJ, Carmichael DW, Rodionov R, Thornton RC, Bartlett P, Vulliemoz S, et al. Mapping pre-ictal and ictal haemodynamic networks using video-electroencephalography and functional imaging. *Brain*. (2012) doi: 10.1093/brain/aws302
21. Sierra-Marcos A, Maestro I, Falcon C, Donaire A, Setoain J, Aparicio J, et al. Ictal EEG-fMRI in localization of epileptogenic area in patients with refractory neocortical focal epilepsy. *Epilepsia*. (2013) 54:1688–98. doi: 10.1111/epi.12329
22. Thornton R, Vulliemoz S, Rodionov R, Carmichael DW, Chaudhary UJ, Diehl B, et al. Epileptic networks in focal cortical dysplasia revealed using electroencephalography-functional magnetic resonance imaging. *Ann Neurol*. (2011) 70:822–37. doi: 10.1002/ana.22535
23. Al-Asmi A, Benar CG, Gross DW, Khani YA, Andermann F, Pike B, et al. fMRI activation in continuous and spike-triggered EEG-fMRI studies of epileptic spikes. *Epilepsia*. (2003) 44:1328–39. doi: 10.1046/j.1528-1157.2003.01003.x
24. Thornton R, Laufs H, Rodionov R, Cannadathu S, Carmichael DW, Vulliemoz S, et al. EEG correlated functional MRI and postoperative outcome in focal epilepsy. *J Neurol Neurosurg Psychiatry*. (2010) 81:922–7. doi: 10.1136/jnnp.2009.196253
25. Tyvaert L, Hawco C, Kobayashi E, LeVan P, Dubeau F, Gotman J. Different structures involved during ictal and interictal epileptic activity in malformations of cortical development: an EEG-fMRI study. *Brain*. (2008) 131:2042–60. doi: 10.1093/brain/awn145
26. Grouiller F, Thornton RC, Groening K, Spinelli L, Duncan JS, Schaller K, et al. With or without spikes: localization of focal epileptic activity by simultaneous electroencephalography and functional magnetic resonance imaging. *Brain*. (2011) 134:2867–86. doi: 10.1093/brain/awr156
27. Carmichael DW, Thornton JS, Rodionov R, Thornton R, McEvoy A, Allen PJ, et al. Safety of localizing epilepsy monitoring intracranial electroencephalograph electrodes using MRI: radiofrequency-induced heating. *J Magn Reson Imaging*. (2008) 28:1233–44. doi: 10.1002/jmri.21583
28. Carmichael DW, Thornton JS, Rodionov R, Thornton R, McEvoy AW, Ordidge RJ, et al. Feasibility of simultaneous intracranial EEG-fMRI in humans: a safety study. *Neuroimage*. (2010) 49:379–90. doi: 10.1016/j.neuroimage.2009.07.062
29. Carmichael DW, Vulliemoz S, Rodionov R, Thornton JS, McEvoy AW, Lemieux L. Simultaneous intracranial EEG-fMRI in humans: protocol considerations and data quality. *Neuroimage*. (2012) 63:301–9. doi: 10.1016/j.neuroimage.2012.05.056
30. Boucousis SM, Beers CA, Cunningham CJ, Gaxiola-Valdez I, Pittman DJ, Goodyear BG, et al. Feasibility of an intracranial EEG-fMRI protocol at 3T: risk assessment and image quality. *Neuroimage*. (2012) 63:1237–48. doi: 10.1016/j.neuroimage.2012.08.008
31. Hawsawi HB, Carmichael DW. Lemieux L. Safety of simultaneous scalp or intracranial EEG during MRI: a review. *Front Phy*. (2017) 5:42. doi: 10.3389/fphy.2017.00042
32. Vulliemoz S, Carmichael DW, Rosenkranz K, Diehl B, Rodionov R, Walker MC, et al. Simultaneous intracranial EEG and fMRI of interictal epileptic discharges in humans. *Neuroimage*. (2011) 54:182–90. doi: 10.1016/j.neuroimage.2010.08.004
33. Cunningham CB, Goodyear BG, Badawy R, Zaamout F, Pittman DJ, Beers CA, et al. Intracranial EEG-fMRI analysis of focal epileptiform discharges in humans. *Epilepsia*. (2012) 53:1636–48. doi: 10.1111/j.1528-1167.2012.03601.x
34. Rosenow F, Luders H. Presurgical evaluation of epilepsy. *Brain*. (2001) 124:1683–700. doi: 10.1093/brain/124.9.1683
35. Duncan JS. Imaging in the surgical treatment of epilepsy. *Nat Rev Neurol*. (2010) 6:537–50. doi: 10.1038/nrneurol.2010.131
36. Wieser HG, Blume WT, Fish D, Goldensohn E, Hufnagel A, King D, et al. ILAE commission report. Proposal for a new classification of outcome with respect to epileptic seizures following epilepsy surgery. *Epilepsia*. (2001) 42:282–6. doi: 10.1046/j.1528-1157.2001.4220282.x
37. Allen PJ, Josephs O, Turner R. A method for removing imaging artifact from continuous EEG recorded during functional MRI. *Neuroimage*. (2000) 12:230–9. doi: 10.1006/nimg.2000.0599
38. Luders H, Noachtar S, Benson JK. *Atlas and Classification of Electroencephalography*. Philadelphia, PA: Saunders (2000).
39. Bettus G, Ranjeva JP, Wendling F, Benar CG, Confort-Gouny S, Regis J, et al. Interictal functional connectivity of human epileptic networks assessed by intracerebral EEG and BOLD signal fluctuations. *PLoS ONE*. (2011) 6:e20071. doi: 10.1371/journal.pone.0020071

40. Chaudhary UJ, Centeno M, Thornton RC, Rodionov R, Vulliemoz S, McEvoy AW, et al. Mapping human preictal and ictal haemodynamic networks using simultaneous intracranial EEG-fMRI. *Neuroimage Clin.* (2016) 11:486–93. doi: 10.1016/j.nicl.2016.03.010
41. Friston KJ, Holmes AP, Worsley KJ, Poline JB, Firth CD, Frackowiak RSJ. Statistical parametric maps in functional imaging: a general linear approach. *Hum Brain Mapp.* (1995) 2:189–210. doi: 10.1002/hbm.460020402
42. Friston KJ, Williams S, Howard R, Frackowiak RS, Turner R. Movement-related effects in fMRI time-series. *Magn Reson Med.* (1996) 35:346–55. doi: 10.1002/mrm.1910350312
43. Chaudhary UJ, Rodionov R, Carmichael DW, Thornton RC, Duncan JS, Lemieux L. Improving the sensitivity of EEG-fMRI studies of epileptic activity by modelling eye blinks, swallowing and other video-EEG detected physiological confounds. *Neuroimage.* (2012) 61:1383–93. doi: 10.1016/j.neuroimage.2012.03.028
44. Birn RM, Cox RW, Bandettini PA. Experimental designs and processing strategies for fMRI studies involving overt verbal responses. *Neuroimage.* (2004) 23:1046–58. doi: 10.1016/j.neuroimage.2004.07.039
45. Jansen M, White TP, Mullinger KJ, Liddle EB, Gowland PA, Francis ST, et al. Motion-related artefacts in EEG predict neuronally plausible patterns of activation in fMRI data. *Neuroimage.* (2012) 59:261–70. doi: 10.1016/j.neuroimage.2011.06.094
46. Johnstone T, Ores Walsh KS, Greischar LL, Alexander AL, Fox AS, Davidson RJ, et al. Motion correction and the use of motion covariates in multiple-subject fMRI analysis. *Hum Brain Mapp.* (2006) 27:779–88. doi: 10.1002/hbm.20219
47. An D, Fahoum F, Hall J, Olivier A, Gotman J, Dubeau F. Electroencephalography/functional magnetic resonance imaging responses help predict surgical outcome in focal epilepsy. *Epilepsia.* (2013) 54:2184–94. doi: 10.1111/epi.12434
48. van Houdt PJ, De Munck JC, Leijten FS, Huiskamp GJ, Colon AJ, Boon PA, et al. EEG-fMRI correlation patterns in the presurgical evaluation of focal epilepsy: a comparison with electrocorticographic data and surgical outcome measures. *Neuroimage.* (2013) 75:238–48. doi: 10.1016/j.neuroimage.2013.02.033
49. Kowalczyk MA, Omidvarnia A, Abbott DF, Tailby C, Vaughan DN, Jackson GD. Clinical benefit of presurgical EEG-fMRI in difficult-to-localize focal epilepsy: a single-institution retrospective review. *Epilepsia.* (2020) 61:49–60. doi: 10.1111/epi.16399
50. Tao JX, Ray A, Hawes-Ebersole S, Ebersole JS. Intracranial EEG substrates of scalp EEG interictal spikes. *Epilepsia.* (2005) 46:669–76. doi: 10.1111/j.1528-1167.2005.11404.x
51. Tao JX, Baldwin M, Hawes-Ebersole S, Ebersole JS. Cortical substrates of scalp EEG epileptiform discharges. *J Clin Neurophysiol.* (2007) 24:96–100. doi: 10.1097/WNP.0b013e31803ecdaf
52. Aghakhani Y, Beers CA, Pittman DJ, Gaxiola-Valdez I, Goodyear BG, Federico P. Co-localization between the BOLD response and epileptiform discharges recorded by simultaneous intracranial EEG-fMRI at 3 T. *Neuroimage Clin.* (2015) 7:755–63. doi: 10.1016/j.nicl.2015.03.002
53. Sharma NK, Pedreira C, Chaudhary UJ, Centeno M, Carmichael DW, Yadee T, et al. BOLD mapping of human epileptic spikes recorded during simultaneous intracranial EEG-fMRI: the impact of automated spike classification. *Neuroimage.* (2019) 184:981–92. doi: 10.1016/j.neuroimage.2018.09.065
54. Deichmann R, Josephs O, Hutton C, Corfield DR, Turner R. Compensation of susceptibility-induced BOLD sensitivity losses in echo-planar fMRI imaging. *Neuroimage.* (2002) 15:120–35. doi: 10.1006/nimg.2001.0985
55. Fahoum F, Zelmann R, Tyvaert L, Dubeau F, Gotman J. Epileptic discharges affect the default mode network–FMRI and intracerebral EEG evidence. *PLoS ONE.* (2013) 8:e68038. doi: 10.1371/journal.pone.0068038
56. Laufs H, Hamandi K, Salek-Haddadi A, Kleinschmidt AK, Duncan JS, Lemieux L. Temporal lobe interictal epileptic discharges affect cerebral activity in "default mode" brain regions. *Hum Brain Mapp.* (2007) 28:1023–32. doi: 10.1002/hbm.20323
57. Disbrow EA, Slutsky DA, Roberts TP, Krubitzer LA. Functional MRI at 1.5 tesla: a comparison of the blood oxygenation level-dependent signal and electrophysiology. *Proc Natl Acad Sci USA.* (2000) 97:9718–23. doi: 10.1073/pnas.170205497
58. Nimsky C, Ganslandt O, Cerny S, Hastreiter P, Greiner G, Fahlbusch R. Quantification of, visualization of, and compensation for brain shift using intraoperative magnetic resonance imaging. *Neurosurgery.* (2000) 47:1070–9. doi: 10.1097/00006123-200011000-00008
59. Jacobs J, Kobayashi E, Boor R, Muhle H, Stephan W, Hawco C, et al. Hemodynamic responses to interictal epileptiform discharges in children with symptomatic epilepsy. *Epilepsia.* (2007) 48:2068–78. doi: 10.1111/j.1528-1167.2007.01192.x
60. Pittau F, Fahoum F, Zelmann R, Dubeau F, Gotman J. Negative BOLD response to interictal epileptic discharges in focal epilepsy. *Brain Topogr.* (2013) 26:627–40. doi: 10.1007/s10548-013-0302-1
61. Ray A, Tao JX, Hawes-Ebersole SM, Ebersole JS. Localizing value of scalp EEG spikes: a simultaneous scalp and intracranial study. *Clin Neurophysiol.* (2007) 118:69–79. doi: 10.1016/j.clinph.2006.09.010
62. Flanagan D, Badawy RA, Jackson GD. EEG-fMRI in focal epilepsy: Local activation and regional networks. *Clin Neurophysiol.* (2013) 125:21–31. doi: 10.1016/j.clinph.2013.06.182
63. Laufs H, Richardson MP, Salek-Haddadi A, Vollmar C, Duncan JS, Gale K, et al. Converging PET and fMRI evidence for a common area involved in human focal epilepsies. *Neurology.* (2011) 77:904–10. doi: 10.1212/WNL.0b013e31822c90f2
64. Moran NF, Lemieux L, Kitchen ND, Fish DR, Shorvon SD. Extrahippocampal temporal lobe atrophy in temporal lobe epilepsy and mesial temporal sclerosis. *Brain.* (2001) 124:167–75. doi: 10.1093/brain/124.1.167
65. Fahoum F, Lopes R, Pittau F, Dubeau F, Gotman J. Widespread epileptic networks in focal epilepsies: EEG-fMRI study. *Epilepsia.* (2012) 53:1618–27. doi: 10.1111/j.1528-1167.2012.03533.x
66. Yamazoe T, von EN, Khoo HM, Huang YH, Zazubovits N, Dubeau F, et al. Widespread interictal epileptic discharge more likely than focal discharges to unveil the seizure onset zone in EEG-fMRI. *Clin Neurophysiol.* (2019) 130:429–38. doi: 10.1016/j.clinph.2018.12.014
67. Vulliemoz S, Lemieux L, Daunizeau J, Michel CM, Duncan JS. The combination of EEG source imaging and EEG-correlated functional MRI to map epileptic networks. *Epilepsia.* (2010) 51:491–505. doi: 10.1111/j.1528-1167.2009.02342.x
68. Chaudhary UJ, Centeno M, Carmichael DW, Vollmar C, Rodionov R, Bonelli S, et al. Imaging the interaction: Epileptic discharges, working memory, and behavior. *Hum Brain Mapp.* (2012) 34:2910–7. doi: 10.1002/hbm.22115
69. Abreu R, Leal A, Lopes da SF, Figueiredo P. EEG synchronization measures predict epilepsy-related BOLD-fMRI fluctuations better than commonly used univariate metrics. *Clin Neurophysiol.* (2018) 129:618–35. doi: 10.1016/j.clinph.2017.12.038
70. Murta T, Hu L, Tierney TM, Chaudhary UJ, Walker MC, Carmichael DW, et al. A study of the electro-haemodynamic coupling using simultaneously acquired intracranial EEG and fMRI data in humans. *Neuroimage.* (2016) 142:371–80. doi: 10.1016/j.neuroimage.2016.08.001

Conflict of Interest: The authors declare that the research was conducted in the absence of any commercial or financial relationships that could be construed as a potential conflict of interest.

frontiers in Neurology

ORIGINAL RESEARCH
published: 08 October 2021
doi: 10.3389/fneur.2021.659081

Identification of Negative BOLD Responses in Epilepsy Using Windkessel Models

Alejandro Suarez[1†], Pedro A. Valdés-Hernández[1†], Byron Bernal[2], Catalina Dunoyer[2], Hui Ming Khoo[3,4], Jorge Bosch-Bayard[3] and Jorge J. Riera[1]*

[1] Neuronal Mass Dynamics Laboratory, Florida International University, Miami, FL, United States, [2] Nicklaus Children Hospital, Miami, FL, United States, [3] Montreal Neurological Institute, McGill University, Montreal, QC, Canada, [4] Department of Neurosurgery, Osaka University, Suita, Japan

Edited by:
Maria Centeno,
University College London,
United Kingdom

Reviewed by:
Borbála Hunyadi,
Delft University of Technology, Netherlands
Antonella Scorziello,
Università di Napoli Federico II, Italy
S. Ottavio Tomasi,
Paracelsus Medical University, Austria

***Correspondence:**
Jorge J. Riera
jrieradi@fiu.edu

† These authors have contributed equally to this work

Specialty section:
This article was submitted to Applied Neuroimaging, a section of the journal Frontiers in Neurology

Received: *27 January 2021*
Accepted: *03 September 2021*
Published: *08 October 2021*

Citation:
Suarez A, Valdés-Hernández PA, Bernal B, Dunoyer C, Khoo HM, Bosch-Bayard J and Riera JJ (2021) Identification of Negative BOLD Responses in Epilepsy Using Windkessel Models. Front. Neurol. 12:659081. doi: 10.3389/fneur.2021.659081

Alongside positive blood oxygenation level–dependent (BOLD) responses associated with interictal epileptic discharges, a variety of negative BOLD responses (NBRs) are typically found in epileptic patients. Previous studies suggest that, in general, up to four mechanisms might underlie the genesis of NBRs in the brain: (i) neuronal disruption of network activity, (ii) altered balance of neurometabolic/vascular couplings, (iii) arterial blood stealing, and (iv) enhanced cortical inhibition. Detecting and classifying these mechanisms from BOLD signals are pivotal for the improvement of the specificity of the electroencephalography–functional magnetic resonance imaging (EEG-fMRI) image modality to identify the seizure-onset zones in refractory local epilepsy. This requires models with physiological interpretation that furnish the understanding of how these mechanisms are fingerprinted by their BOLD responses. Here, we used a Windkessel model with viscoelastic compliance/inductance in combination with dynamic models of both neuronal population activity and tissue/blood O_2 to classify the hemodynamic response functions (HRFs) linked to the above mechanisms in the irritative zones of epileptic patients. First, we evaluated the most relevant imprints on the BOLD response caused by variations of key model parameters. Second, we demonstrated that a general linear model is enough to accurately represent the four different types of NBRs. Third, we tested the ability of a machine learning classifier, built from a simulated ensemble of HRFs, to predict the mechanism underlying the BOLD signal from irritative zones. Cross-validation indicates that these four mechanisms can be classified from realistic fMRI BOLD signals. To demonstrate proof of concept, we applied our methodology to EEG-fMRI data from five epileptic patients undergoing neurosurgery, suggesting the presence of some of these mechanisms. We concluded that a proper identification and interpretation of NBR mechanisms in epilepsy can be performed by combining general linear models and biophysically inspired models.

Keywords: negative BOLD responses, Windkessel models, hemodynamic response function, general linear model, machine learning, epilepsy, EEG-fMRI multimodal

INTRODUCTION

The interest in the concurrent electroencephalography–functional magnetic resonance imaging (EEG-fMRI) method as an important imaging modality in epilepsy surgical planning has increased gradually during the last 20 years (1–3). This method generates whole-brain maps of blood oxygenation level–dependent (BOLD) responses evoked by interictal epileptiform discharges (IEDs), which are then used to locate/identify potential irritative zones (IZs) within the brain. IED-evoked BOLD response analysis is attractive for epilepsy surgery planning, owing to its low invasiveness, accessibility, low cost, and efficiency. The standard clinical protocol for using IED-evoked BOLD signal to demarcate IZs includes (a) concurrent EEG and fMRI recordings while the patient is resting or prompted to sleep; (b) IEDs (spikes and sharp waves) are visually identified by EEG technicians; (c) series of IED onsets are convolved with a canonical hemodynamic response function (HRF, 4) to create a set of regressors; (d) the BOLD signal at each voxel is described as a function of these IED-based regressors *via* a general linear model (GLM) (4); and (e) statistical parametric maps (t-test and F-test) of the linear coefficients are created to detect positive BOLD responses (PBRs). In advanced clinical protocols, IZ detection with the EEG-fMRI technique is performed with flexible parametric HRF models (5–9) to account for voxel and subject variability. Unfortunately, these parametric HRF models misrepresent atypical BOLD responses frequently observed in certain regions of an epileptic brain, e.g., negative BOLD responses (NBRs), precluding detection of the seizure-onset zones (SOZs) in many patients (10–16). Non-parametric HRF models (17–23) could in principle account for HRF misspecification in epilepsy by sacrificing parsimony, but they are computationally intensive, do not include spatial dependencies, and lack mechanistic foundations. These limitations create opportunities to increase the sensitivity of the EEG-fMRI method in epilepsy.

Initial EEG-fMRI clinical studies have associated SOZs with PBRs as a result of a localized hyperemic response triggered by abnormal neuronal excitability [e.g., the pioneer work by (24)]. More recent data suggest NBRs in SOZs might be caused by local circuit inhibitions during after-spike slow-wave components (13), presumably owing to a profound hyperpolarization of pyramidal cells (25, 26) after a fast spike. In general, this is the most accepted mechanism for the NBR found in many experimental paradigms (27–32). The inhibition can occur in the same active region, but exceeding the excitation, provoking negative changes in the overall neuronal activity, resulting in an NBR. For simplicity, we shall refer to these mechanisms as the *enhanced cortical inhibition* (ECI). Clinical [see reviews by (33) and (34)] and preclinical (35) studies of focal epilepsy point out to the existence of abnormal decreases in the hyperemic/metabolic ratio during frequent/strong epileptogenic activity, which might be linked to an NBR according to computer simulations presented in this study. We shall refer to this mechanism as *altered neurometabolic/vascular couplings* (ANCs).

However, not all NBRs might be considered as SOZ candidates during surgical planning. For example, deactivations (or disruption) of normal resting state networks (RSNs), such as the default mode network (DMN), have also been linked to NBRs, a phenomenon reported in epileptic patients during IEDs (11, 36, 37). Here, we refer to this mechanism as *neuronal disruption of network activity* (NDA). Also, an initial work by Harel et al. (38) suggested that *arterial blood stealing* (ABS) could cause an NBR in healthy brain areas as a result of decreases in cerebral blood flow (CBF) and volume (CBV) in a region in close proximity to an IED-evoked PBR. A recent computational model (39) demonstrated that ABS is physically possible in the brain vasculature. More recent studies have corroborated experimentally the existence of ABS (40, 41). Therefore, areas with NDA and ABS types of NBRs are not IZs; hence, they should not be considered during the surgical workup.

Classifying these different types of NBRs from the noise fMRI signal must be challenging. However, it is reasonable to expect they have different HRF waveforms, which could be used as fingerprints of the underlying mechanism. To verify and take advantage of these differences for the identification of the mechanisms, it is advised to have biophysical models. Incorporating biophysical model–based discrimination of disparate NBR types in refractory focal epilepsy may significantly improve the accuracy of the EEG-fMRI method to localize/delineate SOZs, thereby increasing success rates of ablative surgery. Windkessel (balloon) models (42) have been utilized in the last decades for statistical inference of BOLD signals (43, 44) due to their parsimonious capabilities to capture most of the features of the HRFs reported experimentally.

In this article, we propose a comprehensive Windkessel-based model to account for these four possible mechanisms underlying NBRs in patients with focal epilepsy. Using the model, we predict a specific HRF waveform for each of the four NBR mechanisms aforementioned. We also investigate if these HRFs are classifiable from noisy fMRI data. To that end, HRFs were fitted using the near-neighborhood exogenous autoregressive (NN-ARx) (45) model. HRF dimensionality was reduced using the principal component analysis (PCA). We subsequently build a machine learning ensemble classifier that uses the first three principal components as features and their corresponding mechanisms as classes. We evaluate the performance of the classifier in predicting mechanisms from their BOLD signals. Finally, we used this method to evaluate the presence of different NBR types in cases of drug-resistant focal epilepsy.

MATERIALS AND METHODS

EEG-fMRI Data

This is a prospective study duly approved by the Western Institutional Review Board (WIRB #20160218). Parents or legal guardians of 10 patients (9–18 y/o) recruited at Nicklaus Children's Hospital signed a written approved–informed consent. All patients were refractory to pharmacology treatment and exhibited frequent IED. In this context, "frequent" was defined as at least 1 IED per minute. Patients needing sedation or vascular malformations were excluded. In this study, patients exhibiting significant NBRs were only included ($n = 5$). Demographics and clinically relevant findings are summarized in **Table 1**. The results of EEG source localization, positron emission tomography (PET), ictal single-photon emission computed tomography (SPECT), subdural implantation (ECoG/sEEG), MRI diagnosis, and pathology were annotated. The MR-compatible EEG system used in this study is not Food and Drug Administration–approved. Therefore, results obtained from the EEG-fMRI analysis were not used in any form during the surgical evaluation of the patients.

We acquired four 10-min trials of simultaneous EEG-fMRI data from each patient. Using the fMRI trials for which the IEDs were better identified from the EEG, we fitted GLM and NN-ARx to estimate IED-related PBRs and NBRs. The IEDs were visually detected and classified into several subtypes by two experts based on their morphology, the semiology of the patient, and other neuroimaging modalities. The different subtypes of IEDs and other types of events were used as different types of inputs (conditions) in GLM and NN-ARx. In addition, motion correction parameters were included as nuisance regressors.

MRI data were collected in a Philips 1.5-T scanner with a 16-channel SENSE Rx coil. fMRI was acquired with a GE-EPI sequence. Each fMRI scan consists of 21 interleaved slices 6 *mm* thick with a 2-mm gap, in-plane voxel size of 3 × 3 *mm*, and field of view (FOV) = 204 mm. Flip angle (FA) was 90, repetition time (T_R) = 2 *s*, and echo time (T_E) = 45 *ms*. For the purpose of anatomical reference, a high-resolution T1-weighted image was acquired using a spoiled three-dimensional (3D) gradient echo sequence with $T_R = 9.7\ ms$, $T_E = 4\ ms$, and FA = 12. The structural MRIs have 90 to 100 slices, covering the whole brain. In some cases, a T2-weighted 3D image was also acquired with parameters: $T_R = 25\ ms$ and $T_E = 3.732\ ms$, FA = 30, FOV = 240 mm, and 160 2-mm-thick axial slices. 3D fluid-attenuated inversion recovery volumes were acquired in sagittal plane using the following parameters: $T_{\mathrm{R}} = 4{,}800$ ms, T_{E} = shortest; FA = 40°; 230 sagittal cuts, matrix: 212 × 185 × 230 mm; FOV = 250; matrix reconstruction isovoxel 0.98 mm. The fMRI volumes were preprocessed using statistical parametric mapping (SPM) (http://www.fil.ion.ucl.ac.uk/spm/). They were corrected for motion artifacts and spatially smoothed with an 8-mm Gaussian kernel. Both smoothed and unsmoothed images were used in GLM analysis to detect significant voxels. Although the minimum variance estimator of GLM may be biased due to non-Gaussian noise (46), the latter was necessary to detect near PBR and NBR, as it was suggested by Goense et al. (47) and Harel et al. (38) for detecting the NBR of vascular origin. The GLM analysis and the results were masked to the gray matter using the SPM segmentation obtained from the anatomical image (48).

EEG was recorded using a 10–10 system 32-channel EasyCap (BrainAmp MR, Brain Product GmbH). To record EEG data simultaneously with the fMRI signal, we used MRI-compatible EEG amplifiers (BrainAmp MR, Brain Product GmbH). EEG signals were sampled at 5 kHz and digitized (0.5-μV resolution) (BrainVision Recorder 1.4, Brain Products GmbH). The majority of EEG electrodes had impedances lower than 5 kΩ. The electrocardiogram (ECG) was measured with an ECG electrode attached to the middle of the back of the patients. To synchronize the EEG with fMRI scans, a trigger marking the beginning of the scans was sent to the EEG recording laptop. To ensure the highest

TABLE 1 | Patient clinical information.

#	A/G Eth	Seizures	IED	MRI	Nuclear		EEG BSI	ECoG/sEEG	Ictal EEG	Surgery
					PET	***Ictal SPECT***				
1	14/F Cauc	Au/To	54	L-H (Pol-MG)	ND	L-FT	L-ST	ND	Monomorph sharps at C3-P3-CZ	NPY
2	13/F Cauc	Ge/UG	38	NL	R-P	R-F	R-FP	R-P	Bi-F spike/SW at 3–4Hz	R-P
3	17/M Cauc	Pa R-FI	48	NL/(PO) R-PI	ND	R-H	R-FO&T	R-FT>> L-T	R-FT>L-T	R-AT-Lo Hi & AI
4	10/M Cauc	Fo R-Le/Pe	81	Tb	ND	ND	ND	NPY	L-F S&W	NPY
5	9/F Hisp	R-Ar/Ting CP/ESES	572	L-C Cyst (vs. Mal)	L-PaC, Hyper	ND	L-PaC	Concordant	L(C3-P3-FZ) S&W	NPY

Seizures: CP, complex partial; Au, autonomic; To, tonic; Ge, generalized; UG, uncinate gyral; Pa, partial; Fo, focal; Le, leg; Pe, pedaling; Ar, arm; Ting, tingling; Discharges: IED, number of IEDs; SW, slow wave; S&W, spike and wave discharges; Locations: F, frontal; P, parietal; T, temporal; C, central; S(A)T, superior (anterior)–temporal; FP, frontopolar; P(A)I, posterior (anterior)–insular; PaC, paracentral; FT, frontotemporal; FI, frontoinsular; FO, fronto-opercular; Hi, hippocampus. Acronyms: R, right; L, left; H, hemisphere; NL, no lesion; PO, postoperatory; ND, not done; Bi, bilateral; NPY, not performed yet; Lo, lobectomy; Mal, malacia; Pol-MG, polymicrogyria; Tb, tuberous sclerosis; ESES, electric status epilepticus on sleep; A, age; G, gender; Eth, ethnicity; Cauc, Caucasian; Hisp, Hispanic; Symbol: >, effect size.

temporal precision, the clock of the laptop was synchronized to the 10-MHz clock of the MR console using a Syncbox (Brain Products GmbH). The following EEG preprocessing was performed using BrainVision Analyzer 2 (Brain Products GmbH). To remove the MR-related artifact, the EEG data were first subsampled to 50 kHz using *sinc* interpolation to virtually increase its resolution and correct the random phase jittering—of no <0.2-ms resolution determined by the 5-kHz sampling rate—that is present in the scan markers. This phase jittering has significant negative effects in the estimation of the MR gradient artifacts as the latter can change as fast as 0.2 ms. Subsequently, we applied a method for removing the MRI gradient artifacts (49), based on the estimation of an average artifact template. The resultant EEG data were bandpass filtered within 0.5–125 Hz. After marking the R-waves using a semiautomatic tool, we applied a method to detect and remove the effects of the balistocardiogram (50). Finally, we applied ICA based on the Infomax method (51, 52) to remove further artifacts.

As IEDs last ∼70–200 ms, the input $u\left(t\right)$ is modeled as a train of short pulses. To account for the actual time in which the slice containing the region with significant voxels was acquired, the inputs $u\left(t\right)$ were transformed according to $u\left(t+n\frac{T_R}{N_z}\right)$, where n is the position of the slice according to the sequence in which they were acquired, and N_z, the number of slices the whole scan.

Ictal SPECT was performed using a Siemens Multispect 3 gamma camera (Hoffman States, IL). Technetium-HMPAO was used as the radiotracer at a dose of 300 μCi/kg with a minimum dose of 3 mCi and a maximum dose of 20 mCi. PET was performed using a GE Discovery-Dimension ST PET/CT system. FDG was injected at a dose of 140 μCi/kg with a minimum of 1 mCi and maximum of 15 mCi. The stereo-EEG was performed utilizing a Natus Neurology, Natus Medical Incorporated, Excel-Tech Ltd (XLTEK) (Ontario, Canada). The electrode type was a Natus Neuro Grass disposable deep cup electrode (silver chloride, AgAgCl).

The Biophysical Model

The proposed model comprises a two-state dynamic causal modeling component (P-DCM) (53) for principal excitatory cells and inhibitory interneurons, extended to having long-range modulatory excitatory inputs also in the inhibitory population. NDA and ECI types of NBRs are explained by adjusting the time constants of the modulatory synaptic connections in the excitatory and inhibitory population of the extended P-DCM model, respectively. Each brain region has a Windkessel component linked to its neuronal activity through an inducing signaling (i.e., the neurovascular coupling). A viscoelastic non-linear delayed compliance was also included (54). To account for blood stealing effects in brain regions sharing a common supply artery (Option 1, **Supplementary Table A1**), an inductive element was added to connect their respective Windkessel components (39). For regions not sharing a common supplying artery, the two equations for the CBF become independent. For this particular case, a simplified model proposed by Friston et al. (55) is used (Option 2, **Supplementary Table A1**). An oxygen-to-tissue transport (OTT) component was used to account for the dynamics of the oxygen extraction fraction and the O_2 concentrations in both tissue and blood (i.e., the neurometabolic coupling) (56). ABS and ANC types of NBRs are explained by fitting those parameters in the model controlling the stealing effect size and the vascular/metabolic imbalance, respectively. The differential equations describing the biophysical model are shown in **Supplementary Table A1**. **Supplementary Figure A1** shows the flow diagram for the physiological mechanisms with their respective state variables (**Supplementary Table A2**). A graphical representation of all model configurations and defining parameters for each of the four mechanisms is shown in **Supplementary Figure A2**. Values of the parameters for all these particular situations are summarized in **Supplementary Table A3**. All the specifics related to the particular cases of the model can be found in the **Appendix**.

Detecting IZs Using the GLM

The fastest and most widely used method to detect significant BOLD responses is the GLM regression (4):

$$y\left(t_i\right) = \sum_{k=1}^{N_u}\left(\beta_{hrf}^{(k)}\left(h\otimes u_k\right)\left(t_i\right)+\beta_{der}^{(k)}\left(h^{'}\otimes u_k\right)\left(t_i\right)\right.$$
$$\left.+\beta_{disp}^{(k)}\left(d\otimes u_k\right)\left(t_i\right)\right)+\sum_{r=1}^{N_r}\beta_r x_r\left(t_i\right)+\eta\left(t_i\right) \quad (1)$$

where $\{t_i\}_{i=1,\ldots,N}$, being N the number of scans and N_u the number of types of inputs $\{u_k\left(t\right)\}_{k=1,\ldots,N_u}$, $\{x_r\}_{r=1,\ldots,N_r}$ the confounding or nuisance regressors (e.g., the motion parameters), and β_r their effect sizes. h, $h^{'}$, and d are the canonical BOLD HRF (57), its temporal derivative, and its dispersion, respectively. The noise is prewhitened by applying a first-order autoregressive (AR) model to the signal. To demonstrate that the NBR mechanisms are detectable using GLM, we simulated a set of 10-min BOLD signals with a single type of input ($N_u = 1$) consisting of a random Poisson train of pulses with average frequency of 2.6/min. This input was the same across all models and trials. We then created a simulated set of $N = 300$ fMRI scans with $T_R = 2\ s$ by adding the simulated BOLD signals to the voxels of a real EPI image. The trials from the same type of model were added to neighboring voxels to form spatial clusters. The amplitude of the simulated BOLD signal in each cluster was multiplied by a Gaussian spatial kernel [full width at half maximum (FWHM) = 2.5 mm] with the maximum at the center of the cluster. The resultant set of images was further corrupted with colored noise, according to a spectral density given by $1/f^p$, with $0 < p < 1$, to account for biological noise inherent to the BOLD signal but not attributable to the temporal filtering of the HRF (58). No nuisance regressor was included in these simulations, i.e., $x_r = 0$. Following standard fMRI preprocessing procedures, the simulated fMRI scans were spatially smoothed with a Gaussian kernel of 8-mm FWHM. For each voxel, the vectors of coefficient $\beta=\left[\beta_{can}\&\beta_{der}\&\beta_{disp}\right]^T$ of the GLM were estimated using SPM (4). Using an F contrast, we selected the voxels where the null hypothesis, $\mathbf{I}_3\beta = \mathbf{0}$ was rejected with $p <$

0.05, after correcting for multiple comparisons using the family-wise error criterion, i.e., the significant voxels. $\mathbf{I}_3$ is the 3×3 identity matrix, and $\otimes$ denotes temporal convolution.

Estimation of HRFs for the IZs

Although the responses fitted by the GLM, i.e., the first-order Volterra kernel (59), can reconstruct a large variety of HRFs, we used a more adaptable method to accommodate all possible extreme HRF waveforms, the NN-ARx (45), which has been simplified here to extract the HRFs from fMRI time series from the detected IZs. In this particular case, there is no need for a term describing the near-neighbor effect. Under this assumption, the NN-ARx consists of an AR model with an exogenous input s_i, i.e., the IEDs.

$$y_i = \mu_i + \sum_{j=1}^{p} \varphi_j y_{i-j} + \sum_{j=1}^{r} \theta_j s_{i-j-d} + \varepsilon_i \tag{2}$$

With $y_i = y(t_i)$ defining the BOLD signal at discrete time instants. The term μ_i accounts for any drift in the BOLD signal, which is modeled by a polynomial. ε_i represents a normally distribute noise with zero mean and variance σ to be estimated from the fMRI data. This model is suitable to deal with the colored nature of the fMRI time series and the spatial correlation between neighboring voxels in the images. A simple recursive method to estimate the linear coefficient φ_j and θ_j can be found in Riera et al. (45). By minimizing the Akaike information criterion, NN-ARx estimates the orders and coefficients of the AR (p), the order of a polynomial modeling the drift, and the delay of the HRF onset (d). With these, the HRF can be constructed (45). By applying the NN-ARx to the unsmoothed fMRI scans, we extracted the HRF in the IZs with significant PBR and NBR from the GLM.

Classification of Mechanisms

Once the IZs are detected and their HRF estimated using the NN-ARx method, it is necessary to classify them according to the type of NBR mechanism. For this purpose, we propose to build a classifier based on a machine learning algorithm. We simulated $M = 51$ trials of 10-min fMRI signals with $T_R = 2\ s$ with random inputs consisting of trains of short pulses Poisson-distributed in time. To account for the entire span of HRF waveforms, we model the possible intraindividual and interindividual variability in the parameters by randomly sampling their values, for each trial, from a uniform distribution within the intervals specified in **Supplementary Table A3**. For all trials, the NN-ARx–based HRFs were normalized by the maximum of their absolute value. The number of time points of the HRFs was $\frac{T}{T_R} = \frac{32}{2} = 16$. The PCA was used to reduce the dimension of each HRF to just its three most relevant components (features). Then, a final matrix $5M \times 3$ of features was created, with number 5 representing the number of classes (i.e., ECI, NDA, ANC, and ABS). The PBR class was included as reference. This matrix of features and the corresponding vector of classes were used to create a multiclass machine learning ensemble classifier based on support vector machine (SVM) (60, 61). This type of algorithm is a very popular and powerful tool for classification and regression in many of the research fields today (62). We tested the ability of the classifier to differentiate among the five different classes trying with different kernel functions to find the optimal classification.

RESULTS

Predicted Responses for Single Impulses

Figure 1 shows the predicted responses for the mechanisms proposed in this article, and their sensibility to the relevant parameters, following a single IED event. A longer inhibitory recovery creates an ECI type of NBR with smaller amplitude (**Figure 1A**). The recovery time of the network is reflected in the NBR duration of NDA (**Figure 1B**). For ANC, a disproportionately high neurometabolic to neurovascular coupling ratio yields NBR (**Figure 1C**). Regarding the vascular phenomena, the NBR only occurs in the presence of blood resistance in the shared vessel. The higher the resistance, the higher the amplitude of the NBR (39) (**Figure 1D**). As **Supplementary Material**, we uploaded the model codes to the public. The folder includes a pdf file with the documentation that contains user instructions (http://web.eng.fiu.edu/jrieradi/NBR-Model/).

Detection, Estimation, and Classification of NBR Mechanisms

Figure 2 indicates that by using the GLM it is possible to detect voxels exhibiting different simulated NBR types. The mechanism with the least significance is ABS—because its NBR has the smaller amplitude. The ECI mechanism was not included because of the similarity of the HRF with that of the ABS mechanism.

Figure 3 shows the performance of the machine learning classifier based on the SVM analysis of ensembles of simulated HRFs as described in section Materials and Methods. We demonstrate the ability of this classifier to predict new mechanisms using a five-fold cross-validation, i.e., leaving five HRFs out for prediction and using the rest as the training set. Six kernel functions were tested (i.e., linear, quadratic, cubic, fine Gaussian, medium Gaussian, and coarse Gaussian). However, we present here only the results obtained with the coarse Gaussian kernels, which provided the best range of accuracy from a minimum 89% to a maximum 93.7%. Trivially, the PBR response is clearly separable from the NBRs. The ANC is distinguishable from the PBRs, even though its HRF can have a significant positive overshoot. NDA and ANC can be distinguished from each other and from the rest of the NBR types, owing to the prolonged recovery of the former and the fast and bipolar shape of the latter. However, the margin of classification and the confidence of prediction of ECI and ABS are the lowest because of their proximity. This means that it might be difficult to distinguish in some cases, at least merely from fMRI signals. In general, mechanisms were incorrectly classified in ∼6.3% of the cases, only among ECI and ABS types.

NBR Mechanisms Associated With Particular IZs in the Epileptic Patients

In this section, we used the HRF classifier, previously trained with data from the biophysical models, to predict the NBR types in

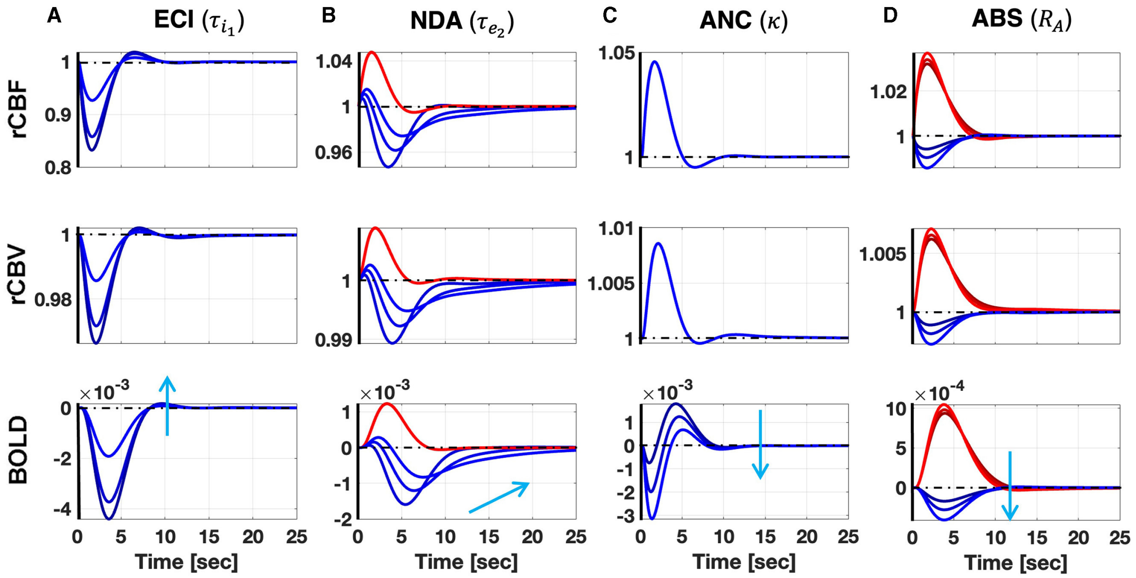

FIGURE 1 | Simulation of the ECI **(A)**, NDA **(B)**, ANC **(C)**, and ABS **(D)** mechanisms after a single short pulse. Red (blue) corresponds to PBR (NBR). Each column corresponds to variation in a parameter that significantly determines the NBR waveform. The sensibility of the responses to these parameters is illustrated with different curves corresponding to three different values of the parameters covering the ranges in **Supplementary Table A3**. The light blue arrow indicates how the NBRs change by increasing the value of the parameters. Besides BOLD responses, we also show other candidate observables in MRI: rCBF and rCBV. Increasing the duration of the inhibitory recovery decreases the amplitude of the ECI mechanism. Expectedly, the longer the recovery time constant in the NDA mechanism, the slower the NBR. We also note that higher neurometabolic coupling gain yields higher NBR amplitudes in the ANC mechanism. Besides, the higher the arterial resistance, relative to the arteriole, in the ABS mechanism, respectively, the higher NBR amplitude.

some particular IZs of five patients with refractory focal epilepsy. For each case, we applied the following pipeline: (a) GLM-based detection of voxels significantly correlated with the IEDs (SPM); (b) selection of the region-of-interest (ROI) for the IZ of interest; (c) estimation of the NN-ARx HRF, averaged inside spheres within the ROIs; (d) classification of the mechanisms using the machine learning (SVM) classifier; and (e) estimation of key parameters of the biophysical model associated with the identified mechanism. To obtain confidence intervals for the HRFs, we estimated the empirical distribution of the null hypothesis of no significant response using a permutation test. This was done by estimating the NN-ARx HRFs from 5,000 trials with random order of the IEDs. For each time point, the lower and upper confidence values were the 5 and 95 percentiles of these null HRF distributions, respectively. Not all IZs detected for each patient by the EEG-fMRI technique are discussed in this study. Results from these five patients are introduced only as proof of concept. This part of the study does not aim at clinically validating our methodology, but rather at illustrating its value.

Patient 1 is a 14-year-old girl with partial autonomic evolving to tonic seizures and left hemisphere polymicrogyria. We found a PBR–NBR pair surrounding the anterior parietal artery (**Figure 4**). Slices showing the thresholded F statistics map built from the estimated coefficients of the GLM using SPM overlaid on the T1-weighted image are presented in panel A. The blue crosshair locates the center of the NBR region in the right postcentral gyrus (PG), whereas the red crosshair locates the center of the PBR region in the right superior parietal lobule (SPL), separated by the postcentral sulcus (another PBR in the left SPL is also shown in this panel). The schematic to the bottom illustrates the ABS mechanism—the regions share the final segment of the anterior parietal artery. The dark gray curve in panel B shows the NN-ARx PBR-HRF and its confidence interval, estimated from the real data, and averaged across the voxels satisfying $F \geq 4.5$ within a 10-mm radius sphere with origin in red crosshair in panel A. The light gray curve shows the estimated NN-ARx NBR-HRF and its confidence interval and averaged across the voxels satisfying $F \geq 5$ within a 10-mm radius sphere with origin in the blue crosshair in panel A. The light red and blue curves show the unnoisy simulated PBR-HRF and NBR-HRF of the fitted ABS model with the estimated value $R_A = 0.17$. In panel C, the temporal behaviors of the ABS simulated BOLD in the PBR and NBR regions (with the aforementioned estimated parameters) overlap the time series of the real fMRI and the 54 IEDs (input) used in the NN-ARx estimation. Note that, to detect this NBR/PBR pair, the unsmoothed images had to be used, considerably decreasing statistical significance. This is however the strategy used in Goense et al. (47) and Harel et al. (38) to detect close BOLD responses with inverted polarities. According to the predicted HRF type, this NBR should not be classified as an IZ.

Patient 2 is a 13-year-old girl with generalized and uncinate gyral seizures. An NBR with ECI type of HRF was found in this patient (**Figure 5**). No lesions were present (A). In concordance with the ictal-SPECT (hyperperfusion, B) and the brain source imaging (EEG-BSI) (C), we found an NBR in the right frontal eye field. sEEG data (C) showed better correspondence with a hypometabolism (interictal PET, B) in the right parietal lobe.

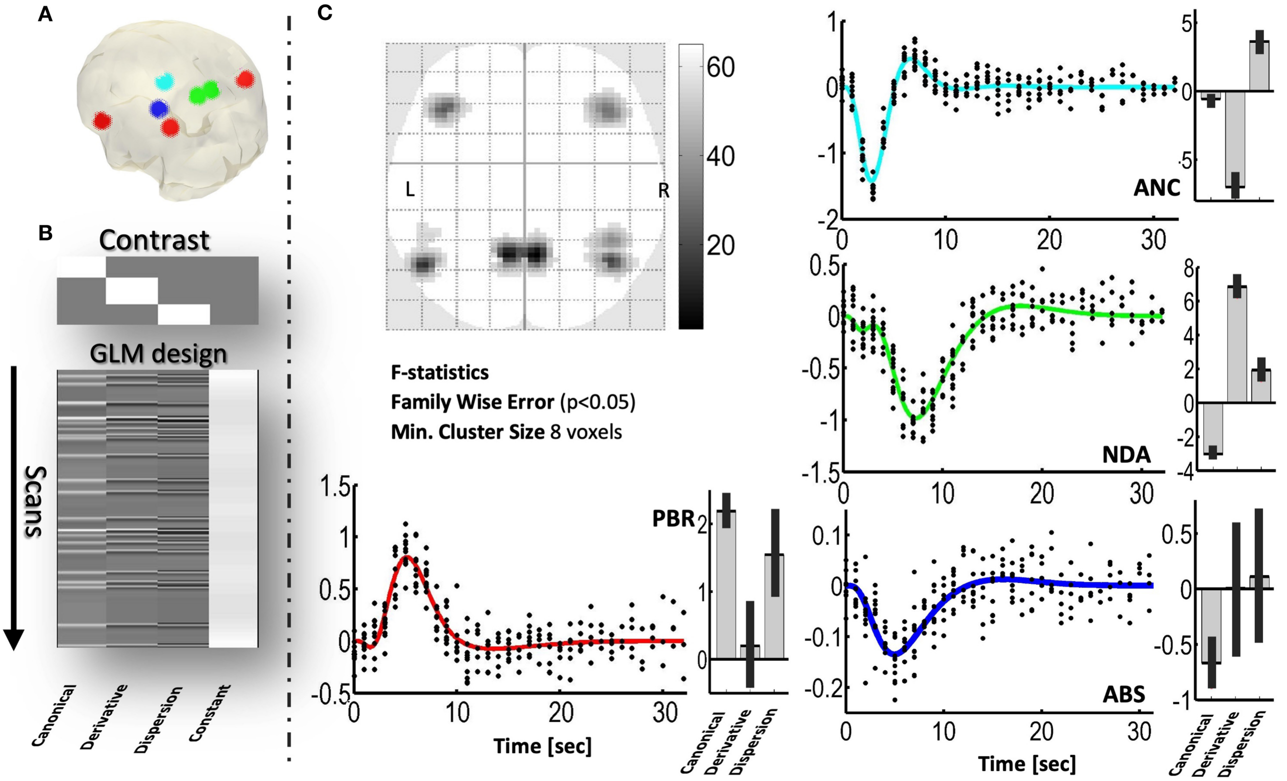

FIGURE 2 | Detection, using the GLM, of simulated spatial distribution of PBRs and three NBRs in a realistic sequence of echoplanar fMRI scans. **(A)** Three-dimensional glass brain showing the regions where the mechanisms were simulated. **(B)** F contrast (the 3-order identity matrix) and design matrix of the GLM, used to detect significant voxels. **(C)** Two-dimensional glass brain showing the *F* statistics. The plots show the responses predicted by the GLM (color curves) and the adjusted data (black dots), for each mechanism. Besides each plot, the estimated values and confidence intervals of the coefficients, β_{can}, β_{der}, and β_{disp}, of the GLM are shown. PBR (red), NDA (green), ANC (cyan), ABS (blue).

Ictal EEG points out to a bifrontal spike/slow wave at 3 to 4 Hz. Our classifier linked this particular NBR-HRF to an ECI mechanism (D). A total of 38 IEDs were used to generate the BOLD signal regressors. The right parietal lobe was removed. The patient was free of seizures for 30 weeks. Thermal ablation of the right posterior cingulate gyrus was performed 7 months later obtaining a reduction of 90% of seizure frequency. According to our hypothesis, the right frontal eye field is an IZ with potential to be the SOZ; hence, seizures could resume. An alternative explanation is that the ECI might be reflecting the presence of an inhibitory mechanism linked to the ictal slow-wave component.

Patient 3 is a 17-year-old boy with partial seizures in the right frontal insula. There are unarguably several regions with NDA type of NBRs linked mainly to the DMN (**Figure 6**). All nodes of the DMN, as well as the superior frontal gyri, the middle frontal gyri, the left inferior frontal gyrus (IFG), part of the right IFG, the right fronto-opercular region, and the right caudate nucleus, were highly significantly deactivated. In addition, PBR was detected in the right IFG, which could be one of the foci of the IEDs, based on the semiology of the patient and their proximity to the EEG electrodes used to detect the IEDs (i.e., spikes with highest amplitude in electrode F8). Other types of events were also marked and used as regressors in the linear models. Panel A shows the thresholded *F* statistics map built from the estimated coefficients of the GLM overlaid on the T1-weighted image. Top left axial slice: green crosshair locating the center of one NBR region in the right lateral parietal node of the DMN—coinciding with the maximum value of the *F* statistics (bottom left sagittal: green crosshair locating another NBR region in the caudate nucleus; right slices: red crosshair locating the center of the PBR region in the right frontal cortex—presumably in the origin of the IEDs). The approximate location of electrode F8 is shown with a green circle in the right axial slice to illustrate the possible relation of the frontal PBR and the IEDs. The right inset shows a short segment of the preprocessed EEG data where 2 IEDs were identified. In panel B, the dark gray curve shows the estimated NN-ARx PBR-HRF and its confidence interval, estimated from the real data around the region marked by the red crosshair in panel A and averaged across voxels satisfying $F \geq 9.5$ within a 7-mm radius sphere. The light gray curve shows the estimated NN-ARx NBR-HRF and its confidence interval, estimated from the real data around the DMN node marked by the green crosshair in the top left slice in in panel A and averaged across the voxels satisfying $F \geq 70$ within a 10-mm radius sphere. The red and green curves show the unnoisy simulated PBR-HRF and NBR-HRF, respectively, of the fitted model with the estimated value of

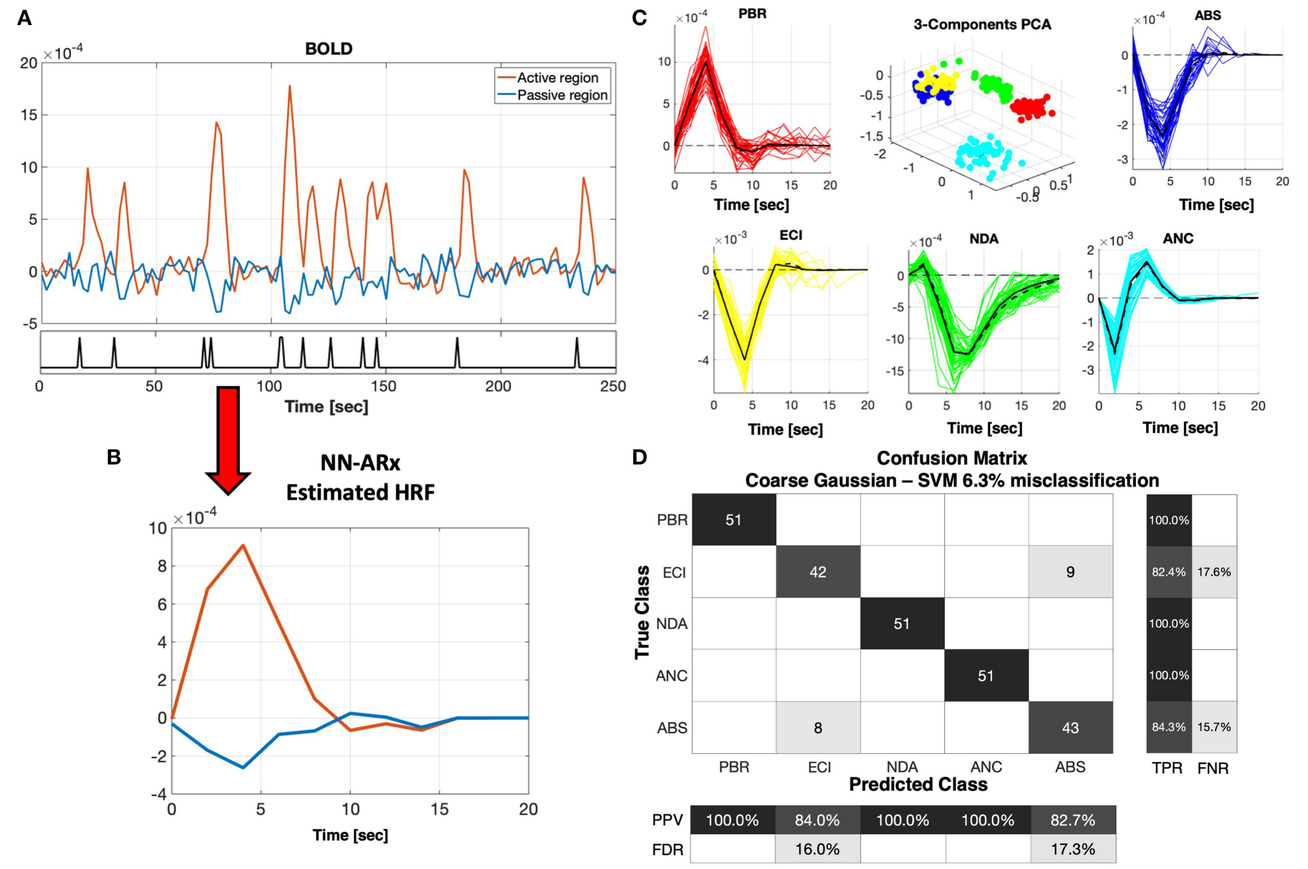

True Class	PBR	ECI	NDA	ANC	ABS	TPR	FNR
PBR	51					100.0%	
ECI		42			9	82.4%	17.6%
NDA			51			100.0%	
ANC				51		100.0%	
ABS		8			43	84.3%	15.7%
PPV	100.0%	84.0%	100.0%	100.0%	82.7%		
FDR		16.0%			17.3%		

FIGURE 3 | NN-ARx estimation and classification of HRFs. **(A)** Example of a portion of simulated fMRI time series for the ABS mechanism. The input $u(t)$ is represented with a black trace at the bottom graph. **(B)** Both positive and negative HRFs estimated using NN-ARx from the example in A. **(C)** Estimated HRFs from all trials. The black continuous curve represents the average across trials, whereas the black dash curve corresponds to a simulation without noise. To geometrically illustrate their separability, the 3D plot depicts the scores of the first three components of the PCA decomposition of the matrix formed by stacking all HRF as row vectors, after normalizing their amplitudes. PBR (red), ECI (yellow), NDA (green), ANC (cyan), and ABS (blue). **(D)** Results of the five-fold cross-validation of the SVM classifier with a coarse Gaussian kernel function resulted in 6.3% of misclassification. Center figure shows the confusion matrix. TPR, true-positive rate; FNR, false-negative rate; PPV, positive predictive value; FDR, false discovery rate. As expected, the PBR is distinguishable from all the NBRs. NDA and ANC mechanisms were also perfectly classified, whereas ECI and ABS are the ones that are closer to each other.

the recovery time constant: $\tau_{e2} = 3s$. For illustration purposes (panel C), we also show the temporal behavior of the simulated BOLD signal in the NBR region (with $\tau_{e2} = 3s$), the time series of the real BOLD signal, and the IEDs (input). To account for the actual relative effect of the IEDs, the amplitude of the input pulses was multiplied by the normalized power of the EEG in F8. The patient underwent a right anterior temporal lobectomy and partial hippocampus/anterior–insular resection. The patient is not yet seizure-free.

Patient 4 is a 10-year-old boy with focal seizures and leg pedaling. The patient exhibits ANC-type NBR (cyan crosshair), just in the edge of a tumor in the left frontal cortex (**Figure 7**). Although the null hypothesis in the significant voxels could not be rejected with a probability corrected by multiple comparisons, this probability was set to a very low value ($p < 0.0005$), and the minimum cluster size of the significant regions was set to five voxels (by decreasing the minimum size of significant voxels, more significant voxels appear in the upper edge of the lesion). Moreover, the HRF was significant according to the permutation test. This HRF corresponded to 50 IEDs identified in electrode F7. Other IEDs, for a total of 81, were also identified and included as regressors in the linear models. Panel A shows an axial slice of the thresholded F statistics map built from the estimated coefficients of the GLM overlying on the T1-weighted image. The IEDs were detected using the EEG signal in electrode F7 (green circle), which was very close to the area with the ANC type of NBR. The right inset shows a short segment of the preprocessed EEG data where 2 of 50 IEDs were identified. The patient suffers from tuberous sclerosis complex (B). The cyan crosshair—the maximum value of the F statistics—locates the center of the NBR region, in the perimeter, and below one of the patient's tumors. The tumor is highlighted with the yellow circle in the axial slice and the red arrow in the coronal slice of the T2-weighted image. In panel C, the gray curve shows the estimated NN-ARx HRF

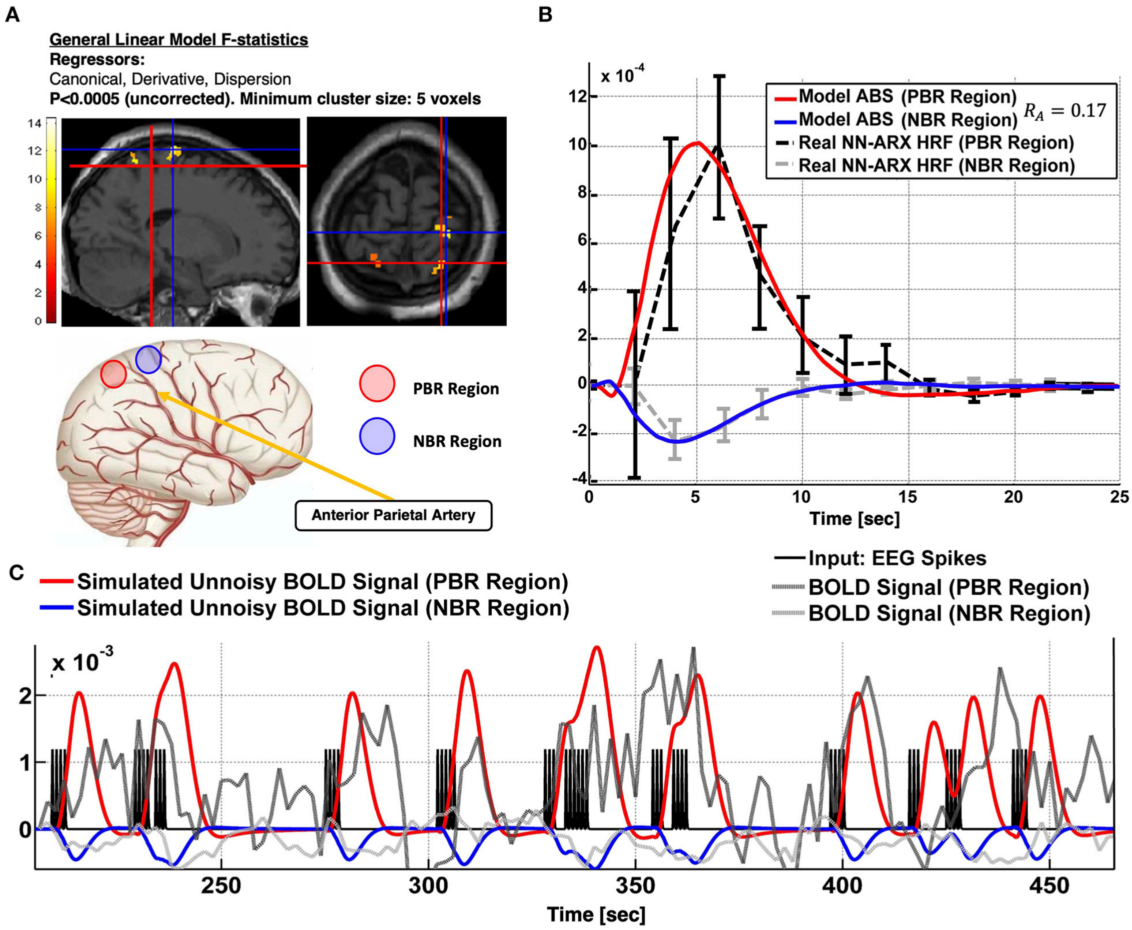

FIGURE 4 | Patient #1 shows an irritative zone with ABS-type HRF. **(A)** Slices showing the thresholded F-statistics map built from the estimated coefficients of the GLM overlaid on the T1-weighted image. The blue crosshair locates the center of the NBR region in the Right Post-central Gyrus; whereas the red crosshair locates the center of the PBR region in the Right Superior Parietal Lobule (SPL). The cartoon at the bottom illustrates the ABS mechanism-the regions share the final segment of the Anterior Parietal Artery. **(B)** The dark gray curve shows the estimated NN-ARx PBR-HRF and its confidence interval, estimated from the real data, and averaged across the voxels within a 10 mm-radius sphere with origin in red crosshair in **(A)**. The light gray curve shows the estimated NN-ARx NBR-HRF and its confidence interval, estimated from the real data, and averaged across the voxels within a 10 mm-radius sphere with origin in the blue crosshair in **(A)**. The light red and blue curves show the unnoisy simulated PBR-HRF, NBR-HRF of the fitted ABS model with the estimated values R_A = 0.17. **(C)** Temporal behavior of the ABS simulated BOLD in the PBR and NBR regions (with the above-mentioned estimated parameters), the time series of the real fMRI and the input used in the NN-ARx estimation.

and its confidence interval, estimated from the real data, and averaged across the voxels satisfying $F \geq 6.5$ within a 10-mm radius sphere with origin in the crosshair in panel A. The cyan curve shows the unnoisy simulated HRF of the fitted OTT model with the estimated value of the neurometabolic coupling gain: $\kappa = 0.51\ s^{-1}$. We also show the simulated temporal behavior of g and the simulated BOLD signal in the NBR region (with $\kappa = 0.51\ s^{-1}$), the time series of the real fMRI, and the IEDs (input). Also, to account for the actual relative effect of the IEDs, the amplitude of the input pulses was multiplied by the normalized power of the EEG in F7. Our EEG-fMRI results predict the SOZ in the periphery of the tumor. The patient has neither been sEEG implanted nor undergone a surgical procedure.

Patient 5 is a 9-year-old girl with electric status epilepticus on sleep and left (C3-P3-FZ) ictal spikes–waves discharges. A very significant PBR was found in the premotor cortex with high probability to be the SOZ (**Figure 8**). There is a non-enhancing cystic lesion in the left posterior frontal lobe (A). Interictal PET (C) reveals hypermetabolism (perhaps due to the high frequency of IEDs) on the left posterior paracentral (both precentral and postcentral sulcus) in agreement with the PBR. EEG-BSI indicates brain sources on the bank of the left central sulcus (C). Hence, we expect total seizure control if this area is resected. In contrast, we found an NBR posterior to the cyst that was classified as ABS. We found a PBR nearby this deactivation, but it was not significant. To illustrate the usefulness of the NN-ARx method, we compared HRFs estimated with it and those obtained with the impulse response function (IRF) method (SPM software). The IRF method was not able to capture underlying HRFs. Results from the EEG-fMRI analysis are shown in panel D.

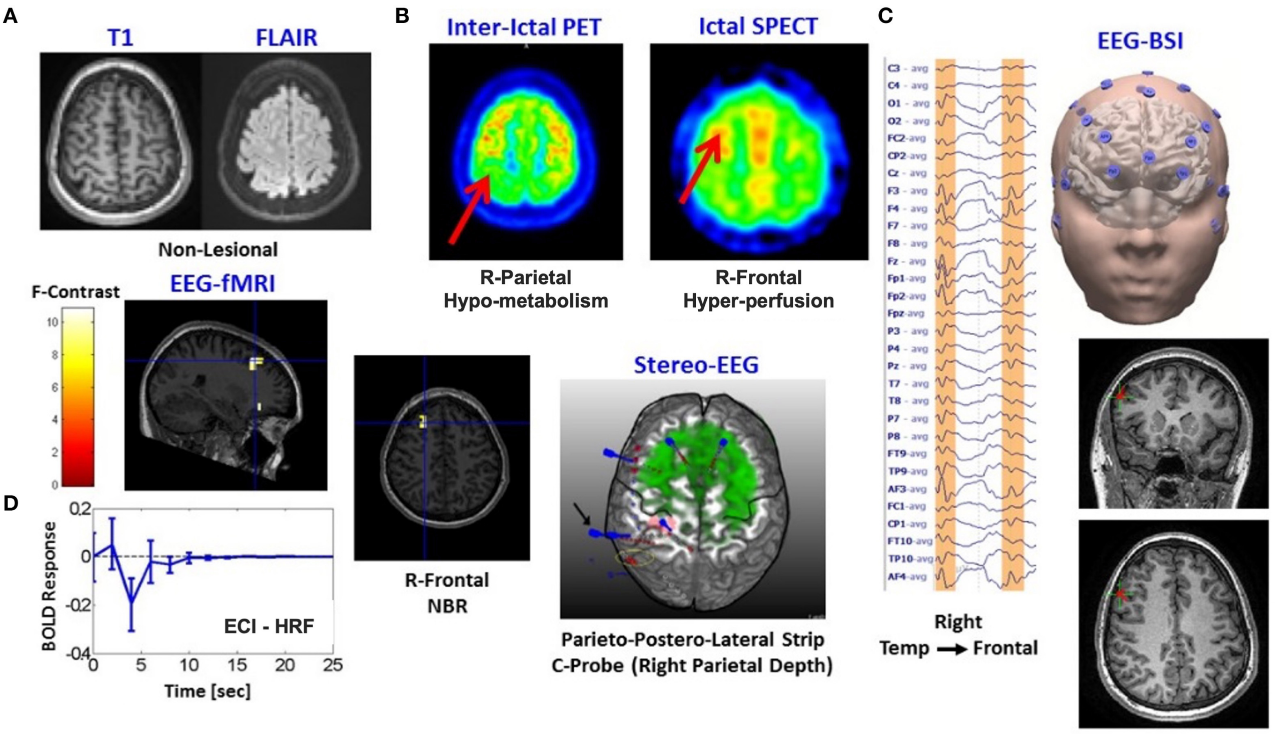

FIGURE 5 | Patients #2 shows an irritative zone with ECI-type HRF with a high probability to be the seizure onset zone. **(A)** Two modalities of fMRI anatomical imaging: left, T1-weighted; right, FLAIR. **(B)** Two modalities of nuclear imaging: left, interictal PET; right, ictal SPECT. **(C)** Left, Ictal EEG points out to a bifrontal spike/slow wave at 3-4Hz; right, brain source imaging (EEG-BSI) in Right Tempo-Frontal. **(D)** Composed panel: left top and center, two slices with the thresholded F-statistics map built from the estimated coefficients of the GLM overlaid on the T1-weighted image with blue crosshair locating the center of one NBR region in the Right Frontal Lobe, left bottom-estimated NN-ARx of this particular NBR-HRF was classified as ECI mechanism, right-stereo EEG (sEEG) electrodes placement is shown as reference.

DISCUSSION

The most accessible, inexpensive, and least-invasive brain imaging method available for localizing seizure foci with high sensitivity (85%) is fMRI combined with EEG. Unfortunately, its benefits remain controversial for many patients, owing to an incomplete understanding of the neuronal, vascular, and metabolic responses in epileptic tissues, decreasing the sensitivity of the biomarker used to locate foci. A large percentage (∼17.4%) of discordance in the use of the EEG-fMRI technique is due to a poor classification of clinically relevant NBR responses (**Table 2**). Here, we hypothesize that NBRs during IEDs could be caused by both clinically and non-clinically relevant mechanisms. A clinically relevant mechanism should be that resulting as a direct consequence of epileptogenic tissues, i.e., an enhanced inhibition and a vascular/metabolic balance mismatch both due to tissue overexcitability. A secondary effect, such as blood flow stealing and resting-state network shutdown, should be considered not clinically relevant and hence not discussed during the surgical workup. Therefore, tools aiming at the classification of these four mechanisms might increase accuracy in the localization of foci for neurosurgical excision, improving success rates. Henceforth, we discuss the rationale and implications of the mechanisms proposed for NBR genesis in epilepsy.

Modeling NBRs With a Neuronal Network Origin

Inhibition-related phenomena, i.e., ECI and NDA, require accounting for the imbalance between the local activation of inhibitory and excitatory neuronal states, which depend on their respective connectivity structure. A two-state model (P-DCM) was used by Havlicek et al. (44, 53) to explain NBR during static and flickering visual stimulation. In this article, we extended the P-DCM model to include an additional external input to the inhibitory population in each brain region of interest and an IED-evoked synaptic modulation of the RSNs. Long-range excitatory (thalamocortical/corticocortical) inputs targeting inhibitory populations in the granular layers of the cerebral cortex have been extensively reported in previous literature. IEDs are mostly initiated by a brief increase in excitatory feedback gains and decrease in the thresholds for firing (63). In many cases, local neuronal excitability is followed by an enhancement in cortical inhibition (e.g., the wave component in the spike-wave events), which has been linked to a robust hyperpolarization in III/V layer pyramidal cells (25, 26). Data by Pittau et al. (13) suggested this type of enhanced inhibition might cause NBR in, or near, the actual IZs. Therefore, we hypothesize NBR with an ECI-HRF type should be included as a potential candidate for ablation in the epilepsy surgical workup. We

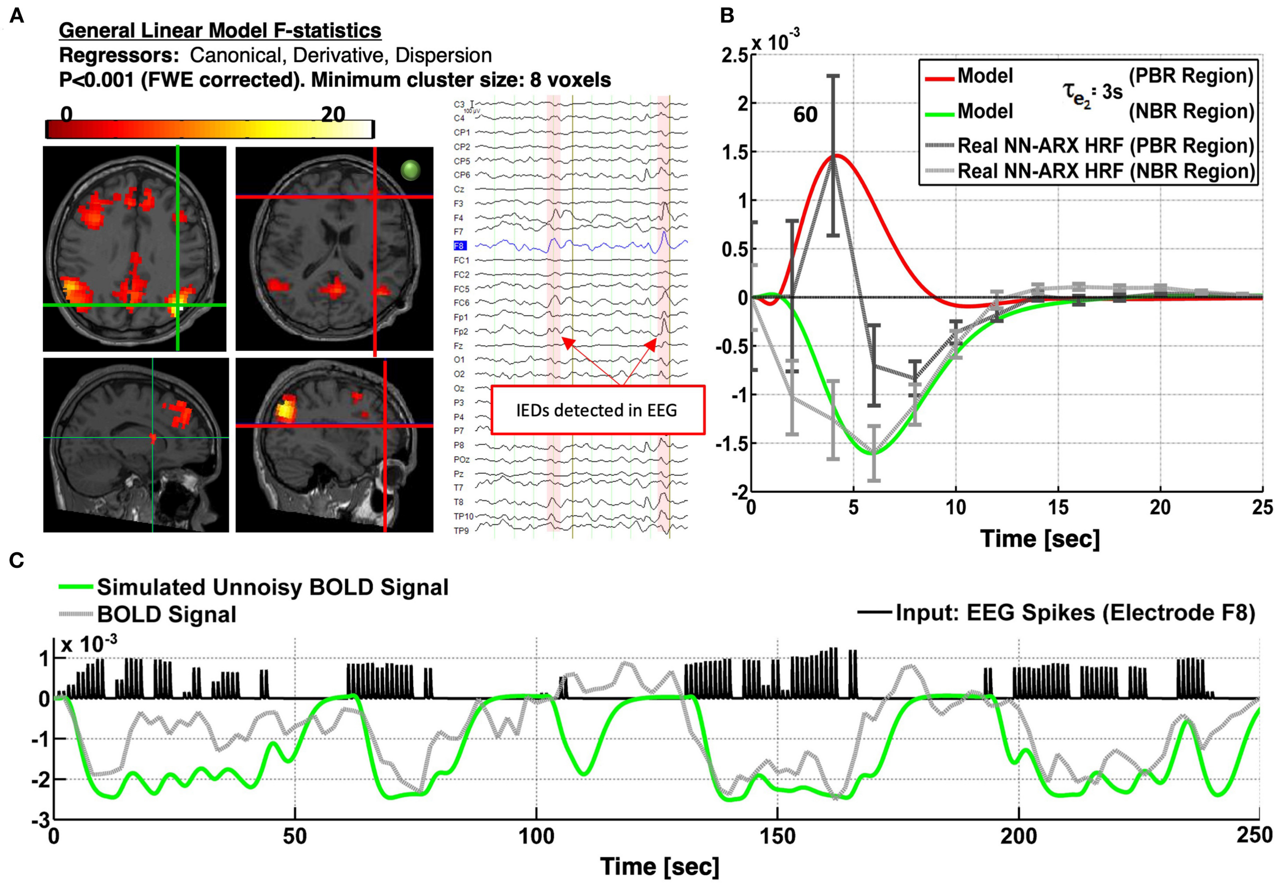

FIGURE 6 | Patients #3 shows an irritative zone with NDA-type HRF in a brain area of the DMN. **(A)** Slices showing the thresholded F-statistics map built from the estimated coefficients of the GLM overlaid on the T1-weighted image. Top left axial slice: green crosshair locating the center of one NBR region in the Right Lateral Parietal node of the DMN—coinciding with the maximum value of the F-statistics. Bottom left sagittal: green crosshair locating another NBR region in the caudate nucleus. Right slices: Red crosshair locating the center of the PBR region in the right frontal cortex-presumably in the origin of the IEDs. The IEDs were detected using the EEG signal in electrode F8. The approximate location of this electrode is shown with a green circle in the right axial slice to illustrate the possible relation of frontal PBR and the IEDs. The right inset shows a short segment of the preprocessed EEG data where 2 IEDs were identified. **(B)** The dark gray curve shows the estimated NN-ARx PBR-HRF and its confidence interval, estimated from the real data around the region marked by the red crosshair in **(A)**. The light gray curve shows the estimated NN-ARx NBR-HRF and its confidence interval, estimated from the real data around the DMN node marked by the green crosshair in the top left slice in **(A)**. The red and green curves show the unnoisy simulated PBR-HRF and NBR-HRF, respectively, for a $\tau_{e2} = 3s$. **(C)** For illustration purposes, we also show the temporal behavior of the simulated neuronal activity and BOLD signal in the NBR region [with $\tau_{e2} = 3s$], the time series of the real fMRI and the input. To account for the actual relative effect of the IEDs, the amplitude of the input pulses was multiplied by the normalized power of the EEG in F8.

believe the NBR results from an abnormal enhancement in the external input to inhibitory populations in the neocortex, which is modeled by a large response time of the inhibitory population τ_{i1}. In this article, the τ_{i1} parameter was fitted using the BOLD data to accurately represent the particular NBR waveform. On the other hand, the recovery of the neuronal activity of the disrupted RSN (NDA) after an IED affects one of its nodes is characterized by a modulation of the excitatory synapses in specific areas within the RSNs, which was characterized by a reduced intralaminar excitatory connectivity $c_{e2} = 0.01$ and a large response time τ_{e2}. The latter actually depends on the way the different nodes interact to effectively "shut down" and recover the network. Note that brain dynamics operate near criticality (64–66), i.e., on the brink to instability. Neuronal activities in this situation require higher recovery time to reach equilibria after perturbed and are associated with large-scale dependencies and scale invariance (67). Therefore, the time response for excitatory τ_{e2} was fitted to the BOLD data to accurately characterize the NDA type of NBRs.

Modeling NBRs With a Vascular/Metabolic Origin

Enhancements in the neurovascular coupling gain ε cause increases in CBF, hence a larger PBR effect. Ictal hyperperfusion has been observed with ^{15}O-H$_2$O PET and ^{99m}Tc-HMPAO/ECD (33, 34). Using invasive recordings from a preclinical model of epilepsy, we have reported increases in the perfusion gain around the SOZs (35). In this previous study, we associated a small value

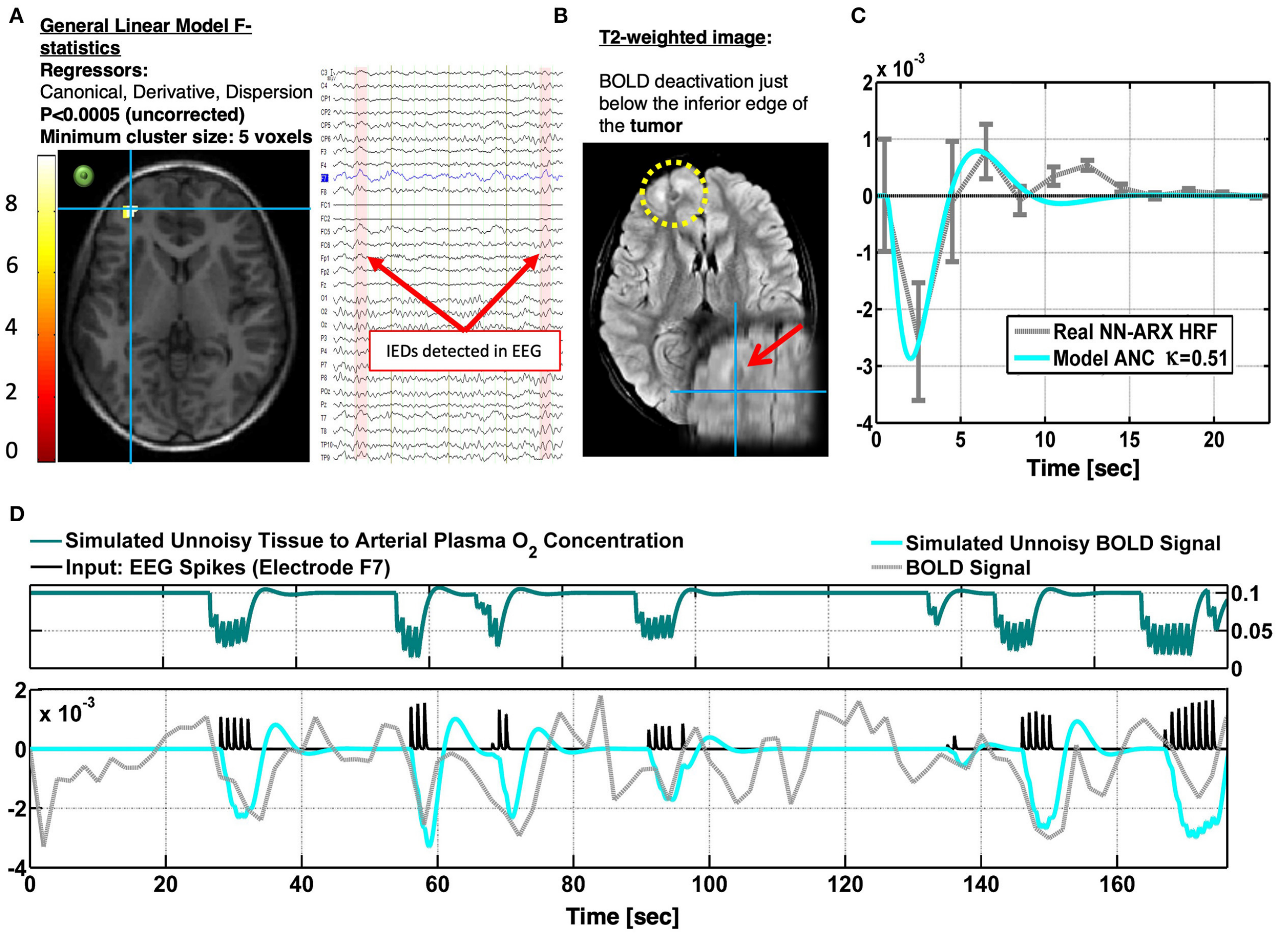

FIGURE 7 | Patients #4 shows an irritative zone with ANC-type HRF in a brain area at the edge of a tumor (TSC). **(A)** Axial slice of the thresholded F-statistics map built from the estimated coefficients of the GLM overlaid on the T1-weighted image. The IEDs were detected using the EEG signal in electrode F7. The approximate location of this electrode is shown with a green circle to illustrate the possible relation between the NBR region and the IEDs. The right inset shows a short segment of the preprocessed EEG data where 2 IEDs were identified. **(B)** The patient suffers from tuberous sclerosis complex. The cyan crosshair—the maximum value of the F-statistics—locates the center of the NBR region, in the perimeter and below one of the patient's tumors. The tumor is highlighted with the yellow circle in the axial slice and the red arrow in the coronal slice of the T2-weighted image. **(C)** The gray curve shows the estimated NN-ARx HRF and its confidence interval, estimated from the real data, and averaged across the voxels within a 10 mm-radius sphere with origin in the crosshair in **(A)**. The cyan curve shows the unnoisy simulated HRF of the fitted OTT model with the estimated value of the neuro-metabolic coupling gain: $\kappa = 0.51\ s^{-1}$. **(D)** For illustration purposes, we also show the simulated temporal behavior of the state variable g and the simulated BOLD in the NBR region [with $\kappa = 0.51\ s^{-1}$], the time series of the real fMRI and the input. To account for the actual relative effect of the IEDs, the amplitude of the input pulses was multiplied by the normalized power of the EEG in F7.

of κ in the SOZ with an increase in the baseline O_2 metabolism, which might be related to reported glucose hypermetabolism in the SOZs from ictal FDG PET. The interplay between O_2/glucose metabolism and blood perfusion during IEDs is still controversial. Several studies have shown a hypometabolism in IZs, whereas others have reported complex glucose metabolism patterns with hypermetabolism also in some SOZ candidates (34, 68). Using $^{15}O\text{-}H_2O$ PET, Bittar et al. (68) showed an increase in blood perfusion during IEDs. However, reductions in perfusion have been also reported in the past (34). If this neurovascular coupling gain is kept constant, the parameter that is highly correlated with NBR amplitude will be κ. A disproportionate increase of this value leads to the ANC type of HRF. In this mechanism, the NBR can be seen as an exaggerated initial dip as a result of an abnormally enhanced O_2 metabolism. It is hypothesized that this particular type of NBR may be clinically relevant while defining IZs. NBR can also have a pure vascular origin *via* an ABS effect. Here, we use a model proposed by Suarez et al. (39) that couples two Windkessels by a common artery to classify ABS types of HRFs. Simulations indicate that the parameter that determines the NBR amplitude is the resistance of the vessel (artery), relative to the total steady state resistance of the vasculature within the tissue, i.e., the arterioles, capillaries, and venules. A vascular anatomical network (VAN) model proposed earlier by Boas et al. (69) predicts also a relative decrease in CBF and O_2 saturation around a brain area undergoing a positive functional hyperemic response. However, the authors are not aware of the application of the VAN model to

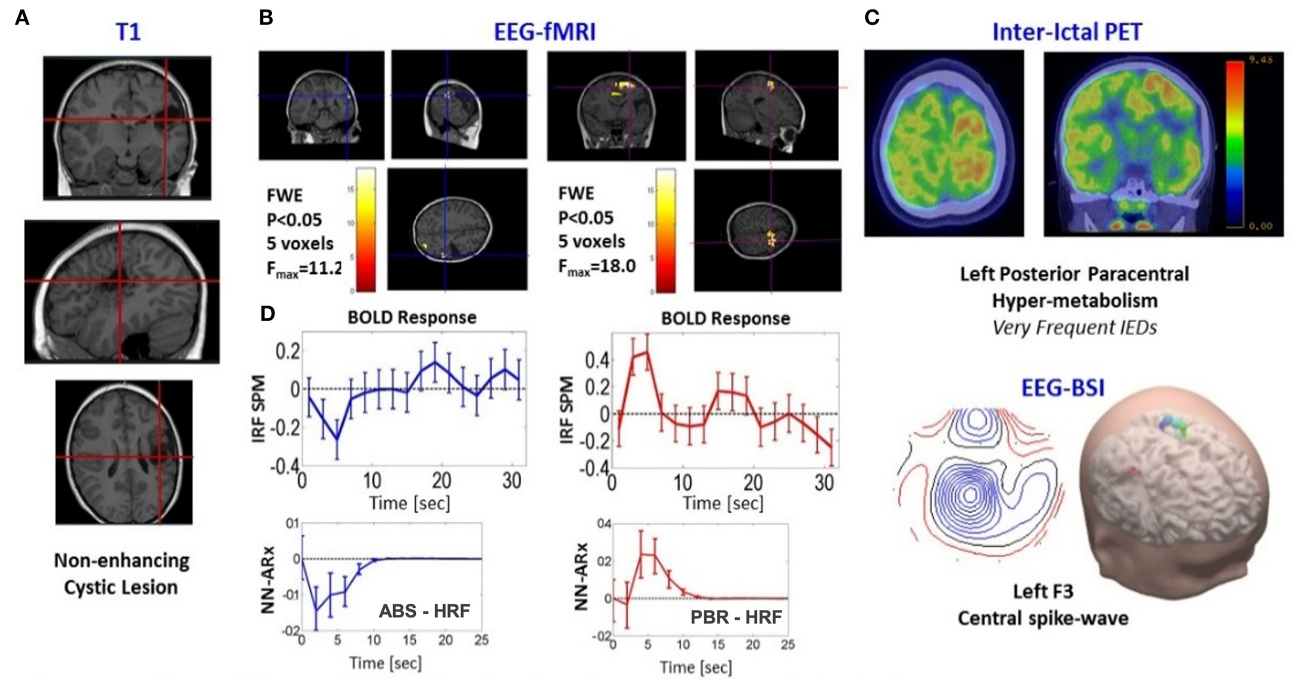

FIGURE 8 | Patients #5 shows an irritative zone with ABS-type HRF. **(A)** Three different slices of anatomical fMRI imaging (T1-weighted) show non-enhancing cystic lesion in the Left Posterior Frontal Lobe (red crosshairs). **(B)** Slices showing the thresholded F-statistics map built from the estimated coefficients of the GLM overlaid on the T1-weighted image; left panel, NBR highlighted with blue crosshairs; right panel, PBR highlighted with red crosshairs. **(C)** Composed panel: top, two slices of nuclear imaging (interictal PET); bottom, EEG-BSI data. **(D)** Comparison between the NN-ARx method with the impulse response function (IRF) method (SPM software). The IRF method was not able to capture underlying HRFs. Results from the NN-ARx were classified as the ABS mechanism.

study NBRs in epilepsy. The existence of ABS effect in the brain have been experimentally demonstrated by several groups (38, 41). Here, we recommend excluding IZs with ABS types of NBRs as potential candidates of SOZ. Some authors have suggested that a type of NBR might also result from the combination of blood backpressure and neuronal inhibition (47, 70). That would explain the presence of the poststimulus overshoot, which is in contrast to those observed in our pure vascular simulations. This undershoot is shown to be determined by the dynamics of the inhibitory neuronal state (44). Other causes including vein delayed compliance might also explain these transient. However, these last mechanisms were not investigated in this study.

NBR Classification

In this article, we focus on the possibility of detecting and classifying the NBR mechanisms using the HRFs extracted from BOLD fMRI signals. We use linear models for the detection and estimation of the HRFs, i.e., GLM and NN-ARx methods, respectively. Under the assumption of the extended balloon model, the validity of the GLM was previously investigated by quantifying the effect size of second-order Volterra kernels (55). Under the same model, the validity of the NN-ARx to estimate HRFs was evaluated in (17, 45). Although linear models have been used to detect and reconstruct BOLD responses for decades, even before addressing the non-linear characteristics of BOLD signals (59, 71), we decided to analyze if linear models are able to accurately characterize PBRs and NBRs in epileptic patients. In general, for balloon/Windkessel models—with sporadic IED events and typical canonical-like responses (57), these linear models are suitable for spatial detection estimation of the HRF. We investigated if the NBR mechanisms can be solely classified from their BOLD responses. This is important for clinical applications when only standard fMRI paradigms are available or designed. **Figure 3D** shows that the machine learning classifier is able to differentiate PBR (red), ECI (yellow), NDA (green), ANC (cyan), and ABS (blue) in 100% of the cases. However, ECI and ABS were undistinguishable in some trials. In practice, this might be worse as there is a loss of sensitivity and specificity related to the usual misclassifications of IEDs, which is expert dependent. Furthermore, we cannot outline the possibility of having more than one NBR mechanism in the same area at the same time. Thus, failing to identify IZs with multiple NBR mechanisms could lead, in the worst-case scenario, to the incorrect clinical assessment. According to our hypothesis, an ABS/ECI misclassification will be the most critical case. However, these mechanisms are different in nature, and our model predicts different responses when using other imaging or recording modalities. At the expense of experimental feasibility, other imaging technique can be combined with our EEG-fMRI methodology to verify the predicted NBR mechanisms. For example, MION (38) and/or VASO (47) can be used to measure CBV concurrent with BOLD signals. Measurements of neuronal activity can be incorporated using ECoG/sEEG and EEG (27). In addition, CBF can be also included using

TABLE 2 | Results from two studies (different laboratories) about the accuracy of the EEG-fMRI technique, with specifications to (a) typical percentage of refractory epileptic patients who will not be able to complete a successful EEG-fMRI study and (b) typical percentage of these patients with a "discordant" NBR result.

References	**No.**	**Removed *[Art, No IED]***	**Concordance (%)**			**Discordant (%)**			**NBR-/Tot *(%)***
			PBR	***NBR***	***Total***	***PBR***	***NBR***	***Total***	
Salek-Haddadi et al. (14)	63	29 (46.0%)	17	4	62%	2	9	32%	9/34 (26%)
An et al. (1)	47	12 (25.5%)	21	6	77%	5	3	23%	3/35 (8%)
Total	110	41 (37.3%)	38	10	69%	7	12	27%	12/69 (17.4)

arterial spin labeling (ASL) (30) and/or FAIR (47). In the case of ABS/ECI misclassification, a radiologist could use EEG concurrently recorded with ASL focused on the particular regions to verify whether there is a decrease in CBF. If no decrease in CBF is observed, ECI mechanisms should be expected. With these multimodal observations, we foresee a significant increase in the margins of classification of the NBR mechanisms, even in the case more than one is present in the same region (47, 72). It is important to highlight that none of the available imaging modalities (**Table 1**) provides conclusive results, and a thorough data evaluation in the surgical workup is needed for each clinical case. Our approach only aims at providing another level of EEG-fMRI data interpretation to improve the accuracy of this technique. To illustrate this, five specific clinical cases are discussed below.

Epileptic Cases Discussion

We found an ABS type of NBR in patients 1 and 5. In patient 1, an NBR was located in the SPL and a PBR in the PG. The NBR was classified as ECI, which would occur *via* either U fibers or pure vascular phenomena. However, we cast doubt on ECI as we believe an inhibitory pathway from SPL to PG is rather weak. Note that the PG hosts the primary somatosensory cortex (S1) (73), which is a granular cortex that mainly receives somatotopic feedforward afferents from the ventral posterolateral and posteromedial relay nuclei (VPL and VPM) of the thalamus (74). In addition, the SPL, involved in transforming visual information in complex motor planning, has efferent pathways mainly to the premotor supplementary motor cortices in the precentral gyrus. A top–down inhibition from higher areas (prefrontal cortex) to the somatosensory area is mainly *via* efferent pathways. Moreover, both difussion spectrum imaging (DSI)-based connectivity (75) and cortical thickness–based connectivity (76) between SPL and PG are rather low. The mechanism might be ABS. Note that the detected BOLD responses are in the vascular domain of the middle central artery, at both sides of the postcentral sulcus. Thus, they might be sharing a final segment of the anterior parietal artery. Although we do not discard the existence of a venous blood backpressure effect, in which the regions could be sharing some anastomotic vein feeding the central sulcal vein or a branch of the superior anastomotic vein of Trolard, it has been reported that venous CBV changes are relevant only for longer stimuli (77). The NBR in patient 5 was found posterior to the cyst. We used data from this patient to illustrate the HRF estimation with the IRF method (SPM) and our NN-ARx method. Because of a probable revascularization around the cyst, angiography data from this patient will be required for a discussion about possible scenarios for the ABS effect. A frontal eye-field NBR with an ECI HRF was found in patient 2, which is most likely due to ictal propagation with frontal slow-wave responses. Slow-wave discharges have been found associated with NBR (13). DMN deactivations, like those found in patient 3, have been systematically reported in the literature for temporal lobe epilepsy (TLE) (11, 37) and for other types of focal epilepsy (36, 78). The pattern of deactivation depicted in **Figure 6**, with a predominance in the parietal node of the DMN ipsilateral to the focus, is similar to that reported ibyn Fahoum et al. (36) for four of five patients, with concomitant decrease of electrophysiological activity. Our results suggest that the PBR region might have afferents on the anterior part of the caudate nucleus that relay to central nodes of the DMN. This is consistent with the hypothesis of widespread secondary inhibition of non-seizing cortical regions *via* basal ganglia (79). The temporal profile of the PBR HRF in the right IFG experienced an unpredicted decay (or rebound) correlated with the amplitude of the NBR in the DMN nodes. This might be seen as an interruption of the PBR mechanism by inhibitory afferents coming from the regions exhibiting NDA, which in this case are present all around the right IFG. This might have implications in the interpretations of BOLD responses during IEDs or stimulation paradigms. If the location of the PBR is close to an affected RSN node, its HRF waveform might be misleading of the actual underlying PBR mechanism, due to either the interaction between mechanisms, i.e., inhibitory inputs from the NBR to the PBR region, or the effect of the BOLD spatial point-spread function. This rebound can be also explained as an increase in dHb due to an increase in neuronal activity in the NBR region, or even a vascular reallocation phenomena, as suggested by Hu and Huang (40). They observed positive and negative optical responses, concurrent with local field potentials (LFP) and multiunit activity (MUA) measurements, in rats during hindlimb electrical stimulation. Finally, it has been hypothesized that NDA is a disruption of RSN provoking a reduction of consciousness and cognitive reserve (36). Interestingly, our results suggest that a recovery from this disrupted state is not instantaneous. In our data, the estimated value for the recovery time constant was $\tau_{e2} = 3s$. The Epilepsy Connectome Project (ECP) (80) constitutes a huge database that contains clinical, neurophysiological, and resting-state fMRI (rs-fMRI) data of 105 patients with TLE and 55 healthy individuals as control.

Using graph (nodes and edges) theory combined with rs-fMRI measures, a characterization of abnormal patterns in the local and global neuronal connectivity in TLE has been possible, thanks to the ECP. Our model-based method to identify different types of NBRs in epilepsy can help provide a neurophysiological foundation to the reported connectivity maps abnormalities. The ANC mechanism, as reported for patient 4, is related to a decrease in the CBF/CMRO$_2$ balance. NBRs in the hippocampus of rats during bicuculline-induced generalized tonic–clonic seizures were associated with this type of mechanism (81). The authors reported that, even with higher LFP/MUA activity in the hippocampus, as compared to the cortex, the CBF was lower, and the CMRO$_2$ was higher, yielding to NBRs in the hippocampus. Quantitatively, the unbalance corresponds to a decrease in the ratio $\frac{\varepsilon}{\kappa}$ in the OTT model (56), which is $\sim\frac{0.4}{0.05} = 8$ for normal positive responses. Song et al. (35) estimated a ratio approximately five-fold smaller in rat with focal cortical seizures. Although the rCBF/CMRO$_2$ coupling was reported to be preserved in human IEDs without any apparent lesion (82), we do not discard the possibility of an unbalance produced by a more critical state of tissue pathology. For example, the typical calcification of the surrounding blood vessels present in TSC tumors (83) could hamper the expected IED-induced increase of rCBF. We estimated $\kappa = 0.51s^{-1}$ for the IED-related ANC mechanism around the lesion, which yields $\frac{0.28}{0.51} = 0.55$, 14 times smaller than the normal values.

Final Remarks

It is worth noting the foreseeable boost that BOLD modeling will have with the advent of new and optimized sequences in high-field spin-echo fMRI, with the considerably improved ability to measure high-resolution layer-dependent BOLD images and correlates of rCBV and rCBF (47, 70, 84–89). This allows for the construction and estimation of more detailed models of BOLD generation, through understanding of the actual role of arteries, capillaries, and veins in the generation of these observables and the possible biases that the variability of neurovascular/metabolic coupling, CBV, and signal-to-noise ratio (SNR) across layers could introduce. For example, it has been reported that the baseline CBV distribution varies over cortical layers biasing fMRI signal to layers with high CBV values (77). This affects the interpretation of what the contribution of the different vascular compartments to the average low-resolution BOLD response is.

DATA AVAILABILITY STATEMENT

The datasets presented in this article are not readily available because they are from clinical cases and this would jeopardize patient privacy. Requests to access the datasets should be directed to jrieradi@fiu.edu.

ETHICS STATEMENT

The studies involving human participants were reviewed and approved by Western IRB, USA. Written informed consent to participate in this study was provided by the participants' legal guardian/next of kin.

AUTHOR CONTRIBUTIONS

AS: data analysis and model development. PV-H: data collecting and data analysis. BB: data analysis and clinic case discussion. CD: IED detection and classification. JB-B: data analysis. JR: research design, discussion, and writing. PV-H: data collecting, data analysis, and model development. All authors contributed to the article and approved the submitted version.

FUNDING

This work was supported by the National Institutes of Health (R56NS094784-01A1).

ACKNOWLEDGMENTS

We appreciate Prof. Pedro A. Valdes-Sosa and Prof. Louis Lemeiux for their useful comments and suggestions during the preparation of this manuscript. Special thanks goes to Professor Jean Gotman and Dr. Nicolas von-Ellenrieder, who substantially helped with the data analysis and interpretation.

SUPPLEMENTARY MATERIAL

The Supplementary Material for this article can be found online at: https://www.frontiersin.org/articles/10.3389/fneur.2021.659081/full#supplementary-material

REFERENCES

1. An D, Fahoum F, Hall J, Olivier A, Gotman J, Dubeau F. Electroencephalography/functional magnetic resonance imaging responses help predict surgical outcome in focal epilepsy. *Epilepsia.* (2013) 54:2184–94. doi: 10.1111/epi.12434
2. Coan AC, Chaudhary UJ, Grouiller F, Campos BM, Perani S, de Ciantis A, et al. EEG-fMRI in the presurgical evaluation of temporal lobe epilepsy. *J Neurol Neurosurg Psychiatry.* (2016) 87:642–9. doi: 10.1136/jnnp-2015-310401
3. Pittau F, Ferri L, Fahoum F, Dubeau F, Gotman J. Contributions of EEG-fMRI to assessing the epileptogenicity of focal cortical dysplasia. *Front Comput Neurosci.* (2017) 11:8. doi: 10.3389/fncom.2017.00008
4. Friston KJ, Holmes AP, Worsley KJ, Poline JB, Frith C, Frackowiak RS. Statistical parametric maps in functional imaging: a general linear approach. *Hum Brain Mapping.* (1995) 2:189–210. doi: 10.1002/hbm.460020402
5. Van Eyndhoven S, Dupont P, Tousseyn S, Vervliet N, Van Paesschen W, Van Huffel S, et al. Augmenting interictal mapping with neurovascular coupling biomarkers by structured factorization of epileptic EEG and fMRI data. *NeuroImage.* (2021) 228:117652. doi: 10.1016/j.neuroimage.2020.117652
6. Lu Y, Grova C, Kobayashi E, Dubeau F, Gotman J. Using voxel-specific hemodynamic response function in EEG-fMRI data analysis: an estimation and detection model. *Neuroimage.* (2007) 34:195–203. doi: 10.1016/j.neuroimage.2006.08.023

7. Grouiller F, Vercueil L, Krainik A, Segebarth C, Kahane P, David O. Characterization of the hemodynamic modes associated with interictal epileptic activity using a deformable model-based analysis of combined EEG and functional MRI recordings. *Human Brain Mapp.* (2010) 31:1157–73. doi: 10.1002/hbm.20925
8. Storti SF, Formaggio E, Bertoldo A, Manganotti P, Fiaschi A, Toffolo GM. Modelling hemodynamic response function in epilepsy. *Clin Neurophysiol.* (2013) 124:2108–18. doi: 10.1016/j.clinph.2013.05.024
9. Proulx S, Safi-Harb M, LeVan P, An D, Watanabe S, Gotman J. Increased sensitivity of fast BOLD fMRI with a subject-specific hemodynamic response function and application to epilepsy. *NeuroImage.* (2014) 93:59–73. doi: 10.1016/j.neuroimage.2014.02.018
10. Bagshaw AP, Aghakhani Y, Bénar, C.-G., Kobayashi E, Hawco C, et al. EEG-fMRI of focal epileptic spikes: analysis with multiple haemodynamic functions and comparison with gadolinium-enhanced MR angiograms. *Hum Brain Mapp.* (2004) 22:179–92. doi: 10.1002/hbm.20024
11. Kobayashi E, Bagshaw AP, Grova C, Dubeau F, Gotman J. Negative BOLD responses to epileptic spikes. *Hum Brain Mapp.* (2006) 27:488–97. doi: 10.1002/hbm.20193
12. Rathakrishnan R, Moeller F, Levan P, Dubeau F, Gotman J. BOLD signal changes preceding negative responses in EEG-fMRI in patients with focal epilepsy. *Epilepsia.* (2010) 51:1837–45. doi: 10.1111/j.1528-1167.2010.02643.x
13. Pittau F, Fahoum F, Zelmann R, Dubeau F, Gotman J. Negative BOLD response to interictal epileptic discharges in focal epilepsy. *Brain Topogr.* (2013) 26:627–40. doi: 10.1007/s10548-013-0302-1
14. Salek-Haddadi A, Diehl B, Hamandi K, Merschhemke M, Liston A, Friston K, et al. Hemodynamic correlates of epileptiform discharges: an EEG-fMRI study of 63 patients with focal epilepsy. *Brain Res.* (2006) 1088:148–66. doi: 10.1016/j.brainres.2006.02.098
15. Pesaresi I, Cosottini M, Belmonte G, Maritato P, Mascalchi M, Puglioli M, et al. Reproducibility of BOLD localization of interictal activity in patients with focal epilepsy: intrasession and intersession comparisons. *Magma.* (2011) 24:285–96. doi: 10.1007/s10334-011-0263-x
16. Beers CA, Williams RJ, Gaxiola-Valdez I, Pittman DJ, Kang AT, Aghakhani Y, et al. Patient specific hemodynamic response functions associated with interictal discharges recorded via simultaneous intracranial EEG-fMRI. *Hum Brain Mapp.* (2015) 36:5252–64. doi: 10.1002/hbm.23008
17. Riera JJ, Watanabe J, Kasuki I, Naoki M, Aubert E, Ozaki T, et al. A state-space model of the hemodynamic approach: nonlinear filtering of BOLD signals. *NeuroImage.* (2004) 21:547–67. doi: 10.1016/j.neuroimage.2003.09.052
18. Makni S, Ciuciu P, Idier J, Poline JB. Joint detection-estimation of brain activity in functional MRI: a multichannel deconvolution solution. *IEEE Trans Signal Process.* (2005) 53:3488–502. doi: 10.1109/TSP.2005.853303
19. Makni A, Idier J, Vincent T, Thirion B, Dehaene-Lambertz G, Ciuciu P. A fully Bayesian approach to the parcel-based detection-estimation of brain activity in fMRI. *NeuroImage.* (2008) 41:941–69. doi: 10.1016/j.neuroimage.2008.02.017
20. Baraldi P, Manginelli AA, Maieron M, Liberati D, Porro CA. An ARX model-based approach to trial by trial identification of fMRI-BOLD responses. *Neuroimage.* (2007) 37:189–201. doi: 10.1016/j.neuroimage.2007.02.045
21. Vincent T, Risser L, Ciuciu P. Spatially adaptive mixture modeling for analysis of fMRI time series. *IEEE Trans Medical Imaging.* (2010) 29:1059–74. doi: 10.1109/TMI.2010.2042064
22. Chaari L, Vincent T, Forbes F, Dojat M, Ciuciu P. Fast joint detection-estimation of evoked brain activity in event-related fMRI using a variational approach. *IEEE Trans Medical Imaging.* (2013) 32:821–37. doi: 10.1109/TMI.2012.2225636
23. Cherkaoui H, Moreau T, Halimi A, Leroy C, Ciuciu P. Multivariate semi-blind deconvolution of fMRI time series. *Neuroimage.* (2021) 241:118418. doi: 10.1016/j.neuroimage.2021.118418
24. Lemieux L, Salek-Haddadi A, Josephs O, Allen P, Toms N, Scott C, et al. Event-related fMRI with simultaneous and continuous EEG: description of the method and initial case report. *Neuroimage.* (2001) 14:780–7. doi: 10.1006/nimg.2001.0853
25. Neckelmann D, Amzica F, Steriade M. Changes in neuronal conductance during different components of cortically generated spike-wave seizures. *Neuroscience.* (2000) 96:475–85. doi: 10.1016/S0306-4522(99)00571-0
26. Pollen DA. Intracellular studies of cortical neurons during thalamic induced wave and spike. *Electroencephalogr Clin Neurophysiol.* (1964) 17:398–404. doi: 10.1016/0013-4694(64)90163-4
27. Maggioni E, Zucca C, Reni G, Cerutti S, Triulzi FM, Bianchi AM, et al. Investigation of the electrophysiological correlates of negative BOLD response during intermittent photic stimulation: an EEG-fMRI study. *Hum Brain Mapp.* (2016) 37:2247–62. doi: 10.1002/hbm.23170
28. Pasley BN, Inglis BA, Freeman RD. Analysis of oxygen metabolism implies a neural origin for the negative BOLD response in human visual cortex. *Neuroimage.* (2007) 36:269–76. doi: 10.1016/j.neuroimage.2006.09.015
29. Schäfer K, Blankenburg F, Kupers R, Grüner JM, Law I, Lauritzen M, et al. Negative BOLD signal changes in ipsilateral primary somatosensory cortex are associated with perfusion decreases and behavioral evidence for functional inhibition. *Neuroimage.* (2012) 59:3119–27. doi: 10.1016/j.neuroimage.2011.11.085
30. Shmuel A, Yacoub E, Pfeuffer J, Van de Moortele PF, Adriany G, Hu X, et al. Sustained negative BOLD, blood flow and oxygen consumption response and its coupling to the positive response in the human brain. *Neuron.* (2002) 36:1195–210. doi: 10.1016/S0896-6273(02)01061-9
31. Smith AT, Williams AL, Singh KD. Negative BOLD in the visual cortex: evidence against blood stealing. *Hum Brain Mapp.* (2004) 21:213–20. doi: 10.1002/hbm.20017
32. Wade AR. The negative BOLD signal unmasked. *Neuron.* (2002) 36:993–5. doi: 10.1016/S0896-6273(02)01138-8
33. Van Paesschen W. Ictal SPECT. *Epilepsia.* (2004) 45:35–40. doi: 10.1111/j.0013-9580.2004.04008.x
34. Sarikaya I. PET studies in epilepsy. *Am J Nucl Med Mol Imaging.* (2015) 5:416–30.
35. Song Y, Torres R, Garcia S, Frometa Y, Bae J, Deshmukh A, et al. Dysfunction of neuro-vascular/metabolic coupling in chronic focal epilepsy. *IEEE Trans Biomed Eng.* (2016) 63:97–110. doi: 10.1109/TBME.2015.2461496
36. Fahoum F, Zelmann R, Tyvaert L, Dubeau F, Gotman J. Epileptic discharges affect the default mode network - fMRI and intracerebral EEG evidence. *PLoS One.* (2013) 8:e68038. doi: 10.1371/journal.pone.0068038
37. Laufs H, Hamandi K, Salek-Haddadi A, Kleinschmidt AK, Duncan JS, Lemieux L. Temporal lobe interictal epileptic discharges affect cerebral activity in "default mode" brain regions. *Hum Brain Mapp.* (2007) 28:1023–32. doi: 10.1002/hbm.20323
38. Harel N, Lee SP, Nagaoka T, Kim DS, Kim SG. Origin of negative blood oxygenation level-dependent fMRI signals. *J Cereb Blood Flow Metab.* (2002) 22:908–17. doi: 10.1097/00004647-200208000-00002
39. Suarez A, Valdes-Hernandez PA, Moshkforoush A, Tsoukias N, Riera J. Arterial blood stealing as a mechanism of negative BOLD response: from the Steady-flow with nonlinear phase separation to a Windkessel-based model. *J Theor Biol.* (2021) 529. doi: 10.1016/j.jtbi.2021.110856
40. Hu D, Huang L. Negative hemodynamic response in the cortex: evidence opposing neuronal deactivation revealed via optical imaging and electrophysiological recording. *J Neurophysiol.* (2015) 114:2152–61. doi: 10.1152/jn.00246.2015
41. Ma Z, Cao P, Sun P, Lu Z, Li L, Chen Y, et al. Negative hemodynamic response without neuronal inhibition investigated by combining optical imaging and electrophysiological recording. *Neurosci Lett.* (2017) 637:161–7. doi: 10.1016/j.neulet.2016.11.029
42. Mandeville JB, Marota JJ, Ayata C, Zaharchuk G, Moskowitz MA, Rosen BR, et al. Evidence of a cerebrovascular postarteriole Windkessel with delayed compliance. *J Cereb Blood Flow Metab.* (1999) 19:679–89. doi: 10.1097/00004647-199906000-00012
43. Buxton RB, Wong EC, Frank LR. Dynamics of blood flow and oxygenation changes during brain activation: the Balloon model. *MRM.* (1998) 39:855–64. doi: 10.1002/mrm.1910390602
44. Havlicek M, Ivanov D, Roebroeck A, Uludag K. Determining excitatory and inhibitory neuronal activity from multimodal fMRI data using a generative hemodynamic model. *Front Neurosci.* (2017) 11:616. doi: 10.3389/fnins.2017.00616
45. Riera J, Bosch J, Yamashita O, Kawashima R, Sadato N, Okada T, et al. fMRI activation maps based on the NN-ARx model. *NeuroImage.* (2004) 23:680–97. doi: 10.1016/j.neuroimage.2004.06.039

46. Friston K. Statistical parametric mapping. In: *Statistical Parametric Mapping: The Analysis of Functional Brain Images*. London: Academia Press; Elsevier (2007). p. 10–31.
47. Goense J, Merkle H, Logothetis NK. High-resolution fMRI reveals laminar differences in neurovascular coupling between positive and negative BOLD responses. *Neuron.* (2012) 76:629–39. doi: 10.1016/j.neuron.2012.09.019
48. Ashburner J, Friston KJ. Unified segmentation. *Neuroimage.* (2005) 26:839–51. doi: 10.1016/j.neuroimage.2005.02.018
49. Allen PJ, Josephs O, Turner R. A method for removing imaging artifact from continuous EEG recorded during functional MRI. *Neuroimage.* (2000) 12:230–9. doi: 10.1006/nimg.2000.0599
50. Allen PJ, Polizzi G, Krakow K, Fish DR, Lemieux L. Identification of EEG events in the MR scanner: the problem of pulse artifact and a method for its subtraction. *Neuroimage.* (1998) 8:229–39. doi: 10.1006/nimg.1998.0361
51. Bell AJ, Sejnowski TJ. An information-maximization approach to blind separation and blind deconvolution. *Neural Comput.* (1995) 7:1129–59. doi: 10.1162/neco.1995.7.6.1129
52. Makeig S, Jung TP, Bell AJ, Ghahremani D, Sejnowski TJ. Blind separation of auditory event-related brain responses into independent components. *Proc Natl Acad Sci USA*. (1997) 94:10979–84. doi: 10.1073/pnas.94.20.10979
53. Havlicek M, Roebroeck A, Friston K, Gardumi A, Ivanov D, Uludag K. Physiologically informed dynamic causal modeling of fMRI data. *Neuroimage.* (2015) 122:355–72. doi: 10.1016/j.neuroimage.2015.07.078
54. Zheng Y, Mayhew J. A time-invariant visco-elastic Windkessel model relating blood flow and blood volume. *Neuroimage.* (2009) 47:1371–80. doi: 10.1016/j.neuroimage.2009.04.022
55. Friston KJJ, Mechelli A, Turner R, Price CJJ. Nonlinear responses in fMRI: the Balloon model, Volterra kernels, and other hemodynamics. *Neuroimage.* (2000) 12:466–77. doi: 10.1006/nimg.2000.0630
56. Zheng Y, Martindale J, Johnston D, Jones M, Berwick J, Mayhew J. A model of the hemodynamic response and oxygen delivery to brain. *Neuroimage.* (2002) 16:617–37. doi: 10.1006/nimg.2002.1078
57. Glover GH. Deconvolution of impulse response in event-related BOLD fMRI. *Neuroimage.* (1999) 9:416–29. doi: 10.1006/nimg.1998.0419
58. Chen C-C, Tyler CW. Spectral analysis of fMRI signal noise. In: Onozuka M, Yen C-T, editors. *Novel Trends in Brain Science: Brain Imaging, Learning and Memory, Stress and Fear, and Pain*. Tokyo: Springer Japan (2008). p. 63–76.
59. Friston KJJ. Bayesian estimation of dynamical systems: an application to fMRI. *Neuroimage.* (2002) 16:513–30. doi: 10.1006/nimg.2001.1044
60. Furey TS, Cristianini N, Duffy N, Bednarski DW, Schummer M, Haussler D. Support vector machine classification and validation of cancer tissue samples using microarray expression data. *Bioinformatics.* (2000) 16:906–14. doi: 10.1093/bioinformatics/16.10.906
61. Mathur A, Foody GM. Multiclass and binary SVM classification: implications for training and classification users. *IEEE Geosci Remote Sensing Lett.* (2008) 5:241–5. doi: 10.1109/LGRS.2008.915597
62. Cervantes J, Garcia-Lamont F, Rodríguez-Mazahua L, Lopez A. A comprehensive survey on support vector machine classification: applications, challenges and trends. *Neurocomputing.* (2020) 408:189–215. doi: 10.1016/j.neucom.2019.10.118
63. Ayala GF, Dichter M, Gumnit RJ, Matsumoto H, Spencer WA. Genesis of epileptic interictal spikes. New knowledge of cortical feedback systems suggests a neurophysiological explanation of brief paroxysms. *Brain Res.* (1973) 52:1–17. doi: 10.1016/0006-8993(73)90647-1
64. Deco G, Jirsa VK, McIntosh AR. Emerging concepts for the dynamical organization of resting-state activity in the brain. *Nat Rev Neurosci.* (2011) 12:43–56. doi: 10.1038/nrn2961
65. Deco G, Jirsa VK. Ongoing cortical activity at rest: criticality, multistability, and ghost attractors. *J Neurosci.* (2012) 32:3366–75. doi: 10.1523/JNEUROSCI.2523-11.2012
66. Ghosh A, Rho Y, McIntosh AR, Kötter R, Jirsa VK. Noise during rest enables the exploration of the brain's dynamic repertoire. *PLoS Comput Biol.* (2008) 4:e1000196. doi: 10.1371/journal.pcbi.1000196
67. Haken H. *Synergetics: An Introduction: Nonequilibrium Phase Transitions and Self-Organization in Physics, Chemistry, and Biology, 3rd ed, Springer Series in Synergetics*. New York, NY: Springer-Verlag (1983).
68. Bittar RG, Andermann F, Olivier A, Dubeau F, Dumoulin SO, Pike GB, et al. Interictal spikes increase cerebral glucose metabolism and blood flow: a PET study. *Epilepsia.* (1999) 40:170–8. doi: 10.1111/j.1528-1157.1999.tb02071.x
69. Boas DA, Jones SR, Devor A, Huppert TJ, Dale AM. A vascular anatomical network model of the spatio-temporal response to brain activation. *Neuroimage.* (2008) 40:1116–29. doi: 10.1016/j.neuroimage.2007.12.061
70. Bandettini PA. The BOLD plot thickens: sign- and layer-dependent hemodynamic changes with activation. *Neuron.* (2012) 76:468–9. doi: 10.1016/j.neuron.2012.10.026
71. Buxton RB, Uludag K, Dubowitz DJ, Liu TT. Modeling the hemodynamic response to brain activation. *Neuroimage.* (2004) 23:S220–33. doi: 10.1016/j.neuroimage.2004.07.013
72. Shmuel A, Augath M, Oeltermann A, Logothetis NK. Negative functional MRI response correlates with decreases in neuronal activity in monkey visual area V1. *Nat Neurosci.* (2006) 9:569–77. doi: 10.1038/nn1675
73. Geyer S, Schormann T, Mohlberg H, Zilles K. Areas 3a, 3b, and 1 of human primary somatosensory cortex. *Neuroimage.* (2000) 11:684–96. doi: 10.1006/nimg.2000.0548
74. Cappe C, Rouiller E, Barone P. Cortical and thalamic pathways for multisensory and sensorimotor interplay. In: *The Neural Bases of Multisensory Processes*. Boca Raton, FL: CRC Press/Taylor & Francis (2011). p. 15–30.
75. Hagmann P, Kurant M, Gigandet X, Thiran P, Wedeen VJ, Meuli R, et al. Mapping human whole-brain structural networks with diffusion MRI. *PLoS ONE.* (2007) 2:e597. doi: 10.1371/journal.pone.0000597
76. Joshi AA, Joshi SH, Dinov I, Shattuck DW, Leahy RM, Toga AW. Anatomical structural network analysis of human brain using partial correlations of gray matter volumes. In: *2010 IEEE International Symposium on Biomedical Imaging: From Nano to Macro*. Rotterdam: IEEE (2010). p. 844–7.
77. Uludag K, Blinder P. Linking brain vascular physiology to hemodynamic response in ultra-high field MRI. *Neuroimage.* (2018) 168:279–95. doi: 10.1016/j.neuroimage.2017.02.063
78. Fahoum F, Lopes R, Pittau F, Dubeau F, Gotman J. Widespread epileptic networks in focal epilepsies: EEG-fMRI study. *Epilepsia.* (2012) 53:1618–27. doi: 10.1111/j.1528-1167.2012.03533.x
79. Norden AD, Blumenfeld H. The role of subcortical structures in human epilepsy. *Epilepsy Behav.* (2002) 3:219–31. doi: 10.1016/S1525-5050(02)00029-X
80. Struck AF, Boly M, Hwang G, Nair V, Mathis J, Nencka A, et al. Regional and global resting-state functional MR connectivity in temporal lobe epilepsy: results from the Epilepsy Connectome Project. *Epilepsy Behav.* (2021) 117:107841. doi: 10.1016/j.yebeh.2021.107841
81. Schridde U, Khubchandani M, Motelow JE, Sanganahalli BG, Hyder F, Blumenfeld H. Negative BOLD with large increases in neuronal activity. *Cereb Cortex.* (2008) 18:1814–27. doi: 10.1093/cercor/bhm208
82. Stefanovic B, Warnking JM, Kobayashi E, Bagshaw AP, Hawco C, Dubeau F, et al. Hemodynamic and metabolic responses to activation, deactivation and epileptic discharges. *Neuroimage.* (2005) 28:205–15. doi: 10.1016/j.neuroimage.2005.05.038
83. Gallagher A, Madan N, Stemmer-Rachamimov A, Thiele EA. Progressive calcified tuber in a young male with tuberous sclerosis complex. *Dev Med Child Neurol.* (2010) 52:1062–65. doi: 10.1111/j.1469-8749.2010.03792.x
84. Feinberg DA, Yacoub E. The rapid development of high speed, resolution and precision in fMRI. *Neuroimage.* (2012) 62:720–5. doi: 10.1016/j.neuroimage.2012.01.049
85. Harel N, Bolan PJ, Turner R, Ugurbil K, Yacoub E. Recent advances in high-resolution MR application and its implications for neurovascular coupling research. *Front Neuroenergetics.* (2010) 2:130. doi: 10.3389/fnene.2010.00130
86. Huber L, Goense J, Kennerley AJ, Ivanov D, Krieger SN, Lepsien J, et al. Investigation of the neurovascular coupling in positive and negative BOLD responses in human brain at 7T. *Neuroimage.* (2014) 97:349–62. doi: 10.1016/j.neuroimage.2014.04.022

87. Huber L, Goense J, Kennerley AJ, Trampel R, Guidi M, Reimer E, et al. Cortical lamina-dependent blood volume changes in human brain at 7T. *Neuroimage.* (2015) 107:23–33. doi: 10.1016/j.neuroimage.2014.11.046
88. Polimeni JR, Uludag K. Neuroimaging with ultra-high field MRI: present and future. *Neuroimage.* (2018) 168:1–6. doi: 10.1016/j.neuroimage.2018.01.072
89. Goense J, Bohraus Y, Logothetis NK. fMRI at High Spatial Resolution: Implications for BOLD-Models. *Front Comput Neurosci*. (2016) 10:66. doi: 10.3389/fncom.2016.00066

Conflict of Interest: The authors declare that the research was conducted in the absence of any commercial or financial relationships that could be construed as a potential conflict of interest.

ORIGINAL RESEARCH
published: 15 November 2021
doi: 10.3389/fneur.2021.695997

Localizing Epileptic Foci Using Simultaneous EEG-fMRI Recording: Template Component Cross-Correlation

Elias Ebrahimzadeh [1,2]*, ***Mohammad Shams*** [3], ***Masoud Seraji*** [4,5], ***Seyyed Mostafa Sadjadi*** [1], ***Lila Rajabion*** [6] ***and Hamid Soltanian-Zadeh*** [1,2,7]

[1] CIPCE, School of Electrical and Computer Engineering, College of Engineering, University of Tehran, Tehran, Iran, [2] School of Cognitive Sciences, Institute for Research in Fundamental Sciences (IPM), Tehran, Iran, [3] Neural Engineering Laboratory, Department of Electrical and Computer Engineering, George Mason University, Fairfax, VA, United States, [4] Center for Molecular and Behavioral Neuroscience, Rutgers University, Newark, NJ, United States, [5] Behavioral and Neural Sciences Graduate Program, Rutgers University, Newark, NJ, United States, [6] School of Graduate Studies, SUNY Empire State College, Manhattan, NY, United States, [7] Image Analysis Laboratory, Departments of Radiology and Research Administration, Henry Ford Health System, Detroit, MI, United States

Edited by:
Brunno Machado De Campos,
State University of Campinas, Brazil

Reviewed by:
Satoshi Maesawa,
Nagoya University, Japan
Taylor J. Abel,
University of Pittsburgh, United States

***Correspondence:**
Elias Ebrahimzadeh
e_ebrahimzadeh@ut.ac.ir;
elias.ebrahimzadeh@ipm.ir
orcid.org/0000-0001-8682-936X

Specialty section:
This article was submitted to Epilepsy,
a section of the journal
Frontiers in Neurology

Received: *15 April 2021*
Accepted: *29 September 2021*
Published: *15 November 2021*

Citation:
Ebrahimzadeh E, Shams M, Seraji M, Sadjadi SM, Rajabion L and Soltanian-Zadeh H (2021) Localizing Epileptic Foci Using Simultaneous EEG-fMRI Recording: Template Component Cross-Correlation. Front. Neurol. 12:695997. doi: 10.3389/fneur.2021.695997

Conventional EEG-fMRI methods have been proven to be of limited use in the sense that they cannot reveal the information existing in between the spikes. To resolve this issue, the current study obtains the epileptic components time series detected on EEG and uses them to fit the Generalized Linear Model (GLM), as a substitution for classical regressors. This approach allows for a more precise localization, and equally importantly, the prediction of the future behavior of the epileptic generators. The proposed method approaches the localization process in the component domain, rather than the electrode domain (EEG), and localizes the generators through investigating the spatial correlation between the candidate components and the spike template, as well as the medical records of the patient. To evaluate the contribution of EEG-fMRI and concordance between fMRI and EEG, this method was applied on the data of 30 patients with refractory epilepsy. The results demonstrated the significant numbers of 29 and 24 for concordance and contribution, respectively, which mark improvement as compared to the existing literature. This study also shows that while conventional methods often fail to properly localize the epileptogenic zones in deep brain structures, the proposed method can be of particular use. For further evaluation, the concordance level between IED-related BOLD clusters and Seizure Onset Zone (SOZ) has been quantitatively investigated by measuring the distance between IED/SOZ locations and the BOLD clusters in all patients. The results showed the superiority of the proposed method in delineating the spike-generating network compared to conventional EEG-fMRI approaches. In all, the proposed method goes beyond the conventional methods by breaking the dependency on spikes and using the outside-the-scanner spike templates and the selected components, achieving an accuracy of 97%. Doing so, this method contributes to improving the yield of EEG-fMRI and creates a more realistic perception of the neural behavior of epileptic generators which is almost without precedent in the literature.

Keywords: simultaneous EEG-fMRI, epileptogenic zone, independent component analysis (ICA), generalized linear model (GLM), blood-oxygen-level dependent imaging (BOLD), epilepsy, source localization

HIGHLIGHTS

- In this study, we succeeded in diminishing limitations through presenting a method in the component domain for localizing epileptic foci, taking into account the clinical application, so that more satisfactory results than the conventional EEG-fMRI methods could be obtained.
- The component-based method plays a more prominent role in eliminating the need for invasive electrode implantations compared to conventional EEG-fMRI analysis.
- The component-based method brings to attention the variations in amplitude and duration of epileptic spikes, whereas the conventional methods simplistically assume that all events are equal.
- The conventional approach overlooks the fact that IED activity is continuous and contains fluctuating sub-threshold epileptic activity that is not clearly observed on surface EEG recordings.
- Such valuable information will be obtained by the ICA algorithm applied as part of the proposed method.

INTRODUCTION

Epilepsy is one of the most common neurological disease worldwide (1). It is generally characterized by an enduring predisposition to recurrent yet spontaneous seizures, defined as brief episodes of signs or symptoms indicating excessive, abnormal, or synchronous neuronal activity in the brain (2). The first course of treatment for this condition is drug therapy. However, about 30% of patients are refractory to antiepileptic medications (2), and those with focal epilepsy may be considered for epilepsy surgery.

To provide successful surgical treatment, an improved preoperative evaluation that delineates the epileptogenic zone (EZ) is a critical prerequisite. Several methods have been proposed in the literature (3–5), among which intracranial electroencephalography recording (icEEG) has gained the most attention and is known as the gold standard for defining the epileptogenic zone (EZ) and localizing the seizure onset zone (SOZ) (6). Although popular, this invasive monitoring technique is not without risks or shortcomings (7): it explores only a small fraction of the brain and tends to be time-consuming as the frequency of seizure occurrence is relatively low compared with interictal epileptiform discharges (IEDs). Consequently, over the past few years, greater attention has been directed toward noninvasive EEG-correlated functional magnetic resonance imaging (EEG-fMRI) method as an additional tool to localize the SOZ (8–11). EEG-fMRI combines the high spatial resolution of blood oxygen level-dependent (BOLD) MRI with the high temporal resolution of the EEG signal. This method is now increasingly available following the resolution of crucial technical challenges such as developing suitable amplifiers and procedures for correcting the scanner-related artifacts in the EEG signal (12–15). There is a clinical need for optimized mapping of the changes in neuronal activity related to epileptic discharges observed on surface EEG (16) considering the subclinical nature of some of the interictal epileptiform activity which makes the events of interest only recognizable on the EEG record. Studying the correlation of these events with the fMRI time series reveals complex patterns of hemodynamic change indicative of brain networks. Studies investigating the spike-related BOLD changes have shown that in addition to characterizing different types of focal and generalized epilepsy, these measures could also improve the presurgical evaluation of patients with refractory focal seizures (17–19).

In epilepsy patients, spike-related BOLD changes can contribute to the localization of the epileptic foci. As shown in the literature, the BOLD signal tends to increase in regions that generate spikes (20), although it is often in the form of widespread responses (21). The study of (22) reports a noticeable rate of 60% in seizure freedom in patients who underwent surgical resections where the cortical tissues responsible for the highest spike-correlated BOLD changes were completely removed. Furthermore, the simultaneous recording and analysis of EEG-fMRI is now an important tool in localizing epileptic generators in patients with nonlesional frontal lobe epilepsy, as confirmed by other imaging modalities (19). The literature has found this technique to be of great value when it comes to clinical decision makings. Pittau et al. (18) demonstrated that EEG-fMRI analysis facilitated the localization of epileptic generators in 64% of the patients and the BOLD responses were concordant with the spike-generating regions in 88% of the patients. In patients who were considered ineligible for surgery according to the conventional clinical decision makings, EEG-fMRI confirmed multifocality in 4 of 5 presumed multifocal patients and improved SOZ localization in 4 of 6 patients with unclear foci (23).

According to the conventional method, the IEDs are considered the primary indicators of epileptic activity (24). So, the conventional analysis begins with identifying and marking the IEDs by trained experts assessing the simultaneous EEG-fMRI. The timing of the detected IEDs is then taken as simple epileptic events and convolved with the hemodynamic response function (HRF) to produce a regressor for a General Linear Model (GLM) analysis. Finally, the estimated activation area with the highest statistical significance will be considered as the spike onset zone, a potential marker of the epileptogenic zone (EZ). Many of the recent studies are still based on the GLM analysis (8–15) and their improvement is in increasing of magnetic field strength (25) or using simultaneous intracranial EEG-fMRI (iEEG-fMRI) (26, 27). Yet, the clinical utility of the conventional EEG-fMRI approach is not completely supported by the published literature (9–13). An important limitation of the conventional IED-based EEG-fMRI analysis is that it only considers the information of epileptic focus activity at the time of the spikes and ignores all the neural activities associated with epileptic generators in other time points. So, the actual neural behavior of epileptic generators over the entirety of the recording is not captured by the conventional method, which is unable to localize the epileptic generator when the spikes do not occur during the EEG recording. The proposed method covers this limitation by considering epileptic neural activity regardless of whether or not a spike occurs, potentially leading to a more accurate localization of the epileptogenic zone.

To improve upon the conventional analysis method, we introduced a new method for analyzing EEG-fMRI data that utilizes the information contained within the entire time series of a relevant EEG source. To do this, we first separated the EEG components using independent component analysis (ICA) and calculated the cross-correlation between the time series of the extracted ICA components and a patient-specific IED spike template to determine the most relevant component. Ultimately, the time series of this component was convolved with the HRF, resampled to the frequency of the fMRI recording, and used in the GLM analysis. To evaluate this method quantitatively, we calculated the distance from the dipole locations in EEG source localization to the BOLD cluster and compared the results to those obtained from the conventional methods.

MATERIALS AND METHODS

Subjects

30 patients from Epilepsy Center, Pars Hospital, Tehran, Iran, who were surgery candidates with focal or generalized epilepsy and also would show at least 10 distinct IEDs during the MRI scanning were included in the study. The ethical approval was obtained from the ethics committee of the Iran University of Medical Sciences, Tehran, Iran, and all patients provided written informed consent.

Long-Term Monitoring (LTM)

All the patients underwent a long-term 64-channel EEG with 500 Hz sampling rates and following the 10–20 standard for electrode placement as a preoperative evaluation at the Epilepsy Center, Pars Hospital, Tehran, Iran. Besides, all the other available information such as the comprehensive clinical record, full neurological examination, neuropsychological assessment, structural MRI, and other non-invasive investigations like ictal SPECT and PET were reviewed to help the localization of irritative zone (IZ) and Seizure Onset Zone (SOZ) through the preoperative evaluation.

EEG-fMRI Acquisition

Simultaneous recording of EEG-fMRI was performed from May 2017 to June 2018 at the National Brain Mapping Laboratory (NBML), Tehran, Iran, in the form of 20-mins sessions with eyes closed. The MRI scanner was the 3 T Siemens Prisma, and the EEG amplifier was a 64-channel BrainAmp MRI-compatible system from Brain Products with 5 kHz sampling rates. The EEG internal clock was synchronized with the MRI clock and the EEG electrodes followed the 10–20 placement system with the reference of Cz. Besides, the ECG signal was recorded using a bipolar lead (10, 28), and a 10-min EEG recording was acquired with eyes closed outside the scanner immediately before the EEG-fMRI session (28). EEG electrodes were equipped with an additional 5 kΩ terminal resistance, and impedances were kept as low as possible to improve the quality of the recording.

For the MRI scanning, a T1 MPRAGE anatomic sequence was first scanned [1 mm slices, 256 × 256 matrices, echo time (TE) = 3.74 ms, repetition time (TR) = 1,810 ms, flip angle = 30°] to use in registering functional images. Functional data was obtained in 20-min runs with patients at rest, using a T2*-weighted gradient-echo (GRE) imaging sequence (234 × 234 matrix, 40 slices, 3 × 3 × 3 mm, TE = 26 ms, TR = 2,500 ms, flip angle = 60°) (29). To minimize the movement of the patient's head and provide comfort, a pillow filled with foam microspheres was used inside the scanner.

EEG Signal Processing—Long Term Monitoring

The EEG signals were preprocessed using the EEGLAB toolbox (https://sccn.ucsd.edu/eeglab/). First, the sampling rate of the signal was reduced to 250 Hz, and a Butterworth high-pass filter at 1 Hz was used to suppress the low-frequency components (30–32). Then, all the channels were reviewed, and those with a standard deviation greater than ±3.1 from the mean standard deviation (across all channels) were excluded as the abnormal channels. For eliminating the power-line noise at 50 Hz, the Clean Line algorithm was used (29). The advantage of this algorithm over the notch filter is that it adaptively estimates and removes sinusoidal artifacts without creating band-holes in the EEG power spectrum (29, 33).

Next, the ICA algorithm was applied on the EEG signal and the irrelevant components corresponding to eye blink, eye movement, cardiac pulsatile, muscular tension, swallowing, or machine vibration were visually identified using the component's scalp map, spectral power activity, and spectral power distribution. **Figure 1** shows typical samples of two such components identified as artifacts. After identifying all the artifact components, the data were re-composed without them.

The resultant cleaned signals were evaluated by a trained expert, and the IEDs were marked for the main analysis. Then, the IEDs were averaged to build patient-specific and morphology-specific IED templates. After band-pass filtering (34) (1–30 Hz) and epoching the spikes with a fixed length of 0.3 s and step size of 1 sample (2.5 ms) to include the negative peak and slow-wave, the template of the spike was set for each subject by hand-selecting and averaging 10–20 spikes from the marked signal by an experienced electroencephalographer. New spikes would then be detected and added to the initial template (29). In case a patient had more than one type of spike, this process is separately done for each different type (35). The match between

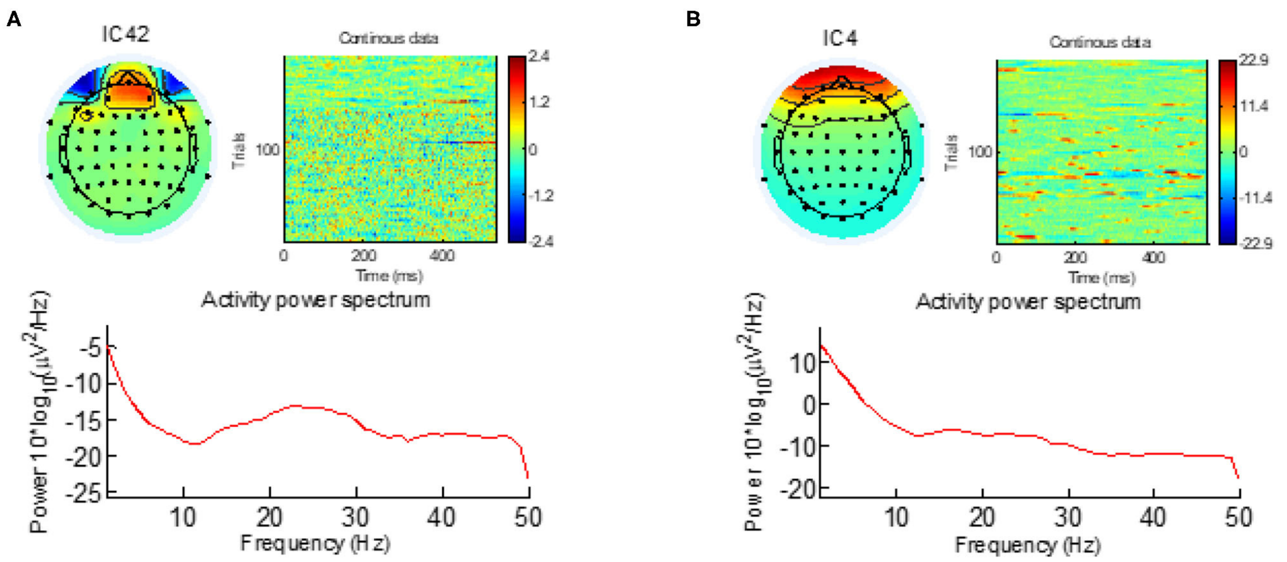

FIGURE 1 | The eye-blinking and eye-movement artifacts are visible both in the scalp map and in the activity power spectrum. **(A)** Eye-blinking artifact. **(B)** Eye-movement artifact.

the template, x, and each 300 ms of candidate component at the times of the IED, y, was defined as the magnitude of the sample correlation, $|r_{xy}|$, presented in Eq. 1.

$$r_{xy} = \frac{\sum_{i=1}^{n} (x_i - \bar{x})(y_i - \bar{y})}{\sqrt{\sum_{i=1}^{n} (x_i - \bar{x})^2 \sum_{i=1}^{n} (y_i - \bar{y})^2}} \tag{1}$$

To add to the initial, hand-selected template, a first pass over the data was performed at a high threshold ($rxy = 0.96$–0.98 depending on the subject) (36).

EEG Signal Processing—Simultaneous EEG/fMRI

For the EEG signals recorded inside the scanner, the MR gradient switching artifact was eliminated using the fMRIb algorithm (https://fsl.fmrib.ox.ac.uk/eeglab/fmribplugin/) which first increases the sampling rate to 20 kHz, and then applies a low-pass filter at 60 Hz (37). Also, the ballistocardiogram (BCG) artifact that occurs because of the movements of the electrodes associated with cardiac pulsations, was detected and removed with the fMRIb toolbox using the heartbeat information from the extra ECG electrode during EEG-fMRI recording. A sample of EEG signals recorded inside the MR scanner before and after removing the MR gradient and BCG artifacts are shown in **Figure 2**.

Template Component Cross-Correlation (TCCC) Method

The general pipeline of the proposed method is summarized in **Figure 3**. First, the EEG signal recorded outside the scanner was preprocessed, and the individual patient-specific IED templates were extracted for each subject. Besides, the EEG signal recorded inside the scanner underwent ICA analysis and was decomposed to its independent components after artifact removal for selecting a set of candidate components representing actual generators of epileptic activity. Different ICA algorithm parameters can lead to various components but if the candidate components are reliable sources, they should be robust to variations in the ICA decomposition process. Therefore, the ICA algorithm was applied 10 times using different arbitrary (random) initialization weights, and the initial candidates selected based on being those seen most often in the 10 repetitions (38). From these, the three components with the highest average λ (weight of extracted independent components) across all 10 iterations were selected as final candidates.

The set of final candidate components of each patient underwent the analysis of cross-correlation with their specific IED templates, built earlier from Long Term Monitoring (LTM) data (**Figure 4A**). The process employed a sliding window of width 0.3 s and step size of 1 sample (the yellow box with the arrow in **Figure 4B**). EEG inside scanner was marked by an experienced electroencephalographer and the marked times were used for the cross-correlation. Components that did not have cross-correlation with the templates at the times of the IED events of at least 0.85 were rejected (**Figure 4C**). Also rejected were the candidates judged to be discordant with the observed IEDs in the EEG (more than 50 mm away) (**Figure 4D**).

The time course of each remaining component was assumed to be the temporal activity of an epileptic source. So, they were convolved with the canonical HRF (**Figure 4E**), resampled to the frequency of the fMRI recording (TR = 2.5 s), and used as the predicted model in the GLM analysis. For multiple spikes, the regressors of the different types were entered simultaneously into a single first-order analysis.

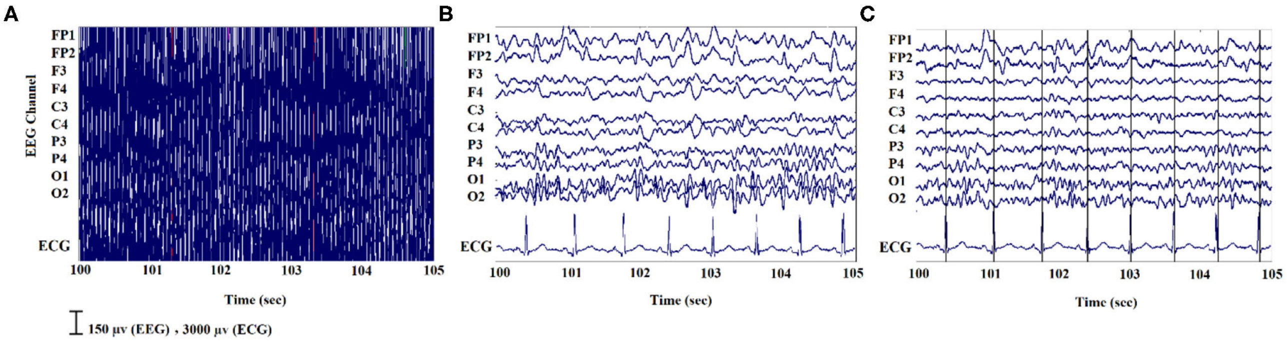

FIGURE 2 | An illustration of EEG signals recorded inside the scanner: **(A)** noisy signal; **(B)** after removing the MR gradient artifact; **(C)** after eliminating the BCG artifacts.

fMRI Analysis

In the conventional analysis, the EEG signals recorded simultaneously with fMRI are reviewed and marked for determining IEDs as zero-duration events, and the resultant time series is convolved with a standard HRF for use in the GLM analysis as the regressor of epileptic activity. However, in our Template Component Cross-Correlation (TCCC) method, the time series of the epileptic-related components are convolved with four HRFs, peaking at 3, 5, 7, and 9 s (12).

The fMRI dataset was preprocessed and analyzed using FSL (FMRI Expert Analysis Tool, Version 6.0.1, FMRIB's Software Library, http://www.fmrib.ox.ac.uk/fsl). Motion correction was done via a 6-parameter rigid-body transformation, and the dataset was spatially smoothed via 6-mm full width at half-maximum. Also, an autoregressive model of order one was used to correct the temporal autocorrelations (39), a third-order polynomial was used to model low-frequency drifts and applied as high-pass temporal filtering. For each fMRI dataset, all of the models built from each of its IED components were included in the same GLM, thus total variance was partitioned amongst the inputs, effectively treating the others as confounds.

All regressors were included in the same GLM in the fMRI analysis (fMRIstat). For each event type, a statistic z-map was created for each regressor using the other regressors as confounds. A combined z-map was created by taking, at each voxel, the maximum z-value from the four z-maps based on four HRFs. The single combined t-map was used for the subsequent analysis. For the second-level analysis, each cluster with at least five contiguous voxels having a z-value >3.1, corresponding to a p value smaller than 0.05 was selected as the significant result. This included correction for multiple comparisons, accounting for the number of voxels and the 4 HRFs. The final statistical maps were then registered to and overlaid on the patient-specific structural MRI. In the z-maps, a yellow-red scale corresponds to positive BOLD responses (activation) and a blue-white scale to negative responses (deactivation). Responses outside the brain were excluded and BOLD responses in the ventricles were excluded using a mask, as they are often interpreted as artifactual findings.

Concordance Between IED Location and Maximal BOLD Response

For evaluating the results of the analysis, the spatial concordance between the BOLD response and the IED field was assessed. First, the locations of the single voxel with maximal z-score of the maximum BOLD cluster and the extracted dipole from ICA algorithm were determined. Next, the distance between the locations was measured and classified into three levels of spatial concordance: (i) concordant (C) for the distance <25 mm; (ii) partially concordant (PC) for the distance between 25 and 50 mm; and (iii) discordant (D) for the distance more than 50 mm (36, 40). To evaluate the distance between dipole and maximum BOLD, the spherical head model has been co-registered to the MNI brain. Spherical dipoles coordinates are also converted to MNI. The fMRI data is also co-registred and normalized into a MNI atlase.

Contribution of TCCC Method

The evaluation of IED sources and seizure onset zone is usually involved in the standard clinical practice for the planning of surgical resection in epilepsy. However, the use of simultaneous EEG-fMRI is not currently part of such standard practice. If it presents meaningful information for more precise localization of the IED sources, it may become a helpful part of the standard clinical practice for presurgical evaluation. Therefore, we have included the evaluation of our final BOLD results for each type of IED in terms of their potential contribution. We defined the BOLD results as contributory if: (i) the BOLD response detected the IED generation field with higher precision and accuracy than EEG source localization, and (ii) the maximum BOLD response was in deep brain structures compared to the surface location of the recorded IED.

If there was no concordance between the BOLD response and the IED field or the results had no new information beyond that provided by the EEG signals, it was not labeled as contributory. Besides, another comparison was made between the the lesional findings of the structural MRI and our BOLD response to ensure precision that possible contributory effects of an MRI lesion on the BOLD response were also taken into account.

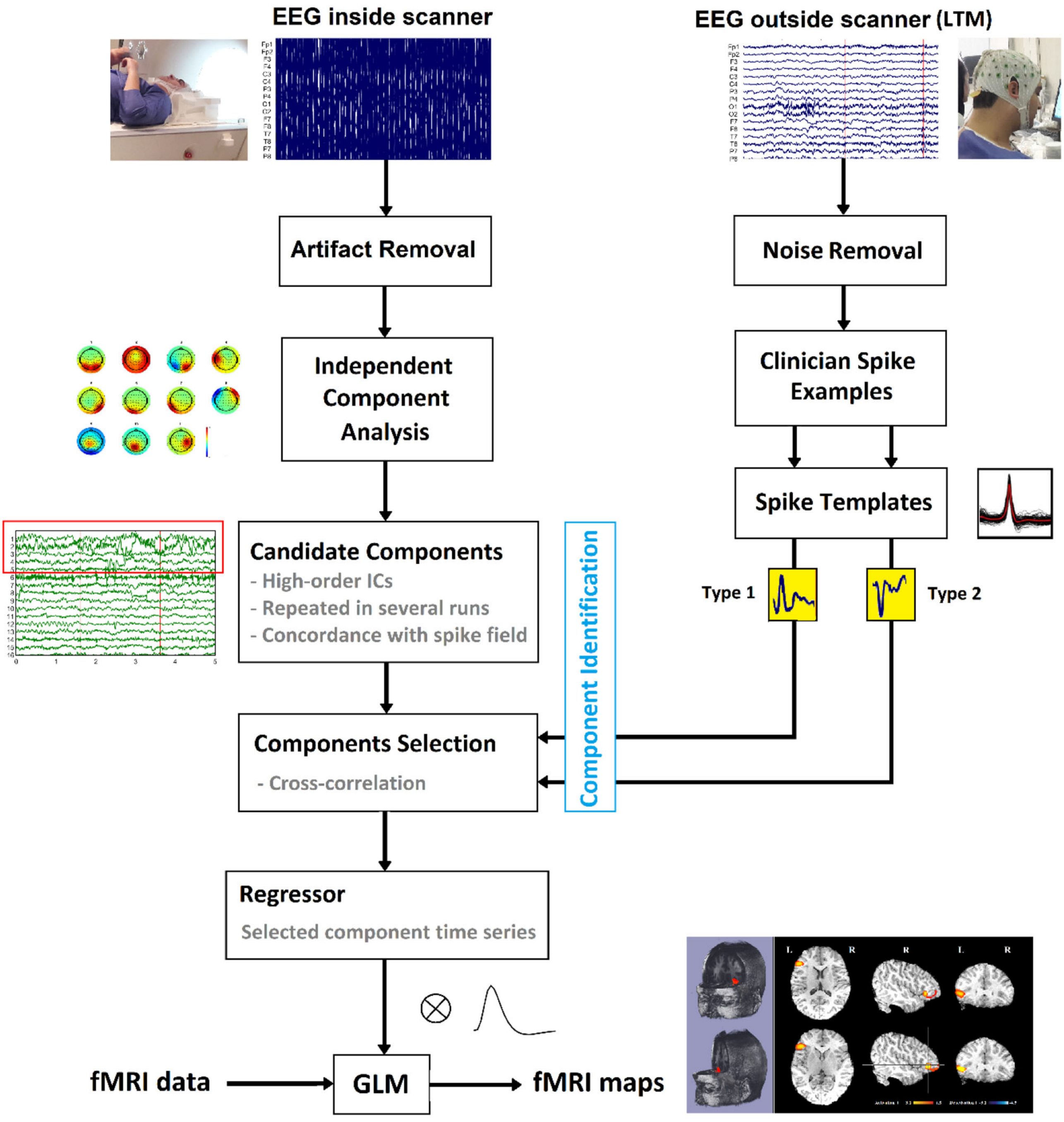

FIGURE 3 | Schematic of the suggested method to localize the epileptic foci using simultaneous EEG-fMRI.

RESULTS

From the total of 34 patients who were recruited for the study and underwent EEG-fMRI, four were not included because of having no clear IEDs during the EEG-fMRI session or significant movement artifact during recording. **Table 1** shows the summarized clinical details for the remaining 30 patients who were 16 females and 14 males (15–48 years with the mean of 27.3 years) and a seizure onset age of 1–22 years (mean of 10.6 years). 28 of the patients had focal epilepsy which 23 of them were unifocal, four were bifocal, and one was multifocal. The other two were generalized epilepsy patients which one of them had continuous spikes and waves during slow sleep (CSWS) and the other one had West's Syndrome. These classifications were done

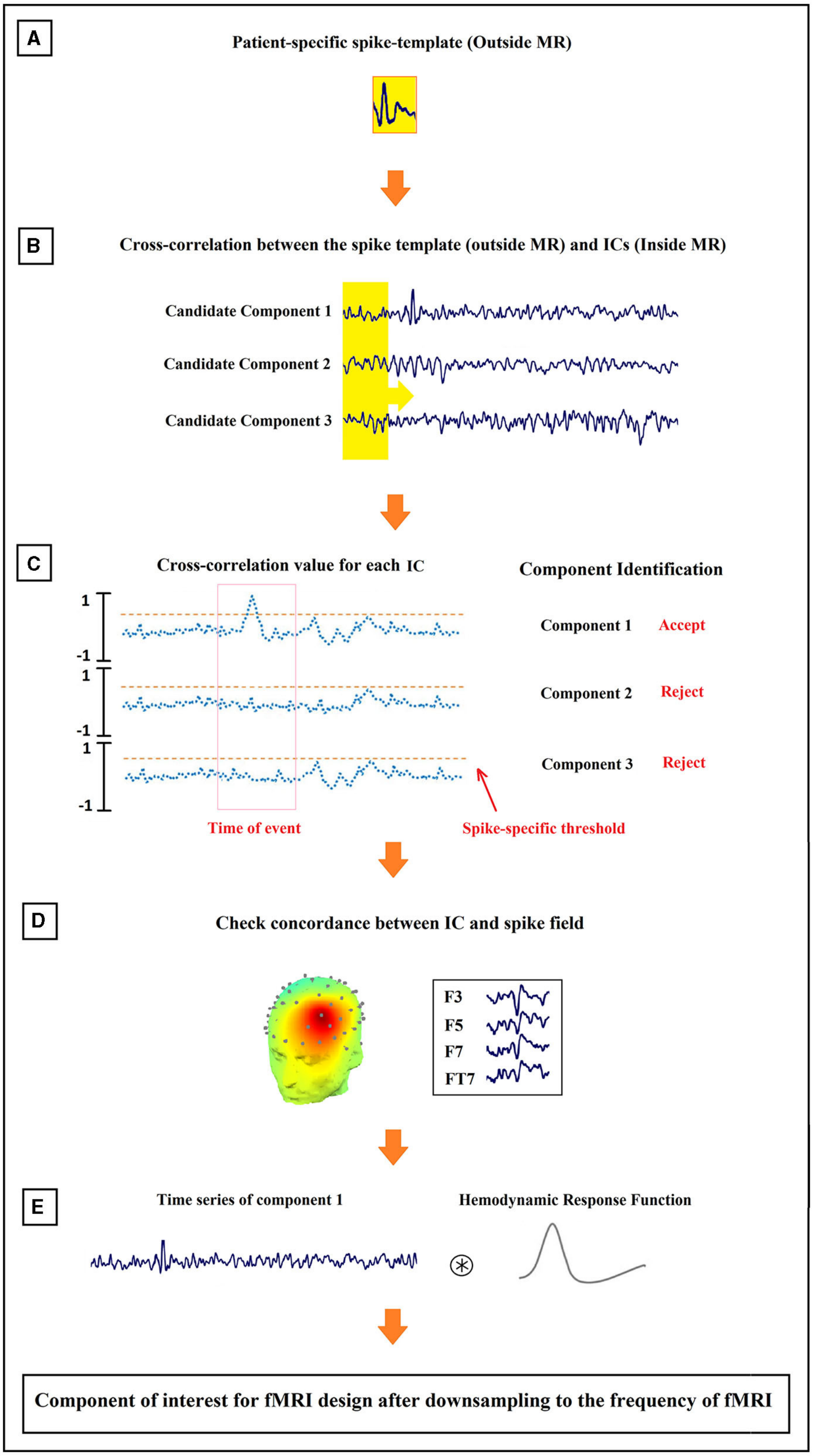

FIGURE 4 | Schematic illustration of the method proposed for the identification of epilepsy-related components. The order of the process from **(A–E)** is shown in the figure.

TABLE 1 | Patients clinical information.

No.	Sex/Age	Age of onset	Type of epilepsy	AED	Ictal EEG Onset	Interictal EEG	No. of spikes in routine EEG	No. of spikes during fMRI
1	F/15	1	TLE, R	VPA, LEV	Tempo. R	Tempo. R	25	17
2	M/14	18	FLE, L	LCM, LTG	Fronto-cent. Bil	Front. L	38	22, 18
3	M/19	10	FLE, R	LCM, OXC, LEV	Front. R	Front. R	49	14, 18, 16
4	F/23	8	PLE, L	OXC, LEV	Pariet. L	Pariet. L	46	38
5	M/34	7	TLE, L	LEV, VPA	Tempo. L	Fronto-tempo. L	33	13, 15
6	F/28	3	IE	OXC, LTG, PT	Bil Gen.	Bil Gen.	36	21
7	F/48	8	FLE, L	LEV	Front. L	Fronto-cent. L	37	18, 9, 11
8	M/32	12	TLE, R	LTG, LCM	Tempo. R	Tempo. R	31	28
9	M/17	1	FLE, R	OXC, VPA, TPM	Front. R/L	Front. L	26	19
10	F/29	20	Unclear	OXC	Hemisphere L	Fronto-temp. L	33	27
11	M/28	16	OLE, R	LTG, OXC	Occip. R	Occip. R	61	14, 18, 25
12	F/18	3	SE	OXC, LTG	Bil. Front.	Bil. Front.	29	13,7
13	M/36	7	Multifocal: P/T	VPA, TPM, LEV	L Pariet./Post Tempo.	L Pariet./Post Tempo.	25	22
14	M/24	15	FLE, R	LTG	Frontopolar R	Fronto-cent. R	34	13, 8, 9
15	F/33	9	TLE, R	CMC, OXC	Tempo. R	Tempo. R	35	38
16	F/40	16	PLE, L	TPM, VPA,	Parieto-occip. L	Pariet. L	26	32
17	F/25	13	Unclear	LEV, OXC	Fronto-cent. Bil	Front. R	38	44
18	F/21	10	FLE, L	LTG, CLO	Fronto-tempo. L	Fronto-tempo. L	41	21, 12, 11
19	M/28	17	PLE, R	CMC, LTG	Pariet. R	Pariet. R	28	35
20	F/19	1	TLE, R	LEV, ESM, ZSM	Tempo. pole	Tempo. R	26	29
21	M/41	16	TLE, R	VPA, CMC	Tempo. R	Tempo. R	28	21
22	M/24	17	FLE, L	LTG	Fronto-tempo. L	Fronto-tempo. and Tempo. L	33	26, 17
23	F/16	3	PLE, R	OXC	Pariet/Occip R	Pariet R	27	10, 19
24	M/18	8	FLE, L	LEV, VPA	Fronto-tempo. L	Front. L	18	13
25	F/28	21	TLE, L	LEV	Tempo. L	Tempo./ Pariet. L	45	28, 16
26	F/32	22	FLE, Bil	LEV, OXC, LCM	Front. Bil.	Front. L>R	17	19
27	M/36	7	TLE, R	OXC	Fronto-tempo. R	Tempo. R	29	32
28	F/26	15	FLE, L	VPA	Front. L	Tempo./ Front. L	25	19
29	F/38	14	TLE, R	VPA, LTG	Tempo. Bil	Tempo. R	37	24, 19
30	M/20	2	OLE, R	TPM, OXC	Pariet./Occip. R	Occip. R	47	43

AED, antiepileptic drug; Bil, bilateral; CMC, carbamazepine; CLO, clobazam; ESM, ethosuximide; FLE, frontal lobe epilepsy; Gen, generalized; IE, idiopathic epilepsy; L, left; LCM, lacosamide; LEV, levetiracetam; LTG, lamotrigine; OLE, occipital lobe epilepsy; OXC, oxcarbazepine; Pariet., Parietal; PT, phenytoin; PLE, parietal lobe epilepsy; R, right; SE, symptomatic epilepsy; P, parietal; TLE, temporal lobe epilepsy; VPA, valproate; TPM, topiramate; ZSM: zonisamide (29).

by two expert neurologists before EEG-fMRI recording, based on structural MRI, EEG signals, and clinical records of patients. 6 of the patients in the focal group had lesions on their MRI scans. For each patient, the number of spikes in the routine EEG and during EEG-fMRI recording is listed in the last columns of **Table 1**.

From the total number of patients, seven had two types of IED, five had three types of spikes, and the rest had one type of spike. We generated one study for each type of spike for the analysis of the TCCC method. Therefore, a total of 792 IEDs from 47 IED-studies underwent EEG-fMRI analysis. Two of the patients with multiple IED types showed no BOLD response. In all of the other 45 studies, at least one BOLD response was observed; 19 had spike-associated activation only (**Figures 5**, **7**, **8**), 9 had spike-associated deactivation only (**Figure 6**), and 17 had spike-associated activation and deactivation.

Concordance Between TCCC-Related BOLD Changes and Identified Component-Related Dipole

After calculating the distance between the center of gravity for maximum BOLD clusters and center of identified component-related dipole for all 45 IED-analyses, the result of statistical analysis showed that the distances between spike field and BOLD cluster for discordant (D) (>50 mm), partially concordant (PC) (25–50 mm), and concordant (C) (<25 mm) groups were significantly distinct from each other ($p < 0.0001$). Overall, 35 types of IED were concordant (13.83 ± 5.37 mm), 9 types of IED were partially concordant (32.44 ± 7.24 mm), and 1 was discordant to the relevant BOLD cluster ($p < 0.0001$).

In 29 patients out of 30 (97%), a minimum of one concordant TCCC-related BOLD response (35 analyses)

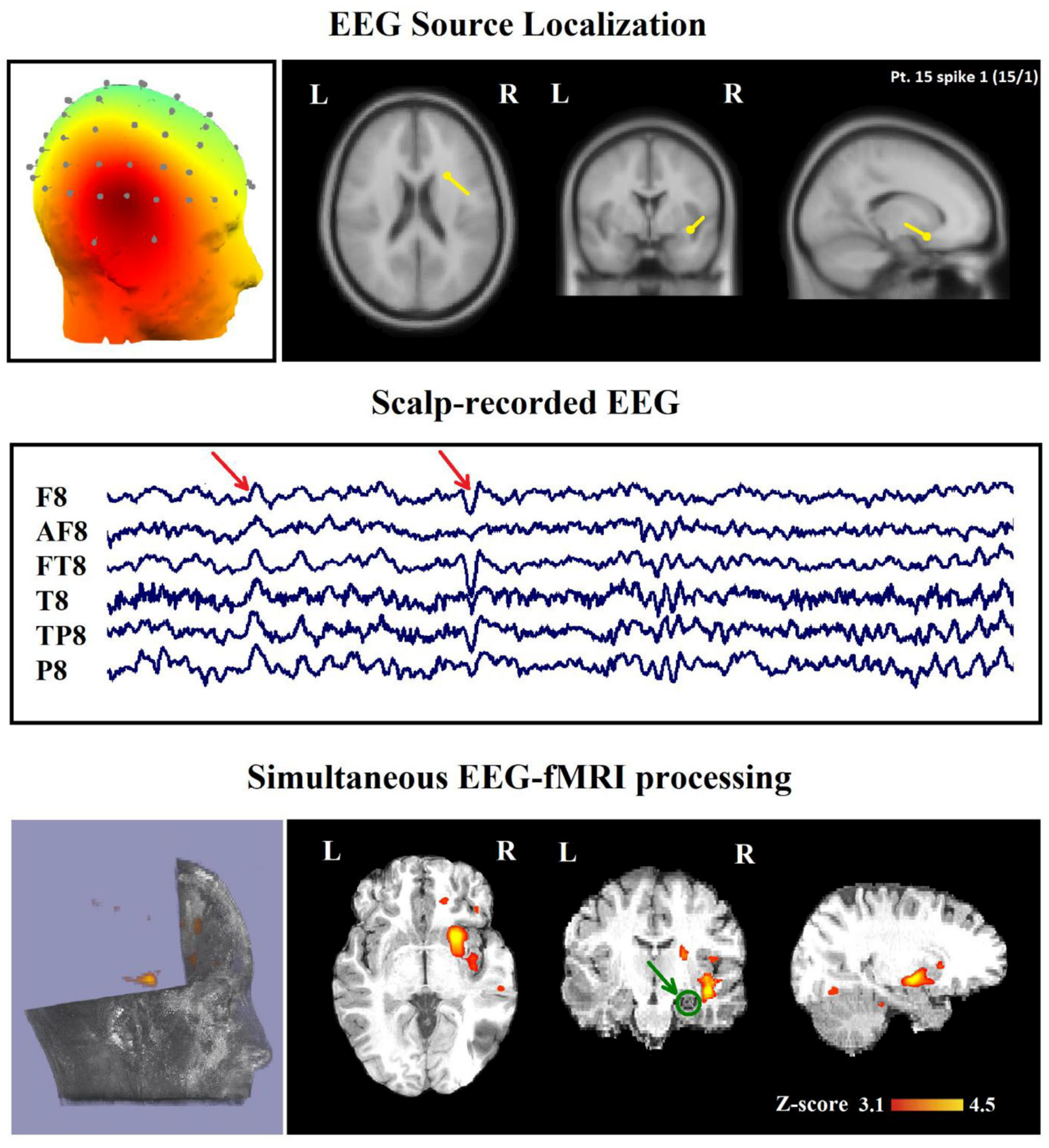

FIGURE 5 | (Patient 15, spike 1) Marked events are F8, FT8 spikes, and the TCCC-related BOLD response shows a neocortical activation in the right head and the superior temporal gyrus. This response is considered concordant with the spike field but not contributory. Based on the mesial temporal sclerosis (MTS), the patient has independent validation information, but the response is invalidated. The green circle shows the MTS area. Top, the component identified on scalp EEG located in the right temporal lobe (left) and the dipole localization of the identified generator in deep brain structures (right) based on analysis of EEG inside the scanner. Middle, scalp recorded EEG. Bottom, Localization of the generator applying simultaneous analysis of EEG-fMRI. The active area is marked with a yellow-red color.

with the identified component location was found (**Figures 5**, **6**). These concordant responses were generalized in 2 patients and focal in 27 ones who had focal discharges. Less significant responses were found in the rostral anterior cingulate gyrus, hypothalamus or posterolateral and occipital areas.

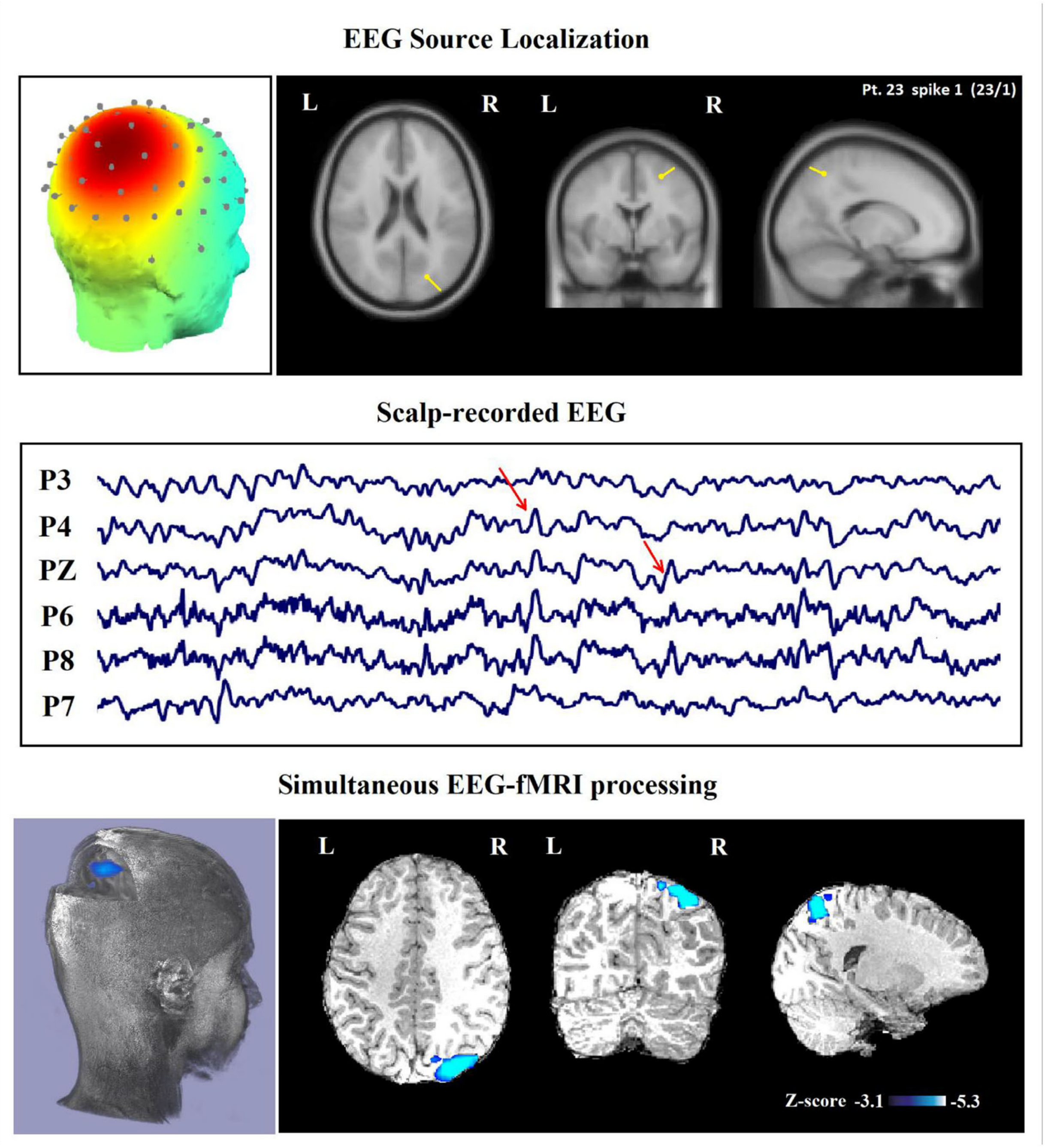

FIGURE 6 | (Patient 23—spike 1) marked events are parietal spikes and wave complexes (referential montage). The TCCC-related BOLD response shows deactivation in the posterior part of the right superior parietal lobule. This BOLD response is considered concordant with the spike field and contributed to a better localization of the epileptic foci compared with the scalp EEG. Top, the component identified on scalp EEG located in the right middle parietal lobe (left) and the dipole localization of the identified generator in brain structures (right) based on analysis of EEG inside the scanner. Middle, scalp recorded EEG. Bottom, Localization of the generator applying simultaneous analysis of EEG-fMRI. The deactivation is marked with a blue-white color.

The highest activations and deactivations were found in four cases who had bilateral diffuse discharges at the posterior cingulate or the parietal areas (default mode regions) and the anterior cingulate or hypothalamus, respectively. Patient 3 had right FLE symptomatic of a small area of focal cortical dysplasia. The BOLD response to the identified components was spatially concordant with the lesion.

Only one of all the 30 patients with one IED-study (patient 10) (3%), who was not a candidate for surgical resection because of poor clinical seizure focus, had a partially concordant BOLD response with the dipole. This patient with left frontotemporal discharge did not show any significant BOLD changes at the region of the identified component. However, a BOLD response was found with a maximum z-score in the contralateral parietal region.

Contribution of TCCC Method to Defining SOZ

In 24 patients (80%), a minimum of one contributory significant BOLD change (29 analyses) was found (**Figures 6**, **7**). In 19 of them, the TCCC-related BOLD change was more capable in comparison with EEG alone to identify the cortical region that generates the spike (**Figure 6**): frontal lobe in 8 (patients 3, 5, 7, 9, 12, 14, 18, and 28), temporal lobe in 4 (patients 1, 20, 25, and 29), parietal lobe in 5 (patients 13, 16, 17, 19, and 23), and occipital lobe in 2 (patient 11 and 30). In the remaining 5 subjects, the maximum TCCC-related BOLD changes were found in deep brain structures, which are most probably involved in the epileptogenic zone (**Figure 7**): basal ganglia and amygdala in 2 (patient 22, 27), and heterotopic tissue in three with nodular heterotopias (patients 2, 8, and 21).

In 16 of the 45 IED studies, the most clinically relevant BOLD response was not contributory. In 9 of them, the TCCC-related BOLD change was partially concordant with the identified component location. In 1 IED study, it was discordant, in 5 IED studies, the BOLD response did not provide any new information in comparison with EEG alone (**Figure 8**), and in the last one (patient 15, spike 1), it was invalidated (**Figure 5**).

For evaluating the TCCC method in patients with an epileptic lesion localized by structural MRI, we drew our attention to six of these patients with focal epilepsy, and it revealed concordant, contributory, and validated BOLD response in five of them. The only subject (patient 15) who showed invalidated response had a right frontal MTS but only a neocortical right temporal activation (**Figure 5**).

In comparison between the TCCC method and conventional EEG-fMRI analysis, the localization of the TCCC-identified component was concordant with the epileptogenic area of conventional analysis for 35 out of 45 IED studies (77%). This clearly shows the accuracy of the TCCC method for detecting the epileptic generators by studying the component of interest, confirming the detected generator's temporal behavior.

Comparison With Conventional Spike-Related Analysis

In **Table 2**, we present a comparison between the spatial distribution of spike-related and TCCC-related BOLD responses. The spatial concordance of the BOLD responses of the conventional method with the electroclinical evaluation was found in 14 of the 30 patients. All of these patients also showed concordant TCCC-related BOLD responses with the results of conventional analysis and validated by clinical records of the patient and the site of the surgical resection. The results of the TCCC method were better than the conventional analysis in 7 patients for determining the cortical spike generator region. No clear IEDs were found during the EEG-fMRI recording in one of them, the significant BOLD changes was not concordant with the spike field in the remaining 6 patients. Unlike other medical information, the results of the conventional analysis in these 6 patients showed no clear foci or multiple potential distinct foci. However, the BOLD responses of the TCCC method revealed a circumscribed foci within the expected region (**Figure 9**). In 3 of the 45 IED studies, the TCCC method was weaker than the conventional analysis (**Figure 10**)

The concordance of the results of the TCCC method and the conventional analysis is shown in **Table 3**. The most obvious information that can be extracted from the table are: (1) a satisfactory agreement between the results of the TCCC method and the conventional method in 32 IED studies; (2) a higher maximum z-score in 28 patients and greater extent of activation in 22 of patients using TCCC method; and (3) different activation regions in three patients with deep located epileptic foci, and no apparent agreement in one patient with deep epileptic foci and also no noticeable activation using the conventional method. This suggests that the conventional method is less effective when the epileptic generator is located remote from the scalp.

Concordance Level Evaluation

The results of localization through TCCC determine 35 C, 9 PC, 1 D, and 2 IED studies had no BOLD response. However, 26 C, 15 PC and 3 D were found through the conventional method and 3 EEG-fMRI studies showed no BOLD response. Comparing the two methods based on concordance level evaluation, in 21 cases, the TCCC method confirmed the results of the conventional method.

In three cases, the proposed method was able to provide satisfactory results with one C and 2 PC, while the conventional method was unable to provide results. In 11 IED studies the results of the two methods were not consistent (**Table 3**, last column); in 10 cases, TCCC improved the results and in only one case (7/2) the conventional method provided better results compared to TCCC (**Figure 10**).

Since the weakness of the proposed method in the mentioned case is due to the automatic selection of the relevant component (**Figure 10**, third row), an improved epileptic foci localization may be obtained by manual selection of the component, which leads to results superior to those of the conventional method (**Figure 10**, fifth row).

DISCUSSION

Conventional methods for localizing epileptic sources usually consider timings of all IEDs for identifying a seizure zone. However, an IED may be produced by multiple sources located at different brain regions. Therefore, only the voxels of a specific region should be examined for the localization of the seizure generator. Since spikes are frequently detected in a specific area of the electrode domain, it will be helpful to filter out the cortical components that do not show epileptic activity and choose the ones that do. In this study, we proposed a new method that incorporates all temporal information of the identified epileptic sources and avoids being deceived by irrelevant or imperfect

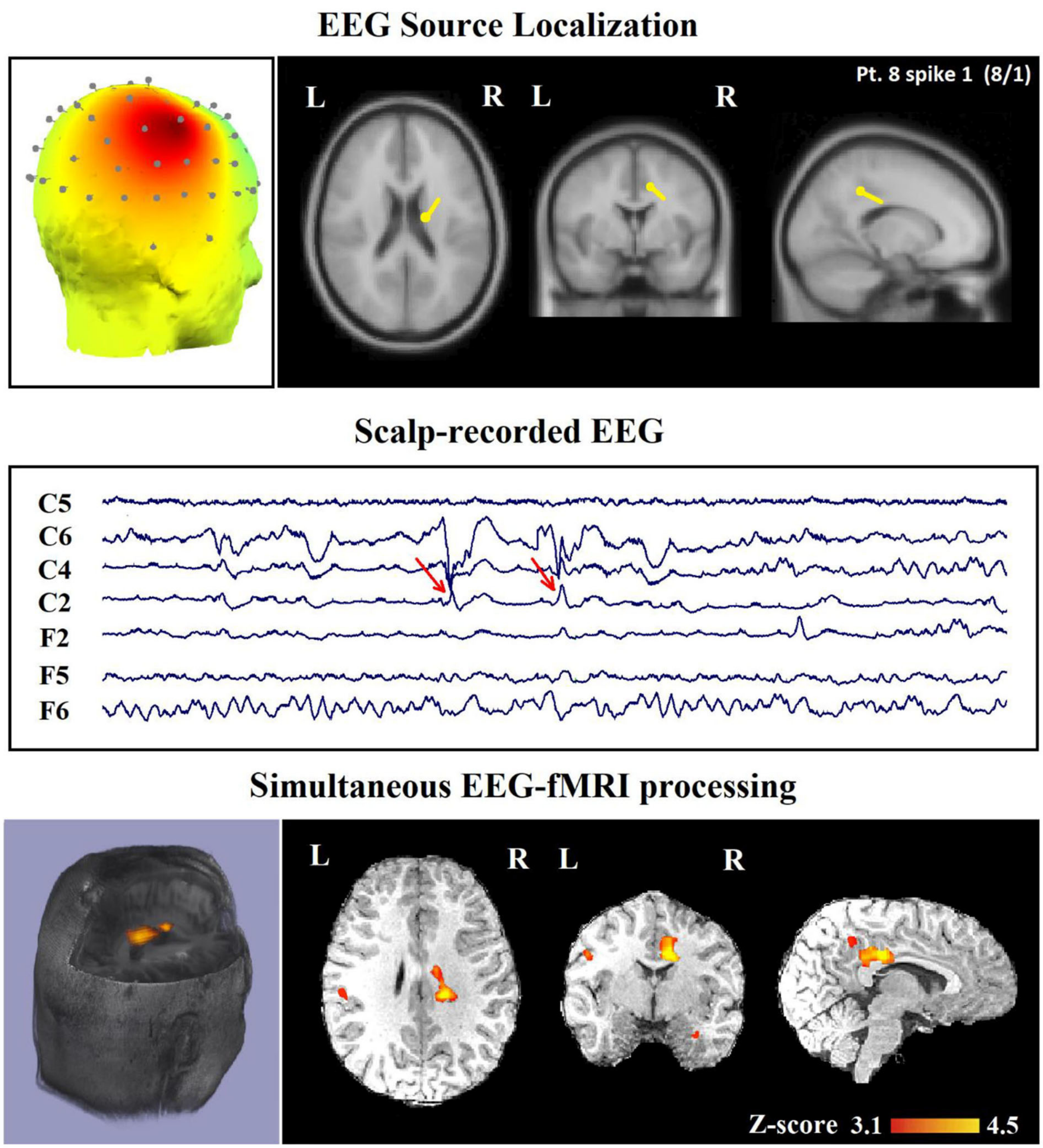

FIGURE 7 | (Patient 8—spike 1) marked events are C4–C6 spikes (referential montage), and TCCC-related BOLD response shows a focal activation in the right head. This response is considered concordant with the spike field and contributory, because it shows the involvement of a deep brain structure, in the epileptic focus, which is not visible on the scalp EEG, based on anatomo-electroclinical correlations. The focus was identified in the cerebral medulla (with matter). Top, the component identified on scalp EEG located in the right temporal lobe and the dipole localization of the identified generator in deep brain structures. The active area is marked with a yellow-red color. Middle, scalp recorded EEG. Bottom, Localization of the generator applying simultaneous analysis of EEG-fMRI.

information and mistakenly recognizing an unrelated source as a generator of epileptic activity.

The epileptic studies using EEG-fMRI are basically different from the task-based studies, as they consider seizure-related events as opposed to stimulation (41). In the epileptic studies, each source of the large spikes should not be inevitably accepted as an epileptic generator. For example, in focal epilepsy, a large spike detected in the frontal region, which is initiated from

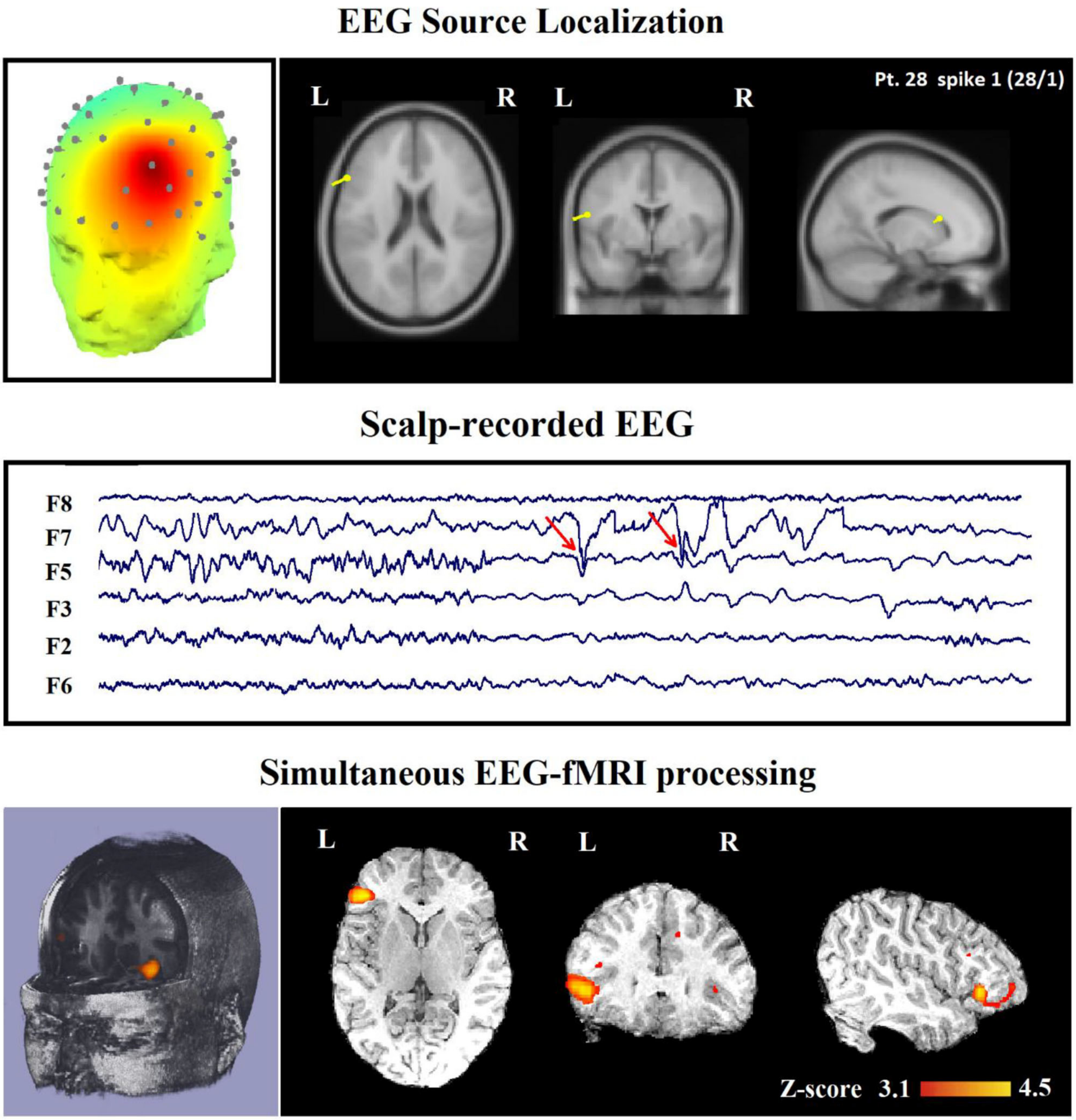

FIGURE 8 | (Patient 28—spike 1) marked events are F3, F5, and F7 spikes (referential montage) and the TCCC-related BOLD response demonstrates a neocortical activation in the inferior frontal gyrus. This response is considered concordant with the spike field but not contributory because it does not add any new information to the scalp EEG. Top, the component identified on scalp EEG located in the left frontotemporal lobe (left) and the dipole localization of the identified generator in deep brain structures (right). Middle, scalp recorded EEG. Bottom, Localization of the generator applying simultaneous analysis of EEG-fMRI. The active area is marked with a yellow-red color.

the source domain of the parietal lobe is not a valid indicator but the conventional analysis cannot distinguish them, because they use all temporal information of IEDs in one regressor regardless of the corresponding regions. We addressed this problem by adding the spatial information associated with the spike generators to ensure the concordance between the position of the accepted epileptic component and the observed spike in EEG. The concordance of results between various localization methods can improve the reliability of planning surgical resection or interictal EEG (iEEG) electrode placement.

TABLE 2 | Comparison of localization between conventional method and TCCC-method.

SOZ (No.)	Epileptic types	TCCC-method	Conventional method
Generalized (2)	CSWS (1)	1	–
	Syndrome (1)	1	1
Unifocal (23)	Non-lesional (17)	10	8
	Lesional (6)	5	3
Bifocal (4)		3	2
Multifocal (1)		1	–
Total	SOZ-based (30)	21, 70%	14, 46%
	Spike-type analysis (45)	29, 64%	21, 46%

The main inspiration for combining fMRI and EEG measurements comes from the ability to benefit from advantages of each modality. For instance, the EEG-derived activity map alone includes just the weighted sum of electrical activation in the brain with a poor spatial resolution and affected by artifacts, voltage drops, and interference with signals caused by non-epileptic sources. While the EEG signal alone is poorly capable of correctly identifying and localizing the epileptic generators, the EEG components time series associated with epileptic activity can be a consistent indicator. Based on this view, we reveal that hemodynamic correlations of EEG components can detect pathological brain activity. Therefore, simultaneous EEG-fMRI recording with patient's medical record form a 'golden package' and extracted component information from scalp EEG that improves the localization of epileptic foci compared to previous methods. This was the case in 90% of the patients in whom the most recent conventional EEG-fMRI analysis was negative, representing that component-related hemodynamic changes could add a more accurate and efficient identification. It is noticeable that in patients who got reasonable results from the conventional analysis, the method of this study also produced similarly concordant results.

In a simultaneous EEG-fMRI acquisition of 34 patients with epilepsy, the TCCC-related BOLD response was observed in all the 30 patients who had IEDs during recording, which makes 90.1% of the whole and is higher performance than that reported in the previous works (18, 42, 43). Also, these responses revealed the epileptic focus in 80% of patients with active EEG (65% of analyzed IEDs), which shows a significant improvement compared to Pittau et al. (18).

Regarding the localization of epileptic generators, Grouiller et al. (44) built an epileptic map by using the spikes detected in the EEG recorded outside the scanner and used it to create a regressor of IEDs from the EEG recorded inside the scanner. Convolving this regressor with an HRF and using it in the GLM analysis revealed concordant BOLD results in 78% (14 of 18) of the patients while this accuracy had a significant rise to 97% using our proposed method. Additional factors also affect the results of analysis, e.g., using higher MRI magnetic field strength which improves the intrasubject reproducibility of EEG-fMRI results (25, 45), using continuous EEG-fMRI instead of spike-triggered which increases the IED-related BOLD response among the patients (46), and using multiple HRFs peaking at 3–9 s after the spike for better localization of the epileptic focus (11, 12, 18).

Drawing on these strategies, our study used multiple HRFs to increase the gain of EEG-fMRI analysis and a high magnetic field MRI scanner to improve the signal-to-noise ratio and reach more informative images. The results showed BOLD responses that were concordant with the spike field in 97% of patients (29 cases out of 30; 74.5% of the analyzed IEDs). This level of concordance which is significantly higher than previous studies (18, 43, 44) is associated with using the component-based approach instead of the linear regressor, multiple HRFs for the fMRI analysis, high-field 3-T scanner for acquiring fMRI data, and effective methods for eliminating artifacts.

However, the definition and evaluation of spatial concordance between the BOLD response and EEG is still to some extent subjective and remains a constant challenge in EEG-fMRI analysis. In our study, the BOLD response is concordant with EEG if the maximum z-value complies with the localization of the EEG spike field. This approach makes the evaluation reliably objective and clinically applicable. All responses have been reported as suggested previously (8, 18). The BOLD responses are more widespread than typical electroclinical findings, due to possible distant or diffuse activations intricate in the epileptic network apart from the focus.

Concordance Level Scrutiny

Our studies have focused on the use of simultaneous EEG-fMRI for SOZ identification in patients with epilepsy. Since SOZs are best characterized using EEG-fMRI, our TCCC method would be suitable to identify presumed SOZ and evaluate its accuracy by comparing it with the IED-related BOLD activation. The concordance between IED-related BOLD activation and presumed SOZ for different brain structures has not been fully characterized using EEG-fMRI. Besides, seizure types have not been reflected as prominent features for precise identification of the SOZ using EEG-fMRI because of the complex pathophysiology of epileptic cerebral structures. Therefore, there is a fundamental need to quantitatively measure the concordance between IED-related BOLD and presumed SOZ for different brain structures to advance SOZ description. This may provide useful information for surgical guidance and better understanding of the mechanisms underlying seizure generation.

This study examined the distance of maximum BOLD clusters to the location of IED (**Figure 10**, third, fourth, and fifth rows). The maximum BOLD clusters appeared to be the most clinically relevant responses for all discharge types. From a clinical standpoint, this would assist in identifying the spike-generating network and hence the presumed SOZ.

Concordant BOLD clusters measured up to 25 mm of distance from the center of gravity to the IED contacts while partly concordant clusters measured between 25 and 50 mm of distance when the BOLD cluster is in the same hemisphere. This methodology was used to comprise two confounding factors: (1) electrophysiological activity that does not completely tie with the associated hemodynamic alterations (47) and (2) susceptibility

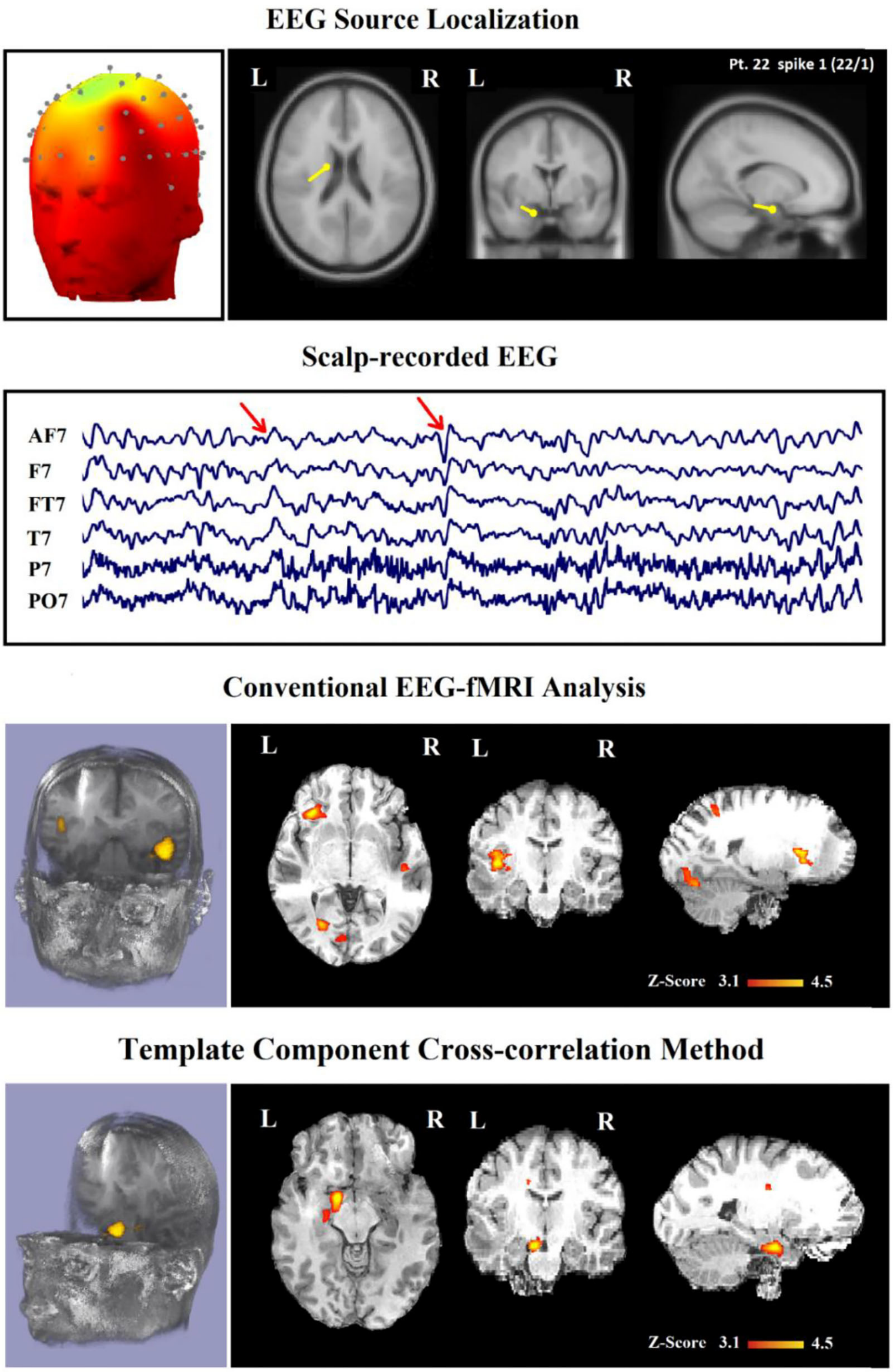

FIGURE 9 | (Patient 22—spike 1) marked events are AF7, T7, and FT7 spikes (referential montage) and the TCCC-related BOLD response demonstrates a neocortical activation in the caudate nucleus and lentiform nucleus for the TCCC method, this response is considered both concordant with the spike field and

(Continued)

FIGURE 9 | contributory duo to it leads to better localization of the epileptic focus compared with the scalp EEG because it adds new information to the scalp EEG, while is considered partially concordance and not contributory for the conventional method. These foci are scattered in three areas. Top, the component identified on scalp EEG located in the left frontotemporal lobe and the dipole localization of the identified generator in deep brain structures. The active area is marked with a yellow-red color. Second row, scalp recorded EEG. Third row, localization of the generator applying simultaneous analysis of EEG-fMRI by the conventional method. Forth row, localization of the generator applying simultaneous analysis of EEG-fMRI by the TCCC.

artifact that distorts the BOLD signal up to 20 mm of the electrodes (48). These measures are coherent with an earlier scalp EEG-fMRI study in which high concordance was defined as a distance between the BOLD response and the spike location on scalp EEG between 20 and 40 mm (49). Other EEG-fMRI studies which compared the location of IEDs with the BOLD responses did not describe the concordance as described in the current study; some used any BOLD cluster rather than separating the maximum for evaluation of concordance (28, 44, 50).

Despite the benefits mentioned, it is worth mentioning that the TCCC method heavily depends on accurate component identification. In case, for any reason, the component is identified in other areas, it will exert influence on the results. Although this study proposes a variety of filters to identify appropriate components, there have still been cases in which inaccurate identification performed by the algorithm has led to inaccurate localization (**Figure 10**, third row). However, the localization improved by the selection of other candidate time series (**Figure 10**, fifth row).

Method Limitations

Notwithstanding the mentioned advantages, it should be noted that since we take the time series of the selected components to detect the respective BOLD changes, there will be a plurality to the number of samples of interest, which inevitably makes the proposed method fairly time consuming. The sampling rate for each component is around 250 Hz while the BOLD signal provides one sample per 2.5 s (each TR time). In order to accelerate the process, we have proposed to reduce the sampling rate for the component of interest to the number of BOLD samples. Therefore, we would have invaluable information of the epileptic activity of each generator with respect to the number of BOLD samples.

In this study, although the simultaneous EEG-fMRI method was compared with the epileptic source localization by EEG only and the conventional EEG-fMRI method and its superiority was demonstrated, basically the post-surgical outcome information or the intracranial EEG recording can lead to more reliable results and it more precisely will approve the improvement of the findings.

Comparison With Other Modalities

Regarding other modalities, PET and SPECT were also used in several studies for the localization of epileptic generators. However, some points need to be considered. For instance, delayed injection in such studies can lead to a misconception of the attained results. Besides, some valuable methods for localizing the epileptic network like interictal FDG PET are not cost-effective while posing risks following radiation exposure.

Generally, although the ictal-based SPECT and PET analyses are suggested and supported by the literature for localizing epileptic foci, their usefulness is limited to revealing regional abnormalities instead of focal epileptic generators (51–54). Besides, our method achieved a BOLD sensitivity of 90% which is higher than those reported for the SPECT and PET studies. However, the obtained specificity might be cooperated by distant BOLD correlations and should be fostered by postsurgical processes. The EEG and MEG source imaging is another promising method that has made incredible development in the number of recorded channels and algorithms to estimate the sources (55–57). The inverse solution of EEG and MEG has reached a sensitivity of around 70% in the study of Knake et al. (58) which is comparable to the EEG-fMRI methods.

Comparison With Other EEG-fMRI-Based Methods

The classical EEG-fMRI method is an event-related design for fMRI analysis based on the time series of constant amplitude and zero duration or block events with the timing of interictal spikes recorded in the simultaneous EEG (43, 59–61). These interictal spikes are found manually or by an automatic spike detection algorithm based on the spike template acquired from the EEG recorded outside the scanner (9, 34, 44, 62–64). Convolving the time series of events with the standard or patient-specific HRFs (65, 66) makes the base regressor for the GLM analysis to localize BOLD responses as the epileptic generators. The main flaws of the conventional method which calls into question 40–70% of EEG-fMRI studies are: (1) existence of insufficient events during recording; and (2) insignificant BOLD correlation with the observed spikes. One of the proposed solutions for the EEG-fMRI studies with no observed spikes during recording was the fMRI data-driven source identification whose specificity was not particularly promising (67). Therefore, there was a limitation in the cases with detectable spikes for applying similar data-driven approaches premised on spatial independent component analysis of fMRI, and the accomplished results revealed high concordance with those from more conventional methods (38, 67–69).

Also, there are a couple of studies that take continuously fluctuating variables to model epileptic behavior, including continuous electrical imaging (70) which was stated to have enhanced EEG/fMRI by 20%. In addition, the spatial correlation coefficient of the reference topography has been considered in a few studies as a continuously fluctuating parameter to be useful in fMRI analysis (44). This approach can act as a spatial filter analogous to using the strength of a dipole source (71) or the current density that was estimated by electrical

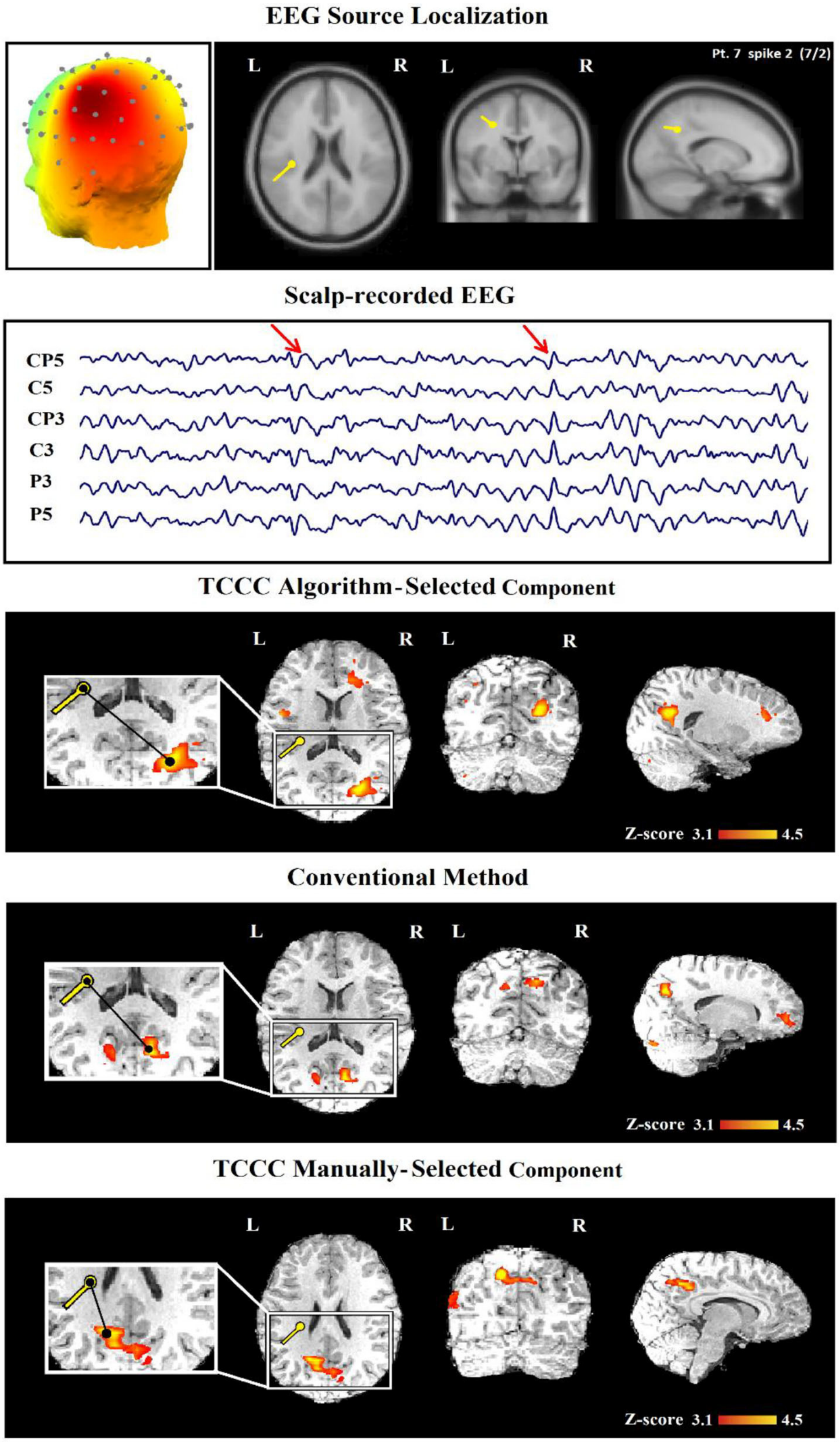

FIGURE 10 | (Patient 22—spike 2) An illustration of a sample result for conventional and TCCC methods both manually and automatically. First row, the identified component and its dipole localization in deep brain structures. Second row, scalp recorded EEG. Third row, TCCC-related BOLD response using auto-identified component (Discordant). The active area is marked with a yellow-red color. Forth row, IED-related BOLD response (conventional method). Fifth row, TCCC-related BOLD response using manually-selected component (Concordance).

TABLE 3 | Comparison of concordance between conventional EEG-fMRI analysis and TCCC method in relation to BOLD response and EEG data of 47 IED studies.

Pt/IED type	IEDs Location	Template Component Cross-correlation EEG-fMRI						Conventional EEG-fMRI						Agreement between TCCC and conventional methods
		Dis.^{a} (mm)	Conc.^{b}	Max Z score for relevant cluster	Max BOLD volume (cm^{3})	BOLD in other location(s)	Contribution	Dis.^{a} (mm)	Conc.^{c}	Max Z score for relevant cluster	Max BOLD volume (cm^{3})	BOLD in other location(s)	Contribution	Concordance^{d}/ Dis. (mm)
1/1	T R	21.33	C	3.84	1.22	L lateral T	Yes	19.52	C	3.63	0.98	L mesial T	Yes	Yes/5.23
2/1	FC bil	17.80	C	4.10	3.51	–	Yes	20.14	C	4.18	2.94	L lateral T	Yes	Yes/6.01
2/2	FC L	14.35	C	2.22	1.12	–	Yes	16.39	C	6.15	1.04	–	No	Yes/4.28
3/1	FT R	19.32	C	3.17	1.94	L mesial P	Yes	28.45	PC	4.52	3.12	–	No	Yes/11.49
3/2	F R	42.15	PC	3.45	2.51	–	No	51.64	D	3.66	2.43	L middle T gyrus	No	Yes/18.54
3/3	Bif	15.25	C	4.07	3.73	–	Yes	18.25	C	4.12	4.26	–	Yes	Yes/7.64
4/1	P L	11.61	C	5.26	4.12	–	No	12.35	C	4.53	1.15	–	Yes	Yes/9.23
5/1	T L	36.42	PC	4.01	0.75	LP–O	No	30.25	–	–	–	–	–	–
5/2	FL	9.34	C	6.95	0.86	–	Yes	14.28	C	5.42	2.51	L anterior P	Yes	Yes/15.81
6/1	Bil generalized	17.55	C	3.87	10.23	–	No	18.41	C	3.54	8.79	–	No	Yes/2.18
7/1	F L	10.48	C	5.16	1.64	L anterior P	Yes	13.25	C	4.56	1.88	Bil F–P	Yes	Yes/22.37
7/2	C L	50.24	D	4.46	2.65	R middle F	No	43.25	PC	3.56	1.02		No	No/12.65
7/3	T R	26.01	PC	5.13	2.41	–	No	18.98	C	16.14	0.89	mesial T–P	Yes	Yes/17.24
8/1	T R	7.61	C	4.38	1.32	L lateral T	Yes	32.27	PC	4.85	5.27	L anterior F	No	No/26.55
9/1	F R/L	8.04	C	6.23	3.18	–	Yes	13.52	C	5.93	3.26	L posterolateral F	Yes	Yes/6.24
10/1	L hemisphere	38.25	PC	3.87	5.44	L P	No	55.14	D	3.36	5.36	–	No	Yes/15.67
11/1	O R	14.32	C	4.29	1.01	L anterior P	Yes	12.62	C	4.11	0.98	L orbito–F	Yes	Yes/8.45
11/2	PO R	–	–	–	–	–	–	51.56	D	2.14	3.14	–	No	–
11/3	P R	23.25	C	6.52	8.42	–	Yes	19.25	C	5.34	2.64	–	Yes	Yes/5.06
12/1	Bifrontal	37.52	PC	5.13	2.80	–	No	35.14	PC	5.09	3.02	–	No	Yes/4.34
12/2	F L	13.46	C	4.58	0.98	–	Yes	13.46	C	6.18	1.06	–	Yes	Yes/0.09
13/1	P L/Post T	16.18	C	3.28	1.62	–	Yes	28.62	PC	4.16	1.15	–	No	No/27.35
14/1	Frontopolar R	22.57	C	4.49	3.46	–	Yes	21.78	C	4.28	3.61	–	Yes	Yes/2.42
14/2	FT R	30.24	PC	4.68	2.16	–	No	32.47	PC	3.74	2.13	–	No	Yes/5.67
14/3	FT L	21.85	C	5.85	0.61	–	Yes	26.85	PC	4.88	0.24	L post T–O	No	No/29.13
15/1	T R	5.34	C	4.57	1.16	R anterior F	No	13.25	C	6.11	0.76	–	No	Yes/10.16

(Continued)

TABLE 3 | Continued

Pt/IED type	IEDs Location	Template Component Cross-correlation EEG-fMRI						Conventional EEG-fMRI						Agreement between TCCC and conventional methods
		Dis.[a] (mm)	**Conc.[b]**	**Max Z score for relevant cluster**	**Max BOLD volume (cm^3)**	**BOLD in other location(s)**	**Contribution**	**Dis.[a] (mm)**	**Conc.[c]**	**Max Z score for relevant cluster**	**Max BOLD volume (cm^3)**	**BOLD in other location(s)**	**Contribution**	**Concordance[d]/ Dis. (mm)**
16/1	PO L	18.62	C	4.36	2.53	–	Yes	19.77	C	4.28	2.84	–	Yes	Yes/3.49
17/1	FC bil	9.48	C	5.61	6.18	–	Yes	28.65	PC	5.24	8.15	–	No	No/28.57
18/1	F L	16.58	C	4.95	2.16	L posterolateral F	No	22.58	C	4.97	2.19	–	Yes	Yes/15.86
18/2	F R	12.87	C	6.03	4.65	–	Yes	18.47	C	3.67	5.27	–	Yes	Yes/3.15
18/3	FT L	–	–	–	–	–	–	18.62	C	3.65	4.50	T L	No	–
19/1	P R	13.13	C	5.72	1.35	–	Yes	31.24	PC	5.34	1.84	–	No	No/27.64
20/1	T pole	15.56	C	3.96	7.52	–	Yes	12.66	C	3.50	7.16	–	Yes	Yes/4.33
21/1	T R	11.68	C	4.26	3.17	L lateral T	Yes	33.92	PC	4.97	0.67	–	No	No/26.85
22/1	FT L	8.26	C	4.16	2.03	–	Yes	48.04	PC	4.36	3.12	L O + R T	No	No/31.75
22/2	T L	25.18	PC	5.39	1.88	–	No	–	–	–	–	–	–	–
23/1	P R	6.23	C	7.18	3.63	–	Yes	14.41	C	3.98	4.65	R middle T	Yes	Yes/10.32
23/2	P R	27.64	PC	4.35	2.12	–	No	31.45	PC	4.11	0.77	–	No	Yes/8.64
24/1	F L	7.65	C	5.18	4.34	–	No	9.17	C	4.50	1.85	Bil Occipital	Yes	Yes/5.93
25/1	T L	24.13	C	3.98	1.05	R lateral T	Yes	21.42	C	4.80	6.54	–	Yes	Yes/5.13
25/2	PO L	18.92	C	5.62	1.54	–	Yes	–	–	–	–	–	–	–
26/1	Bifrontal	13.34	C	6.84	9.25	–	No	33.46	PC	2.98	12.57	L P/R T	No	No/26.21
27/1	FT R	14.42	C	5.34	4.35	–	Yes	10.24	C	4.76	2.64	–	No	Yes/6.95
28/1	F L	7.52	C	3.28	2.46	–	Yes	28.33	PC	5.45	8.34	Bil Occipital	No	No/25.37
29/1	T R	11.62	C	7.26	2.66	R lateral T	Yes	17.46	C	4.13	3.16	–	Yes	Yes/8.62
29/2	FT R	29.85	PC	3.65	2.07	R anterior F	No	31.17	PC	4.80	3.09	L O	No	Yes/10.21
30/1	O R	4.59	C	4.84	2.13	–	Yes	11.09	C	5.12	2.11	–	Yes	Yes/9.64

[a] *Distance from the center of gravity of the relevant BOLD to the dipole location of the identified component.*

[b] *Concordance between the BOLD response and the IED location in the proposed analysis.*

[c] *Concordance between the BOLD response and the IED location in the conventional analysis.*

[d] *Concordance between the BOLD response in the proposed and the conventional analysis.*

Bif, bifrontal; Bil, bilateral; C, concordant; D, discordant; F, frontal; FT, frontotemporal; FC, frontocentral; L, left; O, occipital; P, parietal; PC, partially concordant; PO, parieto-occipital; R, right; T, temporal.

source imaging in a specific region (70). Also, some other approaches based on dynamic causal modeling (DCM) (72) and functional connectivity (73) have played a useful role in this regard.This technique despite improving the sensitivity compared to similar studies has not addressed the localization of epileptic generators. Besides, the results of component-based methods have been better than those of the topographic maps even while the presence of detectable spikes during EEG-fMRI recording (70). The source separation methods have been also considered to localize the epileptic focus in the literature (74, 75). In order to identify the epileptic-related components in this method, the EEG signal collected inside the scanner must include spikes or clear focal slowing. The main challenge in such studies is appropriately recognizing the component(s) associated with epileptic activity without using clinical information. We have addressed this challenge by imposing specific conditions on the components along with the convolution of the spike-template obtained from the outside-of-scanner EEG and the candidate ones.

In the study of Bast et al. (34), a new method was proposed to simplify visual detection of spikes in EEG-fMRI premised on spatiotemporal pattern search. For this aim, the principal component analysis (PCA) was applied on a spike template and then its correlation was evaluated with the EEG recorded inside the scanner. The trials with a spatiotemporal correlation above 0.85 were visually evaluated and false-positive identifications manually detached. Although this is a great method to identify the spikes registered inside the scanner, it still uses a traditional linear regressor of temporal information for the GLM analysis.

In total, the mentioned studies provide an overview of the localization of epileptic generators with reasonable accuracy that can be used in real-life applications. Simultaneous EEG-fMRI is a promising combination of temporal and spatial resolution that allows reaching higher prospects for precise localization of epileptic generators in patients with focal epilepsy. In this study, the source domain has been used instead of the sensor field to provide a more accurate recognition of epileptic foci. The results showed that epileptic-related components can be considered as a representative of epileptic foci activity in the GLM analysis and afford clinically precious information even in cases of datasets with inadequate detectable interictal events.

Accurate epileptic foci localization is an essential step in pre-surgical assessments of patients with medically resistant epilepsy. Measuring BOLD changes using EEG-fMRI offers an advanced technique to adequately record abnormal epileptic activities from localized brain regions while capturing related fluctuations in functional brain activities. Further understanding of the epileptogenic zone using IED-related BOLD responses obtained from EEG-fMRI provides a new avenue for clinicians to accurately identify epileptic foci, guide epilepsy surgery, and improve post-surgical results. This study sheds light on the consideration of EEG-fMRI as an indentifer of the epileptic focus, which can be included as part of the clinical assessment for patients with refractory epilepsy.

CONCLUSION

This study sets out to provide a realistically estimated pattern of epileptic generators. To do so, we shifted the attention from the electrode domain to the source domain, where we extracted the epilepsy-related components through an ICA analysis. Then, we prioritized these components on the basis of (a) the cross-correlation between the spike-template and the time-series of each component, and (b) their alignment with the complementary physiological information. This would yield a set of ranked components that are most likely contributory to the occurrence of spikes, which can well substitute the simplistic linear regressor in conventional approaches. We went on to convolve the time series of the selected components with HRF and used them in the GLM model and checked if the result was consistent with the physiological EEG observations, if so, we accepted the region as a generator of epileptic activity.

In this study, we have also introduced a new EEG-fMRI method which highlights the correlation between the corresponding BOLD alterations and the spike-related EEG components, which were validated against the gold standard for epileptic generators localization. This approach leads to an increase in the EEG-fMRI yield to non-invasively localize the seizure generators, which is particularly useful in the presurgical evaluation of the patients and implantation of intracranial electrodes, allowing a wider range of patients to consider the option of surgery with more confidence.

In future studies, we intend to apply a new approach for EEG-fMRI integration in the field of epilepsy, which incorporates and tests different models of the transfer function between EEG and BOLD signals, hence allowing better predictions of the hemodynamic changes associated with epileptic activity. This work will therefore provide a contribution to our understanding of the link between EEG and BOLD signals as well as for improving the yield of EEG-fMRI studies in epilepsy (76, 77).

DATA AVAILABILITY STATEMENT

The datasets presented in this article are not readily available because due to the nature of this research, participants of this study did not agree for their data to be shared publicly. Requests to access the data should be directed to the corresponding author Elias Ebrahimzadeh, e_ebrahimzadeh@ut.ac.ir.

ETHICS STATEMENT

The studies involving human participants were reviewed and approved by Iran University of Medical Sciences. Written informed consent to participate in this study was provided by the participants' legal guardian/next of kin. Written informed consent was obtained from the individuals, and minors' legal guardian/next of kin, for the publication of any potentially identifiable images or data included in this article.

AUTHOR CONTRIBUTIONS

EE and HS-Z conceived of the presented idea. EE developed the theory and performed the computations. Material preparation, data collection, and analysis were performed by EE. The first draft of the manuscript was written by EE, MSh, MSe, SS and all authors commented on previous versions of the manuscript. MSh, MSe, and HS-Z verified the analytical methods. The visualization and validation were done by EE, LR, and SS. HS-Z supervised the project. All authors provided critical feedback and helped shape the research, analysis, and manuscript. All authors have read and approved the final manuscript.

ACKNOWLEDGMENTS

The EEG-fMRI data used in this study were acquired in the National Brain Mapping Laboratory (NBML), Tehran, Iran. The authors would like to show their gratitude to Dr. Paolo Federico (Department of Clinical Neurosciences, University of Calgary, Calgary, Alberta, Canada) and his group for sharing their pearls of wisdom during the course of this research. They are also immensely grateful to Dr. Negar Tehrani for her valuable comments, although any errors are of our own and should not tarnish the reputation of these esteemed individuals. EE also expresses his gratitude to the Cognitive Science and Technologies Council (COGC), Tehran, Iran for their tremendous support.

REFERENCES

1. de Boer HM, Mula M, Sander JW. The global burden and stigma of epilepsy. *Epilepsy Behav.* (2008) 12:540–546. Available online at: http://ovidsp.ovid.com/ovidweb.cgi?T=JS&PAGE=reference&D=emed8&NEWS=N&AN=2008133201
2. Fisher RS, Van Emde Boas W, Blume W, Elger C, Genton P, Lee P, et al. Epileptic seizures and epilepsy: definitions proposed by the International League Against Epilepsy (ILAE) and the International Bureau for Epilepsy (IBE). *Epilepsia.* (2005) 46:470–2. doi: 10.1111/j.0013-9580.2005.66104.x
3. Mirbagheri M, Hakimi N, Ebrahimzadeh E, Pourrezaei K, Setarehdan SK. Enhancement of optical penetration depth of LED-based NIRS systems by comparing different beam profiles. *Biomed Phys Eng Express.* (2019) 5:065004. doi: 10.1088/2057-1976/ab42d9/meta
4. Mirbagheri M, Hakimi N, Ebrahimzadeh E, Setarehdan SK. Quality analysis of heart rate derived from functional near-infrared spectroscopy in stress assessment. *Informatics Med Unlocked.* (2020) 18:100286. doi: 10.1016/j.imu.2019.100286
5. Mirbagheri M, Hakimi N, Ebrahimzadeh E, Setarehdan SK. Simulation and *in vivo* investigation of light-emitting diode, near infrared Gaussian beam profiles. *J Near Infrared Spectrosc.* (2020) 28:37–50. doi: 10.1177/0967033519884209
6. Rosenow F, Lüders H. Presurgical evaluation of epilepsy. *Brain.* (2001) 124:1683–700. doi: 10.1093/brain/124.9.1683
7. Hamer HM, Morris HH, Mascha EJ, Karafa MT, Bingaman WE, Bej MD, et al. Complications of invasive video-EEG monitoring with subdural grid electrodes. *Neurology.* (2002) 58:97–103. doi: 10.1212/WNL.58.1.97
8. Khoo HM, Hao Y, von Ellenrieder N, Zazubovits N, Hall J, Olivier A, et al. The hemodynamic response to interictal epileptic discharges localizes the seizure-onset zone. *Epilepsia.* (2017) 58:811–23. doi: 10.1111/epi.13717
9. Tousseyn S, Dupont P, Robben D, Goffin K, Sunaert S, Van Paesschen W, et al. reliable and time-saving semiautomatic spike-template-based analysis of interictal EEG-fMRI. *Epilepsia.* (2014) 55:2048–58. doi: 10.1111/epi.12841
10. Pedreira C, Vaudano AE, Thornton RC, Chaudhary UJ, Vulliemoz S, Laufs H, et al. Classification of EEG abnormalities in partial epilepsy with simultaneous EEG-fMRI recordings. *Neuroimage.* (2014) 99:461–76. doi: 10.1016/j.neuroimage.2014.05.009
11. Bagarinao E, Maesawa S, Ito Y, Usui N, Natsume J, Watanabe H, et al. Detecting sub-second changes in brain activation patterns during interictal epileptic spike using simultaneous EEG-fMRI. *Clin Neurophysiol.* (2018) 129:377–89. doi: 10.1016/j.clinph.2017.11.018
12. Hao Y, Khoo HM, von Ellenrieder N, Zazubovits N, Gotman J. DeepIED: an epileptic discharge detector for EEG-fMRI based on deep learning. *NeuroImage Clin.* (2018) 17:962–75. doi: 10.1016/j.nicl.2017.12.005
13. Morano A, Carnì M, Casciato S, Vaudano AE, Fattouch J, Fanella M, et al. Ictal EEG/fMRI study of vertiginous seizures. *Epilepsy Behav.* (2017) 68:51–6. doi: 10.1016/j.yebeh.2016.12.031
14. Ebrahimzadeh E, Soltanian-Zadeh H, Araabi BN. Localization of epileptic focus using simultaneously acquired EEG-FMRI data. *Comput Intellig Electric Eng.* (2018) 9:15–28. doi: 10.22108/ISEE.2018.111024.1123
15. Maziero D, Velasco TR, Salmon CEG, Morgan VL. Two-dimensional temporal clustering analysis for patients with epilepsy: detecting epilepsy-related information in EEG-fMRI concordant, discordant and spike-less patients. *Brain Topogr.* (2018) 31:322–36. doi: 10.1007/s10548-017-0598-3
16. Ives JR, Warach S, Schmitt F, Edelman RR, Schomer DL. Monitoring the patient's EEG during echo planar MRI. *Electroencephalogr Clin Neurophysiol.* (1993) 87:417–20. doi: 10.1016/0013-4694(93)90156-P
17. Kay B, Szaflarski JP. EEG/fMRI contributions to our understanding of genetic generalized epilepsies. *Epilepsy Behav.* (2014) 34:129–35. doi: 10.1016/j.yebeh.2014.02.030
18. Pittau F, Dubeau F, Gotman J. Contribution of EEG/fMRI to the definition of the epileptic focus. *Neurology.* (2012) 78:1479–87. doi: 10.1212/WNL.0b013e3182553bf7
19. Moeller F, Tyvaert L, Nguyen DK, Levan P, Bouthillier A, Kobayashi E, et al. EEG-fMRI: Adding to standard evaluations of patients with nonlesional frontal lobe epilepsy. *Neurology.* (2009) 73:2023–30. doi: 10.1212/WNL.0b013e3181c55d17
20. Bénar CG, Gross DW, Wang Y, Petre V, Pike B, Dubeau F, et al. The BOLD response to interictal epileptiform discharges. *Neuroimage.* (2002) 17:1182–92. doi: 10.1006/nimg.2002.1164
21. Kobayashi E, Bagshaw AP, Bénar CG, Aghakhani Y, Andermann F, Dubeau F, et al. Temporal and extratemporal BOLD responses to temporal lobe interictal spikes. *Epilepsia.* (2006) 47:343–54. doi: 10.1111/j.1528-1167.2006.00427.x
22. Thornton R, Laufs H, Rodionov R, Cannadathu S, Carmichael DW, Vulliemoz S, et al. EEG correlated functional MRI and postoperative outcome in focal epilepsy. *J Neurol Neurosurg Psychiatry.* (2010) 81:922–7. doi: 10.1136/jnnp.2009.196253
23. Zijlmans M, Huiskamp G, Hersevoort M, Seppenwoolde JH, Van Huffelen AC, Leijten FSS. EEG-fMRI in the preoperative work-up for epilepsy surgery. *Brain.* (2007) 130:2343–53. doi: 10.1093/brain/awm141
24. Noachtar S, Borggraefe I. Epilepsy surgery: a critical review. *Epilepsy Behav.* (2009) 15:66–72. doi: 10.1016/j.yebeh.2009.02.028
25. Gholipour T, Moeller F, Pittau F, Dubeau F, Gotman J. Reproducibility of interictal EEG-fMRI results in patients with epilepsy. *Epilepsia.* (2011) 52:433–42. doi: 10.1111/j.1528-1167.2010.02768.x
26. Ridley B, Wirsich J, Bettus G, Rodionov R, Murta T, Chaudhary U, et al. Simultaneous intracranial EEG-fMRI shows inter-modality correlation in time-resolved connectivity within normal areas but not within epileptic regions. *Brain Topogr.* (2017) 30:639–55. doi: 10.1007/s10548-017-0551-5
27. Beers CA, Williams RJ, Gaxiola-Valdez I, Pittman DJ, Kang AT, Aghakhani Y, et al. Patient specific hemodynamic response functions associated with interictal discharges recorded via simultaneous intracranial EEG-fMRI. *Hum Brain Mapp.* (2015) 36:5252–64. doi: 10.1002/hbm.23008
28. Vulliemoz S, Carmichael DW, Rosenkranz K, Diehl B, Rodionov R, Walker MC, et al. Simultaneous intracranial EEG and fMRI

of interictal epileptic discharges in humans. *Neuroimage.* (2011) 54:182–90. doi: 10.1016/j.neuroimage.2010.08.004

29. Ebrahimzadeh E, Soltanian-Zadeh H, Nadjar Araabi B, Hashemi Fesharaki SS, Mehvari Habibabadi J. Component-related BOLD response to localize epileptic focus using simultaneous EEG-fMRI recordings at 3T. *J Neurosci Methods.* (2019) 322:34–49. doi: 10.1016/j.jneumeth.2019.04.010
30. Seraji M, Mohebbi M, Safari A, Krekelberg B. Multiple sclerosis reduces synchrony of the magnocellular pathway. *PLoS ONE.* (2021) 16:e0255324. doi: 10.1371/JOURNAL.PONE.0255324
31. Raeisi K, Mohebbi M, Khazaei M, Seraji M, Yoonessi A. Phase-synchrony evaluation of EEG signals for Multiple Sclerosis diagnosis based on bivariate empirical mode decomposition during a visual task. *Comput Biol Med.* (2020) 117:103596. doi: 10.1016/J.COMPBIOMED.2019.103596
32. Ebrahimzadeh E, Asgarinejad M, Saliminia S, Ashoori S, Seraji M. Predicting clinical response to transcranial magnetic stimulation in major depression using time-frequency EEG signal processing. *Biomed Eng.* (2021). doi: 10.4015/S1016237221500484
33. Ebrahimzadeh E, Shams M, Rahimpour Jounghani A, Fayaz F, Mirbagheri M, Hakimi N, et al. Localizing confined epileptic foci in patients with an unclear focus or presumed multifocality using a component-based EEG-fMRI method. *Cogn Neurodyn.* (2020) 5:1–16. doi: 10.1007/s11571-020-09614-5
34. Bast T, Oezkan O, Rona S, Stippich C, Seitz A, Rupp A, et al. and MEG source analysis of single and averaged interictal spikes reveals intrinsic epileptogenicity in focal cortical dysplasia. *Epilepsia.* (2004) 45:621–31. doi: 10.1111/j.0013-9580.2004.56503.x
35. LeVan P, Tyvaert L, Moeller F, Gotman J. Independent component analysis reveals dynamic ictal BOLD responses in EEG-fMRI data from focal epilepsy patients. *Neuroimage.* (2010) 49:366–78. doi: 10.1016/j.neuroimage.2009.07.064
36. Ebrahimzadeh E, Shams M, Fayaz F, Rajabion L, Mirbagheri M, Nadjar Araabi B, et al. Quantitative determination of concordance in localizing epileptic focus by component-based EEG-fMRI. *Comput Methods Programs Biomed.* (2019) 177:231–41. doi: 10.1016/j.cmpb.2019.06.003
37. Ebrahimzadeh E, Amoozegar S, Asgarinejad M, Dolatabad MR, Bagheri M, Zangeneh Soroush M. Simultaneous EEG-fMRI: a multimodality approach to localize the seizure onset zone in patients with epilepsy. *Int J Biol Med.* (2019) 1:130–9. doi: 10.36811/ijbm.2019.110017
38. LeVan P, Gotman J. Independent component analysis as a model-free approach for the detection of BOLD changes related to epileptic spikes: a simulation study. *Hum Brain Mapp.* (2009) 30:2021–31. doi: 10.1002/hbm.20647
39. Worsley KJ, Liao CH, Aston J, Petre V, Duncan GH, Morales F, et al. General statistical analysis for fMRI data. *Neuroimage.* (2002) 15:1–15. doi: 10.11253/ninchishinkeikagaku1999.3.91
40. Sadjadi SM, Ebrahimzadeh E, Shams M, Seraji M, Soltanian-Zadeh H. Localization of epileptic foci based on simultaneous EEG–fMRI data. *Front Neurol.* (2021) 12:472. doi: 10.3389/fneur.2021.645594
41. Müller-Bardorff M, Bruchmann M, Mothes-Lasch M, Zwitserlood P, Schlossmacher I, Hofmann D, et al. Early brain responses to affective faces: A simultaneous EEG-fMRI study. *Neuroimage.* (2018) 178:660–7. doi: 10.1016/j.neuroimage.2018.05.081
42. Al-Asmi A, Bénar CG, Gross DW, Agha Khani Y, Andermann F, Pike B, et al. fMRI Activation in continuous and spike-triggered EEG-fMRI studies of epileptic spikes. *Epilepsia.* (2003) 44:1328–39. doi: 10.1046/j.1528-1157.2003.01003.x
43. Salek-Haddadi A, Diehl B, Hamandi K, Merschhemke M, Liston A, Friston K, et al. Hemodynamic correlates of epileptiform discharges: an EEG-fMRI study of 63 patients with focal epilepsy. *Brain Res.* (2006) 1088:148–66. doi: 10.1016/j.brainres.2006.02.098
44. Grouiller F, Thornton RC, Groening K, Spinelli L, Duncan JS, Schaller K, et al. With or without spikes: localization of focal epileptic activity by simultaneous electroencephalography and functional magnetic resonance imaging. *Brain.* (2011) 134:2867–86. doi: 10.1093/brain/awr156
45. Krüger G, Kastrup A. Glover GH. Neuroimaging at 15 T and 30 T: comparison of oxygenation-sensitive magnetic resonance imaging. *Magn Reson Med.* (2001) 45:595–604. doi: 10.1002/mrm.1081
46. Lemieux L, Mulert C. *EEG–fMRI Physiological Basis, Technique and Applications*. Berlin: Spriinger. (2009).
47. Disbrow EA, Slutsky DA, Roberts TPL. Krubitzer LA. Functional MRI at 15 tesla: A comparison of the blood oxygenation level-dependent signal and electrophysiology. *Proc Natl Acad Sci USA.* (2000) 97:9718–23. doi: 10.1073/pnas.170205497
48. Boucousis SM, Beers CA, Cunningham CJB, Gaxiola-Valdez I, Pittman DJ, Goodyear BG, et al. Feasibility of an intracranial EEG-fMRI protocol at 3T: risk assessment and image quality. *Neuroimage.* (2012) 63:1237–48. doi: 10.1016/j.neuroimage.2012.08.008
49. Bénar CG, Grova C, Kobayashi E, Bagshaw AP, Aghakhani Y, Dubeau F, et al. EEG-fMRI of epileptic spikes: concordance with EEG source localization and intracranial EEG. *Neuroimage.* (2006) 30:1161–70. doi: 10.1016/j.neuroimage.2005.11.008
50. Aghakhani Y, Beers CA, Pittman DJ, Gaxiola-Valdez I, Goodyear BG, Federico P. Co-localization between the BOLD response and epileptiform discharges recorded by simultaneous intracranial EEG-fMRI at 3 T. *NeuroImage Clin.* (2015) 7:755–63. doi: 10.1016/j.nicl.2015.03.002
51. Wetjen NM, Cascino GD, Fessler AJ, So EL, Buchhalter JR, Mullan BP, et al. Subtraction ictal single-photon emission computed tomography coregistered to magnetic resonance imaging in evaluating the need for repeated epilepsy surgery. *J Neurosurg.* (2006) 105:71–6. doi: 10.3171/jns.2006.105.1.71
52. Willmann O, Wennberg R, May T, Woermann FG, Pohlmann-Eden B. The contribution of 18F-FDG PET in preoperative epilepsy surgery evaluation for patients with temporal lobe epilepsy. A meta-analysis. *Seizure.* (2007) 16:509–20. doi: 10.1016/j.seizure.2007.04.001
53. O'Brien TJ, So EL, Mullan BP, Hauser MF, Brinkmann BH, Bohnen NI, et al. Subtraction ictal SPECT co-registered to MRI improves clinical usefulness of SPECT in localizing the surgical seizure focus. *Neurology.* (1998) 50:445–54. doi: 10.1212/WNL.50.2.445
54. O'Brien TJ, So EL, Mullan BP, Hauser MF, Brinkmann BH, Jack CR, et al. Subtraction SPECT co-registered to MRI improves postictal SPECT localization of seizure loci. *Neurology.* (1999) 52:137–46. doi: 10.1212/wnl.52.1.137
55. Michel CM, Lantz G, Spinelli L, De Peralta RG, Landis T, Seeck M. 128-Channel EEG source imaging in epilepsy: clinical yield and localization precision. *J Clin Neurophysiol.* (2004) 21:71–83. doi: 10.1097/00004691-200403000-00001
56. Michel CM, Murray MM, Lantz G, Gonzalez S, Spinelli L, Grave De Peralta R. EEG source imaging. *Clin Neurophysiol.* (2004) 115:2195–222. doi: 10.1016/j.clinph.2004.06.001
57. Shibasaki H, Ikeda A, Nagamine T. Use of magnetoencephalography in the presurgical evaluation of epilepsy patients. *Clin Neurophysiol.* (2007) 118:1438–48. doi: 10.1016/j.clinph.2007.03.002
58. Knake S, Halgren E, Shiraishi H, Hara K, Hamer HM, Grant PE, et al. The value of multichannel MEG and EEG in the presurgical evaluation of 70 epilepsy patients. *Epilepsy Res.* (2006) 69:80–6. doi: 10.1016/j.eplepsyres.2006.01.001
59. Lemieux L, Salek-Haddadi A, Josephs O, Allen P, Toms N, Scott C, et al. Event-related fMRI with simultaneous and continuous EEG: description of the method and initial case report. *Neuroimage.* (2001) 14:780–7. doi: 10.1006/nimg.2001.0853
60. Gotman J. Epileptic networks studied with EEG-fMRI. *Epilepsia.* (2008) 49:42–51. doi: 10.1111/j.1528-1167.2008.01509.x
61. Bagshaw AP, Hawco C, Bénar CG, Kobayashi E, Aghakhani Y, Dubeau F, et al. Analysis of the EEG-fMRI response to prolonged bursts of interictal epileptiform activity. *Neuroimage.* (2005) 24:1099–112. doi: 10.1016/j.neuroimage.2004.10.010
62. Ebrahimzadeh E, Shams M, Rahimpour Jopungha A, Fayaz F, Mirbagheri M, Hakimi N, et al. Epilepsy presurgical evaluation of patients with complex source localization by a novel component-based EEG-fMRI approach. *Iran J Radiol.* (2019) 16:99134. doi: 10.5812/iranjradiol.99134
63. Ebrahimzadeh E, Soltanian-Zadeh H, Araabi BN, Fesharaki SSH, Habibabadi JM. Localizing epileptic focus through simultaneous EEG-fMRI recording and automated detection of IED from inside-scanner EEG. *Iran J Biomed Eng.* (2019) 13:135–45. doi: 10.22041/ijbme.2019.103479.1447
64. Ebrahimzadeh E, Soltanian-Zadeh H, Araabi BN, Fesharaki SSH, Habibabadi JM. Localizing epileptic focus through simultaneous EEG-fMRI recording and automated detection of interictal epileptiform discharges (IED) from EEG in

inside MRI. In *25th National and 3rd International Iranian Conference on Biomedical Engineering (ICBME 2018)*, 1–6.

65. van Houdt PJ, de Munck JC, Zijlmans M, Huiskamp G, Leijten FSS, Boon PAJM, et al. Comparison of analytical strategies for EEG-correlated fMRI data in patients with epilepsy. *Magn Reson Imaging*. (2010) 28:1078–86. doi: 10.1016/j.mri.2010.03.022
66. Kang JK, Bénar CG, Al-Asmi A, Khani YA, Pike GB, Dubeau F, et al. Using patient-specific hemodynamic response functions in combined EEG-fMRI studies in epilepsy. *Neuroimage*. (2003) 20:1162–70. doi: 10.1016/S1053-8119(03)00290-8
67. Rodionov R, De Martino F, Laufs H, Carmichael DW, Formisano E, Walker M, et al. Independent component analysis of interictal fMRI in focal epilepsy: comparison with general linear model-based EEG-correlated fMRI. *Neuroimage*. (2007) 38:488–500. doi: 10.1016/j.neuroimage.2007.08.003
68. Thornton RC, Rodionov R, Laufs H, Vulliemoz S, Vaudano A, Carmichael D, et al. Imaging haemodynamic changes related to seizures: comparison of EEG-based general linear model, independent component analysis of fMRI and intracranial EEG. *Neuroimage*. (2010) 53:196–205. doi: 10.1016/j.neuroimage.2010.05.064
69. Moeller F, LeVan P, Gotman J. Independent component analysis (ICA) of generalized spike wave discharges in fMRI: comparison with general linear model-based EEG-fMRI. *Hum Brain Mapp*. (2011) 32:209–17. doi: 10.1002/hbm.21010
70. Vulliemoz S, Rodionov R, Carmichael DW, Thornton R, Guye M, Lhatoo SD, et al. Continuous EEG source imaging enhances analysis of EEG-fMRI in focal epilepsy. *Neuroimage*. (2010) 49:3219–29. doi: 10.1016/j.neuroimage.2009.11.055
71. Liston AD, De Munck JC, Hamandi K, Laufs H, Ossenblok P, Duncan JS, et al. Analysis of EEG-fMRI data in focal epilepsy based on automated spike classification and Signal Space Projection. *Neuroimage*. (2006) 31:1015–24. doi: 10.1016/j.neuroimage.2006.01.040
72. Hamandi K, Powell HWR, Laufs H, Symms MR, Barker GJ, Parker GJM, et al. Combined EEG-fMRI and tractography to visualise propagation of epileptic activity. *J Neurol Neurosurg Psychiatry*. (2008) 79:594–7. doi: 10.1136/jnnp.2007.125401
73. Murta T, Figueiredo P, Leal A. EEG-fMRI measures of functional brain connectivity in epilepsy. In *1st Portuguese Meeting in Biomedical Engineering, ENBENG 2011* doi: 10.1109/ENBENG.2011.6026094
74. Jann K, Wiest R, Hauf M, Meyer K, Boesch C, Mathis J, Schroth G, Dierks T, Koenig T. BOLD correlates of continuously fluctuating epileptic activity isolated by independent component analysis. *Neuroimage*. (2008) 42:635–648. Available online at: http://ovidsp.ovid.com/ovidweb.cgi?T=JS&PAGE=reference&D=emed8&NEWS=N&AN=2008357364
75. Marques JP, Rebola J, Figueiredo P, Pinto A, Sales F, Castelo-Branco M, et al. decomposition of EEG signal for fMRI processing in epilepsy. *Hum Brain Mapp*. (2009) 30:2986–96. doi: 10.1002/hbm.20723
76. Abreu R, Leal A, Lopes da. Silva F, Figueiredo P. EEG synchronization measures predict epilepsy-related BOLD-fMRI fluctuations better than commonly used univariate metrics. *Clin Neurophysiol*. (2018) 129:618–35. doi: 10.1016/j.clinph.2017.12.038
77. Leite M, Leal A, Figueiredo P. Transfer function between EEG and BOLD signals of epileptic activity. *Front Neurol*. (2013) 4 JAN: doi: 10.3389/fneur.2013.00001

Conflict of Interest: The authors declare that the research was conducted in the absence of any commercial or financial relationships that could be construed as a potential conflict of interest.

Advantages of publishing in Frontiers

OPEN ACCESS
Articles are free to read
for greatest visibility
and readership

FAST PUBLICATION
Around 90 days
from submission
to decision

HIGH QUALITY PEER-REVIEW
Rigorous, collaborative,
and constructive
peer-review

TRANSPARENT PEER-REVIEW
Editors and reviewers
acknowledged by name
on published articles

Frontiers
Avenue du Tribunal-Fédéral 34
1005 Lausanne | Switzerland

Visit us: www.frontiersin.org
Contact us: frontiersin.org/about/contact

REPRODUCIBILITY OF RESEARCH
Support open data
and methods to enhance
research reproducibility

DIGITAL PUBLISHING
Articles designed
for optimal readership
across devices

FOLLOW US
@frontiersin

IMPACT METRICS
Advanced article metrics
track visibility across
digital media

EXTENSIVE PROMOTION
Marketing
and promotion
of impactful research

LOOP RESEARCH NETWORK
Our network
increases your
article's readership